

Declination (J2000)

63°52'30"

63°52'15"

63°52'00"

63°51'45"

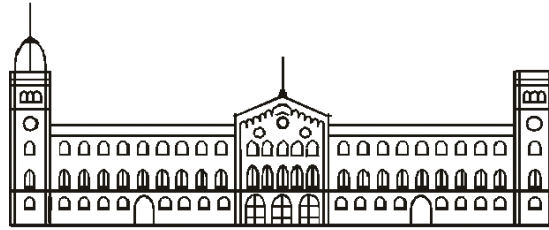
63°51'30"

63°51'15"

$\text{NH}_3(1,1) + \text{CO}(1-0)$

**massive star formation
ionized and molecular gas in the first evolutionary stages**
álvaro sánchez monge

departament d'astronomia i meteorologia
universitat de barcelona



UNIVERSITAT DE BARCELONA

DEPARTAMENT D'ASTRONOMIA I METEOROLOGIA

Massive Star Formation: ionized and molecular gas emission in the first evolutionary stages

Álvaro Sánchez Monge

PH.D. THESIS IN PHYSICS

BARCELONA (SPAIN)

JANUARY 2011

PROGRAMA DE DOCTORAT D'ASTRONOMIA I METEOROLOGIA

2007–2010

Memòria presentada per **Álvaro Sánchez Monge**
per optar al grau de Doctor en Física

Aquesta Tesi Doctoral ha estat dirigida per

Dr. Robert Estalella	Universitat de Barcelona, Spain
Dr. Stan Kurtz	Centro de Radioastronomía y Astrofísica, Mexico
Dra. Aina Palau	Institut de Ciències de l'Espai, Spain

a mi madre y a mi padre

I must not fear.
Fear is the mind-killer.
Fear is the little-death that brings total obliteration.
I will face my fear.
I will permit it to pass over me and through me.
And when it has gone past I will turn the inner eye to see its path.
Where the fear has gone there will be nothing.
Only I will remain.

Litany against fear (Bene Gesserit)

Agradecimientos - Agraïments - Acknowledgements

Siempre me había preguntado qué diría cuando obtuviera o completara algo importante, qué pensaría, a quién le agradecería todo el apoyo recibido, las ayudas. ¿Sería una lista larga de personas? Siempre pensé que la mejor forma de agradecer algo, sin olvidar mencionar a nadie importante sería algo parecido a: *Gracias a todas aquellas personas que de alguna forma u otra han influido en mi vida permitiéndome llegar donde estoy, y conseguir lo que he conseguido.*

... pero ahora, llegado este momento, me doy cuenta que esa frase no es suficiente, y que, a pesar de correr el riesgo de olvidar a alguien importante (pido disculpas), debo agradecer más detalladamente el apoyo recibido por ciertas personas, tal vez aquellas que en los últimos años más me han ayudado a conseguir concluir esta tesis doctoral.

Empezaré agradeciendo el apoyo a mis directores de tesis. Gràcies Robert, moltes gràcies per haver-me introduït en el món de la radioastronomia, de la formació estel·lar, i molt més important, en el món de la investigació. Gràcies per l'ajuda, el suport i la confiança durant aquests (una mica més de) quatre anys. Thanks Stan for make me feeling as if I was at home during the months (one year!) I spent in Mexico, for providing me a different point of view in many different subjects. Moltíssimes gràcies Aina. Fins i tot abans d'estar designada com a co-directora d'aquesta tesis, vas ajudar-me en tot! Sense tu crec que no tindria encara 'tema' de tesis. Gràcies.

Vull agraïr també als membres del grup de 'radio' que estan per Barcelona, i a aquells que, encara que estan una mica (o molt) més lluny i no poden venir a les reunions, encara continuen formant part del grup. Gràcies Chema Torrelles, Josep Miquel Girart, Maite Beltrán, Rosario López, Àngels Riera, Inmma Sepúlveda, i Òscar Morata. I, obviament, gràcies també als estudiants i postdocs: Josep Maria, Felipe, Pau, Marco, i en especial a la Gemma, amb qui he pogut parlar i discutir d'un munt de coses! Gràcies per ajudar-me, i ara ... a continuar per Itàlia.

Gràcies als membres del DAM. Sou molts, així que no podré posar tots els noms. Gràcies a la gent de secretaria (JR, Montse i Rosa) per fer molt més fàcils tots els tràmits i la burocràcia. Gràcies a la gent de suport (Gaby i Jordi) per solucionar els problemes informàtics d'ordinadors, impresores i altres aparells. Gràcies també a molts dels estudiants que han anat passant durant el temps que jo he estat per allà: Carme, Rosa, Laura,

Pol, Pere, Maria, Víctor, Jordi, Sinue, Javi(s), Teresa, Juan Carlos, Adolfo, Kike, Santi, Andreu, Héctor, Nadia, . . . , sou masses persones que fan del DAM un lloc més agradable.

Gracias a los compañeros de México (ya sean del CRyA, del DF o de Ensenada). Gracias a los todos investigadores del CRyA porque desde que llegué por primera vez me demostraron que el ambiente de paz, tranquilidad y armonía que se respira en el CRyA no es solo por su edificio (casi monasterial), sino también por las personas que lo ‘habitan’; y porque me dejaron participar y ayudar en muchas de las tantas miles de actividades de divulgación que realiza el CRyA. Gracias especialmente a los estudiantes con los que he tenido la fortuna de convivir, y que me hicieron sentir como en casa desde que aterricé. Gracias Rosy y Ramiro (sobretudo por darme alojamiento los primeros días); gracias Chente, Karla, Chuy, el Hippie, Charly, Gaby, Lola, Fox, Roberto porque sin vosotros las estancias en México no hubiesen sido lo mismo. La lista de estudiantes a quien agradecer es mucho más larga: Alfonso, Martín, Sergio, Brenda, Arturo, Fátima, Yetli, Carolina, Manuel(es), Citlali, . . . , gracias. Gracias también a los que no están en Morelia: Teresita, Manuel, Paco, Quique, René, . . .

Thank you to all the researchers, students and technical staff I have met during my visits to different institutions, during the stays, the observations, the workshops. Thank to all the people who I met in Heidelberg and Bonn, in Grenoble, in Firenze, in Granada and IRAM, CARMA, ATCA, Sydney, . . . , con mención especial a Ana que ahora me presta su casa para la nueva etapa que empezaré.

No me olvido tampoco de los compañeros con los que empecé el camino hace ahora unos 9 años (sé de alguien que podría precisar más las fechas). Gracias a los compañeros de la licenciatura: Roger Bordoy, Albert Saragossa, Lluc Garcia, Ignasi Reichardt, Ricci, Eloi Cordoní (si si, l’home del temps), Laura Rodríguez, Joan Camuñas, Nacho Moreno, Carlos López, Dani Dagnino, Quico Cortés, Silvia Royo, Carles Conill, Helena Prieto, Ricardo Zarzuela, Escartín, . . . , gracias en especial a los miembros de la *Fila 2* (también a las señoras de la limpieza que cada cierto tiempo nos proporcionaban una superficie limpia donde comentar, escribir y dibujar), por hacer que las clases de la licenciatura se entendieran y fueran más llevaderas.

Muy especialmente, gracias a mis compañeros de *los comederos*, por esperarme (casi siempre) a la 1 para ir a comer (jeje) durante los últimos cuatro años. Gracias David López, Noela Fariña, Toni Luque, Joan Camps, Silvio Morales, Paolo, Maria, Pau, . . . , porque la hora de la comida era uno de los mejores momentos del día (sobretudo para comentar como iba ganando en el SM, incluso cuando alguien – noelurus – me superaba, haciendo trampas seguro). Gracias especialmente a Ricard Matas, por estar siempre ahí, desde el primerísimo día de Universidad, por ayudarme cuando lo necesitaba, por hacer que las clases fueran únicas como un circo, si yo he podido escribir esto, seguro que tú también puedes, ánimo!.

No todo es atronomía en esta vida (por suerte). Así que gracias también a mis amigos de siempre, de Igualada, Barcelona, de otras partes de España y del Mundo, porque de

alguna forma u otra han ayudado e influido en el desarrollo de esta tesis. Gracias a David, Jose, Rubencillo, Carlos, Juanjo, Tati, . . . , porque esos partidos de basket eran, son y espero que sean lo mejor de los sábados por la mañana. Gracias también a Lara y Jan por acogerme en St Andrews durante una de las pocas semanas de vacaciones que he tenido en los últimos tres años. Espero haceros una nueva visita próximamente. Gracias a aquellas personas que me han permitido desconectar del mundo de la astrofísica y volver al mundo real. También agradezco a mis compañeros de AstroAnoia (por este año escaso que llevamos en marcha), porque en la astronomía no todo tiene que ser profesional. Gracias también a mi familia que está lejos de Igualada: gracias a mis tíos/as y primos/as, y en especial a mis abuelos/as. Gracias yaya por disfrutar junto a mi de las estrellas y del cielo aquellas noches de verano.

. . . me acerco al final, y a riesgo de haber olvidado a alguien (a quien le pido disculpas por anticipado), escribiré mis últimas, pero muy importantes, frases de agradecimiento. . .

Gracias Sandra por todo lo pasado y futuro (que será mucho). Simplemente, Te quiero.

Finalmente gracias a mi familia. Gracias Bea y Rafa (los diseñadores de la portada del libro). Gracias Bea por haberme ayudado desde pequeñitos, por ser un modelo a seguir, tanto antes como ahora. Porque creo que no se puede tener a una hermana mejor. Y para concluir, gracias a dos personas básicas, fundamentales y únicas, sin las que esta tesis no hubiera podido existir de ninguna manera. Gracias papá y mamá, por criarme de pequeño, por educarme, por enseñarme a ser buena persona, por enseñarme los valores de la vida, por ayudarme en todo, por estar disponibles en cualquier momento en que os necesitase, por aguantarme durante los días en los que tenía demasiado trabajo, en definitiva, gracias por permitirme llegar a ser lo que soy.

A vosotros os dedico esta tesis.

Contents

Resumen de la tesis	xix
I Introduction	1
1 Massive star formation	3
1.1 Massive star formation	3
1.1.1 Observational massive star-forming features	5
1.2 Ionized gas	9
1.2.1 Thermal emission from ionized gas	9
1.2.2 Non-thermal emission from ionized gas	18
1.3 Molecular gas	19
1.3.1 Ammonia (NH_3) and other dense gas tracers	20
1.3.2 Methyl cyanide (CH_3CN) and other high density tracers	20
1.3.3 Carbon monoxide (CO) and other outflow tracers	21
1.3.4 Water (H_2O) and other maser tracers	22
1.4 About this work	22
1.4.1 Goal of the thesis	22
1.4.2 Approach and strategy	22
1.4.3 Selection of targets	23
1.4.4 Outline of the thesis and status of the different works	24
II Ultracompact H II regions emerging from their natal cloud	29
2 IRAS 00117+6412: an UCH II region at the border of its natal cloud	31
2.1 General overview	31
2.2 Observations	32
2.2.1 Very Large Array	32
2.2.2 Submillimeter Array	33
2.3 Continuum results	35
2.3.1 Centimeter continuum emission	35
2.3.2 Millimeter continuum emission	35

CONTENTS

2.3.3	Spectral energy distribution	38
2.4	Molecular results	40
2.4.1	Molecular outflow gas	40
2.4.2	Molecular dense gas	43
2.4.3	Dense gas analysis	45
2.4.4	Outflow-dense gas interaction	47
2.5	Summary and brief discussion	48
3	IRAS 22134+5834: a small UCH_{II} region disrupting the parental cloud	51
3.1	General overview	51
3.2	Observations	52
3.2.1	Very Large Array	52
3.2.2	Expanded Very Large Array	53
3.2.3	Combined Array for Research in Millimeter-wave Astronomy	53
3.3	Continuum results	54
3.3.1	Centimeter and millimeter continuum results	54
3.3.2	Spectral energy distribution	56
3.4	Molecular results	57
3.4.1	Molecular dense gas: morphology and velocity fields	57
3.4.2	Molecular dense gas: temperature and density	60
3.4.3	Ionized gas emission within the molecular emission	60
3.5	Summary and brief discussion	62
III	Massive embedded compact radio sources driving outflows	65
4	IRAS 22198+6336: a radiojet within an intermediate-mass hot core	67
4.1	General overview	67
4.2	Observations	68
4.2.1	Very Large Array	68
4.2.2	Plateau de Bure Interferometer	69
4.2.3	Submillimeter Array	70
4.3	Continuum results	72
4.3.1	Centimeter and millimeter continuum results	72
4.3.2	Spectral energy distributions	72
4.4	Molecular results	76
4.4.1	Molecular outflow gas	76
4.4.2	Molecular dense gas	78
4.5	Analysis	81
4.5.1	Velocity fields	81
4.5.2	Dense gas analysis	84

4.5.3	Outflow-dense gas interaction	87
4.5.4	Hot molecular core properties	88
4.6	Summary and brief discussion	90
5	G75.78+0.34: compact radio sources embedded in a hot core	93
5.1	General overview	93
5.2	Observations	94
5.2.1	Very Large Array	94
5.2.2	Owens Valley Radio Observatory	96
5.2.3	Submillimeter Array	98
5.3	Continuum results	98
5.3.1	Centimeter continuum emission	98
5.3.2	Millimeter continuum emission	101
5.3.3	Spectral energy distributions	101
5.4	Molecular results	104
5.4.1	Molecular outflow gas	104
5.4.2	Molecular dense gas	107
5.4.3	H ₂ O and CH ₃ OH maser emission	108
5.4.4	Radio recombination lines emission	110
5.5	Analysis	112
5.5.1	Velocity fields	112
5.5.2	Dense gas analysis	114
5.5.3	Hot molecular core properties	116
5.5.4	Nature of the ionized gas emission	120
5.6	Summary and brief discussion	124
6	IRAS 19035+0641: a compact radio source embedded in dense gas	127
6.1	General overview	127
6.2	Observations	128
6.2.1	Very Large Array	128
6.3	Continuum results	129
6.3.1	Centimeter continuum results	129
6.3.2	Spectral energy distributions	131
6.4	Molecular results	133
6.4.1	Molecular dense gas: morphology and velocity fields	133
6.4.2	Molecular dense gas: temperature and density	133
6.4.3	Ionized gas emission within the molecular clump	138
6.5	Summary and brief discussion	139

CONTENTS

7	IRAS 04579+4703: a radio source–outflow system	141
7.1	General overview	141
7.2	Observations	142
7.2.1	Very Large Array	142
7.2.2	Submillimeter Array	143
7.3	Continuum results	143
7.4	Molecular results	146
7.4.1	Molecular outflow gas	146
7.4.2	Molecular dense gas	148
7.5	Summary and brief discussion	153
IV	General discussion	155
8	The sample of massive star-forming regions	157
8.1	Archival data of additional sources	157
8.2	Summary of sources of the sample	158
9	Towards an evolutionary sequence	165
9.1	Ionized gas emission	165
9.2	Dust and molecular gas emission	173
9.3	Spectral energy distribution: bolometric luminosity	176
9.4	Towards an evolutionary sequence	178
9.4.1	‘Color-color’ diagrams	178
9.4.2	Outflow properties	186
9.4.3	Hot molecular core properties	189
9.4.4	Ammonia properties	189
9.4.5	Final discussion: evolutionary stages	191
9.5	Future prospects: open questions	196
	Bibliography	199
A	First steps in VLA continuum data reduction with <i>AIPS</i>	221
A.1	Loading and inspecting the data	222
A.2	Tools for data examination	223
A.3	Calibration strategy	226
A.4	Imaging	232
B	Physical parameters of H II regions	241
B.1	Fundamental equations of H II regions	241
B.2	Physical parameters of optically thin H II regions	243
B.3	Optically thick H II regions	244

B.4	H II regions with density gradient	245
B.5	Program <code>HIregions.f</code>	248
C	Dust mass estimation	251
C.1	Fundamental equations of dust emission	251
D	Molecular Column Density Calculation	255
D.1	Column Density Calculation	255
D.1.1	Radiative transfer equation	255
D.1.2	Optical depth, source function and temperatures	256
D.1.3	Molecular column density	258
D.1.4	Observational terms	259
D.1.5	Molecular (catalogued) terms	262
D.1.6	Summary of equations: step-by-step guide	267
D.2	Rotational diagrams	269
D.3	Resources from databases (CDMS and JPL)	269
D.3.1	The Cologne Database for Molecular Spectroscopy, CDMS	270
D.3.2	Jet Propulsion Laboratory, Molecular Spectroscopy, JPL	271
D.4	Program <code>ColDens.f</code>	272
D.5	Astrophysical constants and conversion factors	273

List of Figures

1.1	Observational massive star forming features (I)	6
1.2	Observational massive star forming features (II)	7
1.3	Different morphologies of UCH II regions	8
1.4	Schematic view for the weak and strong photoevaporated disk model	13
1.5	Images of an equatorial wind and a massive radiojet	15
2.1	Continuum maps for IRAS 00117+6412	34
2.2	Spectral energy distribution of the UCH II region in IRAS 00117+6412 . . .	38
2.3	Outflow maps for IRAS 00117+6412	39
2.4	Spectrum of the ^{12}CO (2–1) outflow emission	40
2.5	Position-velocity plots for the CO (2–1) outflow	41
2.6	NH_3 (1,1) and (2,2) and N_2H^+ (1–0) maps toward IRAS 00117+6412	44
2.7	Ammonia parameters towards IRAS 00117+6412	46
2.8	Outflow/dense gas (ammonia) interactions	47
2.9	Images at infrared wavelengths for IRAS 00117+6412	48
3.1	Continuum maps for IRAS 22134+5834	55
3.2	Spectral energy distribution for IRAS 22134+5834	58
3.3	NH_3 (1,1) and (2,2) and N_2H^+ (1–0) maps toward IRAS 22134+5834	59
3.4	Ammonia parameters towards IRAS 22134+5834	61
3.5	Images at infrared wavelengths for IRAS 22134+5834	63
4.1	Global overview of the region IRAS 22198+6336	71
4.2	Continuum maps for IRAS 22198+6336	73
4.3	Spectral energy distributions for the YSOs in IRAS 22198+6336	75
4.4	IRAS 22198+6336 molecular outflow emission	77
4.5	Intensity maps for molecules detected towards IRAS 22198+6336	79
4.6	Wide-band SMA spectrum toward IRAS 22198+6336	80
4.7	Velocity maps for molecules detected towards IRAS 22198+6336	82
4.8	Linewidth maps for molecules detected towards IRAS 22198+6336	83
4.9	Position-velocity plots toward IRAS 22198+6336	84
4.10	Ammonia parameters towards IRAS 22198+6336	85
4.11	Ammonia affected by the passage of the molecular outflows (I)	86

LIST OF FIGURES

4.12	Ammonia affected by the passage of the molecular outflows (II)	87
4.13	Rotational diagrams for IRAS 22198+6336	88
5.1	Global overview of the star-forming complex G75.78+0.34	97
5.2	G75.78+0.34 centimeter continuum maps	99
5.3	G75.78+0.34 millimeter continuum maps	101
5.4	Spectral energy distributions for the YSOs in G75.78+0.34	102
5.5	G75.78+0.34 molecular outflow emission	104
5.6	Intensity, velocity and linewidths NH ₃ maps towards G75.78+0.34	106
5.7	Intensity maps of the molecules detected towards G75.78+0.34	107
5.8	Wide-band SMA spectrum toward G75.78+0.34	109
5.9	H ₂ O maser distribution in G75.78+0.34	110
5.10	Velocity maps for the molecules detected towards G75.78+0.34	112
5.11	Linewidth maps for the molecules detected towards G75.78+0.34	113
5.12	Ammonia parameters towards G75.78+0.34	115
5.13	Ammonia RGB composite image of G75.78+0.34	116
5.14	Rotational diagram towards G75.78+0.34	117
5.15	Images at infrared wavelengths for G75.78+0.34	121
5.16	Zoom of the images at infrared wavelengths for G75.78+0.34	122
6.1	Continuum maps for IRAS 19035+0641	130
6.2	Spectral energy distributions of VLA1 and VLA2	132
6.3	NH ₃ (1,1) (2,2) and (3,3) maps toward IRAS 19035+0641	134
6.4	Ammonia parameters towards IRAS 19035+0641	135
6.5	Ammonia rotational diagram for IRAS 19035+0641	136
6.6	3-color composite IRAC image overlayed with the ammonia emission	137
6.7	Images at infrared wavelengths for IRAS 19035+0641	138
7.1	Continuum maps for IRAS 04579+4703	144
7.2	Spectral energy distribution for IRAS 04579+4703	146
7.3	Molecular outflow emission toward IRAS 04579+4703	147
7.4	Ammonia emission toward IRAS 04579+4703	148
7.5	Molecular emission toward IRAS 04579+4703	149
7.6	Wide-band SMA spectrum toward IRAS 04579+4703	150
7.7	Molecular line spectra toward IRAS 04579+4703	151
7.8	Position-velocity cuts in IRAS 04579+4703	152
8.1	Continuum maps for the regions from the literature	159
8.2	NH ₃ (1,1) and (2,2) maps toward IRAS 05358+3543	160
8.3	Ammonia parameters towards IRAS 05358+3543	161
9.1	Spectral energy distributions in the centimeter range	166

9.2	Plot of centimeter size versus emission measure	169
9.3	Plot of $S_\nu d^2$ versus L_{bol}	171
9.4	Plot of $S_\nu d^2$ versus \dot{P}	172
9.5	Spectral energy distributions	175
9.6	Graphics of several parameters versus T_{bol}	182
9.7	Graphics of the four main parameters	184
9.8	Graphics of several properties versus L_{bol}	185
9.9	Graphics of several properties versus distance	186
9.10	Presence/absence of outflow against bolometric temperature	187
9.11	Graphics of the outflow momentum rate and collimation	188
9.12	Presence/absence of hot molecular core	189
9.13	Graphics of the ammonia rotational temperature and linewidth	190
9.14	Plot of $S_\nu d^2$ versus L_{bol}	192
9.15	Summarizing table	194
9.16	Sketch of evolutionary stages	195
A.1	Examples of different UVPLT plots	236
A.2	Example of bad data to be flagged	237
A.3	TV display for the IMAGR task	240
B.1	Thermal bremsstrahlung spectra from different H II regions	245
B.2	Scheme for a non-homogeneous H II region	246
B.3	Thermal bremsstrahlung spectra for non-homogeneous H II regions	248
D.1	Two energy level molecular system	256
D.2	Molecular spectroscopic database webpages	269
D.3	Example of CDMS database	270
D.4	Example of JPL database	271

List of Tables

1.1	Sample of regions selected for the study of this Thesis	24
2.1	Main continuum observational parameters of IRAS 00117+6412	33
2.2	Multiwavelength results for the YSOs in IRAS 00117+6412	36
2.3	Parameters of the 1.2 mm subcondensations associated with MM1	37
2.4	Physical parameters of the outflows driven by IRAS 00117+6412	42
3.1	Main VLA continuum observational parameters of IRAS 22134+5834	53
3.2	Multiwavelength results for the YSOs in IRAS 22134+5834	56
3.3	Continuum flux density for VLA1 with the same uv -range	57
4.1	Main VLA continuum observational parameters of IRAS 22198+6336	69
4.2	Main PdBI observational parameters of IRAS 22198+6336	70
4.3	Multiwavelength results for the YSOs in IRAS 22198+6336	74
4.4	Physical parameters of the outflows driven by IRAS 22198+6336	78
4.5	Molecular transitions toward IRAS 22198+6336	89
5.1	Main continuum observational parameters of G75.78+0.34	94
5.2	Main spectral line observational parameters of G75.78+0.34	95
5.3	Multiwavelength results for the YSOs in G75.78+0.34	100
5.4	Physical parameters of the dust and H II regions in G75.78+0.34	103
5.5	Physical parameters for the molecular outflow in G75.78+0.34	105
5.6	22 GHz water and 44 GHz methanol masers in G75.78+0.34	111
5.7	Molecular transitions toward G75.78+0.34	118
5.8	Properties of the hot molecular cores: IRAS 22198+6336 and G75.78+0.34	119
6.1	Main VLA continuum observational parameters of IRAS 19035+0641	128
6.2	Multiwavelength results for the YSOs in IRAS 19035+0641	131
7.1	Main VLA continuum observational parameters of IRAS 04579+4703	143
7.2	Continuum fluxes for the radio source in IRAS 04579+4703	145
7.3	Physical parameters of the outflow driven by IRAS 04579+4703	147
8.1	Radio continuum fluxes from archival data	158

LIST OF TABLES

9.1	Parameters for the ionized gas of the radio continuum sources	167
9.2	Millimeter continuum and molecular gas data	174
9.3	Flux densities at different wavelengths (part I)	176
9.4	Flux densities at different wavelengths (part II)	177
9.5	Parameters of a large sample of sources, observed with interferometers (I) .	180
9.6	Parameters of a large sample of sources, observed with interferometers (II) .	181
A.1	Primary beam of the VLA at different wavelengths	237
A.2	uv -range and antennas per arm for the VLA flux calibrators	238
A.3	Information for the standard VLA flux calibrators	239
B.1	Gamma functions and spectral indices for different density gradients	247
D.1	Nuclear statistical weight factors for C_{2v} and C_{3v} molecules	266

List of abbreviations

2MASS	Two Micron All-Sky Survey
ALMA	Atacama Large Millimeter Array
CARMA	Combined Array for Research in Millimeter Astronomy
DSS	Digital Sky Survey
EVLA	Expanded Very Large Array
FWHM	full width at half maximum
IMYSO	intermediate-mass young stellar object
ISM	interstellar medium
IRAC	Infrared Array Camera (on the Spitzer satellite)
IRAS	Infrared Astronomical Satellite
IRDC	infrared dark cloud
HH object	Herbig-Haro object
H I	neutral hydrogen
H II	ionized hydrogen
HCH II region	hypercompact H II region
HMC	hot molecular core
MIPS	Multiband Imaging Photometer (on the Spitzer satellite)
MSX	Midcourse Space Experiment
PdBI	Plateau de Bure Interferometer
PDR	photodissociated (photon dominated) region
RRL	radio recombination line
SED	spectral energy distribution
SMA	Submillimeter Array
UCH II region	ultracompact H II region
UV	ultraviolet
VLA	Very Large Array
VLBI	very large baseline interferometer
YSO	young stellar object
ZAMS	zero-age main sequence

Resumen de la tesis

Formación estelar masiva

Las estrellas masivas ($M \gtrsim 8 M_{\odot}$) juegan un papel importante en la determinación de las propiedades morfológicas, dinámicas y químicas de las galaxias que las albergan, a través de fuertes vientos estelares, una intensa radiación ultravioleta (UV) y finalmente, explosiones de supernovas. A pesar de su gran importancia, sus primeras etapas evolutivas aún no se conocen en detalle. Los modelos teóricos (e.g., Larson 1969; Shu et al. 1987) que permiten explicar de forma acertada la formación de estrellas de baja masa (similares al Sol), presentan problemas cuando se aplican a las estrellas más masivas.

El principal problema teórico radica en el hecho que las estrellas masivas empiezan a producir reacciones termonucleares en su interior cuando aún están acretando material del disco y de la envoltura. Si la estrella masiva en formación alcanza una determinada luminosidad (equivalente a la de una estrella de tipo espectral B), será capaz de producir un número de fotones ionizantes ($\nu > 13.6 \text{ eV}$) suficiente como para ionizar el gas que la rodea. Esta elevada radiación produce una presión de radiación que impediría la acreción, y por lo tanto, que la estrella alcanzara masas más elevadas (i.e., no deberían existir estrellas de tipo O; Kahn 1974, Wolfire & Cassinelli 1987). Actualmente hay dos modelos teóricos diferentes que tratan de solucionar estos problemas para poder explicar la formación de las estrellas masivas. El primer método conocido como *colapso monolítico* (Yorke & Sonnhalter 2002) intenta aplicar los modelos utilizados para estrellas de baja masa modificando, principalmente, la simetría y las características en la cual es acretado el material. El segundo método, *acreción competitiva* o coalescencia (Stahler et al. 2000), se basa en el hecho que las estrellas masivas se encuentran en cúmulos numerosos, y que éstas se pueden formar, por ejemplo, a partir de la fusión de estrellas de menor masa. Para determinar que modelo se ajusta mejor a la realidad, son necesarias observaciones precisas de varias regiones de formación estelar, lo cual no es sencillo de realizar.

A pesar de las enormes dificultades observacionales (e.g., las estrellas masivas se encuentran generalmente muy lejos: $\gtrsim 2 \text{ kpc}$, embebidas en nubes moleculares con una elevada extinción: $A_V \gtrsim 100$, y en cúmulos con varias estrellas en formación), recientemente se ha conseguido caracterizar algunas propiedades observacionales relevantes en la formación estelar masiva. De este modo, estudiando con detalle objetos como *nubes oscuras en el infrarrojo* (Pillai et al. 2006), *núcleos moleculares calientes* (Cesaroni 2005), *regiones de*

gas ionizado (Kurtz 2005), *flujos moleculares y jets* (Shepherd 2005), y *másers moleculares* (Ellingsen 2007), debería ser posible obtener las piezas suficientes para resolver el rompecabezas e ir comprendiendo mejor el mecanismo de formación de las estrellas más masivas.

Emisión de gas ionizado

De todas las propiedades observacionales que hemos listado, las regiones de gas ionizado (o regiones H II) son las que claramente diferencian las estrellas de alta masa de las estrellas de menor masa, ya que las estrellas menos luminosas no son capaces de generar un número de fotones ionizantes suficiente como para crear una región H II. Esta emisión de gas ionizado es fácilmente identificable durante las primeras etapas evolutivas de las estrellas como emisión de continuo en el rango de las radiofrecuencias (correspondiendo al rango de longitudes de onda centimétricas del espectro electromagnético). Una ventaja de las radio-ondas, respecto a longitudes de onda como el óptico o el infrarrojo, es que no sufren de extinción, y por lo tanto podemos ver aquellas fuentes (estrellas en formación) profundamente embebidas en las nubes moleculares. De este modo, el gas ionizado (emisión de continuo centimétrico) se convierte en un parámetro a observar que puede aportar información fundamental y relevante. A pesar de esto, no toda la emisión de gas ionizado que se observa en las regiones de formación estelar es producida por la presencia de fotones UV ionizantes. Por ejemplo, los choques producidos durante la eyección de materia (jet/outflow), característica de estrellas en formación, con el medio circundante puede producir ionización del gas. Varios mecanismos y modelos se han propuesto para explicar la presencia del gas ionizado en las regiones de formación estelar (e. g., regiones H II, discos fotoevaporados, vientos ionizantes, flujos de acreción ionizados, radiojets térmicos, choques en el medio circundante). Observaciones de continuo centimétrico a diferentes frecuencias, y con una elevada resolución espacial que permita estudiar la morfología de la emisión, resultan necesarias para comprender el mecanismo de ionización, y determinar cual es el que domina en cada etapa de la formación de una estrella masiva.

Emisión de gas molecular

Simultáneamente a la emisión de gas ionizado, es necesario conocer el ambiente que rodea al objeto estelar recién formado, el cual probablemente caracteriza y define a su vez la emisión de gas ionizado. Las propiedades del entorno de la estrella en formación se pueden determinar mediante dos tipos de observaciones (en radio-ondas) diferentes: i) observaciones del polvo interestelar, y ii) observaciones de gas molecular. La emisión de polvo es dominante en el continuo milimétrico, de esta forma, observando la emisión a varias frecuencias milimétricas se puede determinar parámetros como la temperatura y la masa de polvo de la nube o núcleo en el cual se encuentra embebida la estrella en formación. La emisión de gas molecular aporta información que la emisión de polvo no proporciona.

Más de un centenar de moléculas han sido observadas e identificadas en el medio interestelar. Cada una de estas moléculas presenta diferentes transiciones moleculares, con frecuencias bien definidas, que pueden utilizarse para obtener información importante del gas molecular que rodea a los objetos jóvenes. Transiciones moleculares como las del amoníaco (NH_3) proporcionan información detallada de la temperatura y densidad del núcleo denso que alberga a la protoestrella. Moléculas orgánicas más complejas, como el CH_3CN , proporcionan también medidas de la temperatura y densidad, pero en este caso de la región más caliente y densa, próxima a la estrella, permitiendo caracterizar las propiedades de los núcleos moleculares calientes. Otras moléculas más abundantes, como el monóxido de carbono (CO), son fundamentales para estudiar las eyecciones de material asociadas a los jets, o flujos moleculares, que impulsan las estrellas en sus primeras etapas. Finalmente, otras moléculas como el agua (H_2O) presentan emisión máser, la cual permite conocer con detalle la cinemática del gas en regiones de muy elevada densidad y temperatura.

Objetivos, estrategia y organización de la tesis

El objetivo principal de esta tesis es *la caracterización de la emisión de gas ionizado presente en regiones de formación estelar masiva, y su relación con el gas denso circundante*. Mediante observaciones multifrecuencia de continuo y línea espectral, con una elevada resolución angular, se intentará caracterizar la emisión y la naturaleza de los objetos estelares jóvenes en una muestra de once regiones de formación estelar masiva, e investigar como las estrellas recién formadas pueden afectar a su nube molecular materna. El análisis y comparación entre diferentes trazadores de la formación estelar serán la base para identificar y caracterizar diferentes estados de una secuencia evolutiva.

Seis regiones de formación estelar masiva (con luminosidades $\gtrsim 10^3 L_\odot$, y relativamente próximas al Sol) fueron seleccionadas para ser observadas con los mejores radio-interferómetros disponibles actualmente. Los trazadores utilizados en la caracterización de cada una de las regiones de formación estelar han sido: i) emisión de continuo centimétrico que aporta información del gas ionizado, ii) emisión de continuo milimétrico para determinar las propiedades del polvo, iii) emisión de línea del NH_3 para estudiar las propiedades físicas del núcleo denso molecular, iv) emisión de línea de varios trazadores característicos de los núcleos moleculares calientes (como por ejemplo el CH_3CN o el CH_3OH), y v) emisión de línea del CO para estudiar la presencia y propiedades de los flujos moleculares. Como complemento a estas observaciones, se ha buscado información en la literatura y en bases de datos sobre la emisión en el continuo submilimétrico e infrarrojo.

Los resultados obtenidos que se presentan en esta tesis se dividen en tres partes principales (sin contar la introducción). Las dos primeras partes incluyen los resultados detallados de cada una de las seis regiones de formación estelar observadas. Mientras que en la tercera parte se presenta la muestra de once regiones de formación estelar masiva

(las seis estudiadas en esta tesis, más otras cinco de la literatura que fueron observadas en condiciones similares a las nuestras), y la discusión general con las principales conclusiones obtenidas durante este trabajo.

Resultados principales de las regiones estudiadas

Regiones H II ultracompactas emergiendo de la nube materna

De las seis regiones estudiadas, hay dos (IRAS 00117+6412 e IRAS 22134+5834) que presentan emisión de continuo centimétrico (gas ionizado) similar a la encontrada en regiones H II fotoionizadas. Por sus propiedades físicas (determinadas a partir de la distribución espectral de energía) y su tamaño, estas dos regiones H II se corresponden a uno de los tipos de regiones H II más compactas (y presumiblemente jóvenes) conocidas como regiones H II ultracompactas. El gas ionizado no presentan polvo ni gas denso directamente asociado, aunque si parece estar afectando el gas que rodea la región H II.

En el caso de **IRAS 00117+6412**, la región H II está calentando ligeramente una estructura filamentaria que aparece rodeando la región H II por el sur. Este aumento de temperatura en el gas molecular se produce por la intensa radiación UV que genera la estrella B2 en formación. La distribución de gas molecular (rodeando la parte sur y oeste de la región H II) y la forma de cáscara que presenta el gas ionizado, sugieren que la región H II se ha expandido y está dispersando el gas y polvo de la nube molecular original.

Por otro lado, la región H II en **IRAS 22134+5834** forma parte de un gran cúmulo formado por varias estrellas jóvenes visibles en el infrarrojo. Rodeando el cúmulo se observa emisión de diferentes trazadores de gas denso (e.g., NH_3 y N_2H^+) en una estructura circular, presumiblemente formada por los vientos y radiación de las estrellas recién formadas que están dispersando el gas denso. El gas molecular más próximo a la región H II muestra una temperatura y ancho de línea más elevados, sugiriendo la interacción de la fuerte radiación UV de la joven estrella B1 con el gas circundante. Cabe destacar, que ninguna de estas dos regiones H II está asociada con fenómenos de eyección de materia (jets o flujos moleculares), ni con emisión molecular densa y caliente típica de los núcleos moleculares calientes.

Fuentes de radiocontinuo embebidas impulsando flujos moleculares

En esta sección se incluyen las cuatro regiones restantes que han sido observadas en esta tesis. La propiedad común de estas regiones es la presencia de una fuente de radiocontinuo débil, muy compacta, y embebida en gas y polvo. Estas propiedades, así como sus distribuciones espectrales de energía, sugieren que estos objetos podrían ser más jóvenes que las regiones H II mencionadas en la sección anterior.

En la región de formación estelar de masa intermedia llamada **IRAS 22198+6336**, la emisión de radiocontinuo parece estar trazando un radiojet térmico. La fuente está

asociada con dos flujos moleculares detectados en varias moléculas diferentes, y que están perturbando y dando forma al gas molecular circundante (en particular el amoníaco), creando cavidades tras el paso del material eyectado a alta velocidad. En la región más interna y próxima a la fuente de gas ionizado, se descubrió un núcleo caliente y denso, el cual es catalogado como uno de los pocos núcleos moleculares calientes de masa intermedia conocidos hasta la fecha. La emisión de este gas más denso presenta un gradiente de velocidad perpendicular a uno de los dos flujos moleculares, que posiblemente traza la rotación de un disco o toroide entorno al objeto estelar joven.

Una situación similar se encuentra en el complejo de formación estelar masiva en **G75.78+0.34**. Este complejo, mucho más luminoso y situado a una distancia mayor respecto al Sol, presenta varias fuentes de gas ionizado. La más peculiar es una doble fuente embebida en un núcleo molecular denso y caliente con un gradiente de velocidad perpendicular a un flujo molecular, posiblemente impulsado por las fuentes de radiocontinuo. Varios máseres de agua se detectan próximos a las fuentes de radio continuo, posiblemente trazando los efectos del choque entre el material eyectado a alta velocidad y el medio circundante. Las dos fuentes de gas ionizado detectadas podrían ser: la fuente impulsora (es decir, la estrella en formación) y, la otra, el resultado del choque del gas eyectado con el medio. Finalmente, el gas denso trazado por la emisión de amoníaco presenta una morfología que podría interpretarse como el resultado del paso del flujo molecular.

En la región **IRAS 19035+0641**, se detectan dos fuentes de gas ionizado, una parece ser una región H II ultracompacta, similar a las mencionadas en la sección anterior, mientras que la otra (mucho más débil y de menor tamaño) coincide espacialmente con una condensación de amoníaco. El gas denso asociado con la fuente de radiocontinuo presenta un ensanchamiento en la línea alargado en una dirección perpendicular a un gradiente de velocidad. A pesar de no disponer de información observacional precisa de los flujos moleculares (se conoce la presencia de emisión de alta velocidad en la región), podemos sugerir que la fuente de radio continuo podría ser un radiojet térmico impulsando un flujo molecular el cual está afectando el gas denso trazado por el amoníaco.

Finalmente, en la última región, **IRAS 04579+4703**, la emisión de radio continuo que detectamos parece provenir de un radiojet térmico, el cual impulsa un flujo molecular muy colimado. El objeto estelar joven está asociado a un núcleo molecular denso con escasa emisión de líneas moleculares, pero con alguna de ellas trazando un gradiente de velocidad perpendicular a la dirección del flujo molecular (sugiriendo una posible estructura en rotación). Interesantemente, el flujo molecular parece estar deflectado por la presencia de una condensación de metanol (CH_3OH) que se haya ligeramente desplazada respecto la posición del objeto en formación.

En resumen, hemos estudiado seis regiones de formación estelar masiva, centrando nuestro análisis en las fuentes de continuo centimétrico (trazadoras de gas ionizado) y en las propiedades del gas molecular de su entorno.

Discusion general: hacia una secuencia evolutiva

Con la finalidad de obtener conclusiones generales que permitan comprender mejor el proceso de formación estelar masiva, incrementamos la lista de regiones estudiadas en este trabajo con cinco regiones de la literatura, las cuales han sido estudiadas y observadas de forma similar a las nuestras. El resultado final es una muestra de 11 regiones de formación estelar masiva, las cuales contienen un total de 16 fuentes de radio continuo que han sido estudiadas con alta resolución angular y en varios trazadores (e.g., continuo, gas denso, flujos moleculares), para poder determinar las propiedades y características de una posible secuencia evolutiva.

Respecto a la emisión de gas ionizado, encontramos que las fuentes de radio continuo se pueden clasificar principalmente en dos grandes grupos bien diferenciados: i) aquellas que presentan distribuciones espectrales de energía planas (con índices espectrales característicos de emisión ópticamente delgada), con tamaños ~ 0.01 pc, y que parecen estar ionizadas por fotones UV provenientes de la estrella, y ii) aquellas cuya emisión es parcialmente ópticamente gruesa, con tamaños menores (o no resueltas), y que podrían estar ionizadas por choques. El primer grupo se podría definir como regiones H II mientras que los objetos del segundo grupo podrían estar trazando radiojets térmicos o regiones H II hipercompactas.

Respecto a la emisión de polvo y gas molecular, obtenemos otros dos grupos bien diferenciados: i) objetos profundamente embebidos en condensaciones de polvo, asociados a núcleos densos (varios de ellos con características de núcleos moleculares calientes) y a flujos moleculares, y ii) objetos con emisión de polvo débil (o no existente), con el gas denso distribuido a su alrededor en forma de cáscaras o pilares, y sin impulsar flujos moleculares.

Finalmente, con la emisión a longitudes de onda infrarrojas y submilimétricas, hemos construido la distribución espectral de energía de cada objeto para determinar de forma más precisa su luminosidad y temperatura bolométrica, la cual se utiliza como indicador del estado evolutivo en las estrellas de baja masa.

El estudio global de cada región nos permite construir una tabla con los parámetros principales de cada fuente de radio continuo, obtenidos a partir de los diferentes trazadores de formación estelar utilizados (e.g., continuo centimétrico y milimétrico, gas denso, flujo molecular, infrarrojo). La comparación de estos parámetros nos ha permitido encontrar signos de una posible secuencia evolutiva con dos grupos muy bien diferenciados:

- Fuentes de radio continuo débiles, con emisión parcialmente ópticamente gruesa (índices espectrales > 0.3) y muy compacta. Asociadas con una elevada cantidad de polvo. Embebidas en núcleos denso, en la mayoría de casos asociados con los signos característicos de los núcleos moleculares calientes. Impulsando flujos moleculares. Con escasa emisión en el infrarrojo medio o próximo (emitiendo principalmente a longitudes de onda largas), y temperaturas bolométricas bajas (< 70 K). Interesantemente, los objetos con estas propiedades pero sin emisión de núcleo molecular

caleinte, presentan temperaturas bolométricas más elevadas y son visibles en el cercano infrarrojo, indicando que podrían ser más evolucionados.

- Fuentes de radio continuo más intensas, con emisión ópticamente delgada (índices espectrales ~ -0.1) y más extendida. Con escasa emisión de polvo, y sin presencia de gas denso o flujos moleculares impulsados por el objeto joven. La emisión en el infrarrojo es más intensa, y en algunos casos son visibles en el óptico. Las temperaturas bolométricas son más elevadas (> 70 K). Todas estas propiedades indicando que son objetos más evolucionados que los anteriores.

Las correlaciones entre los diferentes parámetros utilizados para caracterizar estos dos grupos son generalmente próximas al 80–90%, por lo que podemos indicar que los parámetros utilizados son buenos indicadores del estado evolutivo de la estrella en formación.

Finalmente, utilizando los principales parámetros que han permitido la diferenciación de los estados evolutivos, hemos analizado las propiedades de los flujos moleculares y del gas denso. A pesar de la escasa estadística disponible, se encuentra una tendencia con los objetos más luminosos impulsando flujos moleculares más energéticos. Se intentó determinar también si los objetos más jóvenes están asociados a flujos moleculares más colimados, pero la ligera tendencia encontrada debe ser estudiada y confirmada con un mayor número de regiones observadas. Por último, la temperatura del gas denso (amoníaco) parece estar directamente relacionada con la luminosidad del objeto: objetos más luminosos son capaces de calentar más el gas circundante. Dentro de esta tendencia se observa que el gas denso afectado por la radiación UV de regiones H II próximas es más caliente en comparación al aumento de temperatura que puede producir la actividad de los flujos moleculares, mientras que los flujos moleculares perturban cinemáticamente el gas denso de forma más eficiente que la radiación producida por las regiones H II.

Part I

Introduction

Massive star formation

1.1 Massive star formation

Massive stars ($M \gtrsim 8 M_{\odot}$) play a major role in shaping the morphological, dynamical, and chemical structure of their host galaxies, through supersonic winds and strong ultraviolet radiation that can ionize the surrounding gas and form H II regions, and finally through supernova explosions. In addition, when observing far galaxies, most of the stars we are able to detect and study with the current instrumentation are, in fact, massive stars. Thus, the properties that we infer for distant galaxies are commonly the result of the study of massive stars. It is clear, then, that massive stars are key to understanding many physical phenomena in our own Galaxy, and other galaxies. However, their first stages of formation are still poorly understood. Observationally, it is not easy to study the formation of a massive star since they tend to form in clustered mode, deeply embedded in molecular dense cores highly obscured by circumstellar dust (with extinctions $A_V \gtrsim 100$), and at far distances ($\gtrsim 1$ kpc). Additionally, from the theoretical point of view, there are some questions that remain unsolved.

In the case of stars with masses of a few solar masses (the so-called low-mass stars), the now-classical theory of star formation set out by Larson (1969) and Shu et al. (1987) is used to explain how a dense core evolves into a star. The initial phase is a condensation of gas in the interstellar medium (ISM) that becomes gravitationally unstable (probably due to compressive turbulent motions in the ISM), forming a bounded dense core. The core will collapse isothermally until it loses its ability to cool efficiently. This happens at densities of $n_{\text{H}_2} \sim 10^{10} \text{ cm}^{-3}$, where the gas becomes optically thick and the excess of energy due to the compression cannot be radiated away anymore. Then, the gas heats

1. Massive star formation

up until a temperature of ~ 2000 K is reached, which corresponds to the dissociation of H_2 molecules. Dissociation of H_2 absorbs the excess of energy, and thus, the collapse can continue until all H_2 is dissociated. The prestellar phase comes to an end, and a protostar has formed. The protostellar evolution proceeds in subsequent phases which can be distinguished observationally by their spectral energy distribution. In the first phase (Class 0), the protostar grows in mass by accreting gas from its surrounding envelope through an accretion disk, and drives bipolar outflows. In the Class I phase, outflows create cavities in the envelope, the protostars increases its temperature and turns visible in the infrared. The envelope is totally removed in the Class II phase and the protostar has stopped accretion. The protostar now starts its pre-main-sequence evolution. The main source of energy for pre-main-sequence stars is gravitational contraction. When the central temperature is sufficient to ignite hydrogen fusion, a main sequence star is born. Reviews on low-mass star formation are Lada (1999); Shu et al. (1999); André et al. (2000).

The above scenario for star formation is accepted for stars with masses $\lesssim 2 M_\odot$ (i.e., low-mass stars), however, it is questioned for stars much more massive than this. The main differences that call into question the above mentioned model, are related to the different Kelvin-Helmholtz timescales. This timescale is the period in which nuclear reactions have not yet been triggered, and the protostar compensates its energy losses by gravitational contraction. The time for this Kelvin-Helmholtz phase (Huang and Yu 1998) is

$$t_{\text{KH}} = \frac{GM^2}{RL}, \quad (1.1)$$

with G being the gravitational constant, M the protostellar mass, R the protostellar radius, and L the luminosity. By numerical calculations Iben (1965) estimates that this time is 5×10^7 yr for a $1 M_\odot$ star, and 6×10^4 yr for a $15 M_\odot$ star. The free-fall timescale (i.e., the period of accretion for the envelope) for low and high-mass stars can be calculated as

$$t_{\text{ff}} \simeq \left(\frac{3\pi}{32 G \rho} \right)^{1/2}, \quad (1.2)$$

resulting in $\sim 4 \times 10^5$ yr, for densities $\sim 10^4 \text{ cm}^{-3}$. Thus, for massive stars $t_{\text{KH}} \ll t_{\text{ff}}$, indicating that the star begins nuclear fusion while it is still accreting more gas (Palla and Stahler 1993; Keto and Wood 2006). In this situation, the main problem arises from the radiative pressure that newly-formed massive stars exert on the surrounding ambient cloud (i.e., the accretion flow) as soon as they ignite, pushing against infalling material. It is the interaction between the accretion flow and the radiation field of the massive protostar that makes massive star formation different from low-mass star formation, and needs to be understood. In the past decades, early spherically symmetric calculations based on the low-mass star-formation scenario, demonstrated that the strong radiation pressure acting on dust grains might be enough to halt the accretion onto the massive protostar (Kahn 1974; Wolfire and Cassinelli 1987; Stahler et al. 2000), and therefore, the theory had to be adapted to account for the formation of massive stars.

There are two main schools of thought in the theory of massive star formation (Zinnecker and Yorke 2007; Krumholz and Bonnell 2007), that differ primarily in the way how the gas that forms the massive star is assembled.

The first method is the so-called **monolithic collapse**, which tries to adapt the mechanism of low-mass star formation to solve the problem of the radiation pressure. Some theoretical works reveal that the cavity created by a jet and outflow can be used by the radiation from the massive protostar to escape without hindering accretion through the disk and onto the protostar (Wolfire and Cassinelli 1987; Tan and McKee 2002; Yorke and Sonnhalter 2002). Additionally, reduced dust opacities and very high accretion rates of 10^{-4} – $10^{-3} M_{\odot} \text{ yr}^{-1}$ (Osorio et al. 1999; Edgar and Clarke 2003), could also overcome the radiation pressure problem. The observation of highly collimated jets and outflows (e.g., Martí et al. 1993; Beuther and Shepherd 2005) and rotating structures (e.g., Patel et al. 2005; Beltrán et al. 2006a) around some massive protostars, support this scenario. However, some authors caution that this scaled-up version of low-mass star formation can be feasible only up to early B stars (see Zinnecker and Yorke 2007).

The second approach to explain the formation of massive stars is the theory of coalescence and **competitive accretion**, based on the fact that massive stars are mostly observed in clusters (e.g., Bonnell et al. 1998, 2007; Stahler et al. 2000). In isolation, a forming star will accrete most of the mass of the parental cloud, which determines its final mass. However, in clusters, stars ‘must’ compete for accreting cloud gas and gain mass. In this scenario, the final mass of a star depends on its accretion domain, i.e., the region from which gas can be gathered; and, simultaneously, the size of the accretion domain depends on the mass of the protostar and the spatial distribution of nearby stars. Thus, a massive star can gather and accrete more mass than a low-mass star, and become even more massive. Under the assumptions of this scenario, the most massive stars found in clusters must be located at the center of the cluster, where the cloud gas falls into the potential well of the whole cluster, increasing the gas reservoir for each individual star. The coalescence scenario, which requires high protostellar densities ($> 10^6$ – 10^8 pc^{-3}), suggests that the merging of two or more low-mass stars can form a more massive star. Although these protostellar densities are not usually found in protostellar clusters, this model naturally explains why massive stars are found in clusters.

1.1.1 Observational massive star-forming features

Observations of massive star-forming regions are completely necessary to confirm which mechanism better explains and controls the formation of massive stars. However, since massive stars are located far away from the Sun, in sites with large extinctions, and in crowded clusters, their observation becomes a hardworking task. In spite of all the difficulties, observational efforts have revealed several features that are commonly found in the formation of massive stars.

1. Massive star formation

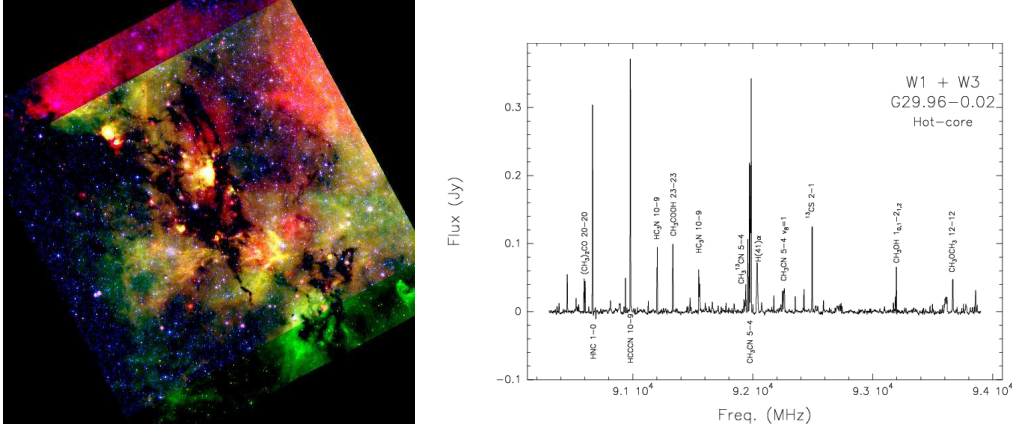


Figure 1.1: Observational massive star forming features. *Left*: Infrared dark cloud G14.2–0.60 seen as an absorption feature against the bright infrared emission (red: 24 μm , green: 8 μm , blue: 4.5 μm); image courtesy of G. Busquet. *Right*: Example of a chemically rich spectrum toward the hot molecular core G29.96–0.02.

- **Infrared Dark Clouds (IRDCs)**: First recognized in mid-infrared images from the Infrared Space Observatory (ISO; Perault et al. 1996) and the Midcourse Space eXperiment (MSX; Egan et al. 1998), infrared dark clouds, seen at infrared wavelengths as absorption features against the bright galactic background, contain thousand of solar masses of dense ($n > 10^5 \text{ cm}^{-3}$) and cold ($T \sim 10\text{--}15 \text{ K}$) gas (e.g., Carey et al. 1998; Pillai et al. 2006). The high density, low temperature and large masses make them a probable birth site for massive stars and clusters. In Figure 1.1 (left panel), we show an example of an IRDC.
- **Hot Molecular Cores (HMCs)**: First discovered in the vicinity of massive protostars (e.g., Osorio et al. 1999; Kurtz et al. 2000; Kurtz 2005b; Cesaroni 2005), hot molecular cores are compact ($\leq 0.1 \text{ pc}$) and dense ($n \gtrsim 10^7 \text{ cm}^{-3}$) objects with relatively high temperatures ($T_k \gtrsim 100 \text{ K}$) that show a very rich chemistry in complex organic molecules (e.g., CH_3CN , CH_3OH , CH_3OCHO ,...). They are considered to be one of the first evolutionary signposts of massive star formation. However, recent works have revealed regions characterized by high temperatures and densities around low-mass protostars (see Ceccarelli 2004 for a review). These so-called hot corinos share many characteristics with HMCs, although being $\sim 10^2$ times less massive. A typical spectrum from a HMC is shown in Figure 1.1 (right panel).
- **H II regions**: These objects are one of the first historical signatures used to search for sites of massive star formation (e.g., Mezger et al. 1967; Yorke 1986; Wood and Churchwell 1989; Kurtz 2005a). Once a massive protostar is formed and reaches the hydrogen burning phase, the large amount of Lyman continuum photons they

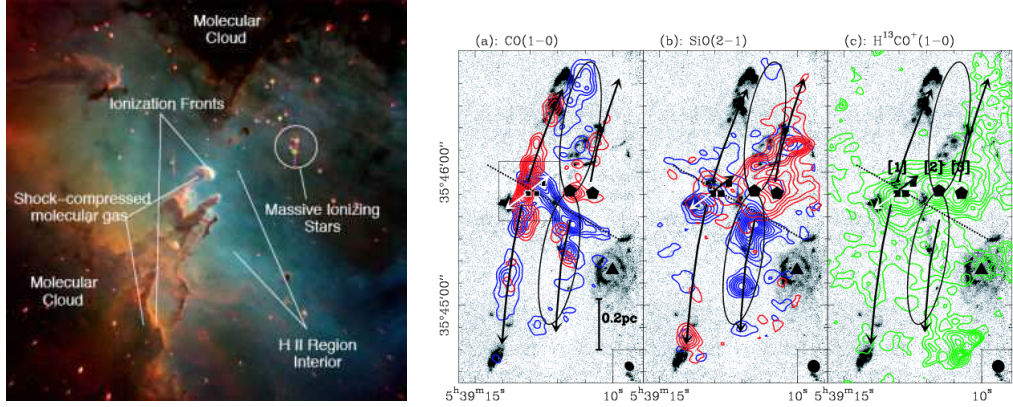


Figure 1.2: Observational massive star forming features. *Left*: Example of an H II region surrounded by molecular gas emission in the Eagle Nebula (M16). *Right*: Example of several collimated molecular outflows in the massive star forming region IRAS 05358+3543; image from Beuther et al. (2002a).

produce have a profound effect on the surrounding material, photoionizing the gas (mainly atomic hydrogen; see Figure 1.2 left). The number of ionizing photons ($h\nu \geq 13.6$ eV) produced by the protostar and the recombinations will determine the size of the H II region. Interestingly, observations reveal that these hot (10^4 K) regions of ionized gas surrounding massive protostars, are found in various shapes and sizes (see Figure 1.3, and Kurtz et al. 1994; Churchwell 2002). The study of ionized gas can provide information about the environment surrounding massive stars. It is interesting to note that low energy photons ($6 \text{ eV} \leq h\nu \leq 13.6 \text{ eV}$) can not ionize hydrogen, but will photodissociate molecules and ionize low ionization-potential atoms (e. g., carbon, silicon) originating photodissociation regions (PDRs; e. g., Hollenbach and Tielens 1997).

- **Molecular outflows and jets:** Similar to the low-mass star formation, different phenomena of mass ejection have been observed associated with massive star-forming sites. The most clear manifestations of outflowing gas associated with protostars are the pc-scale Herbig-Haro (HH) jets and the bipolar molecular outflows. HH objects (Herbig 1951; Haro 1952) are optical nebulosities in star-forming regions, observed in highly excited molecular hydrogen (e. g., Eislöffel 2000), optical forbidden lines (e. g., Anglada et al. 2007), hydrogen Balmer emission lines (e. g., López et al. 2009) and radio continuum (e. g., Torrelles 1991). At smaller scales, close to the YSO where the excitation is too high, radiojets and molecular outflows are the best tracers of mass ejection. Thermal radiojets have been historically found toward low mass YSOs (see Anglada 1995, 1996 for reviews), but recently, several massive protostar show radiocontinuum emission tracing radiojets (e. g., HH 80/81: Martí et al. 1993;

1. Massive star formation

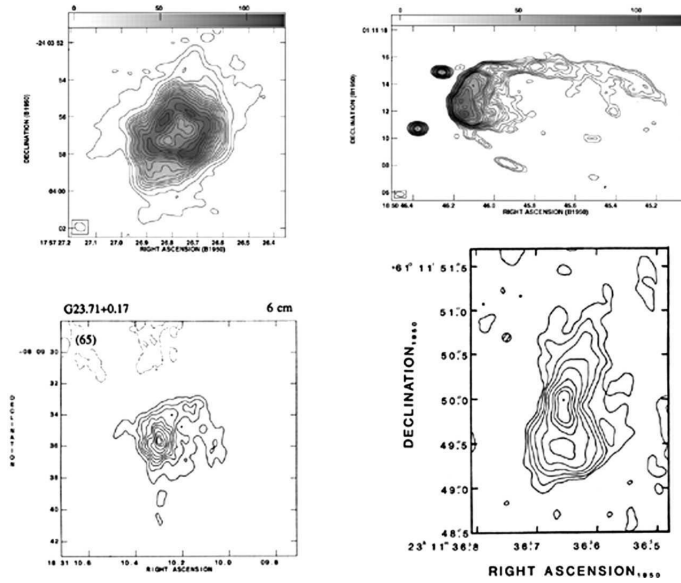


Figure 1.3: Different morphologies of UCH II regions: shell-like (top left), cometary (top right), core-halo (bottom left), and bipolar (bottom right). Figure from Churchwell (2002).

Cepheus A: Garay et al. 1996; IRAS 16547–4247: Rodríguez et al. 2008). More interestingly is the large number of molecular outflows detected in massive star forming region (e.g., Beuther et al. 2002c; López-Sepulcre et al. 2009). In Figure 1.2 (right panel) we show the massive star forming region IRAS 05358+3543 in which up to three distinct outflows have been identified.

- **Molecular masers:** Interstellar masers are one of the best observable signposts of (massive) star formation. They are relatively common, intense, and because they have transitions at centimeter wavelengths, are not affected by the high extinction present in the star-forming sites. Furthermore, the maser emission is compact and intense, which means that it can be studied at very high angular resolution using VLBI techniques. All this makes masers ideal probes of the kinematics of the gas in which they arise (e.g., Torrelles et al. 2005), and the physical conditions of the regions where they are found (e.g., Cragg et al. 2001). However, the complexity of maser pumping schemes introduce significant challenges for a correct interpretation of the results, and thus, complementary information of other tracers observed at high angular resolutions are necessary. Several species of masers have been identified in the ISM: OH, H₂O, CH₃OH, SiO, H₂CO, NH₃ (see Ellingsen 2004, 2005; Ellingsen et al. 2007, for reviews); with some methanol maser transitions probably being only associated with massive star-forming regions (Minier et al. 2003).

1.2 Ionized gas

In the previous Section, we have briefly exposed the classical model for formation of low-mass stars, the recent theories that try to explain the formation of massive stars, and the most important observational signatures associated with massive young stellar objects (YSOs). Among all these observational features, the presence of an H II region is the one that clearly differentiates the bimodality of low-mass and high-mass star formation, since only massive stars can produce enough UV photons to ionize the surrounding gas; and, furthermore, is one of the major effects that complicates the understanding of massive star formation with respect to the models for the low-mass stars. H II regions are mainly ionized gas (hydrogen) regions, with the continuum emission at centimeter wavelengths coming from the interaction of free electrons with charged particles (e. g., protons or ionized hydrogen nuclei). The ionized gas is a good, and necessary, starting point to study massive YSOs; however, not all the continuum centimeter emission we detect in massive star-forming regions comes from H II regions. Thus, it is necessary to comprehend the different mechanisms that can produce radio continuum emission in massive protostars.

In the following, we will describe the mechanisms that can produce radio continuum radiation in star-forming regions. We will make a differentiation between the two major groups in which the electromagnetic radiation is usually categorized: *thermal* and *non-thermal* radiation.

1.2.1 Thermal emission from ionized gas

Thermal radiation can be defined as electromagnetic radiation emitted from all matter due to its possessing thermal energy which is measured by the temperature of the matter. This kind of radiation is essentially produced by the interaction between electrons and atoms: for example, as electrons move from one orbit to another in an atom, or as free electrons interact with the Coulomb field of a charged particle. In general, some ionization or excitation is required to obtain charged particles (e. g., ionized atoms from an initial neutral component), or to change the orbit of the electrons within an atom. The ionization of gas associated with star-forming sites, can be produced by two distinct mechanisms: *photoionization* and *ionization through shocks*. In the following, we list some of the most accepted mechanisms that have been proposed to model the thermal radiocontinuum emission detected toward YSOs.

Homogeneous H II regions —

Massive young stars with temperatures $\gtrsim 10^4$ K and luminosities $\gtrsim 1000 L_{\odot}$, radiate large amounts of UV photons beyond the Lyman limit (912 Å) that can ionize the circumstellar material and form an H II region. Free electrons can recombine with a proton producing new photons, which can ionize new atoms or escape from the region, or they can heat the gas through collisions with other atoms. Thus, an extended region of ionized

1. Massive star formation

gas appears surrounding the massive young star. However, the radiation field decreases with distance from the star due to different effects (e.g., geometrical dilution, isotropy in the reemission of the new UV photons produced in the recombination, or production of two or more less energetic photons after the recombination) and makes the ionized region have a finite size. Classically, different evolutionary stages can be inferred in the formation of an H II region: from the first expansion of the ionizing front (which takes a short time), to the situation in which the ionizing front becomes stationary (see Dyson and Williams 1997 and Stahler and Palla 2005, for details).

The morphology of the H II region depends on the initial distribution of the surrounding medium, and the size depends on the total energy radiated by the protostar. The most standard model to describe the size and properties of H II regions was developed by Strömgren, considering an homogeneous medium formed only by hydrogen. In this scenario, the H II region is a sphere of radius R_S (Strömgren's radius), which is found by equating the number of recombinations and the number of ionizing photons produced by the massive young star

$$\dot{N}_i = (4/3)\pi R_S^3 n_e^2 \alpha^{(2)} \quad (1.3)$$

with \dot{N}_i the number of ionizing photons (i.e., with $\lambda < 912 \text{ \AA}$) per unit of time emitted by the protostar, and $\alpha^{(2)}$ the recombination coefficient to the level 2 or higher (recombinations to level 1 produce an ionizing photon, thus they must not be considered). The value of $\alpha^{(2)}$ is estimated as $2 \times 10^{-13} (T_e)^{-3/4} \text{ cm}^3 \text{ s}^{-1}$, with T_e in units of 10^4 K .

In an ionized environment, electrons accelerate because of the electrostatic interaction with protons and positive ions. The power emitted by a system of charges is given, as a first approximation, by the Larmor equation. Electrons from ionized atoms are free particles, unbounded, so the radiation produced will have a continuum spectrum. This kind of emission is known as thermal bremsstrahlung or free-free emission, and the flux density at radiowavelengths is obtained (see Appendix B) by

$$S_\nu = \int_{\Omega_{\text{source}}} B_\nu(T_e) (1 - e^{-\tau_{ff}(\nu)}) d\Omega, \quad (1.4)$$

with the optical depth of the free-free emission as

$$\tau_{ff}(\nu) \simeq 0.08235 \left[\frac{EM}{\text{cm}^{-6} \text{ pc}} \right] \left[\frac{T_e}{\text{K}} \right]^{-1.35} \left[\frac{\nu}{\text{GHz}} \right]^{-2.1}, \quad (1.5)$$

and the emission measure $EM = \int n_e^2 dl$, with n_e the electron density of the ionized gas. Two different regimes can be identified in the spectral energy distribution of an homogeneous H II region. For low frequencies or high optical depths ($\tau_\nu \gg 1$), the source is optically thick and $S_\nu \propto \nu^{+2}$. On the other hand, for high frequencies or low optical depths ($\tau_\nu \ll 1$), the source is optically thin and $S_\nu \propto \nu^{-0.1}$, as $B_\nu(T_e) \propto \nu^2$. These two regimes are differentiated by the turnover frequency, ν_t , which depends on the electron density as $\nu_t \propto n_e^{0.96}$ (see Appendix B): higher electron densities implicate ν_t is located at higher

frequencies, and thus, the optically thick regime is observed up to higher frequencies. Taking this into account, homogeneous H II regions can show different spectral energy distributions at centimeter wavelengths, depending on their intrinsic properties. The so-called hypercompact H II regions have large electron densities that make their emission be optically thick up to frequencies ~ 100 GHz; however, for compact or ultracompact H II regions (with smaller electron densities) the emission becomes optically thin at frequencies ~ 1 GHz. Equations 1.4 and 1.5 can be used to fit the spectral energy distribution of the H II regions (input parameters: size of the H II region, electron density, and electron temperature) to obtain physical parameters such as the emission measure EM , the mass of ionized gas M_i , and the flux of ionizing photons \dot{N}_i , which can be used to determine the spectral type of the ionizing star (with the tables from Panagia 1973 or Thompson 1984).

Observationally, different morphologies have been identified for H II regions (e. g., Wood and Churchwell 1989): cometary, shell-like, spherical, irregular, core-halo (see Figure 1.3). These different morphologies suggest the gas surrounding newly-born massive stars is not completely homogeneous, and thus, the ionized gas within H II regions could also have a non-homogeneous distribution (see below).

Non-homogeneous H II regions —

As explained above, an homogeneous density distribution is generally assumed to determine the properties of thermal radio continuum emission (assuming it comes from an H II region). In this case, the radio continuum has a well-studied behaviour (see above, and Appendix B), with the asymptotic limits of $S_\nu \propto \nu^{-0.1}$ for $\tau_\nu \ll 1$, and $S_\nu \propto \nu^{+2}$ for $\tau_\nu \gg 1$, and with the change of regime occurring in a narrow frequency range close to ν_t . However, not all the thermal radio continuum sources show this behaviour. For example, our Sun has an almost constant spectral index of +0.7 between 0.3 and 30 GHz. In addition, newly-born stars are surrounded by dense gas with density distributions more complex than the constant density model, implying that the ionized gas can also have a non-homogeneous density distribution. Panagia and Felli (1975), and Olmon (1975) studied how the spectral energy distribution varies with changing the n_e distribution. They assumed a power-law distribution: $n_e \propto r^{-q}$.

In Section B.4 of Appendix B, we present the equations that can be used to solve the flux densities expected from a non-homogeneous H II region with a power-law distribution for n_e . In particular, it is interesting to note that in the case in which $n_e \propto r^{-2}$, the spectrum at radio wavelengths behaves as $\nu^{+0.6}$ over a wide range of frequencies. For steeper density distributions, such as $n_e \propto r^{-4}$, the spectral index results in +1.4. Thus, this simple model can account for the radio emission detected from some young stellar objects, likely tracing stellar winds with spherical symmetry (as it happens in the radio emission from the Sun), or H II regions with density gradients. In particular, hypercompact H II regions, with typical spectral indices of $\sim +1$, have been modeled by Franco et al. (2000) as non-homogeneous H II regions.

1. Massive star formation

Other works (e. g., Ignace and Churchwell 2004) model the radio continuum energy distribution of some H II regions as an ensemble of spherical clumps (i. e., a non-homogeneous distribution of ionized gas). They found that the radio continuum spectral index is governed by the population of clump optical depths $N(\tau)$ such that: i) at frequencies where all clumps are thick, a continuum slope of +2 is found, ii) at frequencies where all clumps are optically thin, a flattened slope of -0.1 is found, and ii) at intermediate frequencies, a power-law segment of significant bandwidth with slopes between these two limiting values can result. With this model, the authors can properly fit the SED of W49N B2, which has a spectral index of +0.9.

Ionized accretion flows —

As explained in Section 1.1, theoretical star-forming models suggest that massive protostars still accrete mass even after starting the nuclear reactions. In addition, molecular line observations toward several massive star-forming regions show evidences for accretion flows around small radio continuum sources (e. g., Guilloteau et al. 1983; Zhang and Ho 1997; Beltrán et al. 2006a). Once the forming star has gained sufficient mass, temperature, and a luminosity equivalent to an early B-type star, the number of emitted Lyman continuum photons will be enough to ionize the gas and produce an H II region. If the star is to accrete the additional mass to become a more massive star (for example, an O-type star), then the accretion must continue past the mass when an H II region forms, resulting in an inevitable fact, the interaction of accretion flows and H II regions in the early evolution of massive stars.

Keto (2002b, 2003, 2007), and previously Walmsley (1995), studied the formation of an H II region within an accretion flow. If the radius of ionization equilibrium r_i (set by the balance between the ionization and recombination within the H II region) is less than the gravitational radius, $r_g = GM_*/c_s^2$, in the accretion flow, then the H II region can be trapped within the accretion flow. This model explains why the development of an H II region does not immediately end the accretion as would be expected in the classic model for the evolution of H II regions by pressure driven expansion, and relies on the momentum of a massive accretion flow to overcome the radiation pressure of the stars. The accretion flow, if not reversed by radiation pressure, will end when the ionization rate, which increases with the increasing mass of the forming star(s), is high enough that the radius of ionization equilibrium increases beyond the gravitational radius. Beyond this point, the H II region expands and the accretion phase ends.

Keto and Wood (2006) extended the model of Keto (2002b) to consider accretion flows with angular momentum. In this model of accretion, the gas spirals in to the star on ballistic trajectories conserving the angular momentum, and as a result a disk develops. In this model, when $r_i > r_g$, the H II region will expand around the disk, and the surface of the disk (except for a small region in the center, where the density is higher) will photoevaporate with an outward flow of ionized gas off the disk, as described in the

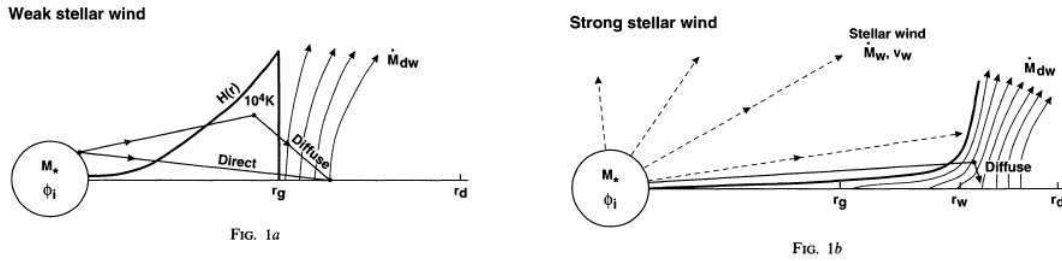


Figure 1.4: Schematic view for the weak (left) and strong (right) photoevaporated disk model. Figure from Hollenbach et al. (1994). *Left*: Weak stellar wind model for a star of mass M_* and Lyman continuum photon luminosity Φ_i . Inside r_g an ionized 10^4 K atmosphere forms with scale height $H(r)$. Diffuse Lyman continuum photons from recombinations in the atmosphere at $\sim r_g$ cause material to evaporate beyond r_g . The disk extends to r_d . *Right*: Strong stellar wind model for a star with a mass-loss rate \dot{M}_w . Material evaporates beyond r_g , but the dominant flow is from r_w , where the stellar wind ram pressure equals the thermal pressure of the ionized flow of the disk. Diffuse photons still dominate the photoevaporation.

models for photoevaporating disks (see below).

The model for H II regions trapped within an accretion flow was developed to explain the observations of the inward flow of ionized gas toward the massive stars forming in G10.6-0.4 (Keto 2002a). The accretion model assumed in Keto (2002b) is a spherical steady-state flow which has a density gradient everywhere less steep than $n_e \propto r^{-3/2}$. It seems that the model of gravitationally trapped H II regions can explain the observations (spectral energy distribution and kinematics of the ionized gas) in G10.6-0.4 and W51e2 (Keto and Klaassen 2008). van der Tak and Menten (2005) also test this model in three other regions, obtaining acceptable fits for the SEDs.

Photoevaporated disk winds —

Hollenbach et al. (1994) and Johnstone et al. (1998) proposed that unresolved UCH II regions, and HCH II regions, could arise from photoevaporating molecular disks. The photoevaporation of circumstellar disks around massive stars occurs when the disk is ionized and heated by the Lyman continuum photons from the star. Within the gravitational radius, $r_g = GM_*/c_s^2$, the heated gas is confined in the gravitational potential well of the star, producing a static ionized dense atmosphere with a temperature $\sim 10^4$ K. For $r > r_g$, the ionized gas can escape and an isothermal evaporative flow is established. The ionized material flows away but is constantly replenished by the photoevaporation of the disk. Depending on the disk mass, this phase can last $\sim 10^5$ yr. The static atmosphere will exist if the wind of the star is weak. If the star has a strong stellar wind, the wind may push the confined gas inside r_g (i.e., the static dense atmosphere) out to a critical radius, r_w , where the ram pressure of the stellar wind is balanced by the thermal pressure of the

1. Massive star formation

photoevaporated flow. In Figure 1.4, we show a schematic view for, both, the weak and strong disk models. Simultaneously to the theoretical models, Yorke and Welz (1996) and Richling and Yorke (1997) made hydrodynamical simulations of the evolution of photoevaporated disks under a variety of conditions. In particular, they found that scattering of ionizing photons on dust grains increases the photoevaporation rate.

Lugo et al. (2004) modeled the density and velocity structure of axisymmetric isothermal winds photoevaporated from a spatially thin Keplerian disk, and calculated the free-free continuum emission expected to arise from the density structure of the weak and strong disk models. Since the model assumes an isothermal wind, the intensity at frequency ν is given by

$$I_\nu = B_\nu(T) (1 - \exp^{-\tau_\nu}), \quad (1.6)$$

where $B_\nu(T)$ is the Planck function at temperature 10^4 K, and τ_ν is the free-free optical depth $\tau_\nu = \int \kappa(\nu) ds$ (see Equations B.1 and B.4). The flux density at frequency ν is given by the integral over the source solid angle, Ω_S , $S_\nu = \int I_\nu d\Omega$. The models of the photoevaporated disk winds depend on several parameters. The solutions depend on the gravitational radius r_g , on the slope of the density profile q , on the value of the normalized z -velocity at the disk surface f_0 , on the inner radius of the disk r_i , and on the radius of the disk r_d . This model can properly reproduce the observed spectral energy distribution of the objects MWC 349 and NGC 7538-IRS1, with a weak and a strong disk model, respectively. Recently, photoevaporated disk model also tries to fit the observed radio recombination lines of MWC 349 (M. Avalos, priv. comm.).

Ionized equatorial winds —

Mass loss appears to be an integral part of the star formation process, determining (by reversing the infall process) the final mass of the star. Luminous YSOs not only drive well-known large-scale bipolar molecular outflows, but also have small-scale ionized stellar winds. They are differentiated from photoionized standard H II regions observationally by their spectral index, which is usually close to that expected for a stellar wind of +0.6, compared to the +2 for optically thick H II regions or −0.1 for optically thin H II regions. Furthermore, stellar wind sources have broad (few 100 km s^{-1}) optically thick near-IR H I emission lines (Persson et al. 1984; Bunn et al. 1995). The ability to resolve the radio emission from the stellar wind sources means that insights can be gained into the geometry of the mass loss. Several works have revealed the presence of elongated structures oriented in the molecular outflow direction, likely tracing thermal radiojets (see below). However, there are some cases where the radio emission does not show the morphology expected for a radiojet.

Hoare et al. (1994) and Hoare (2006) reported (thanks to very high angular resolution observations) the existence of two massive YSOs (S106 IR and S140 IRS1) where the elongation observed in the radiocontinuum emission is opposite to the direction of the bipolar outflow. In Figure 1.5 (left), we show the continuum emission of the equatorial

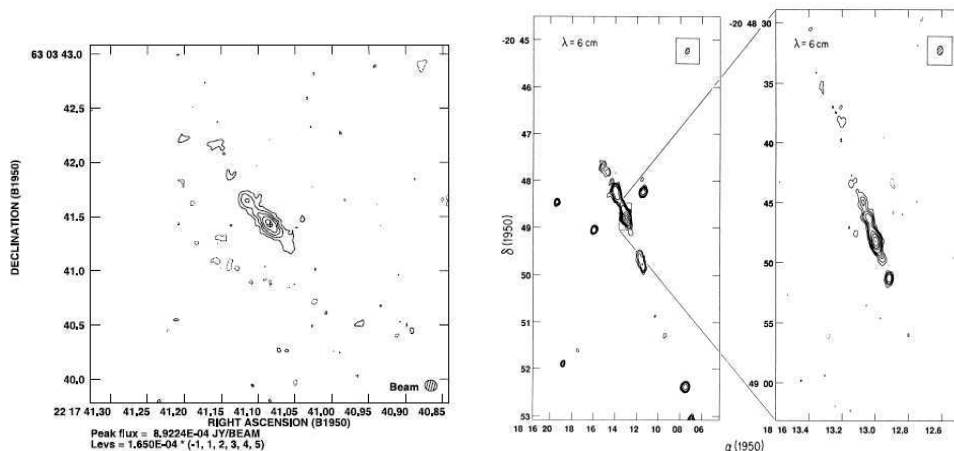


Figure 1.5: *Left*: Continuum image of the equatorial wind S140 IRS1 (Hoare 2006). There are hints of an outflow/jet system in the southeast-northwest direction, perpendicular to the elongation seen in the radio continuum image. *Right*: Continuum images (at 6 and 3.6 cm) of a massive thermal radiojet (HH 80/81: Martí et al. 1993). In this case, the orientation of the molecular outflow is in the same direction as the radio continuum emission.

wind S140 IRS1. They propose that the morphology of these sources is due to the fact that the wind is predominantly equatorial. The radio properties of these objects can be understood in terms of the radiatively driven disk wind model of Drew et al. (1998). The main question is: why some objects have equatorial ionized winds and other massive YSOs have ionized jets? Hoare et al. propose that since most of the radiojets are not visible in the near-IR, while the two proposed equatorial ionized wind sources have a counterpart at such short wavelengths, the differences in the radio continuum morphologies could be due to a different evolutionary stage. Thus, there could be an evolutionary trend in the differentiation between thermal radiojets (younger) and equatorial winds (more evolved). However, a large sample of sources showing properties of equatorial ionized winds is necessary to better constrain their properties, and up to date, only two sources have characteristics similar to those expected for ionized equatorial winds, and scarce examples have been found up to now.

Thermal radiojets —

For low-mass protostars, with luminosities $\lesssim 100 L_{\odot}$, photoionization mechanism by UV stellar photons appears to be insufficient to explain the observed radio continuum emission. Torrelles et al. (1985) propose that radiocontinuum emission from low-luminosity objects can be explained as shocked ionized gas, with UV photons coming from the collision between intense stellar winds and the circumstellar material. Curiel et al. (1987, 1989) modeled this scenario. By assuming stellar winds with mass loss rates of 10^{-5} –

1. Massive star formation

$10^{-7} M_{\odot} \text{ year}^{-1}$, it is possible to generate enough UV photons to produce the centimeter continuum emission observed in low-mass protostars such as IRAS 16293–2422 (Estalella et al. 1991), or L723 (Anglada et al. 1991), see also the reviews of Anglada (1995, 1996). The dependence of the flux density and deconvolved angular size with frequency of these thermal radiojets can be explained with the equations of collimated stellar winds as jet-like winds. Reynolds (1986) considers that the ionization of the material begins at a finite radius, r_0 , with a width w , and assumes power-laws for the width, velocity, density, temperature, and fraction of ionization, with ϵ , q_v , q_T , q_n , and q_X being the power-law indices, respectively. For an isothermal jet, with constant fraction of ionization and velocity, the flux density and the deconvolved major angular axis of the source vary with frequency as

$$S_{\nu} \propto \nu^{1.3-0.7/\epsilon} \quad , \quad \theta_{\text{major}} \propto \nu^{-0.7/\epsilon}. \quad (1.7)$$

Thus, the spectral index for collimated winds varies between -0.1 and $+0.6$, with $\alpha = +0.6$ for a biconical jet ($\epsilon = 1$), which is analogous to the spherical symmetric wind of Panagia and Felli (1975). Anglada (1996) found a correlation between the radio luminosity (calculated as $S_{\nu}d^2$: with S_{ν} the flux density at centimeter wavelengths and d the distance to the source) and the bolometric luminosity of the YSO. The theoretical models of Curiel et al. (1987, 1989) also predicts a correlation between the momentum rate in the outflow (\dot{P}) and the radio luminosity, which is also confirmed by the observational work of Anglada (1996).

For high-luminosity YSOs, the number of UV photons from the massive protostar is enough to ionize the gas and produce the observed radio continuum emission (forming an H II region). However, some massive YSOs have a radio continuum emission several orders of magnitude weaker than expected for an H II region. Furthermore, when observed with high angular resolution, these radio continuum sources show an elongated morphology well aligned with the direction of the molecular outflow (e. g., HH 80/81: Martí et al. 1993, 1998; Cep A2: Rodríguez et al. 1994; Gómez et al. 1999; Curiel et al. 2006; IRAS 16547–4247: Rodríguez et al. 2008). In Figure 1.5 (right), we show the HH 80/81 thermal radiojet. Therefore, the mechanism found in the ionization of thermal radiojets from low-mass YSOs seems to be also present during the formation of massive stars. These massive thermal radiojets seem to show the same correlations between radio luminosity, bolometric luminosity and outflow momentum rate as for low-mass protostars (Anglada et al. in prep.; see Chapter 9).

Dense interstellar shock waves —

Observations and theoretical models propose outflows from young stars to be radiative shock waves driven by mass accretion onto protostars. The shock waves often exhibit ultraviolet, optical, and infrared line emission within Herbig-Haro (HH) bow shocks, being also the responsible of the molecular outflows detected at millimeter wavelengths. At radiowavelengths, several HH bow shocks emit in the centimeter continuum (e. g., HH 1/2:

Pravdo et al. 1985; HH 80/81: Rodríguez and Reipurth 1989; Martí et al. 1993; HH 32: Anglada et al. 1992). As shown above, the centimeter continuum has appeared as a useful tool to study the outflowing emission close to the source (thermal radiojets), when it is deeply embedded in a molecular cloud; similarly these shock waves could also be studied at centimeter wavelengths very close to the driving source.

The free-free radiation produced in these outflows is subject to radiative transfer effects as it propagates through the post-shock gas: resulting that at frequencies $\sim 1\text{--}15$ GHz, the radio continuum from these shocks (with velocities $\gtrsim 100$ km s $^{-1}$, and $n_{\text{H}} \sim 10^3\text{--}10^5$ cm $^{-3}$; Curiel et al. 1995) can be partially optically thick. Ghavamian and Hartigan (1998) modeled the free-free emission from embedded stellar outflows, by solving the radiative transfer equation in conjunction with the ionization, density, and temperature structure of the post-shock gas. The authors present a grid of planar shock models that predict the free-free radio emission for arbitrarily high optical depths, and estimate how the spectral indices in the centimeter domain are influenced by the pre-shock density, shock velocity, and viewing angle. Thus, by knowing the spectral index α , the flux intensity (I_ν) at 1.5, 5 or 15 GHz, and the angular size of the object at one of these frequencies, the reader can apply the models and obtain (as output parameters) the velocity of the shock V_0 , the pre-shock density n_0 , and the viewing angle Θ . Or, in a different way, by fixing V_0 , n_0 and Θ (i. e., fixing the parameters of the model) the observer can try to fit the observational radio continuum parameters (i. e., I_ν , α , and size of the source). This model seems to reproduce the radio continuum properties observed in the massive YSOs DR21(OH) (Araya et al. 2009) and G31.41+0.31 (Araya et al. 2008).

We have presented different mechanisms that can produce thermal radio continuum emission in massive star-forming regions. Among all of them, we can differentiate two categories: those in which the ionization is directly produced by UV photons coming from the protostar (e. g., (non-)homogeneous H II regions, ionized accretion flows, photoevaporated, equatorial disk winds), and those in which it is necessary to have collisions to produce the ionization (e. g., thermal radiojets, dense interstellar shock waves). Some of the models, such as ionized accretion flows, photoevaporated winds and equatorial disk winds, require observations with a high sensitivity and high spatial resolution to properly fit and test them. However, massive star-forming regions are generally located far from us ($\gtrsim 2$ kpc), and thus it is not easy to achieve the necessary angular resolution to test, for example, if the ionized gas emission is or not within the gravitational radius (in the case of the ionized accretion flow). Generally, the observer can only obtain sensitive measurements of the flux density at different wavelengths, and thus construct the spectral energy distribution of the ionized gas. In conclusion, although it is hardworking to achieve high enough spatial resolutions to resolve, for example, the size of the ionization and gravitational radii, we can properly construct the SED and calculate the dependence of the flux density with the frequency, to determine, for example, if the ionized gas has a homogeneous or non-homogeneous density distribution.

1.2.2 Non-thermal emission from ionized gas

Simultaneously to the thermal emission, which is characterized by positive or flat spectral indices (see Rodríguez et al. 1993), radio continuum sources can show negative spectral indices suggestive of the presence of non-thermal radiation. This kind of radiation is usually found toward extragalactic objects such as radio galaxies, pulsars or AGNs (Active Galactic Nuclei), or toward very energetic galactic objects such as microquasars. However, observational studies in star-forming regions have reported the presence of non-thermal radio sources (e.g., Rodríguez et al. 1989; Zapata et al. 2006b). Here we list and briefly explain the mechanisms that can produce non-thermal radio emission in star-forming regions.

Synchrotron and gyrosynchrotron emission —

Non-thermal emission in star-forming regions was initially found toward low-mass YSOs, mainly associated with T Tauri stars (see Feigelson and Montmerle 1999, for a review). Observational studies at different wavelengths of low-mass stars during their early stages of evolution, from protostars through the zero-age main sequence, show highly elevated levels of magnetic activity. The result of strong magnetic activity at radio wavelengths is the presence of powerful non-thermal radiocontinuum flares. This kind of emission, seen in many Class III (and some Class I) objects (e.g., Feigelson and Montmerle 1985; White et al. 1992), is highly variable and sufficiently bright to have detectable circular polarization. The emission mechanism is quite clearly **gyrosynchrotron radiation**, produced by mildly relativistic electrons with energies ~ 1 MeV, spiraling along large-scale and well-ordered magnetic-field lines (within magnetic fields of ~ 1 Gauss; Dulk 1985).

Another mechanism that can produce non-thermal emission is the **synchrotron radiation** produced by electrons accelerated to relativistic velocities. This emission is typical of jets from AGNs and microquasars, where the large velocities allow the electrons to move at ultra-relativistic velocities (several MeVs), which in the presence of a magnetic field can emit linearly polarized synchrotron radiation (Pacholczyk 1970). This emission is characterized at radio wavelengths by negative spectral indices. Some observational works (e.g., Garay et al. 1996) reported the detection of non-thermal radiocontinuum sources close to molecular outflows and thermal radiojets driven by YSOs. This non-thermal emission can be explained as synchrotron radiation coming from the region of interaction between the outflow and the ambient cloud material. In these regions, thermal and non-thermal radiation coexist, but if the density is below a critical value ($\sim 5 \times 10^3 \text{ cm}^{-3}$; Garay et al. 1996; Henriksen et al. 1991), non-thermal emission dominates. Recently, Carrasco-González et al. (2010) report a clear evidence of synchrotron emission in a massive YSO. Radio observations of the large-scale radiojet HH 80/81 reveal that the knots located ~ 0.5 pc away from the central source have linearly polarized emission, indicating the presence of synchrotron emission and implying the presence of relativistic electrons and a magnetic field (which is aligned with the outflow/jet direction).

Very deeply embedded YSOs —

As explained above, radio sources with large negative spectral indices ($\alpha < -0.1$) have been found in star-forming regions. Rodríguez et al. (1993) explored if these negative spectral indices can be obtained from sources of free-free emission with *ad hoc* electron density and temperature distributions. The authors considered inhomogeneous sources with different properties: density distributions, temperature distributions and morphologies; and found that if only free-free emission and absorption are involved, the spectral index will always be $\alpha \geq -0.1$, regardless of the source characteristics.

Rodríguez et al. (1993) also explore the possibility of these large negative spectral indices to be produced by dust absorption. However, the spectral indices become more negative than -0.1 only for very high column densities of absorbing material, which are not usually found in the interstellar medium. In addition, the extremely high column densities required, would make the absorbing gas cloud unstable against gravitational collapse. Thus, even when spectral indices well below -0.1 can be produced, the dust absorption possibility does not seem to be realistic, and, as outlined by the authors, these kind of sources (with negative spectral indices) found in star-forming regions are more naturally interpreted as optically thin synchrotron emitters.

Finally, it is important to note that non-thermal radio sources found in star-forming regions could, in fact, have an extragalactic origin. Distances for each individual source will clarify if these sources are associated with the star-forming region or are located in a galaxy far, far away. However, determination of distances is not a straightforward work. Some works (e. g., Anglada et al. 1998) studied the probability of a radio continuum source, detected within a star-forming region, to have an extragalactic origin. In most cases, the probability of extragalactic contamination is very weak. Furthermore, we can search for positional coincidences of these non-thermal sources with other signposts of star formation, to confirm the galactic origin of these sources.

1.3 Molecular gas

The centimeter continuum emission from YSOs objects can be used to study the contribution from the ionized gas. However, we know the protostar is formed from a large molecular cloud, and in its first evolutionary stages it is still embedded within a molecular envelope. The study of this surrounding environment can be carried out with spectral line observations of different molecules. More than 100 different molecular species have been detected in the ISM, however, not all the molecules can be used in the same way. Depending on which gas content we want to study (e. g., warm dense gas, hot gas, out-flowing gas, rotating gas), we should use some specific molecular transitions to determine the properties of the molecular gas.

1.3.1 Ammonia (NH_3) and other dense gas tracers

The ammonia (NH_3) molecule is a symmetric top, relatively abundant molecule in the ISM ($\sim 10^{-8}$; Herbst and Klemperer 1973). Its critical density, around $2 \times 10^4 \text{ cm}^{-3}$, is similar to the density found in dense cores where stars form. Although the rotational transitions are placed in the infrared regime of the electromagnetic spectra, its peculiar molecular structure allows inversion transitions between different population levels to be placed in the centimeter range (i.e., avoiding the high extinction commonly found in molecular clouds and dense cores). More interestingly, the inversion lines of different rotational transitions have similar frequencies, which allows simultaneous observations of some of them with the same instrumental conditions (up to 6 transitions have frequencies separated by only 1.5 GHz close to 23.7 GHz), and thus, an estimation of the temperature of the gas can be obtained (see Appendix D). Additionally, each inversion transition line shows hyperfine structure, which allows to properly determine the opacity or excitation temperature by observing one single inversion transition. More details of the ammonia molecule can be found in Ho (1972); Ho and Townes (1983); Sepúlveda (2001).

The ammonia molecule, as a nitrogen-bearing molecule, is considered one of the most reliable tracers of the dense gas. Several works (e.g., Tafalla et al. 2004; Pillai et al. 2007; Alonso-Albi et al. 2010) have found that some molecules deplete (freeze onto dust grains) for densities $\sim 10^4\text{--}10^5 \text{ cm}^{-3}$. However, N-bearing species survive in the gas phase at least up to densities $\sim 10^6 \text{ cm}^{-3}$. Thus, NH_3 becomes a perfect tool to study the physical properties (density and temperature) of the dense gas surrounding YSOs. Other useful molecules, with critical densities and abundances similar to ammonia, which can be used to determine the properties of dense cores are N_2H^+ and CS. In addition, a detailed study of the abundance of different molecules can be used to determine the evolutionary stage of dense cores (Caselli et al. 2002; Hotzel et al. 2004; Palau et al. 2007a; Friesen et al. 2010).

1.3.2 Methyl cyanide (CH_3CN) and other high density tracers

Several molecules found in the ISM can be used to trace and study the dense cores where stars form, however, not all the molecules are equally useful. Molecules such as NH_3 or CS can be used to determine the conditions of the dense gas up to densities $\sim 10^5\text{--}10^6 \text{ cm}^{-3}$. However, there are some objects associated with the formation of stars that show higher temperatures and larger densities: the so-called hot molecular cores (HMCs; see Section 1.1). These objects are better traced by complex molecules, that are mainly produced in the hottest and densest regions.

The rotational transitions of methyl cyanide (CH_3CN) have proved to be an excellent tool to estimate the temperature and column density of HMCs (e.g., Loren and Mundy 1984; Hofner et al. 1996; Pankonin et al. 2001; Araya et al. 2005). The symmetric top molecule CH_3CN has a total number of K components for a given $J \rightarrow J - 1$ transition (see Appendix D for details in the quantum numbers) whose relative intensities can directly provide the temperature and column density of the region. The standar

population-diagram (or rotational diagram; Goldsmith and Langer 1999) technique can be used to derive these two physical parameters. Moreover, the K components of a specific J transition are close together in frequency, which allows the observation of all of them in the same bandpass, thus eliminating calibration errors for the line ratios. Among all the J transitions of CH_3CN , the higher levels ($J \gtrsim 12$), with higher energy transitions, are the best suited to properly trace the hot temperatures ($\gtrsim 100$ K) usually found in HMCs (e.g., Purcell et al. 2006).

Other complex (organic) molecules have also been used to determine the physical properties of HMCs. Molecules such as CH_3OH , HCOOH , CH_3OCHO , HNCO , CH_3CCH are abundant in hot cores, and have different rotational transitions (at millimeter and submillimeter wavelengths) that can be used to estimate the hot core temperature.

1.3.3 Carbon monoxide (CO) and other outflow tracers

The carbon monoxide (CO) molecule is the second more abundant molecule ($\sim 8 \times 10^{-5}$; the most abundant molecule is H_2) in the ISM. This molecule has a simple diatomic linear structure, with rotational transitions ($J \rightarrow J - 1$) at frequencies $2B_0J$ (where $B_0 = 57.636$ GHz, and J is the rotational quantum number), which implies that the lower energy transitions are found at 115 GHz and 230 GHz (in the millimeter range). Thanks to its high abundance and low critical density ($\sim 3 \times 10^3 \text{ cm}^{-3}$), the CO molecule is found almost everywhere in the molecular clouds. It turns into a negative aspect, when the emission becomes optically thick, resulting in emission arising only from the outer parts of the molecular cloud (we cannot study the properties of deeply embedded dense cores with the CO molecule). However, the CO molecule can be used with a different aim.

Several works (Bachiller 2009) have revealed that CO is a good tracer of shocks, and is swept out and enhanced by the passage of a jet/outflow. As explained in previous sections, jets and outflows, commonly found in the process of the formation of a star, consist of ejection of mass at high velocities ($\sim 100 \text{ km s}^{-1}$). The CO emission associated with the jet/outflow also reaches large velocities. Thus, although the CO molecular emission can be optically thick at the systemic velocity of the molecular cloud, the CO emission associated with the outflow (with larger velocities) is usually optically thin, allowing us to detect all the high-velocity CO emission. In this Thesis, we have used the CO molecular emission to trace and study the outflowing mass associated with YSOs. Scoville et al. (1986) and Palau et al. (2007b) provide useful tools to estimate the energetics of the outflow.

Carbon monoxide is not the only molecule used to study the outflow emission. Some of its isotopologues (^{13}CO , C^{18}O) have been found to be also good tracers of the outflow emission (e.g., López-Sepulcre et al. 2009). Other molecules such as SiO , HCO^+ , or shocked H_2 gas, are also good tracers of outflows. Furthermore, it is interesting to note that some outflows can be intense in some molecule, but not in other species (e.g., Zapata et al. 2006a).

1. Massive star formation

1.3.4 Water (H₂O) and other maser tracers

Water (H₂O) emission has been found in different astronomical objects, and in particular, toward star-forming regions. It is an abundant molecule in the warm regions surrounding newly-formed stars: the inner protostellar envelopes and the regions where the collapsing matter interacts with the powerful jets driven by the protostar causing violent shocks.

The maser emission (stimulated spectral line emission) of the water molecule emitting at 22 GHz is one of the brightest lines in the radio universe, and can be used to determine the kinematical and physical properties of the regions where it arises. Masers are extremely compact sources, given the special conditions (e. g., high densities and temperatures) required to produce the pumping and maser emission, and thus can be studied in great detail with the highest angular resolutions. By studying the emission of these maser spots during several years, Torrelles et al. (2005, 2011), have obtained the kinematics of the ejecting mass in different YSOs. Other works (e. g., Franco-Hernández et al. 2009) have determined the movements of rotating structures around YSOs thanks to the kinematics of water maser spots. Thus, maser emission has proved to be a useful tool to study the kinematics of the dense gas surrounding YSOs. Several other species of masers have been found in the ISM (see Section 1.1; Ellingsen et al. 2007), being the OH and CH₃OH the most abundants after the H₂O masers. An evolutionary scheme was proposed by Ellingsen et al. (2007) with CH₃OH masers appearing in the earliest evolutionary stages, and the OH and H₂O masers appearing later.

1.4 About this work

1.4.1 Goal of the thesis

Since massive stars are formed within dense cores it is reasonable to think that at some point they will start to interact and ionize the surrounding gas. However, the details of this interaction are not clear and the first footprints that a forming massive star leaves on its dense natal gas are not well established yet.

The main goal of this thesis is *characterizing the ionized gas emission found in massive star-forming regions and its relation with the dense surrounding gas*. Through continuum multiwavelength and spectral line, high spatial resolution observations, we will try to characterize the emission and nature of the YSOs in a sample of eleven massive star-forming regions, and investigate how the massive newly-born stars can affect their natal cloud. The analysis and comparison between different star-forming tracers will be used to identify and characterize different stages of an evolutionary sequence.

1.4.2 Approach and strategy

We have mentioned that massive stars tend to form in clusters, usually located far from the Sun. Thus, it is necessary to achieve high angular resolutions to study in detail

the different members that can be forming in a cluster. Assuming that massive star-forming regions are on average at distances $\gtrsim 1$ kpc, we need angular resolutions of $\lesssim 3''$, which correspond to spatial scales of ~ 5000 AU (or ~ 0.02 pc), good enough to resolve the different members of the cluster. Single-dish telescopes generally provide angular resolutions of a few tens of arcsec (e.g., Effelsberg-100 m has a primary beam of $40''$ at 8.5 GHz; IRAM-30 m has $11''$ at 230 GHz). However, and fortunately, interferometric observations allow us to achieve the requested angular resolutions: obtaining typical values of ~ 0.1 – $4''$ between 8 GHz and 230 GHz. In this Thesis, we have used some of the most powerful radio interferometers available at present. At centimeter wavelengths we used the Very Large Array (VLA), while at millimeter wavelengths we used the Submillimeter Array (SMA), the Plateau de Bure Interferometer (PdBI), and the Combined Array for Research in Millimeter Astronomy (CARMA).

We focused our observations on the study of the ionized gas, the dust, the dense gas, and the molecular outflow emission. Information of the ionized gas and dust content was obtained by observing the continuum emission at centimeter and millimeter wavelengths, respectively. The dense gas was studied mainly by observing different inversion line transitions of the NH_3 molecule, which is a good molecule to trace the physical conditions of the gas where stars form (see Section 1.3.1). Finally, we studied the outflowing gas by observing some transitions of the CO molecule (or other outflow tracers such as SiO and HCO^+). The capabilities of some of the interferometers used, allowed us to simultaneously study the emission of different high density tracers (such as CH_3CN), typically found in hot molecular cores. In addition, we complemented our observations with archival or already published data at submillimeter and infrared wavelengths (from different radiotelescopes and satellites), and with maser emission information.

1.4.3 Selection of targets

As outlined in previous sections, we want to study the ionized gas content in different massive star-forming regions, and its relation with the environment. Furthermore, high spatial resolutions are required, and interferometers are the only instruments that can be used to achieve our goals. To select the scientific targets of our sample, we searched the surveys of Molinari et al. (1996); Mueller et al. (2002); Sridharan et al. (2002); Palau (2006), for those sources with the following characteristics:

- Distances $\lesssim 2$ kpc, to achieve the requested spatial resolutions (~ 5000 AU) necessary for the individual study of the members of the star-forming clusters.
- Regions with bolometric luminosities $\gtrsim 10^3 L_\odot$ (usually determined from IRAS fluxes), to ensure we are observing intermediate/high-mass protostars.
- Strong millimeter emission, from single-dish observations, favouring the presence of a dust cloud characteristic of an early evolutionary stage.

1. Massive star formation

Table 1.1: Sample of regions selected for the study of this Thesis

Region	d (pc)	L (L_{\odot})	cm-continuum references	mm-continuum references
IRAS 00117+6412	1800	1400	Sánchez-Monge et al. (2008)	Sánchez-Monge et al. (2008)
IRAS 04579+4703	2500	4000	Sánchez-Monge et al. (2008)	Sánchez-Monge et al. (2008)
IRAS 19035+0641	2200	8000	Sridharan et al. (2002)	Beuther et al. (2002b)
G75.78+0.34	3800	100000	Carral et al. (1997)	S. Kurtz (priv. comm.)
IRAS 22134+5834	2600	12600	Sridharan et al. (2002)	Beuther et al. (2002b)
IRAS 22198+6336	760	450	Sánchez-Monge et al. (2008)	Jenness et al. (1995)

- Faint radio continuum emission, suggestive of this emission to come from YSOs in their first evolutionary stages (we tried to avoid the presence of large developed H II regions with strong centimeter emission).

We selected five regions that fulfilled these criteria, and added a sixth region which is located farther (3.8 kpc), but for which we obtained higher angular resolution observations, $\sim 0''.5$, corresponding to spatial scales ~ 2000 AU, similar to those obtained in the other regions. In Table 1.1, we list the six selected regions with their distance, luminosity, and references for the previous centimeter and millimeter data.

1.4.4 Outline of the thesis and status of the different works

This Thesis is the result of different works carried out between 2007 and 2010. During this period, we have observed and studied in detail six massive star-forming regions. In the following we outline the different parts of the present Thesis, and explain what is the status of each work. This Thesis is divided in four main parts, with the first one corresponding to this introduction to massive star formation. In the second and third parts, containing Chapters 2–3 and Chapters 4–7 respectively, we show and discuss the results of each of the six studied regions. In the last part, we compile a sample of 11 massive star-forming regions (our six regions, plus five regions from the literature), and present the general conclusions with the aim of searching for an evolutionary sequence.

Part II, entitled “*Ultracompact H II regions emerging from their natal cloud*”, contains the results of two regions in which a developed UCH II region is affecting the surrounding gas, resulting in a temperature enhancement and linewidth broadening, probably due to the UV radiation field.

In **Chapter 2**, we present the study of the nearby intermediate-mass star-forming region IRAS 00117+6412, harbouring three main YSOs in different evolutionary stages and with different properties. Our radio continuum data reveal two objects with centimeter ionized gas emission in two different stages (a shell-like H II region, and a compact thermal radiojet) with clearly differentiated properties regarding the molecular outflow and dense

gas emission. The results of this work have been presented in a paper entitled *Three intermediate-mass young stellar objects with different properties emerging from the same natal cloud in IRAS 00117+6412* and authored by Palau, A., Sánchez-Monge, Á., Busquet, G., Estalella, R., Zhang, Q., Ho, P. T. P., Beltrán, M. T., and Beuther, H., appeared in the *Astronomy & Astrophysics Journal*, 2010, volume 510, page 5A.

In **Chapter 3**, we have analyzed the radio continuum emission and dense gas emission of the massive star-forming region IRAS 22134+5834. The region is associated with a large infrared cluster, with the brightest infrared source showing centimeter continuum emission and likely tracing a cometary H II region. The cluster is surrounded by several dense gas clumps, likely affected by the presence of the H II region. The radio continuum emission and ammonia data of this region will be presented in two different papers (in preparation). The first one will contain the radio continuum emission from this and a few tens massive star forming regions more, while the second paper will be based on the ammonia emission of this region and six other massive star-forming regions.

Part III, entitled “*Deeply embedded compact radio sources driving outflows*”, contains the results of the remaining four regions, in which a faint radio continuum source is embedded in a dense gas clump and associated with molecular outflow emission.

In **Chapter 4**, we show the results for the intermediate-mass star-forming region in IRAS 22198+6336, which was observed with the VLA, the SMA and the PdBI. The continuum observations at millimeter and centimeter wavelengths, together with the vast set of molecular line emission suggest we have detected one of the few intermediate-mass hot cores known up to date. Part of this work has been published in the letter entitled *IRAS 22198+6336: Discovery of an intermediate-mass hot core* authored by Sánchez-Monge, Á., Palau, A., Estalella, R., Kurtz, S., Zhang, Q., Di Francesco, J., and Shepherd, D., appeared in the *Astrophysical Journal Letters*, 2010, volume 721 page 107. The remaining data will be presented in two forthcoming papers.

In **Chapter 5**, we have studied with high-angular resolution and sensitivity, the ionized gas content within the massive star-forming complex G75.78+0.34 (ON 2N). These observations together with molecular line data tracing thermal gas and maser emission, reveal three major sites of star formation, all of them associated with massive YSOs, being the youngest one a hot molecular core driving a molecular outflow and with two very small compact radio sources deeply embedded in. The results of this work will be published in a paper in preparation entitled *Deciphering the ionized gas content in the massive star forming complex G75.78+0.34*. The molecular data will be presented in a second paper.

In **Chapter 6**, we show high angular resolution VLA (continuum and ammonia) observations carried out toward IRAS 19035+0641. Two radio continuum sources with clearly differentiated properties have been identified, both of them embedded in a large ammonia clump. The results of this work (radio continuum and ammonia emission) will be presented together with the results of IRAS 22134+5834 (see above).

1. Massive star formation

In **Chapter 7**, we present the observations carried out toward the massive star-forming site in IRAS 04579+4703. The radiocontinuum data reveal ionized gas at centimeter wavelengths, embedded in a dust condensation at millimeter wavelengths, and associated with dense gas emission likely tracing rotation. The source is driving a powerful and collimated outflow which is probably deflected due to the presence of high dense condensation.

Finally, in **Part IV** we conclude our work with two chapters. **Chapter 8** contains the compilation of a sample of 11 massive star-forming regions (our six sources plus five sources from the literature) studied in detail in the centimeter and millimeter continuum, in dense gas tracers, and in molecular outflow emission. The general discussion and conclusions are presented in **Chapter 9**. In this chapter we compare the results found toward the sample presented in previous chapter. We compare the properties of the ionized gas, and its relation with the dust, dense gas, and molecular outflow emission searching for correlations that will help to determine the main characteristics of different evolutionary stages, and thus establish an evolutionary sequence.

At the end of this Thesis, there are four Appendices used to analyze the observational data, and available for future works. **Appendix A** is a straightforward manual for inspecting, calibrating and imaging VLA continuum data with AIPS. In **Appendix B**, we summarize the main equations that describe the emission of ionized gas in H II regions, and we provide practical equations and a public code to fit the spectral energy distribution and derive physical parameters of homogeneous and non-homogeneous H II regions. In **Appendix C**, we present the fundamental equations used to determine the dust properties from millimeter continuum emission. Finally, in **Appendix D**, we present the basic theory and equations for the calculation of column densities for any molecule. We include a public code that can be used to estimate the molecular column density, by using the information from the most common molecular spectroscopy databases.

Additionally to the thesis work, I have been involved in other projects that have resulted in different publications. Here I list a complete list of the publications in which I have been involved (i.e., containing those of the thesis work and others projects):

- “*Survey of intermediate/high mass star-forming regions at centimeter and millimeter wavelengths*”

Sánchez-Monge, Á., Palau, A., Estalella, R., Beltrán, M. T., Girart, J. M., 2008, *Astronomy & Astrophysics*, 485, 497

- “*Three intermediate-mass young stellar objects with different properties emerging from the same natal cloud in IRAS 00117+6412*”

Palau, A., **Sánchez-Monge, Á.**, Busquet, G., Estalella, R., Zhang, Q., Ho, P. T. P., Beltrán, M. T., Beuther, H., 2010, *Astronomy & Astrophysics*, 510, 5A

- “*The $\text{NH}_2\text{D}/\text{NH}_3$ ratio toward pre-protostellar cores around the UCHII region in IRAS 20293+3952*”
Busquet, G., Palau, A., Estalella, R., Girart, J. M., **Sánchez-Monge, Á.**, Viti, S., Ho, P. T. P., Zhang, Q., 2010, *Astronomy & Astrophysics Letters*, 517, 6L
- “*IRAS 22198+6336: Discovery of an intermediate-mass hot core*”
Sánchez-Monge, Á., Palau, A., Estalella, R., Kurtz, S., Zhang, Q., Di Francesco, J., Shepherd, D., 2010, *The Astrophysical Journal Letters*, 721, 107L
- “*Young starless cores embedded in the magnetically dominated Pipe Nebula*”
Frau, P., Girart, J. M., Beltrán, M. T., Morata, O., Masqué, J. M., Busquet, G., Alves, F. O., **Sánchez-Monge, Á.**, Estalella, R., Franco, G. A. P., 2010, *The Astrophysical Journal*, 723, 1665
- “ *N_2H^+ depletion in the massive protostellar cluster AFGL 5142*”
Busquet, G., Estalella, R., Zhang, Q., Viti, S., Palau, A., Ho, P. T. P., **Sánchez-Monge, Á.**, 2011, *Astronomy & Astrophysics*, 525, A141
- “*Deuteration as an evolutionary tracer in massive star formation*”
Fontani, F., Palau, A., Caselli, P., **Sánchez-Monge, Á.**, et al. in preparation
- “*Deciphering the ionized gas content in the massive star forming complex G75.78+0.34*”
Sánchez-Monge, Á., Kurtz, S., et al. in preparation
- “*Several outflows coming from the intermediate-mass hot core IRAS 22198+6336*”
Sánchez-Monge, Á., Palau, A., et al. in preparation
- “*Disks, outflows, and hot cores at sub-arcsecond resolution*”
Palau, A., Fuente, A., **Sánchez-Monge, Á.**, et al. in preparation

Part II

Ultracompact H II regions emerging from their natal cloud

2

IRAS 00117+6412: an UCH II region at the border of its natal cloud¹

2.1 General overview

IRAS 00117+6412 (hereafter I00117) is a intermediate/high-mass star-forming region with a bolometric luminosity of $1400 L_{\odot}$ and located at a distance of 1.8 kpc (Molinari et al. 1996). Kumar et al. (2006) reported a cluster of infrared sources in the 2MASS. The brightest infrared source is associated with a compact centimeter source, likely tracing an optically thin UCH II region ionized by a B2 ZAMS star (Sánchez-Monge et al. 2008). The UCH II region, located at the edge of a dusty cloud seen at millimeter wavelengths with the IRAM 30 m, seems to be disrupting and dispersing the gas and dust that surround it (Sánchez-Monge et al. 2008). The dusty cloud, located $\sim 15''$ to the west of the centimeter source, shows some substructure with two main peaks and a dust mass of $21\text{--}30 M_{\odot}$. Interferometric millimeter observations carried out with the PdBI (Palau 2006) show two main millimeter sources, MM1 and MM2, separated $\sim 15''$ and coincident with the main peaks observed in the single-dish map. These two millimeter sources are associated with H₂O maser spots (Cesaroni et al. 1988; Wouterloot et al. 1993) and with CO (2–1) bipolar molecular outflow emission (Zhang et al. 2005; Kim and Kurtz 2006), suggesting they harbour YSOs. However, only one millimeter source is associated with near-IR emission, while the other seems to be a deeply embedded object without any infrared counterpart (Palau 2006; Sánchez-Monge et al. 2008). Thus, I00117 seems to be a perfect star-forming

¹This Chapter is based on the results published in Palau, Sánchez-Monge et al. 2010, A&A, 510, 5A.

complex to study intermediate/high-mass YSOs with different properties. Regarding the dense gas emission, Molinari et al. (1996) report the detection of NH₃ (1,1) and (2,2) emission in single-dish. Palau (2006) study the region in the N₂H⁺ (1–0) transition with the PdBI. The N₂H⁺ emission resembles the emission from the dust cloud, with two main condensations associated with MM1 and MM2, and showing a velocity gradient in the southeast-northwest direction.

In this Chapter, we present high-sensitivity radio interferometric observations in the continuum at centimeter and millimeter wavelengths, and in different molecular transitions tracing the dense gas and molecular outflow emission.

2.2 Observations

2.2.1 Very Large Array

I00117 was observed with the Very Large Array (VLA²) at 6.0 and 3.6 cm with 5–8 EVLA antennae in the array (which was in its C configuration). The phase center of these observations was $\alpha(\text{J2000}) = 00^{\text{h}}14^{\text{m}}27^{\text{s}}.725$, and $\delta(\text{J2000}) = +64^{\circ}28'46''.17$. The integration time was about 45 minutes at both wavelengths. Absolute flux calibration was achieved by observing the quasar 3C48, with an adopted flux density of 5.48 Jy at 6 cm, and 3.15 Jy at 3.6 cm. The data reduction followed the VLA standard guidelines for calibration and imaging, using the NRAO package AIPS. Images were performed using different weightings. The robust parameter of Briggs (1995) was set equal to 1 and 3 (almost natural) respectively at 6 and 3.6 cm. In Table 2.1, we list more details of the observations. Searching the archive of the VLA, we found B-array data at 3.6 cm and C-array data at 1.3 cm observed in 1992 (project AC295). The data were reduced with the standard AIPS procedures for high frequency data.

Observations at 7 mm (together with NH₃ observations, see Busquet 2010 for details) were carried out with 9 EVLA antennas in the array. In order to minimize the effects of atmospheric fluctuations, we used the technique of *fast switching* (Carilli and Holdaway 1997) between the source and the phase calibrator over a cycle of 120 seconds, with 80 seconds spent on the target and 40 seconds on the calibrator. The on-source integration time was about 1.8 hours. Absolute flux and phase calibrations were achieved by observing the quasars 3C286 (1.45 Jy) and 0102+584 (see Table 2.1). Data reduction was performed following the VLA guidelines for the calibration of high frequency data, using the NRAO package AIPS. The image was constructed using natural weighting and tapering the *uv*-data at 50 k λ to increase the signal-to-noise ratio. In Table 2.1, we list the synthesized beams and rms noise levels for each image.

²The Very Large Array (VLA) is operated by the National Radio Astronomy Observatory (NRAO), a facility of the National Science Foundation operated under cooperative agreement by Associated Universities, Inc.

Table 2.1: Main continuum observational parameters of IRAS 00117+6412

λ (cm)	Project VLA conf.	Epoch of Observation	Gain cal. / Bootstr. Flux ^a	Flux cal.	Beam (" \times ")	P.A. ($^\circ$)	Rms ^b
6.0	AB1217 C	2006 Oct 27	0102+584 / 2.90(1)	3C48	5.2×4.0	-4	30
3.6	AC295 B	1992 Jan 06	2230+697 / 0.42(2)	3C48	1.0×0.8	-66	100
3.6	AB1217 C	2006 Oct 27	0102+584 / 3.17(1)	3C48	3.1×2.7	+3	20
3.6	AP476 D	2004 Jul 13	0102+584 / 1.89(1)	3C48	14.9×8.5	+76	40
1.3	AC295 C	1992 May 25	0228+673 / 1.77(2)	3C48	1.3×1.0	+50	600
1.3	AP476 C	2004 Jul 13	0102+584 / 2.26(2)	3C48	5.9×4.5	-21	70
0.7	AB1217 B	2007 May 12	0102+584 / 3.08(5)	3C286	4.0×3.0	+64	170
0.32 ^c	PdBI CD	2004 Oct+Dec	0212+735 / 1.15(20)	MWC349	4.3×3.4	+61	180
0.12 ^c	PdBI CD	2004 Oct+Dec	0212+735 / 0.62(20)	MWC349	1.5×1.2	+58	1000
0.13	SMA	2007 Jun 28	0102+584 / 2.58(20)	Uranus	3.2×2.0	+45	800

^a Bootstrapped flux in Jy. In parenthesis: the percentage of error in the flux.

^b Rms noise level in $\mu\text{Jy beam}^{-1}$.

^c Observations from Palau (2006) that will also be used in this chapter.

2.2.2 Submillimeter Array

The Submillimeter Array (SMA³; Ho et al. 2004) in the compact configuration was used to observe the 1.3 mm continuum emission and the $^{12}\text{CO}(2-1)$ molecular transition line (centered at 230.538 GHz, upper sideband) on 2007 June 28. The phase center of the observations was $\alpha(\text{J2000}) = 00^{\text{h}}14^{\text{m}}25^{\text{s}}.80$, and $\delta(\text{J2000}) = +64^\circ28'43''.0$, and the projected baselines ranged from 9 to 78 k λ (12–101 m). System temperatures ranged between 80 and 200 K. The zenith opacities, measured with the NRAO tipping radiometer located at the Caltech Submillimeter Observatory, were good during the track, with $\tau(225 \text{ GHz}) \sim 0.08$. The correlator, with a bandwidth of 1.968 GHz, was set to the standard mode, which provided a spectral resolution of 0.8125 MHz (or 1.06 km s $^{-1}$ per channel) across the full bandwidth. The FWHM of the primary beam at 230 GHz is $\sim 56''$. The flagging and calibration of the data were done with the MIR-IDL⁴ package. The passband response was obtained from observations of 3C454.3. The baseline-based calibration of the amplitudes and phases was performed using the sources 0102+584 and 0014+612. Flux calibration was set by using Uranus, and the uncertainty in the absolute flux density scale was $\sim 20\%$. Imaging and data analysis were conducted using the standard procedures in MIRIAD (Sault et al. 1995) and AIPS (see Table 2.1 for details). The continuum was obtained by averaging all the line-free channels of the upper sideband and the lower sideband.

³The SMA is a joint project between the Smithsonian Astrophysical Observatory and the Academia Sinica Institute of Astronomy and Astrophysics, and is funded by the Smithsonian Institution and the Academia Sinica.

⁴The MIR cookbook by Charlie Qi can be found at <http://cfa-www.harvard.edu/~cqi/mircook.html>

2. IRAS 00117+6412: an UCH II region at the border of its natal cloud

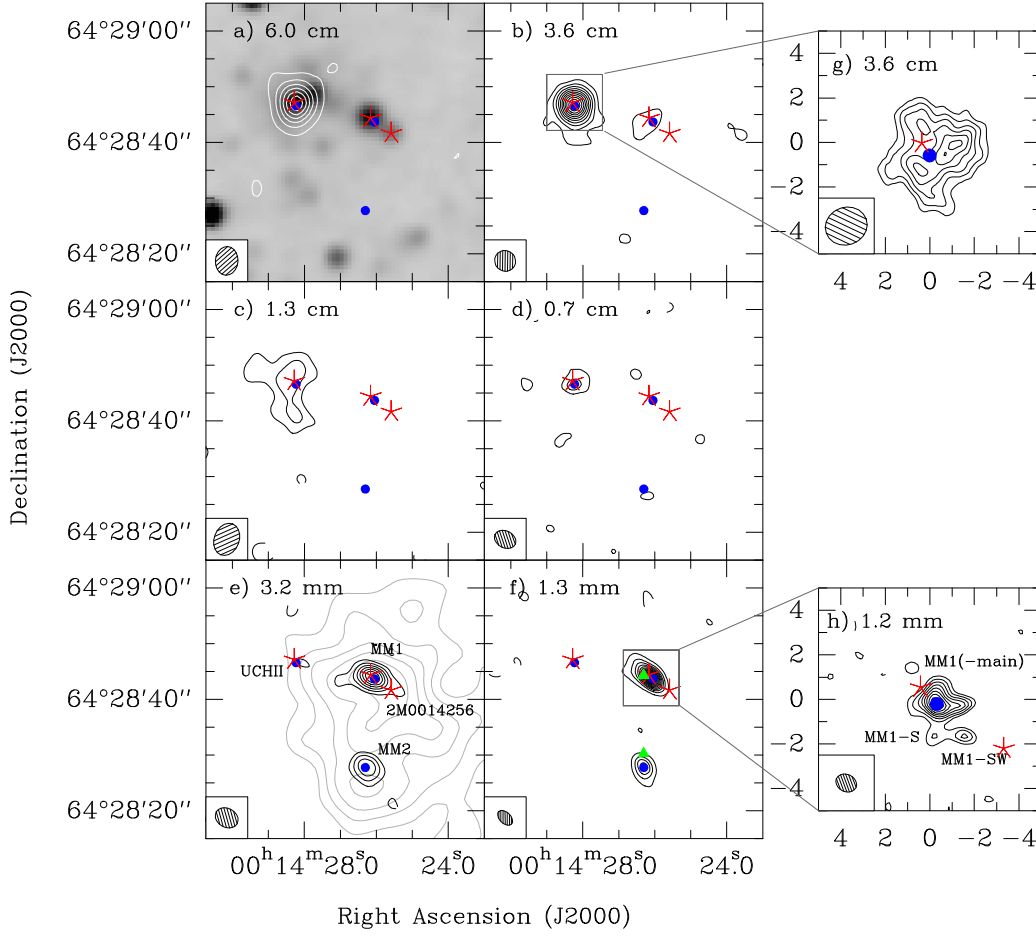


Figure 2.1: IRAS 00117+6412 continuum maps. (a): Grey-scale: 2MASS K_s -band infrared emission. Contours: VLA-C 6 cm continuum emission. Levels are -3 , and 3 to 33 in steps of 6 , times $0.03 \text{ mJy beam}^{-1}$. (b): VLA-CD 3.6 cm continuum emission. Levels are -3 , and 3 to 30 in steps of 3 , times $0.03 \text{ mJy beam}^{-1}$. (c): VLA-D 1.3 cm continuum emission. Levels are -3 , 3 , and 6 times $0.07 \text{ mJy beam}^{-1}$. (d): VLA-D 0.7 cm continuum emission. Levels are -3 , 3 , and 6 times $0.17 \text{ mJy beam}^{-1}$. (e): Black contours: PdBI 3.2 mm continuum emission. Levels are -3 , and 3 to 21 in steps of 3 , times $0.19 \text{ mJy beam}^{-1}$. Grey contours: IRAM 30 m continuum emission tracing the ‘dusty cloud’, from Sánchez-Monge et al. (2008). Levels are 4 , 6 , 8 , 10 , and 12 times the rms of the map, 8 mJy beam^{-1} . (f): SMA 1.3 mm continuum emission. Levels are -3 , and 3 to 69 in steps of 6 , times $0.62 \text{ mJy beam}^{-1}$. Green triangles indicate the position of the H_2O masers in the region (Cesaroni et al. 1988). (g): VLA-BCD 3.6 cm continuum emission. Levels are 3 to 8 in steps of 1 , times $0.05 \text{ mJy beam}^{-1}$. (h): PdBI 1.2 mm continuum emission. Levels are -3 , 3 to 11 in steps of 1 , times $1.1 \text{ mJy beam}^{-1}$. In all panels, five-point red stars indicate the position of 2MASS sources associated with the main centimeter and millimeter sources. Blue dots indicate the position of the UCH II region, MM1-main, and MM2, in order of descending declination. Synthesized beams are shown at the bottom-left corner of each panel, and correspond to those indicated in Table 2.2. Figure from Palau et al. (2010).

2.3 Continuum results

2.3.1 Centimeter continuum emission

We detected centimeter radio continuum emission at all wavelengths. In Figure 2.1a we show the 6 cm continuum emission of the region. The field is dominated by a strong and compact source associated with the brightest infrared source in the field, which is the counterpart of the UCH II region detected at 3.6 cm by Sánchez-Monge et al. (2008). Additionally, the wide field of the VLA at 6 cm allows us to detect two unresolved sources to the north and east of the UCH II region. The northern one, with the coordinates of $\alpha(\text{J2000.0}) = 00^{\text{h}}14^{\text{m}}03^{\text{s}}.21$, and $\delta(\text{J2000.0}) = +64^{\circ}32'26''.5$, has a primary beam corrected flux density of 1.1 ± 0.2 mJy. The eastern one, with the coordinates of $\alpha(\text{J2000.0}) = 00^{\text{h}}14^{\text{m}}57^{\text{s}}.69$, and $\delta(\text{J2000.0}) = +64^{\circ}28'49''.6$, has a primary beam corrected flux density of 0.44 ± 0.09 mJy. Both sources are outside the region shown in Figure 2.1a.

At 3.6 cm, we improved the angular resolution of previous observations by a factor of five. These observations reveal two sources in the field: an eastern source coincident with the UCH II region, and a second and fainter source located $\sim 15''$ to the west. Figure 2.1b shows the resulting image after combining the new VLA C-configuration observations with previous VLA D-configuration observations (Sánchez-Monge et al. 2008). Since the combined dataset has a better uv -coverage, we recovered faint structure to the south of the UCH II region similar to the double-source structure detected at 1.3 cm by Sánchez-Monge et al. (2008). The faint source to the west of the UCH II region is coincident with the main 1.2 mm peak detected with the IRAM 30 m telescope (Sánchez-Monge et al. 2008). By combining the 3.6 cm VLA-C and VLA-D datasets with archival VLA-B data, we improved the angular resolution up to $\sim 1.8''$. With this angular resolution, the faint source $15''$ to the west of the UCH II region is marginally detected, and the UCH II region shows a shell morphology with three main peaks and with the 2MASS source falling at the center of the peaks (see Figure 2.1g). In Figure 2.1c we show, for completeness' sake, the 1.3 cm continuum emission map from Sánchez-Monge et al. (2008). At 7 mm we detected one compact source at the position of the UCH II region (Figure 2.1d).

In Table 2.2, we summarize the main results of the sources detected in the region at different wavelengths. The Table gives for each source the coordinates, peak intensity, flux density, deconvolved size and position angle.

2.3.2 Millimeter continuum emission

Figure 2.1e shows the 3.2 mm PdBI continuum emission of the region. There are two compact strong sources at 3.2 mm: the strongest source, MM1, lying $\sim 15''$ to the west of the UCH II region; and the other source, MM2, being located $\sim 15''$ to the south of MM1. The peak of MM1 is associated with the faint 3.6 cm source shown in Figure 2.1b and with a near-infrared 2MASS source. MM1 is partially extended to the southwest, also spatially

2. IRAS 00117+6412: an UCH II region at the border of its natal cloud

Table 2.2: Multiwavelength results for the YSOs in IRAS 00117+6412

λ (cm)	Beam ('' \times '')	P.A. ($^\circ$)	Rms ^b	$I_\nu^{\text{peak a}}$ (mJy beam ⁻¹)	S_ν^{a} (mJy)	Deconv. Size ('' \times '')	P.A. ($^\circ$)
UCH II $\alpha(J2000.0) = 00^{\text{h}}14^{\text{m}}28^{\text{s}}.23$ $\delta(J2000.0) = +64^\circ28'46''.6$							
6.0	5.2×4.0	-4	30	1.21 ± 0.03	1.72 ± 0.08	$3.1 \times 2.7 \pm 0.5$	95 ± 50
3.6	3.8×3.7	+45	30	1.03 ± 0.03	1.88 ± 0.09	$3.7 \times 3.1 \pm 0.4$	10 ± 60
3.6	1.9×1.7	-70	50	0.43 ± 0.05	1.62 ± 0.16	$3.9 \times 3.7 \pm 0.4$	180 ± 60
1.3 ^c	5.9×4.5	-21	70	0.59 ± 0.07	1.7 ± 0.2	$5.9 \times 5.0 \pm 2.0$	120 ± 50
0.7	4.0×3.0	+64	170	1.35 ± 0.17	1.4 ± 0.3	$2.7 \times 0.0 \pm 1.2$	150 ± 30
0.32	4.3×3.4	+61	180	...	< 1
0.13	3.2×2.0	+45	600	...	< 4
0.12 ^d	1.5×1.2	+58	1000	...	< 25
MM1 $\alpha(J2000.0) = 00^{\text{h}}14^{\text{m}}26^{\text{s}}.05$ $\delta(J2000.0) = +64^\circ28'43''.7$							
6.0	5.2×4.0	-4	30	...	< 0.12
3.6	3.8×3.7	+45	30	0.14 ± 0.03	0.17 ± 0.07	$6.4 \times 3.0 \pm 2.0$	120 ± 30
3.6	1.9×1.7	-70	50	0.21 ± 0.05	0.15 ± 0.06	$4.0 \times 2.2 \pm 1.5$	160 ± 50
1.3	5.9×4.5	-21	70	...	< 0.27
0.7	4.0×3.0	+64	170	...	< 0.69
0.32	4.3×3.4	+61	180	4.16 ± 0.19	5.1 ± 0.9	$3.2 \times 0.0 \pm 0.4$	75 ± 10
0.13	3.2×2.0	+45	600	51 ± 1	71 ± 14	$2.4 \times 1.0 \pm 0.3$	50 ± 10
0.12 ^d	1.5×1.2	+58	1000	21 ± 1	65 ± 10	$2.9 \times 1.6 \pm 0.4$	25 ± 10
MM2 $\alpha(J2000.0) = 00^{\text{h}}14^{\text{m}}26^{\text{s}}.31$ $\delta(J2000.0) = +64^\circ28'27''.8$							
6.0	5.2×4.0	-4	30	...	< 0.12
3.6	3.8×3.7	+45	30	...	< 0.12
3.6	1.9×1.7	-70	50	...	< 0.21
1.3	5.9×4.5	-21	70	...	< 0.27
0.7	4.0×3.0	+64	170	...	< 0.69
0.32	4.3×3.4	+61	180	2.8 ± 0.2	3.2 ± 0.6	$1.6 \times 1.0 \pm 1.0$	160 ± 50
0.13	3.2×2.0	+45	600	19 ± 1	24 ± 5	$2.0 \times 0.0 \pm 0.5$	170 ± 20
0.12 ^d	1.5×1.2	+58	1000	20 ± 5	50 ± 13	$3.5 \times 1.1 \pm 0.8$	140 ± 30

^a Primary beam corrected. Error in intensity is σ . Error in flux density has been calculated as $\sqrt{(\sigma\sqrt{\theta_{\text{source}}/\theta_{\text{beam}}})^2 + (\sigma_{\text{flux-scale}})^2}$, where σ is the rms noise level of the map, θ_{source} and θ_{beam} are the size of the source and the beam respectively, and $\sigma_{\text{flux-scale}}$ is the error in the flux scale, which takes into account the uncertainty on the calibration applied to the flux density of the source ($S_\nu \times \%\text{uncertainty}$).

^b Rms noise level in $\mu\text{Jy beam}^{-1}$.

^c Data from Sánchez-Monge et al. (2008). Deconvolved size and P.A. correspond to the component VLA3 from Sánchez-Monge et al. (2008), which is the component associated with the easternmost 2MASS source shown in Figure 2.1c.

^d 1.2 mm PdBI continuum map done with natural weighting; for flux densities and coordinates for the different subcondensations detected in the uniform-weighted map, see Table 2.3.

Table 2.3: Parameters of the 1.2 mm subcondensations associated with MM1 from the uniform-weighted PdBI map^a

Source	Position		I_{ν}^{peakb} (mJy beam ⁻¹)	S_{ν}^{b} (mJy)	Deconv. Size ^c ('' × '')	P.A. ^c (°)	$M_{\text{env}}^{\text{d}}$ (M_{\odot})
	α (J2000)	δ (J2000)					
MM1-main ^e	00 14 26.051	64 28 43.69	12.8 ± 1.1	39 ± 6	$3.2 \pm 1.8 \times 0.3 \pm 0.3$ $2.1 \pm 0.9 \times 1.0 \pm 0.3$	-89 ± 5 $+3 \pm 13$	1.46
MM1-S	00 14 26.065	64 28 42.26	4.7 ± 1.1	5.4 ± 1.4	$1.6 \pm 0.5 \times 0.8 \pm 0.2$	-30 ± 30	0.20
MM1-SW	00 14 25.861	64 28 42.25	5.9 ± 1.1	6.4 ± 1.5	$1.3 \pm 0.4 \times 0.2 \pm 0.1$	$+85 \pm 9$	0.24

^a Synthesized beam of the uniform-weighted map is $0''.96 \times 0''.77$ with P.A. = $+66^\circ$. The rms noise level of the map is 1.11 mJy beam⁻¹.

^b Primary beam corrected. Error in intensity and flux density as in Table 2.2.

^c Deconvolved sizes and P.A. obtained from a fit with two Gaussian for MM1-main, and one single Gaussian for MM1-S and MM1-SW.

^d Masses derived assuming a dust mass opacity coefficient at 1.2 mm of 0.9 g cm^{-1} (agglomerated grains with thin ice mantles in cores of densities $\sim 10^6 \text{ cm}^{-3}$, Ossenkopf and Henning 1994), and a dust temperature of 30 K. The uncertainty in the masses due to the opacity law is estimated to be of a factor of 2.

^e Throughout all the text, we refer to MM1-main as MM1, for simplicity.

coincident with a second infrared source detected in the 2MASS (J00142558+6428416), hereafter 2M0014256 (cf. Figure 2.1e). Note that the K_s -2MASS image shows no infrared emission toward MM2 (cf. Figure 2.1a).

The SMA map at 1.3 mm shows two compact sources clearly associated with MM1 and MM2 (Figure 2.1f). The 1.2 mm maps from the PdBI, with an angular resolution three times better than the SMA images, but only covering the region of MM1 within the primary beam of $22''$, show that this source splits up into at least three subcondensations: a compact core, MM1-main, elongated in the east-west direction and with faint extensions towards the north and the south; a faint 4σ source about $1''$ to the south of MM1-main, MM1-S; and a faint source at 5σ located $\sim 2''$ to the southwest of MM1-main, MM1-SW (see Figure 2.1h and Table 2.3). We note that the PdBI 1 mm and SMA 1 mm flux densities are completely consistent, if we take into account that the PdBI is filtering out emission at smaller scales than the SMA. In the following we will refer to MM1-main as MM1.

In Table 2.2, we summarize the main results of the sources detected in the region at millimeter wavelengths. For both MM1 and MM2, we estimated the mass of the dust component assuming dust temperatures of 30 K and 20 K for MM1 and MM2, respectively (as a first approximation, since MM1 is associated with near-infrared emission, while MM2 is not), and a dust mass opacity coefficient at 1.3 mm of 0.9 g cm^{-1} (agglomerated grains with thin ice mantles in cores of densities $\sim 10^6 \text{ cm}^{-3}$, Ossenkopf and Henning 1994). With these assumptions, we estimated a mass for MM1 of $\sim 3.0 M_{\odot}$, and a mass for MM2 of $\sim 1.7 M_{\odot}$ (both derived from the (SMA) flux at 1.3 mm given in Table 2.2). In order to properly estimate the spectral index between 3.2 mm (PdBI) and 1.3 mm (SMA), we made the SMA image using the same uv -range as the PdBI data (9–72 k λ). By measuring

2. IRAS 00117+6412: an UCH II region at the border of its natal cloud

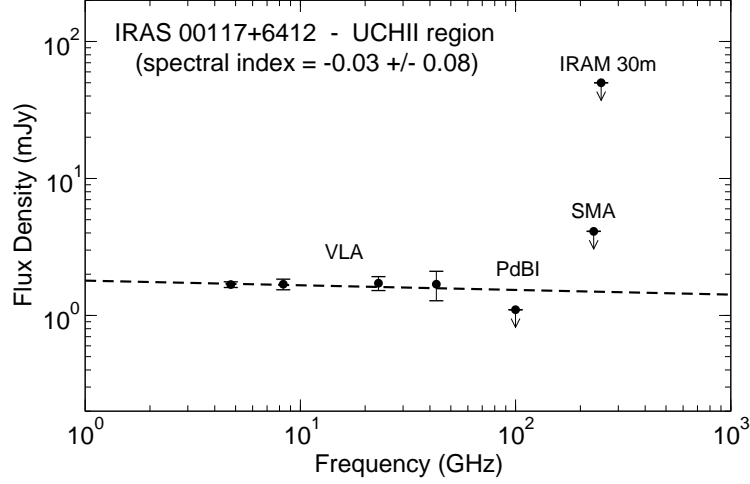


Figure 2.2: Spectral energy distribution in the centimeter and millimeter range for the UCH II region. Dashed line: free-free optically thin fit with a spectral index of -0.03 ± 0.08 . Figure from Palau et al. (2010).

the flux densities in the maps in the common uv -range, we obtained a spectral index of 3.1 ± 0.2 for MM1 and 2.7 ± 0.2 for MM2. Finally, we estimated the fraction of missing flux resolved out by the SMA at 1.3 mm by comparing the total flux of MM1 plus MM2 with the flux density measured with the IRAM 30 m Telescope of 1.2 Jy (Sánchez-Monge et al. 2008), and found that the fraction of flux filtered out by the SMA is 92% (see Appendix of Palau et al. (2010), for details in the calculations).

2.3.3 Spectral energy distribution

The centimeter range (from 6 up to 0.7 cm) of the spectral energy distribution of the UCH II region can be fitted assuming free-free optically thin emission from ionized gas with a spectral index (α , $S_\nu \propto \nu^\alpha$) of -0.03 ± 0.08 (see Figure 2.2). We calculated the physical parameters of the H II region and found a size of 0.03 ± 0.01 pc, an electron density of $2 \times 10^3 \text{ cm}^{-2}$, an emission measure of $1.1 \times 10^5 \text{ cm}^{-6} \text{ pc}$, and a mass of ionized gas of $8.9 \times 10^{-4} M_\odot$. Such an H II region can be ionized by a B2 ZAMS star, with a flux of ionizing photons of $4.4 \times 10^{44} \text{ s}^{-1}$ (Panagia 1973). Regarding the centimeter emission coming from MM1, we only have a detection at 3.6 cm, and thus we cannot measure the spectral index. However, we can estimate a range of possible spectral indices, which is $-0.3 < \alpha_{\text{MM1}} < 1.1$, consistent with thermal free-free emission from ionized gas. More sensitive observations at different wavelengths are necessary to confirm the value of the spectral index in the centimeter range for the MM1 source.

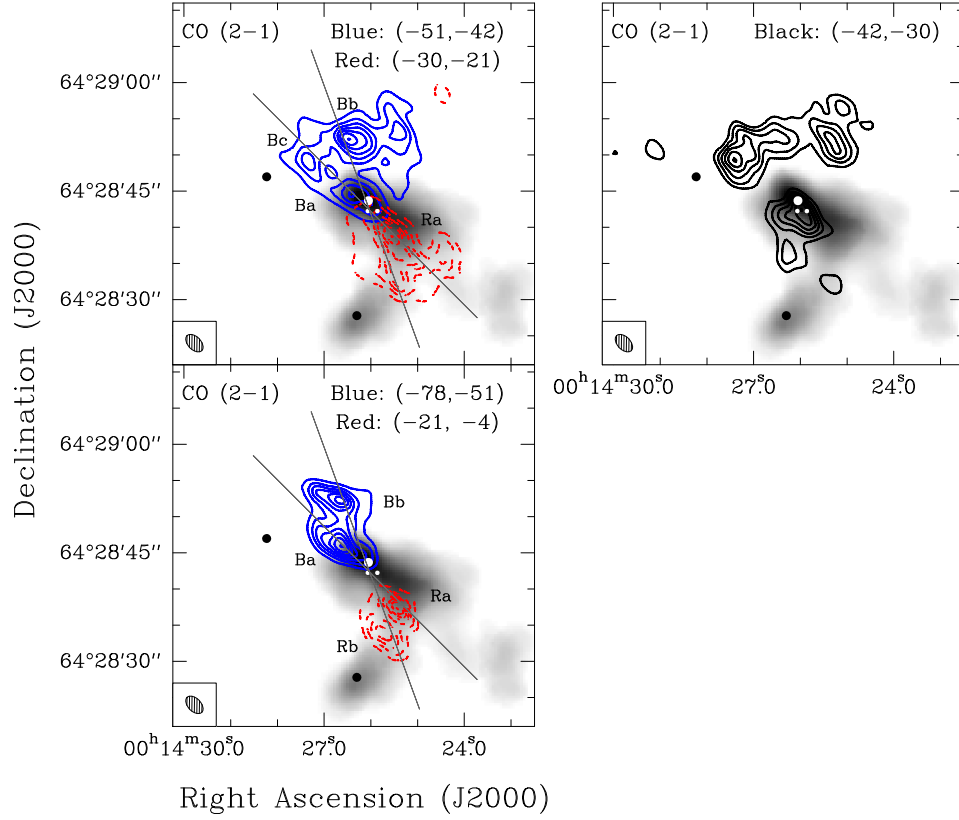


Figure 2.3: *Right*: Contours: CO (2–1) moment-zero map integrated for systemic velocities (between -6 and $+6$ km s^{-1} with respect to the systemic velocity, -36.3 km s^{-1}). Levels start at 24%, increasing in steps of 15% of the peak intensity, 22.9 $\text{Jy beam}^{-1} \text{ km s}^{-1}$. *Top-left*: Idem for moderate velocities. Blue (solid) contours: emission in the velocity range from -6 to -15 km s^{-1} with respect to the systemic velocity. Red (dashed) contours: emission in the velocity range from $+6$ to $+15$ km s^{-1} with respect to the systemic velocity. Levels start at 9%, increasing in steps of 15% of the peak intensity, 32.7 $\text{Jy beam}^{-1} \text{ km s}^{-1}$ and 25.8 $\text{Jy beam}^{-1} \text{ km s}^{-1}$ for the blue and red-shifted velocities, respectively. *Bottom-left*: Idem for high velocities. Blue (solid) contours: emission in the velocity range from -15 km s^{-1} to most negative values with respect to the systemic velocity. Red (dashed) contours: emission in the velocity range from $+15$ km s^{-1} to most positive values with respect to the systemic velocity. Levels start at 9%, increasing in steps of 15% of the peak intensity, 13.0 $\text{Jy beam}^{-1} \text{ km s}^{-1}$ and 11.1 $\text{Jy beam}^{-1} \text{ km s}^{-1}$ for the blue and red-shifted velocities, respectively. In all panels, grey scale: N_2H^+ zero-order moment map; grey solid lines indicate the possible orientation (PA= 45° and 20°) of the outflow(s). Black/white dots indicate the position of the UCH II region, MM1 (main, south, and southwest), and MM2. The synthesized beam, $2''.92 \times 1''.78$ at P.A. = $44^\circ.7$, is shown in the bottom left corner of each panel. Figure from Palau et al. (2010).

2. IRAS 00117+6412: an UCH II region at the border of its natal cloud

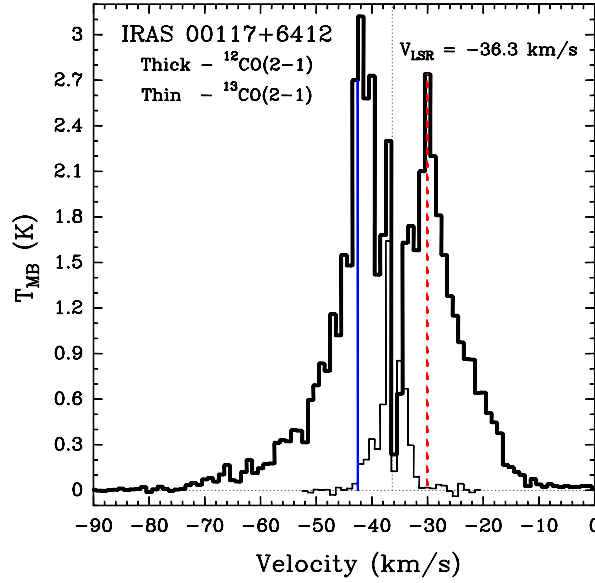


Figure 2.4: Spectrum of the ^{12}CO (2-1) (thick line) and ^{13}CO (2-1) (thin line) emission in the IRAS 00117+6412 region, averaging over all emission of outflow lobes. Blue (solid) and red (dashed) vertical lines indicate the range of velocities (red wing: -30.0 km s^{-1} up to -8.0 km s^{-1} , and blue wing: -72.0 km s^{-1} up to -42.5 km s^{-1}) used to estimate the parameters of the outflow. Figure from Palau et al. (2010).

2.4 Molecular results

2.4.1 Molecular outflow gas

Interferometric CO (2-1) maps reveal emission spanning a wide range of velocities, from -70 up to -14 km s^{-1} with the systemic velocity at -36.3 km s^{-1} (see Figure 2.3). Blueshifted emission appears in different clumps toward the north and northeast of MM1, while redshifted emission appears toward the southwest of MM1, suggesting a bipolar structure centered on MM1.

The spectrum of the region, averaged over all the emission of outflow lobes, is shown in Fig. 2.4, together with a preliminary spectrum of ^{13}CO (2-1). The CO spectrum shows a dip from -6 up to $+6 \text{ km s}^{-1}$ with respect to the systemic velocity, which could be due to self-absorption by cold foreground gas or opacity effects, as the dip is coincident with the peak of the ^{13}CO line. We note that the dip could be partially produced by the missing short-spacing information in the interferometer data as well. In order to make a rough estimate of the fraction of flux filtered out by the SMA (due to the lack of uv sampling at spacings smaller than $9 \text{ k}\lambda$), we compared the single-dish spectrum (from Zhang et al. 2005) at certain velocities with the SMA spectrum (extracted from

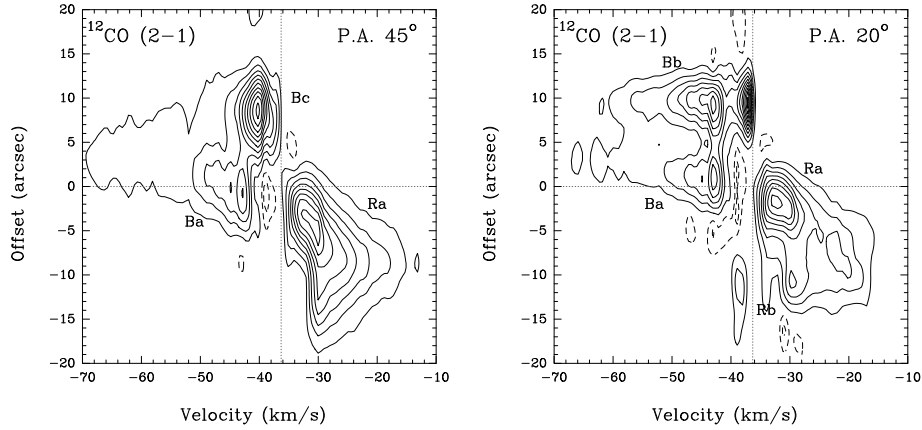


Figure 2.5: *Left*: CO (2–1) pv-plot in the northeast-southwest direction with $\text{P.A.} = 45^\circ$, at the offset position ($3''.36$; $0''.96$), with respect to the phase center. *Right*: CO (2–1) pv-plot in the north-south direction with $\text{P.A.} = 20^\circ$, at the offset position ($2''.07$; $-0''.04$), with respect to the phase center. For both panels, contours are -12% , -6% , 6% to 96% in steps of 10% of the peak intensity, $3.63 \text{ Jy beam}^{-1}$ for the plot at $\text{P.A.} = 45^\circ$, and $3.59 \text{ Jy beam}^{-1}$ for the plot at $\text{P.A.} = 20^\circ$. Both pv-plots have been convolved with a gaussian of $5''.0 \times 2''.0$, at $\text{P.A.} = 135^\circ 0$ and $\text{P.A.} = 110^\circ 0$ respectively. The labeled clumps are identified in Figure 2.3, see Palau et al. (2010) for more details.

the channel maps convolved to the single-dish beam, of $30''$) at the position of the IRAS source. The missing flux is around 99% for the systemic velocities, indicating that at these velocities the CO emission mainly comes from structures much larger than $\sim 10''$, which is the largest angular scale observable by an interferometer whose shortest baseline is $\sim 9 \text{ k}\lambda$ (see Appendix of Palau et al. 2010). On the other hand, the missing flux decreases as one moves to higher velocities. For example, the fraction of missing flux goes down to 50% at -7 and 5 km s^{-1} (with respect to the systemic velocity) for the blueshifted and redshifted sides, respectively; and the SMA recovers all the single-dish flux at -13 and 7 km s^{-1} with respect to the systemic velocity. This indicates that the high-velocity CO (2–1) emission has a characteristic source size $\lesssim 10''$.

In Figure 2.3, we show the zero-order moment maps of the CO emission integrated over three different velocity ranges: (1) systemic velocities from -6 to $+6 \text{ km s}^{-1}$ with respect to the systemic velocity (Figure 2.3 right panel), (2) moderate velocities from -6 to -15 km s^{-1} , and from $+6$ to $+15 \text{ km s}^{-1}$ with respect to the systemic velocity (Figure 2.3 top-left panel), and (3) high velocities from -15 km s^{-1} to most negative velocities, and from $+15 \text{ km s}^{-1}$ to most positive velocities with respect to the systemic velocity (Figure 2.3 bottom-left panel). At systemic velocities the emission appears concentrated in two main structures, a clump associated with the N_2H^+ MM1 ridge (grey scale in the image; see next sections), and a multi-peaked-arc located to the north of MM1, just bor-

2. IRAS 00117+6412: an UCH II region at the border of its natal cloud

Table 2.4: Physical parameters of the outflows driven by IRAS 00117+6412^a

Outflow/lobe (1)	t_{dyn} (2)	size (3)	N_{mol} (4)	M_{out} (5)	\dot{M}_{out} (6)	P_{out} (7)	\dot{P}_{out} (8)	E_{kin} (9)	L_{mech} (10)
Outflow A — P.A.=40°									
CO (2–1) – red	3600	12×9	3.1×10^{16}	0.05	15	1.2	33	2.6	0.46
CO (2–1) – blue	3300	14×7	2.9×10^{16}	0.05	14	1.4	42	4.2	0.85
CO (2–1)	3500	...	6.0×10^{16}	0.10	29	2.6	75	6.7	1.31

^a Parameters are calculated for an inclination with respect to the plane of the sky equal to 0°, and are corrected for opacity effects (following the expressions given in Palau et al. 2007b). Notes and units for each column: (1) blue/red lobe for each molecular species; (2) dynamical age in years; (3) size of the lobe in arcsec; (4) column density of the molecule in cm^{-2} ; (5) outflowing mass in M_{\odot} ; (6) rate of the outflowing mass in $10^{-6} M_{\odot} \text{ yr}^{-1}$; (7) momentum of the outflow in $M_{\odot} \text{ km s}^{-1}$; (8) outflow momentum rate in $10^{-5} M_{\odot} \text{ km s}^{-1} \text{ yr}^{-1}$; (9) kinetic energy in 10^{42} erg ; and (10) mechanical luminosity in L_{\odot} .

dering the N_2H^+ emission. At moderate and high velocities, which are less affected by the missing short spacings in the interferometric data, the emission has a bipolar structure centered near the position of MM1 and is elongated in the northeast-southwest direction (see Figure 2.3 left panels). Note that the position angles of the high-velocity CO emission are almost perpendicular to the direction of the N_2H^+ velocity gradient, found at $\sim 130^\circ$ (see next Section).

We performed different position-velocity (pv) plots close to MM1 in cuts with PA=45° and PA=20° (see Figure 2.5): the two directions indicated in Figure 2.3. Both pv-plots have been convolved with a Gaussian ($5'' \times 2''$ at PA=135° and 110°, respectively). In both plots, positive and negative positions correspond respectively to northeastern and southwestern positions with respect to MM1. In the first cut (45°) we can distinguish a strong velocity gradient from clump Ra to clump Ba (see Figures 2.3 and 2.5 for clump identification), with velocities increasing with distance, following a Hubble-law pattern (up to 34 km s^{-1} with respect to the systemic velocity in the case of clump Ba). We note that in the cut at PA=45°, the clump Bc shows moderate velocity emission of up to 14 km s^{-1} with respect to the systemic velocity. Regarding the pv plot at PA=20°, the redshifted emission and the blueshifted clump Ba also follow a Hubble-law, as in the cut at 45°.

We calculated the energetics of the outflow for each blue and red lobe separately (for the blue lobe we included both clumps Ba and Bb), assuming that all the emission comes from a single outflow, and listed the values in Table 2.4. The expressions used to calculate the outflow CO column density, $N(\text{CO})$, from the transition $J \rightarrow J - 1$, and the outflow mass, M_{out} , are given in Palau et al. (2007b). We adopted an opacity in the line wings of ~ 2 (from preliminary ^{13}CO data). For the red lobe we integrated from -30 to -8 km s^{-1} ,

and for the blue lobe from -72 to -42.5 km s $^{-1}$. The dynamical timescale of the outflow, t_{dyn} , was derived by dividing the size of each lobe by the maximum velocity reached in the outflow with respect to the systemic velocity (28.3 km s $^{-1}$ for the red lobe, and 35.7 km s $^{-1}$ for the blue lobe).

2.4.2 Molecular dense gas

Palau (2006) and Palau et al. (2010) studied the dense gas emission toward I00117 by mapping the N $_2$ H $^+$ (1–0) molecular transition with the PdBI, while Busquet (2010) studied the dense gas emission coming from the NH $_3$ (1,1) and (2,2) inversion line transitions. In Figure 2.6 top panels, we show the zero-order moment (intensity) maps of these dense gas tracers. The NH $_3$ and N $_2$ H $^+$ emission consists of two main clumps named MM1 ridge and MM2. The MM1 ridge, with a size of $\sim 20''$ (~ 0.2 pc at a distance of 1.8 kpc), is elongated in the northeast-southwest direction, i.e., the same direction as the CO (2–1) molecular outflow (cf. Figure 2.3). The N $_2$ H $^+$ main peak (in MM1 ridge) is spatially coincident with the centimeter/millimeter source MM1. This dense core, is resolved into two main components when observed in the ammonia emission. The MM2 clump, located $\sim 20''$ to the south of MM1, is elongated in the southeast-northwest direction, with a length of $\sim 10''$. This clump, coincident with the millimeter source MM2, shows a double peak in the ammonia (1,1) transition. It is worth noting that the MM2 clump is fainter in the (2,2) transition than the MM1 clump. The energy level of the NH $_3$ (2,2) transition is higher than the energy levels of the NH $_3$ (1,1) and N $_2$ H $^+$ (1–0) transitions. Thus, it seems there is no hot gas related to the MM2 clump. Toward the west of this main dense gas structure, there is a third faint clump (western clump) easily detected in the N $_2$ H $^+$ map, and located within the extended emission in the ammonia lines. The emission of NH $_3$ roughly mimics the N $_2$ H $^+$ emission, but being the NH $_3$ emission more extended (possibly as a consequence of the VLA being more sensitive to larger angular scales than the PdBI). Finally, it is worth noting that the dense gas emission is not directly associated with the UCH II region, but close to (and surrounding) the UCH II region, in an elongated structure (seen in ammonia) toward the south of the UCH II region.

In the middle and bottom panels of Figure 2.6, we show the velocity and linewidth maps (obtained from the first and second-order moment maps) of the NH $_3$ and N $_2$ H $^+$ emission. A clear velocity gradient is found in the two main clumps (MM1 ridge and MM2 clump) in the southeast-northwest direction in both cases. These velocity gradients are perpendicular to the direction of the CO (2–1) molecular outflow (cf. Figure 2.3), suggesting the dense gas could be rotating around the two dust condensations. Assuming the Keplerian rotation hypothesis, we estimate the dynamical mass to be $4 M_{\odot}$, with $v_{\text{rot}} = 0.7$ km s $^{-1}$ and $R_{\text{rot}} = 4''$ (we used $M_{\text{dyn}} = v_{\text{rot}}^2 R_{\text{rot}} / G \sin^2 i$, with $i = 90^\circ$). It is interesting to note, that the NH $_3$ (1,1) and N $_2$ H $^+$ (1–0) emission show an enhancement of the linewidth in the direction of the ridge, and along the direction of the molecular outflow, as expected in the case of the outflow being perturbing the dense gas.

2. IRAS 00117+6412: an UCH II region at the border of its natal cloud

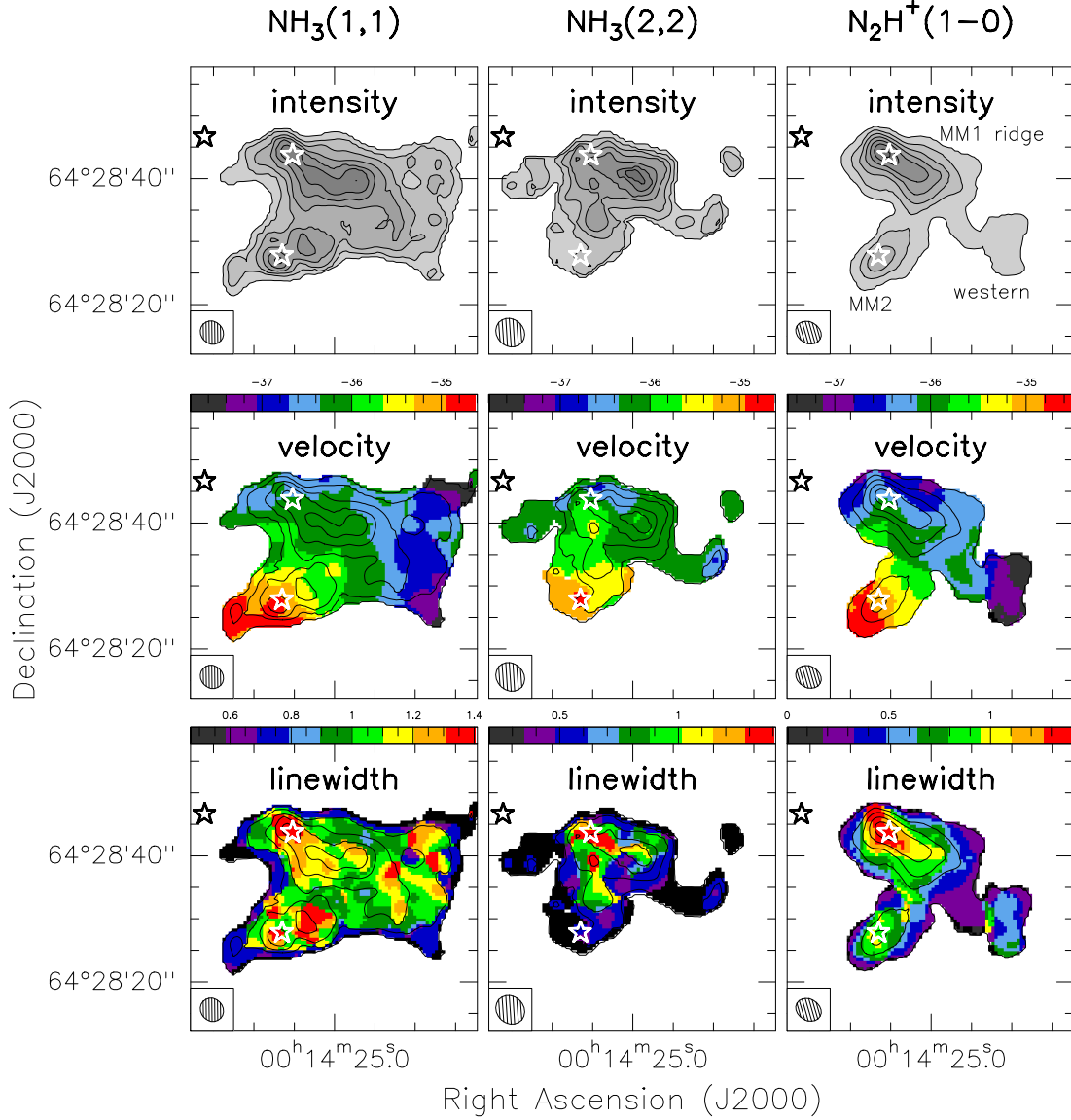


Figure 2.6: $\text{NH}_3(1,1)$ (left-column), $\text{NH}_3(2,2)$ (center-column), and $\text{N}_2\text{H}^+(1-0)$ (right-column) maps toward IRAS 00117+6412. In top panels: we show the zero-order moment (intensity) maps. Levels start at 5%, increasing in steps of 15% the intensity peak: 36, 22, 360 Jy beam⁻¹ m s⁻¹, for $\text{NH}_3(1,1)$, $\text{NH}_3(2,2)$ and N_2H^+ , respectively. In middle panels: we show the first-order moment (velocity field) maps. In bottom panels: we show the second-order moment (linewidth) maps. In middle and bottom panels, contours show the zero-order moment maps in steps of 20%. In all panels, the black star marks the position of the UCH II region, and the white stars mark the position of MM1 and MM2 (see Table 2.2). Synthesized beams are shown in bottom-left corners.

The dense gas associated with MM2 shows some hints of rotation and infall (Palau et al. 2010). This object, with no centimeter continuum emission, no near/mid-IR and no outflow emission, has typical characteristics of starless cores. However, and interestingly, it is associated with a water maser spot (Cesaroni et al. 1988; Á. Sánchez-Monge, priv. comm.), suggesting MM2 could be a very young dense core, harbouring an object in an evolutionary stage between the starless core and the onset of the star formation (see Section 2.4.4 for more details on maser interpretation). In this work, we will focus our analysis in the two centimeter continuum sources and their surroundings. More details in the analysis of the N_2H^+ (1–0) transition are reported in the works of Palau (2006) and Palau et al. (2010). Finally, Busquet (2010) studied the $\text{NH}_3/\text{N}_2\text{H}^+$ ratio toward the different clumps in I00117, finding lowest values of the ratio toward MM1 and higher values toward MM2. Higher values of this ratio are expected in starless cores, while lower values are generally found in dense cores already harbouring a protostar.

The wide band of the SMA is a powerful tool in the detection of several molecular lines, typically tracing hot molecular core emission (see Chapter 1). We searched for other dense gas tracers toward I00117 in the wide SMA band spectrum, and we did not detect dense gas emission associated neither with the UCH II region nor with the MM2 source. At the position of MM1, we only detect emission from the ^{12}CO (2–1), ^{13}CO (2–1) and C^{18}O (2–1) transitions. Thus, no hot core signatures are found toward none of the three main sources in the I00117 star forming complex.

2.4.3 Dense gas analysis

The chemical environment of I00117 has been studied by analyzing the column density, rotational temperature, opacity and velocity of the NH_3 emission. We computed the column density maps by extracting the spectra for positions in a grid of $1''.5 \times 1''.5$. Using CLASS⁵ we fitted the hyperfine structure of each spectrum for NH_3 (1,1) and a single Gaussian for the NH_3 (2,2) transitions. We fitted only those positions with an intensity greater than 5σ for NH_3 (1,1) in order to ensure we are detecting the hyperfine components, whereas for the (2,2) transitions we fitted the spectra with an intensity greater than 4σ .

The hyperfine structure fitting program in CLASS (Forveille et al. 1989) has been used to determine the LSR velocities (v), the intrinsic linewidths (Δv), and opacities of the main line ($\tau_{(1,1)}$; the total opacity for the (1,1) transitions can be obtained from $\tau_T = 2\tau_{(1,1)}$). From the results of the fits of the NH_3 (1,1) and (2,2) spectra, we computed the excitation temperature (T_{ex}), column density (N_{NH_3}), and rotational temperature (T_{rot}) following the procedures described in Ho and Townes (1983) and Harju et al. (1993) (see also Appendix A of Busquet et al. 2009 and Busquet 2010). We assumed a filling factor of 1. In Figure 2.7, we present the resulting maps. The velocity and linewidth maps show similar results as those shown in Figure 2.6, with a broadening of the line at the position of MM1, probably due to the presence of the molecular outflow. The ammonia (1,1)

⁵From the GILDAS packaged, see <http://www.iram.fr/IRAMFR/GILDAS>.

2. IRAS 00117+6412: an UCH II region at the border of its natal cloud

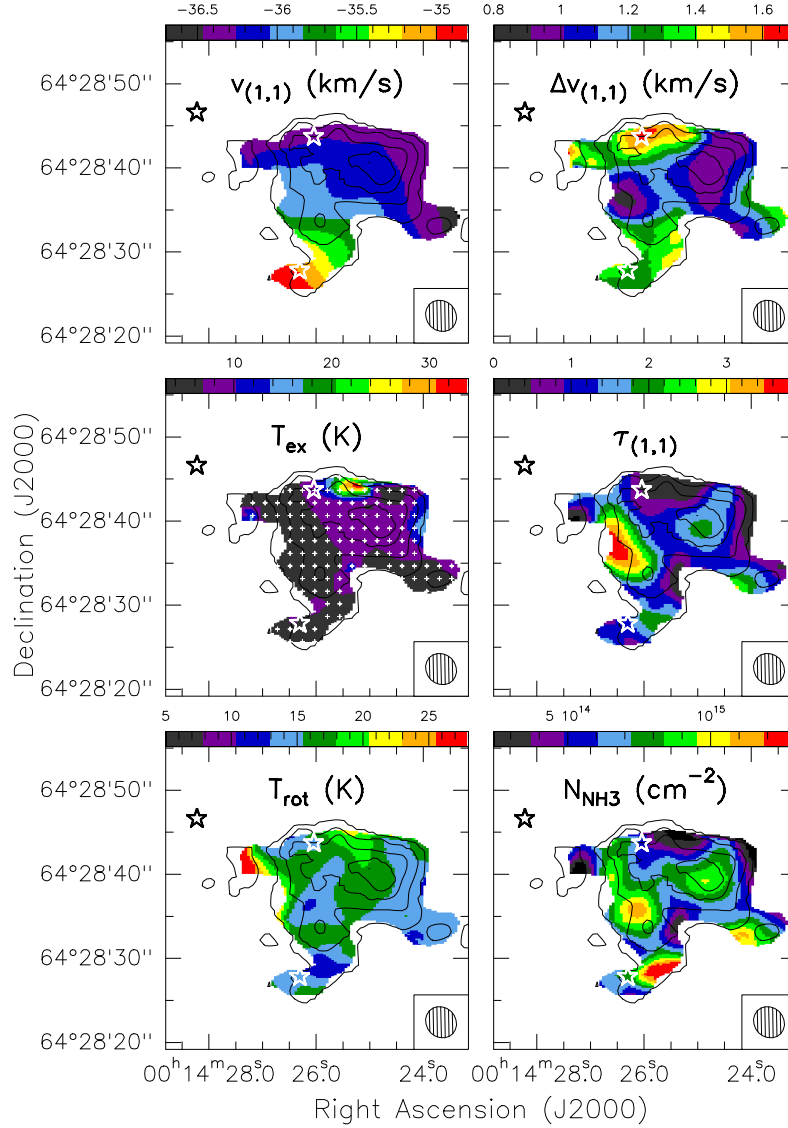


Figure 2.7: Ammonia parameters towards IRAS 00117+6412. From top to bottom, and left to right: velocity map of the NH_3 (1,1) line (units in km s^{-1}); line-width map of the NH_3 (1,1) line (units in km s^{-1}); excitation temperature map from NH_3 (1,1) (units in K); map of the optical depth of the NH_3 (1,1) main line; rotational temperature map from NH_3 (1,1) and NH_3 (2,2) (units in K); and NH_3 column density map (units in cm^{-2}). In all panels, black contours show the intensity map of the NH_3 (2,2) line, the black star marks the position of the UCH II region, and white stars mark the position of MM1 and MM2. The synthesized beam is indicated in the bottom-right corner of each panel. Small white crosses in the T_{ex} map show the position for which we extracted the (1,1) and (2,2) spectra.

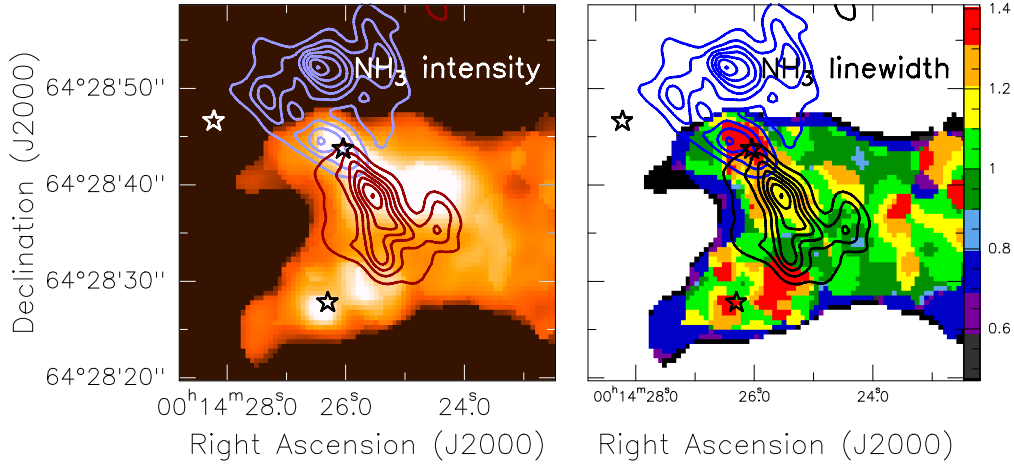


Figure 2.8: *Left panel:* $\text{NH}_3(1,1)$ zero-order moment map (shown in Figure 2.6) in colour scale. Red/blue contours correspond to the redshifted and blueshifted $\text{CO}(2-1)$ molecular outflow emission (as in Figure 2.3, moderate velocities). *Right panel:* Linewidth (FWHM; in km s^{-1}) obtained from the second order moment of the $\text{NH}(1,1)$ emission (as shown in Figure 2.6). Vertical scale units are km s^{-1} . Black/blue contours correspond to the redshifted and blueshifted $\text{CO}(2-1)$ emission (as in left panel). In both panels, the stars mark the position of the three YSOs (UCH II, MM1 and MM2; see Table 2.2).

emission is optically thick ($\tau \sim 1$) in all the cloud, and the column density has a value around $8 \times 10^{14} \text{ cm}^{-2}$, with an enhancement (up to $3 \times 10^{15} \text{ cm}^{-2}$) toward the northwest of MM2 (see next section). The rotational temperature is low (10–18 K) through all the ammonia cloud, reaching values ~ 17 K at the position of MM1, and lower values ~ 12 K towards MM2. It is interesting to note that the temperature rises up to 26 K toward the east of the cloud, close to the UCH II region. At this position, there is a faint filament surrounding the southern part of the H II region. This filament is stronger in the (2,2) transition than in the (1,1) line (cf. Figure 2.6), suggesting this gas is hot (as found in the map of the rotational temperature). The temperature enhancement of the gas could be due to the large UV radiation field produced by the shell-like UCH II region.

2.4.4 Outflow-dense gas interaction

In Figure 2.8, we show an overlay of the outflow emission (in contours) and the ammonia (integrated emission in the left panel, and linewidth in the right panel). It is interesting to note how the red lobe (in black contours) is spatially anticorrelated with respect to the peaks of the ammonia emission, except for the position of the MM1 source. It likely suggests that the outflow is advancing against the dense gas creating cavities in the molecular cloud, or that the outflowing gas can only go through the less dense regions of the cloud.

2. IRAS 00117+6412: an UCH II region at the border of its natal cloud

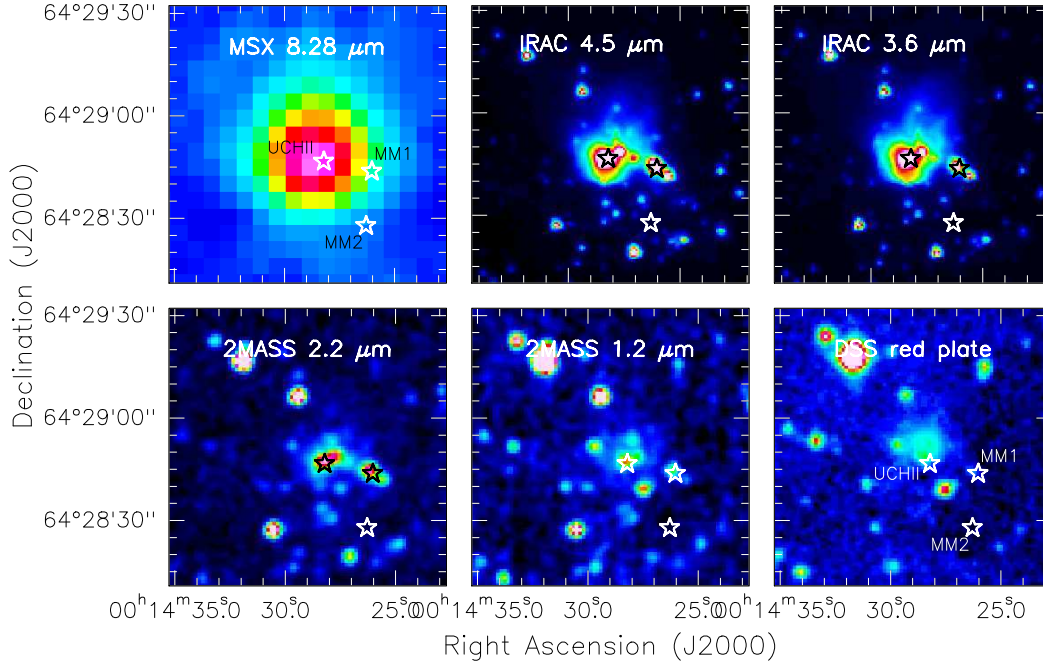


Figure 2.9: Images at infrared wavelengths for IRAS 00117+6412. White/black stars mark the position of the radio continuum sources UCH II, MM1, and MM2 (see Table 2.2). The UCH II region is associated with the strongest IR source, and with faint emission in the red plate of the DSS.

At the position where the outflow reaches the MM2 ammonia clump, an enhancement in intensity and column density (see Figure 2.7) is seen, likely as the result of the collision of the high-velocity outflowing gas with a pre-existing dense core. Furthermore, at this position there is a broadening of the line (up to 1.5 km s^{-1} , see right panel). The water maser emission detected with single-dish telescopes towards MM2 could be, in fact, the result of this collision rather than protostellar activity from MM2. Finally, the ammonia emission close to MM1 and extending toward the southwest, shows a moderate line broadening ($\sim 1.1 \text{ km s}^{-1}$), which could be the result of the passage of the outflow. In conclusion, it seems that the ammonia emission (intensity and kinematics) are determined by the effects of the outflow.

2.5 Summary and brief discussion

We have analyzed with high angular resolution and good sensitivity the centimeter and millimeter continuum, the outflow gas with the CO (2–1) transition, and the dense gas with the N_2H^+ (1–0), NH_3 (1,1) and (2,2) transitions, towards the star-forming region IRAS 00117+6412. Our main conclusions can be summarized as follows.

- Centimeter continuum emission is detected in all the maps, coming from two distinct sources. An UCH II region is located at the border of a dusty cloud, with a shell-like morphology and a flat spectral index of -0.03 ± 0.08 . Its SED can be well fitted by an optically thin H II region with a size of 0.03 pc and an electron density of $2 \times 10^4 \text{ cm}^{-2}$, ionized by a B2 ZAMS star. The second centimeter source, MM1, is located $15''$ to the west of the UCH II region and is embedded in a dust cloud. Although we only detect emission at 3.6 cm, the upper limits at the other wavelengths indicate that the centimeter emission for MM1 is thermal, with a spectral index $-0.3 < \alpha_{\text{MM1}} < 1.1$.
- At millimeter wavelengths we detect two main sources, MM1 and MM2. Both sources seem to be tracing dust envelopes of a few solar masses. The main difference is that MM1 is associated with thermal centimeter continuum emission and with a 2MASS source, while MM2 has no counterparts at infrared or centimeter wavelengths. We searched the *Spitzer* database for observations toward I00117, and found images at 4.5 and 3.6 μm . No emission is detected at these wavelengths at the position of MM2 (see Figure 2.9). Finally, both objects are associated with water maser emission.
- A molecular outflow driven by MM1 is detected in the CO (2–1) transition, with a northeast-southwest orientation. The outflow emission consists of different high velocity condensations in a wide-angle outflow morphology. The physical parameters of the outflow are similar to those found in outflows from intermediate-mass YSOs.
- Dense gas emission is detected in the NH_3 and N_2H^+ lines, coming from a cloud that resembles the morphology of the dusty cloud. The two main dense gas condensations are spatially coincident with the position of MM1 and MM2, and show a velocity gradient in the southeast-northwest direction, perpendicular to the direction of the molecular outflow. A dynamic mass of $4 M_\odot$ is estimated from the velocity gradient at the position of the MM1 source (assuming the gradient is due to Keplerian rotation). The temperature of the gas toward MM1 is $\sim 17 \text{ K}$, while it drops up down to $\sim 12 \text{ K}$ for MM2. Although no dense gas is directly associated with the UCH II region, a faint ammonia filament is detected surrounding the H II region toward the south. Its rotational temperature is $\sim 26 \text{ K}$, suggesting the UV radiation is heating the gas close to the H II region. The global picture suggests that the UCH II region has started to disperse and disrupt its natal cloud. It is interesting to note that faint extended emission in the red band of the DSS is found toward the north of the UCH II region (Figure 2.9), i.e., the opposite site where we find the ammonia filament.
- The morphological distribution seen in the maps of the ammonia intensity (and column density) and linewidth, seems to be the result of the passage of the molecular outflow driven by MM1 through the molecular cloud.

3

IRAS 22134+5834: a small UCH II region disrupting the parental cloud

3.1 General overview

IRAS 22134+5834 (hereafter I22134), with a bolometric luminosity of $12600 L_{\odot}$ at a distance of 2.6 kpc, is located within a compact molecular cloud detected in ^{12}CO and C^{13}O by Dobashi et al. (1994). At millimeter wavelengths, the region is dominated by an extended and elliptical source with a single resolved peak centered on the IRAS source (Chini et al. 2001; Beuther et al. 2002b), and associated with a centimeter compact source of a few mJy (Sridharan et al. 2002). The dusty cloud is associated with an embedded cluster (Kumar et al. 2006), H_2O maser emission (Cesaroni et al. 1988; Wouterloot et al. 1993), and a massive molecular outflow (Dobashi and Uehara 2001; Beuther et al. 2002c), probably associated with H_2 knots (Kumar et al. 2002). Additionally, emission from a vast set of molecular line transitions has been reported in single-dish surveys (Beuther et al. 2002b; Richards et al. 1987; Fuller et al. 2005; Sridharan et al. 2002; López-Sepulcre et al. 2010). Regarding the near-infrared emission, Kumar et al. (2003) find a rich centrally symmetric and flattened embedded cluster and a central dark region, probably an empty cavity, surrounded by a ring of bright and massive stars associated with the FIR/(sub)millimeter emission. All the bright stars in the ring are found to have intrinsic infrared excess emission and are likely to be early-to late-B type stars.

In this Chapter, we present new interferometric continuum and dense gas observations that reveal that I22134 seems to be associated with a small cometary UCH II region, within a large infrared cluster, dispersing the dust and gas that surrounds it.

3.2 Observations

3.2.1 Very Large Array

The I22134 star forming region was observed with the Very Large Array (VLA¹) at 6.0, 3.6, 1.3, and 0.7 cm continuum in the A, B, and C configurations of the array, on 2007 and 2009, with 10–21 EVLA antennas in the array. In Table 3.1 we list the main parameters of the observations. The data reduction followed the VLA standard guidelines for calibration of high frequency data, using the NRAO package AIPS. First images were produced with a natural weighting to obtain a good sensitivity. We complemented our continuum observations with archival data from projects AC295, AB1101 and AS643, and data from the NVSS (Condon et al. 1994), which contains observations of I22134 at 20, 3.6, and 1.3 cm in different configurations (see Table 3.1). Several images were done, by changing the robust weighting parameter of Briggs (1995). We avoided to combine the uv -data sets at the same frequencies due to the large differences between the observations (mainly affecting the rms noise levels, and thus the brightness sensitivity). In order to properly compare the flux density at each frequency of the main source (see Section 3.3) we created images with the same uv -range (15–450 k λ) and convolved with the same synthesized beam ($0''.7 \times 0''.7$). We used only those observations with good angular resolution ($\sim 0''.3$ – $0''.5$) and high sensitivity. In Table 3.3 we provide the resulting synthesized beams and rms noise levels of the combined images.

The VLA was also used to map the $(J, K)=(1,1)$ and $(2,2)$ inversion lines of the ammonia molecule with the array in its D configuration. The archival data (project AK558) were obtained during 2003 May 01. The adopted flux density of the absolute flux calibrator 1331+305 (3C286) was 2.41 Jy at the frequencies of 23.69 and 23.72 GHz. Amplitude and phase calibration were achieved by monitoring 2148+611, resulting in an rms of the phases of $\sim 40^\circ$ and a bootstrapped flux of 0.595 ± 0.004 Jy. The bandpass was fixed by observing the bright quasars 1229+020 (3C273) and 0319+415 (3C84). The 4IF spectral line mode was used, allowing simultaneous observations of NH₃ (1,1) and (2,2) lines with two polarizations for each line. The bandwidth used was 3.1 MHz, with 63 spectral channels with a channel spacing of 48.8 kHz (~ 0.6 km s⁻¹) centered at $v_{\text{LSR}} = -18.3$ km s⁻¹, plus a continuum channel that contains the average of the central 75% of the bandwidth. The data reduction followed the standard guidelines for calibration of high frequency data, using the software package AIPS. Imaging was performed using natural weighting, resulting in a synthesized beam of $3''.7 \times 3''.1$ with a P.A.= $+86^\circ$ and a 1σ rms of 1.7 mJy beam⁻¹ per channel.

¹The Very Large Array (VLA) is operated by the National Radio Astronomy Observatory (NRAO), a facility of the National Science Foundation operated under cooperative agreement by Associated Universities, Inc.

Table 3.1: Main VLA continuum observational parameters of IRAS 22134+5834

λ (cm)	Project VLA conf.	Epoch of Observation	Gain cal. / Bootstr. Flux ^a	Flux cal.	Beam (" \times ")	P.A. ($^\circ$)	Rms ^b
20.0	NVSS D	1995 Mar 12	45. \times 45.	+0	470
6.0	AS1038 D	2010 Apr 23	2148+611 / 1.29(1)	3C48	14.7 \times 11.0	+38	22
6.0	AS902 A	2007 Jun 05	2148+611 / 1.28(1)	3C286	0.41 \times 0.36	-17	45
3.6	AS1038 D	2010 May 07	2148+611 / 1.02(1)	3C48	8.3 \times 5.9	+44	35
3.6	AC295 B	1992 Jan 06	2229+695 / 0.43(1)	3C48	0.74 \times 0.59	-81	123
3.6	AS643 BnA	1998 Jul 02	2320+506 / 1.71(1)	3C286	1.16 \times 0.66	+88	64
3.6	AS902 A	2007 Jun 05	2148+611 / 1.05(1)	3C286	0.24 \times 0.19	+25	24
1.3	AC295 C	1992 May 25	2229+695 / 0.27(3)	3C48	1.29 \times 0.94	+58	674
1.3	AB1274 B	2007 Oct 23	2148+611 / 0.72(3)	3C286	0.30 \times 0.22	+31	76
1.3	AB1101 B	2003 Nov 08	2322+509 / 0.72(3)	3C286	0.35 \times 0.23	+51	135
0.7	AS981 C	2009 Jun 28	2148+611 / 0.68(5)	3C286	0.63 \times 0.39	+68	204
0.7	AB1274 B	2007 Oct 23	2148+611 / 0.50(20)	3C286	0.45 \times 0.32	-63	211

^a Bootstrapped flux in Jy. In parenthesis: the percentage of error in the flux.

^b Rms noise level in $\mu\text{Jy beam}^{-1}$.

3.2.2 Expanded Very Large Array

We also observed I22134 with the new capabilities of the VLA: the Expanded Very Large Array (EVLA). The EVLA was used on 2010 April 23 and May 07 to observe the continuum emission at 6.0 and 3.6 cm in its D configuration, with a bandwidth of 2×256 MHz (up to 5 times better than the standard VLA observations). In Table 3.1, we list the main parameters of these observations. The data reduction followed the EVLA standard guidelines for continuum emission, using the NRAO package CASA. Images were done with the CLEAN procedure in CASA, by setting the robust parameter of Briggs (1995) to +2 (natural) for the 3.6 cm image, and to 0 for the 6 cm image. The resulting rms noise levels and synthesized beams are shown in Table 3.1.

3.2.3 Combined Array for Research in Millimeter-wave Astronomy

The Combined Array for Research in Millimeter-wave Astronomy (CARMA²) was used to observe the 3.2 mm and N_2H^+ (1–0) molecular transition towards I22134. We carried out a 5 hour track on 2008 June 23, with the array (five 10.4 m antennas and nine 6 m antennas) in the D configuration. The phase center was $\alpha(\text{J2000}) = 22^{\text{h}}15^{\text{m}}09^{\text{s}}.23$, and $\delta(\text{J2000}) = +58^\circ49'08''.9$, and the baselines ranged from 9.6 m to 137.6 m. The FWHM of the primary beam at the frequency of the observations was $132''$ for the 6 m

²Supports for CARMA construction was derived from the Gordon and Betty Moore Foundation, the Kenneth t. and Eileen L. Norris Foundation, the Associates of the California Institute of Technology, the states of California, Illinois, and Maryland, and the National Science Foundation. Ongoing CARMA development and operations are supported by the National Science Foundation under a cooperative agreement, and by the CARMA partner universities.

antennas, and 77'' for the 10.4 m antennas. System temperatures were around 200 K. The digital correlator was configured to observe simultaneously the continuum emission and the N₂H⁺ (1–0) group of hyperfine transitions (93.176331 GHz, in the lower sideband). The continuum data were recorded in two 500 MHz units, covering the frequency ranges 93.47–93.91 GHz and 96.06–97.50 GHz. All the hyperfine N₂H⁺ transitions were covered with two overlapping 8 MHz units, with 63 channels each one, providing a spectral resolution of ~ 0.42 km s^{−1}. Bandpass calibration was performed by observing the quasar 3C454.3. Amplitude and phase calibrations were achieved by monitoring BL Lac. The absolute flux density scale was determined from MWC349, with an estimated uncertainty around 20%. Data were calibrated and imaged using the standard procedures in MIRIAD. Imaging was performed using natural weighting, obtaining a synthesized beam of 5''.5 × 4''.2 with a P.A.=−87°, and 1 σ rms of 0.56 mJy beam^{−1} for the continuum, and 45 mJy beam^{−1} per channel for the line.

3.3 Continuum results

3.3.1 Centimeter and millimeter continuum results

We detected radio continuum emission associated with the IRAS source 22134+5834 at all wavelengths. In Figure 3.1, we show a global overview of the region at all radio wavelengths, and at 3.6 μ m of *Spitzer*/IRAC. At the four IRAC bands, the cluster of IR sources reported by Kumar et al. (2003) is visible and appears surrounded by faint emission (dominant at 8 μ m) engulfing all the components of the cluster, and extending in a cometary-like morphology to the west (see Figure 3.1 top panel, and Figure 3.5). At radio wavelengths we will differentiate our observations in low ($\gtrsim 5''$) and high ($\lesssim 1''$) angular resolution. At low angular resolution, the emission is dominated by a strong and compact source (VLA1) associated with one of the strongest IRAC sources located at the head of the infrared cometary structure (see Figure 3.1 middle panels). A second radio continuum source (VLA2) is located $\sim 15''$ to the northwest of VLA1, and is also associated with an IRAC source. In this case the IRAC source is much fainter and is located at the tail of the cometary structure. At 3.2 mm, we only detect emission from VLA1 showing a small extension toward the southeast. VLA2 is not detected at millimeter wavelengths probably due to the low sensitivity of the CARMA observations. In Table 3.2, we list the coordinates, intensity peak, flux density and deconvolved size of the two radio continuum sources.

Our higher angular resolution observations ($\lesssim 1''$) allow us to gain insight into the nature of VLA1. The source appears clearly resolved in a cometary-like morphology, with the head of the cometary arc located to the southeast. It is important to note that the orientation of the centimeter cometary source is similar to the large-scale cometary emission seen at infrared wavelengths. The flux density of VLA1 is almost constant at all the centimeter wavelengths. However, the highest-angular resolution observations (7 mm

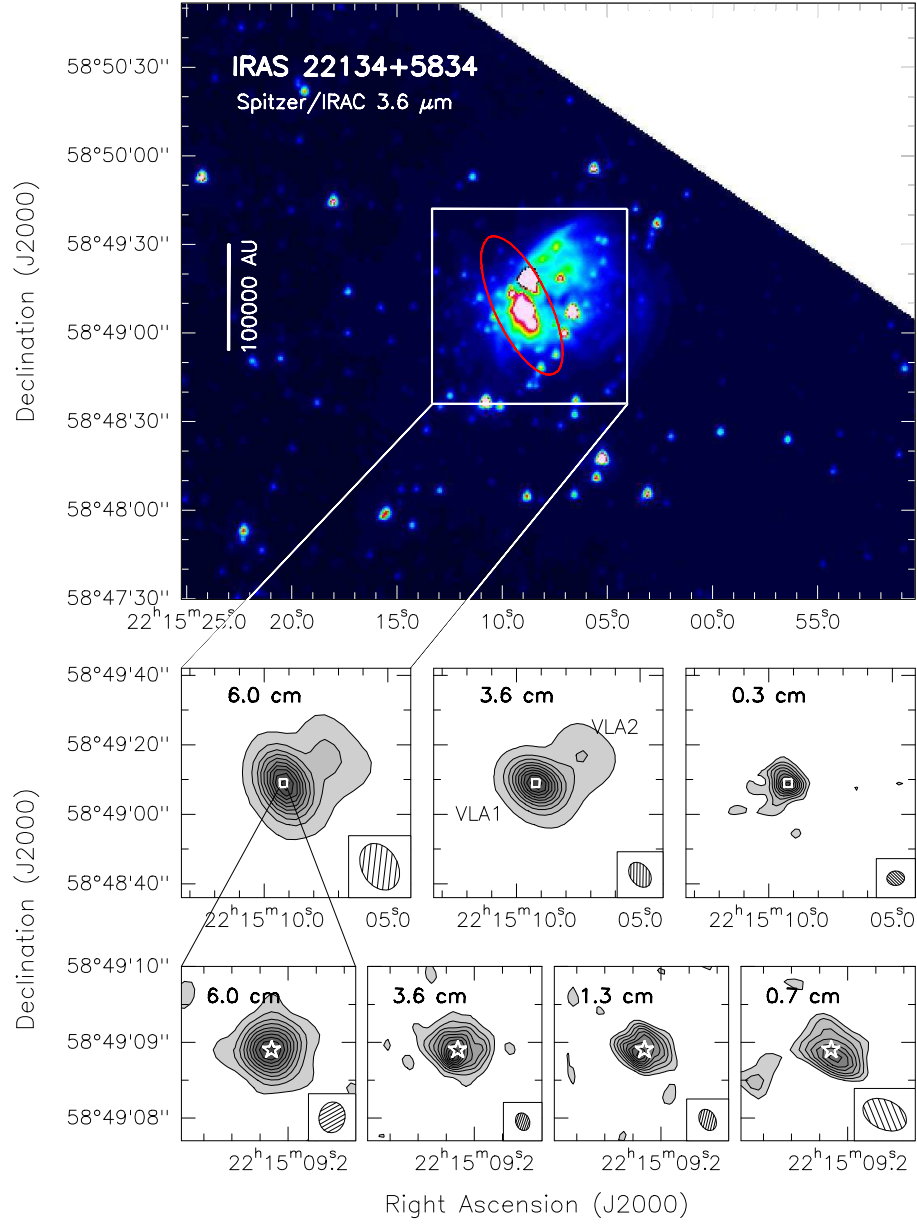


Figure 3.1: Continuum maps for IRAS 22134+5834. *Top*: IRAC/*Spitzer* 3.6 μm image. Red ellipse marks the position of the IRAS source. *Middle panels*: Low-angular resolution images: EVLA (D-config) 6.0 cm continuum image, EVLA (D-config) 3.6 cm continuum image, and CARMA (compact) 3 mm continuum image. Levels start at 3% (15% for 3.2 mm), increasing in steps of 10% the peak intensity: 4.2, 4.0, and 8.6 mJy beam^{-1} , respectively. The white box shows the region zoomed in bottom panels. *Bottom panels*: High-angular resolution images: VLA (A-config) 6.0 cm continuum image, VLA (A-config) 3.6 cm continuum image, VLA (B-config) 1.3 cm continuum image, and VLA (C-config) 0.7 cm continuum image. Levels start at 5% (15% for 1.3 cm, and 35% for 0.7 cm), increasing in steps of 10% of the peak intensity: 1.6, 0.8, 0.8, and 1.5 mJy beam^{-1} , respectively. The white star marks the position of VLA1. Synthesized beams are shown in the bottom-right corner.

3. IRAS 22134+5834: a small UCH II region disrupting the parental cloud

Table 3.2: Multiwavelength results for the YSOs in IRAS 22134+5834

λ (cm)	Beam ('' \times '')	P.A. ($^\circ$)	Rms ^b	I_ν^{peaka} (mJy beam ⁻¹)	S_ν^a (mJy)	Deconv. Size ('' \times '')	P.A. ($^\circ$)
VLA1	$\alpha(J2000.0) = 22^{\text{h}}15^{\text{m}}09^{\text{s}}.23$ $\delta(J2000.0) = +58^\circ49'08''.9$						
20.0	45. \times 45.	+0	470	1.3 \pm 0.9	2.9 \pm 1.4
6.0	14.7 \times 11.0	+38	22	4.3 \pm 0.1	5.1 \pm 0.2	4.2 \times 3.2 \pm 0.3	45 \pm 15
6.0	0.41 \times 0.36	-17	45	1.6 \pm 0.1	3.7 \pm 0.3	0.48 \times 0.38 \pm 0.05	85 \pm 15
3.6	8.3 \times 5.9	+44	35	3.6 \pm 0.1	4.3 \pm 0.2	2.6 \times 1.6 \pm 0.5	50 \pm 15
3.6	0.74 \times 0.59	-81	123	1.6 \pm 0.3	2.1 \pm 0.5	0.43 \times 0.39 \pm 0.2	140 \pm 50
3.6	1.16 \times 0.66	+88	64	2.7 \pm 0.2	3.6 \pm 0.4	0.45 \times 0.42 \pm 0.1	95 \pm 45
3.6	0.27 \times 0.19	+25	24	0.8 \pm 0.1	3.5 \pm 0.2	0.48 \times 0.37 \pm 0.05	85 \pm 15
1.3	1.29 \times 0.94	+58	674	...	< 2.7
1.3	0.30 \times 0.22	+31	76	0.8 \pm 0.2	2.3 \pm 0.5	0.49 \times 0.32 \pm 0.1	90 \pm 20
1.3	0.35 \times 0.23	+51	135	0.7 \pm 0.3	2.4 \pm 0.7	0.71 \times 0.51 \pm 0.2	5 \pm 50
0.7	0.63 \times 0.39	+68	204	1.5 \pm 0.4	2.7 \pm 0.9	0.70 \times 0.45 \pm 0.3	80 \pm 40
0.7	0.45 \times 0.32	-63	211	0.9 \pm 0.4	1.2 \pm 0.8	0.84 \times 0.37 \pm 0.3	130 \pm 40
0.32	5.5 \times 4.2	-87	560	8.6 \pm 1.2	25. \pm 11.	7.8 \times 7.1 \pm 1.2	30 \pm 50
VLA2	$\alpha(J2000.0) = 22^{\text{h}}15^{\text{m}}07^{\text{s}}.26$ $\delta(J2000.0) = +58^\circ49'17''.9$						
6.0	14.7 \times 11.0	+38	22	1.6 \pm 0.1	1.2 \pm 0.1	8.9 \times 5.7 \pm 2.0	150 \pm 30
3.6	8.3 \times 5.9	+44	35	0.4 \pm 0.1	0.5 \pm 0.1	5.5 \times 3.3 \pm 2.5	35 \pm 40

^a Primary beam corrected. Error in intensity is 2σ . Error in flux density has been calculated as $\sqrt{(2\sigma\sqrt{\theta_{\text{source}}/\theta_{\text{beam}}})^2 + (2\sigma_{\text{flux-scale}})^2}$, where σ is the rms noise level of the map, θ_{source} and θ_{beam} are the size of the source and the beam respectively, and $\sigma_{\text{flux-scale}}$ is the error in the flux scale, which takes into account the uncertainty on the calibration applied to the flux density of the source ($S_\nu \times \%$ uncertainty).

^b Rms noise level in $\mu\text{Jy beam}^{-1}$.

with the VLA in its B configuration) filter out almost all the continuum emission (see Table 3.2). In order to properly compare the flux density at different wavelengths, we decided to make images taking into account the same range of projected baselines (15–450 k λ). We convolved the resulting images to the same circular beam of $0''.7 \times 0''.7$. In Table 3.3, we list the flux densities for the images done with the same uv -range. The flux density of VLA1 is ~ 3 mJy, and remains almost constant at all centimeter wavelengths.

3.3.2 Spectral energy distribution

In Figure 3.2, we show the spectral energy distribution (SED) of VLA1 in I22134. At centimeter wavelengths, the flux of the cometary source remains practically constant, with a spectral index (α ; $S_\nu \propto \nu^\alpha$) equal to -0.18 ± 0.08 between 6 and 0.7 cm. The centimeter range of the spectrum is well fitted by an optically thin H II region with a size of 0.01 pc,

Table 3.3: Continuum flux density for VLA1 in IRAS 22134+5834 with the same uv -range

λ (cm)	Beam ($'' \times ''$)	P.A. ($^\circ$)	Rms ^b	$I_\nu^{\text{peak a}}$ (mJy beam ⁻¹)	S_ν^{a} (mJy)	Deconv. Size ($'' \times ''$)	P.A. ($^\circ$)
VLA1	— same uv -range (15–450 k λ), and convolved with a $0.''7 \times 0.''7$ beam						
6.0	0.7×0.7	+0	40	2.7 ± 0.1	3.6 ± 0.2	$0.48 \times 0.38 \pm 0.05$	80 ± 10
3.6	0.7×0.7	+0	35	2.7 ± 0.1	3.5 ± 0.2	$0.44 \times 0.34 \pm 0.05$	80 ± 10
1.3	0.7×0.7	+0	74	2.0 ± 0.2	2.5 ± 0.4	$0.44 \times 0.32 \pm 0.1$	80 ± 25
0.7	0.7×0.7	+0	173	1.9 ± 0.4	2.8 ± 0.8	$0.62 \times 0.37 \pm 0.3$	85 ± 30

^a Primary beam corrected. Error in intensity is 2σ . Error in flux density has been calculated as $\sqrt{(2\sigma\sqrt{\theta_{\text{source}}/\theta_{\text{beam}}})^2 + (2\sigma_{\text{flux-scale}})^2}$, where σ is the rms noise level of the map, θ_{source} and θ_{beam} are the size of the source and the beam respectively, and $\sigma_{\text{flux-scale}}$ is the error in the flux scale, which takes into account the uncertainty on the calibration applied to the flux density of the source ($S_\nu \times \%\text{uncertainty}$).

^b Rms noise level in $\mu\text{Jy beam}^{-1}$.

an electron density of $1.8 \times 10^4 \text{ cm}^{-3}$, an emission measure of $3.3 \times 10^6 \text{ cm}^{-6} \text{ pc}$, an ionized gas mass of $3.8 \times 10^{-4} M_\odot$, and a flux of ionizing photons of $1.7 \times 10^{45} \text{ s}^{-1}$ (corresponding to a B1 ZAMS star; Panagia 1973). At 3.2 mm, the flux increases by a factor of 10 with respect to the centimeter emission³. The millimeter emission can be understood as emission coming from a dust envelope surrounding the cometary H II region. Assuming a source radius of $5''$, a dust emissivity index $\beta = 2$, and a dust mass opacity coefficient of $0.9 \text{ cm}^2 \text{ g}^{-1}$ at 1.3 mm (Ossenkopf and Henning 1994), the mass of gas and dust is $28 M_\odot$, for a dust temperature of 50 K. Higher angular resolution observations at 2 and 1 mm have revealed that the millimeter continuum emission is not directly associated with the H II region, but surrounds it in a shell-like morphology with four main dust condensations (A. Palau, and F. Fontani, priv. comm.). All this suggests that VLA1 is a cometary H II region driven by a B1 ZAMS star, that has started to disrupt the surrounding dust envelope.

3.4 Molecular results

3.4.1 Molecular dense gas: morphology and velocity fields

The zero-order moment (integrated intensity) maps of the NH_3 (1,1) and (2,2) transitions are shown in the top panels of Figure 3.3. We also show the zero-order moment map of the N_2H^+ (1–0) transition in the same figure. The ammonia (1,1) emission in I22134 consists of several clumps with sizes ranging from 0.02 pc to 0.06 pc, forming an extended (almost circular) structure of $\sim 70''$ around the cometary UCH II region, and the cluster

³It is important to note that we are not filtering a large amount of the flux at centimeter wavelengths. The flux density at 6 and 3.6 cm with the EVLA in its D configuration, is only a 20–30% larger than the fluxes listed in Table 3.3 for more extended configurations.

3. IRAS 22134+5834: a small UCH II region disrupting the parental cloud

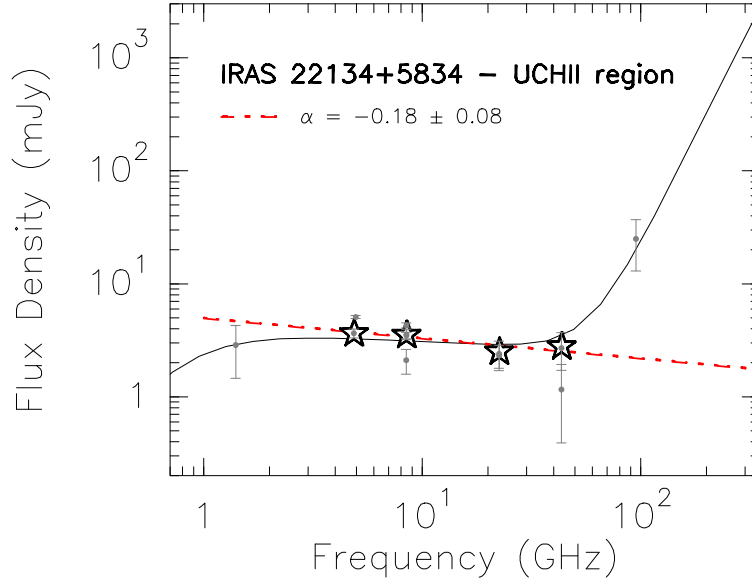


Figure 3.2: Spectral energy distribution for IRAS 22134+5834. Grey dots correspond to the observational data from Table 3.2. Stars correspond to VLA high-angular resolution data, after convolving with a $0''.7 \times 0''.7$ beam, and taking into account only the data in the uv -range 15–450 $k\lambda$ (from Table 3.3). Red dot-dashed line: linear fit ($S_\nu \propto \nu^\alpha$) to the centimeter data (stars) with $\alpha = -0.18 \pm 0.08$. Black solid line: sum of an homogeneous H II region with an electron density of $1.8 \times 10^4 \text{ cm}^{-3}$ and a size of $0''.4$ ($\sim 1000 \text{ AU}$ at 2.6 kpc), and a modified blackbody law for the dust envelope with a dust emissivity index $\beta = 2$, a source radius of $2''$ ($\sim 5200 \text{ AU}$), a dust temperature of 50 K, a dust mass of $28 M_\odot$, and a dust mass opacity coefficient of $0.9 \text{ cm}^2 \text{ g}^{-1}$ at 1.3 mm.

of infrared sources (cf. Figure 3.1). Similarly, the $\text{NH}_3(2,2)$ and $\text{N}_2\text{H}^+(1-0)$ molecular transitions follow the same structure seen in the $\text{NH}_3(1,1)$, but being more compact. It is important to note an elongated filament seen in the $(1,1)$ transition toward the southwest of the UCH II region, and almost at the center of the circular structure. This filament, clearly seen in $\text{NH}_3(1,1)$, is much fainter in the $\text{NH}_3(2,2)$ and N_2H^+ maps. No dense gas is spatially coincident with none of the centimeter continuum sources. However, the cometary UCH II region is surrounded by several dense cores forming a cavity structure around it. It is important to note that the cometary arc of the H II region, located toward the southeast (cf. Figure 3.1) points to the southeastern dense gas condensations, while the tail of the H II region is oriented toward the northwest, i. e., the direction where there are no dense gas clumps close to the UCH II region.

The first-order moment maps tracing the velocity field of the gas (Figure 3.3 middle panels) do not show a clear velocity trend (or gradient) in the different clumps for none of the three molecular transitions. Rather, almost all emission is at -18.5 km s^{-1} , with

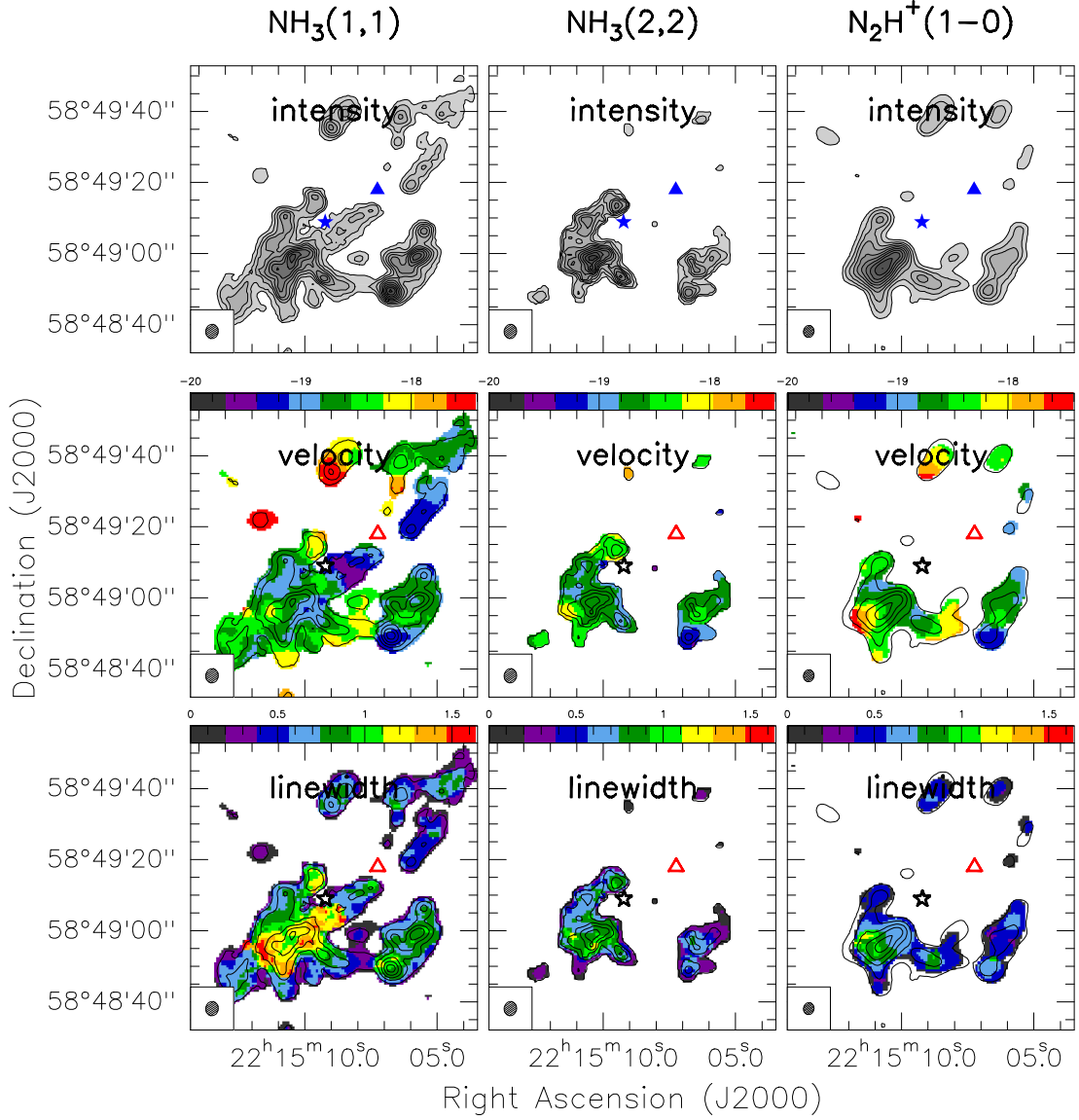


Figure 3.3: $\text{NH}_3(1,1)$ (left-column), $\text{NH}_3(2,2)$ (center-column), and $\text{N}_2\text{H}^+(1-0)$ (right-column) maps toward IRAS 22134+5834. In top panels: we show the zero-order moment (integrated intensity) maps. Levels start at 10% (5% for $\text{NH}_3(2,2)$), increasing in steps of 10% the intensity peak: 0.03, 0.02, and 3.8 Jy beam⁻¹ km s⁻¹, respectively. In middle panels: we show the first-order moment (velocity field) maps. In bottom panels: we show the second-order moment (velocity dispersion) maps. In middle and bottom panels, contours show the zero-order moment maps in steps of 20%. In all panels, the star marks the position of the cometary H II region, and the triangle marks the position of VLA2 (see Table 3.2). Synthesized beams are shown in bottom-left corners.

the exception of the central filament seen in the (1,1) transition, which is blueshifted by $\sim 1 \text{ km s}^{-1}$. Regarding the linewidth, those clumps located close to the UCH II region (toward the southeast and east) show wider spectral lines ($1.5\text{--}2 \text{ km s}^{-1}$) in comparison to the linewidth in the other dense clumps ($0.5\text{--}1 \text{ km s}^{-1}$).

3.4.2 Molecular dense gas: temperature and density

We performed the same chemical study of the ammonia emission toward I22134, as in the previous chapter. See Chapter 2 or Busquet et al. (2009) for details in the method used. We extracted spectra of the NH_3 (1,1) and (2,2) lines for positions in a grid of $1''.4 \times 1''.4$, in order to obtain maps of the rotational temperature, column density, opacity and velocity of the NH_3 emission. In Figure 3.4, we show the resulting maps. The emission is mainly (partially) optically thick ($\tau > 0.5$) for all the ammonia clumps, reaching the higher values (~ 3) in the southwestern clump. Concerning the rotational temperature, there is a clear gradient of the temperature which progressively increases when approaching the UCH II region, achieving the highest value of $30 \pm 5 \text{ K}$ at the position of the cavity that surrounds the centimeter source. On the other hand, the lowest temperatures are found toward the western clumps, with values of $14 \pm 2 \text{ K}$. We can also see the line broadening close to the UCH II region. All this, temperature progressively increasing toward the UCH II region and broad linewidths, suggests that the H II region could be radiatively affecting the surrounding dense gas. Finally, the column density reaches its highest values in the western cloud ($2 \times 10^{15} \text{ cm}^{-2}$), while the surrounding gas close to the UCH II region has a lower column density ($2 \times 10^{14} \text{ cm}^{-2}$), where a cavity is possible created by the UV photons.

Busquet (2010) studied the $\text{NH}_3/\text{N}_2\text{H}^+$ ratio toward the different clumps in I22134, finding that the highest values (around 250–600) are found in the western cores, whereas the main cloud to the southeast of the UCH II region is associated with slightly lower values (in the range of 50–200). Busquet (2010) suggests that the NH_3 could be more affected than the N_2H^+ under a strong UV radiation field (e.g., coming from an H II region). Thus, it seems that the cometary UCH II region is affecting the surrounding gas chemically (the $\text{NH}_3/\text{N}_2\text{H}^+$ ratio) and physically (with an enhancement of the linewidth and the temperature).

3.4.3 Ionized gas emission within the molecular emission

In Section 3.3, we reported the detection of two radio continuum sources in the low angular resolution observations: VLA1 which seems to be a cometary UCH II region (when observed at high angular resolutions), and VLA2 with a flux density decreasing with frequency (the spectral index between 6 and 3.6 cm is ~ -1), and non detected in the high-angular resolution maps. In Figure 3.5, we show the emission in I22134 from submillimeter wavelengths ($850 \text{ }\mu\text{m}$ and $450 \text{ }\mu\text{m}$; Di Francesco et al. 2008) up to the red plate

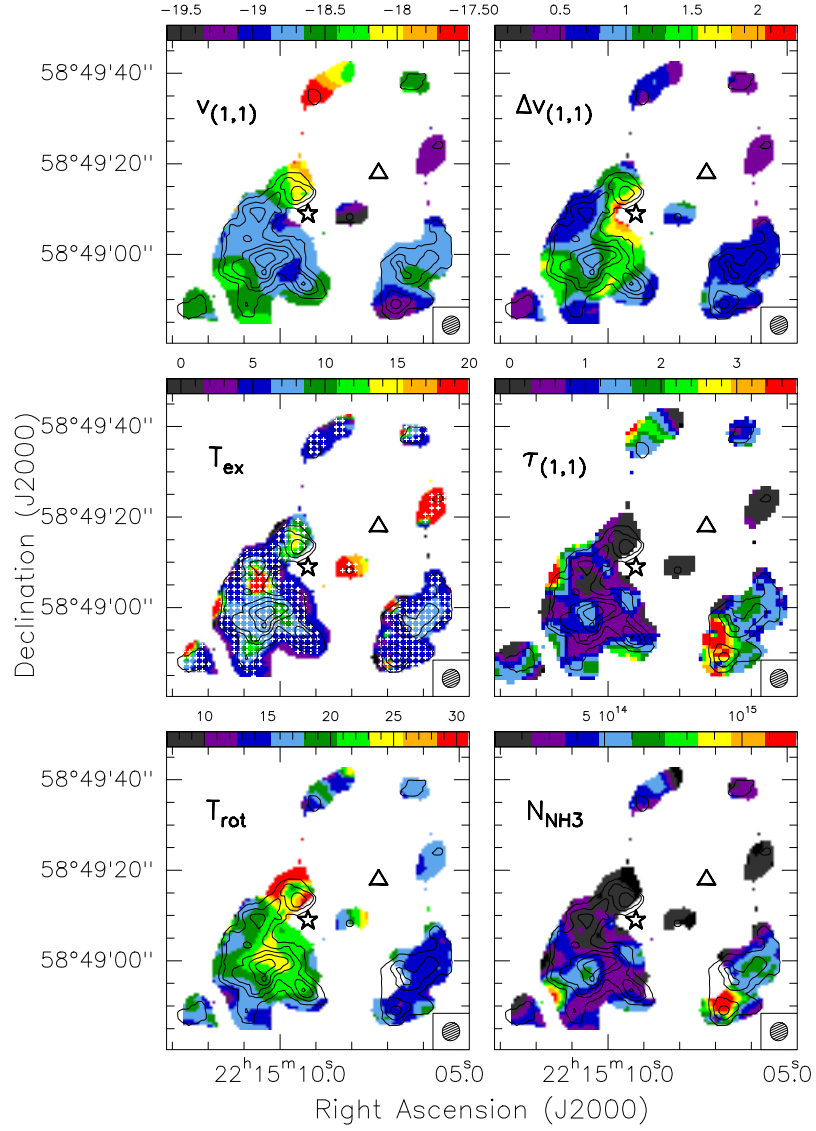


Figure 3.4: Ammonia parameters towards IRAS 22134+5834. From top to bottom, and left to right: velocity map of the NH_3 (1,1) line (units in km s^{-1}); line-width map of the NH_3 (1,1) line (units in km s^{-1}); excitation temperature map from NH_3 (1,1) (units in K); map of the optical depth of the NH_3 (1,1) main line; rotational temperature map from NH_3 (1,1) and NH_3 (2,2) (units in K); and NH_3 column density map (units in cm^{-2}). In all panels, black contours show the intensity map of the NH_3 (2,2) line. The star and the triangle mark the position of the centimeter sources VLA1 and VLA2, respectively (see Table 3.2). The synthesized beam is indicated in the bottom-right corner of each panel. Small white crosses in the T_{ex} map show the position for which we extracted the (1,1) and (2,2) spectra.

3. IRAS 22134+5834: a small UCH II region disrupting the parental cloud

of the DSS (Digital Sky Survey). Both centimeter continuum sources are embedded in a large submillimeter source. However, in the images with a better angular resolution (at $70\ \mu\text{m}$) we see that the emission comes mainly from the UCH II region. In the mid/near-infrared images (from 8.0 up to $2.2\ \mu\text{m}$) we can distinguish the cluster of infrared sources, and the infrared cometary morphology discussed previously. There is an infrared source associated with each of the two radio continuum sources. However, it is interesting to note that the infrared counterpart of the UCH II region is stronger at longer wavelengths and decreases its intensity when approaching the near-infrared or visible regime. On the other hand, the source associated with VLA2 gets stronger at shorter wavelengths, being still visible in the red band of the DSS survey. Thus, VLA2, with a negative spectral index and showing emission in the visible bands, could be a T-Tauri star with synchrotron emission in the centimeter range (Feigelson and Montmerle 1985), or a background source with a possible extragalactic origin; while VLA1 seems to be definitely an UCH II region still associated with some dust.

3.5 Summary and brief discussion

We have presented new high angular resolution observations in the continuum and molecular dense gas tracers of the massive star-forming complex IRAS 22134+5834. We summarize our main conclusions in the following.

- Low angular resolution ($\sim 4''$) observations allow us to detect two centimeter continuum sources within the cluster of infrared sources in I22134. One of the sources, VLA2, has a negative spectral index and is associated with an infrared and optical source. The main radio continuum source, VLA1, shows a cometary morphology when observed with high angular resolution ($< 1''$) and has a spectral index of -0.18 ± 0.08 , consistent with the emission coming from an optically thin UCH II region, ionized by a B1 ZAMS star.
- At millimeter wavelengths, we detect a source coincident with the UCH II region, likely tracing a dust envelope. Higher angular resolution at 2 and 1 mm reveal that the millimeter emission comes from a shell-like structure surrounding the UCH II region (A. Palau and F. Fontani, priv. comm.). Thus, it seems that the cometary UCH II region is already dispersing the dust around it.
- Dense gas emission is detected in the NH_3 and N_2H^+ molecules, coming from several clumps that surround the cluster of infrared sources. The UCH II region lies close to the main dense gas clump, with the cometary arc pointing toward the dense gas. Furthermore, two extended ammonia structures appear surrounding the UCH II region toward the north and south. The dense gas close to the UCH II region shows large linewidths ($1.5\text{--}2\ \text{km s}^{-1}$) and high temperatures ($\sim 30\ \text{K}$). On the other hand, the clumps far from the radio continuum source show narrow lines and low

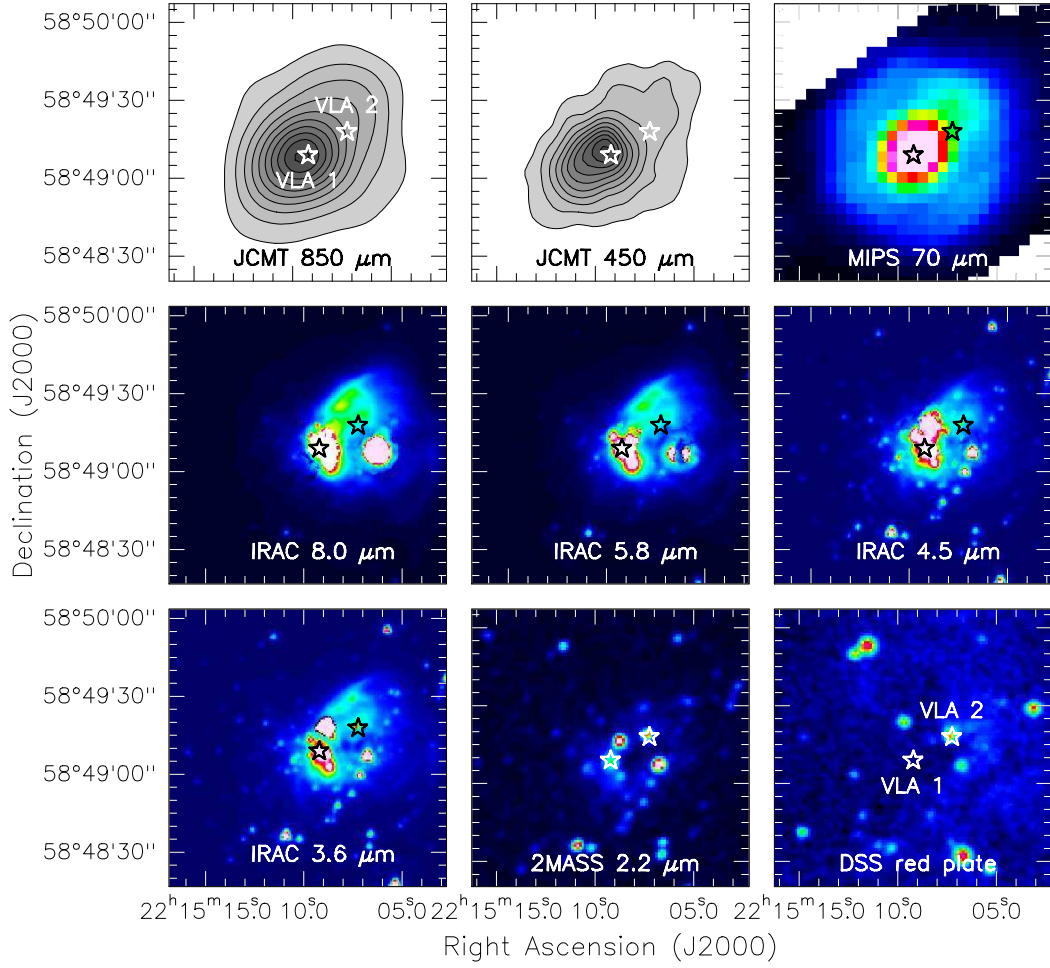


Figure 3.5: Images at infrared/submillimeter wavelengths for IRAS 22134+5834 (from Di Francesco et al. 2008, *Spitzer*, 2MASS, and DSS). The two stars mark the positions of the radio continuum sources VLA1 and VLA2 (see Table 3.2). The infrared emission of VLA1 is stronger at longer wavelengths, while the infrared counterpart of VLA2 is stronger at shorter wavelengths (and still visible in the red plate of the DSS).

temperatures. All this suggests that the UCH II region is radiatively affecting the dense gas, enhancing its temperature and increasing the linewidth.

Part III

Massive embedded compact radio sources driving outflows

4

IRAS 22198+6336: a radiojet within an intermediate-mass hot core¹

4.1 General overview

IRAS 22198+6336 (hereafter I22198) is an intermediate-mass young stellar object located at a distance of 760 pc, in the L1204/S140 molecular complex, with a bolometric luminosity of $\sim 450 L_{\odot}$ (Hirota et al. 2008). The presence of a strong and compact submillimeter dust condensation (Jenness et al. 1995) with no near-infrared neither mid-infrared emission (from 2MASS and MSX surveys) suggests it is a deeply embedded object, classified as an intermediate-mass Class 0 source by Sánchez-Monge et al. (2008). Single-dish telescope observations reveal a CO outflow well centered on the position of the dust condensation (Zhang et al. 2005; Jenness et al. 1995). Sánchez-Monge et al. (2008) detect slightly resolved partially optically thick centimeter emission consistent with a thermal ionized wind (or radiojet). The region is associated with dense gas emission (e.g., NH_3 : Tafalla et al. 1993; CS: Larionov et al. 1999) and H_2O and OH maser emission (Felli et al. 2007; Edris et al. 2007; Valdetaro et al. 2002; Tofani et al. 1995; Palla et al. 1991), but not with CH_3OH maser emission (Fontani et al. 2010). The recent high angular resolution observations of H_2O maser emission performed by Hirota et al. (2008) reveal expanding movements in the region close to the centimeter source ($0''.2$ – $0''.4$), likely tracing the kinematics of the outflow. All this suggest that I22198 is in a very early evolutionary stage.

¹This Chapter is based on the results published in the letter Sánchez-Monge et al. 2010, ApJL, 721, 107L, and in two forthcoming papers: Sánchez-Monge et al. in preparation, and Palau et al. in preparation.

4. IRAS 22198+6336: a radiojet within an intermediate-mass hot core

In this Chapter, we present new interferometric continuum and molecular line observations that reveal that I22198 is associated with an intermediate-mass hot core and two distinct outflows, with the centimeter emission likely tracing a thermal radio jet.

4.2 Observations

4.2.1 Very Large Array

The I22198 star forming region was observed with the Very Large Array (VLA²) at 3.6, 1.3, and 0.7 cm continuum in the D and C configurations of the array, on 2004 and 2008. In Table 4.1, we list the main parameters of the observations. The data reduction followed the VLA standard guidelines for calibration of high frequency data, using the NRAO package AIPS. First images were produced with a natural weighting to obtain a good sensitivity. The D-array 7 mm observations and all the C-array observations were carried out with 8–14 EVLA antennas in the array. We complemented our continuum observations with archival data from projects AO145 and AB601, which contains observations of I22198 at 20, 6.0, and 3.6 cm in different configurations (see Table 4.1). We combined the uv -data sets at the same frequencies to obtain final images with a better uv -coverage, sensitivity and angular resolution. In Table 4.3 we provide the resulting synthesized beams and rms noise levels for the combined uv -data sets.

The VLA was also used to map the $(J, K)=(1,1)$ and $(2,2)$ inversion lines of the ammonia molecule with the array in the C and D configurations. The D-array archival data were obtained during 1999 March 27. The adopted flux density of the absolute flux calibrator 0137+331 (3C48) was 1.05 Jy at the frequencies of 23.69 and 23.72 GHz. Amplitude and phase calibration were achieved by monitoring 2230+697, resulting in an rms of the phases $\sim 40^\circ$ and a bootstrapped flux of 0.426 ± 0.007 Jy. The C-array observations were carried out on 2008 April 21, with 14 EVLA antennas in the array. The flux scale was calibrated with observations of 0137+331 (3C48) and 1331+305 (3C286), with adopted fluxes of 1.11 and 2.52 Jy, respectively. The quasar 2253+161 (3C454.3) was used to correct for the bandpass. Amplitude and phase corrections were achieved by observing 2146+611, resulting in an rms phase $\sim 50^\circ$ and a bootstrapped flux of 0.722 ± 0.018 Jy. In both observations, the 4IF spectral line mode was used, allowing simultaneous observations of the NH_3 (1,1) and (2,2) lines with two polarizations for each line. The bandwidth used was 3.1 MHz, with 63 spectral channels with a channel spacing of 48.8 kHz ($\sim 0.6 \text{ km s}^{-1}$) centered at $v_{\text{LSR}} = -10.5 \text{ km s}^{-1}$ (-11.1 and -6.1 km s^{-1} for the archival (1,1) and (2,2) D-array observations, respectively), plus a continuum channel that contains the average of the central 75% of the bandwidth. The data reduction followed the standard guidelines for calibration of high frequency data, using the software package

²The Very Large Array (VLA) is operated by the National Radio Astronomy Observatory (NRAO), a facility of the National Science Foundation operated under cooperative agreement by Associated Universities, Inc.

Table 4.1: Main VLA continuum observational parameters of IRAS 22198+6336

λ (cm)	Project VLA conf.	Epoch of Observation	Gain cal. / Bootstr. Flux ^a	Flux cal.	Beam (" \times ")	P.A. ($^\circ$)	Rms ^b
20.0	A0145 B	1999 Nov 18+19	2148+611 / 1.78(1)	3C286	5.6×5.2	+25	22
6.0	A0145 B	1999 Nov 18+19	2148+611 / 1.14(1)	3C286	1.6×1.4	+30	20
3.6	AP476 D	2004 Jul 10	2148+611 / 0.97(1)	3C48	10.4×8.8	+7	27
3.6	AB601 D	1991 Mar 31	2230+697 / 0.60(1)	3C286	12.0×8.5	+1	29
3.6	AS926 C	2008 Apr 21	2148+611 / 1.04(2)	3C48	2.7×2.0	+4	32
1.3	AP476 D	2004 Jul 10	2230+697 / 0.60(1)	3C48	3.6×2.9	-5	63
1.3	AS926 C	2008 Apr 21	2148+611 / 0.72(3)	3C48	1.2×0.9	+5	42
0.7	AS896 D	2007 Feb+Mar	2148+611 / 0.53(6)	3C48	2.2×1.3	-43	226
0.7	AS926 C	2008 Mar 21	2148+611 / 1.02(10)	3C48	0.8×0.7	-3	290

^a Bootstrapped flux in Jy. In parenthesis: the percentage of error in the flux.

^b Rms noise level in $\mu\text{Jy beam}^{-1}$.

AIPS. We combined the calibrated D and C uv -data, after taking into account the different v_{LSR} in the observations, to increase the uv -coverage and recover extended and faint NH_3 emission. However, since the spectral rms noise was almost 2 times better for our C-array observations, we decided to use only the C-array data when obtaining spectral NH_3 information at the main core (see next Sections). Imaging was performed using natural weighting, resulting in a synthesized beam of $3''.7 \times 3''.1$ with a P.A. = -41° for the CD combined maps, and $2''.9 \times 2''.5$ with a P.A. = -13° , and 1σ rms of 1.9 mJy beam^{-1} per channel for the C-array observations, after tapering the uv -data at $60\text{ k}\lambda$.

4.2.2 Plateau de Bure Interferometer

The IRAM Plateau de Bure Interferometer (PdBI³) was used to observe the CO (1–0) (115.12 GHz) and SiO (2–1) (86.85 GHz) molecular transitions toward I22198. We carried out 2-pointing mosaic observations (primary beam of $54\text{--}56''$), in 2008 and 2009, with the array in the C and D configurations. The two spectral setups, tuned at 115.27 GHz (2.7 mm) and at 86.85 GHz (3.5 mm), include several molecular transitions. In Table 4.2, we list some of the main observational parameters for the spectral line observations. Additionally, a number of 320 MHz continuum units were used to image the continuum, six at 115 GHz and three at 86 GHz (see Table 4.2). The typical system temperatures for the receivers were $\sim 200\text{ K}$ at 115 GHz and $\sim 100\text{ K}$ at 86 GHz. Bandpass calibration was performed by observing 3C273 and 3C454.3. Amplitude and phase calibrations were achieved by monitoring 0116+731, 1928+738 and 2037+511, resulting in a phase rms of around 30° . The absolute flux density scale was determined from MWC349 and 3C84, with an estimated uncertainty around 25%. The data were calibrated with the program CLIC,

³The Plateau de Bure Interferometer (PdBI) is operated by the Institut de Radioastronomie Millimétrique (IRAM), which is supported by INSU/CNRS (France), MPG (Germany), and IGN (Spain).

4. IRAS 22198+6336: a radiojet within an intermediate-mass hot core

Table 4.2: Main PdBI observational parameters of IRAS 22198+6336

Molecular transition	Frequency (MHz)	Bandwidth (MHz)	Number of channels	Spec. resol. (km s ⁻¹)	Beam (″ × ″)	P.A. (°)	Rms ^a
Spectral line observations							
H ¹³ CN (1–0)	86 340.167	40	512	0.28	4.4 × 4.0	80	7.8
SiO (2–1)	86 847.010	40	512	0.28	4.6 × 4.2	117	9.5
H ¹³ CO ⁺ (1–0)	86 754.330	40	512	0.28	4.6 × 4.6	98	7.8
HCN (1–0)	88 631.847	20	512	0.14	4.4 × 3.9	82	15.
HCO ⁺ (1–0)	89 188.526	40	512	0.28	4.3 × 3.9	64	12.
C ¹⁷ O (1–0)	112 358.780	20	512	0.11	3.0 × 2.6	105	15.
¹² CO (1–0)	115 271.202	40	512	0.21	3.0 × 2.5	80	40.
Continuum observations							
3.5 mm	87 790.295	960	4.5 × 4.0	81	0.3
2.7 mm	113 971.362	1920	3.0 × 2.5	107	0.6

^a Rms noise level in mJy beam⁻¹ for continuum images, and mJy beam⁻¹ per channel for line images.

and imaged with MAPPING, both parts of the GILDAS⁴ software package. Imaging was performed using natural weighting, obtaining the synthesized beams and rms noise levels listed in Table 4.2.

4.2.3 Submillimeter Array

We observed the I22198 star-forming region with the Submillimeter Array (SMA⁵; Ho et al. 2004) in the 1.3 mm (230 GHz) band using the compact array configuration on 2008 June 11. The phase center was $\alpha(\text{J2000}) = 22^{\text{h}}21^{\text{m}}27^{\text{s}}.617$, and $\delta(\text{J2000}) = +63^{\circ}51'42''.18$, and the projected baselines ranged from 7 k λ to 100 k λ . The two sidebands of the SMA covered the frequency ranges of 219.4–221.4 GHz and 229.4–231.4 GHz, with a spectral resolution of ~ 0.5 km s⁻¹. System temperatures ranged between 200 and 300 K. The zenith opacities at 225 GHz were around 0.15 and 0.20 during the track. The FWHM of the primary beam at 1.3 mm was $\sim 56''$. Bandpass calibration was performed by observing the quasar 3C454.3. Amplitude and phase calibrations were achieved by monitoring 0019+734 and 1928+739, resulting in an rms phase of $\sim 30^{\circ}$. The absolute flux density scale was determined from Callisto and Jupiter with an estimated uncertainty around 15%. Data were calibrated and imaged with the MIRIAD software package. The continuum was constructed in the (u, v) domain from the line-free channels. Imaging was performed using natural weighting, obtaining a synthesized beam of $3''.0 \times 2''.2$ with a P.A.= 50° , and 1σ rms of 80 mJy beam⁻¹ per channel, and 3.9 mJy beam⁻¹ for the continuum.

⁴Grenoble Image and Line Data Analysis System, see <http://www.iram.fr/IRAMFR/GILDAS>.

⁵The SMA is a joint project between the Smithsonian Astrophysical Observatory and the Academia Sinica Institute of Astronomy and Astrophysics, and is funded by the Smithsonian Institution and the Academia Sinica.

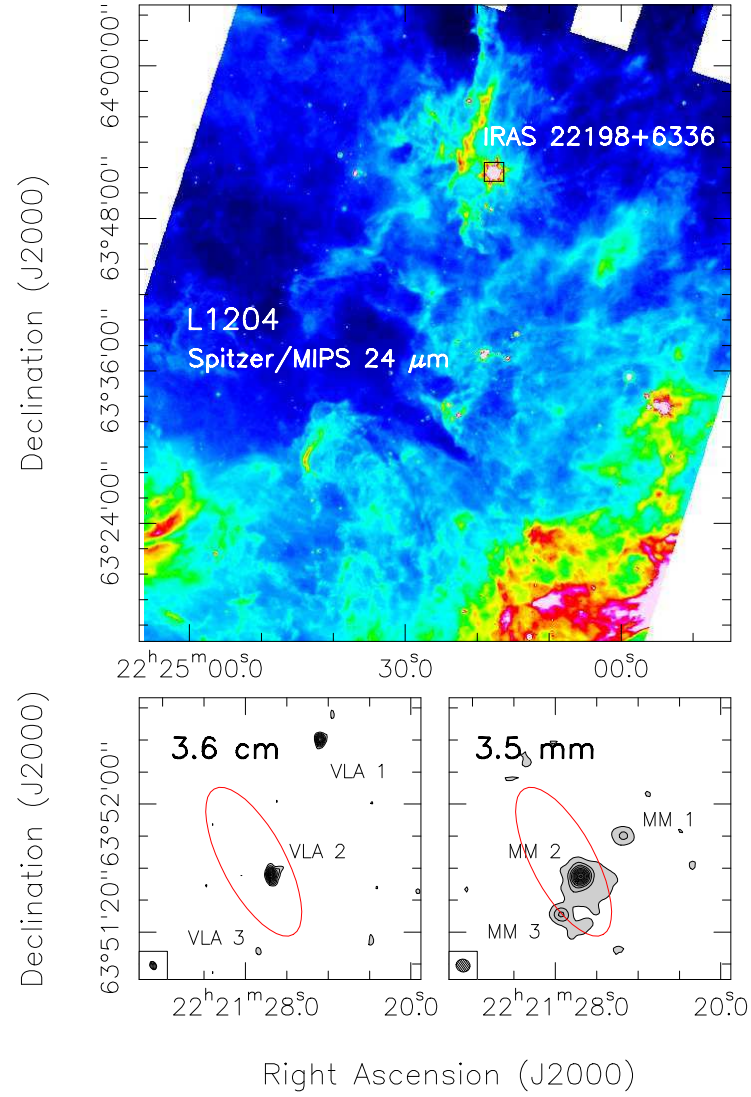


Figure 4.1: L1204/S140 star forming complex (IRAS 22198+6336). *Top*: *Spitzer*/MIPS 24 μm image of the L1204 molecular cloud. The black box marks the region of IRAS 22198+6336, which is zoomed in the bottom panels. *Bottom-left*: VLA 3.6 cm continuum emission. Levels start at 18%, increasing in steps of 10% of the peak intensity $0.41 \text{ mJy beam}^{-1}$. There are three centimeter sources in the field: VLA1, VLA2, and VLA3. Note that VLA3 is stronger at 20 and 6 cm (see Table 4.3). *Bottom-right*: PdBI 3.5 mm continuum emission. Levels start at 5%, increasing in steps of 10% of the peak intensity 15 mJy beam^{-1} . There are three millimeter sources in the field: MM1, MM2, and MM3. Only VLA2 and MM2 are coincident, see Figure 4.2 for a close-up of this source. Red ellipse marks the position of the IRAS source.

4.3 Continuum results

4.3.1 Centimeter and millimeter continuum results

In Figure 4.1 (top panel), we show a global overview of the L1204 star-forming complex at $24\ \mu\text{m}$ (*Spitzer*/MIPS), showing the location of I22198. In the bottom-left panel, we show a close up of the I22198 region at 3.6 cm. We detect centimeter radio continuum emission at all wavelengths. As shown in the figure, there are three main sources: VLA1, VLA2 and VLA3. In Table 4.3, we list their fluxes and sizes together with the beams and rms noise levels of the combined maps. We note that at 20 cm and 6.0 cm, we detect up to 15 different sources, but we will not consider them since they are located further than 0.2 pc from the IRAS source, and in most cases they probably have an extragalactic origin. Regarding the three main centimeter continuum sources, VLA1 and VLA3 have a flux density $\lesssim 1$ mJy decreasing with the frequency (see Table 4.3). Differently, VLA2, which is associated with the IRAS source 22198+6336, and for which we show a close-up at different frequencies in Figure 4.2, has a flux density increasing with frequency (see Figure 4.3). It is interesting to note that at all frequencies, VLA2 is slightly elongated in the southeast-northwest direction with a P.A. $\sim 150^\circ$ (Table 4.3).

At millimeter wavelengths (Figure 4.1 bottom-right panel), the continuum emission is dominated by a compact source, MM2, surrounded by a faint structure extended toward the southwest. The source is clearly detected at 3.5, 2.7, and 1.3 mm and has a similar morphology at the three wavelengths. Toward the northwest and southeast of MM2 there are two faint and compact millimeter continuum sources, MM1 and MM3. The flux densities and deconvolved sizes of the millimeter continuum sources are listed in Table 4.3. For the three sources, the flux increases with frequency, and the emission is likely tracing dust envelopes of young stellar objects, or dust entrained by the passage of molecular outflows (see Section 4.4.1).

Among all the centimeter and millimeter continuum sources, only VLA2 and MM2 are coincident, and directly associated with the IRAS source 22198+6336. However, the primary beam at millimeter wavelengths does not include the coordinates of VLA1 and VLA3, and we cannot ensure there is no millimeter continuum emission associated with these sources. Hereafter, we will refer to VLA2 (or MM2) as I22198.

4.3.2 Spectral energy distributions

We searched the literature for data from 2MASS, MSX, and SCUBA (Di Francesco et al. 2008) to complement our radio continuum observations. For VLA1, VLA3, MM1, and MM3, there is no emission at other wavelengths different from the radio continuum emission reported in this work. Their spectral energy distributions are shown in Figure 4.3 (bottom panels). For the main source, VLA2 or I22198, there is a submillimeter source directly associated with the IRAS source (Jenness et al. 1995), but no near-/mid-infrared

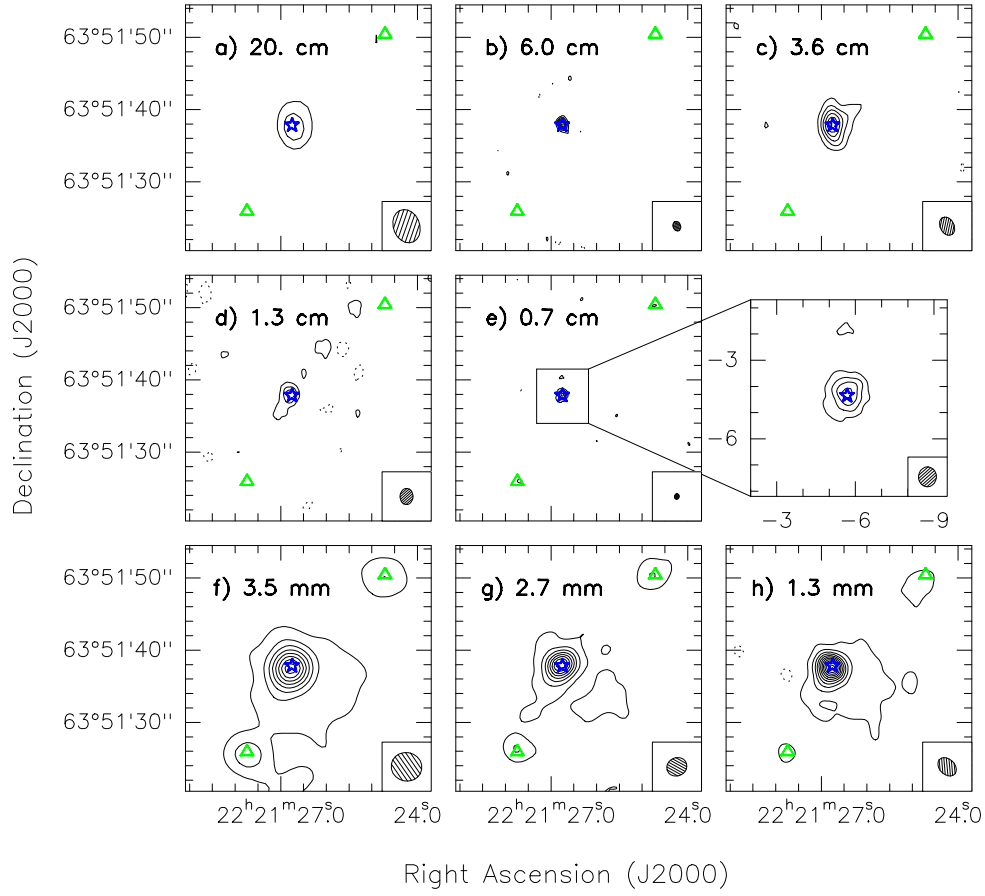


Figure 4.2: IRAS 22198+6336 (VLA2) continuum images. Each panel shows the continuum emission at the wavelength indicated at the top-left corner of the panel. For panels from a) to e), levels are -4 , -3 , and 3 to 9 , in steps of 1 times the rms noise level of the map: 17 , 20 , 23 , 44 , and $170 \mu\text{Jy beam}^{-1}$, respectively. For panels from f) to h), levels are -9 , -3 , and 3 to 63 , in steps of 6 times the rms noise level of the map: 0.3 , 0.6 , and $3.9 \text{ mJy beam}^{-1}$, respectively. For the close-up panel of 0.7 cm emission, $(0,0)$ corresponds to $\alpha(\text{J2000}) = 22^{\text{h}}21^{\text{m}}27^{\text{s}}.617$, and $\delta(\text{J2000}) = +63^{\circ}51'42''.180$. In all panels, the blue star indicates the position of VLA2/MM2: $\alpha(\text{J2000}) = 22^{\text{h}}21^{\text{m}}26^{\text{s}}.758$, and $\delta(\text{J2000}) = +63^{\circ}51'37''.822$, and green triangles mark the positions of MM1 and MM3 (see Table 4.3).

countparts from the 2MASS and MSX catalogues. We searched the *Spitzer* database and found observations from the Spitzer Space Telescope Infrared Array Camera (IRAC; PI: Giovanni Fazio, project: 40147). We retrieved the images using the Leopard⁶ software, and evaluated the fluxes using the MOPEX⁷ software. In Figure 4.3 (top panel), we show

⁶<http://ssc.spitzer.caltech.edu/warmmission/propkit/spot/>

⁷<http://ssc.spitzer.caltech.edu/dataanalysisistools/tools/mopex/>

4. IRAS 22198+6336: a radiojet within an intermediate-mass hot core

Table 4.3: Multiwavelength results for the YSOs in IRAS 22198+6336

λ (cm)	Beam ('' \times '')	P.A. ($^\circ$)	Rms ^b	$I_\nu^{\text{peak a}}$ (mJy beam ⁻¹)	S_ν^{a} (mJy)	Deconv. Size ('' \times '')	P.A. ($^\circ$)
VLA1	$\alpha(J2000.0) = 22^{\text{h}}21^{\text{m}}24.^{\text{s}}43$ $\delta(J2000.0) = +63^\circ52'20''.2$						
20.0	4.8×3.8	+25	17	0.56 ± 0.04	0.56 ± 0.08	$0.6 \times 0.0 \pm 0.6$	65 ± 30
6.0	1.4×1.1	+25	20	0.50 ± 0.05	0.50 ± 0.10	$0.7 \times 0.4 \pm 0.4$	160 ± 40
3.6	3.5×2.5	+0	23	0.35 ± 0.05	0.35 ± 0.09	$0.7 \times 0.0 \pm 0.7$	35 ± 60
MM1	$\alpha(J2000.0) = 22^{\text{h}}21^{\text{m}}24.^{\text{s}}72$ $\delta(J2000.0) = +63^\circ51'50''.4$						
0.35	4.5×4.0	+81	307	3 ± 1	4 ± 2	$2.9 \times 1.8 \pm 0.1$	90 ± 10
0.27	3.0×2.5	107	606	6 ± 1	10 ± 5	$3.7 \times 2.3 \pm 0.1$	130 ± 10
0.13	3.0×2.2	+50	3920	26 ± 8	75 ± 30	$6.2 \times 2.0 \pm 0.8$	140 ± 10
VLA2 ^c	$\alpha(J2000.0) = 22^{\text{h}}21^{\text{m}}26.^{\text{s}}76$ $\delta(J2000.0) = +63^\circ51'37''.8$						
20.0	4.8×3.8	+25	17	0.15 ± 0.04	0.17 ± 0.06	$3.3 \times 0.0 \pm 1.5$	150 ± 40
6.0	1.4×1.1	+25	20	0.39 ± 0.05	0.39 ± 0.09	$0.3 \times 0.0 \pm 0.3$	170 ± 50
3.6	3.5×2.5	+0	23	0.41 ± 0.05	0.62 ± 0.12	$2.7 \times 1.8 \pm 0.5$	170 ± 50
1.3	2.3×1.9	-5	44	0.50 ± 0.09	0.91 ± 0.23	$4.6 \times 1.2 \pm 1.2$	150 ± 10
0.7	1.1×1.0	-24	174	2.2 ± 0.3	2.8 ± 0.9	$0.9 \times 0.7 \pm 0.3$	170 ± 40
0.35	4.5×4.0	+81	307	15 ± 1	31 ± 12	$3.8 \times 2.8 \pm 0.1$	165 ± 10
0.27	3.0×2.5	107	606	30 ± 1	72 ± 27	$2.7 \times 1.9 \pm 0.1$	140 ± 10
0.13	3.0×2.2	+50	3920	260 ± 8	620 ± 150	$2.7 \times 1.8 \pm 0.2$	140 ± 10
VLA3	$\alpha(J2000.0) = 22^{\text{h}}21^{\text{m}}27.^{\text{s}}31$ $\delta(J2000.0) = +63^\circ51'13''.7$						
20.0	4.8×3.8	+25	17	0.68 ± 0.04	0.68 ± 0.05	$2.1 \times 0.8 \pm 0.8$	20 ± 20
6.0	1.4×1.1	+25	20	0.23 ± 0.05	0.23 ± 0.07	$0.7 \times 0.0 \pm 0.7$	70 ± 40
3.6	3.5×2.5	+0	23	0.11 ± 0.05	0.11 ± 0.05	$2.7 \times 1.8 \pm 0.5$	170 ± 50
MM3	$\alpha(J2000.0) = 22^{\text{h}}21^{\text{m}}27.^{\text{s}}75$ $\delta(J2000.0) = +63^\circ51'25''.9$						
0.35	4.5×4.0	+81	307	4 ± 1	5 ± 2	$4.1 \times 2.4 \pm 0.1$	50 ± 10
0.27	3.0×2.5	107	606	6 ± 1	8 ± 4	$2.2 \times 0.7 \pm 0.1$	60 ± 10
0.13	3.0×2.2	+50	3920	18 ± 8	22 ± 13	$4.6 \times 1.7 \pm 1.7$	155 ± 15

^a Primary beam corrected. Error in intensity is 2σ . Error in flux density has been calculated as $\sqrt{(2\sigma\sqrt{\theta_{\text{source}}/\theta_{\text{beam}}})^2 + (2\sigma_{\text{flux-scale}})^2}$, where σ is the rms noise level of the map, θ_{source} and θ_{beam} are the size of the source and the beam respectively, and $\sigma_{\text{flux-scale}}$ is the error in the flux scale, which takes into account the uncertainty on the calibration applied to the flux density of the source ($S_\nu \times \%\text{uncertainty}$).

^b Rms noise level in $\mu\text{Jy beam}^{-1}$.

^c VLA2 and MM2 are coincident. We consider them as the same source, and associated with the IRAS source 22198+6336.

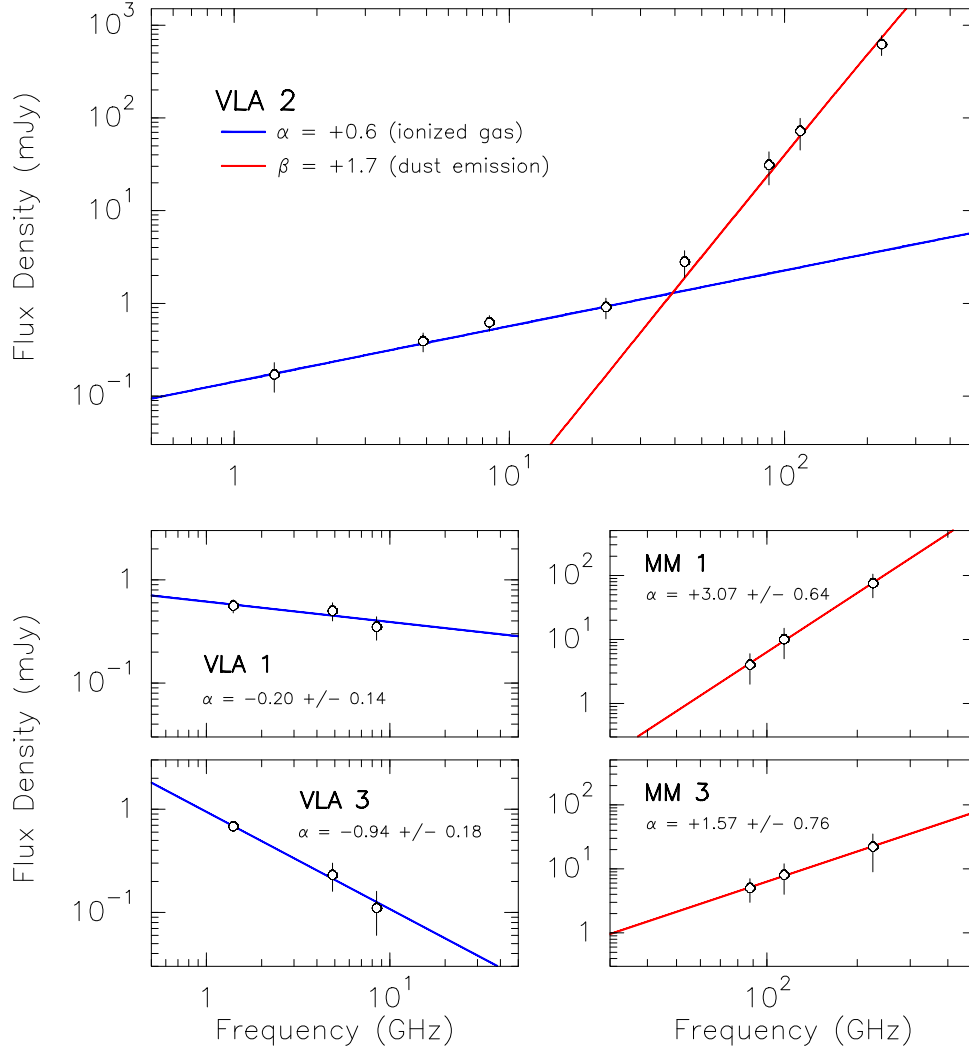


Figure 4.3: *Top:* Spectral energy distribution for VLA2. *Bottom panels:* Spectral energy distributions for VLA1 (top left), VLA3 (bottom left), MM1 (top right), and MM3 (bottom right). Blue and red lines correspond to linear fits to the centimeter and millimeter data, respectively. We indicate the spectral index α ($S_\nu \propto \nu^\alpha$) in all the cases. We note that for MM1 and MM3 (likely tracing dust envelopes) the dust emissivity index β is related to the spectral index by $\beta = \alpha - 2$, assuming the dust emission is optically thin.

the SED for VLA2 in the range of centimeter to millimeter wavelengths (a global SED of VLA2 can be found in Sánchez-Monge et al. 2010; see also Chapter 9). At centimeter wavelengths, the data can be fitted with a power-law distribution ($S_\nu \propto \nu^\alpha$) with $\alpha = +0.6$, while at millimeter wavelengths, the spectral index seems to be 3.7, which would correspond to a dust emissivity index of $\beta = 1.7$ ($\alpha = 2 + \beta$, in the case of optically

thin dust emission). With this dust emissivity index, we estimated the mass of gas and dust at millimeter wavelengths to be $\sim 5 M_{\odot}$, assuming a dust temperature of 36 K (from the global SED fit; Sánchez-Monge et al. 2010), and a dust mass opacity coefficient of $0.9 \text{ cm}^2 \text{ g}^{-1}$ at 1.3 mm (Ossenkopf and Henning 1994).

4.4 Molecular results

4.4.1 Molecular outflow gas

Interferometric ^{12}CO (1–0) and ^{12}CO (2–1) (Figure 4.4 top panels) maps reveal an outflow with a quadrupolar morphology clearly centered on the position of VLA2 (and MM2). The outflow emission spans a velocity range from -25 km s^{-1} to $+5 \text{ km s}^{-1}$ for the $J = 1 \rightarrow 0$ transition and -30 km s^{-1} to $+10 \text{ km s}^{-1}$ for the $J = 2 \rightarrow 1$ transition (the systemic velocity is $v_{\text{LSR}} \simeq -10.5 \text{ km s}^{-1}$). The quadrupolar morphology of the outflow can be interpreted as the walls of a single outflow or as the superposition of two bipolar outflows: outflow A in the southwest-northeast direction (with a P.A.= 40°), and outflow B in the northwest-southeast direction (with a P.A.= 125°). Different to CO outflow emission, high velocity HCO^+ (1–0) maps (Figure 4.4 bottom-left) reveal emission mainly associated with outflow B, spanning a range of velocities similar to the CO (1–0) outflow B emission. Only faint blueshifted emission is also found associated with the blueshifted lobe of outflow A. On the other hand, the integrated high-velocity SiO (2–1) emission, spanning a velocity range from -25 to -13 km s^{-1} (shown in black contours in Figure 4.4 bottom-right panel) is only coincident with the blueshifted lobe of outflow A. No redshifted counterpart is observed for the SiO emission. Additionally, HCN (1–0) emission showing moderate blue/red-shifted velocities (Figure 4.4 bottom-right) is clearly associated with outflow B. Finally, we also note that the IRAC $4.5 \mu\text{m}$ band (grey scale in Figure 4.4) shows extended emission (“green fuzzy”) associated mainly with the blueshifted CO outflow lobes. Such $4.5 \mu\text{m}$ extended emission is thought to be associated with shocked H_2 emission (De Buizer and Vacca 2010). H_2 emission at $2.12 \mu\text{m}$ observed with the 3.5 m Telescope of CAHA (Almería, Spain) reveal a number of H_2 knots coincident with some of the ‘sources’ detected at $4.5 \mu\text{m}$ (*Spitzer*/IRAC), and clearly following the red lobe of outflow B (A. Palau, priv. comm.).

Thus, it seems we are facing two distinct outflows associated with I22198: outflow A in the southwest-northeast direction mainly traced by CO, SiO, HCN, and $4.5 \mu\text{m}$ shocked gas emission, and with faint HCO^+ emission; and outflow B in the northwest-southeast direction traced by CO, HCO^+ , and $4.5 \mu\text{m}$ shocked gas emission. Both outflows are centered on the position of the millimeter continuum source, which could be a millimeter clump harbouring at least two sources. In fact, higher angular resolution observations ($0.4''$ or 300 AU) with the PdBI at 1.3 mm reveal a strong source with indications of a faint extension to the south (Palau et al., in prep.). We estimated the physical parameters of outflows A and B (see Table 4.4) and found values similar to the outflow

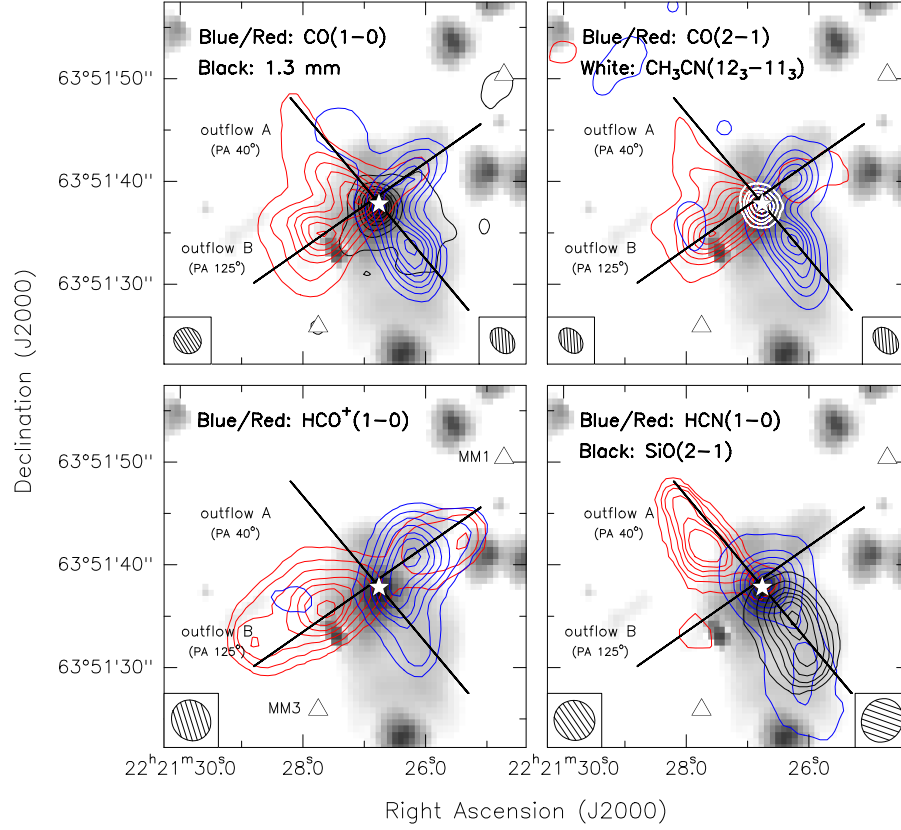


Figure 4.4: IRAS 22198+6336 outflow emission. *Top-left*: Blue/red contours: CO (1–0) intensity map for blue/red-shifted velocities (from -5 to -15 km s $^{-1}$ and from $+5$ to $+15$ km s $^{-1}$ with respect to the v_{LSR}). Black contours: 1.3 mm continuum map. Levels are -4 , and 4 to 60 in steps of 8 , times 3.92 mJy beam $^{-1}$. *Top-right*: Blue/red contours: CO (2–1) intensity map for blue/red-shifted velocities (from -5 to -20 km s $^{-1}$ and from $+5$ to $+20$ km s $^{-1}$ w.r.t. the v_{LSR}). White contours: CH $_3$ CN (12 $_3$ –11 $_3$) intensity map as in Figure 4.5. *Bottom-left*: Blue/red contours: HCO $^+$ (1–0) intensity map for blue/red-shifted velocities (from -5 to -15 km s $^{-1}$ and from $+5$ to $+15$ km s $^{-1}$ w.r.t. the v_{LSR}). *Bottom-right*: Blue/red contours: HCN (1–0) intensity map for blue/red-shifted velocities (from -4 to -7 km s $^{-1}$ and from $+4$ to $+7$ km s $^{-1}$ w.r.t. the v_{LSR}). Black contours: SiO (2–1) intensity map for blueshifted velocities (from -5 to -15 km s $^{-1}$ with respect to the v_{LSR}). In all panels, grey scale: 4.5 μ m IRAC/*Spitzer* image. Levels for blue/red contours start at 5% , increasing in steps of 15% of the peak intensity: $5.2/5.4$, $51/41$, $0.7/0.8$, $0.5/0.1$, and 0.4 Jy beam $^{-1}$ km s $^{-1}$ for CO (1–0), CO (2–1), HCO $^+$, HCN, and SiO, respectively. Synthesized beams are shown in the bottom-left (for the first image listed in the top of the panel) and in the bottom-right (for the second image listed in the top of the panel) corners. The white star marks the position of VLA2, and white triangles mark the positions of MM1 and MM3. Black lines mark the orientations of the pv-cuts shown in Figure 4.9.

4. IRAS 22198+6336: a radiojet within an intermediate-mass hot core

Table 4.4: Physical parameters of the outflows driven by IRAS 22198+6336^a

Outflow/lobe (1)	t_{dyn} (2)	size (3)	N_{mol} (4)	M_{out} (5)	\dot{M}_{out} (6)	P_{out} (7)	\dot{P}_{out} (8)	E_{kin} (9)	L_{mech} (10)
Outflow A — P.A.=40°									
CO (1–0) – red	1200	9×5	1.5×10^{16}	0.002	1.7	0.05	2.0	11.5	0.06
CO (1–0) – blue	1600	11×6	5.7×10^{16}	0.012	7.3	0.26	8.2	58.1	0.23
CO (1–0)	1400	...	7.2×10^{16}	0.014	9.8	0.31	11.1	69.7	0.29
CO (2–1) – red	1100	9×5	2.3×10^{16}	0.003	3.0	0.08	3.6	18.5	0.10
CO (2–1) – blue	1100	11×6	2.7×10^{16}	0.005	4.8	0.16	7.2	48.5	0.26
CO (2–1)	1100	...	5.0×10^{16}	0.009	7.9	0.24	10.9	67.1	0.36
SiO (2–1) – blue	1600	11×6	3.6×10^{12}	0.007	4.6	0.17	5.2	36.8	0.15
HCO ⁺ (1–0) – blue	2700	8×4	2.0×10^{12}	0.003	1.0	0.06	1.0	11.1	0.02
Outflow B — P.A.=125°									
CO (1–0) – red	1300	10×6	2.3×10^{16}	0.004	3.2	0.09	3.4	19.5	0.08
CO (1–0) – blue	1200	8×5	5.0×10^{16}	0.006	5.3	0.14	6.0	30.6	0.17
CO (1–0)	1250	...	7.3×10^{16}	0.010	8.3	0.23	9.2	50.1	0.25
CO (2–1) – red	1200	10×5	3.1×10^{16}	0.005	4.0	0.12	4.8	27.6	0.13
CO (2–1) – blue	1000	10×5	2.0×10^{16}	0.003	3.1	0.09	4.6	28.0	0.17
CO (2–1)	1100	...	5.2×10^{16}	0.008	7.2	0.21	9.5	55.6	0.30
HCO ⁺ (1–0) – red	2000	15×7	1.4×10^{12}	0.002	0.6	0.03	0.6	4.6	0.02
HCO ⁺ (1–0) – blue	1400	10×6	2.3×10^{12}	0.002	0.8	0.03	0.8	4.2	0.02
HCO ⁺ (1–0)	1700	...	3.8×10^{12}	0.003	1.3	0.05	1.3	8.8	0.03

^a Parameters are calculated for an inclination with respect to the plane of the sky equal to 30°, following the expressions given in Palau et al. (2007b). Notes and units for each column: (1) blue/red lobe for each molecular species; (2) dynamical age in years; (3) size of the lobe in arcsec; (4) column density of the molecule in cm^{-2} ; (5) outflowing mass in M_{\odot} ; (6) rate of the outflowing mass in $10^{-6} M_{\odot} \text{ yr}^{-1}$; (7) momentum of the outflow in $M_{\odot} \text{ km s}^{-1}$; (8) outflow momentum rate in $10^{-5} M_{\odot} \text{ km s}^{-1} \text{ yr}^{-1}$; (9) kinetic energy in 10^{42} erg ; and (10) mechanical luminosity in L_{\odot} . We have used the following abundances with respect to H_2 : $X_{\text{CO}} = 10^{-4}$, $X_{\text{SiO}} = 10^{-8}$, and $X_{\text{HCO}^+} = 4 \times 10^{-8}$.

parameters found in other intermediate-mass YSOs (e. g., IC 1396 N: Beltrán et al. 2002; IRAS 22272+6358 A: Beltrán et al. 2006b).

4.4.2 Molecular dense gas

The zero-order moment maps of the NH_3 (1,1) and (2,2) transitions are shown in Figure 4.5. The integrated NH_3 emission consists on one main clump associated with the centimeter source and showing a morphology similar to the extended millimeter continuum emission. Additionally, an extended structure elongated in the southeast-northwest

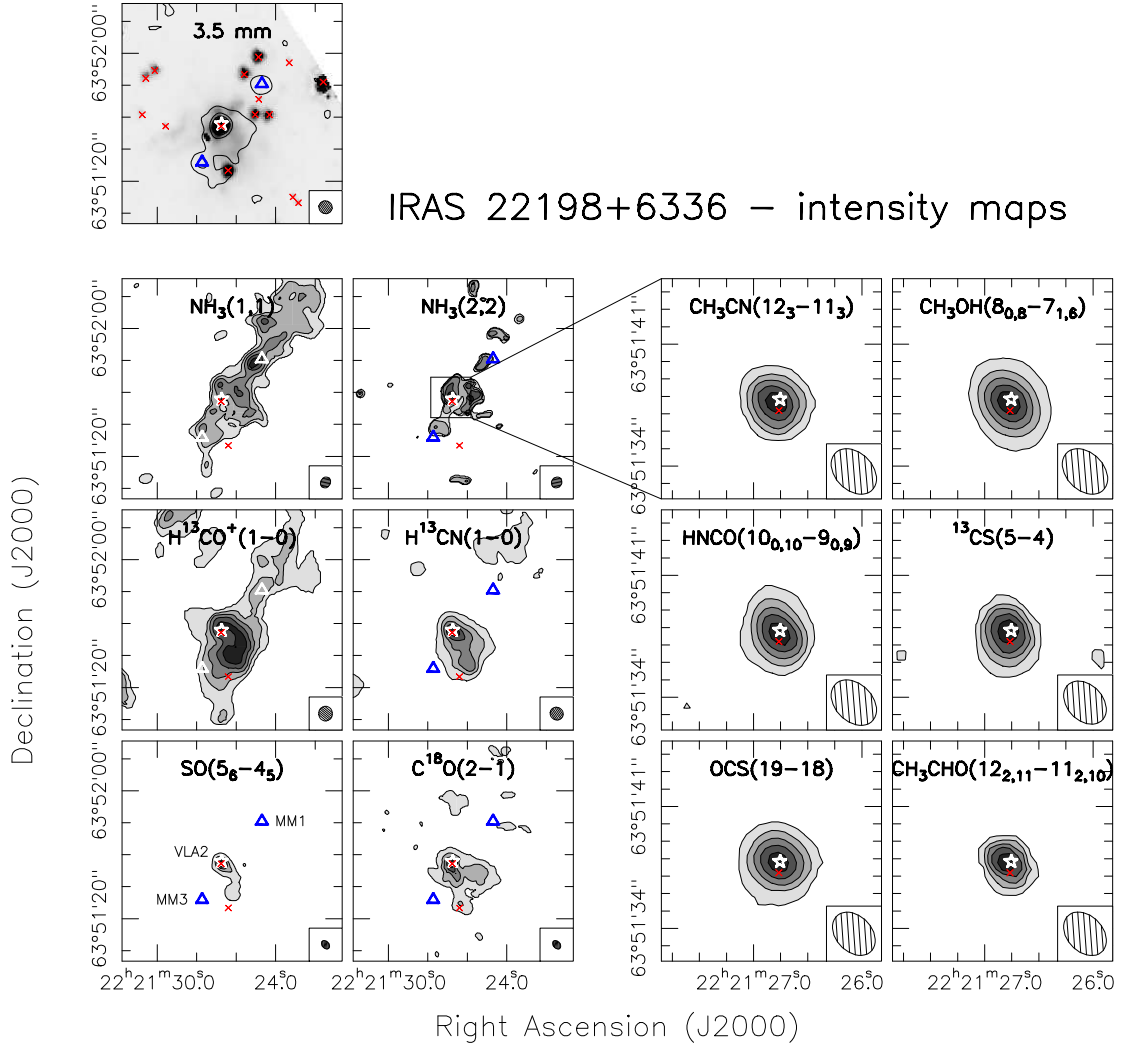


Figure 4.5: Zero-order moment (integrated intensity) maps for different molecules detected towards IRAS 22198+6336. The white star marks the position of the centimeter source, and the blue triangles the position of the millimeter sources. Red crosses are IRAC-*Spitzer* sources. Levels start at 5%, increasing in steps of 20% of the peak intensity. Synthesized beams for each molecule are shown in the bottom-right corner.

direction is clearly seen in the (1,1) ammonia map, being slightly filtered out in the (2,2) transition. Within this elongated structure there are two NH_3 peaks almost coincident with the positions of MM1 and MM3. It is interesting to note, that the main NH_3 clump has a peak directly associated with the centimeter source, surrounded by some condensations and holes or cavities (see next sections for a discussion on the nature of these structures, and for a close-up of the ammonia emission).

4. IRAS 22198+6336: a radiojet within an intermediate-mass hot core

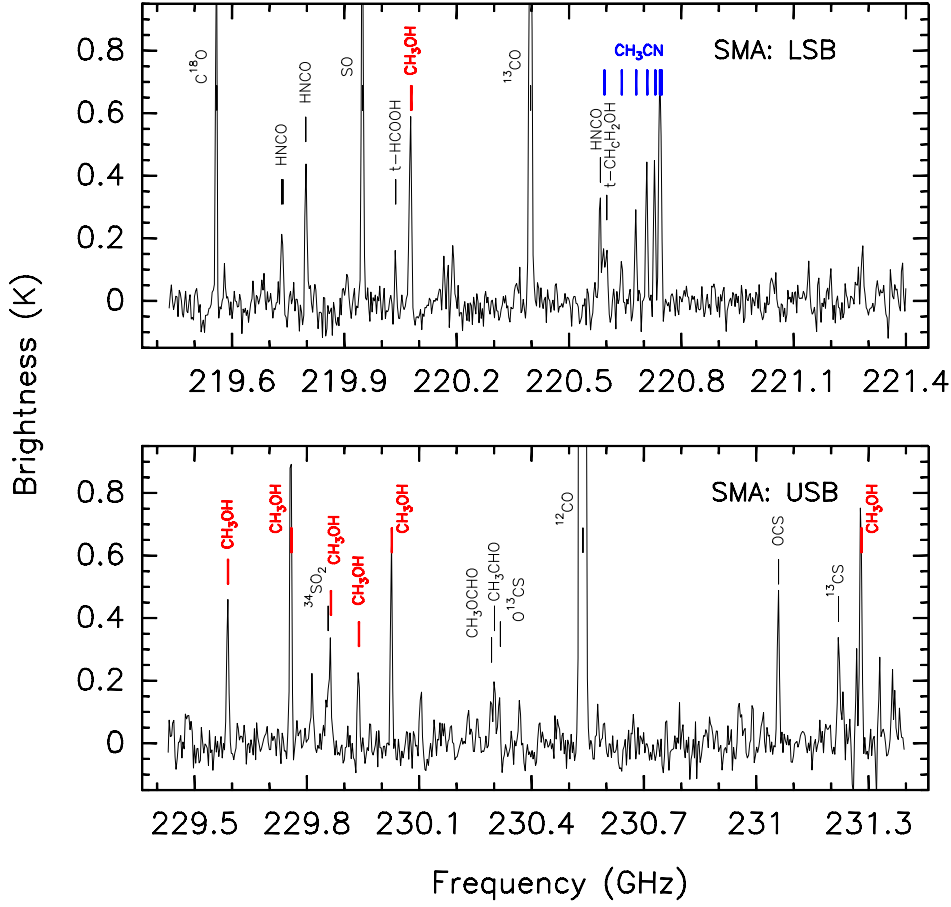


Figure 4.6: 230 GHz continuum-free spectra in the image domain from the SMA data, for the lower sideband (LSB) in the top panel and the upper sideband (USB) in the bottom panel. The molecular transitions used in the rotational diagrams (Figure 4.13) are shown in blue and red.

Similar to the NH_3 emission, the H^{13}CO^+ (1–0) intensity map (see Figure 4.5) consists on a main clump associated with the centimeter source, and elongated components in the southeast-northwest direction. The H^{13}CN (1–0) zero-order moment map resembles the NH_3 (2,2) emission, with the emission mainly contributing to the main clump, and showing some hints of the extended elongated structure $40''$ to the northwest of the main clump. It is interesting to note that in the main clump, the NH_3 (2,2) emission is elongated toward the southeast, while the H^{13}CN emission is elongated toward the southwest, following the direction of outflow A (which was traced by HCN, among other molecules; cf. Figure 4.4). Differently from the NH_3 maps, the H^{13}CO^+ and H^{13}CN emission at the main clump is more compact and does not show the cavities (holes) seen in NH_3 . Other molecules, such as SO and C^{18}O (see Figure 4.5), show emission associated only with the main clump. In

these cases, the emission clearly peaks at the position of the centimeter source, with faint extended emission that matches up with the morphology of the previously discussed dense gas tracers and dust emission.

Several other molecules (e.g., CH_3CN , CH_3OH , HNCO , OCS) have been detected towards I22198, with the emission coming from a compact source ($2''.1 \times 1''.3$, with P.A. = 15°) at the position of the millimeter continuum source and clearly coincident with the centimeter source (see right panels in Figure 4.5). In these cases, there are no hints of extended emission from the envelope of the main clump or from the elongated structure, suggesting this molecular emission arises from a very compact source. In fact, the wide-band SMA spectrum toward the compact molecular core (Figure 4.6) reveals a chemically rich dense core with typical hot core features (e.g., Cesaroni et al. 1999; Gibb et al. 2000). Molecular line transitions detected with $T_{\text{B}} \gtrsim 0.2$ K have been identified and imaged (Figure 4.5). Around 15 different molecular species have been identified in this compact molecular core. We note that the linewidths observed for most of the molecules are 5–8 km s^{-1} .

4.5 Analysis

4.5.1 Velocity fields

In Figures 4.7 and 4.8, we show the first-order moment (velocity) and linewidth (FWHM, obtained from the second-order moment) maps for the molecules shown in Figure 4.5.

Several velocity gradients can be identified in these maps (Figure 4.7). For those molecules with emission elongated in the southeast-northwest direction (NH_3 , H^{13}CO^+), there is a velocity gradient along the extension with velocities similar to the systemic velocity ($\sim -10 \text{ km s}^{-1}$) close to the centimeter source, and slightly blueshifted velocities ($\sim -11.5 \text{ km s}^{-1}$) toward the northwest. In Figure 4.9 (left panels), we show position-velocity plots in a cut with P.A.= 125° (outflow B direction), for these two molecular transitions (NH_3 , H^{13}CO^+) overlayed with the emission from the molecular tracers of outflow B (CO , HCO^+ : in black contours). The bipolar molecular outflow is clearly seen in these pv-plots spanning velocities from -20 up to $+5 \text{ km s}^{-1}$. The velocity gradient detected in the dense gas tracers along the elongated structure (with the blueshifted emission at the position of the blueshifted outflow lobe) is consistent with gas being swept up by the passage of outflow B. It is interesting to note that MM1 and MM3 are roughly situated in the same direction as outflow B. Thus, these two millimeter sources could be tracing dust entrained by outflow B.

In Figure 4.9 (right panels), we show pv-plots in a cut with P.A.= 40° (i.e., in the direction of outflow A, almost perpendicular to the elongation of the NH_3 and H^{13}CO^+ emission). Black contours reveal the emission of outflow A traced by different outflow tracers, spanning velocities from -20 up to $+0 \text{ km s}^{-1}$. The dense gas emission (overlayed as green contours) reveals a small velocity gradient with blueshifted dense gas emission at

4. IRAS 22198+6336: a radiojet within an intermediate-mass hot core

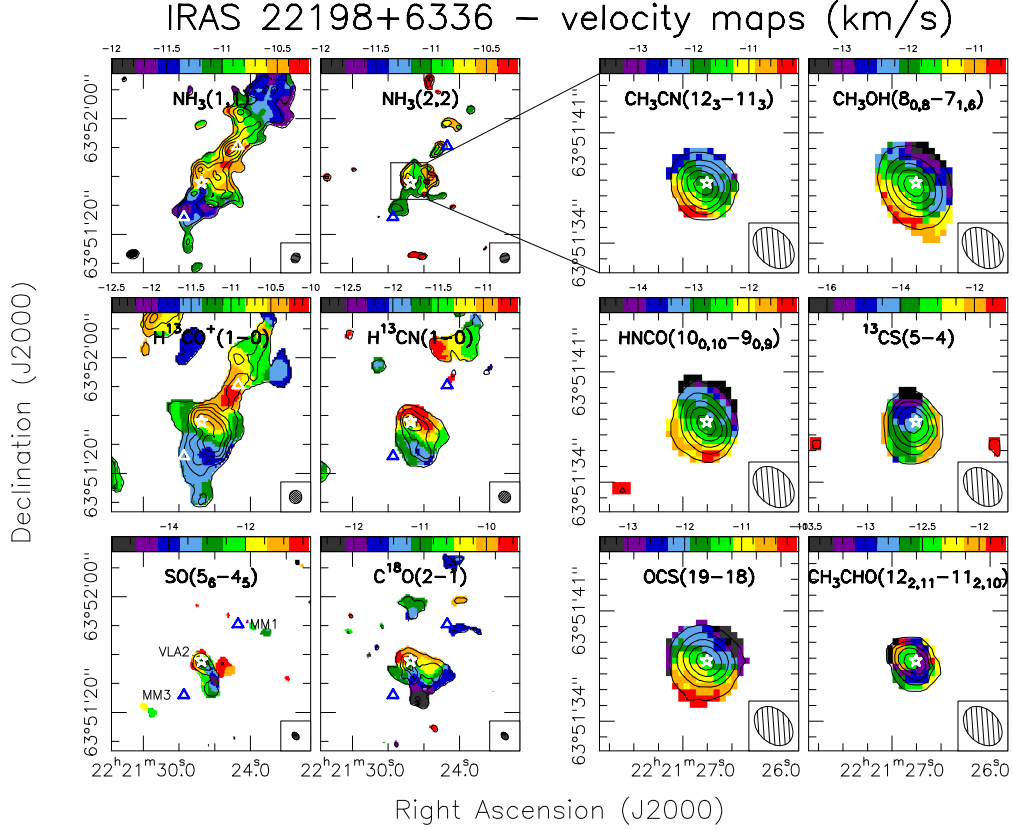


Figure 4.7: First-order moment (velocity) maps for different molecules detected towards IRAS 22198+6336. The white star marks the position of the centimeter source, and the blue triangles the position of the millimeter sources. Contours correspond to the intensity map shown in Figure 4.5.

the position of the blueshifted outflow lobe, consistent with the dense gas being progressively swept up by outflow A. This velocity gradient can also be identified in the first-order moment maps of $C^{18}O$ and $H^{13}CN$ (Figure 4.7). Although the ammonia emission is being perturbed by the outflow, its overall morphology could just be the initial filamentary structure of the cloud (note a second filamentary structure seen at $24\ \mu m$, Figure 4.1 top panel), in the same direction as the NH_3 elongation, toward the northeast of I22198.

At smaller scales, first-order moment maps for high-density tracers (Figure 4.7 right panels) show velocity gradients in the northwest-southeast direction, perpendicular to outflow A, presumably the youngest outflow. SiO high velocity emission is only found associated with outflow A, and SiO generally traces younger outflows since gas-phase SiO abundances may decrease with time (Shang et al. 2006; Klaassen and Wilson 2007; López-Sepulcre et al. 2011). Although the maps of each molecule show a source barely resolved, and we could doubt about this velocity gradient to be an instrumental effect, higher angular

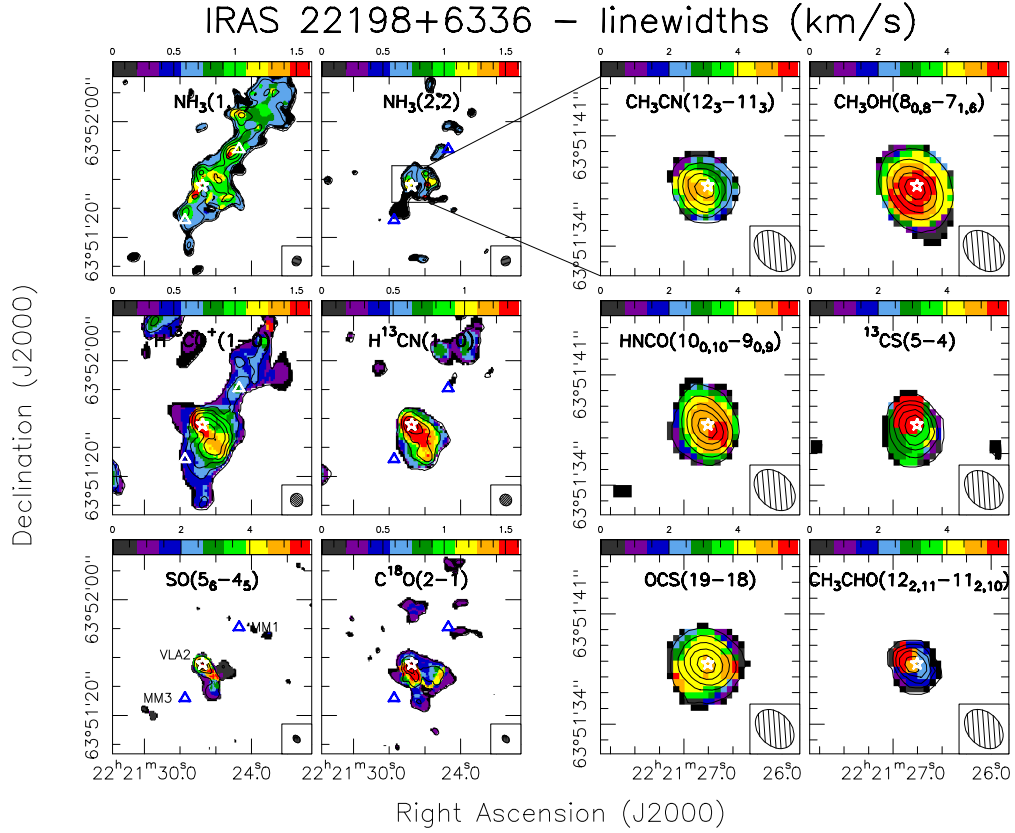


Figure 4.8: Linewidth (FWHM) maps, obtained from the second-order moment, for different molecules detected towards IRAS 22198+6336. The white star marks the position of the centimeter source, and the blue triangles the position of the millimeter sources. Contours correspond to the intensity map shown in Figure 4.5.

resolution observations with the PdBI reveal the same velocity gradient at scales of 300 AU (Palau et al., in prep.). Most of these molecules generally trace disks and/or toroids in other massive YSOs (e.g., Beltrán et al. 2006a). However, the presence of outflow B perpendicular to outflow A makes the interpretation of these velocity gradients uncertain. Assuming that these gradients trace rotation, the dynamical mass has been calculated from the expression $M_{\text{dyn}} = v_{\text{rot}}^2 R_{\text{rot}} / G \sin^2 i$, where v_{rot} is the velocity estimated from the gradient, R_{rot} the radius of the core, G the gravitational constant, and i the inclination angle assumed to be 90° (edge-on). In our case, with $v_{\text{rot}} \simeq 2 \text{ km s}^{-1}$ and $R_{\text{rot}} \simeq 1''$ for the molecules shown in Figure 4.7 right panels, the dynamical mass is $\sim 3.5 M_\odot$. Additionally, following the models of Palla and Stahler (1993), and assuming a luminosity for the object of $\sim 370 L_\odot$ (Sánchez-Monge et al. 2010), the mass of the embedded YSO is about $4\text{--}5 M_\odot$. Thus, the mass of the internal YSO estimated from both methods is $\sim 4 M_\odot$, which is similar to the dust envelope mass ($\sim 5 M_\odot$), as is characteristic of Class 0 objects.

4. IRAS 22198+6336: a radiojet within an intermediate-mass hot core

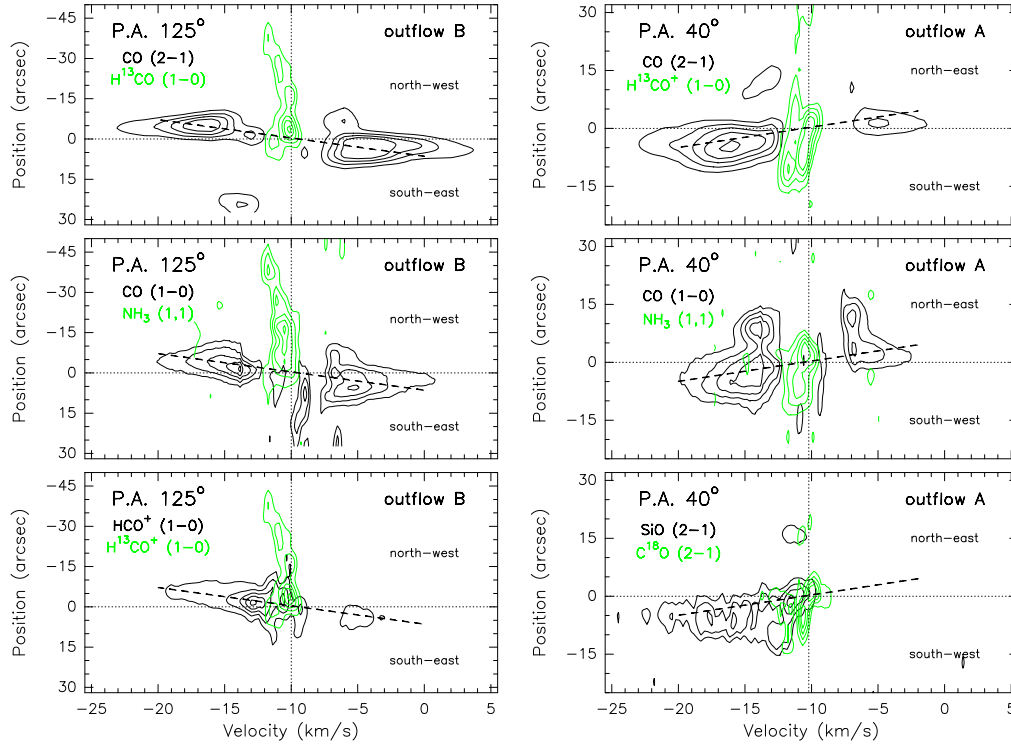


Figure 4.9: IRAS 22198+6336 position-velocity (pv) plots. *Left column:* Pv-plot along outflow B, in a cut with P.A.=125° (northwest-southeast) and centered on the position of the centimeter source VLA2. From top to bottom panels, black contours show the emission of the molecular outflow tracers CO (2–1), CO (1–0) and HCO⁺ (1–0), and green contours show emission from dense gas tracers H¹³CO⁺ (1–0) and NH₃ (1,1). Levels start at 15%, increasing in steps of 20% of the peak intensity: 4.4, 1.4, 0.6, 0.35, 0.04 Jy beam^{−1}. *Right column:* Pv-plot along outflow A, in a cut with P.A.=40° (southwest-northeast) and centered on the position of the centimeter source VLA2. From top to bottom panels, black contours show the emission of the molecular outflow tracers CO (2–1), CO (1–0) and SiO (2–1), and green contours show emission from dense gas tracers H¹³CO⁺ (1–0), NH₃ (1,1), and C¹⁸O (2–1). Levels start at 15%, increasing in steps of 20% of the peak intensity: 6.0, 1.7, 0.1, 0.3, 0.03, 0.9 Jy beam^{−1}.

4.5.2 Dense gas analysis

Following the method used in Chapters 2 and 3, we studied the chemical environment of I22198 by analyzing the column density of several molecular species, and estimating the temperature of the dense gas. We used the NH₃ (1,1) and (2,2) data from the C-array observations to derive the temperature of the extended dense gas emission. We computed the column density maps by extracting the spectra of the (1,1) and (2,2) transition lines for

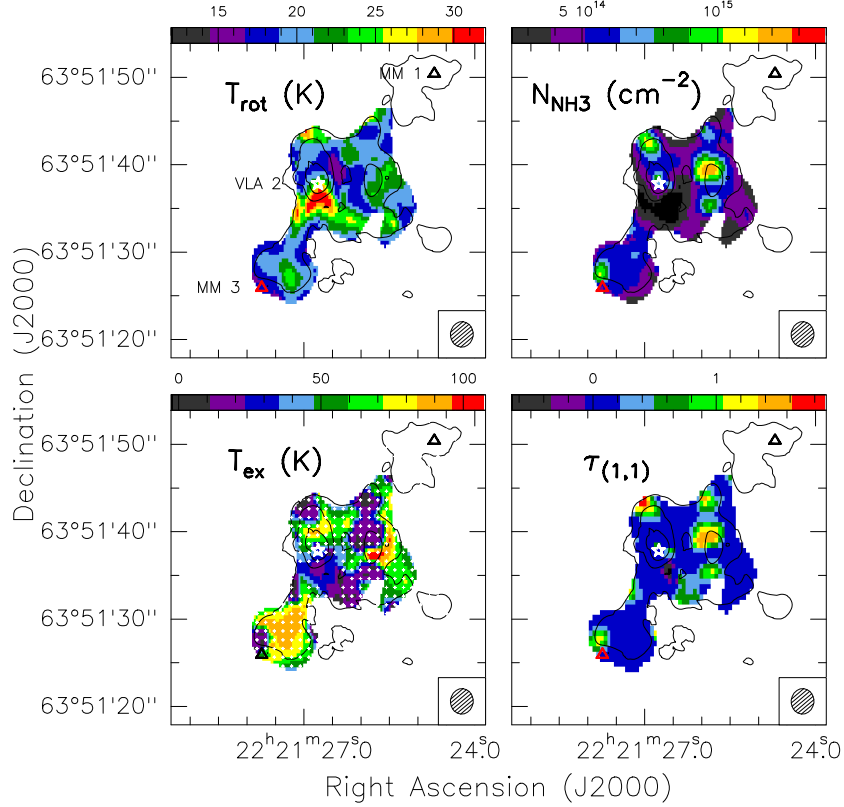


Figure 4.10: Ammonia parameters towards IRAS 22198+6336. From top to bottom, and left to right: rotational temperature map from NH_3 (1,1) and NH_3 (2,2) (units in K); NH_3 column density map (units in cm^{-2}); excitation temperature map from NH_3 (1,1) (units in K); map of the optical depth of the NH_3 (1,1) main line. In all panels, black contours show the intensity map of the NH_3 (2,2) line, and the white star marks the position of the centimeter continuum source. Triangles mark the position of MM1 and MM3. The synthesized beam is indicated in the bottom-right corner of each panel. Small white crosses in the T_{ex} map show the position for which we extracted the (1,1) and (2,2) spectra.

positions in a grid of $1'' \times 1''$ (see Busquet et al. 2009 and Busquet 2010, for more details in the method used). In Figure 4.10, we present the rotational temperature, column density, opacity and excitation temperature maps of the NH_3 emission. The emission of NH_3 (1,1) is essentially optically thin ($\tau_{(1,1)} < 1$) for all the main clump, with higher values close to the position of MM1. Large values of the excitation temperature (up to 80 K) are found in some ammonia condensations, however, this is a low opacity effect. For opacities $\tau < 0.1$, CLASS cannot obtain a reliable opacity value, which turns into a high excitation temperature (see Equation D.42). It is important to note, that the determination of the

4. IRAS 22198+6336: a radiojet within an intermediate-mass hot core

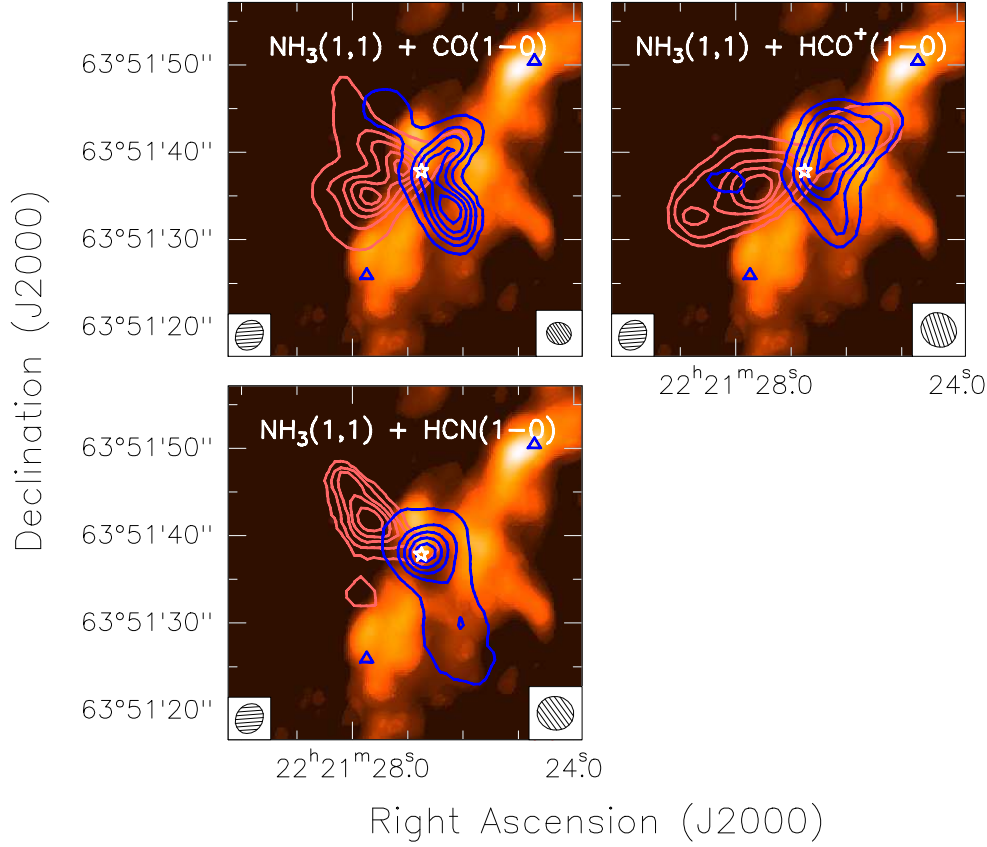


Figure 4.11: In all panels, colour scale show the NH₃ (1,1) zero-order moment map (shown in Figure 4.5). Red/blue contours correspond to the molecular outflows (as in Figure 4.4, but in steps of 20%) traced by CO (1-0) (left), HCO⁺ (1-0) (middle), and HCN (1-0) (right). The synthesized beams of the ammonia and outflow tracers are shown in the bottom left and right corners, respectively. In all panels, white star marks the position of VLA2, and the triangles mark the positions of MM1 and MM3 (see Table 4.3).

rotational temperature and column densities are not affected by this problem⁸. The values of the rotational temperature are close to 15–20 K in all the main clump, with values of the column density close to 10^{15} cm^{-2} . Note the V-shaped structure in T_{rot} with values for the temperature up to 34 K close to the centimeter source VLA2, and the temperature enhancement seen close to MM3 (see next section).

⁸For optical depths < 0.1 , the main beam temperature of the transition is obtained directly from $A \times \tau_m$ (see Equation D.41), and the rotational temperature will depend only on the main beam temperatures of the (1,1) and (2,2) transitions (cf. Equation A.4 in Busquet et al. 2009), and the column density only depends on the rotational temperature.

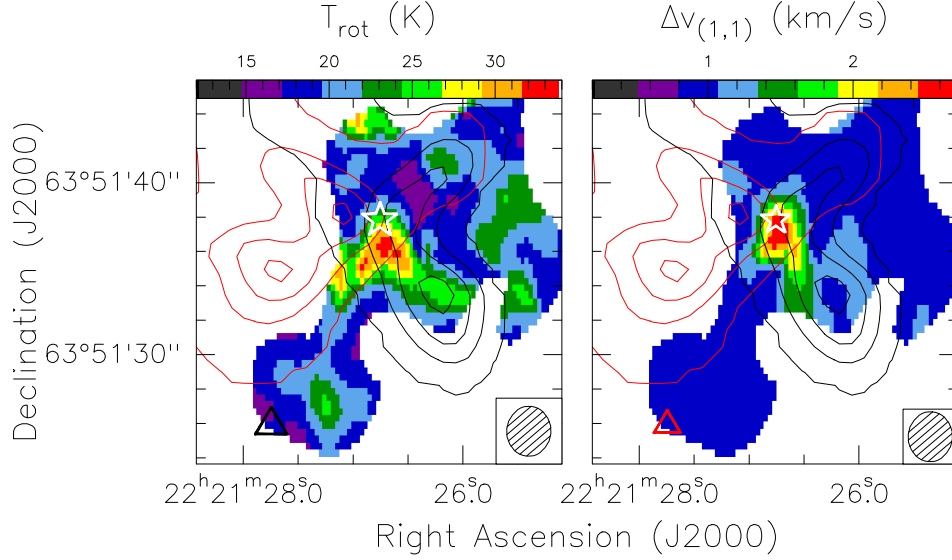


Figure 4.12: Rotational temperature (in K; *left panel*) from the NH_3 (1,1) and (2,2) transitions, and NH_3 (1,1) linewidth (in km s^{-1} ; *right panel*) maps, obtained from the spectral fits done at each pixel (see Section 4.5 and Figure 4.10). In both panels, red/black contours correspond to the molecular outflow traced by CO (1–0) (see Figure 4.4). There is a temperature enhancement and line broadening close to the position of the centimeter source VLA2. In all panels, white star marks the position of VLA2, and the triangles mark the positions of MM1 and MM3 (see Table 4.3).

4.5.3 Outflow-dense gas interaction

As shown in Section 4.5.1 (see also Figure 4.9), the two molecular outflows associated with VLA2 are perturbing kinematically the dense gas emission as traced by NH_3 or H^{13}CO^+ . In addition, we have searched for any hints of perturbation in the morphology of the NH_3 emission. As shown in Figure 4.11, where we show an overlay of the ammonia and outflow emission, the ammonia cores are spatially anticorrelated with the outflow lobes. Thus, and similar to the case of MM1 in IRAS 00117+6412 (see Chapter 2), it seems that the passage of the outflows are affecting morphologically the ammonia emission, creating several cavities and holes around the centimeter source.

Regarding the physical properties of the ammonia (see Figure 4.12), the enhancements, with a V-shaped morphology close to VLA2, in temperature (up to 34 K) and linewidth (up to 2.7 km s^{-1}) seem to be the result of the outflow interaction with the dense gas. Note also that the ammonia clump close to the MM3 dust condensation shows a temperature slightly higher ($\sim 25 \text{ K}$), likely produced by the presence of both outflows.

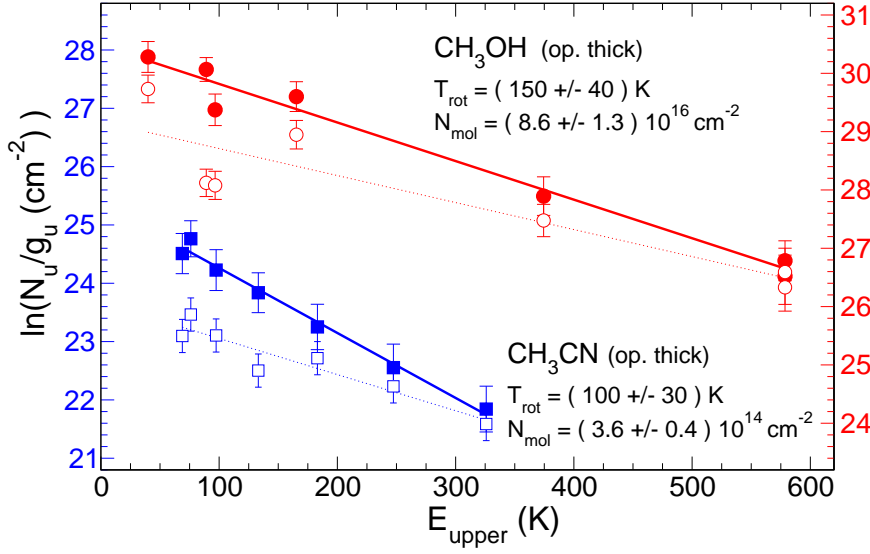


Figure 4.13: CH_3CN (blue squares) and CH_3OH (red circles) rotational diagrams. Open symbols and dashed lines refer to the optically thin approximation, while filled symbols and solid lines refer to the opacity which yields the best linear fit. For the optically thick fit we give the values in the figure, and adopt them in the main text. For the optically thin fit, $T_{\text{rot}} = 160 \pm 30$ K and $N_{\text{mol}} = (1.7 \pm 0.3) \times 10^{14} \text{ cm}^{-2}$ for CH_3CN , and $T_{\text{rot}} = 220 \pm 60$ K and $N_{\text{mol}} = (4.6 \pm 1.6) \times 10^{16} \text{ cm}^{-2}$ for CH_3OH . Vertical left and right axes refer to CH_3CN and CH_3OH , respectively. (Figure from Sánchez-Monge et al. 2010).

4.5.4 Hot molecular core properties

In addition to the NH_3 emission, we used the other observed molecules (detected in the compact core) to better estimate the physical conditions of this object: the hot molecular core. Because of the wide SMA band (Figure 4.6), one can observe several CH_3CN and CH_3OH transitions simultaneously. Following the rotational diagram method (Goldsmith and Langer 1999; Araya et al. 2005), which assumes that all molecular levels are populated according to the same excitation temperature, we can derive this temperature, T_{rot} , and the total column density, N_{mol} , for these molecules. We constructed the rotational diagrams following two methods. First, we assumed optically thin emission (open symbols in Figure 4.13). Second, we estimated the opacity for each transition (following Goicoechea et al. 2006; see also Girart et al. 2002) and we adopted the value that yielded the best linear fit (filled symbols in Figure 4.13). The resulting opacities for the different CH_3CN and CH_3OH transitions range from 0.3 to 3.5 and from 0.2 to 6.5, respectively. In the discussion we will use the results of the latter fit, which are $T_{\text{rot}} = 100 \pm 30$ K and $N_{\text{mol}} = (3.6 \pm 0.4) \times 10^{14} \text{ cm}^{-2}$ for CH_3CN , and $T_{\text{rot}} = 150 \pm 40$ K and $N_{\text{mol}} = (8.6 \pm 1.3) \times 10^{16} \text{ cm}^{-2}$ for CH_3OH . The high temperatures, together with

Table 4.5: Physical parameters derived from the molecular transitions observed

Molecule	Transition	Frequency (MHz)	$\int T dv$ (K km s ⁻¹)	v_{peak} (km s ⁻¹)	Δv (km s ⁻¹)	T_{peak} (K)	T_{ex} (K)	E_u (K)	A_{ul} (s ⁻¹)	N_u (cm ⁻²)	N_{mol} (cm ⁻²)
SMA molecular transitions											
C ¹⁸ O	2 → 1	219 560.354	3.8 ± 0.2	-9.7 ± 0.1	1.5 ± 0.1	2.460	42 ± 2	15.8	6.0 × 10 ⁻⁷	8.5 ± 0.9 × 10 ¹⁴	4.0 × 10 ¹⁵
HNCO	10 _{2,9} → 9 _{2,8}	219 733.850	0.6 ± 0.2	-10.6 ± 0.2	1.6 ± 0.8	0.342	54 ± 2	228.3	1.4 × 10 ⁻⁴	5.4 ± 2.8 × 10 ¹¹	3.5 × 10 ¹⁴
HNCO	10 _{2,8} → 9 _{2,7}	219 737.193	0.8 ± 0.2	-10.3 ± 0.3	2.5 ± 0.7	0.314	50 ± 2	228.3	1.4 × 10 ⁻⁴	7.7 ± 2.4 × 10 ¹¹	6.3 × 10 ¹⁴
HNCO	10 _{0,10} → 9 _{0,9}	219 798.274	3.9 ± 0.2	-12.2 ± 0.2	7.2 ± 0.4	0.514	79 ± 2	58.0	1.5 × 10 ⁻⁴	3.4 ± 0.3 × 10 ¹²	1.2 × 10 ¹⁴
SO	5 ₆ → 4 ₅	219 949.442	11.1 ± 0.2	-11.4 ± 0.1	6.1 ± 0.2	1.713	31 ± 2	35.0	1.3 × 10 ⁻⁴	1.1 ± 0.1 × 10 ¹³	1.9 × 10 ¹⁴
t-HCOOH	10 _{0,10} → 9 _{0,9}	220 037.967	1.0 ± 0.2	-11.7 ± 0.4	4.3 ± 0.8	0.212	36 ± 2	54.6	1.2 × 10 ⁻⁴	1.0 ± 0.2 × 10 ¹²	9.4 × 10 ¹³
CH ₃ OH (<i>E</i>)	8 _{0,8} → 7 _{1,6}	220 078.561	4.5 ± 0.2	-11.1 ± 0.2	6.7 ± 0.3	0.633	69 ± 2	96.6	2.5 × 10 ⁻⁵	1.6 ± 0.1 × 10 ¹³	8.6 × 10 ¹⁶ ‡
¹³ CO	2 → 1	220 398.684	15.9	6.1 × 10 ⁻⁷
HNCO	10 _{1,9} → 9 _{1,8}	220 584.751	2.9 ± 0.7	-10.9 ± 1.0	8.9 ± 2.3	0.308	50 ± 2	101.5	1.5 × 10 ⁻⁴	2.6 ± 0.7 × 10 ¹²	1.7 × 10 ¹⁴
CH ₃ CN	12 ₆ → 11 ₆	220 594.423	1.1 ± 0.5	-11.3 ± 0.2	6.7 ± 0.7	0.156	20 ± 2	325.9	6.9 × 10 ⁻⁴	2.3 ± 2.0 × 10 ¹¹	3.6 × 10 ¹⁴ †
t-CH ₃ CH ₂ OH	13 _{1,13} → 12 _{0,12}	220 601.941	1.1 ± 0.5	-12.4 ± 1.0	4.6 ± 2.7	0.229
CH ₃ CN	12 ₅ → 11 ₅	220 641.084	1.2 ± 0.5	-11.3 ± 0.2	6.7 ± 0.7	0.164	22 ± 2	247.4	7.6 × 10 ⁻⁴	1.9 ± 0.9 × 10 ¹¹	3.6 × 10 ¹⁴ †
CH ₃ CN	12 ₄ → 11 ₄	220 679.287	2.0 ± 0.5	-11.3 ± 0.2	6.7 ± 0.7	0.289	33 ± 2	183.1	8.2 × 10 ⁻⁴	2.7 ± 0.3 × 10 ¹¹	3.6 × 10 ¹⁴ †
CH ₃ CN	12 ₃ → 11 ₃	220 709.017	3.5 ± 0.3	-11.3 ± 0.2	6.7 ± 0.7	0.488	56 ± 2	133.2	8.7 × 10 ⁻⁴	3.8 ± 0.5 × 10 ¹¹	3.6 × 10 ¹⁴ †
CH ₃ CN	12 ₂ → 11 ₂	220 730.261	3.3 ± 0.3	-11.3 ± 0.2	6.7 ± 0.7	0.462	54 ± 2	97.4	9.0 × 10 ⁻⁴	3.4 ± 0.4 × 10 ¹¹	3.6 × 10 ¹⁴ †
CH ₃ CN	12 ₁ → 11 ₁	220 743.011	4.8 ± 0.3	-11.3 ± 0.2	6.7 ± 0.7	0.676	59 ± 2	76.0	9.2 × 10 ⁻⁴	3.6 ± 0.5 × 10 ¹¹	3.6 × 10 ¹⁴ †
CH ₃ CN	12 ₀ → 11 ₀	220 747.261	3.3 ± 0.3	-11.3 ± 0.2	6.7 ± 0.7	0.471	63 ± 2	68.9	9.2 × 10 ⁻⁴	4.5 ± 0.5 × 10 ¹¹	3.6 × 10 ¹⁴ †
CH ₃ OH (<i>E</i>)	15 _{4,11} → 16 _{3,13}	229 589.073	3.4 ± 0.3	-11.9 ± 0.3	6.2 ± 0.5	0.519	58 ± 2	374.4	2.1 × 10 ⁻⁵	1.6 ± 0.2 × 10 ¹³	8.6 × 10 ¹⁶ ‡
CH ₃ OH (<i>E</i>)	8 _{-1,8} → 7 _{0,7}	229 758.760	7.3 ± 0.3	-10.7 ± 0.1	5.1 ± 0.2	1.324	139 ± 3	89.1	4.2 × 10 ⁻⁵	1.7 ± 0.1 × 10 ¹³	8.6 × 10 ¹⁶ ‡
³⁴ SO ₂	4 _{2,2} → 3 _{1,3}	229 857.628	1.1 ± 0.2	-10.0 ± 0.6	7.3 ± 1.5	0.135	25 ± 2	18.7	7.1 × 10 ⁻⁵	2.0 ± 0.5 × 10 ¹²	6.9 × 10 ¹³
CH ₃ OH (<i>A</i> +)	19 _{5,15} → 20 _{4,16}	229 864.190	1.8 ± 0.2	-11.3 ± 0.3	5.1 ± 0.5	0.325	38 ± 2	578.6	2.1 × 10 ⁻⁵	8.4 ± 1.2 × 10 ¹²	8.6 × 10 ¹⁶ ‡
CH ₃ OH (<i>A</i> -)	19 _{5,14} → 20 _{4,17}	229 939.180	1.4 ± 0.2	-11.6 ± 0.4	.60 ± 1.3	0.216	27 ± 2	578.6	2.1 × 10 ⁻⁵	6.5 ± 1.8 × 10 ¹²	8.6 × 10 ¹⁶ ‡
CH ₃ OH (<i>E</i>)	3 _{-2,2} → 4 _{-1,4}	230 027.060	5.3 ± 0.2	-11.2 ± 0.1	6.3 ± 0.3	0.789	85 ± 2	39.8	1.5 × 10 ⁻⁵	3.5 ± 0.2 × 10 ¹³	8.6 × 10 ¹⁶ ‡
CH ₃ OCHO (<i>A</i>)	22 _{9,13} → 22 _{8,14}	230 293.951	1.3 ± 0.3	-10.4 ± 0.7	8.5 ± 2.1	0.142	209 ± 3	203.4	1.6 × 10 ⁻⁵	1.1 ± 0.3 × 10 ¹³	3.5 × 10 ¹⁶
CH ₃ CHO (<i>A</i> -)	12 _{2,11} → 11 _{2,10}	230 301.880	1.8 ± 0.3	-12.1 ± 0.4	6.3 ± 0.9	0.261	43 ± 2	81.0	4.2 × 10 ⁻⁴	5.8 ± 1.0 × 10 ¹³	2.1 × 10 ¹⁴
O ¹³ CS	19 → 18	230 317.527	1.1 ± 0.2	-8.4 ± 0.4	4.6 ± 0.9	0.224	38 ± 2	110.5	3.5 × 10 ⁻⁵	4.3 ± 1.0 × 10 ¹²	2.7 × 10 ¹⁴
¹² CO	2 → 1	230 538.000	16.6	6.9 × 10 ⁻⁷
OCS	19 → 18	231 060.993	3.8 ± 0.3	-11.0 ± 0.2	6.4 ± 0.4	0.554	13 ± 1	110.9	3.6 × 10 ⁻⁵	1.6 ± 0.3 × 10 ¹³	7.8 × 10 ¹⁶
¹³ CS	5 → 4	231 220.685	2.2 ± 0.4	-12.9 ± 0.4	5.8 ± 1.0	0.356	57 ± 2	33.3	2.5 × 10 ⁻⁴	1.2 ± 0.2 × 10 ¹²	1.0 × 10 ¹³
faint line	? → ?	231 270.000	2.3 ± 0.3	-10.2 ± 0.4	5.9 ± 0.9	0.366
CH ₃ OH (<i>A</i> -)	10 _{2,9} → 9 _{3,6}	231 281.100	8.8 ± 0.4	-10.6 ± 0.2	8.0 ± 0.4	1.031	109 ± 3	165.3	1.8 × 10 ⁻⁵	4.7 ± 0.4 × 10 ¹²	8.6 × 10 ¹⁶ ‡

† Molecular column density estimated from the rotational diagram with the 7 rotational transitions of CH₃CN (12–11). We estimate a $T_{\text{rot}} = 100 \pm 30$ K and a $N_{\text{mol}} = 3.6 \pm 0.4 \times 10^{14}$ cm⁻² (see Figure 4.13).

‡ Molecular column density estimated from the rotational diagram with the 7 rotational transitions of CH₃OH. We estimate a $T_{\text{rot}} = 150 \pm 40$ K and a $N_{\text{mol}} = 8.6 \pm 1.3 \times 10^{16}$ cm⁻² (see Figure 4.13).

4. IRAS 22198+6336: a radiojet within an intermediate-mass hot core

the chemically rich spectrum, are clear evidence that I22198 is an intermediate-mass hot core.

Finally, in Table 4.5 we list all the molecules detected in the compact core likely tracing a hot core. Following the procedures indicated in Appendix D we have estimated the column densities of each molecule, except for those molecules with several rotational transitions observed, for which we have listed the column density derived from their rotational diagrams. The molecular abundances can be estimated taking into account the column density of H_2 (obtained from the dust millimeter continuum emission). Assuming $T = 100$ K and a size of $2''.1 \times 1''.3$, which is the deconvolved size of the CH_3CN core, we obtain $N_{\text{H}_2} = 7 \times 10^{23} \text{ cm}^{-2}$. The derived abundances, calculated as $X_{\text{mol}} = N_{\text{mol}}/N_{\text{H}_2}$, for some of the molecules are $X_{\text{C}^{18}\text{O}} = 1 \times 10^{-8}$, $X_{\text{HNCO}} = 8 \times 10^{-10}$, $X_{\text{SO}} = 5 \times 10^{-10}$, $X_{\text{HCOOH}} = 2.4 \times 10^{-10}$, $X_{\text{OCS}} = 2 \times 10^{-7}$, $X_{\text{C}^{13}\text{CS}} = 2.5 \times 10^{-11}$, and $X_{\text{CH}_3\text{CN}} = 9 \times 10^{-10}$, $X_{\text{CH}_3\text{OH}} = 2.2 \times 10^{-7}$, with uncertainties close to a factor of 2 or 4. These abundances are similar to the values found in NGC 7129-FIRS2 (Fuente et al. 2005), an intermediate-mass hot core similar to I22198 (see Sánchez-Monge et al. 2010 for more details).

4.6 Summary and brief discussion

We have studied with high angular resolution observations the nearby intermediate-mass star-forming complex associated with the IRAS source 22198+6336. In the following, we summarize the main conclusions obtained.

- Our radio continuum study has revealed the presence of five sources close ($\lesssim 0.2$ pc) to IRAS 22198+6336. Two of them (VLA1 and VLA3) are only detected at centimeter wavelengths likely tracing non-thermal emission. MM1 and MM3, only detected at millimeter wavelengths, could be tracing dust condensations or dust entrained by the molecular outflows. The main radio continuum source is VLA2 (associated with the IRAS source), with the centimeter emission likely tracing a thermal radiojet or ionized wind (with a spectral index of 0.6) and the millimeter emission tracing a dust envelope of $5 M_{\odot}$ for a dust temperature of 36 K.
- We have detected two distinct outflows in different molecular species, centered on the position of the centimeter (and millimeter) source. Outflow A (P.A. = 40°) traced by CO, SiO, HCN and $4.5 \mu\text{m}$ shocked gas emission, and outflow B (P.A. = 125°) traced by CO, HCO^+ and $4.5 \mu\text{m}$ shocked gas emission. Both outflows have physical properties similar to the values found in other intermediate-mass molecular outflows.
- The cold (15–20 K) dense gas seen at large scales (mainly NH_3 and H^{13}CO^+) seems to be kinematically affected by the passage of the two molecular outflows. Additionally, we have found evidences of the outflows shaping the morphology of the ammonia emission (creating holes and cavities that perfectly match the blue/red lobes of the two outflows). In conclusion, and similar to the case of IRAS 00117+6412, the

ammonia molecule seems to be affected by the passage of the outflows driven by YSOs.

- At smaller scales we have found a compact dense core with emission from 15 different molecular species. This chemically rich and compact emission is characteristic of hot cores. By using the rotational diagram technique we estimated the temperature of this compact core to be 100–150 K. Thus, the chemically rich spectrum and the high rotational temperature, make I22198 one of the few intermediate-mass hot cores (IMHCs) known at present. Finally, a velocity gradient, perpendicular to outflow A, is found in almost all the molecular transitions associated with the hot core. Assuming this velocity gradient traces Keplerian rotation of a disk, we have estimated a central mass for the YSO to be $3.5 M_{\odot}$, which is similar to the dust envelope mass ($\sim 5 M_{\odot}$), as is characteristic for Class 0 objects.

5

G75.78+0.34: compact radio sources embedded in a hot core¹

5.1 General overview

The G75.78+0.34 (hereafter G75) massive star-forming region, close to the IRAS source 20198+3716, is located within the ON-2 molecular cloud at a distance of 3.8 kpc (Ando et al. 2010). At centimeter wavelengths, the region is dominated by a cometary ultracompact (UC) H II region reported by Wood and Churchwell (1989). Hofner and Churchwell (1996) detected a cluster of water masers located about 2'' (10^4 AU) southwest of the UCH II region, coincident with a compact radio continuum source (Carral et al. 1997) with a spectral index from 6 cm through 3 mm of $+1.5 \pm 0.4$. Franco et al. (2000) modeled this compact continuum source as a hypercompact (HC) H II region with a density gradient of $n_e \propto r^{-4}$. Additionally, emission from a vast set of molecular line transitions has been reported in single-dish surveys (e.g., Shirley et al. 2003; Roberts and Millar 2007; Klaassen and Wilson 2007; Bisschop et al. 2007). Interferometric observations of different ammonia transitions reveal that the most of the molecular emission seems to come from the compact radio continuum source associated with the cluster of water masers (Codella et al. 2010). Finally, up to four distinct outflows have been identified in the ON-2N molecular cloud (Shepherd et al. 1997). All this makes G75 an excellent target to study the nature of multiple centimeter continuum sources in a massive star forming region.

In this Chapter, we present high angular resolution VLA centimeter continuum obser-

¹This Chapter is based on the results that will be published in Sánchez-Monge, Kurtz et al. in prep.

5. G75.78+0.34: compact radio sources embedded in a hot core

Table 5.1: Main continuum observational parameters of G75.78+0.34

λ (cm)	Project VLA conf.	Epoch of Observation	Gain cal. / Bootstr. Flux ^a	Flux cal.	Beam ($'' \times ''$)	P.A. ($^\circ$)	Rms ^b
6.0	AF381 B	2001 Apr 23	2015+371 / 2.50(1)	3C48	1.6×1.3	-87	0.49
3.6	AK440 B	1997 Mar 16	2025+337 / 3.50(1)	3C286	1.0×0.7	+6	0.14
3.6	AK490 A	1999 Sep 12+13	2015+371 / 2.01(1)	3C286	0.3×0.2	-73	0.05
2.0	AK423 CnB	1996 Jan 29	2025+337 / 2.72(2)	3C286	1.7×1.4	+66	0.36
2.0	AF381 B	2001 Apr 23	2015+371 / 2.62(1)	3C286	0.6×0.4	-84	0.11
1.3	AK440 B	1997 Mar 16	2025+337 / 3.48(2)	3C286	0.31×0.26	-14	0.12
1.3	AK490 A	1999 Sep 12+13	2015+371 / 1.82(2)	3C286	0.10×0.08	+52	0.13
0.7	AK423 CnB	1996 Jan 29	2025+337 / 2.33(2)	3C286	2.5×0.5	-64	0.46
0.7	AK500 B	1999 + 2000	2015+371 / 2.10(4)	3C286	0.14×0.12	+37	0.25
0.31	OVRO	1997 + 1998	BL Lac / 5.4(20)	Uranus	2.0×1.7	-88	0.59
0.13	OVRO	1997 Sep-Dec	BL Lac / 2.5(30)	Uranus	1.6×1.5	-51	4.0
0.12	SMA	2010 Jun 10	2025+337 / 1.7(15)	Callisto	6.4×2.7	-76	8.4

^a Bootstrapped flux in Jy. In parenthesis: the percentage of error in the flux.

^b Rms noise level in mJy beam⁻¹.

vations, and H₂O and CH₃OH maser emission, together with OVRO and SMA millimeter continuum and spectral line observations toward G75.

5.2 Observations

5.2.1 Very Large Array

G75.78+0.34 was observed with the Very Large Array (VLA²) at 6.0, 3.6, 2.0, 1.3, and 0.7 cm from January 1996 to April 2001, using the array in the CnB, B, and A configurations. In Table 5.1 we report details of the observations. The data reduction followed the VLA standard guidelines for calibration of high frequency data, using the NRAO package AIPS. First images were produced with the robust parameter of Briggs (1995) set to 1. Regarding the angular resolution, we distinguish two groups in our data set: one with $\theta_{\text{beam}} \geq 1''.0$, and the other with $\theta_{\text{beam}} \sim 0''.3$. The continuum images at 1.3 cm and 0.7 cm, from projects AK490 and AK500, were self-calibrated with the strongest H₂O and CH₃OH maser components, respectively, observed simultaneously to the continuum emission (see below). Finally, we combined our uv -data at the same frequencies to obtain final images with a better uv -coverage, sensitivity, and angular resolution. The resulting synthesized beams and rms noise levels are shown in Table 5.3. At 6 cm, the H II region G75.77+0.34 to the southwest (see Figure 5.1) produced non-imageable artifacts. Excluding the short-

²The Very Large Array (VLA) is operated by the National Radio Astronomy Observatory (NRAO), a facility of the National Science Foundation operated under cooperative agreement by Associated Universities, Inc.

Table 5.2: Main spectral line observational parameters of G75.78+0.34

Line	Frequency (GHz)	Bandwidth and Spectral Resol. ^a	v_{ref} (km s ⁻¹)	Beam ('' × '')	P.A. (°)	Rms ^b
H ₂ O (6 ₁₆ -5 ₂₃)	22.235080	1.56 / 0.0244 (0.33)	+1.0	0.07 × 0.07	-67	77.
		6.25 / 0.0977 (1.3)	-10.0	0.10 × 0.07	-69	50.
NH ₃ (1,1)	23.694495	3.13 / 0.0488 (0.6)	-2.0	3.72 × 3.43	-57	2.8
		6.25 / 0.0977 (1.2)	-0.2	1.04 × 0.97	-10	1.7
		1.56 / 0.0061 (0.08)	-3.5	1.03 × 0.96	-63	1.7
NH ₃ (2,2)	23.723360	3.13 / 0.0488 (0.6)	-2.0	3.72 × 3.43	-58	2.5
		3.13 / 0.0244 (0.3)	-0.2	1.06 × 0.93	+27	2.0
NH ₃ (4,4)	24.141748	3.13 / 0.0244 (0.3)	-0.2	1.09 × 0.83	+42	2.5
CH ₃ OH (7 ₀ -6 ₁)	44.069410	1.56 / 0.0244 (0.17)	+3.0	0.11 × 0.10	+32	30.
H40 α	99.022960	128. / 2.0 (6.1)	-8.0	5.6 × 2.8	+33	10.
H30 α	231.900940	128. / 2.0 (2.6)	-8.0	3.9 × 1.8	+29	15.
SMA lines	...	4000. / 0.38 (1.0)	-0.2	6.4 × 2.7	-76	90.

^a Bandwidth in MHz. Spectral resolution in MHz (number in parenthesis in km s⁻¹).

^b Rms noise level per channel, in units of mJy beam⁻¹.

est baselines (< 5 k λ) produced essentially no change in the measured flux density but significantly improved the quality of the map.

The water maser line at 22.23508 GHz (6₁₆ – 5₂₃ transition) was observed with the VLA in the A configuration (project AK490) simultaneously to the 1.3 cm continuum emission. Two different spectral configurations (see Table 5.2) were used providing two different spectral resolutions (0.3 and 1.3 km s⁻¹). The class I methanol maser line at 44.06941 GHz (7₀ – 6₁ A⁺ transition) was observed with the VLA in the B configuration (project AK500) simultaneously to the 0.7 cm continuum emission. Details on the spectral configuration can be found in Table 5.2. The H₂O and CH₃OH maser data were calibrated following the AIPS guidelines for the calibration of high frequency data. Self-calibration was performed on the strongest maser component, and the solutions were applied to the spectral line and continuum data. The images were constructed using uniform and natural weighting to obtain the highest angular resolution and to estimate the intensity of the different maser components, respectively.

The VLA was also used to map the (J, K)=(1,1) (2,2) and (4,4) inversion lines of the ammonia molecule with the array in the C and D configurations. The archival (1,1) and (2,2) line data were obtained during 2002 January 12 (project AF386) with the array in its D configuration. The adopted flux density of the absolute flux calibrator 1331+305 (3C286) was 2.41 Jy at the frequencies of 23.69 and 23.72 GHz. Amplitude and phase calibration were achieved by monitoring 2025+337, resulting in an rms of the phases of $\sim 40^\circ$ and a bootstrapped flux of 2.50 ± 0.04 Jy. The 4IF spectral line mode was used, allowing simultaneous observations of NH₃ (1,1) and (2,2) lines with two polarizations for each line. The bandwidth used was 3.1 MHz, with 63 spectral channels with a channel

5. G75.78+0.34: compact radio sources embedded in a hot core

spacing of 48.8 kHz ($\sim 0.6 \text{ km s}^{-1}$) centered at $v_{\text{LSR}} = -2.0 \text{ km s}^{-1}$, plus a continuum channel that contains the average of the central 75% of the bandwidth. The (1,1) (2,2) and (4,4) inversion lines were observed with the array in the C-configuration on 2009 July (project AS984). The flux scale was calibrated with observations of 1331+305 (3C286), with an adopted flux of 2.40 Jy at 23.87 GHz. The quasar 1642+398 (3C345) was used to correct for the bandpass. Amplitude and phase corrections were achieved by observing 2015+371, resulting in an rms phase of $\sim 40^\circ$ and a bootstrapped flux of 3.81 ± 0.06 Jy. The (1,1) line was observed with two different bandwidths and spectral resolutions (1.2 and 0.08 km s^{-1} ; see Table 5.2). The small bandwidth (1.56 MHz) of the high spectral resolution (1,1) observations, together with the large ($\sim 5 \text{ km s}^{-1}$) linewidth measured in the observations (see next Sections), and the VLA-EVLA aliasing problem, make difficult to properly subtract the continuum baseline to the higher spectral resolution observations. We decided not to use these data, since we have new observations of all the (1,1) hyperfine transitions with a high spectral resolution (0.2 km s^{-1} ; Expanded VLA project: AS1031, in process of calibration). The (2,2) and (4,4) lines were observed simultaneously with a spectral resolution of 0.3 km s^{-1} . See Table 5.2 for more details of the observations. The data reduction followed the standard guidelines for calibration of high frequency data, using the software package AIPS. Imaging was performed using natural weighting, resulting in the synthesized beams and rms noise levels listed in Table 5.2.

5.2.2 Owens Valley Radio Observatory

The Owens Valley Radio Observatory (OVRO³) observations at 3 and 1 mm were made in the L (Low) and H (High) resolution configurations during September, October and December 1997. In March 1998, additional 3 mm observations were made in the uH (ultra-High) resolution configuration. All the observations were made in the double sideband mode, simultaneously observing at 3 and 1 mm. The continuum was observed in two 1 GHz channels, centered at 95.78 GHz and 98.78 GHz for 3 mm and 228.85 GHz and 231.85 GHz for 1 mm. In addition, spectral line modules covered the H40 α (99.02296 GHz) and H30 α (231.90094 GHz) radio recombination lines (RRLs). Each spectral line setup consisted of 62 Hanning smoothed channels of 2 MHz each, providing resolutions of 6.1 and 2.6 km s^{-1} at 3 mm and 1 mm, respectively. The assumed LSR velocity for both lines was -8 km s^{-1} . Bandpass calibration was performed by observing the quasar 3C454.3. Amplitude and phase calibration were achieved by monitoring BL Lac during the different observing tracks. The absolute flux density scale was determined from Uranus, with an estimated uncertainty of 20% at 3 mm and 30% at 1 mm. The data were reduced using a combination of routines from the OVRO reduction package MMA, from MIRIAD, and from AIPS. Imaging was performed with the task IMAGR of AIPS. In Tables 5.1 and 5.2 we list details of the continuum and radio recombination line observations.

³OVRO was operated by the California Institute of Technology with support from the National Science Foundation.

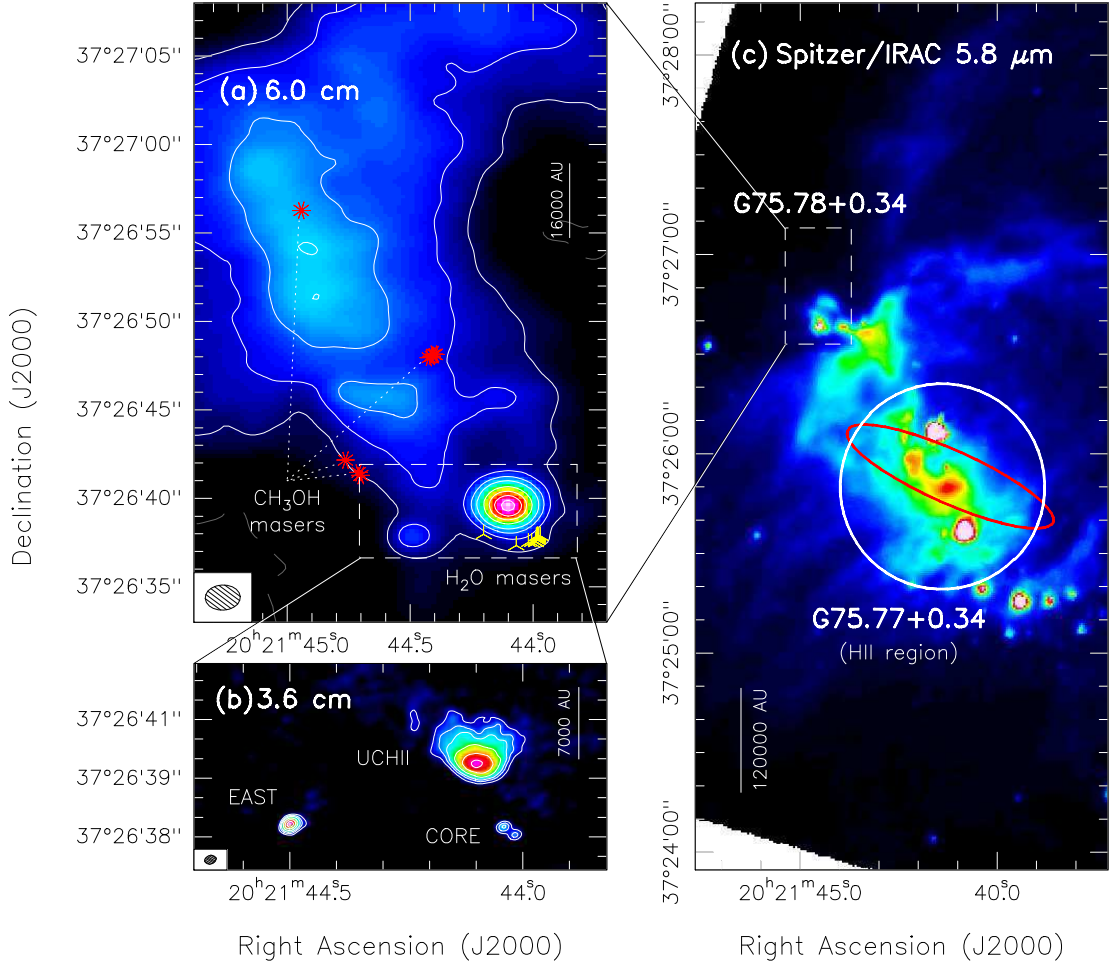


Figure 5.1: G75.78+0.34 star-forming region. (a): VLA 6.0 cm continuum image. Levels are $-3, 3, 6, 10, 15, 25, 35, 45,$ and 55 times $490 \mu\text{Jy beam}^{-1}$. Ten-point red stars indicate CH₃OH masers, and three-point yellow stars indicate H₂O masers. The dashed box shows the region zoomed in the panel b. (b): VLA 3.6 cm continuum image. Levels are $-4, 4, 8, 12, 20, 30,$ and 40 times $50 \mu\text{Jy beam}^{-1}$. Synthesized beams of the continuum images are shown in the bottom-left corner. (c): *Spitzer*/IRAC $5.8 \mu\text{m}$ image. The white circle shows the position of the large H II region G75.77+0.34. The dashed box shows the region of G75.78+0.34, zoomed in panel (a). The red ellipse marks the position of the IRAS source 20198+3716.

5.2.3 Submillimeter Array

G75.78+0.34 was observed with the Submillimeter Array (SMA⁴) in the 1.3 mm (230 GHz) band using the compact configuration on 2010 June 10. A total of 2×4 GHz were used, covering the frequency ranges 218.2–222.2 GHz and 230.2–234.3 GHz, with a spectral resolution of $\sim 1 \text{ km s}^{-1}$. System temperatures ranged between 150 and 250 K. The zenith opacities at 225 GHz were around 0.10 and 0.15 during the 3-hour track. The FWHM of the primary beam at 1.3 mm was $\sim 56''$. Bandpass calibration was performed by observing the quasar 3C454.3. Amplitude and phase calibrations were achieved by monitoring 2025+337 and 2015+371, resulting in an rms phase of $\sim 40^\circ$. The absolute flux density scale was determined from Callisto with an estimated uncertainty around 15%. Data were calibrated and imaged with the MIRIAD software package. The continuum was constructed in the (u, v) domain from the line-free channels. Imaging was performed using natural weighting, resulting in a synthesized beam of $6''.4 \times 2''.7$ with a P.A. = -76° , and 1σ rms of $8.4 \text{ mJy beam}^{-1}$ for the continuum. The wide SMA band includes several molecular transitions in the frequency range 220.2–222.2 GHz and 230.3–232.2 GHz.

5.3 Continuum results

5.3.1 Centimeter continuum emission

In Figure 5.1, we show a global overview of the G75 region at 6.0 cm (panel a), 3.6 cm (panel b), and $5.8 \mu\text{m}$ (panel c). We detected centimeter radio continuum emission at all wavelengths. As seen in the figure, the centimeter continuum emission is dominated by three strong and compact components (UCH II, EAST, and CORE) and by a large and faint extended structure toward the north-east of the three compact sources. In Figure 5.2, we show the maps of the combined images at each frequency for each of the three main centimeter continuum sources, and in Table 5.3 we list their flux densities and sizes, together with the beams, and rms noise levels of the combined images. The strongest source (UCH II) is a cometary UCH II region with an integrated flux density of $\sim 35 \text{ mJy}$ and an angular size of $\sim 1''$ ($\sim 0.02 \text{ pc}$ at a distance of 3800 pc; already imaged by Wood and Churchwell 1989 and Carral et al. 1997). Located $\sim 6''$ to the east, we identify a compact source (EAST), with a flux density of $\sim 4 \text{ mJy}$ and an angular size of $\sim 0.2''$ ($\sim 0.004 \text{ pc}$ at a distance of 3800 pc). Finally, at the head of the cometary arc we find a compact source (CORE) slightly elongated in the northeast-southwest direction, with a flux density of a few mJy increasing with frequency. This source is coincident with the 7 mm continuum source reported by Carral et al. (1997) and with the clump of H_2O masers (Hofner and Churchwell 1996). Our higher angular resolution observations ($\leq 0''.3$)

⁴The SMA is a joint project between the Smithsonian Astrophysical Observatory and the Academia Sinica Institute of Astronomy and Astrophysics, and is funded by the Smithsonian Institution and the Academia Sinica.

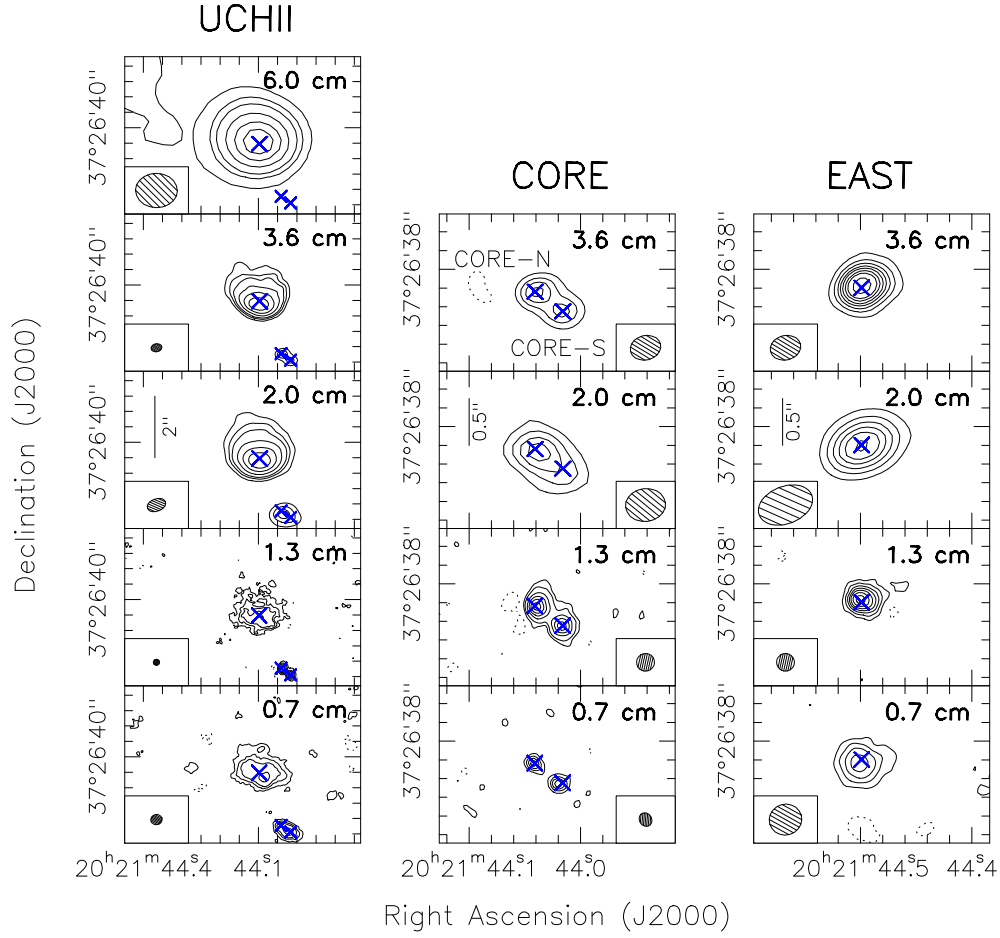


Figure 5.2: **Left column:** UCH II region continuum maps. Each panel shows the continuum emission at the wavelengths observed with the VLA. For all panels, levels are $-4, 4, 8, 12, 20, 30$, and 40 times the rms noise level of the map: $485, 61, 138, 67$, and $159 \mu\text{Jy beam}^{-1}$, for $6.0, 3.6, 2.0, 1.3$, and 0.7 cm maps, respectively. **Middle column:** CORE (North and South) region continuum maps. Each panel shows the continuum emission at the wavelengths observed with the VLA. For all panels, levels are $-3, 3, 6, 12, 18, 24$, and 30 times the rms noise level of the map: $61, 144, 67$, and $186 \mu\text{Jy beam}^{-1}$, for $3.6, 2.0, 1.3$, and 0.7 cm maps, respectively. **Right column:** EAST region continuum maps. Each panel shows the continuum emission at the wavelengths observed with the VLA. For all panels, levels are $-4, 4, 8, 12, 16, 20, 25$, and 30 times the rms noise level of the map: $61, 138, 67$, and $159 \mu\text{Jy beam}^{-1}$, for $3.6, 2.0, 1.3$, and 0.7 cm maps, respectively. See Table 5.3 for details of the flux and beam of each image. Blue crosses indicate the position of the four continuum sources: UCH II, EAST, CORE-N and CORE-S (see Table 5.3). The scale in arcseconds is shown in each 2.0 cm continuum image panel (multiply by 3800 to obtain astronomical units.)

5. G75.78+0.34: compact radio sources embedded in a hot core

Table 5.3: Multiwavelength results for the YSOs in the star-forming region G75.78+0.34

λ (cm)	Beam (" \times ")	P.A. ($^\circ$)	Rms ^b	$I_\nu^{\text{peak a}}$ (mJy beam ⁻¹)	S_ν^{a} (mJy)	Deconv. Size (" \times ")	P.A. ($^\circ$)
UCH II $\alpha(J2000.0) = 20^{\text{h}}21^{\text{m}}44^{\text{s}}098$ $\delta(J2000.0) = +37^\circ26'39''47$							
6.0	1.30×1.11	+89	485	24 ± 1	49 ± 6	$1.3 \times 1.2 \pm 0.4$	60 ± 40
3.6	0.33×0.26	-75	61	30 ± 1	32 ± 4	$1.0 \times 0.8 \pm 0.1$	70 ± 10
2.0	0.60×0.40	-69	138	7 ± 1	34 ± 4	$1.1 \times 0.9 \pm 0.1$	70 ± 10
1.3	0.19×0.19	+33	67	33 ± 1	32 ± 4	$1.0 \times 0.9 \pm 0.1$	80 ± 10
0.7	0.35×0.33	-74	159	4 ± 1	27 ± 4	$1.2 \times 0.8 \pm 0.2$	75 ± 10
0.31	1.96×1.74	-88	579	21 ± 2	34 ± 14	$2.0 \times 0.8 \pm 0.3$	120 ± 10
0.13	1.61×1.49	-51	4000	...	< 16
EAST $\alpha(J2000.0) = 20^{\text{h}}21^{\text{m}}44^{\text{s}}499$ $\delta(J2000.0) = +37^\circ26'37''80$							
6.0	1.30×1.11	+89	485	4.1 ± 1.0	4.5 ± 1.5	$1.3 \times 1.0 \pm 0.7$	130 ± 50
3.6	0.33×0.26	-76	61	2.9 ± 0.2	4.5 ± 0.6	$0.25 \times 0.20 \pm 0.04$	135 ± 40
2.0	0.60×0.40	-69	138	3.8 ± 0.3	3.9 ± 0.7	$0.15 \times 0.0 \pm 0.15$	105 ± 40
1.3	0.19×0.19	+33	67	2.2 ± 0.2	3.9 ± 0.6	$0.20 \times 0.15 \pm 0.05$	90 ± 20
0.7	0.35×0.33	-74	159	2.9 ± 0.4	3.3 ± 0.7	$0.2 \times 0.1 \pm 0.2$	90 ± 50
0.31	1.96×1.74	-88	579	6.0 ± 1.2	9.9 ± 4.7	$2.8 \times 1.7 \pm 0.5$	25 ± 20
0.13	1.61×1.49	-51	4000	...	< 17
CORE $\alpha(J2000.0) = 20^{\text{h}}21^{\text{m}}44^{\text{s}}030$ $\delta(J2000.0) = +37^\circ26'37''67$							
6.0	1.30×1.11	+89	485	...	< 1.9
3.6	0.33×0.26	-76	61	0.8 ± 0.2	1.4 ± 0.3
2.0	0.60×0.40	-69	138	2.1 ± 0.3	3.1 ± 0.7	$0.45 \times 0.23 \pm 0.09$	50 ± 20
1.3	0.19×0.19	+33	67	2.2 ± 0.2	4.8 ± 0.7
0.7	0.35×0.33	-74	159	4.0 ± 0.3	7.9 ± 1.2	$0.6 \times 0.2 \pm 0.1$	55 ± 15
0.31	1.96×1.74	-88	579	23 ± 2	36 ± 14	$2.0 \times 1.4 \pm 0.3$	145 ± 10
0.13	1.61×1.49	-51	4000	98 ± 10	300 ± 100	$4.0 \times 2.2 \pm 0.3$	145 ± 10
CORE-N $\alpha(J2000.0) = 20^{\text{h}}21^{\text{m}}44^{\text{s}}041$ $\delta(J2000.0) = +37^\circ26'37''76$							
3.6	0.33×0.26	-76	61	0.8 ± 0.2	0.8 ± 0.2	$0.4 \times 0.1 \pm 0.1$	50 ± 20
2.0	0.43×0.35	-84	144	2.0 ± 0.3	2.1 ± 0.5	$0.4 \times 0.1 \pm 0.1$	50 ± 15
1.3	0.19×0.19	+33	67	2.2 ± 0.2	2.7 ± 0.4	$0.15 \times 0.08 \pm 0.04$	30 ± 10
0.7	0.15×0.13	+40	186	2.6 ± 0.4	2.6 ± 0.8	$0.05 \times 0.0 \pm 0.05$	55 ± 30
CORE-S $\alpha(J2000.0) = 20^{\text{h}}21^{\text{m}}44^{\text{s}}016$ $\delta(J2000.0) = +37^\circ26'37''55$							
3.6	0.33×0.26	-76	61	0.6 ± 0.2	0.6 ± 0.2	$0.5 \times 0.1 \pm 0.1$	55 ± 15
2.0	0.43×0.35	-84	144	1.8 ± 0.3	1.8 ± 0.5	$0.4 \times 0.1 \pm 0.1$	50 ± 15
1.3	0.19×0.19	+33	67	1.9 ± 0.2	2.1 ± 0.4	$0.20 \times 0.07 \pm 0.05$	45 ± 10
0.7	0.15×0.13	+40	186	2.7 ± 0.4	3.2 ± 0.9	$0.10 \times 0.0 \pm 0.05$	100 ± 30

^a Primary beam corrected. Error in intensity is 2σ . Error in flux density has been calculated as $\sqrt{(2\sigma\sqrt{\theta_{\text{source}}/\theta_{\text{beam}}})^2 + (2\sigma_{\text{flux-scale}})^2}$, where σ is the rms noise level of the map, θ_{source} and θ_{beam} are the size of the source and the beam respectively, and $\sigma_{\text{flux-scale}}$ is the error in the flux scale, which takes into account the uncertainty on the calibration applied to the flux density of the source ($S_\nu \times \%\text{uncertainty}$).

^b Rms noise level in $\mu\text{Jy beam}^{-1}$.

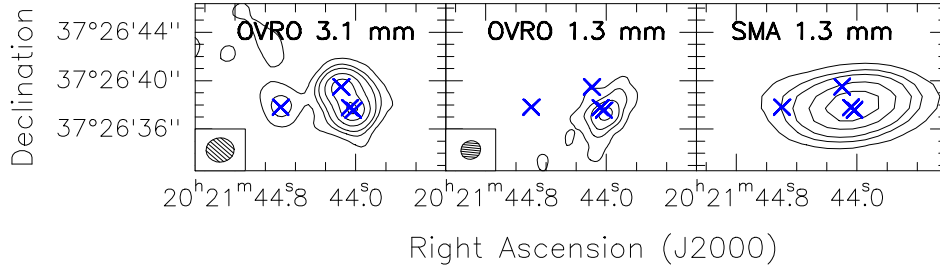


Figure 5.3: G75.78+0.34 millimeter continuum maps. Each panel shows the continuum emission at the millimeter wavelengths observed with OVRO and SMA. Levels are $-4, 4, 8, 12, 20, 30$, and 40 times the rms noise level of the map: $0.6, 4$, and $8.4 \text{ mJy beam}^{-1}$, for OVRO 3.1 mm, OVRO 1.3 mm, and SMA 1.3 mm maps, respectively. See Table 5.3 and Section 5.3.2 for details of the flux and beam of each image. Blue crosses as in Fig. 5.2.

allow us to resolve the CORE source in two different (almost unresolved) condensations: CORE-NORTH and CORE-SOUTH (see Figure 5.2). In Table 5.3, we also provide the flux densities and sizes for these two components.

5.3.2 Millimeter continuum emission

In Figure 5.3, we show the millimeter continuum images of the G75 region (from OVRO and SMA observations). At 3.1 mm we detect emission from the three main sources, with the emission from the UCH II region and the CORE source only slightly separated. At 1.3 mm, we only detect emission associated with the CORE source, probably due to a lack of sensitivity that does not allow to detect (faint) emission coming from the EAST and UCH II sources. The angular resolution achieved in our millimeter continuum images (up to 10–15 times poorer than the angular resolution at centimeter wavelengths) does not allow us to resolve the components CORE-NORTH and CORE-SOUTH. In Table 5.3, we list the flux densities and sizes, and the beams and rms noise levels of the OVRO observations. For the SMA 1.3 mm source, we fit a two-dimensional gaussian obtaining a primary beam corrected flux density of $0.60 \pm 0.17 \text{ Jy}$ with a deconvolved size of $(4 \times 2 \pm 1)''$ at a P.A. = $(75 \pm 10)^\circ$. The SMA 1.3 mm source, although centered on the CORE position, encompasses the UCH II source and shows an extension to the EAST source. We refrain from combining the OVRO and SMA 1.3 mm continuum images due to the low uv -coverage and sensitivity of the SMA image. Higher sensitivity maps are needed to confirm the 1 mm continuum emission associated with the UCH II and EAST sources.

5.3.3 Spectral energy distributions

In Figure 5.4, we show the spectral energy distributions (SEDs) of the radio continuum sources found towards G75. The UCH II source has a flat distribution, with a spectral

5. G75.78+0.34: compact radio sources embedded in a hot core

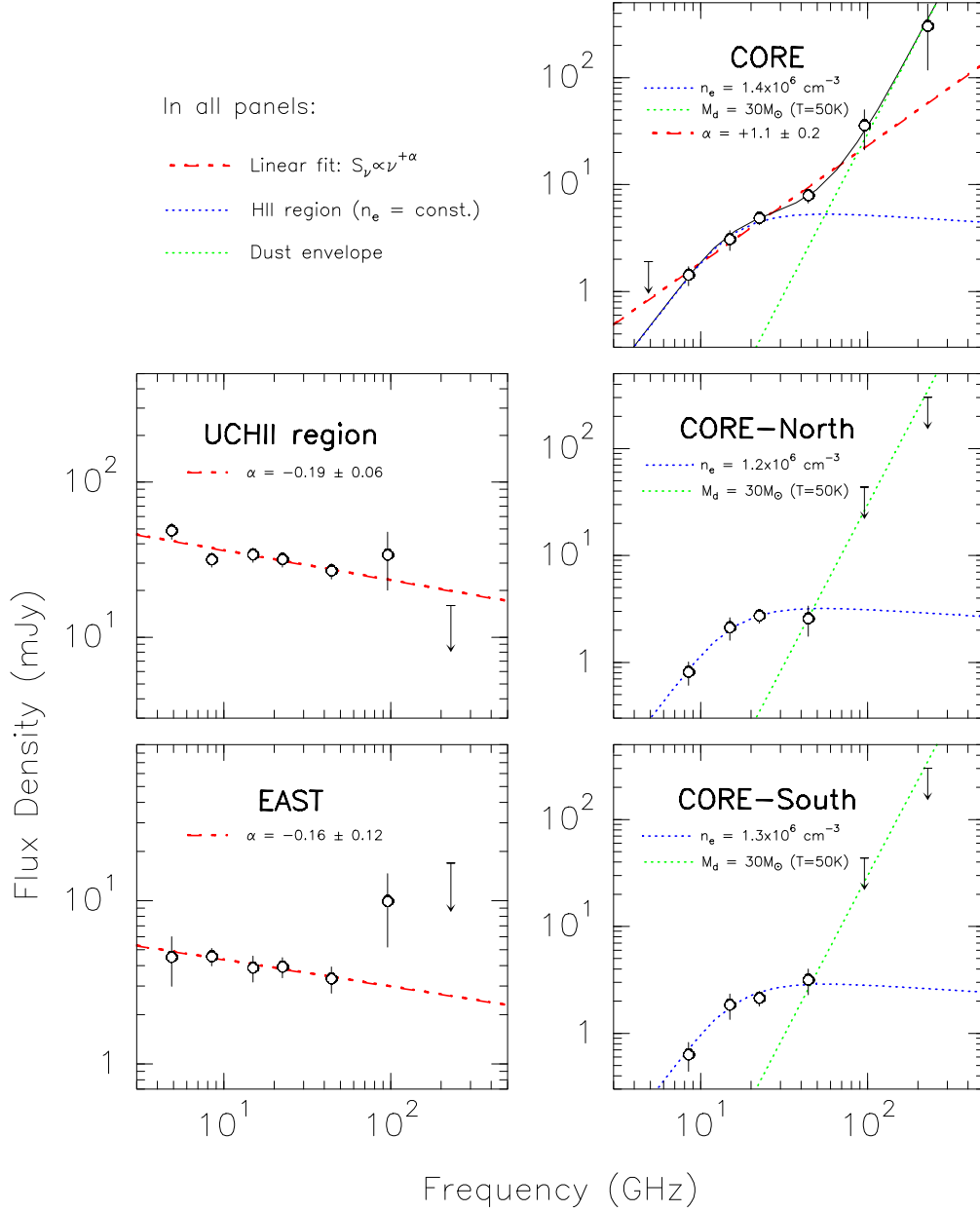


Figure 5.4: Spectral energy distributions. Circles and upper limits correspond to the observational data from Table 5.3. Red dashed lines: linear fit ($S_\nu \propto \nu^\alpha$) to the centimeter data (from 6 up to 0.7 cm; see Table 5.4). Blue dotted lines: homogenous HII region with an electron density specified in the panel. Green dotted lines: modified blackbody law for the dust envelope with a dust emissivity index of $\beta = 1$, a source radius of $3''$, a dust temperature of 50 K, a dust mass of $30 M_\odot$, and a dust mass opacity coefficient of $0.9 \text{ cm}^2 \text{ g}^{-1}$ at 1.3 mm.

Table 5.4: Physical parameters of the H II regions and dust properties for the sources in G75.78+0.34

Source	H II region physical parameters ^a						Dust ^b		
	Diameter (pc)	EM (cm^{-6} pc)	n_e (cm^{-3})	M_i (M_\odot)	\dot{N}_i (s^{-1})	Spectral Type	$S_{\nu 3\text{mm}}^{\text{dust}}$ (mJy)	$S_{\nu 1\text{mm}}^{\text{dust}}$ (mJy)	M_{dust}^c (M_\odot)
UCH II	0.019	2.5×10^7	3.7×10^4	4.7×10^{-3}	4.2×10^{46}	B0	7
EAST	0.004	6.6×10^7	1.3×10^5	1.4×10^{-4}	4.4×10^{45}	B0.5	8	< 12	7–30
CORE	< 0.001	> 2.1×10^9	> 1.4×10^6	< 2.9×10^{-5}	1.1×10^{46}	B0.5	30	190	30
							5	110	17
CORE-N	< 0.001	> 1.2×10^9	> 1.2×10^6	< 1.4×10^{-5}	4.2×10^{45}	B0.5	< 40	< 200	< 30
CORE-S	< 0.001	> 1.4×10^9	> 1.3×10^6	< 1.3×10^{-5}	4.1×10^{45}	B0.5	< 40	< 200	< 30

^a Physical parameters of the H II regions assuming homogeneous ionized gas. For the EAST and UCH II sources we assumed optically thin emission at all centimeter wavelengths (see Figure 5.4). The spectral type is determined from Panagia (1973) using the number of ionized photons, \dot{N}_i .

^b $S_{\nu 3\text{mm}}^{\text{dust}}$ and $S_{\nu 1\text{mm}}^{\text{dust}}$ correspond to the (dust) millimeter continuum flux density after subtracting the contribution from free-free emission (from the fits shown in Figure 5.4). For the CORE source, the first value assumes the centimeter emission is described by an homogeneous H II region, and the second value assumes the centimeter emission is fitted with a power law fit ($S_\nu \propto \nu^\alpha$) with $\alpha = 1.1$.

^c Dust and gas mass estimated from the millimeter emission (after subtracting the contribution of the ionized gas). For the UCH II source, all the millimeter continuum emission is thermal ionized gas emission. For the EAST source we assumed a dust emissivity index of 1.5, a dust mass opacity coefficient of $0.9 \text{ cm}^2 \text{ g}^{-1}$ at 1.3 mm (Ossenkopf and Henning 1994), and a dust temperature of 100 and 30 K, respectively. For CORE, CORE-N and CORE-S sources we provide the mass estimated assuming a dust emissivity index of 1, a dust mass opacity coefficient of $0.9 \text{ cm}^2 \text{ g}^{-1}$ at 1.3 mm, and a dust temperature of 50 K. The upper limits are due to the low angular resolution at millimeter wavelengths that does not allow to resolve the CORE-N and CORE-S sources.

index (α ; $S_\nu \propto \nu^\alpha$) of -0.19 ± 0.06 , typical of optically thin free-free emission. This SED is well fitted by an optically thin H II region with an electron density of $3.7 \times 10^4 \text{ cm}^{-3}$ and a size of $\sim 0.019 \text{ pc}$ (3800 AU), and ionized by an early B0 type star. In Table 5.4, we list the main physical parameters of the cometary UCH II region. At millimeter wavelengths, the emission detected at 3.1 mm and the upper limit at 1.3 mm are consistent with the millimeter continuum emission coming from ionized gas, suggesting that no (or few) dust is directly associated with the cometary UCH II region.

The eastern continuum source (EAST) is almost unresolved showing an irregular (or spherical) shape (cf. Figure 5.2 and Table 5.3), and with a flat spectral distribution ($\alpha = -0.16 \pm 0.12$). Thus, its SED (see Figure 5.4) can be fitted, at centimeter wavelengths, by an optically thin H II region with a size of $\sim 0.004 \text{ pc}$ (900 AU; consistent with the deconvolved size listed in Table 5.3) and an electron density of $1.3 \times 10^5 \text{ cm}^{-3}$, being ionized by at least one B0.5 star. Its physical parameters are listed in Table 5.4. At 3.1 mm there is an excess of continuum emission with respect to the optically thin H II region assumption, probably coming from a dust envelope of $\sim 7\text{--}30 M_\odot$ (see last column in Table 5.4). We refrain from fitting a dust envelope to the millimeter wavelengths of the SED, since at 1.3 mm we only have an upper limit.

Finally, we have constructed the SED for the CORE source (taking into account all the emission) and the SEDs for CORE-N and CORE-S, separately. At centimeter wavelengths, the emission is partially optically thick, with a spectral index of $+1.1 \pm 0.2$ for the entire emission of the CORE. The major difference for the SEDs of CORE, CORE-N and CORE-

5. G75.78+0.34: compact radio sources embedded in a hot core

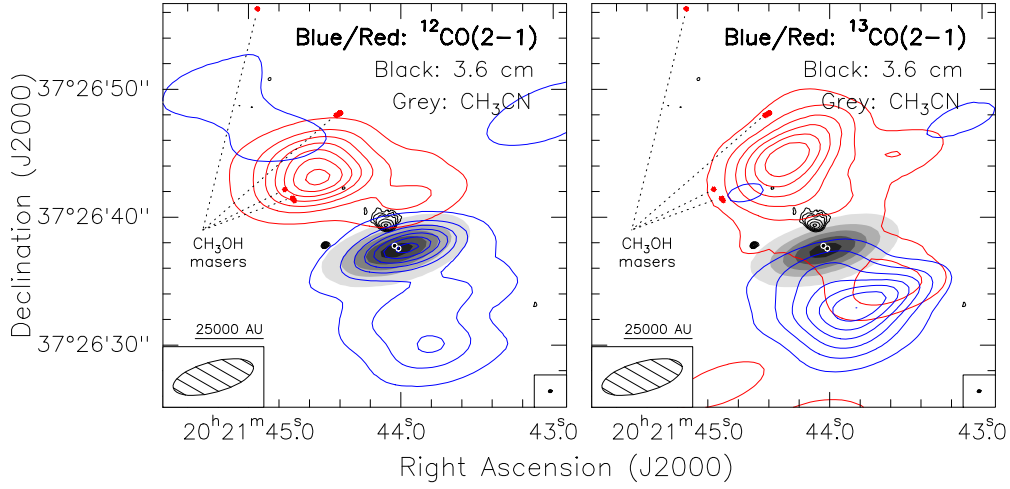


Figure 5.5: Outflow emission G75.78+0.34. *Left*: Blue/red contours: $^{12}\text{CO}(2-1)$ intensity map for blue/red-shifted velocities (from -6 to -60 km s^{-1} and from $+10$ to $+70$ km s^{-1} with respect to the $v_{\text{LSR}} \sim -0.2$ km s^{-1}). Levels start at 5%, increasing in steps of 15% the peak intensity: 107 and 162 $\text{Jy beam}^{-1} \text{km s}^{-1}$, for blue and red respectively. *Right*: Blue/red contours: $^{13}\text{CO}(2-1)$ intensity map for blue/red-shifted velocities (from -6 to -20 km s^{-1} and from $+7$ to $+30$ km s^{-1} w.r.t. the v_{LSR}). Levels start at 10%, increasing in steps of 15% the peak intensity: 30 and 16 $\text{Jy beam}^{-1} \text{km s}^{-1}$, for blue and red respectively. In both panels: Black contours: VLA 3.6 cm continuum map (CORE-N and S sources are identified with white circles). Grey scale: intensity map for the $\text{CH}_3\text{CN}(12-11)$ molecular transition. Ten-points red stars mark the position of methanol Class I masers (see Table 5.6). Synthesized beams for the outflow and continuum emission are shown in the bottom-left and right corners, respectively.

S sources is the flux density at 7 mm. However, in all cases the centimeter emission can be well fitted by an H II region with an electron density of $\sim 10^6 \text{ cm}^{-3}$ and a size < 0.001 pc (see Table 5.4). An H II region with these properties has a turnover frequency at ~ 20 GHz, and thus we can detect the optically thick and thin regimes of the spectrum at centimeter wavelengths: it is an hypercompact H II region. At millimeter wavelengths, where we cannot separate the contribution of CORE-N and CORE-S sources, we have assumed the emission comes from a hot dust envelope (50 K and $30 M_{\odot}$; see Table 5.4).

5.4 Molecular results

5.4.1 Molecular outflow gas

Interferometric SMA $^{12}\text{CO}(2-1)$ and $^{13}\text{CO}(2-1)$ (Figure 5.5) maps reveal an outflow with a clear bipolar morphology centered on the position of the CORE source. The outflow emis-

Table 5.5: Physical parameters for the molecular outflow in G75.78+0.34

Outflow/lobe (1)	t_{dyn} (2)	size (3)	N_{mol} (4)	M_{out} (5)	\dot{M}_{out} (6)	P_{out} (7)	\dot{P}_{out} (8)	E_{kin} (9)	L_{mech} (10)
Outflow — P.A.=30°									
^{12}CO (2–1) – red	2600	10×8	1.6	0.10	3.7	5.7	2.2	3.4	10
^{12}CO (2–1) – blue	3000	10×8	1.1	0.07	2.3	3.7	1.2	2.0	5
^{12}CO (2–1)	2800	...	2.7	0.17	5.9	9.4	3.4	5.4	14
^{13}CO (2–1) – red	4800	8×7	0.2	0.50	10.6	11.6	2.4	2.7	4
^{13}CO (2–1) – blue	7200	8×7	0.2	0.58	8.0	8.2	1.1	1.1	1
^{13}CO (2–1)	6000	...	0.4	1.09	18.1	19.8	3.3	3.8	5

^a Parameters are calculated for an inclination with respect to the plane of the sky equal to 0°, following the expressions given in Palau et al. (2007b). Notes and units for each column: (1) blue/red lobe for each molecular species; (2) dynamical age in years; (3) size of the lobe in arcsec; (4) column density of the molecule in cm^{-2} ; (5) outflowing mass in M_{\odot} ; (6) rate of the outflowing mass in $10^{-5} M_{\odot} \text{ yr}^{-1}$; (7) momentum of the outflow in $M_{\odot} \text{ km s}^{-1}$; (8) outflow momentum rate in $10^{-3} M_{\odot} \text{ km s}^{-1} \text{ yr}^{-1}$; (9) kinetic energy in 10^{45} erg ; and (10) mechanical luminosity in L_{\odot} .

sion spans a velocity range from -60 km s^{-1} to $+70 \text{ km s}^{-1}$ for the ^{12}CO and -20 km s^{-1} to $+30 \text{ km s}^{-1}$ for the ^{13}CO (the systemic velocity is $v_{\text{LSR}} \simeq -0.2 \text{ km s}^{-1}$). At larger scales, Shepherd et al. (1997) identified four distinct outflows in the G75 star-forming region with low angular resolution maps. The ‘central’ outflow of Shepherd et al. (1997) is spatially coincident with the outflow detected in the SMA observations, but more extended toward the northeast. However, at large scales, the red lobe of the ‘central’ outflow is located toward the south, while the blue lobe is located toward the north(east). We have identified, in our interferometric observations, an outflow in roughly the same direction of the ‘central’ outflow (P.A. $\sim 30^\circ$), but with the blue/red lobes reversed. An accurate study of Fig. 7 in Shepherd et al. (1997) reveals some hints of the presence of the outflow we detect in the SMA data. All this confirms that the identification of molecular outflows in clustered star-forming regions is laborious and not straightforward from single-dish observations, due to the presence of a high number of YSOs driving outflows. In Table 5.5, we provide the physical parameters derived for the outflow seen in the SMA maps. The energetics of the outflow are similar to those found in other massive molecular outflows (Shepherd 2005).

5. G75.78+0.34: compact radio sources embedded in a hot core

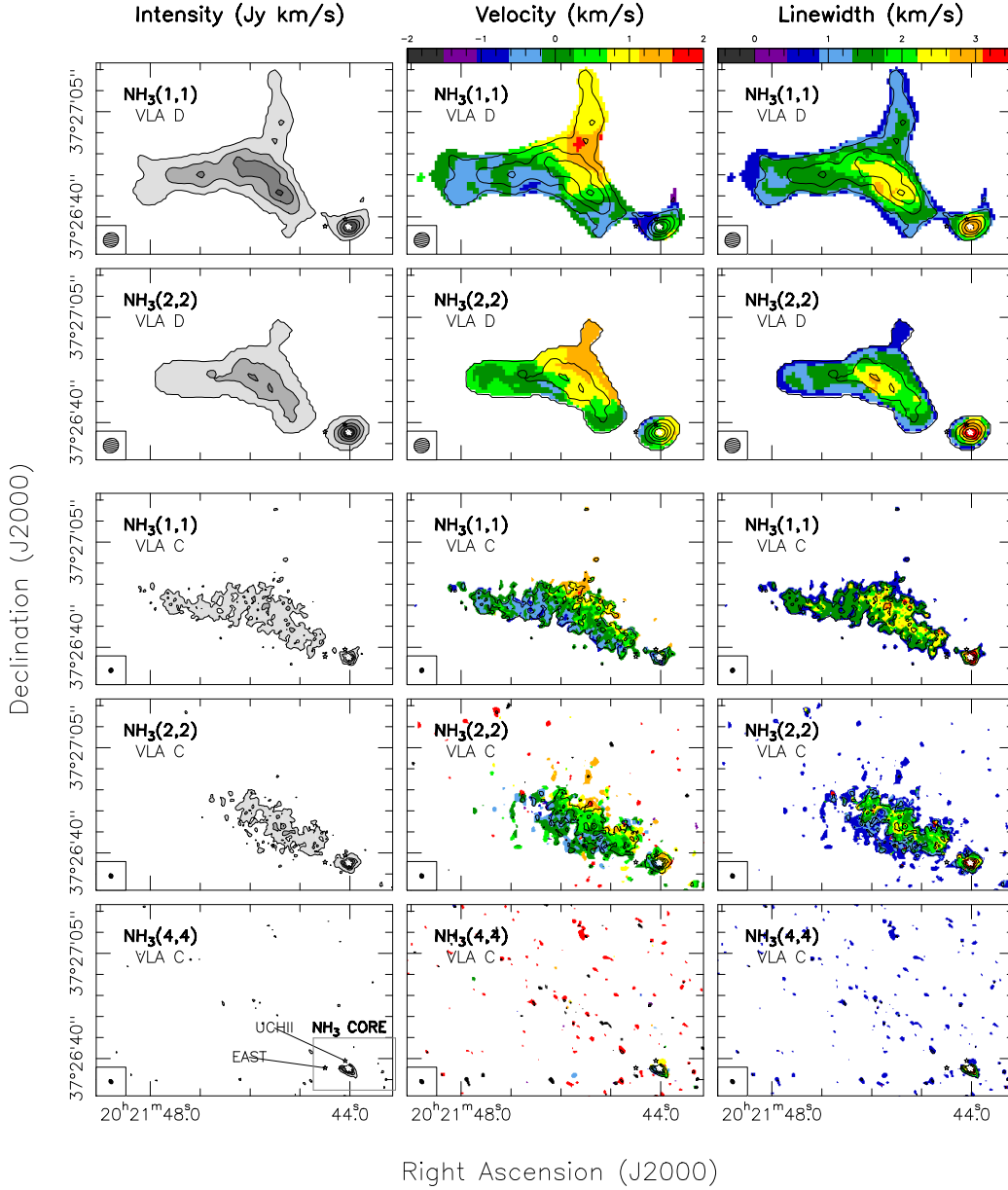


Figure 5.6: *Left columns:* Zero-order moment (integrated intensity) maps for different NH_3 transitions. *Center columns:* First-order moment (velocity field) maps. *Right columns:* Linewidth (FWHM) maps, obtained from the second-order moment. The two top rows correspond to VLA ammonia observations with the array in its most compact configuration (D), while the three bottom rows show the maps of the observations with the array in its C configuration. The grey box in the panel $\text{NH}_3(4,4)$ marks the region of the NH_3 core zoomed in Figure 5.7. In all panels, white and black stars mark the position of the centimeter continuum sources (see Table 5.3). Synthesized beams are always shown in the bottom-left corner.

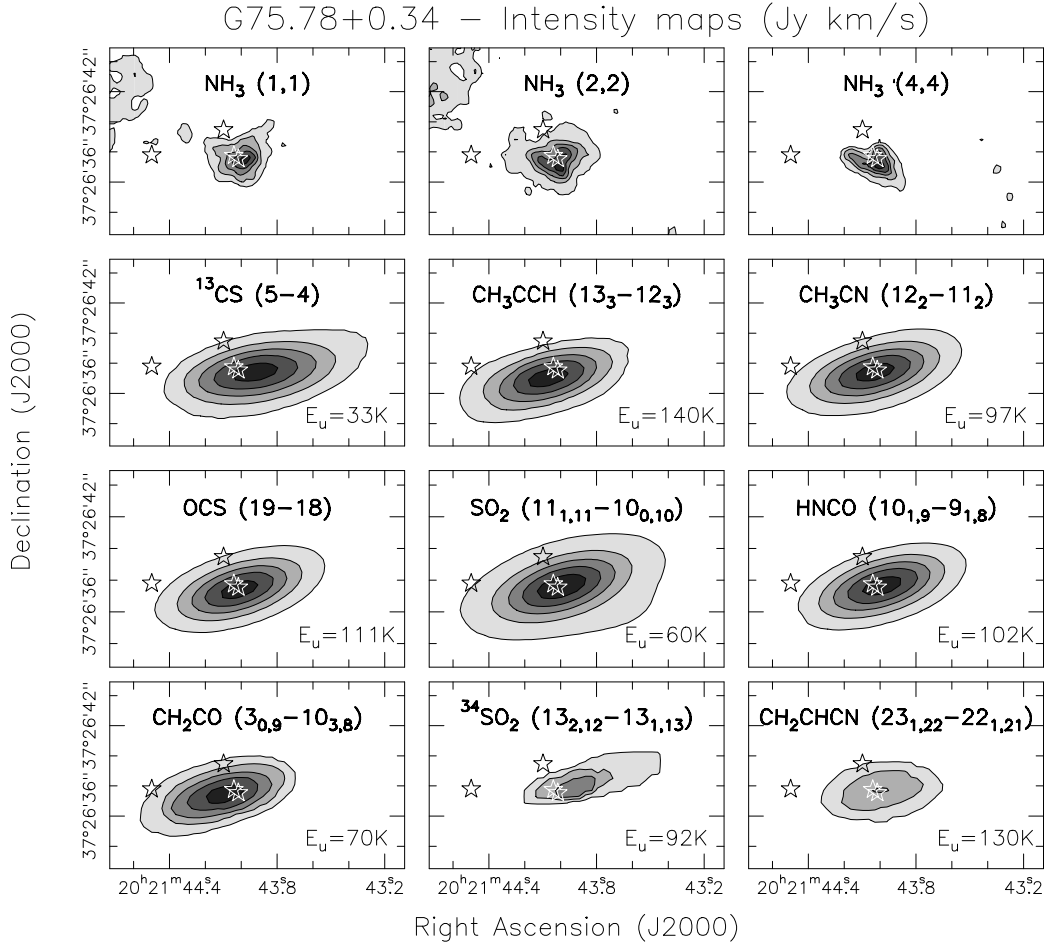


Figure 5.7: Zero-order moment (integrated intensity) maps for different molecules detected towards G75.78+0.34. Levels start at 10%, increasing in steps of 20% the peak intensity. The white/black stars mark the position of the centimeter sources (see Table 5.3). The energy of the upper level for each transition is indicated in the bottom-right corner (in units of K).

5.4.2 Molecular dense gas

The zero-order moment maps of the NH_3 (1,1) and (2,2) transitions (with the VLA in its D configuration) are shown in the top-left panels of Figure 5.6. The dense gas traced by NH_3 reveals a compact core at the position of the CORE/UCH II sources (labeled NH_3 core in Figure 5.6) and a filament extending $\sim 50''$ to the east of the EAST source. A second filamentary structure can be identified in the north-south direction in the (1,1) transition map. When observing with high angular resolution (VLA-C observations; Figure 5.6 bottom rows), the filamentary structure is slightly resolved out in the (1,1) and (2,2) transitions, and practically not detected in the (4,4) ammonia transition maps. The NH_3

core, associated with the radio continuum sources, appears resolved (see Figure 5.7, for a close-up), showing a double-peak in the (2,2) transition and a V-shaped morphology in the (4,4) transition map. It is important to note that there is no NH_3 emission associated with the EAST source. Additionally, the ammonia emission from the dense core, is spatially well-centered on the CORE source, laying the UCH II source at the border of the dense gas condensation. The close-up images in Figure 5.7 reveal that the two centimeter sources (CORE-N and CORE-S) are located exactly in the middle of the double peak, seen in the (2,2) transition, and at the middle of the V-shaped structure, seen in the (4,4) transition.

Several other molecules (e.g., CH_3CN , CH_3OH , CH_3CCH , HNCO , OCS) have been detected towards G75, in the wide SMA band observations. All these molecules show a compact unresolved source (see Figure 5.7) at the position of the SMA 1.3 mm source (see Section 5.3.2). Similar to the dense core seen in ammonia, these other molecular species peak at the position of the CORE source. However, the low angular resolution of the SMA observations does not allow to determine the morphology of this dense gas core in the other molecular tracers. It is important to note that no extended emission (from filaments) is detected in the SMA molecular transitions, suggesting this molecular emission arises from a very compact source. In fact, the wide-band SMA spectrum toward the compact molecular core (Figure 5.8) reveals a chemically rich dense core with typical hot core features (as seen in I22198: Chapter 4 – note that the frequency range is different for I22198 and G75). Molecular line transitions detected with $T_{\text{B}} \gtrsim 0.1$ K have been identified and imaged. Around 16 different molecular species have been identified in this compact molecular core.

5.4.3 H_2O and CH_3OH maser emission

Hofner and Churchwell (1996) reported a cluster of water masers located $2''$ southwest from the UCH II region, at the same position as the CORE source (as reported by Carral et al. 1997). Our H_2O maser observations at 22.235 GHz have a double aim: to cross-calibrate the radio continuum data at 1.3 cm, and to observe the masers with higher angular resolution ($\sim 0''.1$ versus $\sim 0''.4$ of previous observations). Two different spectral resolutions (~ 0.3 and ~ 1.3 km s^{-1}) were used to observe the H_2O maser emission, allowing us to look for maser components in a velocity range of $(-40, +40)$ km s^{-1} . In Figure 5.9, we show the different H_2O maser components (colour circles) with respect to the 1.3 cm continuum sources. All the components appear forming an arc at a distance of $\sim 2''$ from the head of the cometary UCH II region (cf. Figure 5.1), with only a few of them directly associated with the CORE-SOUTH continuum source. We note that there are no instrumental offsets to be considered between the 1.3 cm continuum and the H_2O maser images, since the observations were simultaneous. In Table 5.6 we list the position, intensity, velocity, and integrated intensity of the different H_2O maser components, indicating in the last column at which frequency resolution the component was detected. In Figure 5.9 we use different colours as an indicator of the velocity of the maser component. No clear velocity

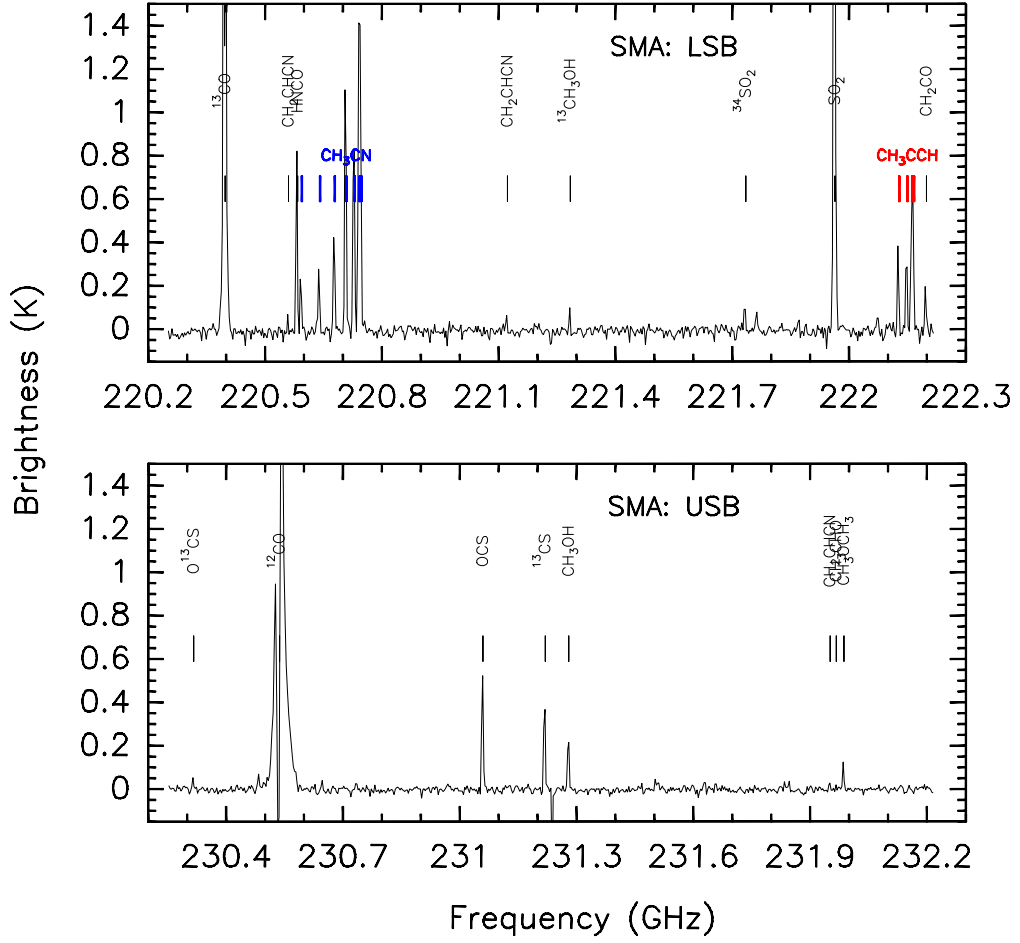


Figure 5.8: 230 GHz continuum-free spectra (for the dense core in G75.78+0.34) in the image domain from the SMA data, for the lower sideband (LSB) in the top panel and the upper sideband (USB) in the bottom panel. The molecular transitions used in the rotational diagrams (Figure 5.14) are shown in blue and red.

gradients are found in the H₂O maser emission, although most of them appear redshifted with respect to the cloud velocity, $v_{\text{LSR}} \sim -0.2 \text{ km s}^{-1}$.

For the class I methanol masers at 44.069 GHz toward G75 we detect four different groups (with a total of 8 different components). However, none of them appear directly associated with any of the three main continuum sources. All the 44 GHz CH₃OH maser components are close to or inside the faint extended continuum centimeter emission (cf. Figure 5.1) at a distance of 10''–20'' (0.2–0.4 pc for a distance of 3800 pc) from the main YSOs in the region. In Table 5.6 we list the position, intensity, velocity, and integrated intensity for all the methanol maser components. As in other star-forming regions (e.g., Kurtz et al. 2004), class I methanol masers rarely coincide with other signposts of star

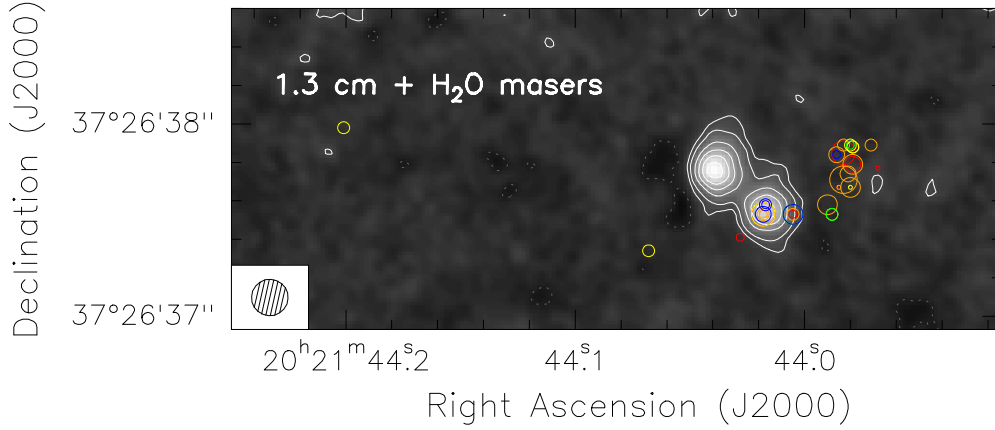


Figure 5.9: H₂O maser distribution. Grey scale and black contours: VLA 1.3 cm continuum image. Levels are $-3, 3, 6, 12, 18, 24,$ and 30 times $67 \mu\text{Jy beam}^{-1}$. Colour circles show the position of water masers (see Table 5.6). Colours indicate different velocity ranges: blue for $(-50, -5) \text{ km s}^{-1}$, green for $(-5, -1) \text{ km s}^{-1}$, yellow for $(-1, +1) \text{ km s}^{-1}$, orange for $(+1, +5) \text{ km s}^{-1}$, and red for $(+5, +30) \text{ km s}^{-1}$. Sizes are correlated with the peak intensity of the maser.

formation (e. g., H II regions, OH masers, class II methanol masers). Theoretical models of methanol masers suggest that the class I masers arise in an environment where collisional processes dominate (Cragg et al. 1992; Pratap et al. 2008). The G75 star-forming region contains up to four different molecular outflows (Shepherd et al. 1997), suggesting that the 44 GHz CH₃OH masers could be pumped by collisions resulting from the molecular outflows. In particular, some of the methanol masers we detect are close to or within the red lobe of the molecular outflow (cf. Figure 5.5). Furthermore, the velocity of these maser components is red-shifted (see Table 5.6) as expected from these masers to have been pumped in the collisions of the red lobe of the molecular outflow.

5.4.4 Radio recombination lines emission

We used the OVRO interferometer to observe the radio recombination lines at 3 mm (H40 α) and 1 mm (H30 α) towards G75, with the main aim of determining the contribution of the ionized gas component at millimeter wavelengths. However, we do not find clear detections of these lines. The channels are dominated by the continuum emission coming from the dust emission discussed in previous sections. Our 1σ rms noise levels for the line (continuum-free emission) are 10 and 15 mJy beam⁻¹ for the H40 α and H30 α , respectively. Although we do not detect emission from the radio recombination lines, the upper limits we can obtain are still useful to determine the ionized gas content in the millimeter range (see Section 5.5.4 for more details).

Table 5.6: 22 GHz water and 44 GHz methanol masers in G75.78+0.34

$\alpha(\text{J2000.0})$ (^h ^m ^s)	$\delta(\text{J2000.0})$ ([°] ['] ^{''})	S_{peak} (Jy)	v_{peak} (km s ⁻¹)	$\int S dv$ (Jy km s ⁻¹)	Notes ^a
H ₂ O maser components					
20 21 43.968	37 26 37.77	0.3	+7.0	0.4	L
20 21 43.971	37 26 37.89	1.5	+3.0	1.7	H
20 21 43.979	37 26 37.79	3.9	+6.9	3.1	H
		15.	+2.3	16.4	H,L
20 21 43.979	37 26 37.88	2.4	+0.0	1.4	H
		1.0	-0.8	1.3	L
20 21 43.980	37 26 37.67	4.5	+2.6	6.3	H
		0.2	+0.5	0.3	L
20 21 43.980	37 26 37.89	1.5	+0.5	2.0	L
		0.7	-2.6	0.6	H,L
20 21 43.990	37 26 37.58	7.5	+3.0	10.5	H,L
20 21 43.981	37 26 37.74	5.1	+1.7	2.6	H
20 21 43.983	37 26 37.71	122.	+3.0	220.	H
20 21 43.983	37 26 37.89	1.7	+1.3	0.9	H
20 21 43.983	37 26 37.85	53.	+6.9	111.	H,L
20 21 43.985	37 26 37.67	0.2	+6.9	0.12	H
		0.3	+4.6	0.6	H,L
20 21 43.986	37 26 37.84	6.5	+4.3	3.9	H,L
		0.6	-11.0	1.6	L
20 21 43.988	37 26 37.53	3.1	+0.3	2.5	H,L
		1.0	-2.3	1.0	H
20 21 44.005	37 26 37.53	0.6	+5.5	0.6	H,L
		1.1	+1.7	0.9	H
		7.2	-1.3	15.1	H,L
		15.	-5.6	20.4	H,L
20 21 44.017	37 26 37.58	0.5	-30.0	0.7	L
		1.4	-36.0	1.8	L
20 21 44.018	37 26 37.53	47.	+7.3	65.5	H,L
		0.4	+4.9	0.2	H
		2.7	+2.0	3.0	H
		56.	-0.7	150.	H,L
		3.7	-6.2	6.7	H,L
20 21 44.028	37 26 37.41	0.7	+14.0	0.9	L
20 21 44.068	37 26 37.34	2.3	+0.3	3.0	H,L
20 21 44.201	37 26 37.98	2.4	+0.7	2.4	H,L
CH ₃ OH maser components					
20 21 44.397	37 26 48.14	0.06	+1.3	0.04	
20 21 44.403	37 26 48.15	0.07	-0.3	0.06	
20 21 44.412	37 26 48.04	0.4	+1.3	0.4	
20 21 44.424	37 26 47.96	1.6	+0.5	2.4	
20 21 44.701	37 26 41.30	6.8	+3.8	5.6	
20 21 44.710	37 26 41.47	1.2	+4.2	1.0	
20 21 44.763	37 26 42.17	5.8	+3.2	6.7	
20 21 44.943	37 26 56.28	1.8	+0.5	1.2	

^a Labels H and L refer to the VLA observations done with a spectral resolution of 0.33 km s⁻¹ and 1.3 km s⁻¹, respectively.

5. G75.78+0.34: compact radio sources embedded in a hot core

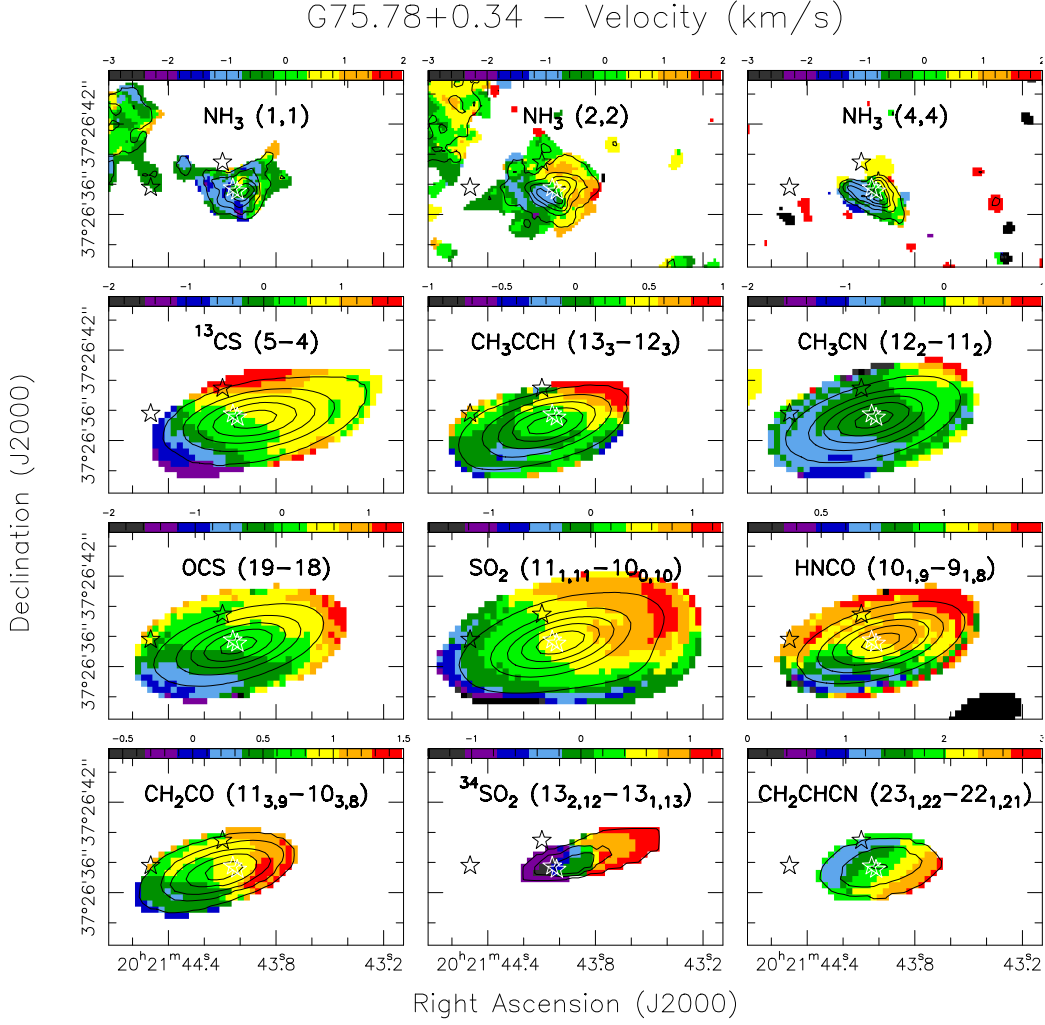


Figure 5.10: First-order moment (velocity field) maps for different molecules detected towards G75.78+0.34. Levels as in Figure 5.7. The white/black stars mark the position of the centimeter sources (see Table 5.3).

5.5 Analysis

5.5.1 Velocity fields

In Figures 5.10 and 5.11, we show the velocity field (first-order moment) and linewidth (FWHM, obtained from the second-order moment) maps, for those molecular transitions shown in Figure 5.7. Almost all the molecular transitions have linewidth $\sim 3\text{--}5\text{ km s}^{-1}$, and show a velocity gradient in the southeast-northwest direction (P.A. $\simeq 130^\circ$, with red-shifted velocities to the northwest). The gas at large scales (NH_3 filament; see Figure 5.6)

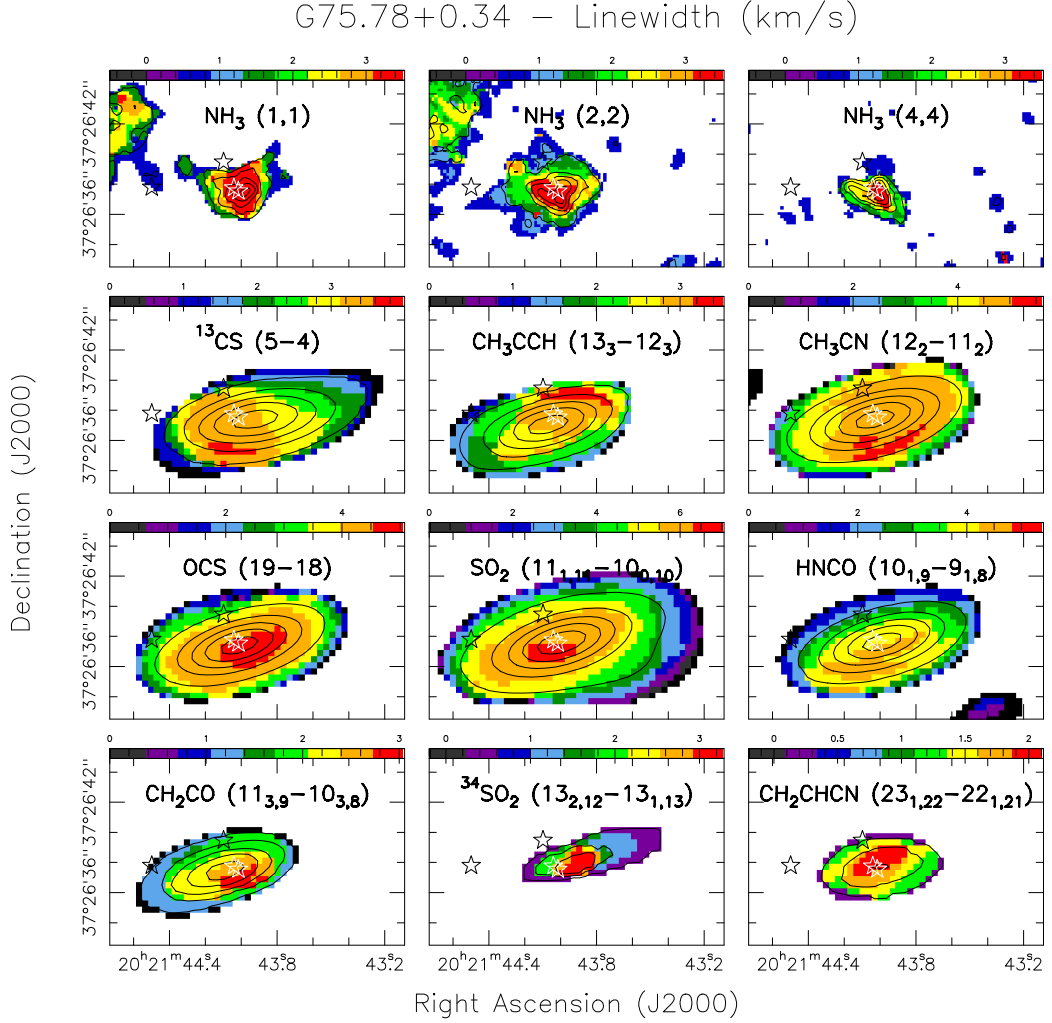


Figure 5.11: Second-order moment (linewidth) maps for different molecules detected towards G75.78+0.34. Levels as in Figure 5.7. The white/black stars mark the position of the centimeter sources (see Table 5.3).

also shows the same velocity gradient in the southeast-northwest direction.

This velocity gradient (seen in almost all the molecules) perpendicular to the outflow, can be interpreted as rotating gas from a molecular disk or toroid. However, for the large-scale eastern filament, we cannot discard the scenario in which the filamentary cloud seen in ammonia corresponds to two distinct filaments with different velocities: a redshifted one in the north-south direction, and a blueshifted one in the east-west direction. High spectral-resolution ammonia observations can help to test the two-filament scenario by searching for two distinct velocity components in the region where the two filaments overlap. Although the two-filament hypothesis must be taken into account, it seems that the dense gas (NH_3)

emission comes from a large rotating cloud that is fragmenting and forming different YSOs. The fact that there is no connection between the dense core and the filamentary structure can be due to the presence of the EAST and UCH II sources. The UV photons of the EAST and UCH II regions could have cleared up the dense gas, and produced this gap in the ammonia emission.

Assuming that the velocity gradient traces Keplerian rotation, the dynamical mass for the dense core has been calculated from the expression $M_{\text{dyn}} = v_{\text{rot}}^2 R_{\text{rot}} / G \sin^2 i$ (see Chapter 4). In this case, with $v_{\text{rot}} \simeq 1 \text{ km s}^{-1}$ and $R_{\text{rot}} \simeq 2''$, the dynamical mass is $\sim 9 M_{\odot}$, for a rotating structure seen edge-on ($i = 90^\circ$). The mass of the internal object ($\sim 9 M_{\odot}$) is similar to the mass of the dust envelope ($\sim 7\text{--}30 M_{\odot}$; see Table 5.4), suggesting that the embedded objects can still accrete an important amount of mass.

5.5.2 Dense gas analysis

As in previous chapters, we studied the chemical environment of G75 by analyzing the column density, rotational temperature, opacity and velocity of the NH_3 emission and other molecular dense gas tracers detected in the dense core. We used the NH_3 (1,1) and (2,2) data from the D-array observations to derive the temperature of the dense gas along the filamentary structure and in the dense core. We computed the column density maps by extracting the spectra for positions in a grid of $0''.9 \times 0''.9$, and using CLASS to fit the hyperfine structure of each spectrum for NH_3 (1,1) and a single Gaussian for the NH_3 (2,2) transitions. See Chapter 2 or Busquet (2010) for more details in the procedures used.

In Figure 5.12, we present the rotational temperature, column density, opacity and excitation temperature maps of the NH_3 emission for the large cloud seen in G75. A close-up of the dense core region is shown in the four bottom panels of Figure 5.12. The emission is essentially optically thin ($\tau_{(1,1)} < 1$) in all the filamentary structure, while in the dense core the emission appears partially thick at the east of the CORE-N and CORE-S sources, and optically thin towards the west. This differentiation (also seen in the T_{rot} , N , and T_{ex} maps) could be understood as different ammonia components in the dense core, however there are no hints of a double component in the spectrum (down to a spectral resolution of 0.6 km s^{-1}). The high excitation temperatures ($\sim 80 \text{ K}$) are due to the low opacities measured in some parts of the cloud (see Section 4.5.2 in Chapter 4 for more details). The column density is 2 or 3 times lower in the filament than in the dense core, in which it reaches values $\sim 4 \times 10^{15} \text{ cm}^{-2}$. Regarding the rotational temperature: the filament has values between 15 and 25 K, while the dense core has hotter temperatures, between 30 and 45 K. The temperature of 25 K for the filament could be due to internal heating of embedded YSOs (in fact, several IRAC sources are found at the positions of the temperature enhancements; cf. Figure 5.12 top panels), or, alternatively, the passage of outflows could play a role as well (several outflows have been indentified in this region; Shepherd et al. 1997). In order to see in more detail the distribution of the gas temperature along the dense core, we have constructed a RGB composite image

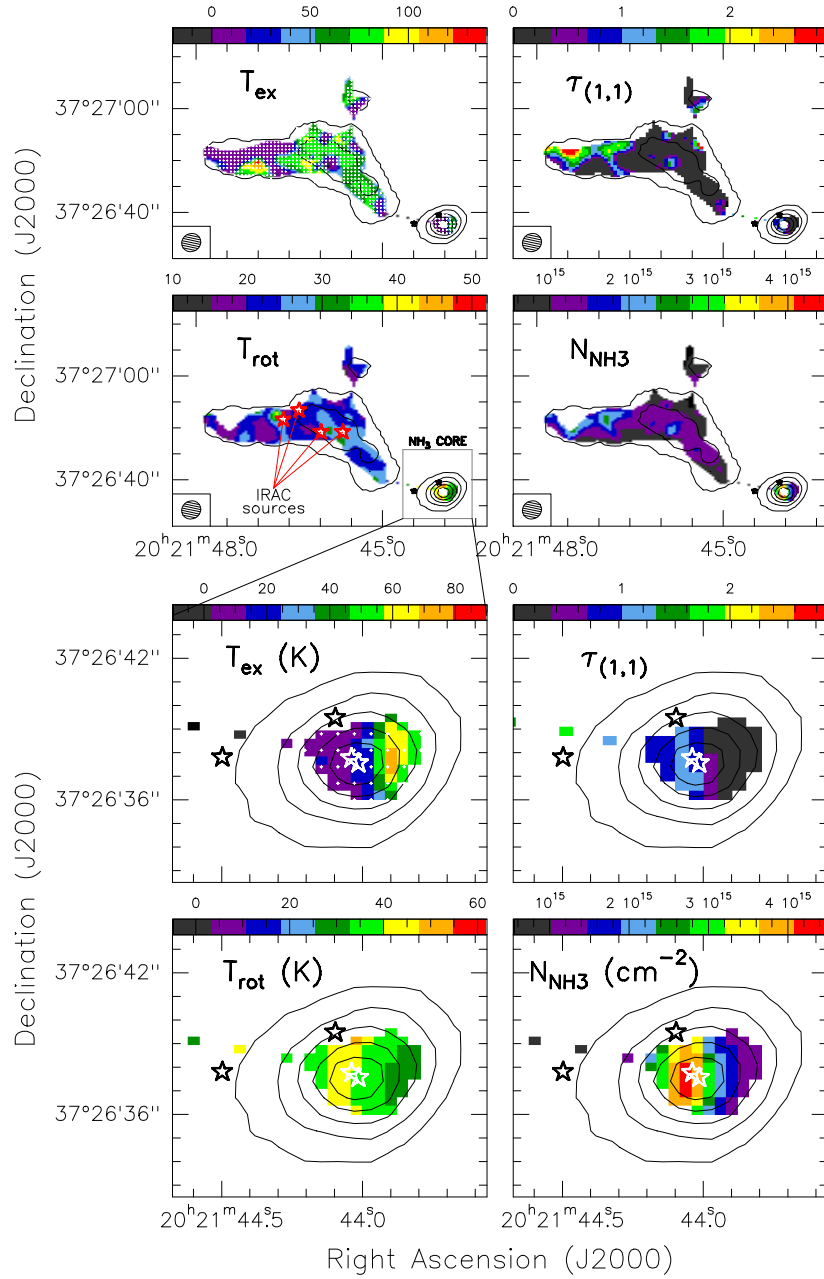


Figure 5.12: *Four top panels:* Ammonia parameters towards G75.78+0.34. From top to bottom, and left to right: excitation temperature map from NH₃ (1,1) (units in K); map of the optical depth of the NH₃ (1,1) main line; rotational temperature map from NH₃ (1,1) and NH₃ (2,2) (units in K); NH₃ column density map (units in cm^{-2}). In all panels, black contours are zero-order (intensity) map of the NH₃ (2,2) line, and white/black star marks the position of the centimeter continuum sources. The synthesized beam is indicated in the bottom-right corner of each panel. *Four bottom panels:* Close-up of the NH₃ dense core. Maps and symbols are the same as for the top panels.

5. G75.78+0.34: compact radio sources embedded in a hot core

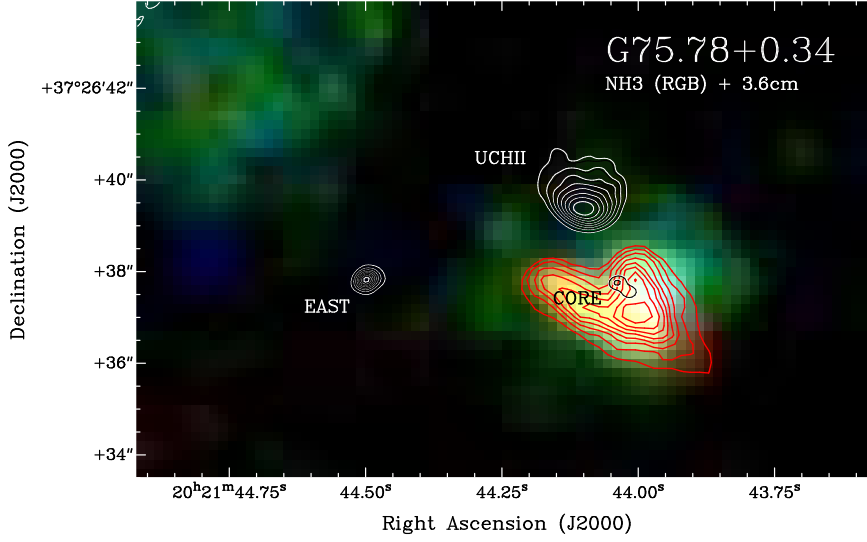


Figure 5.13: Ammonia RGB composite image of G75.78+0.34. Blue: NH₃ (1,1) C-array observations; Green: NH₃ (2,2) C-array observations; Red: NH₃ (4,4) C-array observations. Red contours: NH₃ (4,4) C-array integrated emission (see Figure 5.7). White/black contours: 3.6 cm continuum emission.

with the NH₃ (1,1) (blue), NH₃ (2,2) (green) and NH₃ (4,4) (red) emission from the C-array observations (Figure 5.13). Since there are no ortho/para effects between the (1,1) (2,2) and (4,4) ammonia transitions (all are para transitions), a direct comparison of the intensity of each line can be used as an indicator of the temperature. Those regions with emission from the (4,4) line will be hotter than those regions with only emission from the (1,1) and/or (2,2) lines. As can be seen in Figure 5.13, the reddened regions do not spatially peak in the CORE-N and CORE-S sources, but appear surrounding them. Thus, the enhancements of the temperature could be due to shocks in the molecular outflow in combination to the presence of the YSOs. Such a scenario in which the hot ammonia appears surrounding the YSOs, is consistent with the gas being disrupted (or pushed away) by the YSOs, as in the case of I22198 (see Chapter 4).

5.5.3 Hot molecular core properties

Additionally to the NH₃ emission, we used the other molecules detected in the NH₃ core to better estimate the physical conditions of this object. The wide SMA band shown in Figure 5.8 includes a large list of different rotational transitions of the same molecule, in particular we have detected more than 3 different transitions for CH₃CN and CH₃CCH. Additionally, we used the three transitions of the NH₃ molecule observed with the VLA in its C configuration. Following the rotational diagram method (Goldsmith and Langer

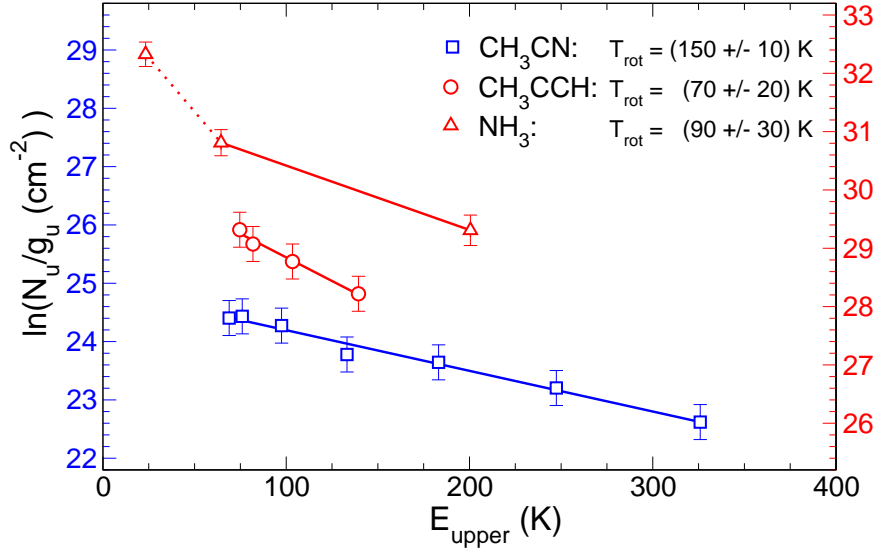


Figure 5.14: Rotational diagrams towards G75.78+0.34. CH_3CN in blue squares, CH_3CCH in red circles, and NH_3 in red triangles. CH_3CN and CH_3CCH were fitted assuming optically thin emission, while NH_3 was fitted using the derived opacities from the hyperfine transitions. Note that the NH_3 can be fitted by two different temperature components. A hotter one at ~ 90 K likely tracing the gas close to the hot core, and a colder one at ~ 30 K likely tracing the outer layers of the gas envelope. Vertical (blue) left axis refers to CH_3CN , while vertical (red) right axis refers to CH_3CCH and NH_3 .

1999; Araya et al. 2005) which assumes that all molecular levels are populated according to the same excitation temperature, we can derive this temperature, T_{rot} , and the total column density, N_{mol} , for these molecules. In Figure 5.14, we show the rotational diagrams for three molecular species: CH_3CN , CH_3CCH , and NH_3 . It is interesting to note that for low energy transitions (e.g., NH_3 (1,1) and (2,2)) the derived temperature is ~ 30 K, similar to the temperature derived from the ammonia analysis in Figure 5.12. However, those transitions with higher energy levels (from 100 up to 300 K) provide a temperature estimation of ~ 100 K. Thus, it seems we are detecting two different dense gas components: a cold/warm envelope observed in the lower molecular transitions, with $T_{\text{rot}} \sim 30$ K, and a hotter component with $T_{\text{rot}} \sim 100$ K. All this indicates that not all the molecular transitions can be used as thermometers to estimate temperatures of hot gas. Finally, the high temperature derived for the dense core in G75, together with the chemically-rich spectrum shown in Figure 5.8, are evidences of G75 harbouring a hot molecular core. The derived molecular column densities are $4.6 \times 10^{14} \text{ cm}^{-2}$, $3.5 \times 10^{16} \text{ cm}^{-2}$, and $1.3 \times 10^{16} \text{ cm}^{-2}$ for CH_3CN , CH_3CCH , and NH_3 , respectively. At this point, it is important to remember that the temperature derived from the ammonia emission does not peak at the position of the two radio continuum sources (cf. Figure 5.13). Higher angular

Table 5.7: Physical parameters derived from the molecular transitions observed

Molecule	Transition	Frequency (MHz)	$\int T dv$ (K km s ⁻¹)	v_{peak} (km s ⁻¹)	Δv (km s ⁻¹)	T_{peak} (K)	T_{ex} (K)	E_u (K)	A_{ul} (s ⁻¹)	N_u (cm ⁻²)	N_{mol} (cm ⁻²)
SMA molecular transitions											
¹³ CO	2 → 1	220 398.684	15.9	6.1×10^{-7}
CH ₂ CHCN	24 _{1,24} → 23 _{1,23}	220 561.394	0.5 ± 0.4	$+2.1 \pm 1.6$	2.4 ± 1.2	0.192	110 ± 11	134.9	8.9×10^{-4}	$2.7 \pm 1.9 \times 10^{11}$	1.2×10^{14}
HNCO	10 _{1,9} → 9 _{1,8}	220 584.751	4.9 ± 0.8	$+1.5 \pm 0.3$	3.8 ± 0.7	1.202	102 ± 10	101.5	1.5×10^{-4}	$1.7 \pm 0.6 \times 10^{13}$	1.1×10^{15}
CH ₃ CN	12 ₆ → 11 ₆	220 594.423	1.9 ± 0.7	-0.1 ± 0.1	5.1 ± 0.2	0.353	20 ± 2	325.9	6.9×10^{-4}	$1.3 \pm 2.0 \times 10^{13}$	$4.6 \times 10^{14} \dagger$
CH ₃ CN	12 ₅ → 11 ₅	220 641.084	1.9 ± 0.7	-0.1 ± 0.1	5.1 ± 0.2	0.349	22 ± 2	247.4	7.6×10^{-4}	$1.2 \pm 0.9 \times 10^{13}$	$4.6 \times 10^{14} \dagger$
CH ₃ CN	12 ₄ → 11 ₄	220 679.287	3.2 ± 0.4	-0.1 ± 0.1	5.1 ± 0.2	0.583	33 ± 2	183.1	8.2×10^{-4}	$1.9 \pm 0.3 \times 10^{13}$	$4.6 \times 10^{14} \dagger$
CH ₃ CN	12 ₃ → 11 ₃	220 709.017	7.6 ± 0.4	-0.1 ± 0.1	5.1 ± 0.2	1.407	56 ± 2	133.2	8.7×10^{-4}	$4.4 \pm 0.5 \times 10^{13}$	$4.6 \times 10^{14} \dagger$
CH ₃ CN	12 ₂ → 11 ₂	220 730.261	6.5 ± 0.4	-0.1 ± 0.1	5.1 ± 0.2	1.197	54 ± 2	97.4	9.0×10^{-4}	$3.6 \pm 0.4 \times 10^{13}$	$4.6 \times 10^{14} \dagger$
CH ₃ CN	12 ₁ → 11 ₁	220 743.011	7.8 ± 0.4	-0.1 ± 0.1	5.1 ± 0.2	1.433	59 ± 2	76.0	9.2×10^{-4}	$4.2 \pm 0.5 \times 10^{13}$	$4.6 \times 10^{14} \dagger$
CH ₃ CN	12 ₀ → 11 ₀	220 747.261	7.6 ± 0.4	-0.1 ± 0.1	5.1 ± 0.2	1.402	63 ± 2	68.9	9.2×10^{-4}	$4.1 \pm 0.5 \times 10^{13}$	$4.6 \times 10^{14} \dagger$
³⁴ SO ₂	22 _{2,20} → 22 _{1,21}	221 114.897	0.6 ± 0.1	$+0.4 \pm 0.4$	5.0 ± 0.7	0.117	69 ± 7	247.8	9.4×10^{-5}	$3.2 \pm 1.1 \times 10^{12}$	1.7×10^{15}
CH ₂ CHCN	23 _{1,22} → 22 _{1,21}	221 123.856	0.4 ± 0.1	$+1.3 \pm 0.2$	1.5 ± 0.3	0.239	135 ± 13	130.2	8.9×10^{-4}	$2.1 \pm 0.8 \times 10^{11}$	1.1×10^{14}
³⁴ SO ₂	13 _{2,12} → 13 _{1,13}	221 735.715	0.8 ± 0.1	$+1.1 \pm 0.2$	2.9 ± 0.4	0.258	146 ± 14	92.4	6.1×10^{-5}	$6.4 \pm 2.2 \times 10^{12}$	9.0×10^{14}
CH ₂ CHCN	24 _{0,24} → 23 _{0,23}	221 766.035	0.5 ± 0.2	$+2.0 \pm 0.4$	3.1 ± 1.1	0.148	85 ± 8	134.5	9.0×10^{-4}	$2.6 \pm 1.5 \times 10^{11}$	1.1×10^{14}
SO ₂	11 _{1,11} → 10 _{0,10}	221 965.220	26.8 ± 0.2	$+0.7 \pm 0.1$	5.9 ± 0.2	4.305	95 ± 8	60.4	1.1×10^{-4}	$1.3 \pm 0.3 \times 10^{14}$	1.2×10^{16}
CH ₃ CCH	13 ₃ → 12 ₃	222 128.815	2.0 ± 0.1	$+0.6 \pm 0.1$	3.0 ± 0.1	0.618	63 ± 2	139.7	4.0×10^{-5}	$2.7 \pm 0.5 \times 10^{14}$	$3.6 \times 10^{16} \ddagger$
CH ₃ CCH	13 ₂ → 12 ₂	222 150.010	1.8 ± 0.1	$+0.6 \pm 0.1$	3.0 ± 0.1	0.554	63 ± 2	103.5	4.0×10^{-5}	$2.3 \pm 0.5 \times 10^{14}$	$3.5 \times 10^{16} \ddagger$
CH ₃ CCH	13 ₁ → 12 ₁	222 162.730	2.5 ± 0.1	$+0.6 \pm 0.1$	3.0 ± 0.1	0.762	63 ± 2	81.9	4.0×10^{-5}	$3.2 \pm 0.5 \times 10^{14}$	$3.5 \times 10^{16} \ddagger$
CH ₃ CCH	13 ₀ → 12 ₀	222 166.971	3.1 ± 0.1	$+0.6 \pm 0.1$	3.0 ± 0.1	0.979	63 ± 2	74.6	4.0×10^{-5}	$4.0 \pm 0.5 \times 10^{14}$	$3.5 \times 10^{16} \ddagger$
CH ₂ CO	11 _{3,9} → 10 _{3,8}	222 199.883	1.0 ± 0.1	$+0.9 \pm 0.2$	2.9 ± 0.4	0.320	63 ± 2	68.9	9.2×10^{-4}	$4.5 \pm 0.5 \times 10^{11}$	3.6×10^{14}
CH ₂ CO	11 _{3,8} → 10 _{3,7}	222 200.213	1.0 ± 0.1	$+0.9 \pm 0.2$	2.9 ± 0.4	0.320	63 ± 2	68.9	9.2×10^{-4}	$4.5 \pm 0.5 \times 10^{11}$	3.6×10^{14}
O ¹³ CS	19 → 18	230 317.527	0.5 ± 0.1	$+0.6 \pm 0.2$	2.7 ± 0.5	0.185	106 ± 10	110.5	3.5×10^{-5}	$7.9 \pm 3.1 \times 10^{12}$	2.1×10^{14}
¹² CO	2 → 1	230 538.000	16.6	6.9×10^{-7}
OCS	19 → 18	231 060.993	7.4 ± 0.1	$+0.1 \pm 0.1$	5.0 ± 0.1	1.388	117 ± 11	110.9	3.6×10^{-5}	$1.1 \pm 0.3 \times 10^{14}$	3.0×10^{15}
¹³ CS	5 → 4	231 220.685	4.8 ± 0.2	$+0.6 \pm 0.1$	3.8 ± 0.2	1.179	30 ± 2	33.3	2.5×10^{-4}	$1.2 \pm 0.3 \times 10^{12}$	8.8×10^{13}
CH ₃ OH (A-)	10 _{2,9} → 9 _{3,6}	231 281.100	3.2 ± 0.2	-0.9 ± 0.1	3.3 ± 0.2	0.897	170 ± 16	165.3	1.8×10^{-5}	$9.2 \pm 2.4 \times 10^{13}$	3.6×10^{16}
t-HCOOH	10 _{1,9} → 9 _{1,8}	231 505.608	0.5 ± 0.1	-0.3 ± 0.3	3.3 ± 0.5	0.153	89 ± 8	64.5	1.4×10^{-4}	$2.1 \pm 0.7 \times 10^{12}$	2.9×10^{14}
CH ₃ OCH ₃	13 _{0,13} → 12 _{1,12}	231 987.933	1.5 ± 0.1	-0.4 ± 0.2	3.7 ± 0.3	0.375	74 ± 7	80.9	9.1×10^{-5}	$8.7 \pm 2.5 \times 10^{12}$	1.5×10^{16}

† Molecular column density estimated from the rotational diagram with the 7 rotational transitions of CH₃CN(12–11). We estimate a $T_{\text{rot}} = 150 \pm 10$ K and a $N_{\text{mol}} = 4.6 \pm 1.0 \times 10^{14}$ cm⁻² (see Figure 5.14).

‡ Molecular column density estimated from the rotational diagram with the 4 rotational transitions of CH₃CCH(13–12). We estimate a $T_{\text{rot}} = 70 \pm 20$ K and a $N_{\text{mol}} = 3.5 \pm 1.0 \times 10^{16}$ cm⁻² (see Figure 5.14).

Table 5.8: Properties of the hot molecular cores: IRAS 22198+6336 and G75.78+0.34^a

	IRAS 22198+6336	G75.78+0.34
distance (pc)	760	3800
L_{bol} (L_{\odot})	370	73000
T_{bol} (K)	61	50
M_{env} (M_{\odot})	5	27
clustering (mm)	no	no
IRAC source	yes	yes
L_{cm} (mJy kpc ²)	0.36	20
outflow	yes	yes
<i>hot core information</i>		
T_{rot} (K)	100–150	100–150
N_{H_2} (cm ⁻²)	4×10^{23}	1.6×10^{23}
$X_{\text{CH}_3\text{CN}}$	9×10^{-10}	3×10^{-9}
$X_{\text{CH}_3\text{OH}}$	2×10^{-7}	2×10^{-7}
X_{HNCO}	8×10^{-10}	7×10^{-9}
X_{OCS}	2×10^{-7}	2×10^{-8}
$X_{^{13}\text{CS}}$	3×10^{-11}	6×10^{-10}
<i>outflow information</i>		
t_{dyn} (yr)	1300 / 1200	2800
\dot{M} ($10^{-6} M_{\odot} \text{ yr}^{-1}$)	10 / 8	59
P ($M_{\odot} \text{ km s}^{-1}$)	0.3 / 0.2	9.4

^a References are Chapter 4 and the current Chapter. For details in the estimation of the bolometric luminosity and temperature, see Chapter 9.

resolution observations at millimeter wavelengths are necessary to determine how is the morphology of the hottest dense gas and its temperature distribution. Recently, Zapata et al. (2010) reveal, thanks to the morphological distribution of the dense gas tracers, that the ‘hot core’ in Orion KL seems to be not a *real* hot core, i. e., the hot and dense gas is not heated by an internal embedded object but by outside objects or powerful shocks. The morphology of the NH_3 (2,2) and (4,4) emission in G75, together with the presence of the molecular outflow and water masers, make this object an excellent candidate to study if the ‘hot core’ molecular emission is internally or externally heated. A similar case is the intermediate-mass hot core in I22198 (see Chapter 4), in which the ammonia emission shows a morphology affected by the presence of the outflows, but in this case with the hot core being compact and directly associated with the YSO (i. e., the hot core seems to be produced by internal heating in I22198). Higher angular resolution observations of hot core tracers, with the SMA in more extended configurations or ALMA, are necessary to

5. G75.78+0.34: compact radio sources embedded in a hot core

unveil the origin of the hot molecular core emission in G75.

In Table 5.7, we list all the molecules detected with the SMA in the dense core. Following the procedures indicated in Appendix D we have estimated the column density for each molecule. In order to derive molecular abundances, we used the dust millimeter continuum emission to calculate the column density of H_2 , which is $1.6 \times 10^{23} \text{ cm}^{-2}$ (assuming a dust temperature of 150 K, and a size of $5''$). In Table 5.8, we list the calculated abundances and show a comparative of the properties of the hot molecular cores in I22198 and G75 (we also list some additional information on the centimeter, millimeter, infrared and outflow properties). These two sources are clearly different, in distance and luminosity, however their hot molecular core properties are rather similar for molecules such as CH_3CN or CH_3OH , but different (up to 1 order of magnitude) in other species such as ^{13}CS or OCS . A complete chemical analysis of these two hot molecular cores, together with other objects from the literature, can be useful to search for differences in this star-forming features seen in low, intermediate and high-mass stars.

5.5.4 Nature of the ionized gas emission

In Section 5.3, we reported the detection of four distinct radio continuum sources: UCH II, EAST, CORE-N and CORE-S (the last two corresponding to the CORE source when the angular resolution is not good enough).

The UCH II and EAST sources seem to be two H II regions with a size (0.019 and 0.004 pc) and physical properties (n_e of 3.7×10^4 and 1.3×10^5) characteristic of ultracompact H II regions (Kurtz 2005a), probably ionized by B0 and B0.5 ZAMS stars, respectively, and with the emission at centimeter wavelengths being optically thin (i.e., spectral index of -0.1). However, there are some differences, regarding the morphology and infrared properties, between the two sources. The UCH II source has a clear cometary shape, while the EAST source seems to be spherical or irregular (with a smaller size). Regarding the infrared emission, in Figures 5.15 and 5.16, we show some infrared maps of the G75 star-forming complex. An infrared source between 8 and $3.6 \mu\text{m}$ is clearly associated with the EAST source, however, there is no infrared emission at these wavelengths associated with the cometary UCH II. This is surprising because both sources have similar properties in the centimeter range or even that the EAST source should be younger than the UCH II, as it is visible at millimeter wavelengths (cf. Figure 5.3 and Table 5.3) and at mid-infrared wavelengths. However, if the cometary UCH II region was a more evolved source, having already dispersed the dust (no emission at millimeter wavelengths, neither at mid-infrared), it should be visible at (near)infrared wavelengths, while there is no infrared counterpart. We can think that the UCH II is not visible at infrared due to the presence of a large dusty cloud which obscures the region. This large dusty cloud is detected at submillimeter wavelengths in emission (Di Francesco et al. 2008), and at infrared wavelengths as a dark (obscured) region (cf. the obscured region to the northeast in the infrared panels of Figure 5.15).

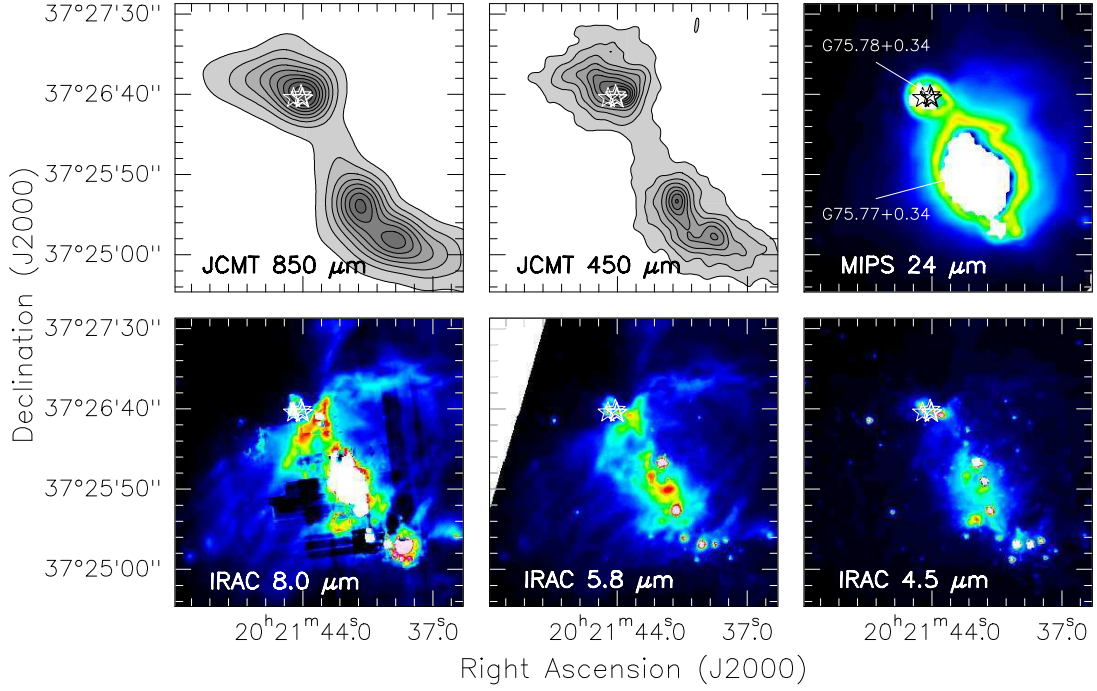


Figure 5.15: Images at infrared wavelengths for G75.78+0.34. The stars mark the position of the radio continuum sources: UCH II, EAST and CORE (N and S); see Table 5.3. The large infrared and submillimeter source toward the southwest of the images correspond to the H II region G75.77+0.34. A dark region is seen toward the northeast in the infrared images (at the position of the radio continuum sources discussed in this Chapter). At the same position of this infrared dark region there is a strong submillimeter source, detectable at 850 and 450 μm . The images at 24 μm and 8 μm are saturated at the position of the large H II region G75.77+0.34.

Regarding the emission from the CORE (N and S) source, we test different models to explain the mechanism that is producing the ionized gas. Franco et al. (2000) modeled the CORE source as an H II region with a density distribution $n_e \propto r^{-4}$, with partially optically thick centimeter continuum emission up to frequencies ~ 100 GHz. However, our new observational data seem to indicate that the ionized gas emission becomes optically thin at frequencies ~ 30 GHz (Figure 5.4). The upper limits for the RRLs at 99 and 232 GHz (cf. Section 5.4.4) can be used to confirm if the emission is optically thin at $\nu > 40$ GHz. Assuming optically thin emission for line and continuum, and 3σ upper limits for H30 α and H40 α (i.e., 30 and 45 mJy beam $^{-1}$, respectively), we can calculate the expected continuum emission from ionized gas with (Rohlfs and Wilson 2004)

$$\left[\frac{S_L}{S_C} \right] = 6940 \left[\frac{\Delta v}{\text{km s}^{-1}} \right]^{-1} \left[\frac{T_e}{\text{K}} \right]^{-1.15} \left[\frac{\nu}{\text{GHz}} \right]^{1.1}, \quad (5.1)$$

where S_L is the line flux density, S_C is the continuum flux density, Δv is the width of

5. G75.78+0.34: compact radio sources embedded in a hot core

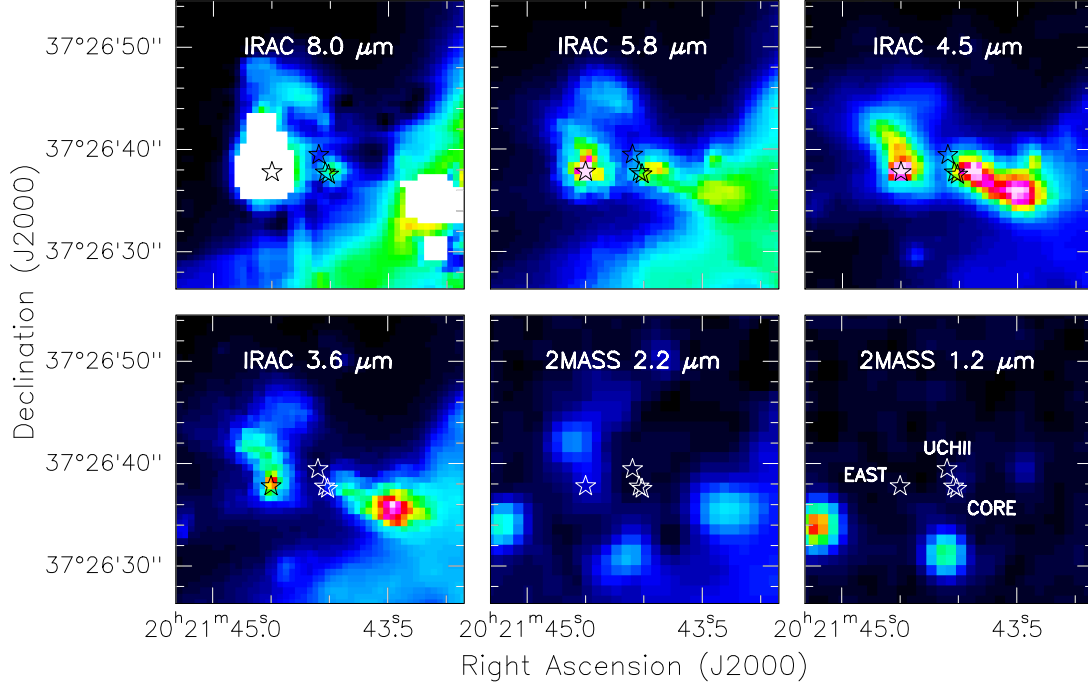


Figure 5.16: Zoom of the images at infrared wavelengths for G75.78+0.34. The stars mark the position of the radio continuum sources: UCH II, EAST and CORE (N and S); see Table 5.3). No infrared emission is associated with the cometary UCH II region. The image at 8 μ m is saturated at the center of the EAST source.

the radio recombination line (assumed to be 30 km s⁻¹; Kurtz 2005a), T_e is the electron temperature assumed to be 10⁴ K, and ν is the frequency of the line. We obtain that the continuum flux density of ionized gas at 3 and 1 mm could be < 30 and < 18 mJy, respectively. These values are in agreement with the homogeneous H II region fits discussed in Section 5.3.3, for which the expected fluxes at 3 and 1 mm for free-free emission are ~ 3 mJy (i. e., $\ll 18$ mJy). Thus, we can assume the ionized gas emission becomes optically thin for frequencies > 30 GHz (as seem to suggest the observations at 7 mm).

From the SED analysis done in Section 5.3.3, we can fit the centimeter emission of each of the two sources by using a simple model of homogenous H II region, with sizes $\lesssim 0.001$ pc and electron densities of $\simeq 10^6$ cm⁻³. Both sources would be ionized by a B0.5 ZAMS star, and separated by a distance of 0''.36 (1400 AU at a distance of 3.8 kpc). This scenario implies a close massive binary system. We searched the literature for similar systems, with two close massive radio continuum sources, and found that in the massive star-forming complex G31.41+0.31 there is a system of two centimeter continuum sources separated by 0''.19 (1500 AU at 7.9 kpc; Araya et al. 2008); in G10.47+0.03 there are two similar sources separated by 0''.53 (5700 AU at 10.8 kpc; Cesaroni et al. 2010); and

in DR21(OH) a similar system is separated by only $0''.45$ (900 AU at 2 kpc; Araya et al. 2009). Thus, it seems that it is not unusual to detect double radio continuum sources, separated by ~ 1000 AU in massive star-forming regions.

At this point, it is important to note that the double radio continuum source of some of the previous listed systems, is not always explained as emission coming from homogenous H II regions. Araya et al. (2009) propose that the radio continuum emission in DR(21)OH is, in fact, free-free radiation coming from interstellar shock waves. In Chapter 1, we discussed this mechanism (see also Ghavamian and Hartigan 1998 for more details). In this scenario, the ionized emission arises from shocked emission instead of photoionized gas. The molecular outflows and collimated jets originated in the star formation process, produce shocks when interacting with the surrounding environment, typically seen as HH objects in the optical. Ghavamian and Hartigan (1998) provide some graphs that can be used to test their model. The input parameters are the flux density at 1.5, 5 or 15 GHz, the angular size of the source at one of these frequencies, and the spectral index between some pairs of these frequencies. In our case, assuming a flux of ~ 2 mJy beam $^{-1}$ at 15 GHz (or 22 GHz), an angular size of $0''.05$, and a spectral index between 5 and 15 GHz of 1.1, we can roughly estimate that we need a preshock density of 10^6 – 10^7 cm $^{-3}$, with shock velocities of 100–250 km s $^{-1}$. These parameters are consistent with the presence of the dense (and hot) core traced by several molecules (cf. Section 5.5.2), for which we estimated an H $_2$ density of $\sim 2 \times 10^6$ cm $^{-3}$ from the 1.3 mm continuum emission), and with the velocities for the molecular outflow (~ 70 km s $^{-1}$ for the CO). In conclusion, it seems that the radio continuum emission from CORE-N and S sources could be due to shocks between the jet/outflow and the molecular surrounding gas. In addition, it is interesting to note the elongated structure visible between 3.6 and 5.8 μ m (see Figure 5.16), and ‘emanating’ from the position of the CORE source. This elongated structure is more prominent at 4.5 μ m, as expected for shocked H $_2$ emission (the H $_2$ shocked emission lines are more abundant and bright in the 4.5 μ m IRAC band). This emission seems to favor the presence of shocked gas related to the CORE source, and following the outflow blue lobe detected by us with the SMA.

Other mechanisms that can also be tested to explain the centimeter emission from CORE N and S (see Chapter 1). Equatorial winds (Hoare 2006) or thermal radiojets (Anglada 1996) typically predict constant spectral indices of +0.6 and a relation between the size of the source and the frequency. However, our observations suggest spectral indices $\sim +1$, and we cannot test the dependence of size with frequency since we only revolve the source at one wavelength. Photoevaporated disk has been proposed to explain the continuum emission of the double peak source (hour-glass morphology) MWC 349. The CORE source with the two peaks (N and S sources) could be fitted as a photoevaporated disk. However, recent studies indicate that the double peak of the hour-glass morphology from a photoevaporated disk should change its separation, getting closer for larger frequencies (M. Avalos, priv. comm.). In our case, the peak position of N and S sources does not

change up to a precision of $\sim 0''.02$ from 3.6 up to 0.7 cm. In addition, the double continuum peak morphology is not consistent with the outflow orientation, in a photoevaporated disk scenario.

In conclusion, the centimeter continuum emission from CORE (N and S) source can be well-fitted as homogeneous H II regions likely tracing hypercompact H II regions around two B0.5 ZAMS star, or as free-free radiation coming from interstellar shock waves produced by the interaction of a jet/outflow system with the surrounding environment. The water maser spots reported in Figure 5.9 can help up disentangling which scenario is most probable. While the CORE-S source has some maser spots associated with, the N source has no maser emission directly associated. In some regions, water masers have been found to trace the kinematics of jets/outflows, and associated with centimeter continuum sources likely tracing shocked gas emission (e.g., IRAS 20126+4104: Hofner et al. 2007). G75-CORE could be a similar case, with the CORE-S continuum source tracing a shock between the jet and the dense gas, which would enhance the water maser emission. In this situation the shock would be produced in a region of high density, as is likely suggested by the V-shaped morphology seen in ammonia. The CORE-N source could be the driving source, or a secondary shock produced in a less dense region, without enhancement of maser emission. This scenario can be tested with future centimeter continuum observations with the EVLA, to confirm if the CORE-S source (and water maser spots) have been displaced with respect to the other continuum sources. In less than five years, we should be capable to disentangle the movement of CORE-S, assuming a velocity of the jet of $\sim 100 \text{ km s}^{-1}$.

5.6 Summary and brief discussion

We have studied the massive star-forming complex G75.78+0.34 achieving high angular resolutions for centimeter and millimeter continuum emission, and complemented these observations with spectral line data, tracing ionized gas (radio recombination lines), molecular outflows, and dense gas emission. We summarize our main conclusions in the following.

- Our radio continuum data revealed the presence of four distinct centimeter sources. The strongest one, UCH II, is a cometary UCH II region, with a size of 0.02 pc, an electron density of $3.7 \times 10^4 \text{ cm}^{-3}$ and ionized by a B0 ZAMS star. A second source, EAST (located $\sim 6''$ to the east), can also be fitted as an UCH II region with a smaller size (0.004 pc) and $n_e = 10^5 \text{ cm}^{-3}$ probably ionized by a B0.5 ZAMS star. The remaining two sources (CORE-N and S) are found very close ($0''.36$, 1400 AU) and show similar properties: flux density increasing with the frequency, and unresolved emission. When observed with lower angular resolution both sources appear as in a single compact source labelled CORE. The ionized gas emission could be produced by two HCH II regions ionized by B0.5 ZAMS star, or by the collisions between a jet and its environment.

- The continuum emission at millimeter wavelengths seems to have different origins for each source. For the UCH II source all the emission is likely tracing the ionized gas of the cometary UCH II region, however, for the EAST source there is an excess at 3 mm suggesting that this second UCH II region is still embedded in dust. Finally, the strong millimeter clump detected at the position of the CORE source is well fitted by a dust core of $\sim 30 M_{\odot}$.
- A molecular outflow has been identified in the ^{12}CO and ^{13}CO (2–1) transitions, with a northeast-southwest orientation likely powered by the CORE source. The energetics of the outflow are similar to those of other massive molecular outflows.
- A dense core, traced by different molecules, is found associated with the CORE source. The ammonia data, with higher angular resolution, reveal a double peak or V-shaped morphology surrounding the two continuum sources. The emission of other dense gas tracers, observed with lower angular resolution, comes from a compact (unresolved) core with the peak coincident with the CORE source. The richness in complex organic molecules and the high temperature ($T \sim 100$ K) derived from rotational diagrams confirms that there is a hot molecular core associated with the CORE continuum source. Finally, a velocity gradient, perpendicular to the outflow direction, is seen in all the molecular tracers, likely tracing a rotating structure.
- We also have reported high angular resolution observations of H_2O and class I CH_3OH maser emission. Several water maser spots have been associated close to the CORE N and S sources, with only a few of them spatially coincident with the S source. The class I methanol maser spots are found far from any of the radiocontinuum sources, but close to the red lobe of the molecular outflow. Furthermore, the velocity of these methanol masers is redshifted, suggesting they could have been pumped by the collisions of the outflow.

6

IRAS 19035+0641: a compact radio source embedded in dense gas

6.1 General overview

IRAS 19035+0641 (hereafter I19035) is a massive star-forming region, with a bolometric luminosity of $8000 L_{\odot}$ at a distance of 2.2 kpc (Sridharan et al. 2002; Osterloh et al. 1997), observed in several continuum, molecular and maser line surveys. At (sub)millimeter wavelengths, single-dish maps reveal a compact and strong source with extended emission toward the north, likely tracing a dust envelope of $\sim 300\text{--}900 M_{\odot}$ (Beuther et al. 2002b; Williams et al. 2004). I19035 is also detected at far and mid-infrared wavelengths (De Buizer et al. 2005; IRAS, MSX and *Spitzer* GLIMPSE and MIPS GAL surveys). Fazal et al. (2008) modeled the SED spanning the mid-infrared to millimeter wavelengths as an envelope with a high accretion rate. Several molecular line transitions have been detected in the region (CS, C^{34}S : Bronfman et al. 1996; Larionov et al. 1999; Beuther et al. 2002b; CH_3CN , H_2CO : Araya et al. 2005, 2007; HCO^+ , N_2H^+ : Fuller et al. 2005). CO single-dish maps reveal a velocity gradient in the (south)east-(north)west direction likely tracing a massive molecular outflow (Beuther et al. 2002c; López-Sepulcre et al. 2010). Finally, the region is very rich in maser emission: 6.7 GHz (class II) methanol, water, and 1.6 and 6.7 GHz hydroxyl masers (e.g., Caswell and Vaile 1995; Szymczak et al. 2000; Sridharan et al. 2002; Beuther et al. 2002d; Fish et al. 2005; Fish and Reid 2006; Edris et al. 2007 have been found associated with the peak of the dust condensation, as clear evidence of star formation activity. At centimeter wavelengths one compact source of a few mJy has been reported close to the dust peak (Hughes and MacLeod 1989; Sridharan et al. 2002).

6. IRAS 19035+0641: a compact radio source embedded in dense gas

Table 6.1: Main VLA continuum observational parameters of IRAS 19035+0641

λ (cm)	Project VLA conf.	Epoch of Observation	Gain cal. / Bootstr. Flux ^a	Flux cal.	Beam (" \times ")	P.A. ($^\circ$)	Rms ^b
20.0	NVSS D	1996 Jul 04	45. \times 45.	+0	620
20.0	AR177 DnC	1988 May 15	2029+121 / 0.85(1)	3C286	20. \times 14.	-3	3060
6.0	AR177 DnC	1988 May 15	2029+121 / 0.77(1)	3C286	5.0 \times 3.8	-6	84
6.0	AS902 A	2007 Jun 05	1922+155 / 0.62(1)	3C286	0.41 \times 0.35	-60	48
6.0	AH329 A	1988 Oct 29	1923+210 / 1.69(1)	3C286	0.50 \times 0.40	-65	49
3.6	AS643 BnA	1998 Jul 02	1920+154 / 0.81(1)	3C286	1.04 \times 0.74	+50	62
3.6	AS902 A	2007 Jun 05	1922+155 / 0.58(1)	3C286	0.23 \times 0.22	-7	32
2.0	AH329 A	1988 Oct 29	1923+210 / 1.86(5)	3C286	0.41 \times 0.34	+59	141
1.3	AB1274 B	2007 Oct 23	1851+005 / 0.90(3)	3C286	0.29 \times 0.26	-13	81
0.7	AS981 C	2009 Jun 29	1856+061 / 0.21(5)	3C286	0.54 \times 0.42	+44	213
0.7	AB1274 B	2007 Oct 23	1851+005 / 0.76(20)	3C286	0.41 \times 0.35	-10	211

^a Bootstrapped flux in Jy. In parenthesis: the percentage of error in the flux.

^b Rms noise level in $\mu\text{Jy beam}^{-1}$.

In this Chapter, we present VLA continuum and NH_3 line observations that reveal the presence of two radio continuum sources in I19035, one of them being deeply embedded in a dense ammonia and dust clump.

6.2 Observations

6.2.1 Very Large Array

The I19035 star-forming region was observed with the Very Large Array (VLA¹) at 6.0, 3.6, 1.3, and 0.7 cm continuum in the A, B, and C configurations of the array, on 2007 and 2009, with 10–21 EVLA antennas in the array. In Table 6.1 we list the main parameters of the observations. The data reduction followed the VLA standard guidelines for calibration of high frequency data, using the NRAO package AIPS. First images were produced with a natural weighting to obtain a good sensitivity. We complemented our continuum observations with archival data from projects AR177, AH329 and AS643, and data from the NVSS (Condon et al. 1994), which contain observations of I19035 at 20, 6.0, 3.6, and 2.0 cm in different array configurations (see Table 6.1). We combined the uv -data sets at the same frequencies to obtain final images with a better uv -coverage, sensitivity and angular resolution. In Table 6.2 we provide the resulting synthesized beams and rms noise levels for the combined uv -data sets. We did not combine the 0.7 cm observations due to the low sensitivity of the B-array observations.

¹The Very Large Array (VLA) is operated by the National Radio Astronomy Observatory (NRAO), a facility of the National Science Foundation operated under cooperative agreement by Associated Universities, Inc.

The region was observed with the VLA to map the $(J, K)=(1,1)$ (2,2) and (3,3) inversion lines of the ammonia molecule with the array in a compact configuration. The archival (1,1) and (2,2) line data were obtained during 2002 January 01 (project AF386) with the array in its D configuration. The adopted flux density of the absolute flux calibrator 1331+305 (3C 286) was 2.41 Jy at the frequencies of 23.69 and 23.72 GHz. Amplitude and phase calibration were achieved by monitoring 1849+005, resulting in an rms of the phases $\sim 40^\circ$ and a bootstrapped flux of 0.814 ± 0.007 Jy. The 4IF spectral line mode was used, allowing simultaneous observations of NH_3 (1,1) and (2,2) lines with two polarizations for each line. The bandwidth used was 3.1 MHz, with 63 spectral channels with a channel spacing of 48.8 kHz ($\sim 0.6 \text{ km s}^{-1}$) centered at $v_{\text{LSR}} = +31.0 \text{ km s}^{-1}$, plus a continuum channel that contains the average of the central 75% of the bandwidth. The (3,3) inversion line was observed with the array in the C-configuration on 2005 September 19 (project AC787). The flux scale was calibrated with observations of 1331+305 (3C 286), with an adopted flux of 2.40 Jy at 23.87 GHz. The quasar 1229+020 (3C 273) was used to correct for the bandpass. Amplitude and phase corrections were achieved by observing 1851+005, resulting in an rms phase $\sim 50^\circ$ and a bootstrapped flux of 0.928 ± 0.010 Jy. The bandwidth used was 3.1 MHz, with 127 spectral channels with a channel spacing of 24.4 kHz ($\sim 0.3 \text{ km s}^{-1}$) centered at $v_{\text{LSR}} = +32.4 \text{ km s}^{-1}$, plus a continuum channel that contains the average of the central 75% of the bandwidth. In both observational projects, the data reduction followed the standard guidelines for calibration of high frequency data, using the software package AIPS. Imaging was performed using natural weighting, resulting in a synthesized beam of $4''.0 \times 3''.7$ with a P.A. $= -12^\circ$ and a 1σ rms of $1.4 \text{ mJy beam}^{-1}$ per channel for the D-array maps, and $3''.4 \times 3''.1$ with a P.A. $= -15^\circ$ and 1σ rms of $2.5 \text{ mJy beam}^{-1}$ per channel for the C-array observations, after tapering the data at 60 k λ .

6.3 Continuum results

6.3.1 Centimeter continuum results

We detect centimeter radio continuum emission at all wavelengths, except at 20 cm, maybe due to the low sensitivity of the images (see Figure 6.1 and Table 6.2). At 6 cm, with the VLA in a compact configuration, we detect only an unresolved source centered at $\alpha(J2000.0) = 19^{\text{h}}06^{\text{m}}01^{\text{s}}50$ and $\delta(J2000.0) = +06^\circ46'35''.6$, and with an intensity peak of $2.6 \pm 0.4 \text{ mJy beam}^{-1}$, in agreement with the observations of Hughes and MacLeod (1989) and Sridharan et al. (2002). The source is slightly displaced ($1''.3$) of an *Spitzer*/IRAC source (see Figure 6.1 top panel). When observed at higher angular resolution, the radio continuum source splits into two components: VLA1 and VLA2 (see bottom panels in Figure 6.1). In Table 6.2, we list their coordinates, fluxes and sizes, together with the beams and rms noise levels of the (combined, when available) maps.

The brightest radio source, VLA1, has a similar flux density (of a few mJy) and is

6. IRAS 19035+0641: a compact radio source embedded in dense gas

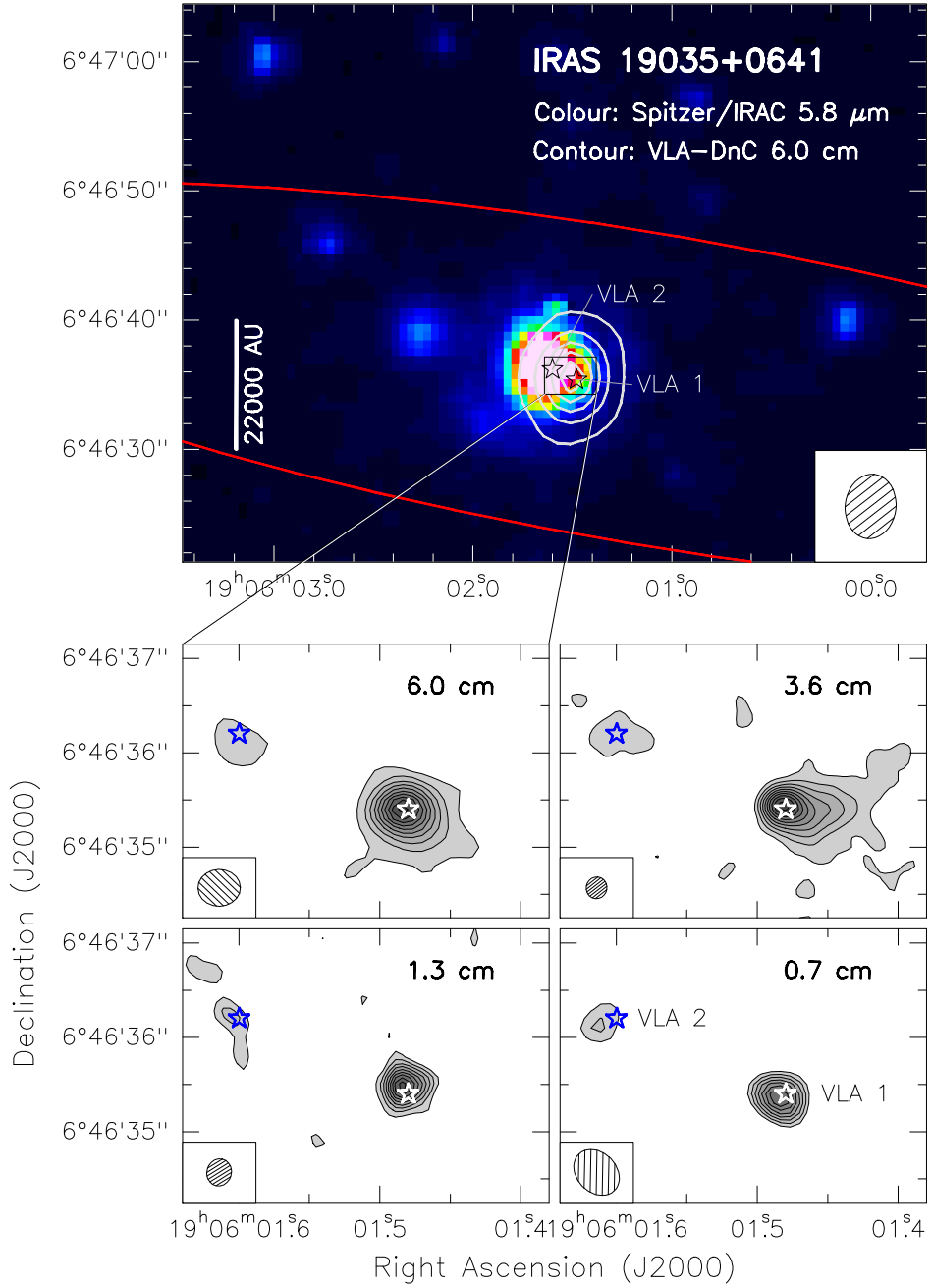


Figure 6.1: Continuum maps for IRAS 19035+0641. **Top:** Colour scale: 5.8 μm *Spitzer*/IRAC map. White contours: VLA-DnC 6.0 cm continuum map. Levels start at 5%, increasing in steps of 20% of the peak intensity $2.6 \text{ mJy beam}^{-1}$. The synthesized beam is shown in the bottom-right corner. The (part of) red ellipse mark the IRAS source. The spatial scale is indicated, and the black box marks the region shown in the bottom panels. **Bottom:** For all panels, grey scale and contours: VLA continuum maps. Levels start at 5%, increasing in steps of 10% of the peak intensity: 1.8, 1.2, 1.1, and 1.9 mJy beam^{-1} , for 6, 3.6, 1.3, and 0.7 cm, respectively. Synthesized beams are shown in the bottom-left corner. The stars in all panels mark the position of sources VLA1 and VLA2 (see Table 6.2).

Table 6.2: Multiwavelength results for the YSOs in IRAS 19035+0641

λ (cm)	Beam ($'' \times ''$)	P.A. ($^\circ$)	Rms ^b	$I_\nu^{\text{peak a}}$ (mJy beam ⁻¹)	S_ν^{a} (mJy)	Deconv. Size ($'' \times ''$)	P.A. ($^\circ$)
VLA1	$\alpha(J2000.0) = 19^{\text{h}}06^{\text{m}}01.^{\text{s}}48$ $\delta(J2000.0) = +06^\circ46'35''.4$						
20.0	45. \times 45.	+0	620	...	< 2.5
6.0	0.45 \times 0.39	-89	36	1.8 \pm 0.1	2.5 \pm 0.2	0.33 \times 0.20 \pm 0.05	55 \pm 10
3.6	0.30 \times 0.29	+1	34	1.2 \pm 0.1	2.8 \pm 0.3	0.50 \times 0.24 \pm 0.05	80 \pm 20
2.0	0.41 \times 0.34	+59	141	0.9 \pm 0.3	1.4 \pm 0.6	0.40 \times 0.30 \pm 0.30	75 \pm 45
1.3	0.29 \times 0.26	-13	81	0.3 \pm 0.2	1.9 \pm 0.4	0.28 \times 0.23 \pm 0.07	75 \pm 30
0.7	0.54 \times 0.42	+44	213	1.9 \pm 0.4	1.9 \pm 0.7
VLA2	$\alpha(J2000.0) = 19^{\text{h}}06^{\text{m}}01.^{\text{s}}60$ $\delta(J2000.0) = +06^\circ46'36''.2$						
20.0	45. \times 45.	+0	620	...	< 2.5
6.0	0.45 \times 0.39	-89	36	0.21 \pm 0.06	0.21 \pm 0.13
3.6	0.30 \times 0.29	+1	34	0.15 \pm 0.05	0.19 \pm 0.10
2.0	0.41 \times 0.34	+59	141	...	< 0.6
1.3	0.29 \times 0.26	-13	81	0.31 \pm 0.11	0.35 \pm 0.25
0.7	0.54 \times 0.42	+44	213	0.81 \pm 0.27	0.81 \pm 0.54

^a Primary beam corrected. Error in intensity is 2σ . Error in flux density has been calculated as $\sqrt{(2\sigma\sqrt{\theta_{\text{source}}/\theta_{\text{beam}}})^2 + (2\sigma_{\text{flux-scale}})^2}$, where σ is the rms noise level of the map, θ_{source} and θ_{beam} are the size of the source and the beam respectively, and $\sigma_{\text{flux-scale}}$ is the error in the flux scale, which takes into account the uncertainty on the calibration applied to the flux density of the source ($S_\nu \times \%$ uncertainty).

^b Rms noise level in $\mu\text{Jy beam}^{-1}$.

elongated in the (north)east-(south)west direction (axis ratio of ~ 1.5 and $\text{PA} \sim 75^\circ$) at all wavelengths. The elongation is probably due to the cometary morphology of the source, seen at 3.6 cm (Figure 6.1). Around 1''.5 to the east of VLA1, we detect VLA2 (at a level of 3–4 σ in all the maps). Its flux density, of a few tenths of mJy, is almost constant between 6 and 1.3 cm (taking into account the uncertainties) and increases at 7 mm, suggesting that at this wavelength we could have contribution of dust emission. The cometary source VLA1 is clearly located displaced of the strongest IRAC source, but VLA2 is spatially coincident with the infrared source, which is detected in all the four *Spitzer*/IRAC bands. In a 3-colour composite image (blue: 3.6 μm ; green: 4.5 μm ; red: 8.0 μm) this IRAC source appears as a red object (see Figure 6.6), suggesting that emission from larger infrared wavelengths dominates, as expected in YSOs deeply embedded in dust.

6.3.2 Spectral energy distributions

In Figure 6.2, we show the spectral energy distributions (SEDs) of VLA1 and VLA2, in the centimeter range. VLA1 has a flat distribution, with a spectral index (α ; $S_\nu \propto \nu^\alpha$) of

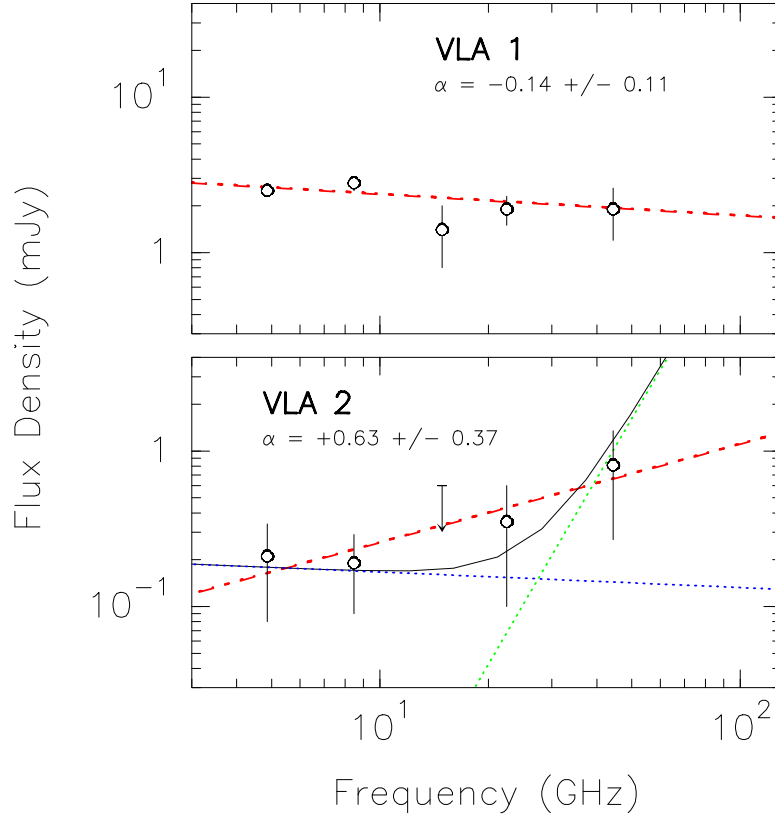


Figure 6.2: Spectral energy distributions for the YSOs VLA1 and VLA2 in IRAS 19035+0641. Circles and upper limits correspond to the observational data from Table 6.2. Red dashed lines: linear fit ($S_\nu \propto \nu^\alpha$) to the centimeter data (from 6 up to 0.7 cm). The value of the spectral index α is indicated in each panel. Blue dotted line: homogenous H II region with an electron density of $7 \times 10^3 \text{ cm}^{-3}$. Green dotted lines: modified blackbody law for the dust envelope with a dust emissivity index of $\beta = 2$, a source radius of $10''$, a dust temperature of 20 K, a dust mass of $40 M_\odot$, and a dust mass opacity coefficient of $0.9 \text{ cm}^2 \text{ g}^{-1}$ at 1.3 mm.

-0.14 ± 0.11 , typical of optically thin free-free emission. This SED can be produced by an H II region with a size of 0.005 pc , an electron density of $2.7 \times 10^4 \text{ cm}^{-3}$, an emission measure of $4.7 \times 10^6 \text{ cm}^{-6} \text{ pc}$, an ionized gas mass of $1.5 \times 10^{-4} M_\odot$, and flux of ionizing photons of 10^{45} s^{-1} (corresponding to a B1 ZAMS star; Panagia 1973). On the other hand, the flux of VLA2 seems to increase with the frequency. In Figure 6.2 we show its SED. A linear fit to the centimeter SED provides an spectral index of $+0.63 \pm 0.37$, typical of partially thick emission (as found in thermal radio jets or non-homogeneous H II regions with a density gradient $n_e \propto r^2$, see Appendix B). However, the large uncertainties in the fluxes of VLA2, makes the interpretation of its SED challenging. It can also be fitted by optically thin free-free emission, with the 7 mm excess in the flux density coming from

a dust envelope. In this case, the optically thin emission would be produced by an H II region with a size of 0.006 pc, an electron density of $7 \times 10^3 \text{ cm}^{-3}$, an emission measure of $3.1 \times 10^5 \text{ cm}^{-6} \text{ pc}$, and flux of ionizing photons of $6.4 \times 10^{43} \text{ s}^{-1}$ (corresponding to a B3 ZAMS star; Panagia 1973). More sensitive observations are necessary to better estimate the flux density of VLA2 at different frequencies, and thus better determine its spectral distribution, and the nature of the ionized gas.

6.4 Molecular results

6.4.1 Molecular dense gas: morphology and velocity fields

The zero-order moment (integrated intensity) maps of the NH_3 (1,1), (2,2) and (3,3) transitions are shown in Figure 6.3 (top panels). As can be seen from the (1,1) line, the ammonia emission shows one major clump surrounded by three fainter clumps located toward the north, east and (south)west. All the four clumps are located within a larger and fainter structure consisting of two major filaments: one in the east-west direction, and the other with a north-south orientation. The emission of (2,2) and (3,3) inversion lines, is mainly associated with the main clump, although there are some hints of faint extended emission tracing the same morphology seen in NH_3 (1,1). It is important to note that the two radio continuum sources lie within the main NH_3 clump (cf. white stars in Figure 6.3). VLA1 is displaced $1''.5$ to the west of the dense clump with the cometary arc of the H II region directly facing the dense clump. More interestingly, VLA2 is spatially coincident with the peak of the NH_3 emission. We note that the IRAC source, likely tracing dust emission from an embedded YSO, is spatially coincident with VLA2 and the NH_3 main clump.

In the middle and bottom panels of Figure 6.3, we show the first-order moment (velocity field) and second-order moment (linewidth) maps for the three ammonia transitions. A velocity gradient ($\sim 2 \text{ km s}^{-1}$) can be identified in the southeast-northwest direction, well centered at the position of the main ammonia clump and the source VLA2. Single-dish observations of the CO (2–1), HCO^+ (1–0) and C^{18}O (2–1) molecular transitions reveal a velocity gradient, in the same direction as the ammonia velocity gradient, which was interpreted as a molecular outflow (Beuther et al. 2002c; López-Sepulcre et al. 2010). New interferometric observations of outflow tracers are necessary to confirm the outflow direction, and thus better interpret the nature of the ammonia velocity gradient. The highest velocity dispersion (corresponding to linewidths of $\sim 5 \text{ km s}^{-1}$) is found at the position of VLA2, possibly indicating that NH_3 gas is affected by outflow motions.

6.4.2 Molecular dense gas: temperature and density

As in previous chapters, we studied the chemical environment of I19035 by analyzing the column density, rotational temperature, opacity and velocity of the NH_3 emission: the

6. IRAS 19035+0641: a compact radio source embedded in dense gas

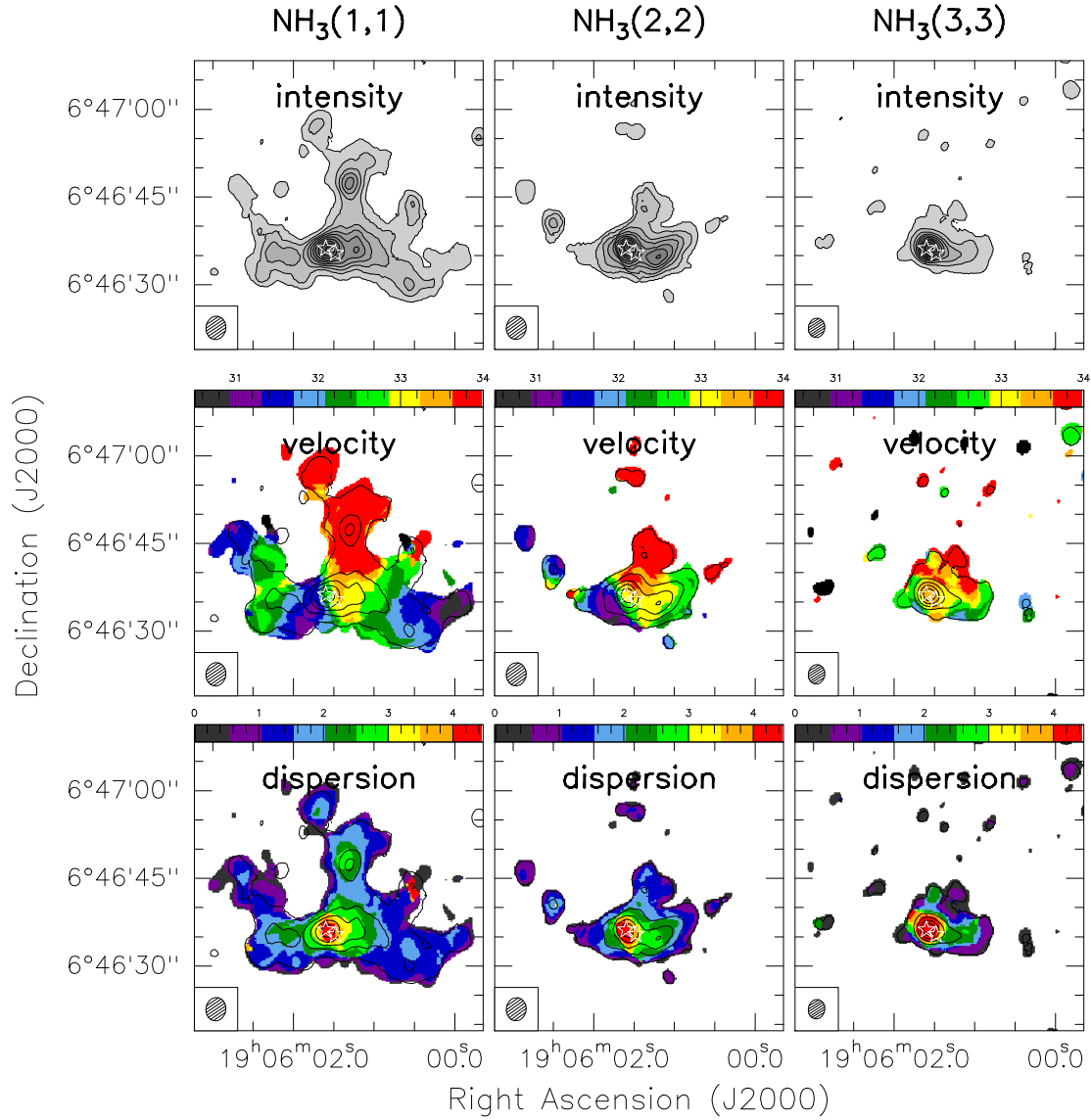


Figure 6.3: $\text{NH}_3(1,1)$ (*left-column*), $\text{NH}_3(2,2)$ (*center-column*), and $\text{NH}_3(3,3)$ (*right-column*) maps toward IRAS 19035+0641. In top panels: we show the zero-order moment (integrated intensity) maps. Levels start at 5%, increasing in steps of 10% the intensity peak: 0.38, 0.16, and 0.18 Jy beam⁻¹ km s⁻¹, respectively. In middle panels: we show the first-order moment (velocity field) maps. In bottom panels: we show the second-order moment (linewidth) maps. In middle and bottom panels, contours show the zero-order moment maps in steps of 20%. In all panels, the white stars mark the position of the centimeter continuum sources VLA1 and VLA2 (see Table 6.2). Synthesized beams are shown in bottom-left corners.

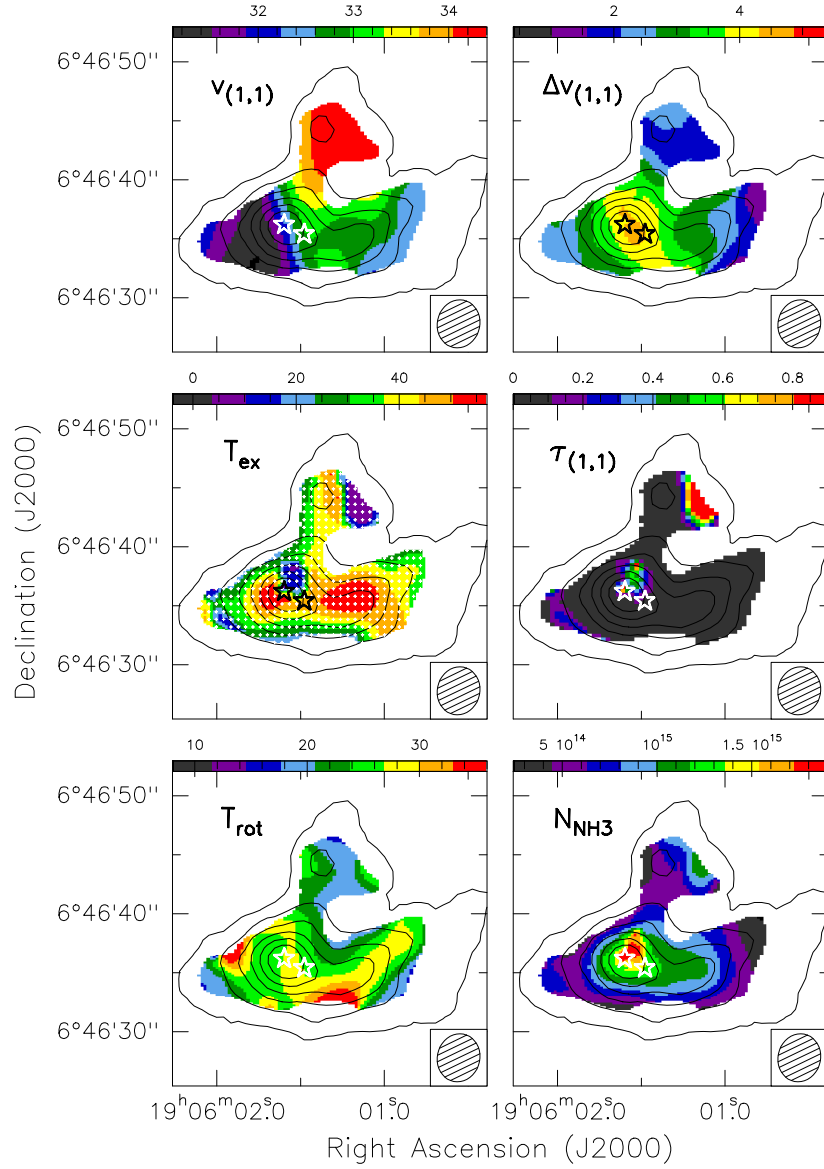


Figure 6.4: Ammonia parameters towards IRAS 19035+0641. From left to right, and top to bottom: velocity map of the $\text{NH}_3(1,1)$ line (units in km s^{-1}); linewidth map of the $\text{NH}_3(1,1)$ line (units in km s^{-1}); excitation temperature map from $\text{NH}_3(1,1)$ (units in K); map of the optical depth of the $\text{NH}_3(1,1)$ main line; rotational temperature map from $\text{NH}_3(1,1)$ and $\text{NH}_3(2,2)$ (units in K); and NH_3 column density map (units in cm^{-2}). In all panels, black contours are zero-order (integrated intensity) map of the $\text{NH}_3(2,2)$ line, and the white/black stars mark the position of the centimeter continuum sources. The synthesized beam is indicated in the bottom-right corner of each panel.

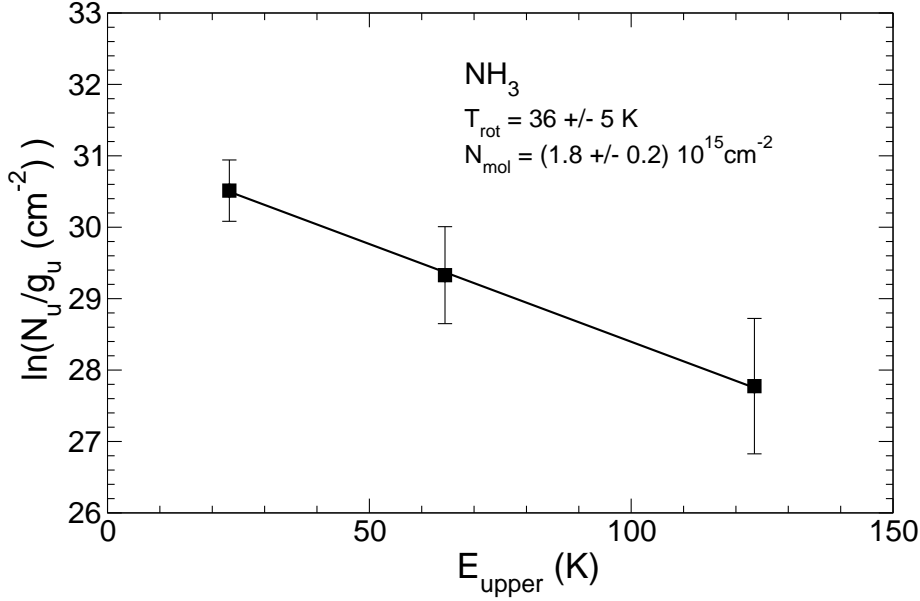


Figure 6.5: NH_3 rotational diagram for main ammonia peak toward IRAS 19035+0641. The linear fit corresponds to $T_{\text{rot}} = 36 \pm 5 \text{ K}$ and $N_{\text{mol}} = (1.8 \pm 0.1) \times 10^{15} \text{ cm}^{-2}$, in agreement with the values obtained from the (1,1) and (2,2) analysis shown in Figure 6.4.

(1,1) and (2,2) ammonia spectra were extracted for positions in a grid of $1'' \times 1''$. See Chapter 2 or Busquet et al. (2009) for a more detailed description about the methods used in the analysis. In Figure 6.4, we present the resulting maps. The emission of NH_3 (1,1) is essentially optically thin ($\tau_{(1,1)} < 1$) for all the main clump, and it increases to opacities of ~ 0.5 close to the peak (near the position of VLA2), yielding to an ammonia column density of $1.8 \times 10^{15} \text{ cm}^{-2}$ at the position of VLA2. Regarding the rotational temperature, it is around 20 and 30 K in all the clump, with higher values toward VLA2 and along a north(east)-south(west) direction (centered on VLA2). As for the kinematics a clear velocity gradient is seen associated also with VLA2, where line broadening is also noticeable. The high temperature and column density, the change in velocity and the line broadening found at the position of VLA2 suggest that this source is perturbing the dense gas, possibly through the presence of a molecular outflow (already imaged in single-dish; Beuther et al. 2002c; López-Sepulcre et al. 2010). Other regions where the ammonia is perturbed by the passage of an outflow are IRAS 20126+4104 (Busquet 2010; Cesaroni et al. 1999), IRAS 20293+3952-MM1 (Palau et al. 2007a), AFGL5142 (Zhang et al. 2002, 2007), and I22198 or I00117 (see Chapters 4 and 2 of this work).

Using the three ammonia observed transitions, we constructed the rotational diagram for the NH_3 molecule at the peak of the ammonia main clump. In Figure 6.5, we show the rotational diagram constructed following the technique explained in Goldsmith and Langer

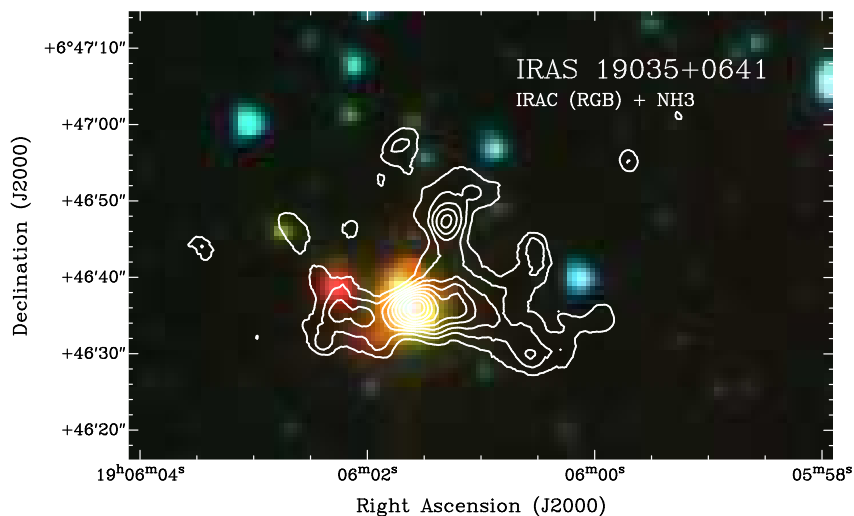


Figure 6.6: Colour scale: 3-color RGB composite image of the Spitzer-IRAC image (red: $8.0 \mu\text{m}$, green: $4.5 \mu\text{m}$, blue: $3.6 \mu\text{m}$). White contours: zero-order moment NH_3 (1,1) image. Levels start at 5%, increasing in steps of 10% the peak intensity.

(1999), (see also Chapter 4). The estimated temperature is $36 \pm 5 \text{ K}$ and the molecular column density is $(1.8 \pm 0.1) \times 10^{15} \text{ cm}^{-2}$, in agreement with the values obtained from the (1,1) and (2,2) transitions analysis. Araya et al. (2005) observed this region with the SEST single-dish telescope in the CH_3CN (6_K-5_K) transitions. Only the $K = 0$ and 1 rotational transitions (those with the lower energy) are detected, but this does not mean that there is no hot molecular emission associated with I19035. Some works have revealed that hot cores can show low temperatures in low-energy transitions (e. g., Purcell et al. 2006) which typically trace colder/warmer envelopes, rather the inner hot core. Thus, observations at higher rotational transitions (e. g., CH_3CN (12–11)) are necessary to confirm the presence of a hot core in I19035.

In order to study the relation of the dense NH_3 gas with the mid-infrared emission at IRAC bands we overplotted the moment-zero NH_3 map on the 3-color RGB composite Spitzer-IRAC image (Figure 6.6; red: $8.0 \mu\text{m}$, green: $4.5 \mu\text{m}$, blue: $3.6 \mu\text{m}$). A main conclusion from the figure is that the infrared emission associated with the NH_3 dense gas has a clear infrared excess, indicative of the region being deeply embedded in dust.

Interestingly, in many cases the NH_3 emission extends until it finds an IRAC source with no IR excess (i. e., rather blue in the figure). The best example of this behaviour is the blue star to the west of the field, which is remarkably well bordered by the extended NH_3 emission. This indicates a close relation between the NH_3 gas and the forming cluster of IR stars, suggesting that the NH_3 emission is tracing in fact the bulk of the true natal cloud, which seems to be shaped by the nascent stars.

6. IRAS 19035+0641: a compact radio source embedded in dense gas

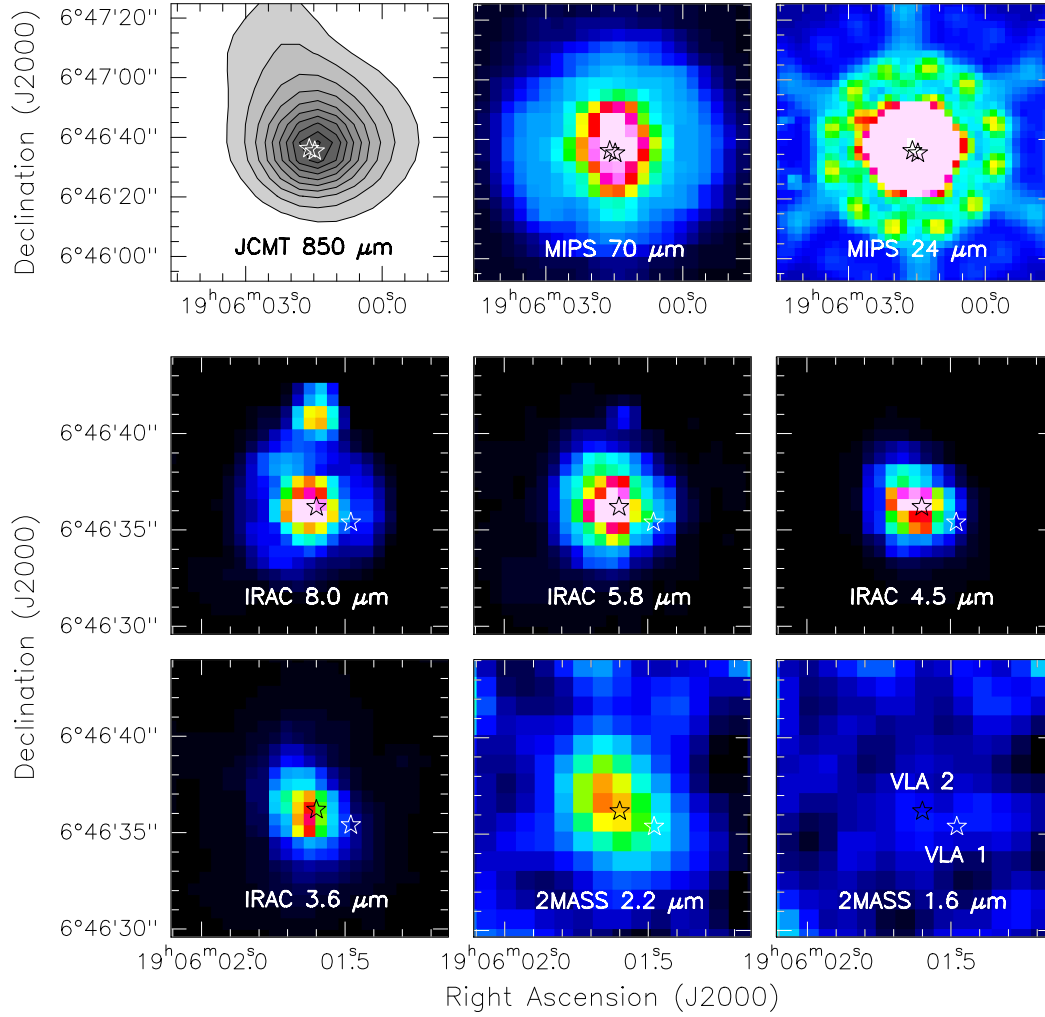


Figure 6.7: Images at infrared wavelengths for IRAS 19035+0641. The two stars mark the positions of the radio continuum sources VLA1 and VLA2 (see Table 6.2). VLA2 is clearly associated with an infrared source. The image at $24\ \mu\text{m}$ is saturated at the center. Note that the top panels show a region of the sky larger than bottom panels.

6.4.3 Ionized gas emission within the molecular clump

In Section 6.3, we reported the presence of two radio continuum sources: VLA1 seems to be a cometary UCH II region offset from the peak of the ammonia emission, and VLA2 is an unresolved and faint continuum source clearly located at the peak of the main ammonia clump. VLA2 is located at the center of the ammonia velocity gradient and at the position where the linewidth achieves its higher values, i. e., VLA2 seems to be located at the center of the possible molecular outflow discussed in previous sections, thus being the driving

source. In this scenario, the centimeter emission could be tracing a thermal radiojet, with the typical spectral index of +0.6 and a faint flux density at centimeter wavelengths (see Section 6.3.2 and Chapter 9 for more details). However, since our radio continuum maps are not sensitive enough, we can not infer the morphology of VLA2 (and search for the elongated morphology characteristic of radiojets). Interferometric observations of molecular outflow tracers are still necessary to confirm this hypothesis.

On the other side, VLA1 seems to be a small cometary UCH II region. We searched for the infrared counterpart of the centimeter continuum source, but we do not find any source associated with it. In Figure 6.7, we show maps from 850 μm up to 1.6 μm . There is an infrared source associated with VLA2, but there is no emission (except for images with large beams, such as 850 μm and 70 μm) at the position of the cometary source. This case is similar to the cometary UCH II region in G75.78+0.34 (see Chapter 5). The presence of a large dust and gas envelope, could be masking the infrared emission of the young star that is producing the H II region, while for VLA2 the infrared source that we clearly detect at mid/near-infrared wavelengths would be dust from the surrounding envelope. Thus, it seems that VLA2 is still associated with dust, while the cometary source VLA1 would have faint or no dust associated with. However, interferometric observations at millimeter wavelengths are necessary to confirm this scenario through observations of outflow tracers, such as CO, and millimeter continuum.

6.5 Summary and brief discussion

We have studied the massive star-forming region IRAS 19035+0641 with the VLA, in the continuum and in three ammonia transitions. In the following, we summarize the main conclusions obtained in this study.

- Two centimeter continuum sources are found associated with the IRAS source. VLA1 is a cometary UCH II region with a small size of 0.006 pc and an electron density of $2.7 \times 10^4 \text{ cm}^{-2}$, ionized by a B1 ZAMS star. The second source, VLA2, is much fainter and unresolved. Its spectral index between 6 and 0.7 cm is $+0.63 \pm 0.37$, characteristic of thermal radiojets driven by YSOs.
- Ammonia emission is found coming from different clumps, with the strongest one spatially associated with VLA2. The cometary arc of VLA1 is oriented towards the position of this main ammonia clump. The rotational temperature close to VLA1 and VLA2 is 25–30 K, while the NH_3 column density is $\sim 10^{15} \text{ cm}^{-2}$, reaching a maximum value of $1.8 \times 10^{15} \text{ cm}^{-2}$ at the position of VLA2.
- A velocity gradient (of $\sim 2 \text{ km s}^{-1}$) is seen in the NH_3 emission, with a southeast-northwest direction, with VLA2 located at the center. Furthermore, the linewidth of the ammonia emission increases up to 4–5 km s^{-1} at the position of the faint

6. IRAS 19035+0641: a compact radio source embedded in dense gas

centimeter continuum source, and along a northeast-southwest direction (perpendicular to the velocity gradient). This could suggest that the ammonia gas is being perturbed by the passage of a molecular outflow, and VLA2 could be the radiojet driving this outflow. Interferometric observations of molecular outflow tracers are necessary to confirm this scenario.

IRAS 04579+4703: a radio-source–outflow system

7.1 General overview

IRAS 04579+4703 (hereafter I04579), with a bolometric luminosity of $4000 L_{\odot}$ at a distance of 2.5 kpc (Molinari et al. 1996), was identified as a possible luminous YSO by Campbell et al. (1989). The region is associated with a dense core detected in ammonia emission (Molinari et al. 1996) and with several water maser components (e.g., Wouterloot and Brand 1989; Palla et al. 1991; Brand et al. 1994), but no emission is detected in the 6.7 and 12.2 GHz maser transitions (Wouterloot et al. 1993; Fontani et al. 2010). The presence of molecular outflow emission has been detected in the CO (1–0) transition (Wouterloot and Brand 1989), but failed to be detected in CO (2–1) (Zhang et al. 2005). At radiowavelengths, Sánchez-Monge et al. (2008) report partially optically thick centimeter continuum emission associated with the IRAS source. A single-dish 1.2 mm map shows a main dust condensation of $23 M_{\odot}$ engulfing the centimeter emission, with the peak slightly displaced ($< 5''$) to the east of the centimeter source. Sánchez-Monge et al. (2008) report a cluster of infrared (2MASS) sources within the dust emission, showing high and moderate infrared excess and with the strongest 2MASS source associated with the centimeter emission. Recently, the near-infrared study of Varricatt et al. (2010) confirmed the existence of a compact cluster of reddened stars, with faint H_2 and $Br\gamma$ emission likely tracing an outflow in the southeast–northwest direction powered by the strongest infrared source. All this suggests that I04579 contains a very young massive YSO surrounded by lower-mass YSOs that are likely in the first phases of formation.

In this Chapter, we present interferometric continuum and molecular line observations that confirm the existence of a forming cluster and a molecular outflow consistent with the shocked gas in H_2 maps.

7.2 Observations

7.2.1 Very Large Array

I04579 was observed with the Very Large Array (VLA¹) at 3.6, 1.3, and 0.7 cm in 2004 and 2007, using the array in the D configuration. We complemented our observations with archival data from projects AM462, AC216 and AC295, at 6.0 and 3.6 cm. In Table 7.1 we report details of the observations. The data reduction followed the VLA standard guidelines for calibration of high frequency data, using the NRAO package AIPS. First images were produced with the robust parameter of Briggs (1995) set to 0, for an optimal compromise between sensitivity and angular resolution. At 6.0 and 3.6 cm we combined the uv -data sets to obtain final images with a better uv -coverage, sensitivity and angular resolution. However, the higher angular resolution observations at these wavelengths did not improve the quality of the combined images. We decided to use only the individual 6.0 cm VLA-DnC and the 3.6 cm VLA-D uv -data sets.

The VLA was also used to map the $(J, K)=(1,1)$ and $(2,2)$ inversion lines of the ammonia molecule during 2007 April 21, with the array in its D configuration. The observations were carried out with 8 EVLA antennas in the array, but with the old correlator. The adopted flux density of the absolute flux calibrator 0137+331 (3C 48) was 1.05 Jy at the frequencies of 23.69 GHz and 23.72 GHz. The quasar 0319+415 (3C 84) was used to correct for the bandpass. Amplitude and phase calibration were achieved by monitoring 0502+416, resulting in an rms phase of $\sim 50^\circ$. We used the 4IF spectral line mode, which allows simultaneous observations of NH_3 (1,1) and (2,2) lines with two polarizations for each line. The bandwidth used was 3.1 MHz, with 63 spectral channels with a channel spacing of 48.8 kHz ($\sim 0.6 \text{ km s}^{-1}$) centered at $v_{\text{LSR}} = -16.5 \text{ km s}^{-1}$, plus a continuum channel that contains the average of the central 75% of the bandwidth. The data reduction followed the standard guidelines for calibration of high frequency data. Imaging was performed with natural weighting and tapering the uv -data at $30 \text{ k}\lambda$, with an rms noise level of 2 mJy beam^{-1} per channel, and a synthesized beam of $7''.5 \times 6''.3$ with a P.A. = -50° . No NH_3 emission was detected at the systemic velocity (-16.5 km s^{-1}), but there is a condensation at a velocity of -5 km s^{-1} . A problem with the doppler tracking could be the cause in v_{LSR} to be not well determined (see next sections).

¹The Very Large Array (VLA) is operated by the National Radio Astronomy Observatory (NRAO), a facility of the National Science Foundation operated under cooperative agreement by Associated Universities, Inc.

Table 7.1: Main VLA continuum observational parameters of IRAS 04579+4703

λ (cm)	Project VLA conf.	Epoch of Observation	Gain cal. / Bootstr. Flux ^a	Flux cal.	Beam (" \times ")	P.A. ($^\circ$)	Rms ^b
6.0	AC216 DnC	1988 Apr 04	0438+488 / 0.508(1)	3C48	4.2×3.6	-27	45
6.0	AM462 CnB	1994 Oct 04	0555+398 / 6.139(1)	3C48	5.8×1.6	-63	110
3.6	AP476 D	2004 Jul 10	0423+418 / 1.986(1)	3C48	8.7×8.3	+33	60
				3C286			
3.6	AC295 B	1992 Jan 07	0359+509 / 1.484(2)	3C48	1.5×1.1	-65	90
1.3	AP476 D	2004 Jul 10	0423+418 / 1.617(1)	3C48	5.2×4.4	+45	100
				3C286			
0.7	AS896 D	2007 Feb+Mar	0502+416 / 0.424(3)	3C48	3.8×3.1	+34	115

^a Bootstrapped flux in Jy. In parenthesis: the percentage of error in the flux.

^b Rms noise level in $\mu\text{Jy beam}^{-1}$.

7.2.2 Submillimeter Array

We observed the I04579 region with the Submillimeter Array (SMA²; Ho et al. 2004) in the 1.3 mm (230 GHz) band using the compact array configuration on 2008 March 21. The phase center was $\alpha(\text{J2000}) = 05^{\text{h}}01^{\text{m}}39^{\text{s}}.92$, and $\delta(\text{J2000}) = +47^\circ 07' 21''.1$, and the projected baselines ranged from 7 k λ to 100 k λ . The two sidebands of the SMA covered the frequency ranges of 219.4–221.4 GHz and 229.4–231.4 GHz, with a spectral resolution of $\sim 0.5 \text{ km s}^{-1}$. System temperatures ranged between 200 and 300 K. The zenith opacities at 225 GHz were around 0.15 and 0.25 during the 7 hours track. The FWHM of the primary beam at 1.3 mm was $\sim 56''$. Bandpass calibration was performed by observing the quasar 3C 279. Amplitude and phase calibrations were achieved by monitoring 0533+483 and 0359+509, resulting in an rms phase of $\sim 50^\circ$. The absolute flux density scale was determined from Saturn’s moon Titan with an estimated uncertainty around 20% (we flagged data corresponding to frequencies 230–231, due to the large CO (2–1) emission coming from the moon’s atmosphere). Data were calibrated and imaged with the MIRIAD software package. The continuum was constructed in the (u, v) domain from the line-free channels. Imaging was performed using natural weighting, obtaining a synthesized beam of $3''.6 \times 2''.6$ with a P.A. = -63° , and 1σ rms of 60 mJy beam^{-1} per channel, and 1 mJy beam^{-1} for the continuum.

7.3 Continuum results

In this region we detect radio continuum emission from 6 cm up to 1.2 mm (see Figure 7.1 bottom panels). A single compact (almost unresolved) and faint centimeter continuum

²The SMA is a joint project between the Smithsonian Astrophysical Observatory and the Academia Sinica Institute of Astronomy and Astrophysics, and is funded by the Smithsonian Institution and the Academia Sinica.

7. IRAS 04579+4703: a radio-source–outflow system

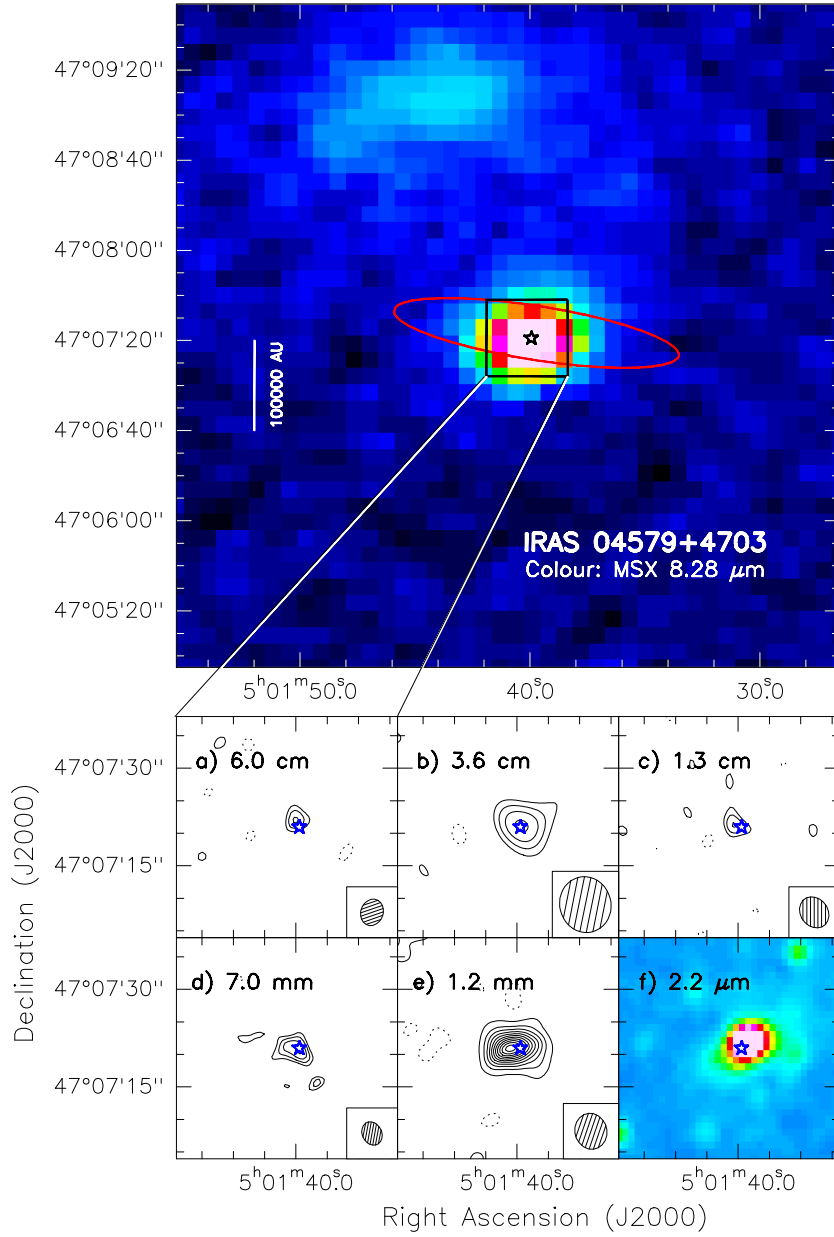


Figure 7.1: Continuum maps for IRAS 04579+4703. *Top:* MSX 8.28 μm image for IRAS 04579+4703. The black box marks the region zoomed in the lower panels. Red ellipse marks the IRAS source. *Bottom:* Each panel shows the continuum emission at the wavelengths shown at the top-left corner. For a), b), c) and d) panels (VLA), levels are -4 , -3 , and 3 to 9 , in steps of 1 times the rms noise level of the map: 45 , 60 , 100 , and $115 \mu\text{Jy beam}^{-1}$, respectively. For e) panel (SMA), levels are -9 , -3 , and 3 to 66 , in steps of 6 times the rms noise level of the map: 1 mJy beam^{-1} . In panel f) we show the 2MASS K_s -band image. Color stars indicate infrared sources with infrared excess. In all panels, the star indicates the position of the radio continuum source (see Table 7.2).

Table 7.2: Continuum fluxes for the radio source in IRAS 04579+4703

λ (cm)	Beam (" \times ")	P.A. ($^\circ$)	Rms ^b	$I_\nu^{\text{peak a}}$ (mJy beam ⁻¹)	S_ν^{a} (mJy)	Deconv. Size (" \times ")	P.A. ($^\circ$)
VLA1	$\alpha(J2000.0) = 05^{\text{h}}01^{\text{m}}39^{\text{s}}.95$ $\delta(J2000.0) = +47^\circ07'20''.9$						
6.0	4.2×3.6	-27	45	0.23 ± 0.09	0.25 ± 0.14	$2.4 \times 1.3 \pm 2.4$	100 ± 50
3.6	8.7×8.3	+33	60	0.37 ± 0.12	0.37 ± 0.15	$4.1 \times 2.2 \pm 4.1$	115 ± 50
1.3	5.2×4.4	+45	100	0.51 ± 0.20	0.51 ± 0.23	$3.5 \times 0.0 \pm 3.5$	180 ± 50
0.7	3.8×3.1	+34	115	0.70 ± 0.23	1.35 ± 0.49	$6.5 \times 3.1 \pm 1.5$	70 ± 30
0.13	3.6×2.6	-63	1000	13 ± 2	173 ± 70	$5.2 \times 2.9 \pm 0.5$	90 ± 10

^a Primary beam corrected. Error in intensity is 2σ . Error in flux density has been calculated as $\sqrt{(2\sigma\sqrt{\theta_{\text{source}}/\theta_{\text{beam}}})^2 + (2\sigma_{\text{flux-scale}})^2}$, where σ is the rms noise level of the map, θ_{source} and θ_{beam} are the size of the source and the beam respectively, and $\sigma_{\text{flux-scale}}$ is the error in the flux scale, which takes into account the uncertainty on the calibration applied to the flux density of the source ($S_\nu \times \%\text{uncertainty}$).

^b Rms noise level in $\mu\text{Jy beam}^{-1}$.

source is found associated with the IRAS source 04579+4703 and with an MSX source (see Figure 7.1 top panel), with its flux density increasing with frequency (see Table 7.2). At 7 mm the source is slightly resolved with a P.A. of 70° . The SMA 1.3 mm continuum image reveals the presence of a compact source clearly elongated in the east-west direction (consistent with the P.A. of the 7 mm source). It is worth to note that the peak of the centimeter source is associated with a near-infrared source (2MASS-K_s and Varricatt et al. 2010), while the millimeter continuum source has its peak displaced $2''$ to the east. This offset and the east-west elongation of the millimeter emission could be due to the presence of two sources, or it could be dust entrained by the molecular outflow (see Section 7.4.1).

In Figure 7.2, we show the spectral energy distribution (SED) of I04579 in the centimeter and millimeter range. Taking into account the uncertainties in the flux densities, the SED can be fitted by two distinct models. First (left panel), we fitted an homogeneous H II region with a small radius of $0''.03$ (158 AU in diameter at a distance of 2.5 kpc, consistent with our ‘unresolved’ size from the observations) and a high electron density of $5 \times 10^5 \text{ cm}^{-2}$ (corresponding to an emission measure of $1.5 \times 10^8 \text{ cm}^{-6} \text{ pc}$). These properties are characteristic of hypercompact (HC) H II regions surrounding massive stars, and in this case the ionizing star would be an intermediate-mass star (B2 ZAMS star; Panagia 1973). At 7 and 1.3 mm we would have contribution of a dust envelope with a mass of $15 M_\odot$, assuming a temperature of 30 K, a dust emissivity index of 2, and a dust mass opacity coefficient of $0.9 \text{ cm}^2 \text{ g}^{-1}$ (Ossenkopf and Henning 1994). The second model used to fit the SED (Figure 7.2 right panel) consists of a thermal radiojet or a non-homogeneous H II region, with a resulting spectral index of $+0.6$ consistent with the spectral index derived from the observations between 6 and 1.3 cm ($\alpha = 0.4 \pm 0.2$), plus a dust envelope

7. IRAS 04579+4703: a radio source–outflow system

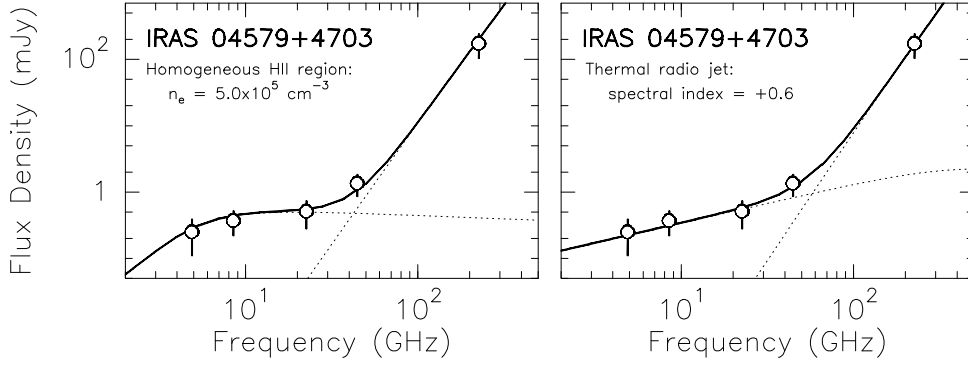


Figure 7.2: Spectral energy distribution for IRAS 04579+4703. Circles: VLA and SMA continuum data (see Table 7.2). *Left panel*: Black solid line: sum of the modified blackbody law and the homogeneous H II region, with a source radius of $0''.03$ and an electron density of $5 \times 10^5 \text{ cm}^{-3}$. *Right panel*: Black solid line: sum of the modified blackbody law and the thermal radio jet, with a spectral index $\alpha = +0.6$ ($S_\nu \propto \nu^\alpha$). In both panels, the modified blackbody law for the dust envelope is constructed with a dust emissivity index of $\beta = 1.8 \pm 0.2$, a source radius of $5''.0$, a dust temperature of $30 \pm 2 \text{ K}$, a dust mass of $15 \pm 2 M_\odot$, and a dust mass opacity coefficient of $0.9 \text{ cm}^2 \text{ g}^{-1}$ at 1.3 mm .

with a mass of $15 M_\odot$ and a temperature of 30 K (as in the previous model). More sensitive and higher angular resolution observations are necessary to determine the size of the centimeter source, and thus better establish the origin of the ionized emission: thermal radiojet versus HCH II region.

7.4 Molecular results

7.4.1 Molecular outflow gas

In Figure 7.3, we show the interferometric map of the ^{12}CO (2–1) transition. Blueshifted emission, spanning a velocity range from -38 km s^{-1} to -20 km s^{-1} , is located toward the northwest of the centimeter/millimeter source, clearly elongated and collimated (with an axis ratio of $\simeq 15/3 \simeq 5$ an P.A. $\simeq 120^\circ$). Redshifted emission, spanning a velocity range from -12 km s^{-1} to $+6 \text{ km s}^{-1}$ with respect to the v_{LSR} , is found to the southeast/south, showing also an elongated morphology, but with a P.A. $\simeq 170^\circ$. In Table 7.3, we list the physical parameters of the outflow.

The shocked H_2 emission, reported by Varricatt et al. (2010), likely tracing the direction of an outflow is consistent with the elongated morphology we found in the ^{12}CO emission (cf. black circles tracing the shocked H_2 emission in Figure 7.3). However, the red-shifted CO emission has a different orientation with respect to the blue-shifted CO and the H_2 emission. The distinct H_2 features also show a slightly different orientation

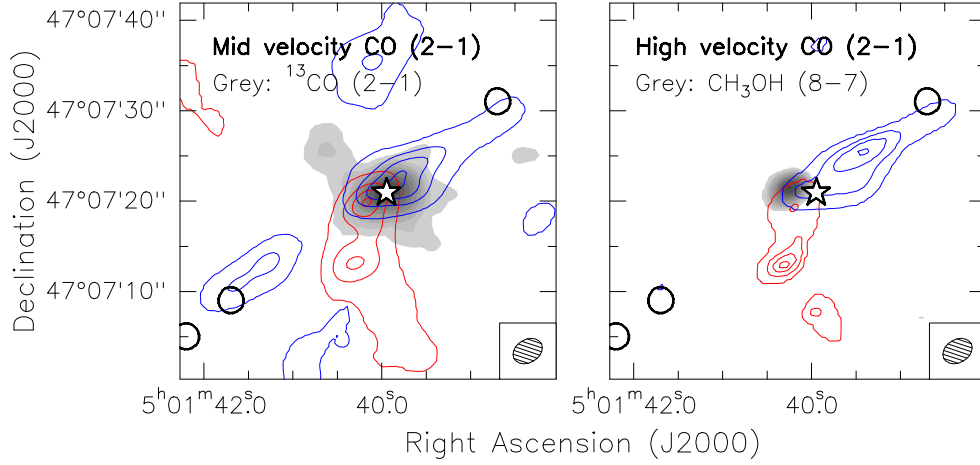


Figure 7.3: Molecular outflow emission toward IRAS 04579+4703. *Left panel:* Grey scale: $^{13}\text{CO}(2-1)$ zero-order moment (integrated intensity). Blue/red contours: $^{12}\text{CO}(2-1)$ moderate blue/red-shifted emission in the velocity range of -4 to -7.5 km s^{-1} and $+4$ to $+7.5$ km s^{-1} with respect to the systemic velocity ($v_{\text{LSR}} = -16.5$ km s^{-1}), respectively. *Right panel:* Grey scale: $\text{CH}_3\text{OH}(8-7)$ zero-order moment (integrated intensity) map (see Figure 7.5). Blue/red contours: $^{12}\text{CO}(2-1)$ high blue/red-shifted emission in the velocity range of -7.5 to -21.5 km s^{-1} and $+7.5$ to $+21.5$ km s^{-1} with respect to the systemic velocity, respectively. In both panels, levels for blue/red contours start at 5% increasing in steps of 30% the peak intensity: 21/18 (left) 7.7/5.3 (right) $\text{Jy beam}^{-1} \text{ km s}^{-1}$. The $^{12}\text{CO}(2-1)$ synthesized beam is shown in the bottom-right corner. The star marks the position of the centimeter source. Black circles correspond to shocked H_2 emission (Varricatt et al. 2010).

Table 7.3: Physical parameters of the outflow driven by IRAS 04579+4703^a

Outflow/lobe (1)	t_{dyn} (2)	size (3)	N_{mol} (4)	M_{out} (5)	\dot{M}_{out} (6)	P_{out} (7)	\dot{P}_{out} (8)	E_{kin} (9)	L_{mech} (10)
Outflow — P.A.=120°									
CO (2-1) – red	3500	15×7	2.4×10^{15}	0.008	2.4	0.38	5.5	17.6	0.33
CO (2-1) – blue	6700	20×7	5.6×10^{15}	0.026	3.9	0.88	6.6	29.8	0.31
CO (2-1)	5100	...	8.0×10^{15}	0.034	6.7	1.27	12.4	47.4	0.63

^a Parameters are calculated for an inclination angle equal to 30° , following the expressions given in Palau et al. (2007b). Notes and units for each column: (1) blue/red lobe for each molecular species; (2) dynamical age in years; (3) size of the lobe in arcsec; (4) column density of the molecule in cm^{-2} ; (5) outflowing mass in M_\odot ; (6) rate of the outflowing mass in $10^{-6} M_\odot \text{ yr}^{-1}$; (7) momentum of the outflow in $M_\odot \text{ km s}^{-1}$; (8) outflow momentum rate in $10^{-5} M_\odot \text{ km s}^{-1} \text{ yr}^{-1}$; (9) kinetic energy in 10^{42} erg; and (10) mechanical luminosity in L_\odot .

7. IRAS 04579+4703: a radio source–outflow system

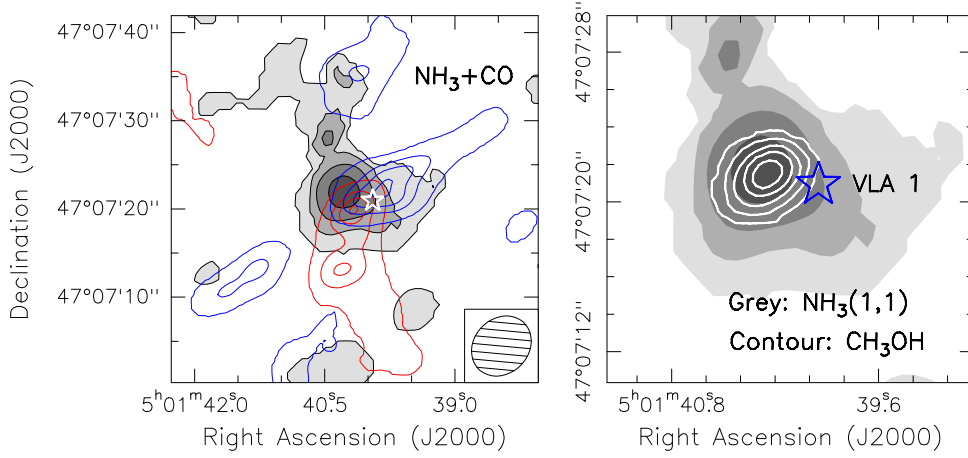


Figure 7.4: *Left panel:* Grey scale and black contours: $\text{NH}_3(1,1)$ zero-order moment (integrated intensity) map (see text for details). Synthesized beam is shown in the bottom-right corner. Blue/red contours: $^{12}\text{CO}(2-1)$ blue/red-shifted emission shown in Figure 7.3 left panel. *Right panel:* Close-up of the ammonia emission (in grey scale) overlaid with the $\text{CH}_3\text{OH}(8-7)$ zero-order moment map (in white contours; see Figure 7.5) The white/blue star marks the position of the centimeter continuum source.

toward the northwest with respect to the signatures found in the southeast (see Figure A2 from Varricatt et al. 2010). However, this difference in position angle is much larger in the CO emission than in the H_2 images. It is worth noting that we also detect outflow CO emission close to the H_2 features toward the southeast.

7.4.2 Molecular dense gas

Molinari et al. (1996) report the detection of the ammonia (1,1) and (2,2) inversion lines, using the 100-m Radiotelescope in Effelsberg (Bonn, Germany) with a line velocity of -16.5 and -17 km s^{-1} , respectively. Our VLA ammonia observations, however, do not have line emission at these velocities, but at $\sim -5 \text{ km s}^{-1}$. It seems that problems with the doppler tracking setup (due to the combined EVLA-VLA baselines during the observations) could be affecting the ammonia observational data (see Section 7.2.1). In Figure 7.4, we show the emission we detect in our VLA observations (at the velocity of -5 km s^{-1}). This faint compact source could be: i) sporadic high noise rather than ammonia emission, ii) emission coming from the main hyperfine $\text{NH}_3(1,1)$ transition line, or iii) emission from one of the satellites of the ammonia hyperfine structure. The compact emission appears almost coincident with the centimeter continuum source (VLA1), and well positioned at the center of the blue/red lobes of the outflow described in previous section, suggesting it is ammonia emission. However, the small offset ($\sim 2''$) to the east, with respect to the centimeter source, calls into question if the emission we detect is real

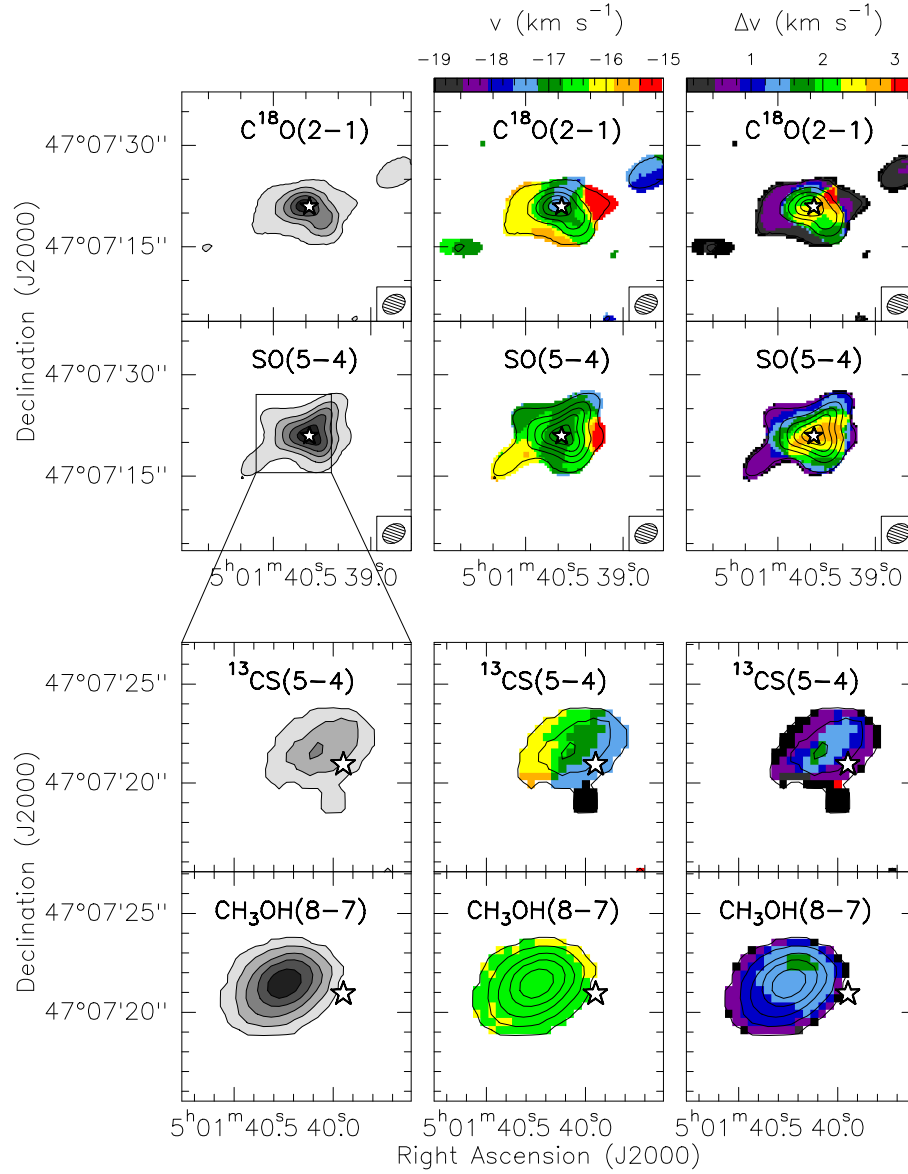


Figure 7.5: Molecular emission toward IRAS 04579+4703. *Left column:* Zero-order moment (integrated intensity) maps for different molecules. Levels and grey scale range from 5 to 85%, in steps of 20% of the peak intensity: 5.3, 8.2, 1.2 and 1.2 Jy beam⁻¹ km s⁻¹, for $\text{C}^{18}\text{O}(2-1)$, $\text{SO}(5-4)$, $^{13}\text{CS}(5-4)$ and $\text{CH}_3\text{OH}(8-7)$, respectively. *Middle column:* First-order moment (velocity field) maps. *Right column:* Second-order moment (linewidth) maps. In all panels, the white star indicates the position of the radio continuum source (see Table 7.2). The synthesized beams are shown in the bottom-right corners of each panel. In the first panel, color stars refer to the 2MASS sources as in Figure 7.1.

7. IRAS 04579+4703: a radio source–outflow system

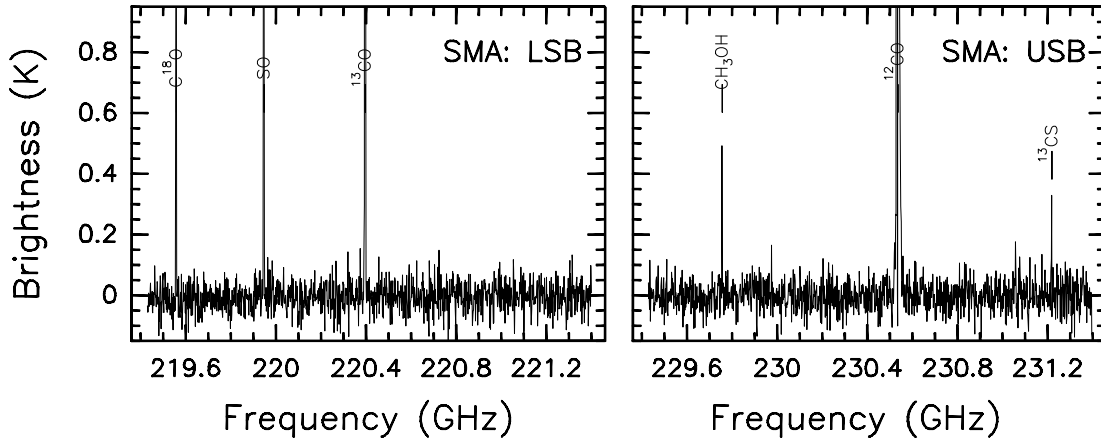


Figure 7.6: 230 GHz continuum-free spectra in the image domain from the SMA data, for the lower sideband (LSB) in the top panel and the upper sideband (USB) in the bottom panel. Note that the frequency coverage is the same as for I22198 (see Chapter 4) for which we detect a rich chemistry, different to the I04579 case.

or not. At this point, it is important to note that methanol emission (see below and Figure 7.5) has the peak at exactly the same position as the ‘ammonia’ emission (cf. Figure 7.4 right panel), and that the fainter extended structure resembles that of other molecules such as ^{13}CO or SO (see below and Figure 7.5). In conclusion, it seems that the emission we detect at -5 km s^{-1} , is in fact ammonia emission. However, problems with the doppler tracking could be affecting the reference velocity, and we can not ensure if this emission comes from the main or some satellite lines of the ammonia hyperfine structure. Thus, we will not go further in the analysis of this emission. New observations must be done to confirm the presence of NH_3 associated with this centimeter continuum source.

The SMA observations, allow us to detect molecular line emission from different molecules, with line velocities $\sim -16 \text{ km s}^{-1}$ (confirming that the velocity measured by Molinari et al. 1996 in their single-dish ammonia observations is correct, and there is a technical problem in our VLA observations). In Figure 7.5, we show the zero-order moment (integrated intensity), the first-order moment (velocity field) and the second-order moment (linewidth) maps of molecules detected toward I04579. A clear compact condensation is found associated with the centimeter/millimeter continuum source. The molecular emission is resolved for the C^{18}O and SO lines, but it is unresolved in the case of high density tracers such as ^{13}CS and CH_3OH . Note that the methanol core is slightly offset ($\sim 2''$ toward the east) with respect to the centimeter source. We searched for more molecules in the wide SMA band spectrum (see Figure 7.6), but, distinctly to I22198 and G75 and similar to I00117, we do not detect many molecular lines, suggesting that this dense core has not properties of hot molecular cores. In Figure 7.7, we show the spectra for each molecule

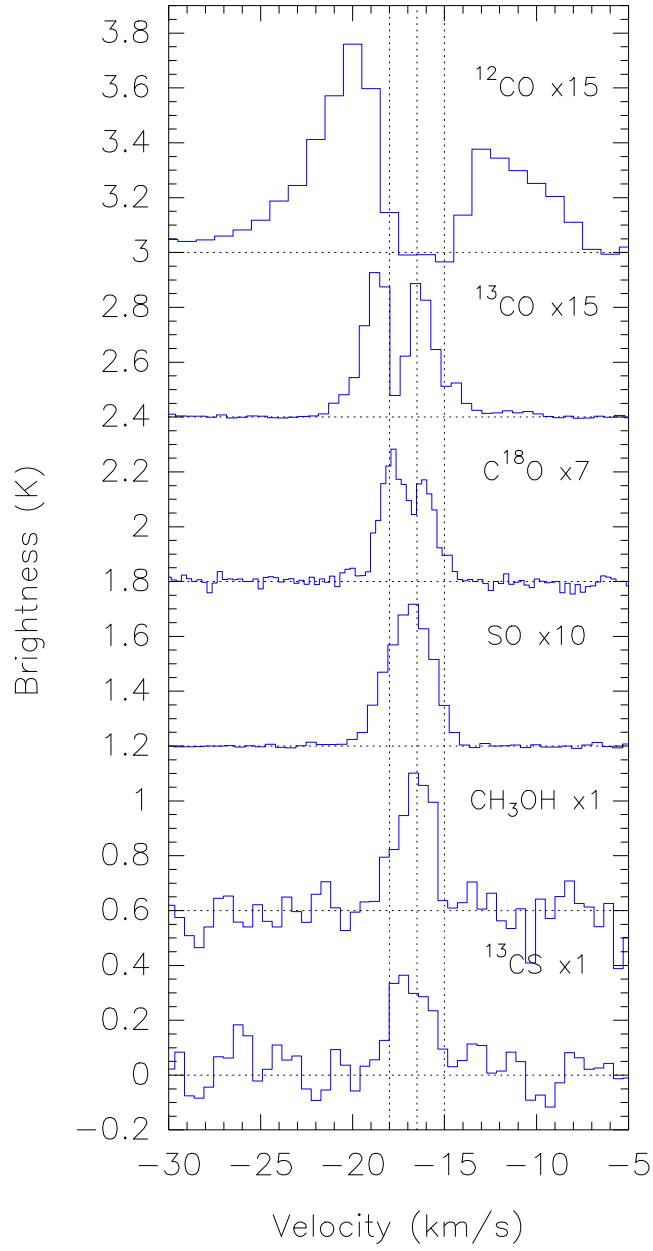


Figure 7.7: Spectra for the different molecules detected towards IRAS 04579+4703 (averaged over the region of emission). The spectra of ^{12}CO and ^{13}CO must be multiplied by 15 to obtain the line temperature, while the C^{18}O spectra must be multiplied by 7, and the SO spectra by 10. Vertical dotted lines are used only as a reference, and correspond to velocities of -18 , -16.5 (systemic), and -15 km s^{-1} .

7. IRAS 04579+4703: a radio source–outflow system

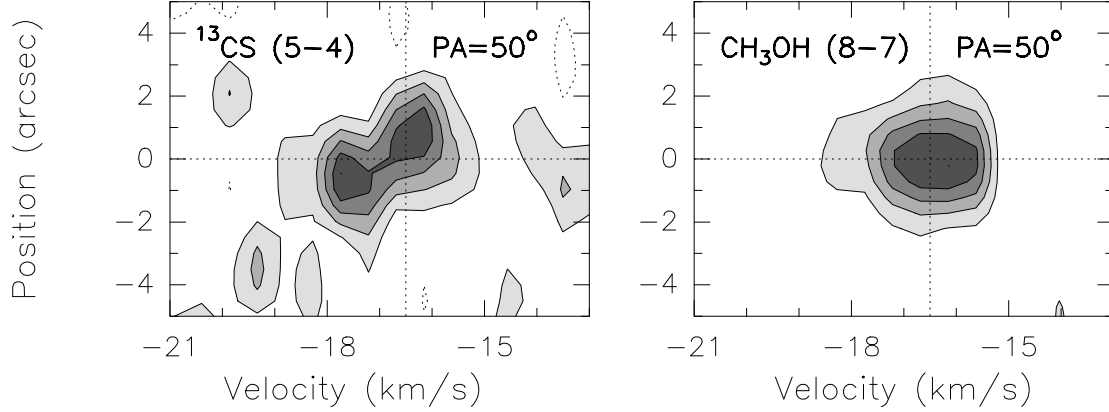


Figure 7.8: *Left:* Position-velocity (pv) cut with P.A. = 50° for the ^{13}CS (5–4) transition. Levels start at 20%, increasing in steps of 20% the peak intensity 0.3 Jy beam^{-1} . The cut is centered on $\alpha(\text{J2000}) = 05^{\text{h}}01^{\text{m}}40^{\text{s}}04$, and $\delta(\text{J2000}) = +47^\circ07'21''.9$, which corresponds to the peak of the ^{13}CS condensation. *Right:* Pv-plot with P.A. = 50° for the CH_3OH (8–7) emission. Levels start at 20%, increasing in steps of 20% the peak intensity 0.5 Jy beam^{-1} . The cut is centered on $\alpha(\text{J2000}) = 05^{\text{h}}01^{\text{m}}40^{\text{s}}27$, and $\delta(\text{J2000}) = +47^\circ07'21''.5$, which corresponds to the peak of the CH_3OH condensation.

detected toward I04579. The ^{12}CO , ^{13}CO , and C^{18}O lines show absorption features at the systemic velocity (between -2 and $+2 \text{ km s}^{-1}$ with respect to v_{LSR}), which could be due to self-absorption by cold foreground gas or opacity effects. We note that the dip could also be partially produced by the missing short-spacing information in the interferometer data. The CO isotopologues show small blue/red-shifted wings in the spectra, however, these molecules do not show the bipolar and collimated morphology seen in ^{12}CO , but show a more compact structure. It is interesting to note the blue-asymmetry in the C^{18}O spectra, which is typical of infall motions (e. g., Bernard et al. 1999). For the other three molecular transitions (i. e., SO, ^{13}CS , CH_3OH), we fitted a gaussian to the line to derive the column density of each molecule, obtaining $N_{\text{SO}} = 1.3\text{--}0.2 \times 10^{15} \text{ cm}^{-2}$ for opacities between 0.01 and 0.3, and $N_{^{13}\text{CS}} = 0.32\text{--}1.8 \times 10^{13} \text{ cm}^{-2}$ and $N_{\text{CH}_3\text{OH}} = 0.35\text{--}29.9 \times 10^{14} \text{ cm}^{-2}$ for $\tau = 0.01\text{--}0.1$.

Regarding the velocity field of the dense core, no clear velocity gradients are found in the C^{18}O and SO lines (see Figure 7.5 middle panels). However, the compact ^{13}CS core seems to show a gradient in the northeast-southwest direction, perpendicular to the outflow direction. In Figure 7.8, we show a position-velocity (pv) cut with P.A. = 50° , centered at the dense core peak for the ^{13}CS and CH_3OH molecular transitions (note that the (0,0) position is different for each pv-plot, we centered the cut at the center of each condensation). The ^{13}CS cut shows a clear velocity gradient of $\sim 1.5\text{--}2 \text{ km s}^{-1}$, which is perpendicular to the direction of the molecular outflow. Assuming that this

gradient traces keplerian rotation, the dynamical mass, estimated from the expression $M_{\text{dyn}} = v_{\text{rot}}^2 R_{\text{rot}} / G \sin^2 i$, for an edge-on disk with $v_{\text{rot}} \simeq 1 \text{ km s}^{-1}$ and $R_{\text{rot}} \simeq 1''.5$ is around $4 M_{\odot}$. For the methanol condensation, no clear evidences of rotation are found. However, the methanol profile shows a small blue-shifted wing (see Figure 7.7; also visible in the pv-plot, Figure 7.8 right panel), suggesting that outflow/rotation motions could affect the emission of this molecule.

At this point it is important to note that the methanol condensation is offset with respect to the centimeter source and the other dense gas tracers (cf. Figure 7.5). Furthermore, the position of the methanol core spatially coincides with the position at which the red lobe of the molecular outflow traced by CO changes its direction (cf. Figure 7.3). Thus, it seems that the molecular outflow traced by CO could have been deflected by the presence of a dense condensation traced by CH₃OH. The blueshifted profile seen in the methanol transition could be interpreted as this condensation being displaced toward us, due to the collision with the outflowing gas. Additionally to the deflection of the red lobe, some outflowing material could have changed its direction toward us (blue-shifted emission) resulting in the blue-shifted CO emission that is detected $\sim 10''$ to the southeast of the centimeter source. A similar case of outflow deflection produced by the presence of a dense gas condensation is found in IRAS 21319+5802 (Beltrán et al. 2002).

7.5 Summary and brief discussion

We have studied with high angular resolution observations the massive star-forming region in IRAS 04579+4703. In the following, we summarize the main conclusions obtained.

- We detect a radio continuum source from 6 up to 0.7 cm, with its flux density increasing with the frequency, which can be fitted by an hypercompact H II region ionized by a B2 ZAMS star (and with a very small size, 150 AU) or by a thermal radiojet with the characteristic spectral index of +0.6. Higher angular and more sensitive observations are needed to better estimate the size of the centimeter source, and thus confirm the nature of the ionized gas. The source is associated with a millimeter source likely tracing a dust envelope of $15 \pm 2 M_{\odot}$, and with an infrared source (from the 2MASS survey, the region has not been observed by *Spitzer*) showing high infrared excess.
- A highly collimated molecular outflow is detected in the ^{12}CO (2–1) transition with a southeast-northwest orientation, consistent with the H₂ shocked gas reported by Varricatt et al. (2010). The outflow has physical parameters similar to the parameters found in other intermediate/high-mass molecular outflows. The red CO lobe seems to be deflected toward the south, changing the main position angle measured for the blue lobe.

7. IRAS 04579+4703: a radio-source–outflow system

- A dense core is found in different molecules (e. g., C^{18}O , SO , ^{13}CS) with the emission from ^{13}CS (5–4) showing a velocity gradient perpendicular to the main direction of the molecular outflow. Assuming keplerian rotation, the velocity gradient implies a mass of $4 M_{\odot}$ for the central object.
- Methanol emission is detected in a condensation slightly offset ($2''$ to the east) with respect to the other dense gas tracers and the centimeter source. Interestingly, the ammonia observations (although with some instrumental setup problems) show a compact core at the same position. This condensation, placed at the position where the CO molecular outflow is deflected, could be responsible for the change in direction of the outflow (similar to the massive star-forming region IRAS 21391+5802; Beltrán et al. 2002). Furthermore, the spectra of the methanol emission shows a blue-shifted wing profile, probably produced by the shock/collision of the outflow.

Part IV

General discussion

8

The sample of massive star-forming regions

8.1 Archival data of additional sources

In this Thesis, we have studied a sample of six massive star-forming regions with high angular resolutions ($\lesssim 5''$), in the centimeter and millimeter continuum, and in different dense gas and outflow tracers, with the aim of deciphering their ionized and molecular gas content. We have focused our study on those sources showing faint centimeter continuum emission, likely tracing early evolutionary stages in the formation of massive stars.

We plan to carry out a comparison of the properties (i. e., continuum, dense gas, outflow gas, and infrared emission) of the detected centimeter continuum sources, in order to search for common characteristics, and try to establish an evolutionary sequence. In order to improve the statistics, we have added to our sample five other massive-star forming regions from the literature, which have been studied with similar spatial resolutions (~ 1000 – 5000 AU) and continuum/molecular tracers as the sources studied in this Thesis. A brief description of these regions is shown in Section 8.2. In some cases, we retrieved continuum data from the archive of the VLA to complement the already published information. The results of the centimeter continuum archival data are shown in Table 8.1 and Figure 8.1. We also searched for archival ammonia observations toward IRAS 05358+3543, for which there is no information in the literature. The resulting images are shown in Figure 8.2. We performed the same analysis to study the ammonia emission as in previous sources, obtaining the results that are shown in Figure 8.3.

8. The sample of massive star-forming regions

Table 8.1: Radio continuum fluxes for archival data toward the regions from the literature^a

λ (cm)	Beam (" × ")	P.A. (°)	Rms ^b	$I_{\nu}^{\text{peak}^b}$ (mJy beam ⁻¹)	S_{ν}^b (mJy)	Deconv. Size (" × ")	P.A. (°)
IRAS 05358+3543 — VLA1				$\alpha(J2000.0) = 05^{\text{h}}39^{\text{m}}13^{\text{s}}.07$ $\delta(J2000.0) = +35^{\circ}45'51''.2$			
3.6	0.28×0.22	-80	21	0.56 ± 0.04	0.63 ± 0.11	$0.09 \times 0.00 \pm 0.09$	125 ± 30
2.0	4.67×4.57	-1	105	1.3 ± 0.2	1.4 ± 0.5	$2.70 \times 0.00 \pm 1.10$	105 ± 20
1.3	3.63×3.28	+75	88	1.4 ± 0.2	1.9 ± 0.5	$2.44 \times 1.94 \pm 0.80$	90 ± 50
IRAS 20293+3952 — IRS1				$\alpha(J2000.0) = 20^{\text{h}}31^{\text{m}}11^{\text{s}}.20$ $\delta(J2000.0) = +40^{\circ}03'09''.9$			
3.6	0.87×0.86	+32	30	0.34 ± 0.06	4.5 ± 0.4	$3.90 \times 3.40 \pm 0.30$	160 ± 20
IRAS 20293+3952 — IRS2				$\alpha(J2000.0) = 20^{\text{h}}31^{\text{m}}10^{\text{s}}.31$ $\delta(J2000.0) = +40^{\circ}03'16''.5$			
3.6	0.87×0.86	+32	30	0.26 ± 0.06	0.30 ± 0.11	$0.38 \times 0.00 \pm 0.38$	135 ± 50
IRAS 20343+4129 — IRS3				$\alpha(J2000.0) = 20^{\text{h}}36^{\text{m}}07^{\text{s}}.25$ $\delta(J2000.0) = +41^{\circ}39'52''.4$			
3.6	2.45×0.81	+60	50	0.63 ± 0.10	1.21 ± 0.34	$2.50 \times 0.80 \pm 0.80$	85 ± 20
1.3	3.02×2.98	-14	87	0.96 ± 0.17	0.96 ± 0.35	$1.70 \times 0.00 \pm 1.50$	25 ± 30
0.7	4.67×4.57	-39	261	...	< 1.04

^a VLA archival data projects. IRAS 05358+3543: AC295, AS643 and AS831; IRAS 20293+3952: AS831; and IRAS 20343+4129: AS643, AP525 and AP533.

^b Primary beam corrected. Error estimated as in Table 2.2; and rms noise level in $\mu\text{Jy beam}^{-1}$.

8.2 Summary of sources of the sample

In the following, we will make a brief summary of each region (those studied in this work, and those from the literature), emphasizing the properties of the emission associated with the centimeter continuum sources. The regions studied in this work are:

IRAS 00117+6412 — This intermediate-mass star-forming region is associated with an IRAS source located at a distance of 1.8 kpc and with a bolometric luminosity of $1400 L_{\odot}$. The region is dominated by a shell-like UCH II region, with a size of 0.03 pc and $n_e \sim 2 \times 10^3 \text{ cm}^{-3}$, associated with a strong near-infrared source showing some infrared excess, but nor with dust neither dense gas emission. The UCH II region is located at the border of a large cloud detectable in dense gas and dust, with a temperature of $\sim 28 \text{ K}$ for the gas that surrounds the ionizing source. Embbeded in the cloud, there is a faint centimeter source within a dust envelope of $\sim 3 M_{\odot}$, MM1, driving a molecular outflow and associated with a colder ($\sim 17 \text{ K}$) dense clump, showing a velocity gradient perpendicular to the direction of the outflow.

References.- Chapter 2 of this Thesis, and references therein.

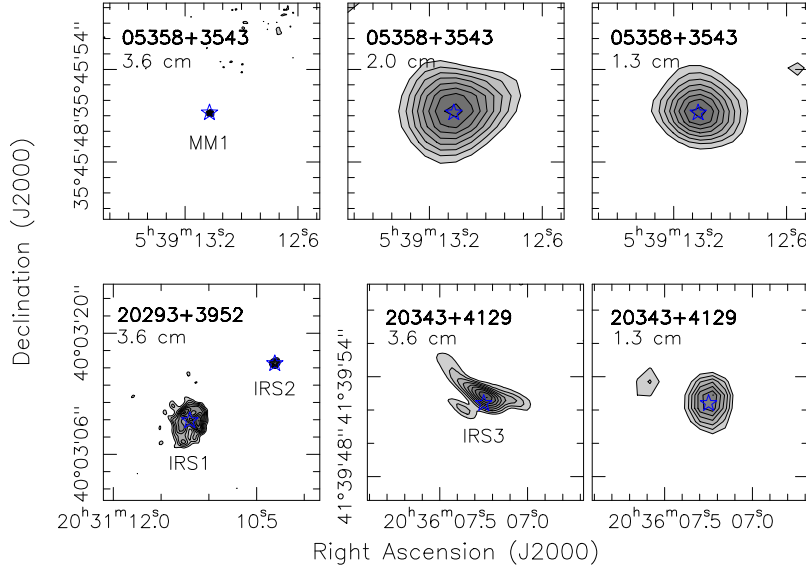


Figure 8.1: Continuum maps for the regions from the literature. See Table 8.1 for the measured flux densities and synthesized beams. Levels start at 20%, increasing in steps of 10%, the peak intensity, indicated in the Table. The stars in all panels correspond to the centimeter continuum sources, see their coordinates in Table 8.1.

IRAS 04579+4703 — The region, located at a distance of 2.5 kpc with a bolometric luminosity of $4000 L_{\odot}$, has a cluster of embedded infrared sources, showing high infrared excess. The brightest source is associated with partially optically thick centimeter continuum emission, likely tracing a thermal radiojet. This source, VLA1, is embedded in a dust envelope of $15 \pm 2 M_{\odot}$, and seems to be the driving source of a highly collimated molecular outflow. Some dense gas tracers are found associated with the source, with the ^{13}CS molecule showing a velocity gradient perpendicular to the direction of the molecular outflow. The molecular outflow is deflected by the presence of a methanol condensation.

References.- Chapter 7 of this Thesis, and references therein.

IRAS 19035+0641 — The region is located at a distance of 2.2 kpc with a bolometric luminosity of $8000 L_{\odot}$. At centimeter wavelengths we detect two different sources. VLA1 is a cometary UCH II region with a small size of 0.005 pc , $n_e \sim 2.7 \times 10^4 \text{ cm}^{-3}$, and ionized by a B1 ZAMS star. VLA2 is a faint source with partially optically thick emission, located at the peak of a warm ($\sim 29 \text{ K}$) and dense clump traced by ammonia. The dense gas shows a velocity gradient in the southeast-northwest direction, and an enhancement in the linewidth perpendicular to the velocity gradient. The region is also associated with singledish outflow emission.

References.- Chapter 6 of this Thesis, and references therein.

8. The sample of massive star-forming regions

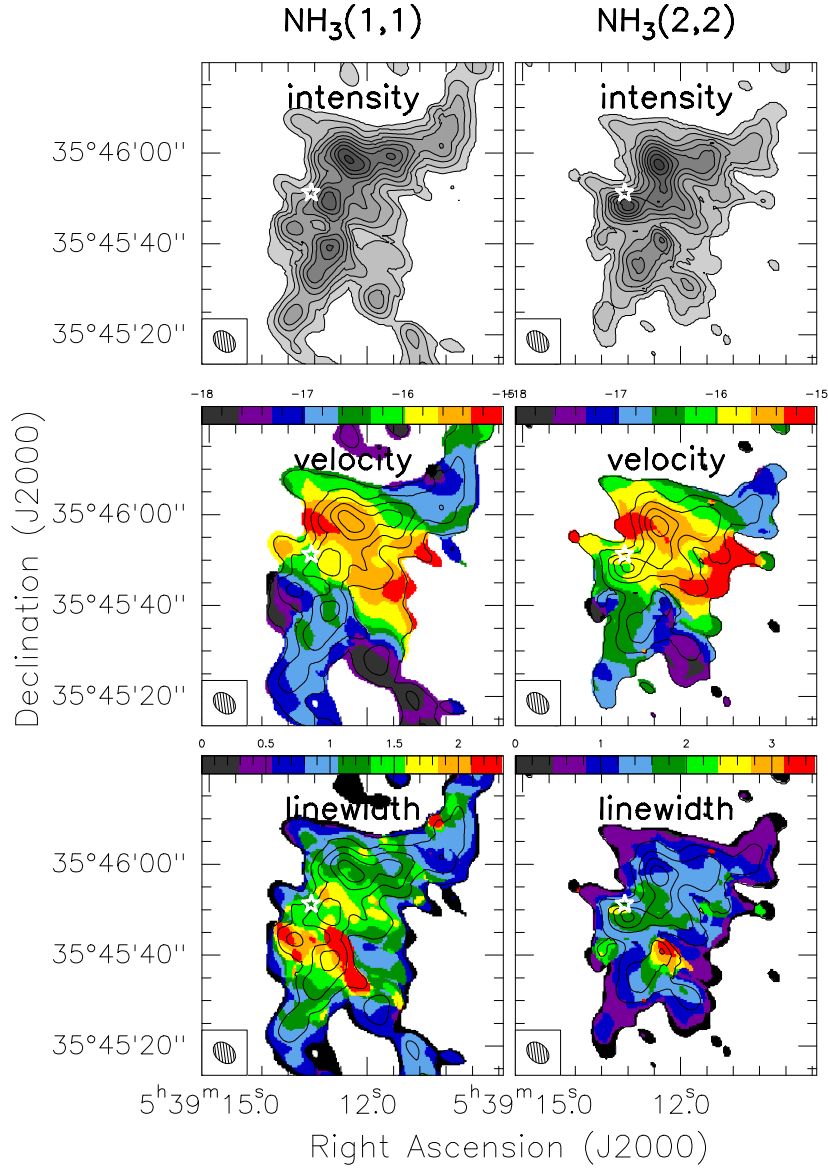


Figure 8.2: $\text{NH}_3(1,1)$ (*left-column*) and $\text{NH}_3(2,2)$ (*right-column*) maps toward IRAS 05358+3543. In top panels: we show the zero-order moment (intensity) maps. Levels start at 5%, increasing in steps of 10% the intensity peak: 0.23, and 0.19 $\text{Jy beam}^{-1} \text{ km s}^{-1}$, respectively. In middle panels: we show the first-order moment (velocity field) maps. In bottom panels: we show the second-order moment (linewidth) maps. In middle and bottom panels, contours show the zero-order moment maps in steps of 20%. In all panels, the white stars mark the position of the centimeter continuum source (see Table 8.1). Synthesized beams are shown in bottom-left corners.

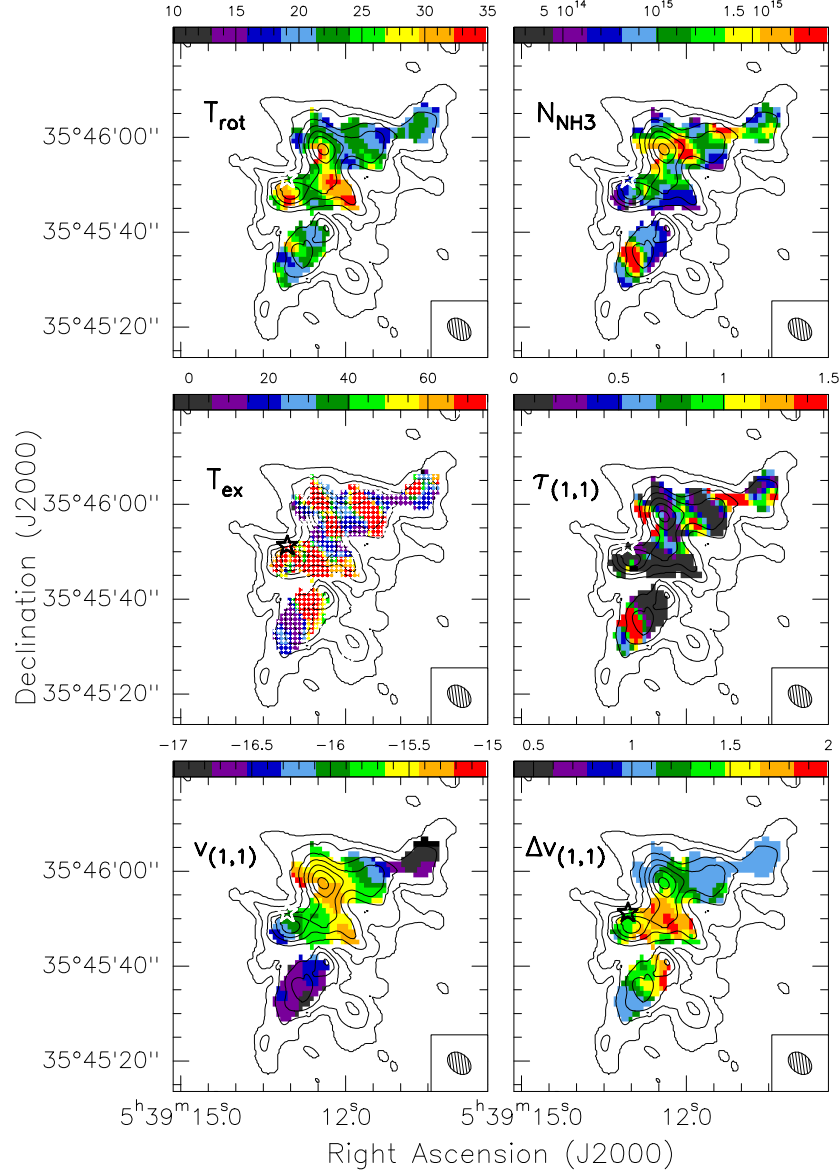


Figure 8.3: Ammonia parameters towards IRAS 05358+3543. From top to bottom, and left to right: rotational temperature map from $\text{NH}_3(1,1)$ and $\text{NH}_3(2,2)$ (units in K); NH_3 column density map (units in cm^{-2}); excitation temperature map from $\text{NH}_3(1,1)$ (units in K); map of the optical depth of the $\text{NH}_3(1,1)$ main line; velocity map of the $\text{NH}_3(1,1)$ line (units in km s^{-1}); and line-width map of the $\text{NH}_3(1,1)$ line (units in km s^{-1}). In all panels, black contours show the intensity map of the $\text{NH}_3(2,2)$ line, and the star marks the position of the centimeter continuum sources (see Table 8.1). The synthesized beam is indicated in the bottom-right corner of each panel. Small white crosses in the T_{ex} map show the position for which we extracted the (1,1) and (2,2) spectra.

8. The sample of massive star-forming regions

G75.78+0.34 — This massive star-forming complex is located at a distance of 3.8 kpc close to the IRAS source 20198+3716 (with a bolometric luminosity of $100000 L_{\odot}$). At centimeter wavelengths the region is dominated by a cometary UCH II region with a size of 0.02 pc, $n_e \sim 3.7 \times 10^4 \text{ cm}^{-3}$, and ionized by a B0 ZAMS star. Located $6''$ to the east, there is a second UCH II region, labelled EAST, with a smaller size (0.004 pc) and a higher electron density ($n_e \sim 1.3 \times 10^5 \text{ cm}^{-3}$). The EAST source is associated with strong mid-infrared emission likely tracing a dust envelope of $7\text{--}30 M_{\odot}$, also detectable at millimeter wavelengths. Finally, $2''$ to the south of the cometary arc of the main source, there are two (almost unresolved) centimeter continuum sources likely tracing two HCH II regions or gas ionized by shocks. These two continuum sources, associated with water masers and a molecular outflow, are embedded in a hot (~ 100 K) and dense molecular core, with a velocity gradient perpendicular to the direction of the outflow.

References.- Chapter 5 of this Thesis, and references therein.

IRAS 22134+5834 — This massive star-forming region, located at a distance of 2.6 kpc and with a bolometric luminosity of $12600 L_{\odot}$, is associated with a large cluster of infrared sources. One of the brightest infrared sources is associated with a cometary UCH II region with a size of 0.006 pc, $n_e \sim 5 \times 10^4 \text{ cm}^{-3}$, and ionized by a B1 ZAMS star. The cometary morphology of the centimeter source is in agreement with the orientation of the cometary shape seen in the cluster of infrared sources. The UCH II region is surrounded by millimeter continuum emission, likely tracing a dust envelope at the beginning of its disruption, probably due to the development of the H II region. Dense gas emission from NH_3 and N_2H^+ is detected in several clumps surrounding the infrared cluster, with the higher temperatures (~ 30 K) and linewidths close to the position of the cometary UCH II region.

References.- Chapter 3 of this Thesis, and references therein.

IRAS 22198+6336 — This intermediate-mass star-forming region, with a bolometric luminosity of $450 L_{\odot}$ at a distance of 0.76 kpc, is dominated at centimeter wavelengths by a partially optically thick source, likely tracing a thermal radiojet and embedded in a dust envelope of $\sim 5 M_{\odot}$. Two bipolar molecular outflows are associated with this source, and detected in many different molecules. Warm (20–25 K) dense gas traced by ammonia appears perturbed by the passage of the outflows, while a compact core of hot (~ 100 K) dense gas is detected in several organic molecules tracing one of the few known intermediate-mass hot cores. The dense gas tracers associated with the hot molecular core show a velocity gradient perpendicular to one (probably the youngest) of the molecular outflows, likely tracing rotation.

References.- Chapter 4 of this Thesis, and references therein.

The five regions selected from the literature are listed (and briefly described) below:

AFGL 5142 — Located in the Perseus arm at a distance of 1.8 kpc, this high-mass star-forming region is close to the IRAS source 05274+3345 with a bolometric luminosity of $3800 L_{\odot}$. Faint partially optically thick radio continuum emission is detected about $30''$ to the east of the IRAS source, coinciding with the peak position of a dust and ammonia condensation. In the near-infrared, a cluster of 44 embedded sources is reported close the position of the centimeter source, in a region of 0.3 pc of radius. Three collimated molecular outflows are reported in different molecules, all of them being originated at the position of the millimeter source, which is in fact, a cluster of several radio continuum sources. The extended structure of the NH_3 and N_2H^+ emission has an hour-glass morphology, likely originated by the passage of the molecular outflows. The ammonia condensation associated with the millimeter clump has a temperature of 20 K, however, a hot (~ 200 K) dense molecular core is detected in several organic species.

References.- Torrelles et al. (1992); Estalella et al. (1993); Hunter et al. (1995, 1999); Zhang et al. (2002, 2007); Goddi et al. (2007); Qiu et al. (2008); Busquet (2010); Busquet et al. (2011).

IRAS 05358+3543 — The region, located at a distance of 1.8 kpc and with a bolometric luminosity of $6300 L_{\odot}$, has strong evidences of massive star formation, as evidenced by maser emission from different molecules and multiple outflow activity. In the centimeter range, there exists a faint radio continuum source, with its flux density increasing with the frequency. This source, located at the border of a molecular cloud traced by ammonia and with temperatures ~ 28 K close to the centimeter source (see Figures 8.2 and 8.3), is also associated with a cluster of millimeter sources, being MM1 the one that spatially coincides with it. When observed with higher angular resolution, MM1 splits up into different components, with the strongest one still associated with the centimeter source. Finally, several complex organic molecules have been detected at the position of the radio continuum source, likely tracing a hot molecular core with a temperature of ~ 220 K.

References.- Beuther et al. (2002a, 2007); Leurini et al. (2007) Figures 8.1 and 8.2 and Table 8.1 of this Thesis.

IRAS 20126+4104 — This massive star-forming region, with a bolometric luminosity of $13000 L_{\odot}$, is located in the Cygnus X complex at a distance of 1.7 kpc. High-angular resolution observations at centimeter wavelengths reveal the presence of three components, likely tracing ionized gas from the shocks of a thermal radiojet. A well-collimated molecular outflow, in the southeast-northwest direction, has been identified in a wide variety of tracers, including the proper motions of water masers. The source is embedded in a compact dusty cloud with some extended structure. The dense gas emission as traced by NH_3 , consists of a compact core with a temperature of 22 K at the position of the centimeter source, while emission coming from a large variety of molecular dense gas tracers has been reported and identified as emission

8. The sample of massive star-forming regions

from a hot molecular core with a temperature of ~ 200 K.

References.- Zhang et al. (1998); Cesaroni et al. (1997, 1999, 2005); Hofner et al. (1999, 2007); Moscadelli et al. (2000, 2005); Busquet (2010).

IRAS 20293+3952 — In this region, located at a distance of 2.0 kpc and with a bolometric luminosity of $6300 L_{\odot}$, the star formation is taking place in a closely-packed environment. The main source in the centimeter domain, is a UCH II region, ionized by a B1 ZAMS star and located at the edge of a large molecular cloud, with its UV radiation heating the dense gas close to it (which achieves a temperature ~ 38 K). Several clumps harbouring YSOs in different evolutionary stages, have been detected in NH_3 and N_2H^+ within the molecular cloud, and chemically studied, finding an evolutionary trend from the most evolved objects close to the UCH II region to starless cores in the outer region of the cloud. A second centimeter continuum source is detected $\sim 10''$ to the northwest of the UCH II region. Although several molecular outflows are found in the region, none of them is associated with the centimeter continuum sources. The two centimeter sources are associated with the brightest infrared sources in the field, but with faint millimeter dust emission, suggesting that both objects are H II regions that have started to disperse the natal cloud.

References.- Sridharan et al. (2002); Kumar et al. (2002); Beuther et al. (2002b, 2004); Palau (2006); Palau et al. (2007a); Busquet (2010); Busquet et al. (2010); Table 8.1 and Figure 8.1 in this Thesis.

IRAS 20343+4129 — This massive star forming region, with a bolometric luminosity of $3200 L_{\odot}$ at a distance of 1.4 kpc, is dominated by three infrared sources. The southern one, IRS3, is associated with optically thin centimeter continuum emission likely tracing an H II region ionized by a B2 ZAMS star. This source, also visible in the red band of the DSS, is surrounded by several dust clumps forming a shell-like or cavity morphology. Several dense gas tracers (e.g., N_2H^+ ; F. Fontani, priv. comm.) also present the same cavity structure around the infrared/centimeter source. A molecular outflow is found associated with a younger source, IRS1, located $15''$ to the north, but there is no high velocity molecular emission associated with the H II region. The H II region associated with IRS3 seems to have disrupted its natal cloud forming a cavity around it.

References.- Miralles et al. (1994); Carral et al. (1999); Sridharan et al. (2002); Kumar et al. (2002); Beuther et al. (2002b); Fuller et al. (2005); Palau (2006); Palau et al. (2007b); Table 8.1 and Figure 8.1 in this Thesis.

In conclusion, we have compiled a list of 11 massive star-forming regions, studied in detail in the radio continuum and in different molecular lines. Within this sample, we can identify 16 (faint) centimeter continuum sources likely tracing ionized gas from young stellar objects in their first evolutionary stages.

9

Towards an evolutionary sequence

9.1 Ionized gas emission

In this Section, we will focus on the analysis of the properties of the centimeter continuum emission detected in a sample of 11 massive star-forming regions, which were listed (and briefly summarized) in Chapter 8. In Table 9.1, we present a list of the 16 detected centimeter continuum sources, with their coordinates and main properties regarding the radio continuum emission. For almost all the sources, we have information of their flux density at different wavelengths in the range from 21 cm to 0.7 cm. Thus, we can test the models described in Chapter 1 by constructing and fitting their spectral energy distributions in the centimeter domain. It is important to note that not all the models are easily applicable. For some models it is necessary to have information about the size of the source at different wavelengths, but most of our sources are faint and unresolved, or only resolved at one wavelength. As outlined in Chapter 1, we can distinguish two major different groups of models: (1) the classical model developed by Strömgren for an homogeneous H II region, and (2) those models that assume the ionized gas has not a uniform density distribution (e. g., non-homogeneous ionized gas, thermal radiojets, ionized accretion flows, for which we can use a density distribution of $n_e \propto r^{-q}$).

We have developed a simple code to fit these two density distributions. In Appendix B, there are some notes about the models used: homogeneous and non-homogeneous. The results obtained by fitting the spectral energy distributions are shown in the last columns of Table 9.1. From columns (7) to (10), we list the parameters of the homogeneous H II region fit. The main inputs of the model are the source size (listed as the diameter of the source) and its electron density, which is assumed to be constant for all the source (we assume an

9. Towards an evolutionary sequence

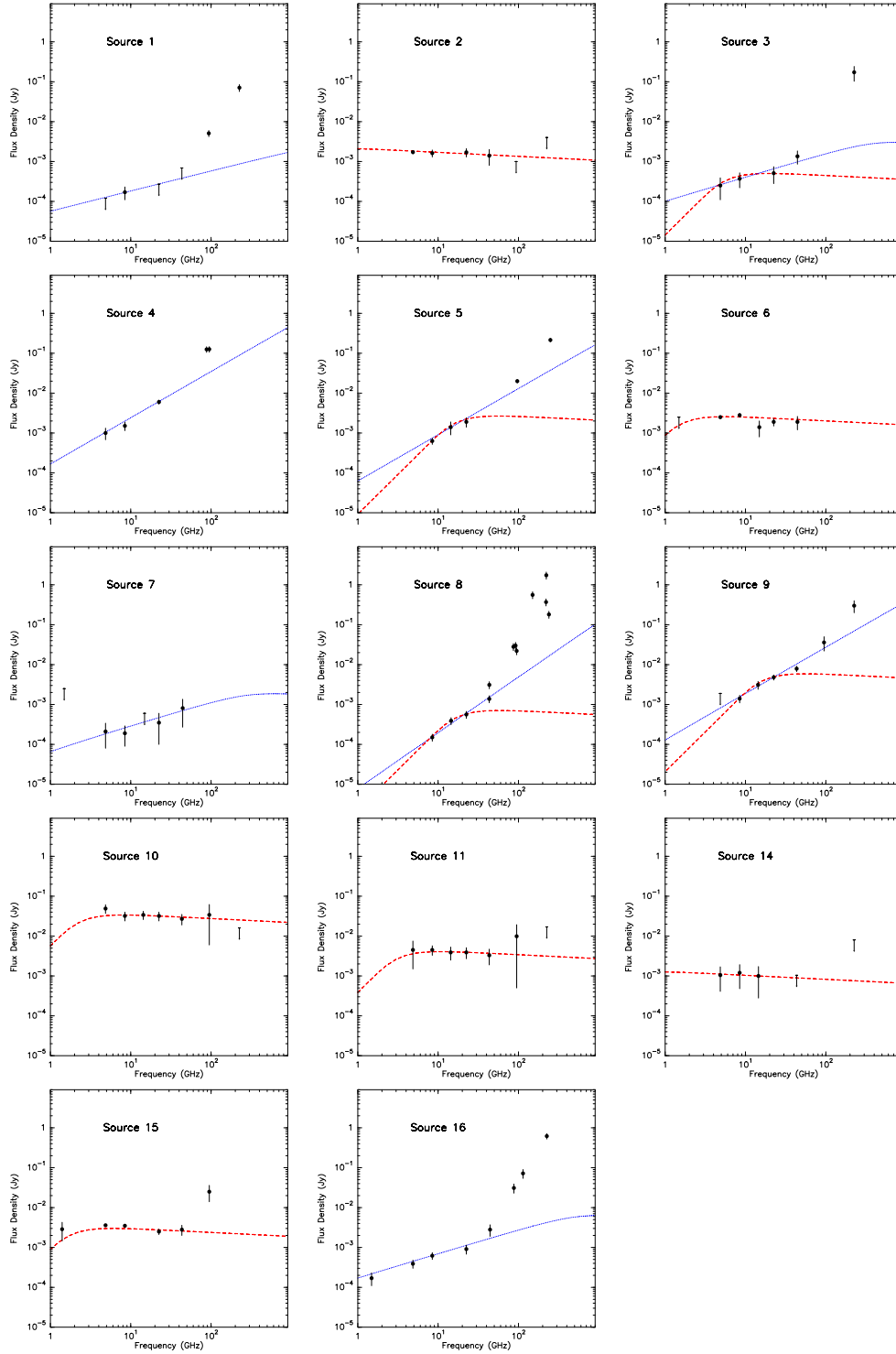


Figure 9.1: Spectral energy distributions in the centimeter range. Blue dotted line: non-homogeneous fit. Red dashed line: homogeneous fit (see Table 9.1 for parameters of the fits). See Tables 9.3 and 9.4 for the data used.

Table 9.1: Parameters for the ionized gas of the radio continuum sources^a

# (1)	Region-Source (2)	$\alpha(J2000)$ (^h ^m ^s) (3)	$\delta(J2000)$ ([°] ['] ^{''}) (4)	S_ν (mJy) (5)	α (6)	Homogeneous ^b				Non-homogeneous ^b		
						diameter (pc) (7)	n_e (cm ⁻³) (8)	EM (cm ⁻⁶ pc) (9)	Spectral Type (10)	q (11)	n_0 (cm ⁻³) (12)	r_0 (^{''}) (13)
1	00117+6412-MM1	00 14 26.05	64 28 43.7	0.17 ± 0.06	-0.3 < α < 1.1	2	50	1.5
2	00117+6412-UCH II	00 14 28.23	64 28 46.6	1.62 ± 0.16	-0.03 ± 0.08	0.0280	2 × 10 ³	1.1 × 10 ⁵	B2	0
3	04579+4703-VLA1	05 01 40.02	47 07 21.2	0.37 ± 0.15	+0.4 ± 0.2	0.0006	5 × 10 ⁵	1.5 × 10 ⁸	B2	2	30	2
4	AFGL 5142	05 30 48.01	33 47 54.1	1.5 ± 0.4	+1.0 ± 0.3	3	270	0.45
5	05358+3543-MM1	05 39 13.07	35 45 51.2	0.63 ± 0.11	+1.1 ± 0.4	0.0003	2 × 10 ⁶	1.0 × 10 ⁹	B2	3	10	0.9
6	19035+0641-VLA1	19 06 01.48	06 46 35.4	2.8 ± 0.3	-0.14 ± 0.11	0.0046	3 × 10 ⁴	4.7 × 10 ⁶	B1	0
7	19035+0641-VLA2	19 06 01.60	06 46 36.2	0.19 ± 0.10	+0.6 ± 0.4	2	2300	0.2
8	20126+4104	20 14 26.04	41 13 32.5	0.15 ± 0.02	+1.4 ± 0.2	0.0002	3 × 10 ⁶	1.5 × 10 ⁹	B2	4	100	0.11
9	G75.78+0.34-CORE	20 21 44.04	37 26 37.8	1.4 ± 0.3	+1.1 ± 0.2	0.0011	1 × 10 ⁶	1.1 × 10 ⁹	B0.5	3	2700	0.16
10	G75.78+0.34-UCH II	20 21 44.10	37 26 39.5	32 ± 4	-0.19 ± 0.06	0.0190	4 × 10 ⁴	2.3 × 10 ⁷	B0	0
11	G75.78+0.34-EAST	20 21 44.50	37 26 37.8	4.5 ± 0.6	-0.16 ± 0.12	0.0050	1 × 10 ⁵	5.3 × 10 ⁷	B0.5	0
12	20293+3952-IRS2	20 31 10.31	40 03 16.5	>0.28 ± 0.11	?	0.0048	1 × 10 ⁴	5.9 × 10 ⁵	B3	?
13	20293+3952-UCH II	20 31 11.20	40 03 09.9	4.5 ± 0.4	?	0.0350	2 × 10 ³	1.8 × 10 ⁵	B1	?
14	20343+4129-IRS3	20 36 07.25	41 39 52.4	1.2 ± 0.4	-0.02 ± 0.30	0.0115	4 × 10 ³	2.2 × 10 ⁵	B2	0
15	22134+5834-VLA1	22 15 09.23	58 49 08.9	3.6 ± 0.4	-0.18 ± 0.08	0.0055	5 × 10 ⁴	1.1 × 10 ⁷	B1	0
16	22198+6336-VLA2	22 21 26.76	63 51 37.8	0.62 ± 0.12	+0.6 ± 0.2	2	250	1.1

^a Information for the columns: (1) identification number; (2) name of the region and centimeter source; (3) right ascension; (4) declination; (5) flux density (in mJy) at 3.6 cm; (6) spectral index of the cm radio continuum emission ($S_\nu \propto \nu^\alpha$). From columns (7) to (10), information about a fit of the centimeter spectral distribution assuming an homogeneous ionized gas source (for details, see Appendix B: (7) diameter size (in pc) of the cm source; (8) electron density (in cm⁻³) of the homogeneous ionized source; (9) emission measure (in cm⁻⁶ pc); (10) spectral type of the ionizing star estimated from the ionizing photons rate and Panagia (1973). From columns (11) to (14), information about the fit of the centimeter spectral distribution assuming a non-homogeneous ionized gas source (for details, see Appendix B): (11) index of the power law used for the density distribution ($n_e = n_0 (r/r_0)^{-q}$); (12) electron density (in cm⁻³) at the reference radius r_0 ; (13) reference radius (in arcsec) used in the power-law distribution.

^b The symbol '...' is shown when the homogeneous or non-homogeneous ionized gas model was not possible to be fitted to the observational data. Empty spaces (for the sources in 20293+5932) are due to the lack of centimeter continuum emission at different wavelengths, there are only measures at 3.6 cm (due to the high angular resolutions in 20293+5932 continuum images we can be filtering faint and extended emission in IRS2, and thus we consider its flux density as a lower limit). In these cases, the physical parameters derived for the homogeneous H II region have been calculated assuming the emission at 3.6 cm is optically thin.

9. Towards an evolutionary sequence

electron temperature of 10^4 K). For completeness, we also list the emission measure, which is estimated from the electron density and the size of the source, and the spectral type (estimated using the tables of Panagia (1973), and the flux of ionizing photons) of a single star that can ionize the gas and create the H II region that we are detecting at centimeter wavelengths. From columns (11) to (13), we list the parameters of the non-homogeneous fit: q , n_0 and r_0 are three constants used in equation $n_e = n_0(r/r_0)^{-q}$ that defines the density distribution. To solve the integral equations used in this model, it is necessary the use of two additional parameters: r_{\min} and r_{\max} (see Appendix B). r_{\min} was set to a minimal value (typically $0''.005$), while r_{\max} was set to have the same value as r_0 . Finally, note that in column (6) we provide the spectral index (α ; $S_\nu \propto \nu^\alpha$) estimated from a linear fit to the flux densities between 20 cm and 1.3 cm (we do not use the 7 mm data to avoid possible contamination from dust emission). In Figure 9.1, we show the spectral energy distribution for each source, and the homogeneous and non-homogeneous fits listed in Table 9.1.

From the results shown in Table 9.1 and Figure 9.1, we can see some differences between groups of sources. Sources with optically thin emission ($\alpha \sim -0.1$) can be well fitted by an homogeneous H II region model, while sources with partially optically thick emission ($\alpha > +0.3$) are better fitted by non-homogeneous density distributions. We note that optically thin emission can also be fitted with any power-law density distribution, since we do not have any observational evidence about the optically thick regime, which determines the properties of the density gradient. However, we favoured the homogeneous fit because it depends on a smaller number of parameters, in comparison with the non-homogeneous model.

In Figure 9.2, we show a plot of the main physical parameters (emission measure and size) for the homogeneous H II regions fitted in Table 9.1. As several works have revealed (see Kurtz 2005a, for a review), the physical parameters of H II regions span orders of magnitude in scale. Assuming an electron temperature (e.g., 10^4 K), these homogeneous H II regions are determined by only two parameters: the size and the emission measure (or electron density). Thus, taking into account these two parameters, we can define different classes of H II regions: giant, classical, compact, ultracompact (UC), and hypercompact (HC) H II regions; with the classes most closely linked to the first stages of the star formation probably being the smallest and densest, i.e., ultracompact and hypercompact H II regions. In Figure 9.2, we have marked different regions with coloured boxes, corresponding to the different classes of H II regions. The black dots correspond to the centimeter continuum sources studied in this work (see Table 9.1), while grey dots show the data from the survey of H II regions carried out by Kurtz et al. (1994). It is interesting to note, that our sources split up into two groups. A group of sources, with sizes between 0.004 and 0.04 pc and emission measures between 10^5 and 10^8 cm $^{-6}$ pc, has physical parameters typical of UCH II regions. The other group, with four sources with sizes < 0.002 pc and emission measures $> 10^8$ cm $^{-6}$ pc, show properties similar to those

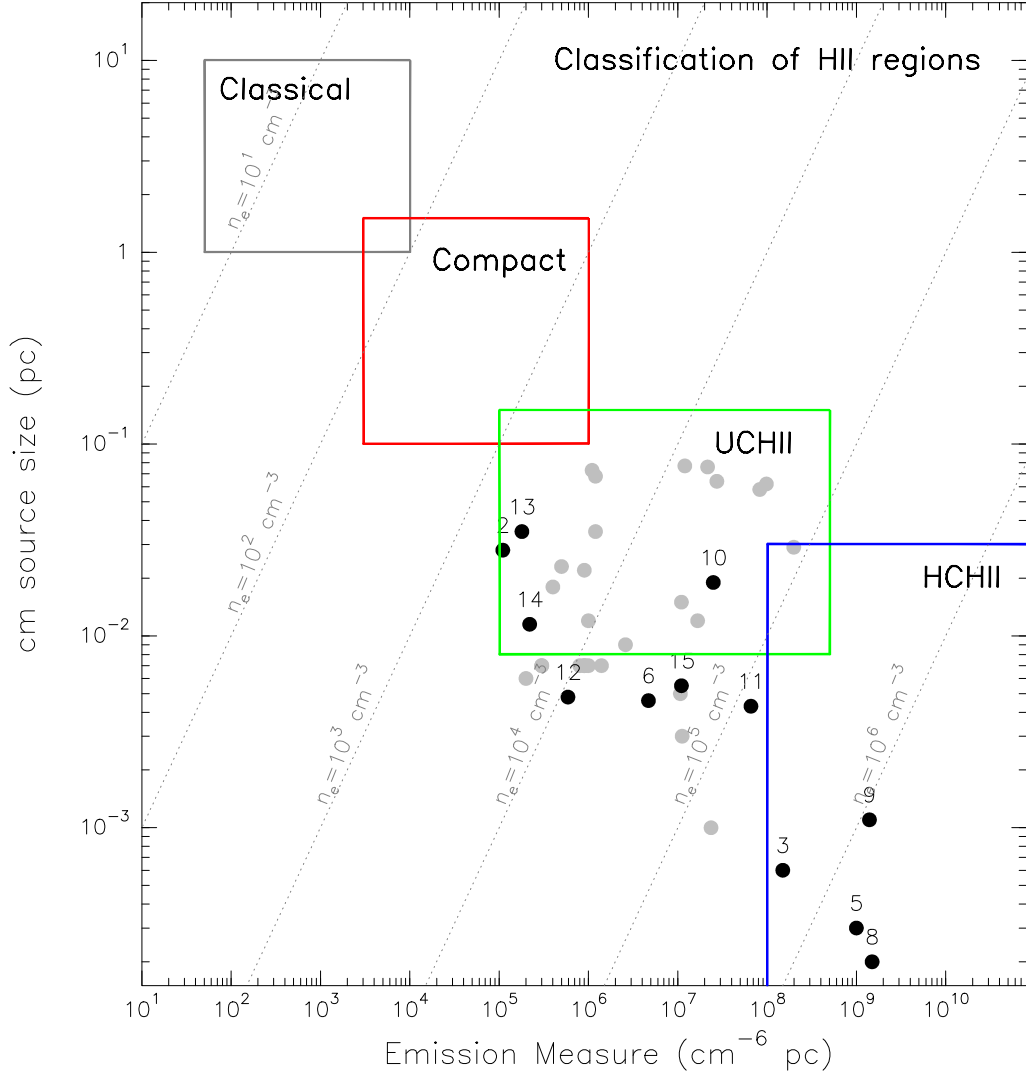


Figure 9.2: Plot of the centimeter size versus the emission measure, of those centimeter continuum sources with a spectral energy distribution fitted by an homogeneous H II region. Black dots correspond to the data of this Thesis (see Table 9.1), while grey dots correspond to data from a survey of ultracompact (UC) H II regions carried out by Kurtz et al. (1994). The colored boxes indicate the different categories (determined by the size and emission measure) in which an H II is usually classified. The youngest ones are presumably the hypercompact (HC) H II regions. Grey dotted lines indicate the electron density, remember that $EM = \int n_e dl$, with l the size of the H II region.

9. Towards an evolutionary sequence

found toward HCH II regions. It is also worth noting that most of the sources lying close to the UCH II box, have small sizes (almost one order of magnitude smaller than typical values for UCH II regions): similar to the sizes found in HCH II regions. However, these sources show moderate values of the emission measure (or electron density): similar to the values found in ultracompact H II regions, and far from the large densities measured in HCH II regions. Which kind of H II regions are we detecting? One possibility could be that we are observing the ionized gas from intermediate-mass stars (B2–B5 ZAMS stars), which creates faint and small H II regions. With the improvement in the efficiency of current interferometers, and with high enough sensitivity observations, we should be capable of detecting (easily) these small H II regions. Thus, these small but low-density objects can be the population of H II regions produced by B2–B5 ZAMS stars. Alternatively, we can think about an evolution between HCH II and UCH II regions, with these particular faint objects being an intermediate evolutionary stage. The two proposed scenarios for these small and faint radio continuum sources, can be tested, for example, by comparing the observed size of the centimeter emission with the radius derived in the classical Strömgren H II region model¹. If the emission comes from an UCH II region ionized by a B-type star we should find R_S to be similar to the observed size, however, if the emission comes from an intermediate stage between HC and UC H II regions we could find that the observed size is smaller than R_S . With the improvement in bandwidth (sensitivity) of the new EVLA, it is expected that we will start to detect more of these H II regions, which could be studied in detail allowing us to assess their true nature. The advent of the EVLA and ALMA will allow to study with high angular resolution and high sensitivity the continuum and radio recombination line emission toward these objects.

We have analyzed the structure of the ionized gas emission (non-homogeneous and homogeneous density distributions) for the centimeter continuum sources studied in this Thesis. However, we have still not considered which is the physical mechanism that can produce the ionization. As explained in Chapter 1, two mechanisms can be responsible for the ionization of the gas surrounding YSOs: *photoionization* and *ionization through shocks*. The classical example of photoionization is the H II region, where the UV photons (with energies > 13.6 eV) coming from the newly-born massive star can ionize the atomic hydrogen. On the other hand, the ionization through shocks in YSOs is expected to arise from the interaction of the jet with the environment. Thermal radiojets are the classic example of ionization through shocks. Anglada (1995, 1996) study the dependence of the radio luminosity ($S_\nu d^2$; being S_ν the flux density at centimeter wavelengths, and d the distance) with the bolometric luminosity of the source (see grey dots in Figure 9.3). Recently, Anglada et al. (in prep.) are studying some radiojets associated with massive YSOs, obtaining a correlation between the radio and bolometric luminosities, similar to

¹The Strömgren radius, R_S , can be measured using Equation B.17, with \dot{N}_i estimated from the flux density (see Equation B.18) and n_e estimated from the observations of radio recombination lines at different frequencies (e.g., Keto et al. 2008).

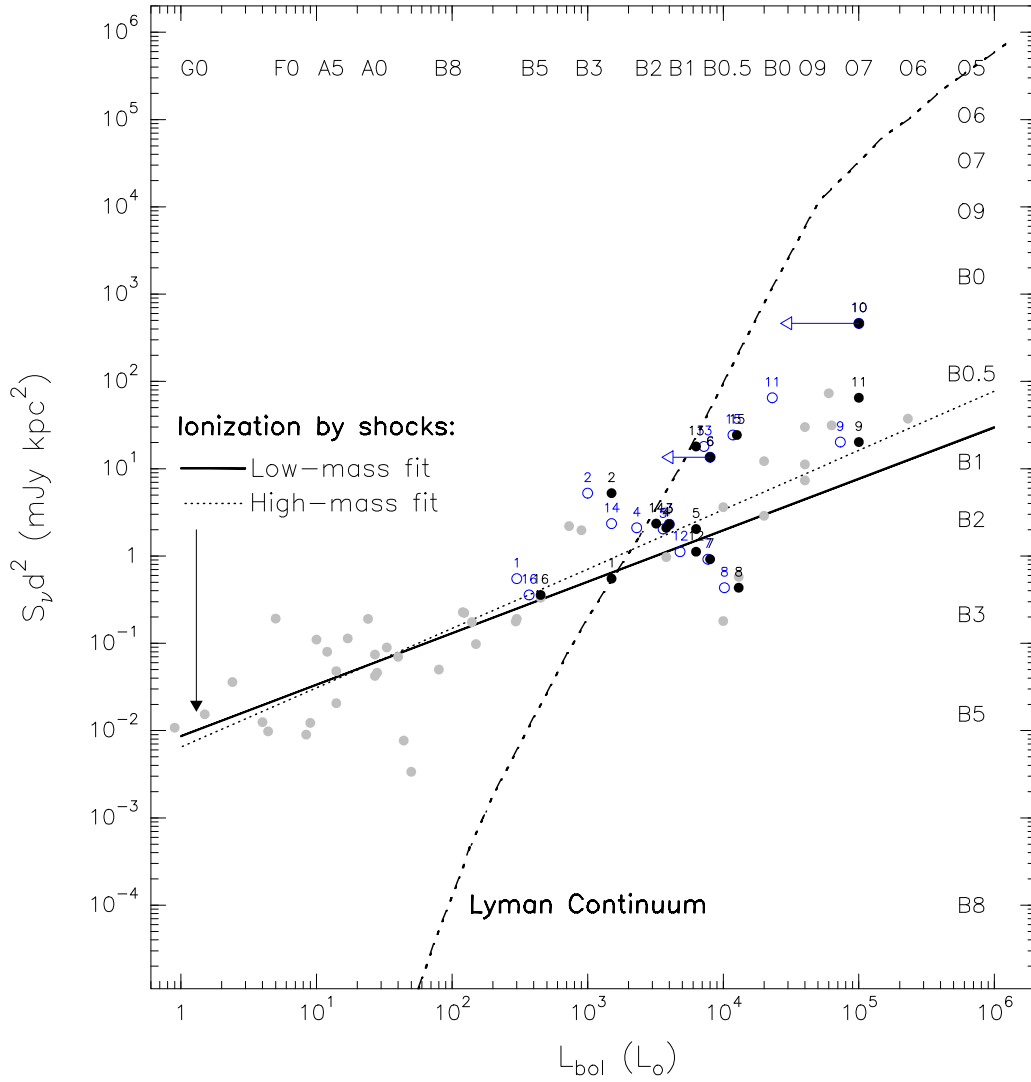


Figure 9.3: Observed radio continuum luminosity, $S_\nu d^2$, as a function of the bolometric luminosity, L_{bol} . S_ν is the observed flux density at centimeter wavelengths (in particular at 3.6 cm) and d is the distance to the source. Grey dots represent data on low luminosity YSOs (Anglada 1996) and high luminosity radio jets (Anglada et al. in prep.). Black dots correspond to the data of the sources studied in this Thesis (see Table 9.1), while blue circles correspond to the same sources but changing the value of the bolometric luminosity, see text (from Table 9.3 and 9.4). The black solid and dotted lines are least square fits to the data of low luminosity and high luminosity YSOs, respectively. Dot-dashed line represents the values expected from Lyman continuum radiation for a zero-age main-sequence star of the given bolometric luminosity (Thompson 1984). At the top and right axes you can find the spectral type corresponding to a given centimeter luminosity (or flux of ionizing photons) and a given bolometric luminosity.

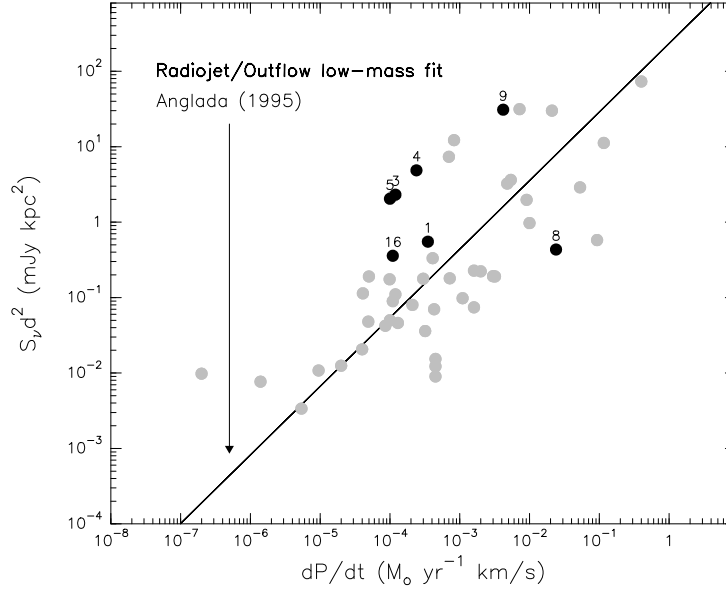


Figure 9.4: Observed radio continuum luminosity, $S_\nu d^2$ (as in Figure 9.3), as a function of the outflow momentum rate, \dot{P} . Grey dots represent data on low luminosity objects (Anglada 1995) and high-mass radiojets (Anglada et al., in prep.). Black dots correspond to the data from Table 9.1. Black solid line is a least square fit to the data of low luminosity YSOs.

the low-mass case. This observational correlation can be used to investigate the origin of the ionization in our sources. Black dots in Figure 9.3, correspond to the sources studied in this Thesis (see Table 9.1). It is interesting to see that some of these sources lie close to the linear fit obtained for radiojets, suggesting that the ionized gas emission for these sources is due to shocks. This is the case of I22198-VLA2 or I20126. On the other hand, there are other sources for which the ionization that we detect can easily be explained by photoionization from a H II region. For example: I00117-UCH II, I20293-UCH II, and I22134-VLA1. However, most of our sources have bolometric luminosities between $500 L_\odot$ and $10000 L_\odot$. In this regime, it is difficult to confirm if the ionization is produced by photons or by shocks, and, thus, it is necessary to obtain more information about the characteristics of the centimeter continuum sources (e. g., information about the morphology of the source, proper motions, molecular outflow emission). In addition, large uncertainties in the bolometric luminosity make still more difficult to properly confirm the ionization mechanism. Blue circles in Figure 9.3, correspond to the sources studied in this Thesis, but taking into account the bolometric luminosity of the specific source (see Section 9.3), instead of the luminosity of all the region. Clusters are common in massive star forming regions and thus, typical bolometric luminosities estimated from IRAS fluxes do not correspond to the real luminosity of a specific source within the cluster. We can see that some sources change their position in the diagram. The clear cases mentioned above

keep the initial classification we have given. But with the new bolometric luminosity, we can disentangle the mechanism for other sources. For example, I00117–MM1 appears as a clear example of ionization through shocks, while G75–EAST seems to be produced by photoionization.

Finally, we can also test the shock-ionization mechanism by comparing the radiocontinuum flux with the outflow momentum rate, for which a relation was obtained in the theoretical works of Curiel et al. (1987, 1989). In Figure 9.4, we compare the results for our sources (those associated with molecular outflow emission) with the results obtained in well-known thermal radiojets. All the considered sources lie close to the theoretical relationship, suggesting that the centimeter emission that we detect in sources like I00117–MM1 or I22198–VLA2, can be produced by a thermal radiojet.

To summarize, we have investigated the ionized gas content in our sample of sources, and found that our centimeter continuum sources can be differentiated in two major groups. Sources with optically thin emission can be fitted with homogeneous H II region models, and their ionization seems to be produced by UV photons. On the other hand, there are sources with partially optically thick emission that in most of the cases can only be fitted by non-homogeneous density distributions for the ionized gas, and their ionization seems to be produced by shocks.

9.2 Dust and molecular gas emission

In the previous section, we have analyzed the properties of the ionized gas of our sample of massive YSOs. We will focus now on the properties of the dust and molecular gas emission associated with each centimeter continuum source. All the regions (except one) have been observed with interferometers at millimeter wavelengths, providing us with 1 mm (or 3 mm) continuum information, i.e., the regime in which the dust typically dominates the emission. In Table 9.2, we list the flux density at millimeter wavelengths from interferometric observations. Following Appendix C, we have used the flux density at millimeter wavelengths to estimate the mass of dust and the column density of H₂ for two different temperatures (listed in the table). The range of temperatures has been chosen taking into account the temperature estimated from different dense gas tracers (mainly NH₃ and CH₃CN).

The last four columns in Table 9.2 refer to the molecular gas emission. We indicate if the centimeter source is associated with: dense gas typically traced by ammonia (in column 6, we describe the morphology of this dense gas); other denser gas tracers, such as CH₃CN, likely tracing a hot molecular core; and high-velocity molecular emission, usually traced by CO, indicating the presence of a molecular outflow.

It is interesting to note that the sources can be grouped in two different categories, as found in the previous section. Sources with strong millimeter emission are associated with dense gas cores, drive molecular outflows, and in most of the cases they are associated with

9. Towards an evolutionary sequence

Table 9.2: Millimeter continuum and molecular gas data^a

# (1)	Dust emission ^b				Molecular gas			
	S_ν (mJy) (2)	M_{dust} (M_\odot) (3)	N_{H_2} (cm^{-2}) (4)	T_{dust} (K) (5)	morphology dense gas (6)	NH_3 (7)	CH_3CN (8)	CO (9)
1	71 ± 14	7–3	$1.9\text{--}0.9 \times 10^{24}$	16–30	core	Y	-	Y
2	< 4	pillar	-	-	-
3	173 ± 70	24–10	$5.6\text{--}2.4 \times 10^{23}$	20–40	core	-	-	Y
4	126 ± 10^c	300–29	$3.3\text{--}0.3 \times 10^{25}$	20–200	core	Y	Y	Y
5	215 ± 22	12–1	$3.0\text{--}0.3 \times 10^{24}$	25–220	displaced	Y	Y	Y
6					displaced	Y		
7					core	Y		
8	181 ± 20	10–1	$7.3\text{--}0.7 \times 10^{24}$	22–200	core	Y	Y	Y
9	300 ± 100	41–10	$7.1\text{--}1.7 \times 10^{23}$	40–150	core	Y	Y	Y
10	< 16	displaced	-	-	-
11	< 17	displaced	-	-	-
12	2.4 ± 1.0^c	9–4	$1.2\text{--}0.6 \times 10^{24}$	17–34	displaced	-	-	-
13	2.4 ± 1.0^c	9–4	$1.2\text{--}0.6 \times 10^{24}$	17–34	pillar	-	-	-
14	< 8	cavity	-	-	-
15	25 ± 11^c	11–5	$6.1\text{--}2.9 \times 10^{23}$	25–50	cavity	-		
16	620 ± 150	8–2	$6.2\text{--}1.0 \times 10^{24}$	20–100	core	Y	Y	Y

^a Information for the columns: (1) identification number; (2) flux density (in mJy) generally at 1.3 mm; (3) dust mass (in M_\odot) estimated for two distinct temperatures; (4) column density of H_2 (in cm^{-2}) estimated for two distinct temperatures; (5) two different temperatures (in K) used to derived the mass of dust, the values correspond to the temperature measured with different molecular dense gas tracers; (6) morphology of the dense gas emission (mainly ammonia); (7) detection of NH_3 with radio interferometers; (8) detection of CH_3CN as a hot molecular core tracer; (9) detection of CO as a molecular outflow tracer. For the last three columns: ‘Y’ indicates detection, ‘-’ indicates non detection, and an empty space means it has not been observed.

^b The dust mass and molecular column density have been calculated following Appendix C, assuming a dust mass opacity of $0.09 \text{ cm}^2 \text{ g}^{-1}$ at 230 GHz (Ossenkopf and Henning 1994), and a dust emissivity index of 2.

^c Flux density in mJy, at 3.2 mm.

hot molecular core signatures. Differently, sources that are not associated with outflow emission, show no (or faint) millimeter continuum emission, and are located displaced from the main dense gas condensations, which appear forming a cavity (or pillar structure) around (or close to) the centimeter continuum source.

9.2. Dust and molecular gas emission

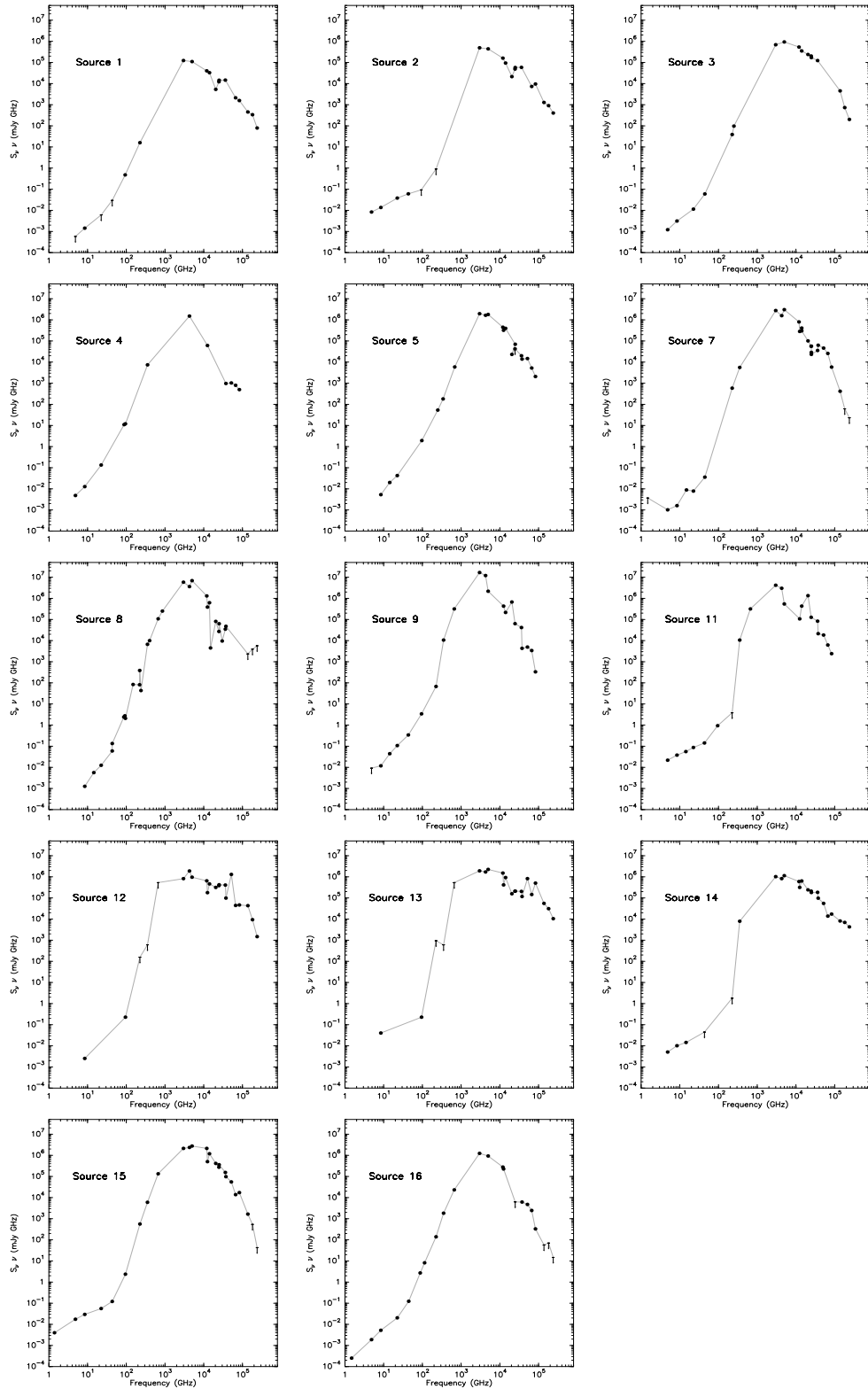


Figure 9.5: Spectral energy distributions with the data from Tables 9.3 and 9.4.

9. Towards an evolutionary sequence

Table 9.3: Flux densities at different wavelengths for the centimeter continuum sources (I)^a

λ (mm)	ν (GHz)	Flux density at different wavelengths (Jy)							
		#1	#2	#3	#4	#5	#6	#7	#8
$L_{\text{bol}} (L_{\odot})$		300	1000	4000	2300	3600	?	7700	10200
$T_{\text{bol}} (\text{K})$		85	> 90	123	57	62	?	66	59
2.00 ⁽⁺²⁾	1.49 ⁽⁺⁰⁾						<2.50 ⁽⁻³⁾	<2.50 ⁽⁻³⁾	
6.00 ⁽⁺¹⁾	4.86 ⁽⁺⁰⁾						2.50 ⁽⁻³⁾	2.10 ⁽⁻⁴⁾	
3.60 ⁽⁺¹⁾	8.46 ⁽⁺⁰⁾	<1.20 ⁽⁻⁴⁾	1.72 ⁽⁻³⁾	2.50 ⁽⁻⁴⁾	1.00 ⁽⁻³⁾		2.80 ⁽⁻³⁾	1.90 ⁽⁻⁴⁾	1.50 ⁽⁻⁴⁾
2.00 ⁽⁺¹⁾	1.49 ⁽⁺¹⁾					6.30 ⁽⁻⁴⁾	1.40 ⁽⁻³⁾	<6.00 ⁽⁻⁴⁾	3.90 ⁽⁻⁴⁾
1.30 ⁽⁺¹⁾	2.24 ⁽⁺¹⁾	<2.70 ⁽⁻⁴⁾	1.70 ⁽⁻³⁾	5.10 ⁽⁻⁴⁾	6.00 ⁽⁻³⁾	1.90 ⁽⁻³⁾	1.90 ⁽⁻³⁾	3.50 ⁽⁻⁴⁾	5.60 ⁽⁻⁴⁾
7.00 ⁽⁺⁰⁾	4.43 ⁽⁺¹⁾	<6.90 ⁽⁻⁴⁾	1.40 ⁽⁻³⁾	1.35 ⁽⁻³⁾			1.90 ⁽⁻³⁾	8.10 ⁽⁻⁴⁾	3.10 ⁽⁻³⁾
3.40 ⁽⁺⁰⁾	8.80 ⁽⁺¹⁾				1.25 ⁽⁻¹⁾				2.80 ⁽⁻²⁾
3.20 ⁽⁺⁰⁾	9.50 ⁽⁺¹⁾	5.10 ⁽⁻³⁾	<1.00 ⁽⁻³⁾		1.26 ⁽⁻¹⁾	2.00 ⁽⁻²⁾			2.20 ⁽⁻²⁾
2.70 ⁽⁺⁰⁾	1.14 ⁽⁺²⁾								
2.00 ⁽⁺⁰⁾	1.49 ⁽⁺²⁾								5.60 ⁽⁻¹⁾
1.30 ⁽⁺⁰⁾	2.30 ⁽⁺²⁾	7.10 ⁽⁻²⁾	<4.00 ⁽⁻³⁾	1.73 ⁽⁻¹⁾				2.60 ⁽⁺⁰⁾	1.74 ⁽⁺⁰⁾
1.20 ⁽⁺⁰⁾	2.49 ⁽⁺²⁾			3.90 ⁽⁻¹⁾		2.15 ⁽⁻¹⁾			1.81 ⁽⁻¹⁾
8.75 ⁽⁻¹⁾	3.42 ⁽⁺²⁾					5.29 ⁽⁻¹⁾			
8.50 ⁽⁻¹⁾	3.54 ⁽⁺²⁾				2.10 ⁽⁺¹⁾	3.52 ⁽⁺¹⁾		1.59 ⁽⁺¹⁾	1.90 ⁽⁺¹⁾
4.50 ⁽⁻¹⁾	6.66 ⁽⁺²⁾					1.53 ⁽⁺²⁾			1.62 ⁽⁺²⁾
1.00 ⁽⁻¹⁾	2.99 ⁽⁺²⁾	4.13 ⁽⁺¹⁾	1.66 ⁽⁺²⁾	2.31 ⁽⁺²⁾		6.55 ⁽⁺³⁾		9.23 ⁽⁺²⁾	1.95 ⁽⁺³⁾
7.00 ⁽⁻²⁾	4.28 ⁽⁺³⁾				3.53 ⁽⁺²⁾	3.85 ⁽⁺²⁾		3.70 ⁽⁺²⁾	8.44 ⁽⁺²⁾
6.00 ⁽⁻²⁾	4.99 ⁽⁺³⁾	2.21 ⁽⁺¹⁾	8.85 ⁽⁺¹⁾	1.88 ⁽⁺²⁾		3.61 ⁽⁺²⁾		6.10 ⁽⁺²⁾	1.38 ⁽⁺³⁾
2.50 ⁽⁻²⁾	1.20 ⁽⁺⁴⁾	3.35 ⁽⁺⁰⁾	1.34 ⁽⁺¹⁾	4.49 ⁽⁺¹⁾		3.73 ⁽⁺¹⁾		6.67 ⁽⁺¹⁾	1.09 ⁽⁺²⁾
2.40 ⁽⁻²⁾	1.25 ⁽⁺⁴⁾				4.90 ⁽⁺⁰⁾	2.57 ⁽⁺¹⁾		2.27 ⁽⁺¹⁾	3.10 ⁽⁺¹⁾
2.13 ⁽⁻²⁾	1.41 ⁽⁺⁴⁾	2.34 ⁽⁺⁰⁾	6.69 ⁽⁺⁰⁾	2.50 ⁽⁺¹⁾		2.82 ⁽⁺¹⁾		2.91 ⁽⁺¹⁾	4.43 ⁽⁺¹⁾
2.08 ⁽⁻²⁾	1.49 ⁽⁺⁴⁾							2.15 ⁽⁺¹⁾	3.00 ⁽⁻¹⁾
1.46 ⁽⁻²⁾	2.05 ⁽⁺⁴⁾	2.61 ⁽⁻¹⁾	1.05 ⁽⁺⁰⁾	1.17 ⁽⁺¹⁾		1.13 ⁽⁺⁰⁾		4.94 ⁽⁺⁰⁾	3.98 ⁽⁺⁰⁾
1.21 ⁽⁻²⁾	2.47 ⁽⁺⁴⁾	4.95 ⁽⁻¹⁾	1.98 ⁽⁺⁰⁾	8.21 ⁽⁺⁰⁾		<1.72 ⁽⁺⁰⁾		2.29 ⁽⁺⁰⁾	1.10 ⁽⁺⁰⁾
1.20 ⁽⁻²⁾	2.49 ⁽⁺⁴⁾	5.80 ⁽⁻¹⁾	2.32 ⁽⁺⁰⁾	6.82 ⁽⁺⁰⁾		2.81 ⁽⁺⁰⁾		2.27 ⁽⁺⁰⁾	2.53 ⁽⁺⁰⁾
1.17 ⁽⁻²⁾	2.49 ⁽⁺⁴⁾	5.80 ⁽⁻¹⁾	2.32 ⁽⁺⁰⁾	6.82 ⁽⁺⁰⁾		2.81 ⁽⁺⁰⁾		1.16 ⁽⁺⁰⁾	
1.10 ⁽⁻²⁾	2.50 ⁽⁺⁴⁾	5.80 ⁽⁻¹⁾	2.32 ⁽⁺⁰⁾	6.82 ⁽⁺⁰⁾		2.81 ⁽⁺⁰⁾		9.30 ⁽⁻¹⁾	
8.28 ⁽⁻²⁾	3.62 ⁽⁺⁴⁾	4.05 ⁽⁻¹⁾	1.62 ⁽⁺⁰⁾	3.41 ⁽⁺⁰⁾		5.53 ⁽⁻¹⁾		9.82 ⁽⁻¹⁾	9.65 ⁽⁻¹⁾
8.00 ⁽⁻³⁾	3.75 ⁽⁺⁴⁾				2.60 ⁽⁻²⁾	3.71 ⁽⁻¹⁾		1.68 ⁽⁺⁰⁾	1.27 ⁽⁺⁰⁾
5.80 ⁽⁻³⁾	5.17 ⁽⁺⁴⁾				2.00 ⁽⁻²⁾	2.86 ⁽⁻¹⁾		8.92 ⁽⁻¹⁾	
4.50 ⁽⁻³⁾	6.66 ⁽⁺⁴⁾	3.20 ⁽⁻²⁾	1.10 ⁽⁻¹⁾		1.20 ⁽⁻²⁾	7.90 ⁽⁻²⁾		3.86 ⁽⁻¹⁾	
3.60 ⁽⁻³⁾	8.33 ⁽⁺⁴⁾	1.90 ⁽⁻²⁾	1.15 ⁽⁻¹⁾		6.00 ⁽⁻³⁾	2.50 ⁽⁻²⁾		7.00 ⁽⁻²⁾	
2.17 ⁽⁻³⁾	1.38 ⁽⁺⁵⁾	3.29 ⁽⁻³⁾	9.28 ⁽⁻³⁾	3.28 ⁽⁻²⁾				3.03 ⁽⁻³⁾	<1.70 ⁽⁻²⁾
1.65 ⁽⁻³⁾	1.82 ⁽⁺⁵⁾	1.86 ⁽⁻³⁾	4.99 ⁽⁻³⁾	4.04 ⁽⁻³⁾				<3.40 ⁽⁻⁴⁾	<2.17 ⁽⁻²⁾
1.25 ⁽⁻³⁾	2.40 ⁽⁺⁵⁾	3.30 ⁽⁻⁴⁾	1.69 ⁽⁻³⁾	8.41 ⁽⁻⁴⁾				<9.60 ⁽⁻⁵⁾	<2.38 ⁽⁻²⁾

^a In this Table we list the flux densities at different wavelengths/frequencies for the 16 centimeter continuum sources. The two first columns correspond to the wavelengths (in mm) and the frequency (in GHz). The number must be read as follows: 2.00⁽⁺²⁾ corresponds to $2.00 \times 10^{+2}$ (i. e., 200 mm, or 20 cm); or for the frequency: 1.49⁽⁺⁰⁾ corresponds to 1.49×10^0 GHz. For each wavelength, we provide the flux density, or an upper limit, (in Jy) if the source has been observed. The source is identified by its identification number (see Table 9.1) at the header of each column. Finally, we also provide the bolometric luminosity (in L_{\odot}) and bolometric temperature (in K) for each centimeter continuum source (see text for details in the calculation). This Table continues in Table 9.4.

9.3 Spectral energy distribution: bolometric luminosity

In previous sections, we have briefly introduced the problems in determining the bolometric luminosity of massive YSOs, which are usually found in crowded clusters containing other (generally less massive) YSOs. We have compiled information at submillimeter and

9.3. Spectral energy distribution: bolometric luminosity

Table 9.4: Flux densities at different wavelengths for the centimeter continuum sources (II)^a

λ (mm)	ν (GHz)	Flux density at different wavelengths (Jy)							
		#9	#10	#11	#12	#13	#14	#15	#16
$L_{\text{bol}} (L_{\odot})$		73000	?	23000	4800	7200	1500	11800	370
$T_{\text{bol}} (\text{K})$		50	?	70	141	136	101	90	61
2.00(+2)	1.49(+0)							2.87(-3)	1.70(-4)
6.00(+1)	4.86(+0)	<1.90(-3)	4.90(-2)	4.50(-3)			1.05(-3)	3.65(-3)	3.90(-4)
3.60(+1)	8.46(+0)	1.40(-3)	3.20(-2)	4.50(-3)	3.00(-4)	4.80(-3)	1.20(-3)	3.56(-3)	6.20(-4)
2.00(+1)	1.49(+1)	3.10(-3)	3.40(-2)	3.90(-3)			1.00(-3)		
1.30(+1)	2.24(+1)	4.80(-3)	3.20(-2)	3.90(-3)				2.40(-3)	9.10(-4)
7.00(+0)	4.43(+1)	7.90(-3)	2.70(-2)	3.30(-3)			<1.04(-3)	1.16(-3)	2.80(-3)
3.40(+0)	8.80(+1)						<8.00(-3)		3.10(-2)
3.20(+0)	9.50(+1)	3.60(-2)	3.40(-2)	9.90(-3)	2.40(-3)	2.40(-3)		2.50(-2)	
2.70(+0)	1.14(+2)								7.20(-2)
2.00(+0)	1.49(+2)								
1.30(+0)	2.30(+2)	3.00(-1)	<1.60(-2)	<1.70(-2)	<7.00(-1)	<4.20(+0)		2.50(+0)	6.20(-1)
1.20(+0)	2.49(+2)								
8.75(-1)	3.42(+2)								
8.50(-1)	3.54(+2)	3.02(+1)		3.02(+1)	<1.72(+0)	<1.72(+0)	2.25(+1)	1.70(+1)	5.20(+0)
4.50(-1)	6.66(+2)	4.76(+2)		4.76(+2)	<8.04(+2)	<8.04(+2)		2.02(+2)	3.50(+1)
1.00(-1)	2.99(+3)			1.40(+3)	2.75(+2)	6.42(+2)	3.42(+2)	7.13(+2)	4.15(+2)
7.00(-2)	4.28(+3)	2.81(+3)		7.03(+2)	4.43(+2)	3.99(+2)	1.93(+2)	5.55(+2)	
6.00(-2)	4.99(+3)	4.36(+2)		1.09(+2)	1.93(+2)	4.50(+2)	2.28(+2)	5.53(+2)	1.87(+2)
2.50(-2)	1.20(+4)				5.41(+1)	1.26(+2)	5.01(+1)	1.78(+2)	2.33(+1)
2.40(-2)	1.25(+4)			8.59(+0)	1.43(+1)	3.34(+1)	2.54(+1)	4.05(+1)	1.82(+1)
2.13(-2)	1.41(+4)	1.53(+1)		3.06(+1)	3.30(+1)	6.60(+1)	4.54(+1)	8.50(+1)	
2.08(-2)	1.49(+4)								
1.46(-2)	2.05(+4)	3.29(+1)		6.58(+1)	1.55(+1)	7.74(+0)	1.19(+1)	2.03(+1)	
1.21(-2)	2.47(+4)	2.57(+0)		5.14(+0)	1.55(+1)	8.46(+0)	8.56(+0)	1.11(+1)	
1.20(-2)	2.49(+4)				1.69(+1)	8.46(+0)	7.27(+0)	1.44(+1)	<2.50(-1)
1.17(-2)	2.49(+4)								
1.10(-2)	2.50(+4)								
8.28(-2)	3.62(+4)	1.15(+0)		2.31(+0)	1.13(+1)	5.65(+0)	5.12(+0)	4.29(+0)	
8.00(-3)	3.75(+4)	1.15(-1)		5.71(-1)	2.64(+0)	3.13(+0)	2.62(+0)	2.62(+0)	1.65(-1)
5.80(-3)	5.17(+4)	9.60(-2)		3.56(-1)	2.53(+1)	1.60(+1)	1.07(+0)	1.07(+0)	9.22(-2)
4.50(-3)	6.66(+4)	5.10(-2)		9.30(-2)	6.65(-1)	2.19(+0)	2.08(-1)	2.08(-1)	3.70(-2)
3.60(-3)	8.33(+4)	4.00(-3)		2.90(-2)	5.61(-1)	6.08(+0)	2.08(-1)	2.08(-1)	3.98(-3)
2.17(-3)	1.38(+5)				3.14(-1)	4.02(-1)	5.90(-2)	1.20(-2)	<4.17(-4)
1.65(-3)	1.82(+5)				5.18(-2)	1.72(-1)	3.84(-2)	<2.99(-3)	<3.91(-4)
1.25(-3)	2.40(+5)				6.18(-3)	4.38(-2)	1.79(-2)	<1.79(-4)	<6.20(-5)

^a Continuation of Table 9.3.

infrared wavelengths for our 16 radiocontinuum sources. By inspecting the images at each wavelength we have calculated the emission at each wavelength coming from our specific source. In Tables 9.3 and 9.4, we show the flux densities obtained at each wavelength for each source (catalogued with the identification number of Table 9.1). We note that in some cases the uncertainty in the flux density is large (up to 40% or 50%), but generally it is close to 10% or 20%. With these flux densities, we have derived the bolometric luminosities and bolometric temperatures for each source.

The bolometric luminosity, L_{bol} , is calculated by integrating over the full observed spectral energy distribution,

$$L_{\text{bol}} = 4\pi d^2 \int_0^{\infty} S_{\nu} d\nu, \quad (9.1)$$

with the flux densities at each frequency obtained from Tables 9.3 and 9.4. It is important

9. Towards an evolutionary sequence

to note that for two sources (G75–UCH II and I19035–VLA1), we were not able to estimate the bolometric luminosity, since there is no clear infrared emission associated with these two sources (see Chapters 5 and 6 for details on the interpretation of these sources, and their emission at infrared wavelengths).

The bolometric temperature, T_{bol} , is defined as the temperature of a blackbody with the same flux-weighted mean frequency as the source (Myers and Ladd 1993; Dunham et al. 2008). A practical expression to calculate T_{bol} is

$$T_{\text{bol}} = 1.25 \times 10^{-11} \frac{\int_0^\infty \nu S_\nu d\nu}{\int_0^\infty S_\nu d\nu} \text{ K.} \quad (9.2)$$

The bolometric temperature has been used as a standard evolutionary indicator (e.g., Chen et al. 1995; Dunham et al. 2008). For low-mass YSOs, bolometric temperatures < 70 K are associated with Class 0 objects (young); while temperatures > 70 K are measured for Class I objects (more evolved). Although T_{bol} is not usually used for the high-mass star formation case, it is a measure of the importance of the (sub)millimeter flux relative to the infrared flux, thus we will adopt T_{bol} in this work as an indicator of how much the protostar is embedded in cold dust and gas. These two parameters, L_{bol} and T_{bol} , are listed in Tables 9.3 and 9.4, for each of the centimeter continuum sources of our sample (except for the particular cases G75–UCH II and I19035–VLA1). In Figure 9.5, we show the SED for each radio continuum source.

9.4 Towards an evolutionary sequence

9.4.1 ‘Color-color’ diagrams

In Sections 9.1 to 9.3, we have analyzed the ionized gas, dust, molecular gas, and infrared properties of a sample of 16 faint radiocontinuum sources associated with massive YSOs. The main parameters obtained for each source have been compiled and listed in Tables 9.5 and 9.6.

Table 9.5 contains basic information regarding the centimeter continuum source, such as its identification number (column 1), its name (column 2) and the heliocentric distance (column 3). We also list some general (bolometric) parameters such as L_{bol} (column 4) and T_{bol} (column 5). Centimeter and millimeter properties are listed in the following columns (columns 6–10, and columns 11–13, respectively). We note that, similar to the radio luminosity at centimeter wavelengths, we have estimated the luminosity at millimeter wavelengths as $S_\nu d^2$, with S_ν being the flux density at 1.3 mm and d the distance. Finally, in the last column (14) we indicate if the source is visible in the optical red band of the DSS, in the near-infrared, and in the mid-infrared.

In Table 9.6, we list, for the same centimeter continuum sources, the properties inferred from the dense gas (NH_3 and hot core tracers), outflow and maser emission. For the ammonia emission (columns 15–19) we indicate information about the morphological

distribution of the dense gas, its positional offset with respect to the centimeter source (in the case where a dense ammonia clump is found associated with the radio continuum source, we list an upper limit of $1''$ for the offset), the linewidth, the column density, and the rotational temperature derived from the (1,1) and (2,2) inversion transition lines. For the hot core emission (columns 20–22), we list the temperatures derived from CH_3CN observations in the $(6 \rightarrow 5)$ transition (obtained in most of the cases from single-dish observations²), and in the $(12 \rightarrow 11)$ transition (derived from interferometric observations, see previous Chapters of this Thesis). For the outflow emission (columns 23–25), we list the outflow momentum rate (either from the literature or derived in this work; note that for all the sources we give the value of the outflow momentum rate assuming optically thin emission), its collimation (measured for all the sources as the ratio of the outflow's length to its width), and notes on the molecular species that have been found tracing the high velocity emission. In the last column (26), we list information about maser (H_2O , OH and CH_3OH , respectively) emission detected in the region.

In order to study a possible evolution with time for the different parameters listed in the table, we have plotted the parameters against the bolometric temperature, supposed to be a reasonable indicator of how much the protostar is embedded (see Section 9.3). We did not plot the millimeter source size against T_{bol} due to significantly different beam sizes of the observations, and we neither plotted the hot core temperature against T_{bol} because we could only determine this parameter for very few sources. For the case of the flux density at millimeter and centimeter wavelengths we have constructed parameters which are not dependent on the distance (i.e., luminosities) and which are expected, in general terms, to evolve with time. The analyzed parameters to evaluate the centimeter and millimeter emission are:

- **centimeter-to-bolometric luminosity ratio**, $L_{\text{cm}}/L_{\text{bol}}$: this parameter is related to the intensity of the centimeter continuum emission in comparison to the bolometric luminosity of the YSO (taking into account the distance of the source). In the high-mass regime, for example, a luminous object with an already developed H II region is expected to have a $L_{\text{cm}}/L_{\text{bol}}$ larger than a luminous object with no H II region or with faint centimeter continuum emission (e.g., tracing a thermal radiojet).
- **millimeter-to-centimeter luminosity ratio**, $L_{\text{mm}}/L_{\text{cm}}$: this parameter evaluates the dust content with respect to the ionized gas, in a similar way to the disruption degree parameter used by Sánchez-Monge et al. (2008). A deeply embedded source will have a $L_{\text{mm}}/L_{\text{cm}}$ larger than a similar source that has already disrupted its natal cloud.

²I am involved in a project to study the deuteration in a large sample of massive young stellar objects in different evolutionary stages. The observations of deuterated species, carried out with the IRAM 30 m telescope, also include data for the CH_3CN (6–5) transitions. The PI of the project, F. Fontani, kindly provided me with the CH_3CN data to derive the T_{rot} using the rotational diagram technique.

Table 9.5: Parameters of a large sample of sources, observed with interferometers (I)^a

#	Source	d (kpc)	L_{bol} (L_{\odot})	T_{bol} (K)	cm					mm			
					morphology	size (AU)	α	q	L_{cm} (mJy kpc ²)	morphology	size (AU)	L_{mm} (Jy kpc ²)	red/IR
(1)	(2)	(3)	(4)	(5)	(6)	(7)	(8)	(9)	(10)	(11)	(12)	(13)	(14)
1	I00117-MM1	1.8	300	85	unresolved	<5000	thermal	2	0.55	compact	3900	0.23	N YY
2	I00117-UCH II	1.8	1000	>90	shell-like	6800	-0.03	0	5.3	no dust	...	<0.013	Y YY
3	I04579-VLA1	2.5	4000	123	unresolved	<6800	+0.4	2	2.3	compact	9700	1.1	N YY
4	A5142	1.8	2300	57	double	2600	+1.0	3	2.7	comp multipeak	4600	1.9	N NY
5	I05358-MM1	1.8	3600	62	compact	3900	+1.1	3	2.0	compact	2900	0.70	N NY
6	I19035-VLA1	2.2	?	?	cometary	1000	-0.14	0	14.				N NY
7	I19035-VLA2	2.2	7700	66	unresolved	<700	+0.6	2	0.92				N YY
8	I20126	1.7	10200	59	double	450	+1.4	4	0.43	compact	1000	0.52	N NY
9	G75-CORE	3.8	73000	50	double	450	+1.1	3	15.	compact	8000	4.5	N NY
10	G75-UCH II	3.8	?	?	cometary	3800	-0.19	0	500.	no dust	...	<0.23	N NY
11	G75-EAST	3.8	23000	70	compact	1600	-0.16	0	70.	compact	12000	0.30	N NY
12	I20293-IRS2	2.0	4800	141	unresolved	800	?	?	>1.2	faint dust	...	0.10	N YY
13	I20293-UCHII	2.0	7200	136	shell-like	7300	?	?	19.	faint dust	...	0.10	Y YY
14	I20343-IRS3	1.4	1500	101	unresolved	2400	-0.02	0	2.0	no dust	...	<0.01	Y YY
15	I22134-VLA1	2.6	11800	90	cometary	1200	-0.18	0	24.	surrounding	19000	<3.4	N YY
16	I22198-VLA2	0.76	370	61	sligh resolv	1700	+0.6	2	0.36	compact envel	1900	0.32	N NY

^a Information for the columns: (1) identification number; (2) name of the source; (3) distance (in kpc); (4) bolometric luminosity (in L_{\odot}) estimated taking into account the different contribution of the mid/far-IR sources to each source in the field (see text), typical errors are around 20–30%; (5) bolometric temperature (in K) estimated in a similar way to the bolometric luminosity (see text), typical errors are around 20–30%; (6) morphology of the cm source, unresolved reads for sources with no deconvolved size determination from the task JMFIT in AIPS, while compact reads for sources with a deconvolved size (from JMFITS) with an error of 100%; (7) diameter size of the cm source (in AU) taking into account radio continuum maps with similar spatial resolution; (8) spectral index of the cm radio continuum emission; (9) index of the power-law distribution for the electron density, $n_e \propto r^{-q}$, as explained in Appendix B; (10) radio continuum luminosity (in mJy kpc², estimated from the flux density at 3.6 cm and the distance of the source; (11) morphology of the mm source; (12) size of the mm source (in AU); (13) luminosity at millimeter wavelengths (in Jy kpc²) estimated from the flux density at 1.3 mm and the distance of the source; (14) IR and optical information (Y: yes and N: no), first subcolumn refers to emission in the red band of the DSS survey, second refers to near-IR emission (between 1.2 and 3 μm), and third to mid-IR emission (between 3 and 50 μm). Continues in Table 9.6.

Table 9.6: Parameters of a large sample of sources, observed with interferometers (II)^a

# (1)	morphology (15)	NH ₃ dense gas				Hot core			Molecular outflow			
		offset (pc) (16)	Δv (km s ⁻¹) (17)	N_{NH_3} (cm ⁻²) (18)	T_{rot} (K) (19)	T_{6-5} (K) (20)	T_{12-11} (K) (21)	size (AU) (22)	\dot{P} (M_{\odot} km s ⁻¹ yr ⁻¹) (23)	collimation (axis ratio) (24)	molecular species (25)	Masers (26)
1	peak	<0.009	1.6	0.7×10^{15}	17	41	3.5×10^{-4}	13/10 = 1.3	CO	Y--
2	pillar	0.090	0.7	0.4×10^{15}	28		N--
3	no detect	1.2×10^{-4}	15/4 = 4	CO	Y-N
4	peak	<0.009	4.7	2.6×10^{15}	20	60	200	3600	2.4×10^{-4}	14/4 = 3.5	CO, SiO, ...	Y-Y
5	~peak	0.017	1.3	1.0×10^{15}	28	38	220	3000	1.0×10^{-4}	40/7 = 6	CO, H ₂ , ...	Y-Y
6	~peak	0.020	3.3	1.2×10^{15}	25	...						YYY
7	peak	<0.011	4.2	1.8×10^{15}	29	...						YYY
8	peak	<0.008	2.7	2.6×10^{15}	22	150	200	5000	2.4×10^{-2}	10/2 = 5	CO, SiO, ...	Y-Y
9	V-shaped	<0.018	4.0	3.8×10^{15}	40	65	150	<12000	3.4×10^{-3}	10/(< 6) > 1.7	CO	Y-N
10	displaced	0.045	...	3.3×10^{15}	42		N-N
11	displaced	0.115	N-N
12	displaced	0.080	Y--
13	pillar	0.050	2.4	1.3×10^{15}	38		Y--
14	cavity	0.070	1.0	1.2×10^{15}	20		Y--
15	cavity	0.060	1.5	0.3×10^{15}	30	30						Y--
16	~peak	<0.004	2.0	0.9×10^{15}	25	31	100	1700	1.1×10^{-4}	10/4 = 2.5	CO, SiO, ...	YYN

^a Continuation from Table 9.5. Information for the columns: (1) identification number as in Table 9.5; (15) morphology of the NH₃ emission; (16) offset (in pc) of the cm source with respect to the NH₃ gas emission, for sources directly associated with a peak of ammonia emission we assumed an accuracy uncertainty of 1''; (17) linewidth (in km s⁻¹) of the ammonia emission, for sources not directly associated with a clump we list the linewidth of the emission closer to the cm source; (18) ammonia column density in (cm⁻²), for sources not associated with a clump we list the column density of the ammonia gas closer to the cm source; (19) rotational temperature (in K) estimated from the NH₃ (1,1) and (2,2) observations with the VLA; (20) rotational temperature (in K) derived from the CH₃CN (6_K-5_K) transitions, observed with the IRAM 30 m (Sánchez-Monge, priv. comm.); (21) rotational temperature (in K) derived from the CH₃CN (12_K-11_K) transitions, observed with the SMA; (22) size (in AU) of the hot core; (23) momentum rate of the outflow (in M_{\odot} km s⁻¹ yr⁻¹); (24) collimation of the outflow estimated from the axis ratio; (25) molecular species detected in the outflow; (26) masers (H₂O, OH, CH₃OH) associated with the outflow (Y: yes, N: no, -: not observed).

9. Towards an evolutionary sequence

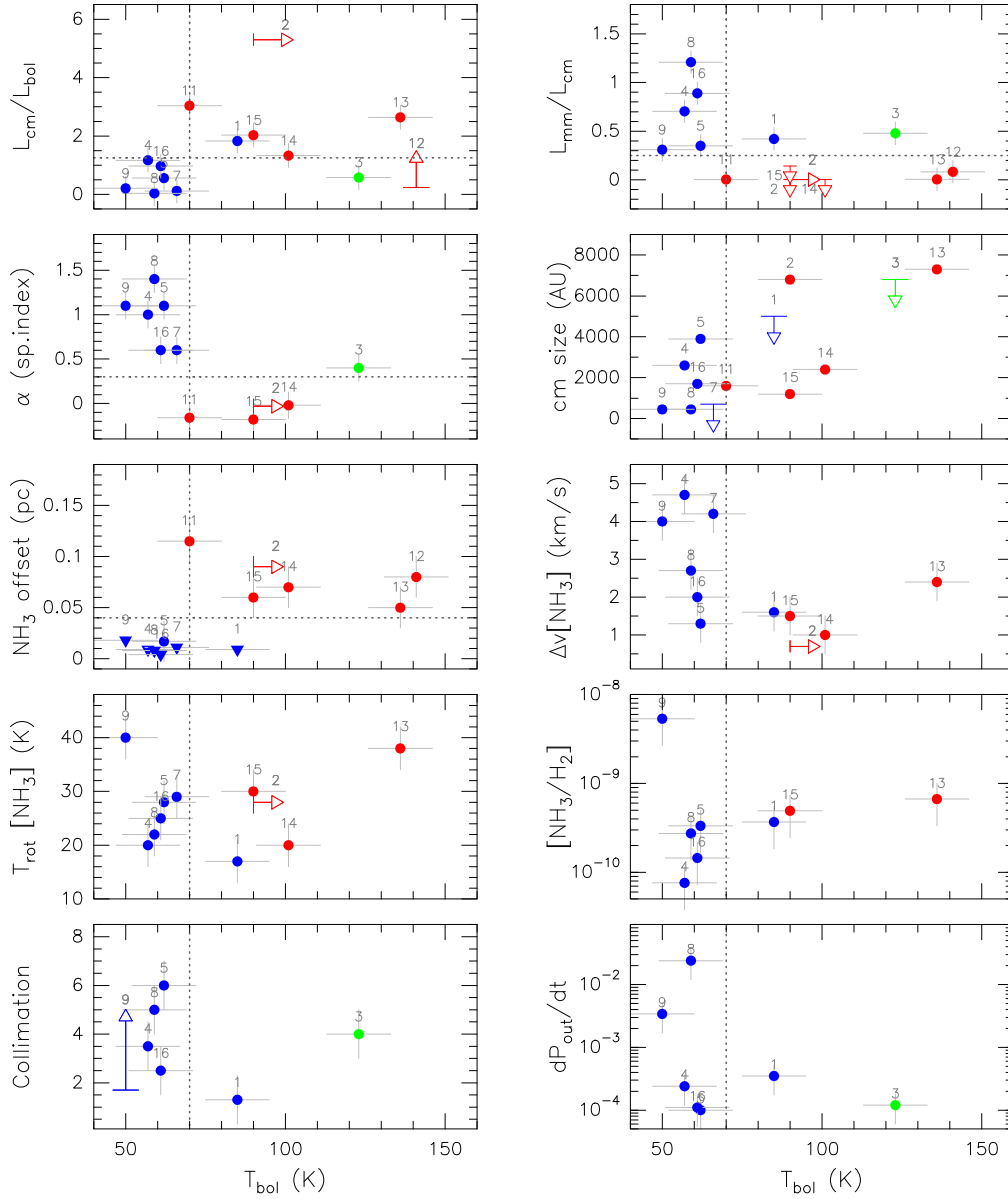


Figure 9.6: Graphics of several parameters versus T_{bol} . From left to right and top to bottom, we present the $L_{\text{cm}}/L_{\text{bol}}$ (in 10^{-3} mJy kpc²/ L_{\odot}), the $L_{\text{mm}}/L_{\text{cm}}$ (in mJy kpc²/Jy kpc²), the cm spectral index, the cm source size, the offset between the NH₃ peak and the cm source, the ammonia linewidth, the rotational temperature derived from ammonia, the abundance of ammonia with respect to H₂, the collimation of the outflow, and the outflow momentum rate (in M_{\odot} km s⁻¹ yr⁻¹). Numbers correspond to the identification number of each centimeter continuum source. Blue dots correspond to those centimeter sources associated with outflow emission (plus the I19035–VLA2 source; see text). Red dots correspond to those centimeter sources not associated with outflow emission. The green dot corresponds to the case of I04579–VLA1. Dotted lines correspond to different thresholds that divide the sources in groups.

It is worth remembering that each of the parameters plotted in the following figures, has been obtained from different star formation tracers, at different frequencies, and tracing different components (e. g., ionized gas, dust, dense gas, outflow, infrared), assessing thus different aspects of the star formation process. In the following figures there is a number located at the top of each dot (data), corresponding to the identification number for the centimeter continuum source (see Table 9.1 or 9.5). Furthermore, we have used different colors for the dots to make easier the discussion. Blue dots correspond to those centimeter sources associated with outflow emission, plus the I19035–VLA2 source, which, despite the lack of interferometric outflow observations, it is highly probable that it is associated with a molecular outflow (see Chapter 6 for more details). Red dots correspond to those centimeter sources not associated with outflow emission. Finally, the green dot corresponds to the particular case of I04579–VLA1 for which we do not have a dataset comparable to the datasets of the other sources (see Chapter 7).

Figure 9.6 shows the results of the plots of the parameters of Tables 9.5 and 9.6 with respect to T_{bol} . From the figure, it is remarkable the fact that the sources driving no outflows (red dots) in general have larger bolometric temperatures, compared to the sources driving outflows (blue dots), indicating that the outflow-driving sources tend to be more embedded and fainter in the infrared, thus being probably less evolved. Furthermore, for certain parameters the sources are joined up into two groups, one associated with smaller bolometric temperatures and a given value of the parameter, and the other group, of larger values of bolometric temperature, showing a different value of the parameter. In particular, the parameters $L_{\text{cm}}/L_{\text{bol}}$, $L_{\text{mm}}/L_{\text{cm}}$, the NH_3 offset, and the centimeter spectral index seem to success fully in separate into two groups the sources of our sample. The other parameters do not separate so clearly the sample. For example, the average centimeter source size of the sources driving outflows is < 4000 AU, and the size of UCH II regions covers the range 2000–8000 AU. Concerning T_{rot} , Δv , and the outflow parameters (\dot{P} and collimation) it is not obvious their relation with T_{bol} , and we will discuss them in subsequent sections. Finally, since the behavior of the NH_3 abundance in massive star-forming regions involves complex physical and chemical processes (e. g., Busquet 2010), we refrain from considering this parameter for further discussion in this work.

To summarize, Figure 9.6 shows that there are mainly four parameters ($L_{\text{cm}}/L_{\text{bol}}$, $L_{\text{mm}}/L_{\text{cm}}$, NH_3 offset, and cm spectral index) which seem to separate the sources with small T_{bol} from the sources with larger T_{bol} . The advantage of these 4 parameters is that they are easily determined from the observations (considering that L_{bol} is known) and easily comparable among different samples of sources. This is not the case of T_{bol} , for which one needs be sure to equally sample the SED of the objects that are being compared, as T_{bol} depends on the sampling of the SED (Kauffmann et al. 2008)³. Thus, to investigate a 4-dimension parameter space we will do 2-dimension projections plotting each one of

³Note that the SEDs of the sources of this work are sampled wuite similarly for most of the sources (see Section 9.3) and thus T_{bol} is comparable among them.

9. Towards an evolutionary sequence

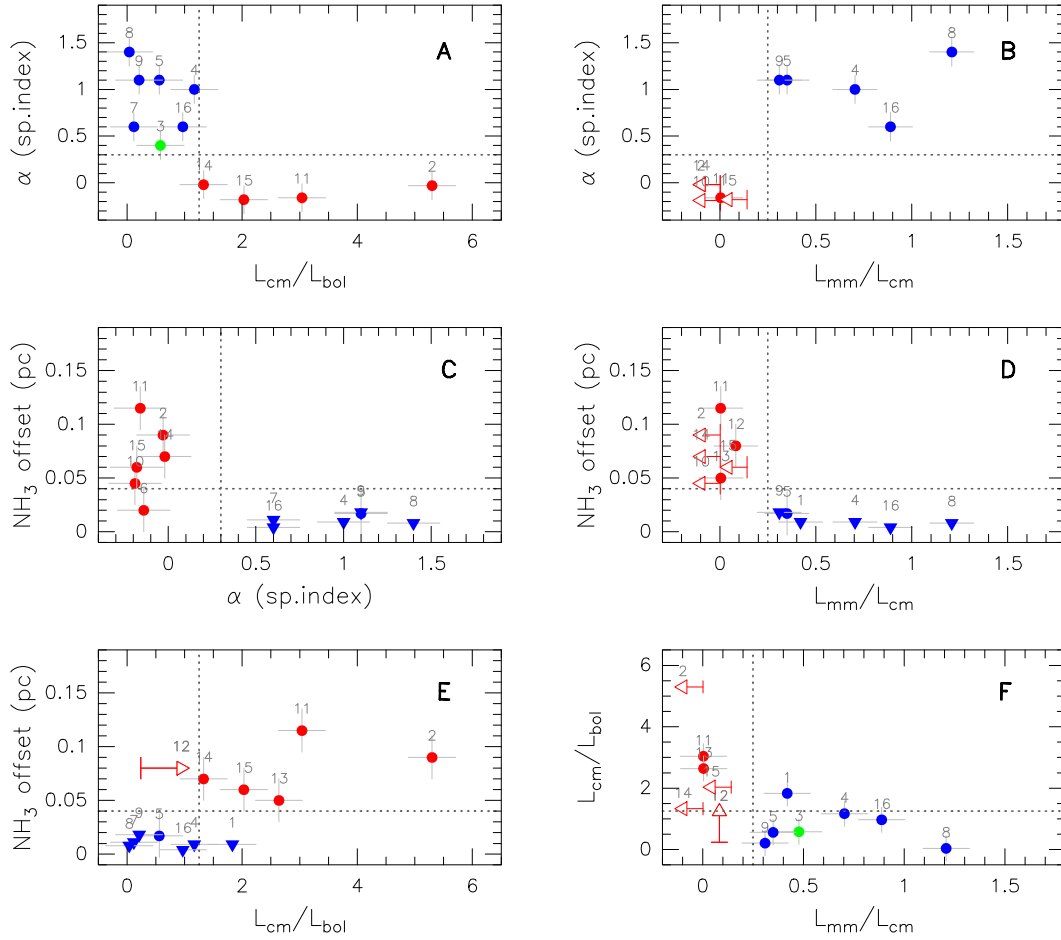


Figure 9.7: Graphics of the four main parameters discussed in the text: $L_{\text{cm}}/L_{\text{bol}}$, $L_{\text{mm}}/L_{\text{cm}}$, NH_3 offset, and cm spectral index. Symbols as in Figure 9.6. See text for more details and interpretation of each panel.

these 4 parameters against another parameter, in a similar way to the color-color diagrams in the infrared or optical. The six 2-D projections of this 4-D parameter space are plotted in Figure 9.7.

Our sample of sources is well split up into two groups for the six panels of Figure 9.7, and these two groups correspond to the outflow driving sources and the no-outflow sources. For example, from panel A (spectral index vs $L_{\text{cm}}/L_{\text{bol}}$) it is seen that the sources with larger cm spectral index are also the sources with fainter centimeter luminosity, suggesting that the fainter ionized gas (relative to L_{bol}) is typically associated with partially optically thick emission (cm spectral index larger than 0.3), while the sources with stronger cm continuum emission (relative to L_{bol}) typically show optically thin emission. In addition, the sources with larger cm spectral index show the largest millimeter luminosities (relative

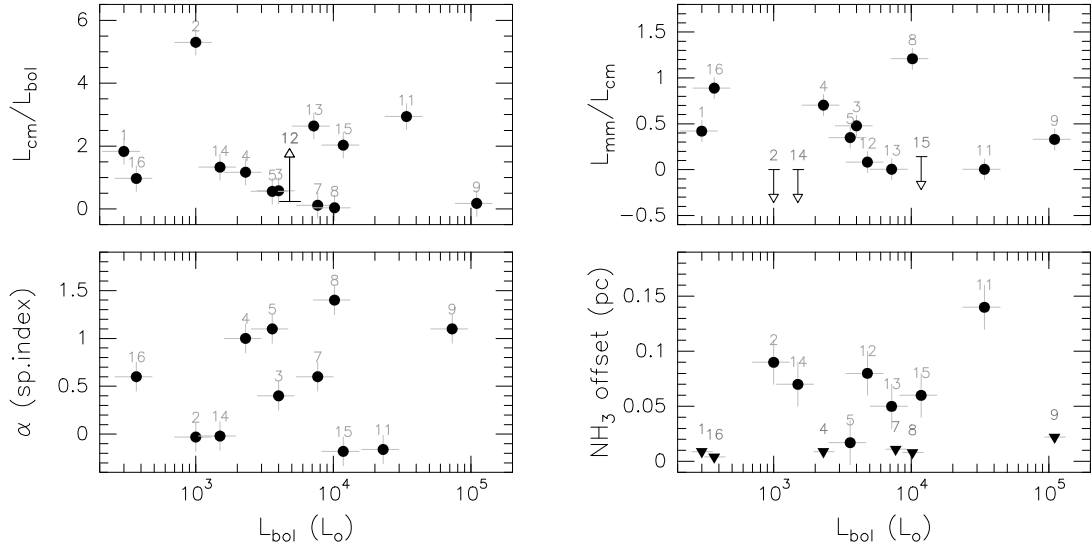


Figure 9.8: Graphics of $L_{\text{cm}}/L_{\text{bol}}$ (in $10^{-3} \text{ mJy kpc}^2/L_{\odot}$), $L_{\text{mm}}/L_{\text{cm}}$ (in $\text{mJy kpc}^2/\text{Jy kpc}^2$), cm spectral index, and NH_3 offset (in pc), versus the bolometric luminosity (in L_{\odot}). Data (black dots) obtained from Tables 9.5 and 9.6. Numbers correspond to the identification number of each centimeter continuum source. No clear correlations are found in these graphics, indicating that the data do not have biases with respect to the bolometric luminosity.

to L_{cm} , see panel B), and are found associated with an NH_3 core (see panel C), and the opposite behavior is found for the sources with no outflows (faint L_{mm} and large NH_3 offset). Thus, the cm spectral index seems to move from optically thick (> 0.3) to optically thin (-0.1) as the nascent protostar progressively gets rid of its natal cloud. The relation between the millimeter emission and the NH_3 emission is eminent in panel D, where the sources with strong L_{mm} (relative to L_{cm}) or with a large amount of dust associated (blue dots) are also the sources found embedded in an NH_3 core. Finally, as expected from the previous trend, panels E and F indicate that the faintest centimeter sources are found embedded in dust and dense NH_3 gas. Therefore, sources driving outflows (blue dots) are in general associated with faint and optically thick centimeter emission which is embedded in dense gas and dust, while sources with no outflows (red dots) seem to be rather associated with strong and optically thin centimeter emission and small amounts of gas and dust. At this point it is important to note that the faint optically thick cm sources are most likely tracing thermal radiojets and/or hypercompact H II regions, while the strong optically thin centimeter sources seem to be more evolved ultracompact H II regions, already in the process of dispersing the natal cloud.

As a final test for the validity of these four parameters, we must ensure that biases are not affecting our conclusions. The main biases can be produced by the different distances and bolometric luminosities of our sample. In Figures 9.8 and 9.9, we show the plots of

9. Towards an evolutionary sequence

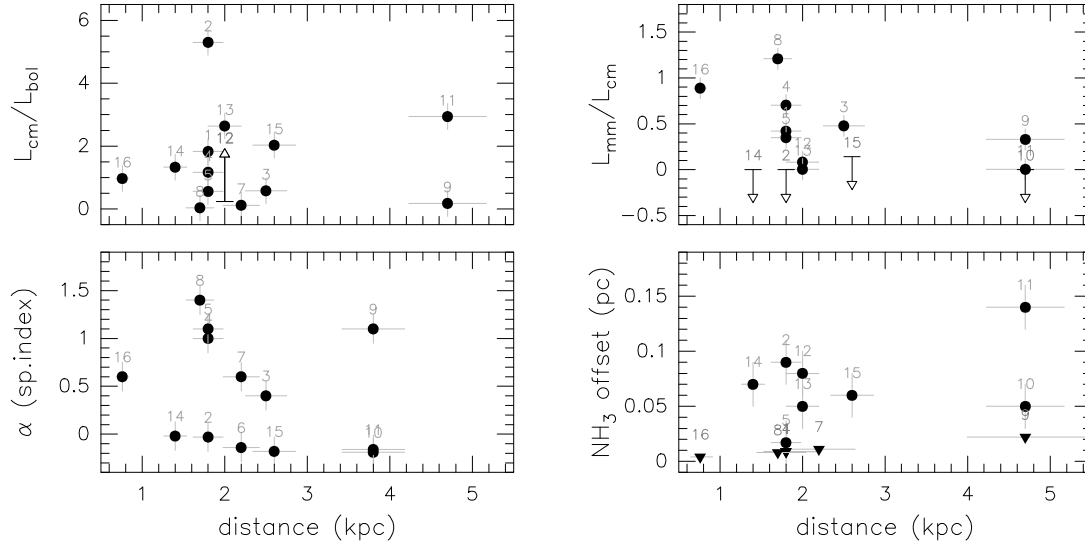


Figure 9.9: Graphics of $L_{\text{cm}}/L_{\text{bol}}$ (in $10^{-3} \text{ mJy kpc}^2/L_{\odot}$), $L_{\text{mm}}/L_{\text{cm}}$ (in $\text{mJy kpc}^2/\text{Jy kpc}^2$), cm spectral index, and NH_3 offset (in pc), versus the distance (in kpc). Data (black dots) obtained from Tables 9.5 and 9.6. Numbers correspond to the identification number of each centimeter continuum source. No clear correlations are found in these graphics, indicating that the data do not have biases with respect to the heliocentric distance of the source.

the four parameters ($L_{\text{cm}}/L_{\text{bol}}$, $L_{\text{mm}}/L_{\text{cm}}$, spectral index, and NH_3 offset) with respect to the bolometric luminosity and to the heliocentric distance. No clear correlations are found in these graphics, indicating that there are no biases (in distance and L_{bol}) in our list of parameters. Thus, the four selected parameters seem to be well-suited to separate the most embedded massive protostars.

In the following we will discuss the general properties of outflows, hot core and dense gas NH_3 emission for the sample of massive star-forming regions studied in this work.

9.4.2 Outflow properties

In the previous section we have seen that the sources with faint and optically thick centimeter emission are the sources driving outflows (blue dots in Figure 9.7), and that these sources are deeply embedded in dust and gas. This would suggest that the sources driving outflows should have the smallest T_{bol} . In Figure 9.10 we test this relation, finding that in general outflow-driving sources have small T_{bol} ($< 70 \text{ K}$) and sources without outflows have large T_{bol} ($> 70 \text{ K}$). However, a couple of sources (I00117-MM1 and I04579) are associated with outflows and have bolometric temperatures in the range 90–120 K, indicating that the outflow phase is still active when the infrared emission starts to be important compared to the (sub)millimeter emission.

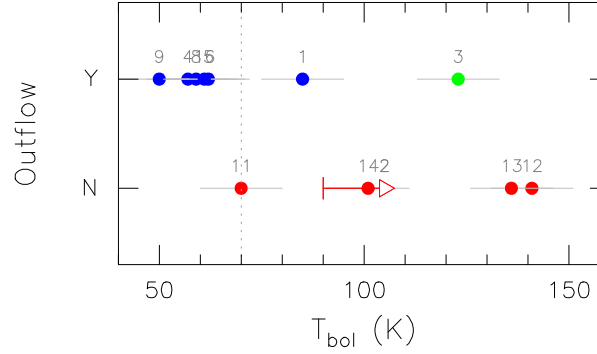


Figure 9.10: Presence/absence of outflow against bolometric temperature. Sources with a small T_{bol} are driving molecular outflows, while, generally, sources with a larger T_{bol} are not found associated with outflows.

Since we have found that several parameters (T_{bol} and the 4 parameters discussed in Figure 9.7, see Section 9.4.1) seem to be appropriate to separate between the most embedded sources and sources deprived of gas and dust, we consider here the possibility that these parameters allow us to search for evolutionary trends in the outflow properties (only available for the most embedded sources).

For the low-mass star formation case, the outflow momentum rate has been proposed to decrease as time evolves (e.g., Bontemps et al. 1996; Wu et al. 2004). In Figure 9.11, we plot the outflow momentum rate vs T_{bol} on one hand, and $L_{\text{cm}}/L_{\text{bol}}$ and the cm spectral index on the other hand, these last as indicators directly related to the emission of possible thermal radiojets (which is supposed to be related to the outflow momentum rate, see Section 9.1 and Figure 9.4). As seen in Figure 9.11 (left-column panels), the two sources with largest outflow momentum rate (G75-CORE and I20126) are on average the sources with smallest T_{bol} , smallest $L_{\text{cm}}/L_{\text{bol}}$, and largest cm spectral index (as expected for the less evolved sources), possibly indicating that, as in the low-mass case, the outflow momentum rate could be decreasing with time. However, it is important to note that the two sources with largest \dot{P} are exactly the two sources with largest L_{bol} (see Table 9.5), and in fact a trend of \dot{P} with L_{bol} has been observed in the high-mass regime in many cases (e.g., Beuther et al. 2002c; Wu et al. 2005; Takahashi et al. 2008), although using single-dish telescopes. Clearly, a larger number of regions is required to properly study these relations with high angular resolution.

Another outflow parameter which has been proposed to evolve with time, both from the theoretical (e.g., Shang et al. 2006) and the observational (e.g., Jørgensen et al. 2007; Seale and Looney 2008) point of view, is the collimation of the outflow, supposed to decrease (angle opening) with time. For the high-mass regime, some authors (e.g., Beuther and Shepherd 2005; Keto 2007) have proposed a similar trend. In Figure 9.11 (right-column panels) we present the collimation against T_{bol} , $L_{\text{cm}}/L_{\text{bol}}$, and the cm spectral index.

9. Towards an evolutionary sequence

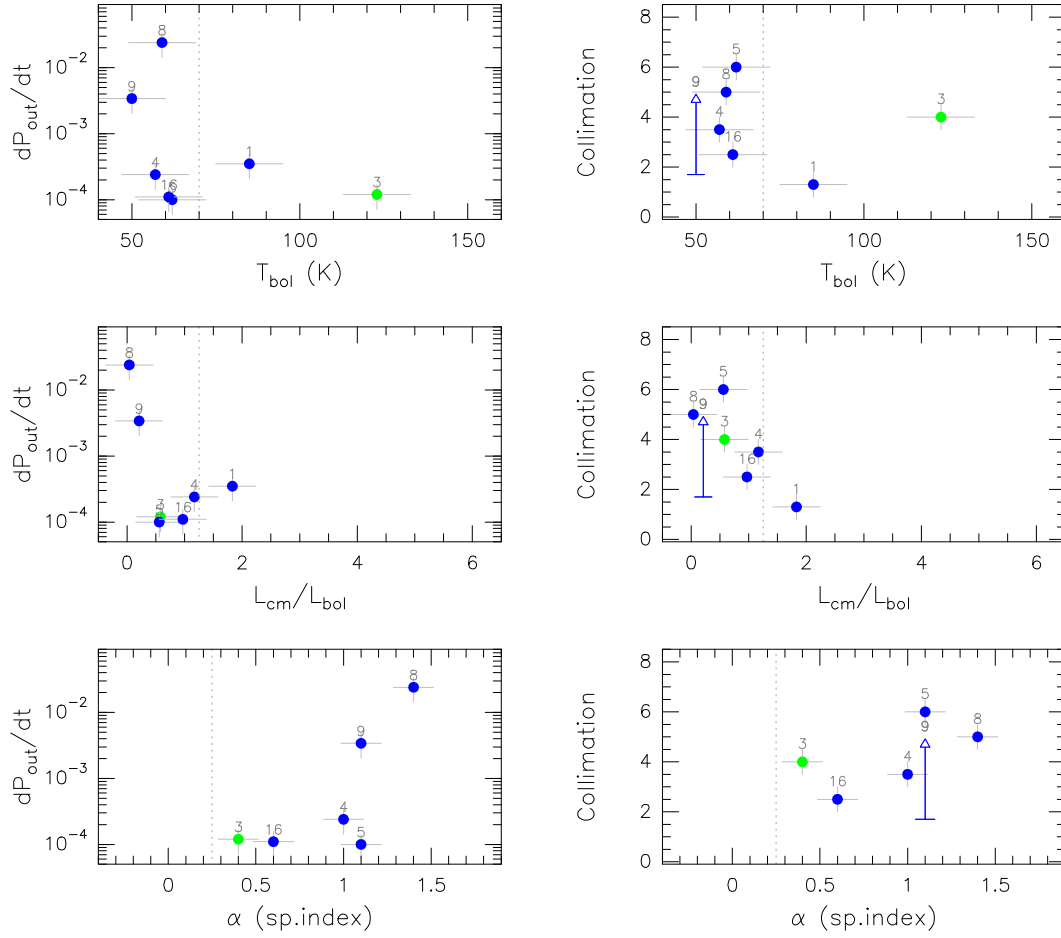


Figure 9.11: Graphics of the outflow momentum rate (*left-column panels*) and collimation (*right-column panels*) against the bolometric temperature, $L_{\text{cm}}/L_{\text{bol}}$, and the cm spectral index. Vertical dotted line typically separate outflow-driving and no-outflow sources (blue and red dots in Figures 9.6 and 9.7). Note that we have no plotted red dots, since these sources are not associated with outflows.

Although we would need a larger number of sources to make a statistical study, the plot of collimation against $L_{\text{cm}}/L_{\text{bol}}$ shows a possible trend of larger collimation with fainter centimeter emission (relative to L_{bol}), which should be further studied. The outflow collimation vs T_{bol} and the spectral index do not show any clear trend, and we would need a larger sample to study if sources with less collimated outflows show higher values of T_{bol} , and if there is a relation of the cm spectral index with the collimation of the outflow.

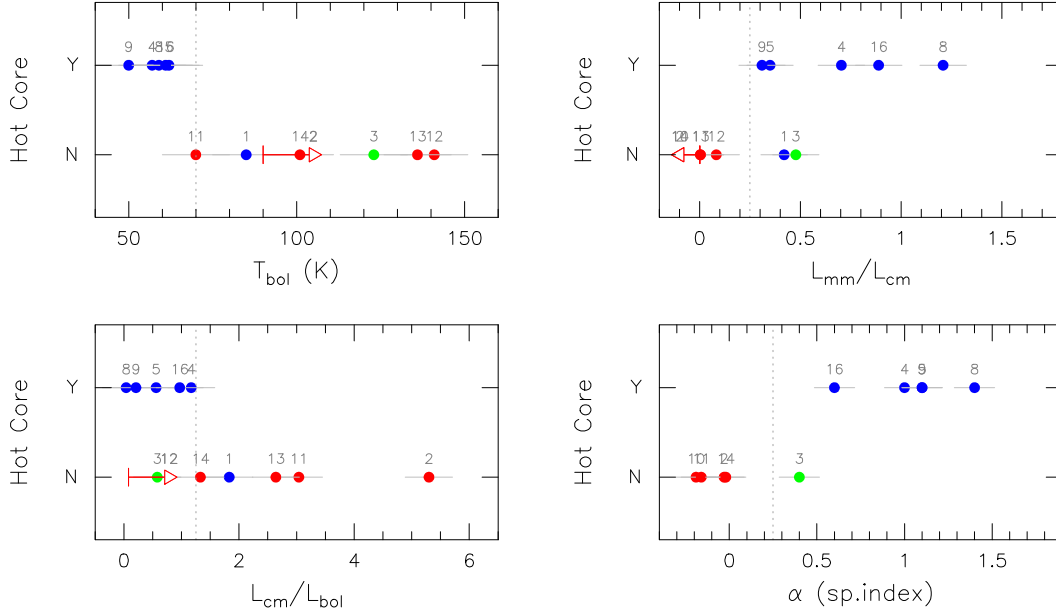


Figure 9.12: Presence/absence of hot molecular core versus T_{bol} , $L_{\text{mm}}/L_{\text{cm}}$, $L_{\text{cm}}/L_{\text{bol}}$, and cm spectral index. Symbols as in Figure 9.6. See Section 9.4.3 for more details and interpretation of each panel.

9.4.3 Hot molecular core properties

We study in this section the presence/absence of hot core in our source sample related to other parameters discussed in previous sections (see Section 9.4.1). As seen in Figure 9.12, all the sources with hot cores have small T_{bol} (< 70 K), have strong $L_{\text{mm}}/L_{\text{cm}}$ (thus are embedded in dust), and show faint and (partially) optically thick centimeter emission. Interestingly, all these sources with hot core emission are driving outflows, indicating that both phenomena (outflow and hot core) seem to be co-eval. However, there are two sources (I00117-MM1 and I04579) associated with molecular outflows and with no hot core emission. It is worth noting that these two sources are the same two that show bolometric temperatures > 90 K and still outflow emission. Consequently, our data seem to suggest that the hot core phase could be short-lived and may vanish before the outflow phase.

9.4.4 Ammonia properties

Finally, we will search for evolutionary trends in the dense gas physical parameters derived from the ammonia emission, in particular the rotational temperature derived from the (1,1) and (2,2) ammonia inversion lines and the linewidth.

We study now how the ammonia linewidth can be affected by the presence of a newly-

9. Towards an evolutionary sequence

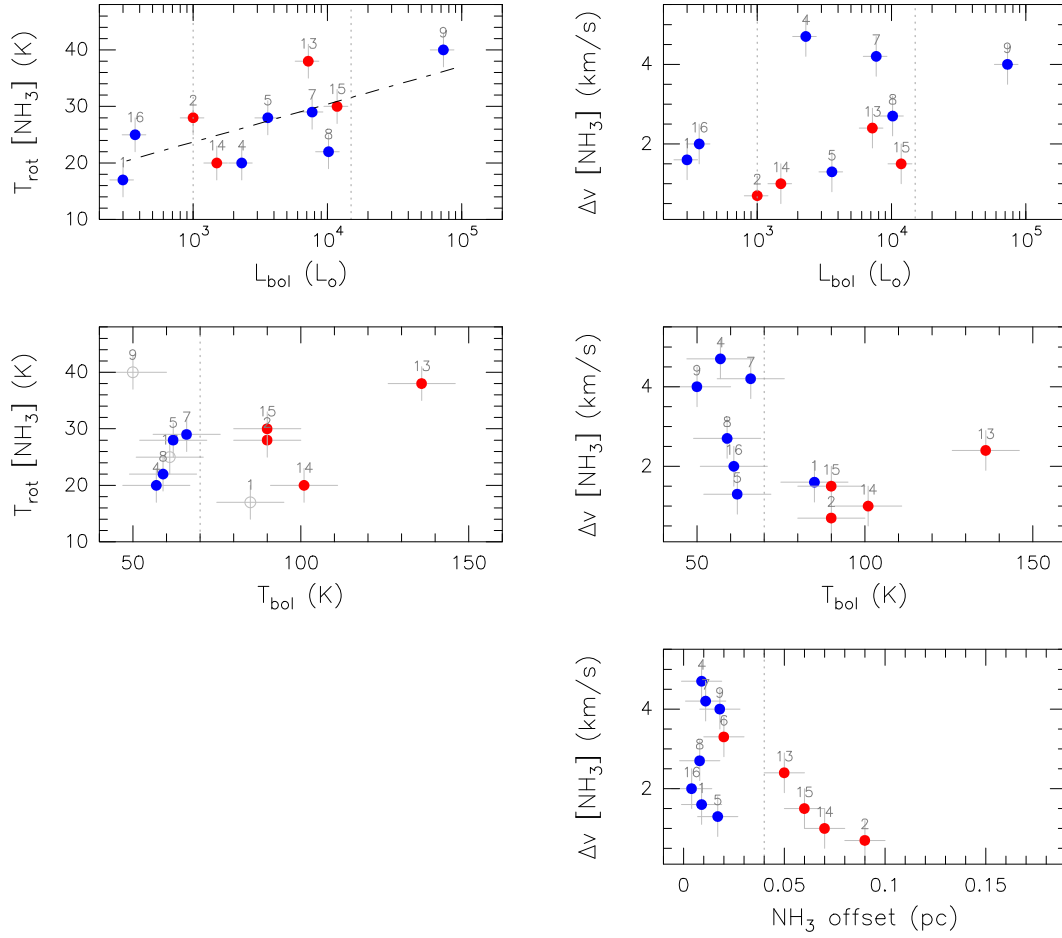


Figure 9.13: Graphics of the ammonia rotational temperature (*left-column panels*) against L_{bol} and T_{bol} ; and linewidth (*right-column panels*) against L_{bol} , T_{bol} and NH_3 offset. Symbols as in Figure 9.6. See Section 9.4.4 for more details.

born massive protostar (see Figure 9.13 right-column panels). In this case (top-right panel) there is no a clear trend between the linewidth and the luminosity of the young stellar object. However, it is worth noting (middle-right panel) that on average sources with larger T_{bol} are associated with less perturbed dense gas (with typical linewidths of 1.7 km s^{-1}), while sources with smaller T_{bol} and driving outflows are associated with dense gas showing larger linewidths (up to $\sim 4 \text{ km s}^{-1}$). In addition (see bottom-right panel), the dense gas surrounding UCHII regions has larger linewidths if it is found closer to the massive protostar, and linewidth decreases as the gas is found spatially farther away from the massive YSO. Thus, it seems that the dense gas is more perturbed when it is closely associated with the massive protostar (typically driving outflows) and when it is less evolved. Among possible mechanisms of line broadening for the sources of our sample,

mainly infall and outflow, we suggest that outflows can play an important role as seen in previous chapters that the NH_3 seems to be perturbed by the passage of the outflow.

Regarding T_{rot} , in Figure 9.13 (top-left panel) we find that sources with large luminosities (e.g., G75-CORE) show higher rotational temperatures (~ 40 K), while less-luminous objects (e.g., I00117-MM1 and I22198) are embedded in colder dense gas ($T_{\text{rot}} \sim 22$ K). In fact, all the data seem to suggest a trend in which the temperature derived from the ammonia gas is directly related to the luminosity of the young stellar object. In order to avoid the effects of the luminosity and search for evolutionary trends, we decided to consider only those sources with similar bolometric luminosities (in the range between 10^3 and $10^4 L_{\odot}$). In middle-left panel, we do not find any clear trend of T_{rot} evolving with T_{bol} , indicating that T_{rot} seems to be mainly determined by the luminosity of the object rather by an evolutionary effect. The main heating mechanisms of dense gas for sources of our sample seem to be radiative heating from a nearby massive YSO (e.g., I00117-UCH II, I20293-UCH II, I22134) or from embedded internal objects (e.g., I00117-MM1, I05358, G75-CORE), or heating through shocks of molecular outflows (e.g., I22198, G75-CORE, AFGL5142, I20126).

9.4.5 Final discussion: evolutionary stages

In this last Chapter of the thesis, we have analyzed different massive star formation tracers, with the aim of searching for signposts of different evolutionary stages in the process of formation of a massive star. The sources of our sample can be mainly divided into two well-differentiated groups: on one hand, sources with faint and (partially) optically thick centimeter emission are found embedded in dense gas and dust, driving outflows and in most of the cases associated with hot molecular cores; while on the other hand, sources with strong and optically thin centimeter emission, do not have dense gas or dust directly associated, but dispersed surrounding them, and are not found associated with outflows or hot cores, suggesting they are more evolved. This suggests the following question: which is the main ionizing mechanism dominating in each of these two groups of sources?

In Section 9.1, we have shown a plot of the centimeter luminosity (L_{cm} or $S_{\nu}d^2$) against the bolometric luminosity (L_{bol}) which can be a useful tool to answer this question. In Figure 9.14, we show this kind of plot (similar to that shown in Figure 9.3) where three main distinct regimes can be identified: low-mass thermal radiojets, massive thermal radiojets, and photoionized H II regions (Anglada 1996, Anglada et al. in prep., Thompson 1984). For the low-mass star formation case (with luminosities $< 100 L_{\odot}$) it seems acceptable to assume that the (thermal) radiocontinuum emission we detect toward protostars is due to the presence of thermal radiojets. However, for the high-mass case, the picture becomes a bit more complex. On one hand, for the most luminous objects ($> 10^5 L_{\odot}$) the centimeter luminosity expected for a thermal radiojet is more than 2 orders of magnitude fainter than the luminosity expected for the Lyman continuum. Thus, the measurement of the centimeter emission for such a luminous object should allow us to distinguish which is the

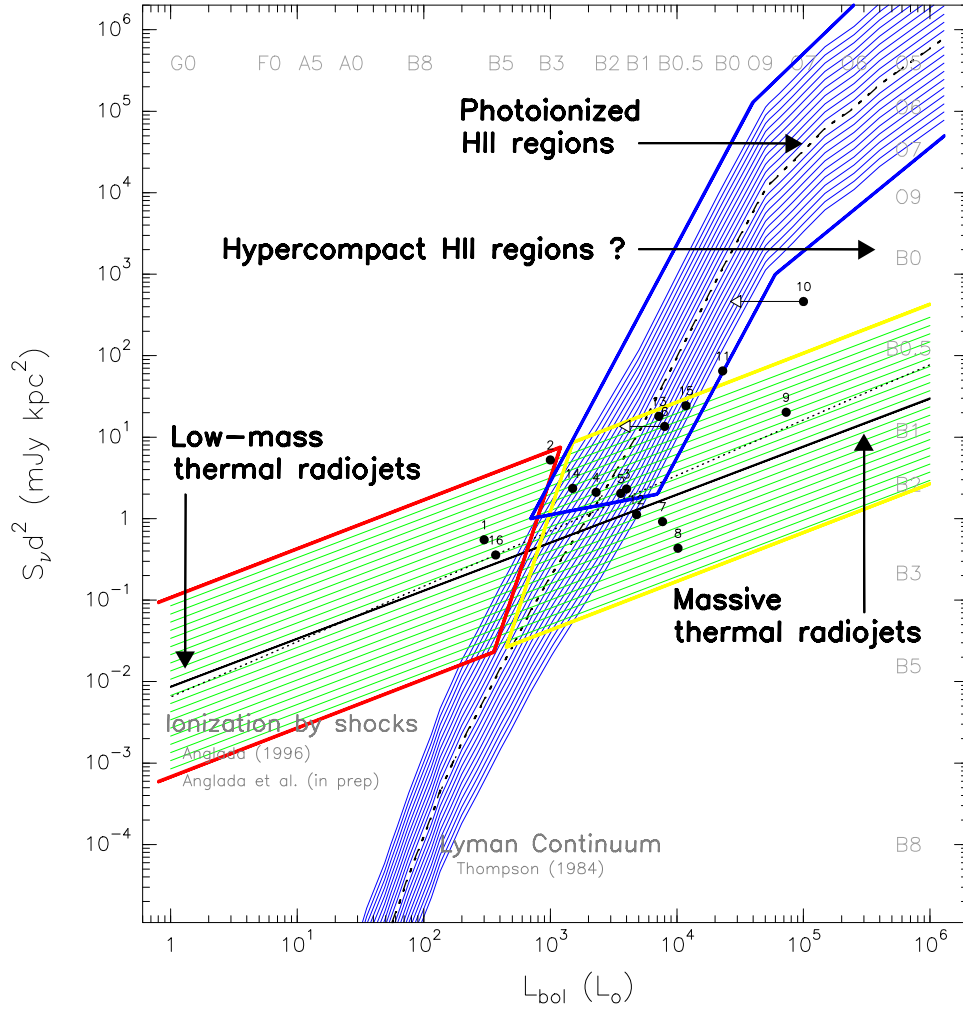


Figure 9.14: Observed radio continuum luminosity, $S_\nu d^2$, as a function of the bolometric luminosity, L_{bol} , as in Figure 9.3. We indicate the regions in which it is expected to find low-mass thermal radiojets, massive (intermediate/high-mass) thermal radiojets, and photoionized H II regions. The hypercompact H II regions can be probably found in the region in between the massive thermal radiojets and more evolved H II regions.

mechanism that produces the ionization. However, in the very first stages of massive star formation the development of an H II region could be slowed down due to a high mass accretion rate, resulting in a trapped or quenched H II region (Keto 2007; Walmsley 1995) with a faint centimeter luminosity (similar to that expected for a thermal radiojet). Thus, for a luminous object with faint centimeter emission we cannot easily disentangle which mechanism produces the ionization. The new and upgraded instruments (such as EVLA and ALMA), providing a sensitivity more than one order of magnitude better than the

current instrumentation, would allow us to study the emission and morphology of these objects helping to understand the ionizing mechanism.

On the other hand, for objects with luminosities from 10^3 to $10^4 L_{\odot}$, the expected centimeter emission from thermal radiojets is overlapping with the centimeter luminosity expected for the Lyman continuum, and thus the centimeter emission alone is not enough to elucidate the ionization mechanism nor the evolutionary stage. Consequently, for regions in this luminosity range, information from other star formation tracers (outflow, dense gas, hot core, dust, SED) is essential to have a first approximation on the nature of these sources.

As shown in Sections 9.4.1 to 9.4.4, information on the dust, dense gas, outflow, hot core and infrared has allowed us to distinguish groups of sources with different properties suggesting their evolutionary stage. In particular we used the ‘color-color’ diagrams presented in Figure 9.7, and information about the presence/absence of hot cores and outflows. All the plots that can be done with the main parameters from Tables 9.5 and 9.6, are *statistically* summarized in the table shown in Figure 9.15. The table is divided by a line of grey cells: the numbers shown in the bottom-left cells refer to the total number of sources (of our sample) that fulfill the criteria of each pair of parameters, while in the top-right cells of the table we list the percentage of sources. By using this table, one can easily identify how many sources have, for example, a bolometric temperature < 70 K and a $L_{\text{cm}}/L_{\text{bol}}$ smaller than $1.25 \times 10^{-3} \text{ mJy kpc}^2/L_{\odot}$ (in this example: 6 sources, or a 43% of the total of sources). In the cells with the percentage values (top-right cells with respect to the line of grey cells), we have bolded those percentages that are significant (over a 33%) just to find easier the correlations discussed in previous sections. The bimodality in each pair of parameters turns evident, with typical correlation factors of $\sim 80\text{--}90\%$. We have marked in blue the cells that refer to the ‘color-color’ diagrams of Figure 9.7, in red the cells that compare the main 4 parameters (‘color-color’ diagrams) with T_{bol} , and in green the cells that provide information about the presence/absence of hot core and outflow. In summary, by analyzing different star formation tracers one can make a first estimate, using the table, of the evolutionary stage of a particular massive protostar.

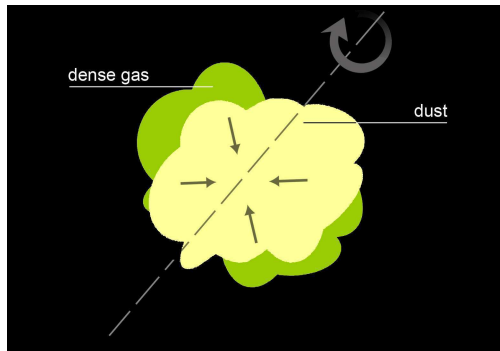
After this analysis, and focusing first on the ionized gas (Figure 9.14), we propose a scenario where the forming massive protostar, which is deeply embedded in an infalling envelope and driving outflows, first ionizes the surrounding medium through shocks. This object would be located in the ‘massive thermal radiojet’ box (yellow box) of Figure 9.14. As the forming massive protostar grows in mass, it eventually will start to radiate UV photons and ionize the medium creating an hypercompact H II region. This region, at the beginning, could be trapped or quenched, but when infall has decreased enough it will develop to a classical H II region. This final object would appear in the ‘photoionized H II region’ box in the plot (blue box in Figure 9.14). Therefore, we would expect to find some sources in the intermediate region of the plot (between the yellow and blue boxes)

9. Towards an evolutionary sequence

		T_{bol}		$L_{\text{cm}}/L_{\text{bol}}$		α		$L_{\text{mm}}/L_{\text{cm}}$		NH_3 offshot		core		outflow		red/IR		
		<70	≥ 70	<1.25	≥ 1.25	≥ 0.3	<0.3	<0.25	≥ 0.25	<0.04	≥ 0.04	Y	N	Y	N	MIR	NIR	red
T_{bol}	<70			43	0	55	0	0	39	46	0	42	0	42	0	21	21	0
	≥ 70			14	43	9	36	46	15	8	46	0	58	16	42	0	37	21
$L_{\text{cm}}/L_{\text{bol}}$	<1.25	6	2			64	0	8	46	46	8	42	16	50	8	21	37	0
	≥ 1.25	0	6			0	36	38	8	8	38	0	42	8	34	0	21	21
α	≥ 0.3	6	1	7	0			0	55	50	0	50	10	55	0	23	32	0
	<0.3	0	4	0	4			45	0	8	42	0	40	0	45	15	15	15
$L_{\text{mm}}/L_{\text{cm}}$	<0.25	0	6	1	5	0	5			0	46	0	46	0	46	7	21	21
	≥ 0.25	5	2	6	1	6	0			54	0	38	15	54	0	21	30	0
NH_3 offs	<0.04	6	1	6	1	6	1	0	7			42	8	50	0	27	27	0
	≥ 0.04	0	6	1	5	0	5	6	0			0	50	0	50	6	20	20
hot core	Y	5	0	5	0	5	0	0	5	5	0			38	0	23	15	0
	N	0	7	2	5	1	4	6	2	1	6			16	46	8	31	23
outflow	Y	5	2	6	1	6	0	0	7	6	0	5	2			23	31	0
	N	0	5	1	4	0	5	6	0	0	6	0	6			8	15	23
red/IR	MIR	3	0	3	0	3	2	1	3	4	1	3	1	3	1			
	NIR	3	5	5	3	4	2	3	4	4	3	2	4	4	2			
	red	0	3	0	3	0	2	3	0	0	3	0	3	0	3			
		Number of sources																
		Percentages																

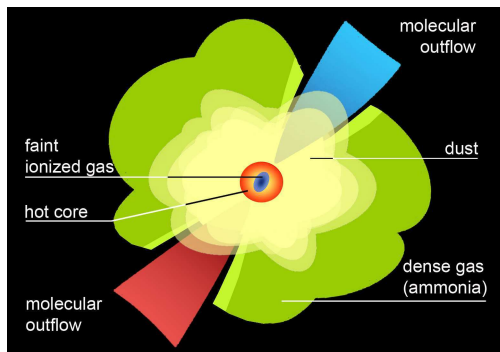
Figure 9.15: In this Table we summary the statistics obtained in this observational work. We show some of the main parameters estimated for each centimeter continuum source, presented in Tables 9.5 and 9.6, and discussed in Chapter 9. Definitions for each parameters are provided in Section 9.4. Units for each parameters: T_{bol} in K; $L_{\text{cm}}/L_{\text{bol}}$ in 10^{-3} mJy kpc²/ L_{\odot} ; α is the spectral index at centimeter wavelengths; $L_{\text{mm}}/L_{\text{cm}}$ in Jy kpc²/mJy kpc²; NH_3 offset in pc; hot core refers to yes or no hot molecular core signatures; outflow refers to yes or not molecular outflow emission; red/IR refers to source associated only with MIR (MIR), with MIR+NIR (NIR), with MIR+NIR and red emission from the DSS (red). In the bottom-left cells of the Table we show the number of centimeter sources, while in the top-right cells we show the percentage of sources. For example, by combining the T_{bol} and $L_{\text{cm}}/L_{\text{bol}}$ parameters we have found that 6 sources (43%) have a low T_{bol} and faint $L_{\text{cm}}/L_{\text{bol}}$; 2 sources (14%) have a high T_{bol} and faint $L_{\text{cm}}/L_{\text{bol}}$; and 6 sources (43%) have a high T_{bol} and strong $L_{\text{cm}}/L_{\text{bol}}$.

9.4. Towards an evolutionary sequence



- rotating and collapsing core
- dust and dense gas
- NO ionized gas

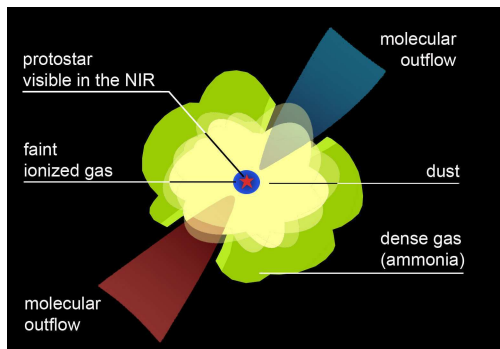
Sources of this thesis in this evolutionary stage



- faint ionized gas (thermal radiojet / HCHII region)
- strong dust emission
- embedded in dense gas
- molecular outflow
- hot molecular core
- small bolometric temperature

Sources of this thesis in this evolutionary stage

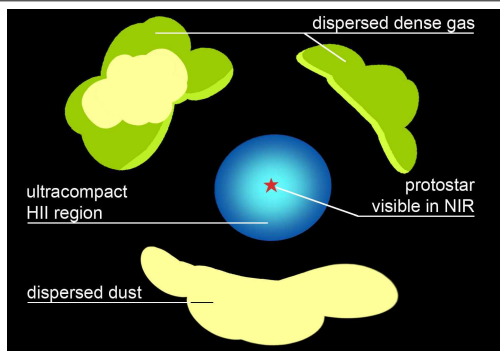
[AFGL5142 / I05358-MM1 / I19035-VLA2 / I20126 / G75-CORE / I22198-VLA2](#)



- faint ionized gas (thermal radiojet / HCHII region)
- associated with dust emission
- embedded in (less) dense gas
- molecular outflow
- large bolometric temperature
- protostar visible in the near-infrared

Sources of this thesis in this evolutionary stage

[I00117-MM1 / I04579-VLA1](#)



- strong ionized gas (UCHII region)
- dust and dense gas dispersed around the protostar
- NO molecular outflow
- large bolometric temperature
- protostar visible in the near-infrared

Sources of this thesis in this evolutionary stage

[I00117-UCHII / I20293-UCHII / I20343-IRS3 / I20293-IRS2 / G75-EAST / G75-UCHII / I22134-VLA1](#)

Figure 9.16: Sketch for the evolutionary stages proposed in this work.

9. Towards an evolutionary sequence

tracing possible evolutionary tracks from the massive thermal radiojets zone up to the photoionized H II regions zone.

This sequence, based on the ionized gas content, can be fitted within a more general context taking into account the different star formation tracers analyzed in this work. In Figure 9.16, we show a sketch of the main evolutionary stages that can be inferred from the results of this work. The *first stage* (top panel in the figure) would consist of a contracting and rotating massive dense core, with still no (or very faint) ionized gas emission, and thus not considered in this work. In the *second stage*, during the first phases in which ionized gas is detectable (second panel in the figure), the newly-formed massive protostar appears deeply embedded in dust and dense gas. The faint ionized gas likely tracing thermal radiojets or hypercompact H II regions has partially optically thick emission and a very small size. The forming star drives a molecular outflow that interacts (heating and perturbing) the dense gas as traced by ammonia, and is associated with hot molecular cores. Regarding the infrared properties, the protostar is generally not detected at near infrared wavelengths resulting in small bolometric temperatures. The *third stage* (corresponding to the third panel of the figure) would be mainly differentiated from the previous stage due to the absence of a hot core associated with the protostar. The source is still associated with faint centimeter continuum emission (from a radiojet or a HCH II region); appears embedded in (less) dust and dense gas; drives a molecular outflow (which is expected to be less energetic); and becomes visible in the near-infrared, resulting in larger bolometric temperatures. Finally, the *last stage* starts when the ionization of the massive (proto)star is dominated by the UV photons, and an ultracompact or compact H II region has developed (thus the main contribution to the centimeter emission comes from photoionization rather than ionization through shocks). The outflow activity (and accretion) has been halted, and the dust and dense gas do not appear associated with the UCH II region but surrounding it in cavities or pillar structures. The protostar is visible in the near-infrared (and in some cases in the optical), resulting in larger bolometric temperatures.

9.5 Future prospects: open questions

In this section, we suggest a few points and questions to take into account for further work aimed at better establishing the properties of different evolutionary stages in the formation of massive stars.

- **Improve statistics.** Several surveys of star formation tracers toward massive protostars have been carried out in the last decades, most of them using single-dish telescopes or low angular resolutions. However, the complexity of the massive star-forming regions require high-angular resolution interferometric observations to understand the scenario in which massive stars form. A large sample (hundreds of sources?) studied in great detail is necessary to confirm and extend the results

presented in this thesis. We note that not only a large number of sources is important, but also a careful comparison of observations and results from the different regions, ensuring the use of the same techniques and methods in the analysis of the properties.

- **From radiojets to UCH II regions.** Different questions arise when considering the ionized gas content in massive star-forming sites. One of the main ‘open’ questions is based on the existence of UCH II regions driving molecular outflows. Although first (low angular resolution) observations suggested the association of UCH II regions with massive molecular outflows, the improvement in angular resolution thanks to the interferometers revealed that in several cases the outflows are not driven by the UCH II region but by YSOs located close to it. The results of our work also point in this direction (no UCH II regions driving outflows are found). If this scenario is confirmed, it would suggest that the transition between the phase in which the molecular outflow is active (with faint ionized gas likely coming from thermal radiojets or HCH II regions) and the phase in which an UCH II region dominates the radio continuum emission must be fast. More accurate observations, and models, are necessary to study and understand this transition between thermal radiojets or HCH II regions and the UCH II regions: when does the photoionization start to dominate over the ionization through shocks? Can radiojets be photoionized before the development of an H II region? Does the photoionization affect the properties of molecular outflows? Higher sensitivity and angular resolution observations provided by EVLA and ALMA will contribute for sure to answer these questions.
- **Hot molecular core phase.** Almost one half of the sources studied in this work (the presumably younger ones) have revealed hot molecular core signatures (large temperatures and a rich chemistry). Although the number of hot core detections has increased in the last years thanks to the advent of new instruments, several questions remain still open regarding this kind of objects: do all protostars (both low and high-mass) undergo the hot molecular core phase? When does it start and how long does it take? What is the mechanism that produces this emission (shocks or internal heating)? Are there (important) differences between the hot corinos and the massive hot cores? Observational surveys of reliable hot core tracers toward large samples of sources will help to answer these questions.

Bibliography

- Alonso-Albi, T., Fuente, A., Crimier, N., Caselli, P., Ceccarelli, C., Johnstone, D., Planesas, P., Rizzo, J. R., Wyrowski, F., Tafalla, M., Lefloch, B., Maret, S., and Dominik, C. (2010). Chemical study of intermediate-mass (IM) Class 0 protostars. CO depletion and N₂H⁺ deuteration. *Astronomy and Astrophysics*, 518:A52+.
- Altenhoff, W., Mezger, P. G., Wendker, H., and Westerhout, G. (1960). *Veroff. Univ. Sternwarte Bonn*, 59:48.
- Ando, K., Nagayama, T., Omodaka, T., Handa, T., Imai, H., Nakagawa, A., Nakanishi, H., Honma, M., Kobayashi, H., and Miyaji, T. (2010). Astrometry of Galactic Star-Forming Region ON2N with VERA: Estimation of the Galactic Constants. *ArXiv e-prints*.
- André, P., Ward-Thompson, D., and Barsony, M. (2000). From Prestellar Cores to Protostars: the Initial Conditions of Star Formation. *Protostars and Planets IV*, pages 59–+.
- Anglada, G. (1995). Centimeter Continuum Emission from Outflow Sources. In S. Lizano & J. M. Torrelles, editor, *Revista Mexicana de Astronomia y Astrofisica Conference Series*, volume 1 of *Revista Mexicana de Astronomia y Astrofisica*, vol. 27, pages 67–+.
- Anglada, G. (1996). Radio Jets in Young Stellar Objects. In A. R. Taylor & J. M. Paredes, editor, *Radio Emission from the Stars and the Sun*, volume 93 of *Astronomical Society of the Pacific Conference Series*, pages 3–7.
- Anglada, G., Estalella, R., Rodríguez, L. F., Torrelles, J. M., Lopez, R., and Cantó, J. (1991). A double radio source at the center of the outflow in L723. *Astrophysical Journal*, 376:615–617.
- Anglada, G., López, R., Estalella, R., Masegosa, J., Riera, A., and Raga, A. C. (2007). Proper Motions of the Jets in the Region of HH 30 and HL/XZ Tau: Evidence for a Binary Exciting Source of the HH 30 Jet. *Astronomical Journal*, 133:2799–2814.
- Anglada, G., Rodríguez, L. F., Cantó, J., Estalella, R., and Torrelles, J. M. (1992). Radio continuum from the powering sources of the RNO 43, HARO 4-255 FIR, B335, and PV Cephei outflows and from the Herbig-Haro object 32A. *Astrophysical Journal*, 395:494–500.

BIBLIOGRAPHY

- Anglada, G., Villuendas, E., Estalella, R., Beltrán, M. T., Rodríguez, L. F., Torrelles, J. M., and Curiel, S. (1998). Spectral Indices of Centimeter Continuum Sources in Star-forming Regions: Implications on the Nature of the Outflow Exciting Sources. *Astronomical Journal*, 116:2953–2964.
- Araya, E., Hofner, P., Goss, W. M., Linz, H., Kurtz, S., and Olmi, L. (2007). A Search for Formaldehyde 6 cm Emission toward Young Stellar Objects. II. H₂CO and H110alpha Observations. *Astrophysical Journal, Supplement*, 170:152–174.
- Araya, E., Hofner, P., Kurtz, S., Bronfman, L., and DeDeo, S. (2005). CH₃CN Observations toward Southern Massive Star-forming Regions. *Astrophysical Journal, Supplement*, 157:279–301.
- Araya, E., Hofner, P., Kurtz, S., Olmi, L., and Linz, H. (2008). Thermal Methanol Observations of the Outflow from the G31.41+0.31 Hot Molecular Core. *Astrophysical Journal*, 675:420–426.
- Araya, E. D., Kurtz, S., Hofner, P., and Linz, H. (2009). Radio Continuum and Methanol Observations of DR21(OH). *Astrophysical Journal*, 698:1321–1329.
- Bachiller, R. (2009). *Molecular Outflows: Observations*, pages 381–393.
- Beckwith, S. V. W., Sargent, A. I., Chini, R. S., and Guesten, R. (1990). A survey for circumstellar disks around young stellar objects. *Astronomical Journal*, 99:924–945.
- Beltrán, M. T., Cesaroni, R., Codella, C., Testi, L., Furuya, R. S., and Olmi, L. (2006a). Infall of gas as the formation mechanism of stars up to 20 times more massive than the Sun. *Nature*, 443:427–429.
- Beltrán, M. T., Girart, J. M., and Estalella, R. (2006b). Who is eating the outflow? High-angular resolution study of an intermediate-mass protostar in L1206. *Astronomy and Astrophysics*, 457:865–876.
- Beltrán, M. T., Girart, J. M., Estalella, R., Ho, P. T. P., and Palau, A. (2002). IRAS 21391+5802: The Molecular Outflow and Its Exciting Source. *Astrophysical Journal*, 573:246–259.
- Bernard, J. P., Dobashi, K., and Momose, M. (1999). Outflow and disk around the very young massive star GH2O 092.67+03.07. *Astronomy and Astrophysics*, 350:197–203.
- Beuther, H., Leurini, S., Schilke, P., Wyrowski, F., Menten, K. M., and Zhang, Q. (2007). Interferometric multi-wavelength (sub)millimeter continuum study of the young high-mass protocluster IRAS 05358+3543. *Astronomy and Astrophysics*, 466:1065–1076.

- Beuther, H., Schilke, P., Gueth, F., McCaughrean, M., Andersen, M., Sridharan, T. K., and Menten, K. M. (2002a). IRAS 05358+3543: Multiple outflows at the earliest stages of massive star formation. *Astronomy and Astrophysics*, 387:931–943.
- Beuther, H., Schilke, P., Menten, K. M., Motte, F., Sridharan, T. K., and Wyrowski, F. (2002b). High-Mass Protostellar Candidates. II. Density Structure from Dust Continuum and CS Emission. *Astrophysical Journal*, 566:945–965.
- Beuther, H., Schilke, P., Menten, K. M., Motte, F., Sridharan, T. K., and Wyrowski, F. (2005). Erratum: “High-Mass Protostellar Candidates. II. Density Structure from Dust Continuum and CS Emission”. *Astrophysical Journal*, 633:535–535.
- Beuther, H., Schilke, P., Sridharan, T. K., Menten, K. M., Walmsley, C. M., and Wyrowski, F. (2002c). Massive molecular outflows. *Astronomy and Astrophysics*, 383:892–904.
- Beuther, H., Schilke, P., and Wyrowski, F. (2004). High Spatial Resolution CN and CS Observation of Two Regions of Massive Star Formation. *Astrophysical Journal*, 615:832–839.
- Beuther, H. and Shepherd, D. (2005). Precursors of UCHII Regions and the Evolution of Massive Outflows. In M. S. N. Kumar, M. Tafalla, & P. Caselli, editor, *Cores to Clusters: Star Formation with Next Generation Telescopes*, pages 105–119.
- Beuther, H., Walsh, A., Schilke, P., Sridharan, T. K., Menten, K. M., and Wyrowski, F. (2002d). CH₃OH and H₂O masers in high-mass star-forming regions. *Astronomy and Astrophysics*, 390:289–298.
- Bisschop, S. E., Jørgensen, J. K., van Dishoeck, E. F., and de Wachter, E. B. M. (2007). Testing grain-surface chemistry in massive hot-core regions. *Astronomy and Astrophysics*, 465:913–929.
- Bonnell, I. A., Bate, M. R., and Zinnecker, H. (1998). On the formation of massive stars. *Monthly Notices of the RAS*, 298:93–102.
- Bonnell, I. A., Larson, R. B., and Zinnecker, H. (2007). The Origin of the Initial Mass Function. *Protostars and Planets V*, pages 149–164.
- Bontemps, S., André, P., Terebey, S., and Cabrit, S. (1996). Evolution of outflow activity around low-mass embedded young stellar objects. *Astronomy and Astrophysics*, 311:858–872.
- Brand, J., Cesaroni, R., Caselli, P., Catarzi, M., Codella, C., Comoretto, G., Curioni, G. P., Curioni, P., di Franco, S., Felli, M., Giovanardi, C., Olmi, L., Palagi, F., Palla, F., Panella, D., Pareschi, G., Rossi, E., Speroni, N., and Tofani, G. (1994). The Arcetri catalogue of H₂O maser sources update. *Astronomy and Astrophysics, Supplement*, 103:541–572.

BIBLIOGRAPHY

- Briggs, D. S. (1995). *High fidelity deconvolution of moderately resolved sources*. PhD thesis, The New Mexico Institute of Mining and Technology.
- Bronfman, L., Nyman, L., and May, J. (1996). A CS(2-1) survey of IRAS point sources with color characteristics of ultra-compact HII regions. *Astronomy and Astrophysics, Supplement*, 115:81–+.
- Bunn, J. C., Hoare, M. G., and Drew, J. E. (1995). Observations of the IR recombination line emission from massive young stellar objects. *Monthly Notices of the RAS*, 272:346–354.
- Busquet, G. (2010). *Timing the chemical evolution of dense gas in high-mass star-forming regions*. PhD thesis, Univeritat de Barcelona.
- Busquet, G., Estalella, R., Zhang, Q., Viti, S., Palau, A., Ho, P. T. P., and Sánchez-Monge, Á. (2011). N₂H⁺ depletion in the massive protostellar cluster AFGL 5142. *Astronomy and Astrophysics*, 525:A141+.
- Busquet, G., Palau, A., Estalella, R., Girart, J. M., Anglada, G., and Sepúlveda, I. (2009). Low-mass protostars and dense cores in different evolutionary stages in IRAS 00213+6530. *Astronomy and Astrophysics*, 506:1183–1198.
- Busquet, G., Palau, A., Estalella, R., Girart, J. M., Sánchez-Monge, Á., Viti, S., Ho, P. T. P., and Zhang, Q. (2010). The NH₂D/NH₃ ratio toward pre-protostellar cores around the UC H II region in IRAS 20293+3952. *Astronomy and Astrophysics*, 517:L6+.
- Campbell, B., Persson, S. E., and Matthews, K. (1989). Identification of new young stellar objects associated with IRAS point sources. III - The northern Galactic plane. *Astronomical Journal*, 98:643–658.
- Carey, S. J., Clark, F. O., Egan, M. P., Price, S. D., Shipman, R. F., and Kuchar, T. A. (1998). The Physical Properties of the Midcourse Space Experiment Galactic Infrared-dark Clouds. *Astrophysical Journal*, 508:721–728.
- Carilli, C. L. and Holdaway, M. A. (1997). *Millimeter Array Techincal Memo*, 173.
- Carral, P., Kurtz, S., Rodríguez, L. F., Martí, J., Lizano, S., and Osorio, M. (1999). VLA Continuum Observations of Suspected Massive Hot Cores. *Revista Mexicana de Astronomia y Astrofisica*, 35:97–+.
- Carral, P., Kurtz, S. E., Rodríguez, L. F., de Pree, C., and Hofner, P. (1997). Detection of 7 Millimeter Sources near Cometary H II Regions. *Astrophysical Journal, Letters*, 486:L103+.
- Carrasco-González, C., Rodríguez, L. F., Anglada, G., Martí, J., Torrelles, J. M., and Osorio, M. (2010). A Magnetized Jet from a Massive Protostar. *Science*, 330:1209–.

- Caselli, P., Benson, P. J., Myers, P. C., and Tafalla, M. (2002). Dense Cores in Dark Clouds. XIV. N_2H^+ (1-0) Maps of Dense Cloud Cores. *Astrophysical Journal*, 572:238–263.
- Caswell, J. L. and Vaile, R. A. (1995). Excited-state OH masers at 6.035 GHz. *Monthly Notices of the RAS*, 273:328–346.
- Ceccarelli, C. (2004). The Hot Corinos of Solar Type Protostars. In D. Johnstone, F. C. Adams, D. N. C. Lin, D. A. Neufeld, & E. C. Ostriker, editor, *Star Formation in the Interstellar Medium: In Honor of David Hollenbach*, volume 323 of *Astronomical Society of the Pacific Conference Series*, pages 195–+.
- Cesaroni, R. (2005). Hot molecular cores. In R. Cesaroni, M. Felli, E. Churchwell, & M. Walmsley, editor, *Massive Star Birth: A Crossroads of Astrophysics*, volume 227 of *IAU Symposium*, pages 59–69.
- Cesaroni, R., Felli, M., Jenness, T., Neri, R., Olmi, L., Robberto, M., Testi, L., and Walmsley, C. M. (1999). Unveiling the disk-jet system in the massive (proto)star IRAS 20126+4104. *Astronomy and Astrophysics*, 345:949–964.
- Cesaroni, R., Felli, M., Testi, L., Walmsley, C. M., and Olmi, L. (1997). The disk-outflow system around the high-mass (proto)star IRAS 20126+4104. *Astronomy and Astrophysics*, 325:725–744.
- Cesaroni, R., Hofner, P., Araya, E., and Kurtz, S. (2010). The structure of hot molecular cores over 1000 AU. *Astronomy and Astrophysics*, 509:A50+.
- Cesaroni, R., Neri, R., Olmi, L., Testi, L., Walmsley, C. M., and Hofner, P. (2005). A study of the Keplerian accretion disk and precessing outflow in the massive protostar IRAS 20126+4104. *Astronomy and Astrophysics*, 434:1039–1054.
- Cesaroni, R., Palagi, F., Felli, M., Catarzi, M., Comoretto, G., di Francos, Giovanardi, C., and Palla, F. (1988). A catalogue of H₂O maser sources north of $\delta = -30^\circ$. *Astronomy and Astrophysics, Supplement*, 76:445–458.
- Chen, H., Myers, P. C., Ladd, E. F., and Wood, D. O. S. (1995). Bolometric temperature and young stars in the Taurus and Ophiuchus complexes. *Astrophysical Journal*, 445:377–392.
- Chini, R., Ward-Thompson, D., Kirk, J. M., Nielbock, M., Reipurth, B., and Sievers, A. (2001). Mm/Submm images of Herbig-Haro energy sources and candidate protostars. *Astronomy and Astrophysics*, 369:155–169.
- Churchwell, E. (2002). Ultra-Compact HII Regions and Massive Star Formation. *Annual Review of Astron and Astrophys*, 40:27–62.

BIBLIOGRAPHY

- Codella, C., Cesaroni, R., López-Sepulcre, A., Beltrán, M. T., Furuya, R., and Testi, L. (2010). Looking for high-mass young stellar objects: H₂O and OH masers in ammonia cores. *Astronomy and Astrophysics*, 510:A86+.
- Condon, J. J., Cotton, W. D., Greisen, E. W., Yin, Q. F., Perley, R. A., and Broderick, J. J. (1994). The NRAO VLA Sky Survey. In D. R. Crabtree, R. J. Hanisch, & J. Barnes, editor, *Astronomical Data Analysis Software and Systems III*, volume 61 of *Astronomical Society of the Pacific Conference Series*, pages 155–+.
- Cox, A. N. (1999). *Allen’s astrophysical quantities*.
- Cragg, D. M., Johns, K. P., Godfrey, P. D., and Brown, R. D. (1992). Pumping the interstellar methanol masers. *Monthly Notices of the RAS*, 259:203–208.
- Cragg, D. M., Sobolev, A. M., Ellingsen, S. P., Caswell, J. L., Godfrey, P. D., Salii, S. V., and Dodson, R. G. (2001). Multitransition study and new detections of class II methanol masers. *Monthly Notices of the RAS*, 323:939–951.
- Curiel, S., Cantó, J., and Rodríguez, L. F. (1987). A model for the thermal radio continuum emission produced by a shock wave and its application to the Herbig-Haro objects 1 and 2. *Revista Mexicana de Astronomía y Astrofísica*, 14:595–602.
- Curiel, S., Ho, P. T. P., Patel, N. A., Torrelles, J. M., Rodríguez, L. F., Trinidad, M. A., Cantó, J., Hernández, L., Gómez, J. F., Garay, G., and Anglada, G. (2006). Large Proper Motions in the Jet of the High-Mass YSO Cepheus A HW2. *Astrophysical Journal*, 638:878–886.
- Curiel, S., Raymond, J. C., Wolfire, M., Hartigan, P., Morse, J., Schwartz, R. D., and Nisenson, P. (1995). Molecular H₂ Emission in HH 47A: Hubble Space Telescope GHRS and FOC Observations. *Astrophysical Journal*, 453:322–+.
- Curiel, S., Rodríguez, L. F., Cantó, J., and Torrelles, J. M. (1989). A search for radio sources near double Herbig-Haro objects. *Revista Mexicana de Astronomía y Astrofísica*, 17:137–141.
- De Buizer, J. M., Osorio, M., and Calvet, N. (2005). Observations and Modeling of the 2–25 μ m Emission from High-Mass Protostellar Object Candidates. *Astrophysical Journal*, 635:452–465.
- De Buizer, J. M. and Vacca, W. D. (2010). Direct Spectroscopic Identification of the Origin of “Green Fuzzy” Emission in Star-forming Regions. *Astronomical Journal*, 140:196–202.
- Di Francesco, J., Johnstone, D., Kirk, H., MacKenzie, T., and Ledwosinska, E. (2008). The SCUBA Legacy Catalogues: Submillimeter-Continuum Objects Detected by SCUBA. *Astrophysical Journal, Supplement*, 175:277–295.

- Diaz-Miller, R. I., Franco, J., and Shore, S. N. (1998). Photoionized and Photodissociated Regions around Main-Sequence Stars. *Astrophysical Journal*, 501:192–+.
- Dobashi, K., Nozawa, S., Hayashi, Y., Sato, F., and Fukui, Y. (1994). A molecular cloud and a CO outflow associated with IRAS 22134+5834. *Astronomical Journal*, 107:2148–2152.
- Dobashi, K. and Uehara, H. (2001). A CO Outflow and a Molecular Cloud Core Associated with a Young Massive Star IRAS 22134+5834. *Publications of the ASJ*, 53:799–809.
- Drew, J. E., Proga, D., and Stone, J. M. (1998). A radiation-driven disc wind model for massive young stellar objects. *Monthly Notices of the RAS*, 296:L6+.
- Dulk, G. A. (1985). Radio emission from the sun and stars. *Annual Review of Astron and Astrophys*, 23:169–224.
- Dunham, M. M., Crapsi, A., Evans, II, N. J., Bourke, T. L., Huard, T. L., Myers, P. C., and Kauffmann, J. (2008). Identifying the Low-Luminosity Population of Embedded Protostars in the c2d Observations of Clouds and Cores. *Astrophysical Journal, Supplement*, 179:249–282.
- Dyson, J. E. and Williams, D. A. (1997). *The physics of the interstellar medium*.
- Edgar, R. and Clarke, C. (2003). A new algorithm for radiative feedback and its application to the formation of massive stars. *Monthly Notices of the RAS*, 338:962–972.
- Edris, K. A., Fuller, G. A., and Cohen, R. J. (2007). A survey of OH masers towards high mass protostellar objects. *Astronomy and Astrophysics*, 465:865–877.
- Egan, M. P., Shipman, R. F., Price, S. D., Carey, S. J., Clark, F. O., and Cohen, M. (1998). A Population of Cold Cores in the Galactic Plane. *Astrophysical Journal, Letters*, 494:L199+.
- Eisloffel, J. (2000). Parsec-scale molecular H₂ outflows from young stars. *Astronomy and Astrophysics*, 354:236–246.
- Ellingsen, S. P. (2004). Masers: High Resolution Probes of Massive Star Formation. In M. G. Burton, R. Jayawardhana, & T. L. Bourke, editor, *Star Formation at High Angular Resolution*, volume 221 of *IAU Symposium*, pages 133–+.
- Ellingsen, S. P. (2005). The relationship between class I and class II methanol masers. *Monthly Notices of the RAS*, 359:1498–1516.
- Ellingsen, S. P., Voronkov, M. A., Cragg, D. M., Sobolev, A. M., Breen, S. L., and Godfrey, P. D. (2007). Investigating high-mass star formation through maser surveys. In J. M. Chapman & W. A. Baan, editor, *IAU Symposium*, volume 242 of *IAU Symposium*, pages 213–217.

BIBLIOGRAPHY

- Estalella, R. and Anglada, G. (1999). *Introducción a la física del medio interestelar*.
- Estalella, R., Anglada, G., Rodríguez, L. F., and Garay, G. (1991). Multifrequency VLA observations of radio continuum from IRAS 16293 - 2422. *Astrophysical Journal*, 371:626–630.
- Estalella, R., Mauersberger, R., Torrelles, J. M., Anglada, G., Gomez, J. F., Lopez, R., and Muters, D. (1993). The Molecular Cores in the L1287, AFGL 5142, and IRAS 20126+4104 Regions. *Astrophysical Journal*, 419:698–+.
- Fazal, F. M., Sridharan, T. K., Qiu, K., Robitaille, T., Whitney, B., and Zhang, Q. (2008). Spectral Energy Distributions of High-Mass Protostellar Objects: Evidence of High Accretion Rates. *Astrophysical Journal, Letters*, 688:L41–L44.
- Feigelson, E. D. and Montmerle, T. (1985). An extremely variable radio star in the rho Ophiuchi cloud. *Astrophysical Journal, Letters*, 289:L19–L23.
- Feigelson, E. D. and Montmerle, T. (1999). High-Energy Processes in Young Stellar Objects. *Annual Review of Astron and Astrophys*, 37:363–408.
- Felli, M., Brand, J., Cesaroni, R., Codella, C., Comoretto, G., di Franco, S., Massi, F., Moscadelli, L., Nesti, R., Olmi, L., Palagi, F., Panella, D., and Valdetaro, R. (2007). Water maser variability over 20 years in a large sample of star-forming regions: the complete database. *Astronomy and Astrophysics*, 476:373–664.
- Fish, V. L. and Reid, M. J. (2006). Full-Polarization Observations of OH Masers in Massive Star-forming Regions. II. Maser Properties and the Interpretation of Polarization. *Astrophysical Journal, Supplement*, 164:99–123.
- Fish, V. L., Reid, M. J., Argon, A. L., and Zheng, X. (2005). Full-Polarization Observations of OH Masers in Massive Star-forming Regions. I. Data. *Astrophysical Journal, Supplement*, 160:220–271.
- Fontani, F., Cesaroni, R., and Furuya, R. S. (2010). Class I and Class II methanol masers in high-mass star-forming regions. *Astronomy and Astrophysics*, 517:A56+.
- Forveille, T., Guilloteau, S., and Lucas, R. (1989). *CLASS Manual (Grenoble: IRAM)*.
- Franco, J., Kurtz, S., Hofner, P., Testi, L., García-Segura, G., and Martos, M. (2000). The Density Structure of Highly Compact H II Regions. *Astrophysical Journal, Letters*, 542:L143–L146.
- Franco-Hernández, R., Moran, J. M., Rodríguez, L. F., and Garay, G. (2009). The Rotating Molecular Structures and the Ionized Outflow Associated with IRAS 16547-4247. *Astrophysical Journal*, 701:974–983.

- Frau, P., Girart, J. M., Beltrán, M. T., Morata, O., Masqué, J. M., Busquet, G., Alves, F. O., Sánchez-Monge, Á., Estalella, R., and Franco, G. A. P. (2010). Young Starless Cores Embedded in the Magnetically Dominated Pipe Nebula. *Astrophysical Journal*, 723:1665–1677.
- Friesen, R. K., Di Francesco, J., Shimajiri, Y., and Takakuwa, S. (2010). The Initial Conditions of Clustered Star Formation. II. N_2H^+ Observations of the Ophiuchus B Core. *Astrophysical Journal*, 708:1002–1024.
- Fuente, A., Neri, R., and Caselli, P. (2005). Detection of a hot core in the intermediate-mass Class 0 protostar NGC 7129-FIRS 2. *Astronomy and Astrophysics*, 444:481–493.
- Fuller, G. A., Williams, S. J., and Sridharan, T. K. (2005). The circumstellar environment of high mass protostellar objects. III. Evidence of infall? *Astronomy and Astrophysics*, 442:949–959.
- Garay, G., Ramírez, S., Rodríguez, L. F., Curiel, S., and Torrelles, J. M. (1996). The Nature of the Radio Sources within the Cepheus A Star-forming Region. *Astrophysical Journal*, 459:193–+.
- Gayet, R. (1970). On the Average Gaunt Factor for Free-Free Emission. *Astronomy and Astrophysics*, 9:312–+.
- Ghavamian, P. and Hartigan, P. (1998). Free-Free Radiation from Dense Interstellar Shock Waves. *Astrophysical Journal*, 501:687–+.
- Gibb, E., Nummelin, A., Irvine, W. M., Whittet, D. C. B., and Bergman, P. (2000). Chemistry of the Organic-Rich Hot Core G327.3-0.6. *Astrophysical Journal*, 545:309–326.
- Girart, J. M., Viti, S., Williams, D. A., Estalella, R., and Ho, P. T. P. (2002). The molecular condensations ahead of Herbig-Haro objects. I. Multi-transition observations of HH 2. *Astronomy and Astrophysics*, 388:1004–1015.
- Goddi, C., Moscadelli, L., Sanna, A., Cesaroni, R., and Minier, V. (2007). Associations of H_2O and CH_3OH masers at milli-arcsec angular resolution in two high-mass YSOs. *Astronomy and Astrophysics*, 461:1027–1035.
- Goicoechea, J. R., Pety, J., Gerin, M., Teyssier, D., Roueff, E., Hily-Blant, P., and Baek, S. (2006). Low sulfur depletion in the Horsehead PDR. *Astronomy and Astrophysics*, 456:565–580.
- Goldsmith, P. F. and Langer, W. D. (1999). Population Diagram Analysis of Molecular Line Emission. *Astrophysical Journal*, 517:209–225.

BIBLIOGRAPHY

- Gómez, J. F., Sargent, A. I., Torrelles, J. M., Ho, P. T. P., Rodríguez, L. F., Cantó, J., and Garay, G. (1999). Disk and Outflow in Cepheus A-HW2: Interferometric SiO and HCO⁺ Observations. *Astrophysical Journal*, 514:287–295.
- Gordon, M. A. (1988). The continuum spectra of warm cloud complexes associated with radio-bright H II regions. *Astrophysical Journal*, 331:509–522.
- Gordy, W. and Cook, R. L. (1984). *Microwave molecular spectra*.
- Guilloteau, S., Stier, M. T., and Downes, D. (1983). Ammonia absorption toward W3(OH) - 0.3 arcsec resolution maps in the (2,2) line. *Astronomy and Astrophysics*, 126:10–15.
- Harju, J., Walmsley, C. M., and Wouterloot, J. G. A. (1993). Ammonia clumps in the Orion and Cepheus clouds. *Astronomy and Astrophysics, Supplement*, 98:51–75.
- Haro, G. (1952). Herbig’s Nebulous Objects Near NGC 1999. *Astrophysical Journal*, 115:572–+.
- Henriksen, R. N., Mirabel, I. F., and Ptuskin, V. S. (1991). Bipolar radio sources in star-forming regions? *Astronomy and Astrophysics*, 248:221–226.
- Herbig, G. H. (1951). The Spectra of Two Nebulous Objects Near NGC 1999. *Astrophysical Journal*, 113:697–699.
- Herbst, E. and Klemperer, W. (1973). The Formation and Depletion of Molecules in Dense Interstellar Clouds. *Astrophysical Journal*, 185:505–534.
- Herzberg, G. (1991). *Molecular spectra and molecular structure, Vol 2*.
- Hildebrand, R. H. (1983). The Determination of Cloud Masses and Dust Characteristics from Submillimetre Thermal Emission. *Quarterly Journal of the RAS*, 24:267–+.
- Hirota, T., Ando, K., Bushimata, T., Choi, Y. K., Honma, M., Imai, H., Iwadate, K., Jike, T., Kamenno, S., Kameya, O., Kamohara, R., Kan-Ya, Y., Kawaguchi, N., Kijima, M., Kim, M. K., Kobayashi, H., Kuji, S., Kurayama, T., Manabe, S., Matsui, M., Matsumoto, N., Miyaji, T., Miyazaki, A., Nagayama, T., Nakagawa, A., Namikawa, D., Nyu, D., Oh, C. S., Omodaka, T., Oyama, T., Sakai, S., Sasao, T., Sato, K., Sato, M., Shibata, K. M., Tamura, Y., Ueda, K., and Yamashita, K. (2008). Astrometry of H₂O Masers in Nearby Star-Forming Regions with VERA III. IRAS 22198+6336 in Lynds1204G. *Publications of the ASJ*, 60:961–.
- Ho, P. T. P. (1972). *Study of the ammonia molecule in the interstellar medium*. PhD thesis, Massachusetts Institute of Technology.
- Ho, P. T. P., Moran, J. M., and Lo, K. Y. (2004). The Submillimeter Array. *Astrophysical Journal, Letters*, 616:L1–L6.

- Ho, P. T. P. and Townes, C. H. (1983). Interstellar ammonia. *Annual Review of Astron and Astrophys*, 21:239–270.
- Hoare, M. G. (2006). An Equatorial Wind from the Massive Young Stellar Object S140 IRS 1. *Astrophysical Journal*, 649:856–861.
- Hoare, M. G., Drew, J. E., Muxlow, T. B., and Davis, R. J. (1994). Mapping the radio emission from massive young stellar objects. *Astrophysical Journal, Letters*, 421:L51–L54.
- Hofner, P., Cesaroni, R., Olmi, L., Rodríguez, L. F., Martí, J., and Araya, E. (2007). Sub-arcsecond resolution radio continuum observations of IRAS 20126+4104. *Astronomy and Astrophysics*, 465:197–205.
- Hofner, P., Cesaroni, R., Rodríguez, L. F., and Martí, J. (1999). A double system of ionized jets in IRAS 20126+4104. *Astronomy and Astrophysics*, 345:L43–L46.
- Hofner, P. and Churchwell, E. (1996). A survey of water maser emission toward ultracompact HII regions. *Astronomy and Astrophysics, Supplement*, 120:283–299.
- Hofner, P., Kurtz, S., Churchwell, E., Walmsley, C. M., and Cesaroni, R. (1996). Massive Star Formation in the Hot, Dense Cloud Core of G9.62+0.19. *Astrophysical Journal*, 460:359–+.
- Hollenbach, D., Johnstone, D., Lizano, S., and Shu, F. (1994). Photoevaporation of disks around massive stars and application to ultracompact H II regions. *Astrophysical Journal*, 428:654–669.
- Hollenbach, D. J. and Tielens, A. G. G. M. (1997). Dense Photodissociation Regions (PDRs). *Annual Review of Astron and Astrophys*, 35:179–216.
- Hotzel, S., Harju, J., and Walmsley, C. M. (2004). The NH₃/N₂H⁺ abundance ratio in dense cores. *Astronomy and Astrophysics*, 415:1065–1072.
- Huang, R. Q. and Yu, K. N. (1998). *Stellar astrophysics*.
- Hughes, V. A. and MacLeod, G. C. (1989). The use of IRAS data to define H II regions. *Astronomical Journal*, 97:786–800.
- Hunter, T. R., Testi, L., Taylor, G. B., Tofani, G., Felli, M., and Phillips, T. G. (1995). A multiwavelength picture of the AFGL 5142 star-forming region. *Astronomy and Astrophysics*, 302:249–+.
- Hunter, T. R., Testi, L., Zhang, Q., and Sridharan, T. K. (1999). Molecular Jets and H₂O Masers in the AFGL 5142 Hot Core. *Astronomical Journal*, 118:477–487.

BIBLIOGRAPHY

- Iben, Jr., I. (1965). Stellar Evolution. I. The Approach to the Main Sequence. *Astrophysical Journal*, 141:993–+.
- Ignace, R. and Churchwell, E. (2004). Free-Free Spectral Energy Distributions of Hierarchically Clumped H II Regions. *Astrophysical Journal*, 610:351–360.
- Jenness, T., Scott, P. F., and Padman, R. (1995). Studies of Embedded Far Infrared Sources in the Vicinity of H₂O Masers - I. Observations. *Monthly Notices of the RAS*, 276:1024–+.
- Johnstone, D., Hollenbach, D., and Bally, J. (1998). Photoevaporation of Disks and Clumps by Nearby Massive Stars: Application to Disk Destruction in the Orion Nebula. *Astrophysical Journal*, 499:758–+.
- Jørgensen, J. K., Bourke, T. L., Myers, P. C., Di Francesco, J., van Dishoeck, E. F., Lee, C., Ohashi, N., Schöier, F. L., Takakuwa, S., Wilner, D. J., and Zhang, Q. (2007). PROSAC: A Submillimeter Array Survey of Low-Mass Protostars. I. Overview of Program: Envelopes, Disks, Outflows, and Hot Cores. *Astrophysical Journal*, 659:479–498.
- Kahn, F. D. (1974). Cocoons around early-type stars. *Astronomy and Astrophysics*, 37:149–162.
- Kauffmann, J., Bertoldi, F., Bourke, T. L., Evans, II, N. J., and Lee, C. W. (2008). MAMBO mapping of Spitzer c2d small clouds and cores. *Astronomy and Astrophysics*, 487:993–1017.
- Keto, E. (2002a). An Ionized Accretion Flow in the Ultracompact H II Region G10.6-0.4. *Astrophysical Journal*, 568:754–760.
- Keto, E. (2002b). On the Evolution of Ultracompact H II Regions. *Astrophysical Journal*, 580:980–986.
- Keto, E. (2003). The Formation of Massive Stars by Accretion through Trapped Hypercompact H II Regions. *Astrophysical Journal*, 599:1196–1206.
- Keto, E. (2007). The Formation of Massive Stars: Accretion, Disks, and the Development of Hypercompact H II Regions. *Astrophysical Journal*, 666:976–981.
- Keto, E. and Klaassen, P. (2008). The Ionization of Accretion Flows in High-Mass Star Formation: W51e2. *Astrophysical Journal, Letters*, 678:L109–L112.
- Keto, E. and Wood, K. (2006). Observations on the Formation of Massive Stars by Accretion. *Astrophysical Journal*, 637:850–859.
- Keto, E., Zhang, Q., and Kurtz, S. (2008). The Early Evolution of Massive Stars: Radio Recombination Line Spectra. *Astrophysical Journal*, 672:423–432.

- Kim, K. and Kurtz, S. E. (2006). Occurrence Frequency of CO Outflows in Massive Protostellar Candidates. *Astrophysical Journal*, 643:978–984.
- Klaassen, P. D. and Wilson, C. D. (2007). Outflow and Infall in a Sample of Massive Star-forming Regions. *Astrophysical Journal*, 663:1092–1102.
- Krumholz, M. R. and Bonnell, I. A. (2007). Models for the Formation of Massive Stars. *ArXiv e-prints 0712.0828*.
- Kumar, M. S. N., Bachiller, R., and Davis, C. J. (2002). H₂ Emission around Massive Young Stellar Objects with Outflows. *Astrophysical Journal*, 576:313–322.
- Kumar, M. S. N., Keto, E., and Clerkin, E. (2006). The youngest stellar clusters. Clusters associated with massive protostellar candidates. *Astronomy and Astrophysics*, 449:1033–1041.
- Kumar, M. S. N., Ojha, D. K., and Davis, C. J. (2003). A Ring-shaped Embedded Young Stellar (Proto)Cluster. *Astrophysical Journal*, 598:1107–1111.
- Kurtz, S. (2005a). Hypercompact HII regions. In R. Cesaroni, M. Felli, E. Churchwell, & M. Walmsley, editor, *Massive Star Birth: A Crossroads of Astrophysics*, volume 227 of *IAU Symposium*, pages 111–119.
- Kurtz, S. (2005b). The Young Massive Star Environment. In D. C. Lis, G. A. Blake, & E. Herbst, editor, *Astrochemistry: Recent Successes and Current Challenges*, volume 231 of *IAU Symposium*, pages 47–56.
- Kurtz, S., Cesaroni, R., Churchwell, E., Hofner, P., and Walmsley, C. M. (2000). Hot Molecular Cores and the Earliest Phases of High-Mass Star Formation. *Protostars and Planets IV*, pages 299–+.
- Kurtz, S., Churchwell, E., and Wood, D. O. S. (1994). Ultracompact H II regions. 2: New high-resolution radio images. *Astrophysical Journal, Supplement*, 91:659–712.
- Kurtz, S., Hofner, P., and Álvarez, C. V. (2004). A Catalog of CH₃OH 70-61 A+ Maser Sources in Massive Star-forming Regions. *Astrophysical Journal, Supplement*, 155:149–165.
- Lada, C. J. (1999). The Formation of Low Mass Stars: An Observational Overview. In C. J. Lada & N. D. Kylafis, editor, *NATO ASIC Proc. 540: The Origin of Stars and Planetary Systems*, pages 143–+.
- Larionov, G. M., Val’tts, I. E., Winnberg, A., Johansson, L. E. B., Booth, R. S., and Golubev, V. V. (1999). Survey of bipolar outflows and methanol masers in the C(32) S (2-1) and C(34) S (2-1) lines in the Northern sky. *Astronomy and Astrophysics, Supplement*, 139:257–275.

BIBLIOGRAPHY

- Larson, R. B. (1969). Numerical calculations of the dynamics of collapsing proto-star. *Monthly Notices of the RAS*, 145:271–+.
- Laurini, S., Beuther, H., Schilke, P., Wyrowski, F., Zhang, Q., and Menten, K. M. (2007). Multi-line (sub)millimetre observations of the high-mass proto cluster IRAS 05358+3543. *Astronomy and Astrophysics*, 475:925–939.
- López, R., Estalella, R., Gómez, G., Riera, A., and Carrasco-González, C. (2009). The nature of HH 223 from long-slit spectroscopy. *Astronomy and Astrophysics*, 498:761–769.
- López-Sepulcre, A., Cesaroni, R., and Walmsley, C. M. (2010). A comparative study of high-mass cluster forming clumps. *Astronomy and Astrophysics*, 517:A66+.
- López-Sepulcre, A., Codella, C., Cesaroni, R., Marcelino, N., and Walmsley, C. M. (2009). Molecular outflows towards O-type young stellar objects. *Astronomy and Astrophysics*, 499:811–825.
- López-Sepulcre, A., Walmsley, C. M., Cesaroni, R., Codella, C., Schuller, F., Bronfman, L., Carey, S. J., Menten, K. M., Molinari, S., and Noriega-Crespo, A. (2011). SiO outflows in high-mass star forming regions: A potential chemical clock? *Astronomy and Astrophysics*, 526:L2+.
- Loren, R. B. and Mundy, L. G. (1984). The methyl cyanide hot and warm cores in Orion - Statistical equilibrium excitation models of a symmetric-top molecule. *Astrophysical Journal*, 286:232–251.
- Lugo, J., Lizano, S., and Garay, G. (2004). Photoevaporated Disks around Massive Young Stars. *Astrophysical Journal*, 614:807–817.
- Martí, J., Rodríguez, L. F., and Reipurth, B. (1993). HH 80-81: A Highly Collimated Herbig-Haro Complex Powered by a Massive Young Star. *Astrophysical Journal*, 416:208–+.
- Martí, J., Rodríguez, L. F., and Reipurth, B. (1998). Proper Motions of the Inner Condensations in the HH 80-81 Thermal Radio Jet. *Astrophysical Journal*, 502:337–+.
- Mezger, P. G., Altenhoff, W., Schraml, J., Burke, B. F., Reifenshtein, III, E. C., and Wilson, T. L. (1967). A New Class of Compact H II Regions Associated with OH Emission Sources. *Astrophysical Journal, Letters*, 150:L157+.
- Mezger, P. G., Sievers, A., and Zylka, R. (1991). Dust Emission from Star Forming Clouds: a Progress Report. In E. Falgarone, F. Boulanger, & G. Duvert, editor, *Fragmentation of Molecular Clouds and Star Formation*, volume 147 of *IAU Symposium*, pages 245–+.

- Minier, V., Ellingsen, S. P., Norris, R. P., and Booth, R. S. (2003). The protostellar mass limit for 6.7 GHz methanol masers. I. A low-mass YSO survey. *Astronomy and Astrophysics*, 403:1095–1100.
- Miralles, M. P., sRodríguez, L. F., Tapia, M., Roth, M., Persi, P., Ferrari-Toniolo, M., and Curiel, S. (1994). VLA observations of CYG OB2 No. 5: Detection of a weak radio companion and new observations and models for the main component. *Astronomy and Astrophysics*, 282:547–553.
- Molinari, S., Brand, J., Cesaroni, R., and Palla, F. (1996). A search for precursors of ultracompact HII regions in a sample of luminous IRAS sources. I. Association with ammonia cores. *Astronomy and Astrophysics*, 308:573–587.
- Moscadelli, L., Cesaroni, R., and Rioja, M. J. (2000). Tracing the root of the bipolar jet in IRAS 20126+4104: VLBA observations of H₂O masers. *Astronomy and Astrophysics*, 360:663–670.
- Moscadelli, L., Cesaroni, R., and Rioja, M. J. (2005). Water masers in the massive protostar IRAS 20126+4104: ejection and deceleration. *Astronomy and Astrophysics*, 438:889–898.
- Mueller, K. E., Shirley, Y. L., Evans, II, N. J., and Jacobson, H. R. (2002). The Physical Conditions for Massive Star Formation: Dust Continuum Maps and Modeling. *Astrophysical Journal, Supplement*, 143:469–497.
- Müller, H. S. P., Schlöder, F., Stutzki, J., and Winnewisser, G. (2005). The Cologne Database for Molecular Spectroscopy, CDMS: a useful tool for astronomers and spectroscopists. *Journal of Molecular Structure*, 742:215–227.
- Müller, H. S. P., Thorwirth, S., Roth, D. A., and Winnewisser, G. (2001). The Cologne Database for Molecular Spectroscopy, CDMS. *Astronomy and Astrophysics*, 370:L49–L52.
- Myers, P. C. and Ladd, E. F. (1993). Bolometric temperatures of young stellar objects. *Astrophysical Journal, Letters*, 413:L47–L50.
- Olson, F. M. (1975). Thermal bremsstrahlung radiospectra for inhomogeneous objects, with an application to MWC 349. *Astronomy and Astrophysics*, 39:217–223.
- Osorio, M., Lizano, S., and D’Alessio, P. (1999). Hot Molecular Cores and the Formation of Massive Stars. *Astrophysical Journal*, 525:808–820.
- Ossenkopf, V. and Henning, T. (1994). Dust opacities for protostellar cores. *Astronomy and Astrophysics*, 291:943–959.

BIBLIOGRAPHY

- Osterloh, M., Henning, T., and Launhardt, R. (1997). Infrared Images and Millimeter Data from Cold Southern IRAS Sources. *Astrophysical Journal, Supplement*, 110:71–+.
- Pacholczyk, A. G. (1970). *Radio astrophysics. Nonthermal processes in galactic and extragalactic sources.*
- Palau, A. (2006). *Star formation in cluster environments at mm and submm wavelengths.* PhD thesis, Univeritat de Barcelona.
- Palau, A., Estalella, R., Girart, J. M., Ho, P. T. P., Zhang, Q., and Beuther, H. (2007a). Star formation in a clustered environment around the UCH {II} region in IRAS 20293+3952. *Astronomy and Astrophysics*, 465:219–233.
- Palau, A., Estalella, R., Ho, P. T. P., Beuther, H., and Beltrán, M. T. (2007b). Unveiling the nature and interaction of the intermediate/high-mass YSOs in IRAS 20343+4129. *Astronomy and Astrophysics*, 474:911–922.
- Palau, A., Sánchez-Monge, Á., Busquet, G., Estalella, R., Zhang, Q., Ho, P. T. P., Beltrán, M. T., and Beuther, H. (2010). Three intermediate-mass young stellar objects with different properties emerging from the same natal cloud in IRAS 00117+6412. *Astronomy and Astrophysics*, 510:A5+.
- Palla, F., Brand, J., Comoretto, G., Felli, M., and Cesaroni, R. (1991). Water masers associated with dense molecular clouds and ultracompact H II regions. *Astronomy and Astrophysics*, 246:249–263.
- Palla, F. and Stahler, S. W. (1993). The Pre-Main-Sequence Evolution of Intermediate-Mass Stars. *Astrophysical Journal*, 418:414–+.
- Panagia, N. (1973). Some Physical parameters of early-type stars. *Astronomical Journal*, 78:929–934.
- Panagia, N. and Felli, M. (1975). The spectrum of the free-free radiation from extended envelopes. *Astronomy and Astrophysics*, 39:1–5.
- Pankonin, V., Churchwell, E., Watson, C., and Bieging, J. H. (2001). A Methyl Cyanide Search for the Earliest Stages of Massive Protostars. *Astrophysical Journal*, 558:194–203.
- Patel, N. A., Curiel, S., Sridharan, T. K., Zhang, Q., Hunter, T. R., Ho, P. T. P., Torrelles, J. M., Moran, J. M., Gómez, J. F., and Anglada, G. (2005). A disk of dust and molecular gas around a high-mass protostar. *Nature*, 437:109–111.
- Perault, M., Omont, A., Simon, G., Seguin, P., Ojha, D., Blommaert, J., Felli, M., Gilmore, G., Guglielmo, F., Habing, H., Price, S., Robin, A., de Batz, B., Cesarsky, C., Elbaz, D., Epchtein, N., Fouque, P., Guest, S., Levine, D., Pollock, A., Prusti, T., Siebenmorgen, R., Testi, L., and Tiphene, D. (1996). First ISOCAM images of the Milky Way. *Astronomy and Astrophysics*, 315:L165–L168.

- Persson, S. E., Geballe, T. R., McGregor, P. J., Edwards, S., and Lonsdale, C. J. (1984). Brackett-alpha line profiles of young stellar objects. *Astrophysical Journal*, 286:289–301.
- Pickett, H. M. (1991). The fitting and prediction of vibration-rotation spectra with spin interactions. *J.Molec.Spectroscopy*, 148:371–377.
- Pickett, H. M., Poynter, I. R. L., Cohen, E. A., Delitsky, M. L., Pearson, J. C., and Muller, H. S. P. (1998). Submillimeter, millimeter and microwave spectral line catalog. *Journal of Quantitative Spectroscopy and Radiative Transfer*, 60:883–890.
- Pillai, T., Wyrowski, F., Carey, S. J., and Menten, K. M. (2006). Ammonia in infrared dark clouds. *Astronomy and Astrophysics*, 450:569–583.
- Pillai, T., Wyrowski, F., Hatchell, J., Gibb, A. G., and Thompson, M. A. (2007). Probing the initial conditions of high mass star formation. I. Deuteration and depletion in high mass pre/protocluster clumps. *Astronomy and Astrophysics*, 467:207–216.
- Pratap, P., Shute, P. A., Keane, T. C., Battersby, C., and Sterling, S. (2008). Class I Methanol Masers: Signposts of Star Formation? *Astronomical Journal*, 135:1718–1730.
- Pravdo, S. H., Rodríguez, L. F., Curiel, S., Cantó, J., Torrelles, J. M., Becker, R. H., and Sellgren, K. (1985). Detection of radio continuum emission from Herbig-Haro objects 1 and 2 and from their central exciting source. *Astrophysical Journal, Letters*, 293:L35–L38.
- Purcell, C. R., Balasubramanyam, R., Burton, M. G., Walsh, A. J., Minier, V., Hunt-Cunningham, M. R., Kedziora-Chudczer, L. L., Longmore, S. N., Hill, T., Bains, I., Barnes, P. J., Busfield, A. L., Calisse, P., Crighton, N. H. M., Curran, S. J., Davis, T. M., Dempsey, J. T., Derragopian, G., Fulton, B., Hidas, M. G., Hoare, M. G., Lee, J., Ladd, E. F., Lumsden, S. L., Moore, T. J. T., Murphy, M. T., Oudmaijer, R. D., Pracy, M. B., Rathborne, J., Robertson, S., Schultz, A. S. B., Shobbrook, J., Sparks, P. A., Storey, J., and Travouillon, T. (2006). A CH₃CN and HCO⁺ survey towards southern methanol masers associated with star formation. *Monthly Notices of the RAS*, 367:553–576.
- Qiu, K., Zhang, Q., Megeath, S. T., Gutermuth, R. A., Beuther, H., Shepherd, D. S., Sridharan, T. K., Testi, L., and De Pree, C. G. (2008). Spitzer IRAC and MIPS Imaging of Clusters and Outflows in Nine High-Mass Star Forming Regions. *Astrophysical Journal*, 685:1005–1025.
- Reynolds, S. P. (1986). Continuum spectra of collimated, ionized stellar winds. *Astrophysical Journal*, 304:713–720.
- Richards, P. J., Little, L. T., Heaton, B. D., and Toriseva, M. (1987). HCO(+) survey of unassociated compact molecular clouds in the IRAS Point Source Catalog. *Monthly Notices of the RAS*, 228:43–54.

BIBLIOGRAPHY

- Richling, S. and Yorke, H. W. (1997). Photoevaporation of protostellar disks. II. The importance of UV dust properties and ionizing flux. *Astronomy and Astrophysics*, 327:317–324.
- Roberts, H. and Millar, T. J. (2007). A survey of $[D_2CO]/[H_2CO]$ and $[N_2D^+]/[N_2H^+]$ ratios towards protostellar cores. *Astronomy and Astrophysics*, 471:849–863.
- Rodríguez, L. F., Curiel, S., Moran, J. M., Mirabel, I. F., Roth, M., and Garay, G. (1989). Large proper motions in the remarkable triple radio source in Serpens. *Astrophysical Journal, Letters*, 346:L85–L88.
- Rodríguez, L. F., Garay, G., Curiel, S., Ramírez, S., Torrelles, J. M., Gómez, Y., and Velazquez, A. (1994). Cepheus A HW2: A powerful thermal radio jet. *Astrophysical Journal, Letters*, 430:L65–L68.
- Rodríguez, L. F., Martí, J., Cantó, J., Moran, J. M., and Curiel, S. (1993). Possible radio spectral indices from inhomogeneous free-free sources. *Revista Mexicana de Astronomía y Astrofísica*, 25:23–29.
- Rodríguez, L. F., Moran, J. M., Franco-Hernández, R., Garay, G., Brooks, K. J., and Mardones, D. (2008). The Collimated Jet Source in IRAS 16547-4247: Time Variation, Possible Precession, and Upper Limits to the Proper Motions Along the Jet Axis. *Astronomical Journal*, 135:2370–2379.
- Rodríguez, L. F. and Reipurth, B. (1989). Detection of radio continuum emission from the Herbig-Haro objects 80 and 81 and their suspected energy source. *Revista Mexicana de Astronomía y Astrofísica*, 17:59–63.
- Rohlfs, K. and Wilson, T. L. (2004). *Tools of radio astronomy*.
- Sánchez-Monge, Á., Palau, A., Estalella, R., Beltrán, M. T., and Girart, J. M. (2008). Survey of intermediate/high mass star-forming regions at centimeter and millimeter wavelengths. *Astronomy and Astrophysics*, 485:497–515.
- Sánchez-Monge, Á., Palau, A., Estalella, R., Kurtz, S., Zhang, Q., Di Francesco, J., and Shepherd, D. (2010). IRAS 22198+6336: Discovery of an Intermediate-mass Hot Core. *Astrophysical Journal, Letters*, 721:L107–L111.
- Sault, R. J., Teuben, P. J., and Wright, M. C. H. (1995). A Retrospective View of MIRIAD. In R. A. Shaw, H. E. Payne, & J. J. E. Hayes, editor, *Astronomical Data Analysis Software and Systems IV*, volume 77 of *Astronomical Society of the Pacific Conference Series*, pages 433–+.
- Scoville, N. Z., Sargent, A. I., Sanders, D. B., Claussen, M. J., Masson, C. R., Lo, K. Y., and Phillips, T. G. (1986). High-resolution mapping of molecular outflows in NGC 2071, W49, and NGC 7538. *Astrophysical Journal*, 303:416–432.

- Seale, J. P. and Looney, L. W. (2008). Morphological Evolution of Bipolar Outflows from Young Stellar Objects. *Astrophysical Journal*, 675:427–442.
- Sepúlveda, I. (2001). *Ammonia emission and outflow activity in young stellar objects*. PhD thesis, Univeritat de Barcelona.
- Shang, H., Allen, A., Li, Z., Liu, C., Chou, M., and Anderson, J. (2006). A Unified Model for Bipolar Outflows from Young Stars. *Astrophysical Journal*, 649:845–855.
- Shepherd, D. (2005). Massive star outflows. In R. Cesaroni, M. Felli, E. Churchwell, & M. Walmsley, editor, *Massive Star Birth: A Crossroads of Astrophysics*, volume 227 of *IAU Symposium*, pages 237–246.
- Shepherd, D. S., Churchwell, E., and Wilner, D. J. (1997). A High Spatial Resolution Study of the ON2 Massive Star-forming Region. *Astrophysical Journal*, 482:355–+.
- Shirley, Y. L., Evans, II, N. J., Young, K. E., Knez, C., and Jaffe, D. T. (2003). A CS J=5-4 Mapping Survey Toward High-Mass Star-forming Cores Associated with Water Masers. *Astrophysical Journal, Supplement*, 149:375–403.
- Shu, F. H., Adams, F. C., and Lizano, S. (1987). Star formation in molecular clouds - Observation and theory. *Annual Review of Astron and Astrophys*, 25:23–81.
- Shu, F. H., Allen, A., Shang, H., Ostriker, E. C., and Li, Z. (1999). Low-Mass Star Formation: Theory. In C. J. Lada & N. D. Kylafis, editor, *NATO ASIC Proc. 540: The Origin of Stars and Planetary Systems*, pages 193–+.
- Spitzer, L. (1978). *Physical processes in the interstellar medium*.
- Sridharan, T. K., Beuther, H., Schilke, P., Menten, K. M., and Wyrowski, F. (2002). High-Mass Protostellar Candidates. I. The Sample and Initial Results. *Astrophysical Journal*, 566:931–944.
- Stahler, S. W. and Palla, F. (2005). *The Formation of Stars*.
- Stahler, S. W., Palla, F., and Ho, P. T. P. (2000). The Formation of Massive Stars. *Protostars and Planets IV*, pages 327–+.
- Szymczak, M., Hrynek, G., and Kus, A. J. (2000). A survey of the 6.7 GHz methanol maser emission from IRAS sources. I. Data. *Astronomy and Astrophysics, Supplement*, 143:269–301.
- Tafalla, M., Bachiller, R., and Martin-Pintado, J. (1993). Dense cores in L1204/S140 - Star formation and velocity shifts. *Astrophysical Journal*, 403:175–182.

BIBLIOGRAPHY

- Tafalla, M., Myers, P. C., Caselli, P., and Walmsley, C. M. (2004). On the internal structure of starless cores. I. Physical conditions and the distribution of CO, CS, N₂H⁺, and NH₃ in L1498 and L1517B. *Astronomy and Astrophysics*, 416:191–212.
- Takahashi, S., Saito, M., Ohashi, N., Kusakabe, N., Takakuwa, S., Shimajiri, Y., Tamura, M., and Kawabe, R. (2008). Millimeter- and Submillimeter-Wave Observations of the OMC-2/3 Region. III. An Extensive Survey for Molecular Outflows. *Astrophysical Journal*, 688:344–361.
- Tan, J. C. and McKee, C. F. (2002). The Formation of Massive Stars and Star Clusters. In P. Crowther, editor, *Hot Star Workshop III: The Earliest Phases of Massive Star Birth*, volume 267 of *Astronomical Society of the Pacific Conference Series*, pages 267–+.
- Thompson, R. I. (1984). Lyman and Balmer continuum ionization in zero-age main-sequence stars - Applications to the line excess phenomenon. *Astrophysical Journal*, 283:165–168.
- Tofani, G., Felli, M., Taylor, G. B., and Hunter, T. R. (1995). Exploring the engines of molecular outflows. Radio continuum and H₂O maser observations. *Astronomy and Astrophysics, Supplement*, 112:299–+.
- Torrelles, J. M. (1991). Radio Continuum and Molecular Line Observations Toward Herbig-Haro Objects. In A. D. Haschick & P. T. P. Ho, editor, *Atoms, Ions and Molecules: New Results in Spectral Line Astrophysics*, volume 16 of *Astronomical Society of the Pacific Conference Series*, pages 257–+.
- Torrelles, J. M., Gomez, J. F., Anglada, G., Estalella, R., Mauersberger, R., and Eiroa, C. (1992). The powering sources of the molecular outflows in the AFGL 437, AFGL 5142, and AFGL 5157 regions. *Astrophysical Journal*, 392:616–621.
- Torrelles, J. M., Ho, P. T. P., Rodríguez, L. F., and Cantó, J. (1985). VLA observations of ammonia and continuum in regions with high-velocity gaseous outflows. *Astrophysical Journal*, 288:595–603.
- Torrelles, J. M., Patel, N., Gómez, J. F., Anglada, G., and Uscanga, L. (2005). VLBI Water Maser Proper Motion Measurements in Star-Forming Regions. *Astrophysics and Space Science*, 295:53–63.
- Torrelles, J. M., Patel, N. A., Curiel, S., Estalella, R., Gómez, J. F., Rodríguez, L. F., Cantó, J., Anglada, G., Vlemmings, W., Garay, G., Raga, A. C., and Ho, P. T. P. (2011). A wide-angle outflow with the simultaneous presence of a high-velocity jet in the high-mass Cepheus A HW2 system. *Monthly Notices of the RAS*, 410:627–640.
- Townes, C. H. and Schawlow, A. L. (1975). *Microwave spectroscopy*.

- Vacca, W. D., Garmany, C. D., and Shull, J. M. (1996). The Lyman-Continuum Fluxes and Stellar Parameters of O and Early B-Type Stars. *Astrophysical Journal*, 460:914–+.
- Valdettaro, R., Palla, F., Brand, J., Cesaroni, R., Comoretto, G., Felli, M., and Palagi, F. (2002). Long-term study of water maser emission associated with young stellar objects. I. The database. *Astronomy and Astrophysics*, 383:244–266.
- van der Tak, F. F. S. and Menten, K. M. (2005). Very compact radio emission from high-mass protostars. II. Dust disks and ionized accretion flows. *Astronomy and Astrophysics*, 437:947–956.
- Varricatt, W. P., Davis, C. J., Ramsay, S., and Todd, S. P. (2010). A near-IR imaging survey of intermediate- and high-mass young stellar outflow candidates. *Monthly Notices of the RAS*, 404:661–720.
- Walker, C. K., Adams, F. C., and Lada, C. J. (1990). 1.3 millimeter continuum observations of cold molecular cloud cores. *Astrophysical Journal*, 349:515–528.
- Walmsley, M. (1995). Dense Cores in Molecular Clouds. In S. Lizano & J. M. Torrelles, editor, *Revista Mexicana de Astronomia y Astrofisica Conference Series*, volume 1 of *Revista Mexicana de Astronomia y Astrofisica*, vol. 27, pages 137–+.
- White, S. M., Pallavicini, R., and Kundu, M. R. (1992). A 5 GHz radio survey of selected POST T Tauri and naked T Tauri stars. *Astronomy and Astrophysics*, 257:557–566.
- Williams, S. J., Fuller, G. A., and Sridharan, T. K. (2004). The circumstellar environments of high-mass protostellar objects. I. Submillimetre continuum emission. *Astronomy and Astrophysics*, 417:115–133.
- Wolfire, M. G. and Cassinelli, J. P. (1987). Conditions for the formation of massive stars. *Astrophysical Journal*, 319:850–867.
- Wood, D. O. S. and Churchwell, E. (1989). The morphologies and physical properties of ultracompact H II regions. *Astrophysical Journal, Supplement*, 69:831–895.
- Wouterloot, J. G. A. and Brand, J. (1989). IRAS sources beyond the solar circle. I - CO observations. *Astronomy and Astrophysics, Supplement*, 80:149–187.
- Wouterloot, J. G. A., Brand, J., and Fiegle, K. (1993). IRAS sources beyond the solar circle. III - Observations of H₂O, OH, CH₃OH and CO. *Astronomy and Astrophysics, Supplement*, 98:589–636.
- Wu, Y., Wei, Y., Zhao, M., Shi, Y., Yu, W., Qin, S., and Huang, M. (2004). A study of high velocity molecular outflows with an up-to-date sample. *Astronomy and Astrophysics*, 426:503–515.

BIBLIOGRAPHY

- Wu, Y., Zhang, Q., Chen, H., Yang, C., Wei, Y., and Ho, P. T. P. (2005). CO J = 2-1 Maps of Bipolar Outflows in Massive Star-forming Regions. *Astronomical Journal*, 129:330–347.
- Yorke, H. W. (1986). The dynamical evolution of H II regions - Recent theoretical developments. *Annual Review of Astron and Astrophys*, 24:49–87.
- Yorke, H. W. and Sonnhalter, C. (2002). On the Formation of Massive Stars. *Astrophysical Journal*, 569:846–862.
- Yorke, H. W. and Welz, A. (1996). Photoevaporation of protostellar disks. I. The evolution of disks around early B stars. *Astronomy and Astrophysics*, 315:555–564.
- Zapata, L. A., Ho, P. T. P., Rodríguez, L. F., O'Dell, C. R., Zhang, Q., and Muench, A. (2006a). Silicon Monoxide Observations Reveal a Cluster of Hidden Compact Outflows in the OMC 1 South Region. *Astrophysical Journal*, 653:398–408.
- Zapata, L. A., Rodríguez, L. F., Ho, P. T. P., Beuther, H., and Zhang, Q. (2006b). In Search of Circumstellar Disks around Young Massive Stars. *Astronomical Journal*, 131:939–950.
- Zapata, L. A., Schmid-Burgk, J., and Menten, K. M. (2010). Orion KL: The hot core that is not a "Hot Core". *ArXiv e-prints 1009.1426*.
- Zhang, Q. and Ho, P. T. P. (1997). Dynamical Collapse in W51 Massive Cores: NH 3 Observations. *Astrophysical Journal*, 488:241–+.
- Zhang, Q., Hunter, T. R., Beuther, H., Sridharan, T. K., Liu, S., Su, Y., Chen, H., and Chen, Y. (2007). Multiple Jets from the High-Mass (Proto)stellar Cluster AFGL 5142. *Astrophysical Journal*, 658:1152–1163.
- Zhang, Q., Hunter, T. R., Brand, J., Sridharan, T. K., Cesaroni, R., Molinari, S., Wang, J., and Kramer, M. (2005). Search for CO Outflows toward a Sample of 69 High-Mass Protostellar Candidates. II. Outflow Properties. *Astrophysical Journal*, 625:864–882.
- Zhang, Q., Hunter, T. R., and Sridharan, T. K. (1998). A Rotating Disk around a High-Mass Young Star. *Astrophysical Journal, Letters*, 505:L151–L154.
- Zhang, Q., Hunter, T. R., Sridharan, T. K., and Ho, P. T. P. (2002). A Disk/Jet System toward the High-Mass Young Star in AFGL 5142. *Astrophysical Journal*, 566:982–992.
- Zinnecker, H. and Yorke, H. W. (2007). Toward Understanding Massive Star Formation. *Annual Review of Astron and Astrophys*, 45:481–563.



First steps in VLA continuum data reduction with *AIPS*

The NRAO Astronomical Image Processing System (*AIPS*) is a software package for interactive calibration and editing of radio interferometric data and for calibration, construction, display and analysis of astronomical images made using Fourier synthesis methods. A more complete and detailed description of this software and a cookbook manual can be found in the web <http://www.aips.nrao.edu/>.

Here we present some basic steps to be done during the calibration and edition of **VLA radio continuum interferometric data**. It is important to note that the present manual is not an exhaustive guide of the *AIPS* software. With the aim of making an easy manual which could be followed with no major problems, only the tasks and inputs more relevant during the reduction of interferometric data are indicated. Full explanations of these and other tasks and inputs can be found in the *AIPS Cookbook* or in the **EXPLAIN** task available for each task in the *AIPS* software.

The first and main step is to get a *uv*-data file with VLA observations. Archive VLA data files can be downloaded from the web <https://archive.nrao.edu/archive/advquery.jsp>. Once we have the *uv*-data file, the next step is to load it in *AIPS*. To do this, it is necessary to assign in the linux terminal a variable name to the path of the directory where the VLA data file is saved. For example, if our observation data file is located in */home/username/aips_data*, we should export a variable (for example, the variable *Z*):

```
> export Z='/home/username/aips_data/'
```

Hereafter, we will consider that our astronomical data is contained in two files named *AS896_1*, and *AS896_2*. The science targets are named *source1* and *source2*. The interferometer phase is calibrated by observations of the calibrators *cal1* and *cal2*. The flux density scale is calibrated by observing the flux calibrator *fluxcal*. Finally, we can enter to the *AIPS* system by typing:

```
> aips tv=local:0
```

A.1 Loading and inspecting the data

To load typical *uv*-data files from VLA observations it is common to use the **FILLM** task, although other similar tasks, as **FITLD**, which allow to load FITS files, are also good options. Some inputs in **FILLM** may change if our observations correspond to high frequency, typically 0.7 and 1.3 cm in the VLA, or centimeter frequencies, from 3.6 cm to 21 cm. Additionally, with the new EVLA antennas some differences must take into account when loading and calibrating the data.

FILLM Using the **FILLM** task we load a *uv*-data file into *AIPS*. Multiple VLA archive files may be loaded at the same time.

> TASK 'FILLM'; INP	to review the inputs
> DATAIN 'Z:AS896_	to load a set of files <i>AS896_1,... AS896_n</i> . Let the in-
	verted commas opened to read lower-case
> DOUVCOMP -1	if we want the data to be compressed, put 1
> DOALL 1	to include all data
> NCOUNT <i>n</i>	<i>n</i> is the number of files to be loaded
> DOWEIGHT 10	to apply weights
> CPARM 0	default
> BPARM 0	default
> GO FILLM	to run the program

For high frequency observations you must use:

> CPARM(8) 0.05	to use a short time in the CL-table entries; in minutes
> BPARM 20, 1	to apply opacity and gain curve corrections

If you have some EVLA antennas in the array during the observations:

> CPARM(2) 2	to use back-end T_{sys}
> CPARM(8) 0.05	only if you have high frequency observations
> BPARM 0	default; tipping curves for opacity determination are not implemented yet on the EVLA antennas

More information about the treatment of EVLA antennas in observations and calibration can be found in the web <http://www.vla.nrao.edu/astro/guides/evlareturn/>

A file with an associated *catalog slot number* will be created in *AIPS* for each band observed (L, X, K, ...) in the observational project. This *catalog slot number* differentiates each file from the others. To list all the files we can use:

> PCAT	to list all files catalogued (<i>uv</i> -data and image files)
> UCAT	to list only <i>uv</i> -data files
> MCAT	to list only image files

In order to obtain more information of each file loaded in *AIPS*, and to look for the tables associated to each file, we can use the **IMHEADER** command.

> GETN <i>i</i>	to select the file, <i>i</i> is the catalog slot number
> IMHEADER	to list header information

In case we need to delete a file in *AIPS*, we have to do:

> GETN <i>i</i>	to select the file, <i>i</i> is the catalog slot number
> ZAP	to delete the file... definitely!

Finally, you can reinitialize all the input parameters with **RESTORE** command.

> RESTORE 0	to initialize all the input parameters
-------------	--

VLANT Determines the antenna position corrections applied by the VLA operations staff after your observation. It copies a CL table and applies the correction to the antenna phases.

> TASK 'VLANT'; INP	to review the inputs
> GETN <i>i</i>	to specify the input file
> GAINVER 0	to select the last CL table version
> GO VLANT	to run the program

A.2 Tools for data examination

Once we have loaded all our files, it is important to print the array configuration. The task **PRTAN** prints the antenna (**AN**) table, and allows us to know the antenna position, baseline parameters in meters, and which antennas were out of operation. This information will be useful when selecting a reference antenna, which should be located in the central part of the array, and must have not too many problems (it can be explored using **UVPLT** and **LISTR** tasks, see below).

> TASK 'PRTAN'; INP	to review the inputs
> GETN <i>i</i>	to specify the input file
> DOCRT 132	use -1 to print in a printer or in an output file
> GO PRTAN	to run the program

Now we have to explore carefully the data received for each antenna, during each scan, for each frequency (**IF**), for each polarization (identified with the Stokes parameters), and for each source. To do this, there are different tasks, being **LISTR** and **UVPLT** the most common ones.

LISTR First of all, it is useful to print, for each observed band, all the source names and coordinates and the integration times of each scan.

> TASK 'LISTR'; INP	to review the inputs
> GETN <i>i</i>	to specify the input file
> OPTYPE 'SCAN'	to list all the observed scans
> DOCRT 132	use -1 to print in a printer or in an output file
> GO LISTR	to run the program

A. First steps in VLA continuum data reduction with *AIPS*

With LISTR we can print information of a *uv*-data file in a variety of forms. By using OPTYPE 'MATX', it prints out the amplitude or phase data, and their rms values, once per scan in a matrix format.

> TASK 'LISTR'; INP	to review the inputs
> GETN <i>i</i>	to specify the input file
> OPTYPE 'MATX'	to select matrix listing format
> SOURCE ' <i>source</i> '	to select the source, ' ' means all sources. To select only one source, we must specify the name, for example: ' <i>source1</i> ' or ' <i>cal1</i> ' or ' <i>flxcal</i> '
> CALCODE ' '	to select all kind of sources, default
> ANTEN 0	to list data for all antennas
> TIMER 0	to select an interval of time; 0 means all the observation
> STOKES ' <i>stokes</i> '	to select the polarization, different options are 'RR', 'LL'
> BIF 1	to list the first IF
> DPARM <i>dp₁ dp₂ 0</i>	it allows to print different information, for example: 3 1 0 to print amplitude and rms, scalar scan averaging 4 1 0 to print phase and rms, scalar scan averaging use -1 to print in a printer or in an output file
> DOCRT 132	to run the program
> GO LISTR	
> BIF 2	to list the second IF, each IF must be listed separately
> WAIT; GO LISTR	to wait for the previous execution and rerun the program

To locate the bad data more precisely you might rerun LISTR with the following new inputs:

> OPTYPE 'LIST'	to select column listing format
> SOURCE ' <i>source</i> '	to select the source; ' ' means all sources. To select only one source, we must specify the name, for example: ' <i>source1</i> ' or ' <i>cal1</i> ' or ' <i>flxcal</i> '
> ANTEN <i>a</i> , 0	to select the antenna <i>a</i> , where <i>a</i> is the number of the antenna. It is possible to select more than one antenna at the same time
> TIMER 0	to select an interval of time; 0 means all the observation
> STOKES ' <i>stokes</i> '	to select the polarization, different options are 'RR', 'LL'
> BIF 0	to list the IFs, beginning with the first IF
> EIF 0	to list the IFs, ending with the last IF
> DPARM 0	to select amplitudes with no averaging
> DOCRT 132	to print the information in the shell command
> GO LISTR	to run the program

These inputs produce a column listing, in your terminal, of the amplitude for the antenna A for all baselines. It is possible to select only some baselines with the input BASEL, which works similarly to the ANTEN input.

Another tool for examining the data is by plotting it in the TV display. UVPLT is the most basic task that allows us to plot the *uv*-data in a great variety of forms.

UVPLT This task complements the information provided by LISTR. Usually, UVPLT allows us to detect easily bad data by plotting it in the TV display.

> TASK 'UVPLT'; INP	to review the inputs
> GETN <i>i</i>	to specify the input file
> SOURCE ' <i>source</i> '	to select the source; ' ' means all sources. To select only one source, we must specify the name, for example: ' <i>source1</i> ' or ' <i>cal1</i> ' or ' <i>flxcal</i> '
> BIF 0	to plot the IFs, beginning with the first IF
> EIF 0	to plot the IFs, ending with the last IF
> ANTEN <i>a</i> , 0	to print the antenna <i>a</i> ; ANTEN 0 mean all antennas
> BASEL <i>b</i> , 0	to print the baseline <i>b</i> ; BASEL 0 mean all baselines
> TIMER <i>d h m s d' h' m' s'</i>	to specify the beginning day, hour, minute, and second; and ending day, hour, minute, and second. 0 means all the timerange
> UVRANG <i>min max</i>	to specify the minimum and maximum range of projected baselines; 0 means all the range
> BPARM <i>bp₁ bp₂ 0</i>	it allows to print different information, for example: 11 1 0, to print amplitude versus time 11 2 0, to print phases versus time 0, to print amplitude versus <i>uv</i> -distance 6 7 2 0, to print the <i>uv</i> coverage See Fig. A.1
> D03COL 1	to plot each IF/STOKES with a different colour
> DOTV 1	to plot the data in the TV display
> DOWEIGHT 1	default
> GO UVPLT	to run the program

During the exploration of the data we have to look for bad data, i. e., points that have anomalous amplitude or phase values which may corrupt the final calibrated data due to their presence. This data have to be *flagged*. To FLAG data different tasks can be used.

QUACK Usually, bad data can be found at the beginning of each scan. To flag the first seconds of each scan we can use the QUACK task.

> TASK 'QUACK'; INP	to review the inputs
> GETN <i>i</i>	to specify the input file
> DATAIN ' '	default
> SOURCE ' <i>source</i> '	to select the source
> ANTEN 0	to select all antennas
> TIMER 0	to select the scans of all the observation
> FLAGVER 1	to put all the flags in the version 1 of FG table
> OPCODE 'BEG'	to specify the beginning
> APARM 0 <i>m</i> 0	to flag the first <i>m</i> minutes; for example <i>m</i> =1/10
> GO QUACK	to run the program

A. First steps in VLA continuum data reduction with *AIPS*

UVFLG The next step is to flag bad data (e.g., timeranges, antennas, stokes) found during the exploration with the LISTR and UVPLT tasks. To do this we can use two tasks: UVFLG and TVFLG. TVFLG is a more interactive one that allows you to flag the data using the TV display, the reader is referred to the *AIPS Cookbook* and to the EXPLAIN task in *AIPS* for a complete understanding of TVFLG. Here we will present the UVFLG task. See also Fig. A.2.

> TASK 'UVFLG'; INP	to review the inputs
> GETN <i>i</i>	to specify the input file
> SOURCE ' <i>source</i> '	to select the source with bad data
> DATAIN ' '	you can specify bad <i>uv</i> -points from an external file
> TIMER <i>d h m s d' h' m' s'</i>	range of time to be flagged
> BIF <i>bif</i>	initial bad IF
> EIF <i>eif</i>	last bad IF
> ANTEN <i>a</i> , 0	antennas to be flagged
> BASEL <i>b</i> , 0	baselines to be flagged
> STOKES ' <i>stokes</i> '	bad stokes parameter; <i>stokes</i> can be RR, LL, RL, LR
> OUTFGVER 1	to put all the flags in the version 1 of the FG table
> APARM 0	to ignore amplitude in flagging
> OPCODE 'FLAG'	to flag the data
> GO UVFLG	to run the program

If we have flagged erroneously some good data, we can undo our error by running the UVFLG task with the same inputs, and changing the OPCODE to 'UFLG'.

A.3 Calibration strategy

Once we have examined all data and flagged bad points or antennas, we can begin the calibration. As the calibration procedures change if we have or not have high-frequency data, we will expose two different techniques. First, the basic calibration strategy, for centimeter wavelengths. Second, the procedure that should be used to reduce 7 mm (and sometimes 1.3 cm) data.

Global calibration process

SETJY To enter/calculate the flux density of each primary flux density calibrator, *fluxcal*.

> TASK 'SETJY'; INP	to review the inputs
> GETN <i>i</i>	to specify the input file
> SOURCE ' <i>fluxcal</i> '	to select the flux calibrator
> OPTYPE 'CALC'	to perform the calculation of the flux density
> APARM 0	default
> BPARM 0	default
> GO SETJY	to run the program

After running SETJY, the flux density for each calibrator and for each IF will appear in the message window. These values should be written and saved to be checked later.

CALRD Usually, the *AIPS* software provides a model for the main flux calibrators. Using a model during the calibration will produce better results. To load the model we must do:

> CALDIR	it will list all the available models
> TASK 'CALRD'; INP	to review the inputs
> OBJECT '3C???'	see Table A.3 to know the name of your flux calibrator
> BAND 'band'	the band of our observations
> OUTDISK 1	to write the model image on disk 1
> GO CALRD	to run the program

If we type PCAT, we will find a new file that corresponds to the image of the model loaded.

CALIB The CALIB task writes the amplitudes and phases for all the calibrators in a SN (solution) table, in order to be used later during the creation of the CL (calibration) table. We run first the CALIB task over our flux calibrators.

> TASK 'CALIB'; INP	to review the inputs
> GETN <i>i</i>	to specify the input file
> CALSOUR ' <i>fluxcal</i> '	to select the flux calibrator
> TIMER 0	or that corresponding to the observation
> ANTEN <i>a b ...</i>	antennas per arm (Tables A.2 & A.3); ANTENA 0 default
> UVRANGE 0 0	default if you are using a model, if not see next CALIB
> DOCAL 2	to apply the CL calibration to the data
> GAINUSE 0	to apply latest CL table
> FLAGVER 1	to apply flags from FG table 1
> GET2N <i>j</i>	<i>j</i> is the catalog slot number of the model
> FLUX 0	default
> REFANT <i>r</i>	one antenna centered in the array and with no problems
> SOLINT 0	default
> APARM 0	default
> CPARM 0	default
> SOLMODE 'A&P'	to do amplitude and phase calibration
> SNVER 1	to write the solutions in SN table 1
> GO CALIB	to run the program

CALIB Now we have to do the same for the phase calibrators.

> TASK 'CALIB'	to review the inputs
> GETN <i>i</i>	to specify the input file
> CALSOUR ' <i>cal1</i> ' ' <i>cal2</i> '	to select the phase calibrators
> TIMER 0	or that corresponding to the observation
> ANTEN 0	to select all the antennas
> UVRANGE <i>min max</i>	if the source has a limited uvrage; it can be checked in: http://www.vla.nrao.edu/astro/calib/manual/csource.html , sources with different UVRANGE must be run separately
> DOCAL 2	to apply the CL calibration to the data
> GAINUSE 0; FLAGVER 1	to apply latest CL table, and flags from FG table 1

A. First steps in VLA continuum data reduction with *AIPS*

> clr2n	to clear out the model
> REFANT <i>r</i>	to select the reference antenna
> SNVER 1	to write solutions in SN table 1
> GO CALIB	to run the program

GETJY This task is used to determine the flux density of the secondary calibrators, i.e., the phase calibrators, from the primary flux calibrator, based on the flux densities in the SU (source) table and the antenna gain solutions in the SN tables.

> TASK 'GETJY'; INP	to review the inputs
> GETN <i>i</i>	to specify the input file
> SOURCE ' <i>cal1</i> ' ' <i>cal2</i> '	phase calibrators
> CALSOUR ' <i>flxcal</i> '	flux calibrator
> BIF 0; EIF 0	to select all the IFs
> TIMER 0	or that corresponding to the observation
> SNVER 1	to use the data from SN table 1
> GO GETJY	to run the program

After running GETJY, the flux density for each IF of each phase calibrator will appear in the message window. These values should be copied and saved to be checked later.

CLCAL At this point we have gain and phase solutions for the times of all calibrator scans, including the corrected flux density for the phase calibrators. The next step is to interpolate the solutions derived from the calibrators into the CL table for all the sources. This is done by using the CLCAL task. First, you can self-calibrate all the calibrators individually.

> TASK 'CLCAL'; INP	to review the inputs
> GETN <i>i</i>	to specify the input file
> SOURCE ' <i>flxcal</i> '	first we will look for solutions on the <i>flxcal</i>
> CALSOUR ' <i>flxcal</i> '	to calibrate its solutions with itself (self-calibration)
> BIF 0; EIF 0	to select all the IFs
> TIMER 0	or that corresponding to the observation
> GAINVER 1	input CL version; 2 if you have baseline corrections
> GAINUSE 2	output CL version; 3 if you have baseline corrections
> INTERP 'self'	to select the interpolation method
> OPCODE 'CALI'	to combine SN tables into a CL table
> GO CLCAL	to run the program

We can do the same for the phase calibrators:

> SOURCE ' <i>cal1</i> '	calibrating <i>cal1</i>
> CALSOUR ' <i>cal1</i> '	using itself for self-calibration
> GO CLCAL	to run the program
> SOURCE ' <i>cal2</i> '	calibrating <i>cal2</i>
> CALSOUR ' <i>cal2</i> '	using itself for self-calibration
> GO CLCAL	to run the program

Now we can calibrate the science targets, interpolating with the solutions of the phase calibrators:

```
> TASK 'CLCAL'; INP          to review the inputs
> GETN i                    to specify the input file
> SOURCE 'source1' 'source2' all the science targets
> CALSOUR 'cal1' 'cal2'    all the phase calibrators
> BIF 0; EIF 0              to select all the IFs
> TIMER 0                   or that corresponding to the observation
> GAINVER 1                  input CL version; 2 if you have baseline corrections
> GAINUSE 2                  output CL version; 3 if you have baseline corrections
> INTERP '2pt'              to select the interpolation method
> OPCODE 'CALI'             to combine SN tables into a CL table
> GO CLCAL                  to run the program
```

After finishing the calibration process, it is important to check amplitudes and phases for all the calibrators and sources. The flux of the calibrators should be in agreement with those obtained with the SETJY and GETJY tasks. It is possible that data have still wrong amplitudes or phases after this first calibration, and we can use again the UVPLT or LISTR tasks to detect the new bad data, and flag it with UVFLG. We can use the same inputs as explained in § A.2 for UVPLT and LISTR tasks, but changing:

```
> DOCAL 2                   to apply the calibration
> GAINUSE 2                  input CL version; 3 if you have baseline corrections
```

EXTDEST If some data is bad and must be flagged for some calibrator, we must delete the SN and CL tables, and start again the calibration. To delete the SN and CL tables we have to do:

```
> TASK 'EXTDEST'; INP      to review the inputs
> INEXT 'SN'               or 'CL', to delete a table
> INVER inv                to delete the last version of the table; version 1 of the
                           CL table should not be deleted
> GO EXTDEST               to run the program
```

Remember to reset INTEXT ' ' and INVERS 0, to avoid future problems.

SPLIT Once we have done all the calibration, and checked that there is no more flagging to be done, we can create an specific (calibrated) *uv*-data file for each source.

```
> TASK 'SPLIT'; INP        to review the inputs
> GETN i                   to specify the input file
> SOURCE ' '               to do a split for all the sources
> CALCODE ' '              default
> STOKES ' '               all the stokes
> BIF 0; EIF 0             all the IFs
> TIMER 0                  all the time range, or that corresponding to the obser-
                           vation
```

A. First steps in VLA continuum data reduction with *AIPS*

> DOCAL 2	to apply the calibration
> GAINUSE 2	input CL table; 3 if you have baselines corrections
> FLAGVER 1	to apply the flags of FG table 1
> APARM 0	default
> GO SPLIT	to run the program

If we list the files with PCAT we will find a SPLIT file for each source. These files are what we need to construct images.

High frequency (and/or high resolution) calibration process

When reducing high frequency data, the standard procedure can be a source of frustration. The main reason for more complication calibration lies in the achieved high resolution and the rapid phase atmospheric fluctuations. Remember that FILLM task have to be run with special inputs. Once we have run appropriately FILLM and tasks VLANT, PRTAN, LISTR, QUACK, UVPLT and UVFLG, we can start the calibration for high-frequency (or high-resolution) data

SETJY With the same input parameters as for the global calibration procedure.

CALRD As in the standard calibration it is posible to use models for the flux calibrators.

CALIB Run CALIB to correct for phase only, with a small solution interval (e. g., 20 seconds) on all you calibrator sources, except for the flux calibrators, if you want to use a model for them. The inputs you must change with respect to the global calibration are:

> CALSOUR 'cal1', ...	all your calibrators (without models)
> DOCAL 2	to apply the CL calibration to the data
> GAINUSE 0	to apply latest CL table
> REFANT <i>r</i>	one antenna centered in the array and with no problems
> SOLINT 20/60	interval of 20 seconds, it is useful to try some values
> SOLMODE 'P'	to do phase calibration only
> SNVER 1	to write the solutions in SN table 1
> clr2n	to clear out any model previously used

For the absolute flux calibrators, you have to use the above inputs together with:

> CALSOUR ' <i>fluxcal</i> '	your flux calibrator
> GET2N <i>j</i>	<i>j</i> is the catalog slot number of the model
> INVERS 0; NCOMP 0	to use all the components of the latest CC version

It is useful to try different SOLINT values, or change the REFANT or UVRANG, in order to obtain a larger relative portion of good versus bad solutions. During all the proofs you may be performing, we recommend you to delete all the extra SN tables you are creating with CALIB using EXTDEST, you can use IMHEAD to see how many SN tables do you have. Once you have run CALIB with a model, remember to do clr2n in order to clear out the model.

CLCAL Once you are satisfied with the solutions from **CALIB**, it is time to apply phase corrections in your calibrator scans before you determine the absolute flux density scale. The inputs you must change with respect the global calibration are:

```
> SOURCE ' '; SOUCOD '*'      to correct phases only for calibrator sources
> CALSOUR ' '; CALCOD '*'     include all your calibrators, flux and phase
> OPCODE 'CALI'              to merge solutions from SN into CL table
> INTERP 'self'              to self-calibrate in the interpolation method
> SNVER 1                    to use data from SN table 1
> GAINVER 1                   input CL version; 2 if you have baseline corrections
> GAINUSE 2                   output CL version; 3 if you have baseline corrections
> REFANT  $r$                   to select the reference antenna
```

CALIB Now we have to rerun task **CALIB** with the corrected phases to obtain the flux density scale. Thus, we will calibrate now amplitudes and phases.

```
> CALSOUR 'cal1', ...        all your calibrators (without models)
> DOCAL 2                    to apply the CL calibration to the data
> GAINUSE 0                   to apply the latest CL table
> REFANT  $r$                   to select the reference antenna
> SOLINT 0                   scan lengths; phase variations are applied
> SOLMODE 'A&P'              to do full calibration to get the flux densities
> SNVER 2                    to collect solutions in a new SN table (2)
```

For the absolute flux calibrators (with models) use the previous inputs together with:

```
> CALSOUR 'fluxcal', ...     your flux calibrators (with models)
> GET2N  $j$                    $j$  is the catalog slot number of the model
```

GETJY Run **GETJY** to obtain the secondary calibrator flux densities.

```
> SOURCE 'cal1', ...        all your phase calibrators
> CALSOUR 'fluxcal'         your flux calibrators
> SNVER 2                   to use the version 2 of the SN table
```

CLCAL The final flux density calibration table is obtained by running **CLCAL** again, first self-calibrating the calibrators:

```
> SOURCE ' '; SOUCOD '*'     all the calibrators
> CALSOUR ' '; CALCOD '*'    all the calibrators
> INTERP 'self'             to self-calibrate in the interpolation method
> SNVER 2                   to use data from SN table 2
> GAINVER 2                 input CL version; 3 if you have baseline corrections
> GAINUSE 3                 output CL version; 4 if you have baseline corrections
```

...and now we interpolate for the science targets:

A. First steps in VLA continuum data reduction with *AIPS*

> SOURCE ' '; SOUCOD ' '	all the sources
> CALSOUR 'cal1', ...	all the calibrators, including flux and phase
> CALCOD ' '	default
> INTERP '2pt'	to select the interpolation method
> SNVER 2	to use data from SN table 2
> GAINVER 2	input CL version; 3 if you have baseline corrections
> GAINUSE 3	output CL version; 4 if you have baseline corrections

From here you can continue as usual according to the standard procedure. Checking, with `UVPLT` and `LISTR` tasks, the amplitudes and phases after the calibration. And splitting the data into single source data sets with `SPLIT` task.

A.4 Imaging

To elaborate maps, the `IMAGR` task can be used. Two main inputs: `IMSIZE` and `CELLSIZE`, which correspond to the size in pixels of the map, and the size in arcseconds of a pixel, respectively, must be carefully chosen. Here we show how to calculate these two parameters.

By knowing the frequency of our observations we can calculate the primary beam, θ_{PB} (i.e., the area of the sky observed with the telescope). Usually it is interesting to plot a region 3 times larger than the primary beam. The size of the map in arcseconds can be estimated by using

$$\left[\frac{\text{size of the map}}{\text{arcsec}} \right] = \left[\frac{8100}{\nu_{\text{GHz}}} \right]. \quad (\text{A.1})$$

How to determine the `CELLSIZE`? Using the `UVPLT` task with `BPARM 0` and selecting the newly-created `SPLIT` file, we can determine the longest uv -distance (in $k\lambda$). The inverse of this distance will be the size of the synthesized beam in radians, and we can convert it into arcseconds. To obtain a good image we can make the size of each pixel (`CELLSIZE`) 4 times less than the size of the beam. Consider now an example where the longest uv -distance is 25 $k\lambda$. Then

$$\text{beam size} = \frac{1}{25000} = 4 \cdot 10^{-5} \text{ rad} = 4 \cdot 10^{-5} \frac{3600 \cdot 360}{2\pi} = 8''.25, \quad (\text{A.2})$$

$$\text{cellsize} = \frac{\text{beam size}}{4} \simeq 2''/\text{pixel}. \quad (\text{A.3})$$

How to determine the `IMSIZE`? Dividing the size (in arcseconds) of the map by the `CELLSIZE` we will find the value for the size of the map in pixels (`IMSIZE`). Typical values for the `IMSIZE` are powers of 2 (e.g., 128, 256, 512, 1024).

IMAGR Now we can start to make the image map using the `IMAGR` task. This task is one of the most important tasks in the imaging process, as it offers a wide range of options for cleaning.

> TASK 'IMAGR'; INP	to review the inputs
> GETN <i>i</i>	to specify the input file, it is usually a <code>.split</code> file

> STOKES 'I'	to do a map of intensity (stokes parameter I)
> CELLSIZE <i>cs cs</i>	to specify the <i>cellsize</i> (<i>cs</i>)
> IMSIZE <i>is is</i>	to specify the <i>imsize</i> (<i>is</i>)
> UVTAPER <i>u v</i>	to specify widths in <i>u</i> and <i>v</i> directions of a gaussian function to weight down long baselines; the default is 0
> UVRANGE <i>min max</i>	to specify minimum and maximum project baselines to include; 0 is the default and recommended
> ROBUST <i>R</i>	it can take a value between -5 and +5 >+4 is close to natural weighting <-4 is close to uniform weighting
> GAIN 0.1	0.3 for compact and strong sources 0.05 for extended sources
> FLUX <i>flux</i>	to stop the cleaning process when residual image maximum is < <i>flux</i> ; 0 is the default and recommend
> NITER <i>N</i>	a long number, for example 10000
> DOTV 1	to do cleaning interactively using the TV display
> GO IMAGR	to run the program

Read the EXPLAIN IMAGR task in *AIPS* to obtain help in every input.

With the TV display on (DOTV 1), you can follow the progress of your imaging. Furthermore, a menu of interactive options is also displayed (see Fig. A.3). To select an option from the menu, click with the mouse on the name of the option and press A or F3 in the keyboard. Some of the most common options in this menu are: **tvflame** to change the grey scale into a fire scale (i.e., a more beautiful color to work with, i think); **tvzoom** to make a zoom of a region of the map, press A (or F3) to zoom in and B (or F4) to zoom out; **tvbox** to define different boxes when cleaning. To begin the cleaning you must select **continue clean** (select it with the mouse and press A or F3). During the cleaning process, look in detail the message window, some important values appear during each cleaning iteration: the *total flux cleaned* and the number of clean components (or iterations). For each iteration the total cleaned flux is expected to rise. When this value becomes estable or starts to decrease, you should stop the cleaning. To stop the process you must select **stop cleaning**. The IMAGR task will create two files (you can list them by using PCAT). The .IBM001 (.ibm) file corresponds to the beam image, and the .ICL001 (.icl) file to the cleaned map. This last file is the image we were expecting to get since the begining of the manual... hooray!

Using the TVL0D or TVALL tasks we can plot the image in the TV. TVALL allows us to modify the color of the grey scale, and the contrast level. There are two tasks that provide some information about the image, they are the IMSTAT and TVSTAT tasks.

IMSTAT To read a portion of an image and print the mean and rms brightnesses found. It also prints the location and value of the maximum and minimum brightness in that portion.

> TASK 'IMSTAT'; INP	to review the inputs
> GETN <i>i</i>	to select the cleaned image, it is usually a .icl
> BLC <i>x_{min} y_{min}</i>	bottom left corner; 0 for the minimum corner
> TRC <i>x_{max} y_{max}</i>	top right corner; 0 for the maximum corner
> IMSTAT	to run the program

TVSTAT Similar to the IMSTAT task, but TVSTAT uses the current TV image rather than an image specified, and it determines the values over irregular regions (not only boxes or circles).

> GETN <i>i</i>	to select the cleaned image, it is usually a .icl
> tvinit	to initialize the TV screen
> TVLOD	to load the image on the TV screen
> TVSTAT	with the mouse click on the TV image, and press A (or F3) to select the first vertex of the area. Repeat three, four or as many times as you want. At the end press D (or F6) to close the area and estimate the rms

The IMPOS task allows you to read a celestial (also pixels) position from a TV image using the cursor. By clicking on the TV screen with the mouse, and typing A (or F3), it prints in the terminal the celestial coordinates of that point, and the pixel coordinates. These pixel coordinates can be used to define BLC and TRC positions. TVWIN can be used to set BLC and TRC with the mouse.

KNTR To plot a contour and/or grey-scale plot for one or two images. We will consider only plotting one image.

> TASK 'KNTR'; INP	to review the inputs
> GETN <i>i</i>	to select the cleaned image, it is usually a .icl
> DOCONT 1	to plot countours
> DOVECT -1	use 1 to plot polarized vectors
> DOGREY -1	use 1 to plot a grey scale map
> BLC x_{\min} y_{\min}	bottom left corner
> TRC x_{\max} y_{\max}	top right corner
> PLEV 0	percent of peak for the contour increment; use 0 if you want to indicate the rms noise level in the CLEV input
> CLEV <i>rms</i>	<i>rms</i> of the map, for example: 5e-5, 5e-4, or 5e-3
> LEVS l_1, l_2, l_3, \dots	the levels to be plotted, one example is: -5, -4, -3, 3, 4, 5, 7, 9, 12, 15, 20
> FACTOR 0	default; used in polarization
> CBPLOT 1	to plot the beam at bottom left corner
> DOTV 1	to plot directly on the TV screen
> tvinit	to initialize the TV screen
> GO KNTR	to run the program

To print in the printer the map generated with KNTR we have to do:

> TASK 'KNTR'; INP	to review the inputs
> DOTV -1	to select the printer or and output file
> GO KNTR	to run the program
> GO LWPLA	to print the file created with KNTR

JMFIT This task allows you to fit a gaussian function to a portion of an image, for example to your source. By doing this you can obtain basic physical parameters of your source as the peak intensity, flux density, deconvolved size, celestial position of the source, and so on.

> TASK 'JMFIT'; INP	to review the inputs
> GETN <i>i</i>	to select the cleaned image, it is usually a .icl
> BLC x_{\min} y_{\min}	coordinates of the bottom left corner
> TRC x_{\max} y_{\max}	coordinates of the top right corner
> NGAUSS 0	you can fit up to 4 gaussians in a portion of an image
> NITER 1000	use up to 2000 to fit one gaussian
> DOCRT 132	to print the result of the fit in the message window
> GO JMFIT	to run the program

You must specify a portion of the map by using the BLC and TRC inputs. It is possible to define a portion of the box by loading the image with TVALL and then by using TVWIN to define over the window the portion you want to analyze. It is important to note also, that with IMHEADER you can find information of the synthesized beam.

IMFIT is a task similar to JMFIT, although with little differences. If your source has extended and a complex structure, it is obvious that fitting a gaussian is not a good procedure to estimate the flux density. In these cases, you can use TVSTAT (as explained before) to select the portion of the image that have emission from your source.

At this point I have to say... Congratulations! You have calibrated your data, you have made an image and a map of your source, and finally you have estimated some physical parameters of your source. Now you can submit it to your favourite astronomical journal.

And remember... *AIPS* is your friend!

If you have any question, any suggestion, or any problem when using this manual, do not hesitate to contact me at asanchez@am.ub.es. It would be a pleasure for me to help you.

UVPLT examples with different BPARM inputs

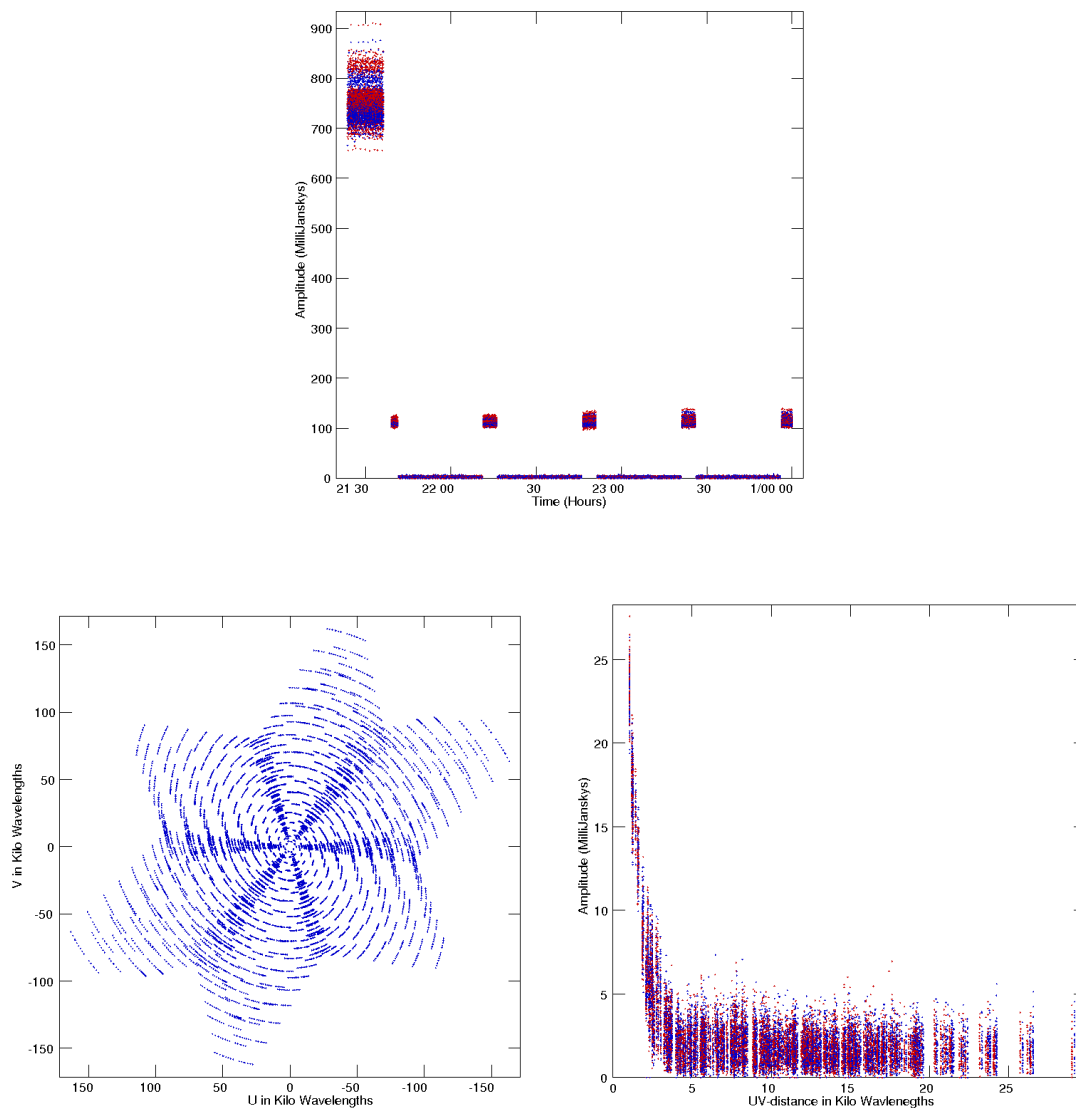


Figure A.1: UVPLT plots with different BPARM options *Top*: BPARM 11 1 0, which correspond to amplitude versus time in hours. By plotting all the sources we can distinguish the flux calibrator (in this case it has an amplitude of ~ 750 mJy), the phase calibrator (it has an amplitude of ~ 120 mJy), and the source (it has an amplitude of ~ 0 mJy). *Bottom-left*: BPARM 6 7 2 0, which correspond to the uv -coverage of a single source. *Bottom-right*: BPARM 0, which correspond to the amplitude versus the uv -distance for a single source.

Bad points in your map... use UVFLG

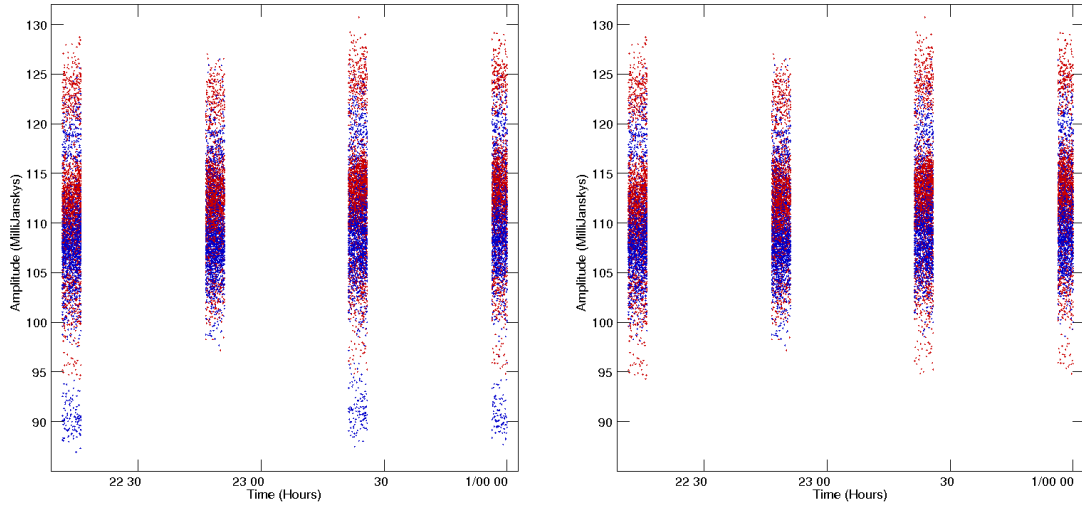


Figure A.2: Example of plots to show typical bad data points to be flagged with UVFLG task. In *right* panel we can find some points with an amplitude of 90–95 mJy. By inspecting the data carefully we found that the IF number 2 of the antenna 22 is the responsible. If we flag this IF of this antenna, we obtain the plot shown in *left* panel. Now, all points seem to be good points.

Table A.1: Primary beam of the VLA at different wavelengths

Band	Wavelength (cm)	Frequency (GHz)	Primary Beam $45/\nu_{\text{GHz}}$ (arcmin)	Size of the map (arcmin)
P	90.0	0.33	130	~ 410
L	20.0	1.4	30	~ 90
C	6.0	5.0	9	~ 27
X	3.6	8.5	5	~ 15
U	2.0	15	3	~ 9
K	1.3	23	2	~ 6
Q	0.7	45	1	~ 3

Table A.2: Information of the uv -range and antennas per arm for the flux calibrators

3C48, 3C147, 3C138					
Band		uv -range (k λ)	Configuration	Antennas per arm	Notes
P	90 cm	0 – 40	All	All	
L	20 cm	0 – 40	A	7	
		0 – 40	B ,C, D	All	
C	6.0 cm	0 – 40	A	3	
		0 – 40	B, C, D	All	
X	3.6 cm	0 – 40	A	2	
		0 – 40	B	6	
		0 – 40	C, D	All	
U	2.0 cm	0 – 40	A	1	Not recommended
		0 – 40	B	4	
		0 – 40	C, D	All	
K	1.3 cm	0 – 40	A	1	Not recommended
		0 – 40	B	3	
		0 – 40	C, D	All	
3C286					
Band		uv -range (k λ)	Configuration	Antennas per arm	Notes
P	90 cm	0 – 18	A	7	
		0 – 18	B, C, D	All	
L	20 cm	0 – 18	A	4	
		0 – 18	B, C, D	All	
		90 – 180	A	All	Reduce flux 6%
C	6.0 cm	0 – 25	A	1	Not recommended
		0 – 25	B	4	
		0 – 25	C, D	All	
		150 – 300	A	All	Reduce flux 2%
X	3.6 cm	50 – 300	A	3	Reduce flux 1%
		50 – 300	B	4	Reduce flux 1%
		50 – 300	C	All	Reduce flux 1%
		0 – 15	D	All	
U	2.0 cm	0 – 150	A	3	
		0 – 150	B, C, D	All	
K	1.3 cm	0 – 185	A	2	
		0 – 185	B	7	
		0 – 185	C, D	All	

Table A.3: Information for the standard VLA flux calibrators

3C48	0137+331	J2000				01 ^h 37 ^m 41 ^s .299431	33° 09' 35".132990	
	0134+329	J1950				01 ^h 34 ^m 49 ^s .826400	32° 54' 20".259000	
	BAND	A	B	C	D	FLUX (Jy)	UVMIN (kλ)	UVMAX (kλ)
	P 90 cm	S	S	S	S	42.00		
	L 20 cm	X	P	P	P	16.50		40
	C 6.0 cm	X	S	P	P	5.48		40
	X 3.6 cm	X	X	S	P	3.25		40
	U 2.0 cm	X	X	S	P	1.78		40
	K 1.3 cm	X	X	X	S	1.13		100
	Q 7 cm	X	X	X	S	0.64		100
3C286	1331+305	J2000				13 ^h 31 ^m 08 ^s .287984	30° 30' 32".958850	
	1328+307	J1950				13 ^h 28 ^m 49 ^s .657700	30° 45' 58".640000	
	BAND	A	B	C	D	FLUX (Jy)	UVMIN (kλ)	UVMAX (kλ)
	P 90 cm	S	S	S	S	26.00		
	L 20 cm	S	S	P	P	15.00		
	C 6.0 cm	S	S	S	P	7.47		
	X 3.6 cm	S	P	P	P	5.23		400
	U 2.0 cm	S	S	S	S	3.40		
	K 1.3 cm	X	S	S	P	2.59		
	Q 7 cm	X	S	P	P	1.45		300
3C138	0521+166	J2000				05 ^h 21 ^m 09 ^s .886021	16° 38' 22".051220	
	0518+165	J1950				05 ^h 18 ^m 16 ^s .514100	16° 35' 26".834000	
	BAND	A	B	C	D	FLUX (Jy)	UVMIN (kλ)	UVMAX (kλ)
	P 90 cm	S	S	S	S	17.50		
	L 20 cm	X	S	P	P	8.47		45
	C 6.0 cm	X	X	S	P	3.78		45
	X 3.6 cm	X	X	S	S	2.52		45
	U 2.0 cm	X	X	X	S	1.56		45
	Q 7 cm	X	X	?	?	0.40		
3C147	0542+498	J2000				05 ^h 42 ^m 36 ^s .137916	49° 51' 07".233560	
	0538+498	J1950				05 ^h 38 ^m 43 ^s .517500	49° 49' 42".837000	
	BAND	A	B	C	D	FLUX (Jy)	UVMIN (kλ)	UVMAX (kλ)
	P 90 cm	S	S	S	S	52.30		
	L 20 cm	X	S	P	P	22.50		50
	C 6.0 cm	X	X	S	P	7.94		50
	X 3.6 cm	X	X	S	P	4.84		50
	U 2.0 cm	X	X	X	S	2.78		50
	Q 7 cm	X	?	?	?	0.91		

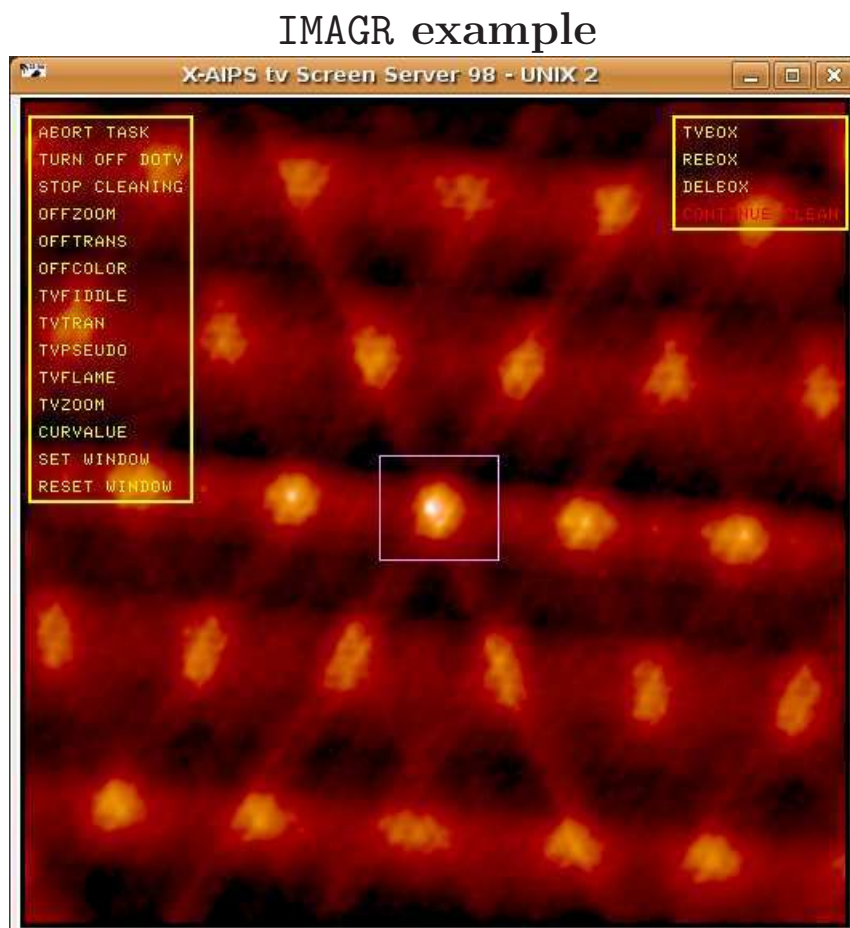


Figure A.3: TV display for the IMAGR task. When executing IMAGR with DOTV 1, you can interactively clean your image. An image similar to the one in the figure will appear in your TV display. You have different menus (words in yellow) to select. You must click with the mouse in one menu, and then press A (or F3) to select it. In some case you have to press D (or F6) to get out of the selected option. The main options are: `tvflame` to change frew scale into a fire scale; `tvzoom` to mke a zoom in the region of interest; `tvbox` to define different boxes, i. e., regions that you want to clean, because you know there is a source (in the figure there is a box defined at center of the image, the source is inside the box); `continue clean` to iterate cleaning the image, and `stop cleaning` to stop the cleaning. You usually will have your source at the center of the image, and an hexagonal patern all around the map. These *extra* sources are due to the secondary lobes. You will see that they start to disappear when cleaning your source. You should finish cleaning when your image shows a uniform colour scale (i. e., all is noise, there are no more sources).

B

Physical parameters of H II regions

The emission at centimeter wavelengths of young stellar objects is majorly dominated by free–free continuum emission and radio recombination lines from ionized gas. Two major mechanisms are responsible for the ionization: *photoionization* and *ionization through shocks*. The former is associated with the large amount of ultraviolet (UV) photons coming from newly-born early-type stars, and the latter is associated with collisions between intense stellar winds and/or outflows and the circumstellar medium. In this Appendix, we will focus our attention on the continuum emission coming from regions of gas (mainly hydrogen) ionized by UV photons, the so-called H II regions.

B.1 Fundamental equations of H II regions

In an ionized environment, electrons accelerate because of the electrostatic interaction with protons and positive ions. The power emitted by a system of charges is given, as a first approximation, by the Larmor equation. Ionized electrons are free particles, unbounded, so the radiation produced will have a continuum spectrum. This kind of emission is known as thermal bremsstrahlung or free–free emission.

The free–free absorption coefficient at radio frequencies is given by (Gordon 1988)

$$\kappa_{ff}(\nu) = \frac{n_e n_i}{\nu^2} \frac{8 Z^2 e^6}{3\sqrt{3} m_e^3 c} \left(\frac{\pi}{2}\right)^{1/2} \left(\frac{m_e}{kT_e}\right)^{3/2} \langle g \rangle, \quad (\text{B.1})$$

where n_e and n_i are the electron and ion densities (for pure hydrogen $n_e = n_i$), ν is the frequency, Z is the ion charge (for hydrogen $Z = 1$), e is the elementary electron charge, m_e is the mass of electron, c is the speed of light, k is the Boltzmann constant, T_e is the

B. Physical parameters of H II regions

kinetic temperature of electrons and $\langle g \rangle$ is the Gaunt factor, which can be defined, for temperatures $\lesssim 10^6$ K, as (Gayet 1970)

$$\langle g \rangle \simeq \frac{\sqrt{3}}{\pi} \ln \left[\left(\frac{2kT_e}{\epsilon m_e} \right)^{3/2} \frac{m_e}{\pi \epsilon Z e^2 \nu} \right], \quad (\text{B.2})$$

with ϵ the Euler constant equal to $e^{(0.577)}$. At radio frequencies, the absorption coefficient can be approximated as (Altenhoff et al. 1960)

$$\left[\frac{\kappa_{ff}(\nu)}{\text{pc}^{-1}} \right] \approx 0.08235 \left[\frac{n_e n_i}{\text{cm}^{-6}} \right] \left[\frac{T_e}{\text{K}} \right]^{-1.35} \left[\frac{\nu}{\text{GHz}} \right]^{-2.1}. \quad (\text{B.3})$$

By integrating Equation B.3 along the line of sight, l , we obtain the optical depth of the free-free emission

$$\tau_{ff}(\nu) = \int_{\text{line of sight}} \kappa_{ff}(\nu) dl = 0.08235 \left[\frac{EM}{\text{cm}^{-6} \text{ pc}} \right] \left[\frac{T_e}{\text{K}} \right]^{-1.35} \left[\frac{\nu}{\text{GHz}} \right]^{-2.1}, \quad (\text{B.4})$$

where EM is the emission measure along the line of sight, $EM = \int_{\text{line of sight}} n_e n_i dl$.

For a source with thermal free-free emission, the general solution of the radiative transfer equation for the continuum intensity, $I_{ff}(\nu)$, is

$$\begin{aligned} I_{ff}(\nu) &= I_0 e^{-\tau_{ff}(\nu)} + \int_0^{\tau_{ff}(\nu)} \mathcal{S}_\nu e^{-\tau'} d\tau' \\ &= (\mathcal{S}_\nu - I_0) (1 - e^{-\tau_{ff}(\nu)}), \end{aligned} \quad (\text{B.5})$$

where I_0 is the background intensity and \mathcal{S}_ν is the source function of the H II region. The second equality in Equation B.5 is true for an uniform medium. The source function, \mathcal{S}_ν , for the free-free radiation can be defined as

$$\mathcal{S}_\nu = B_\nu(T_e) = \frac{2h\nu^3}{c^2} \frac{1}{e^{h\nu/kT_e} - 1}, \quad (\text{B.6})$$

with h the Planck constant and $B_\nu(T_e)$ the Planck function at a temperature T_e . At radio frequencies, where the Rayleigh-Jeans approximation ($h\nu \ll kT_e$) is valid, Equation B.6 becomes

$$\mathcal{S}_\nu = B_\nu(T_e) \simeq \frac{2kT_e\nu^2}{c^2}. \quad (\text{B.7})$$

By integrating the specific intensity, $I_{ff}(\nu)$, from Equation B.5 over the angular size of the source, Ω_{source} , we obtain the flux density, S_ν ,

$$S_\nu = \int_{\Omega_{\text{source}}} I_{ff}(\nu) d\Omega = \int_{\Omega_{\text{source}}} (\mathcal{S}_\nu - I_0) (1 - e^{-\tau_{ff}(\nu)}) d\Omega. \quad (\text{B.8})$$

Taking into account that the background radiation will generally have a temperature of ~ 2.7 K and the source function of the H II region has $\sim 10^4$ K, we can assume $\mathcal{S}_\nu \gg I_0$, obtaining

$$S_\nu = \int_{\Omega_{\text{source}}} \mathcal{S}_\nu (1 - e^{-\tau_{ff}(\nu)}) d\Omega. \quad (\text{B.9})$$

For an homogeneous H II region, with constant density, Equation B.9 is expressed as

$$S_\nu = \mathcal{S}_\nu (1 - e^{-\tau_{ff}(\nu)}) \Omega_{\text{source}}. \quad (\text{B.10})$$

B.2 Physical parameters of optically thin H II regions

Depending on the optical depth, and thus on the frequency, we can observe two different behaviours. The frequency for which the optical depth is $\tau_\nu = 1$, is known as the turnover frequency, ν_t , and can be given in practical units, from Equation B.4, as

$$\left[\frac{\nu_t}{\text{GHz}} \right] = 0.627 \left[\frac{EM}{10^6 \text{ cm}^{-6} \text{ pc}} \right]^{0.48} \left[\frac{T_e}{10^4 \text{ K}} \right]^{-0.64}. \quad (\text{B.11})$$

For low frequencies, $\nu \ll \nu_t$, (or optical depths $\tau_\nu \gg 1$) the source is **optically thick**, and the flux density can be written, in the Rayleigh-Jeans approximation, as

$$S_\nu \cong \frac{2kT_e\nu^2}{c^2} \Omega_{\text{source}}. \quad (\text{B.12})$$

For high frequencies, $\nu \gg \nu_t$, (or optical depths $\tau_\nu \ll 1$) the source is **optically thin**, and the flux density, expanding the exponential of Equation B.10, can be expressed as

$$S_\nu \cong \frac{2kT_e\nu^2}{c^2} \tau_{ff}(\nu) \Omega_{\text{source}}. \quad (\text{B.13})$$

When observing typical H II regions at centimeter wavelengths, $\nu > 5 \text{ GHz}$, we can usually consider optically thin emission. With this assumption, we can estimate some physical parameters of H II regions. Let us consider an optically thin source of angular diameter θ_S , corresponding to an angular size of the source $\Omega_{\text{source}} = (\pi/4 \ln 2) \theta_S^2$, observed at a frequency ν . The emission measure can be estimated from

$$\left[\frac{EM}{\text{cm}^{-6} \text{ pc}} \right] = 1.682 \times 10^7 \left[\frac{S_\nu}{\text{Jy}} \right] \left[\frac{\nu}{\text{GHz}} \right]^{0.1} \left[\frac{T_e}{\text{K}} \right]^{0.35} \left[\frac{\theta_S}{\text{arcsec}} \right]^{-2}. \quad (\text{B.14})$$

If the source has a geometrical depth, L , equal to its diameter, which can be estimated from the observed angular diameter, θ_S , and its distance, D ; the electron density, considering a spherical geometry, is given by

$$\left[\frac{n_e}{\text{cm}^{-3}} \right] = 5.563 \times 10^2 \left[\frac{EM}{\text{cm}^{-6} \text{ pc}} \right]^{1/2} \left[\frac{D}{\text{pc}} \right]^{-1/2} \left[\frac{\theta_S}{\text{arcsec}} \right]^{-1/2}. \quad (\text{B.15})$$

From the electron density, and considering a spherical geometry, the mass of ionized gas, $M_i = \int n_e m_H dV$, is

$$\left[\frac{M_i}{M_\odot} \right] = 1.472 \times 10^{-18} \left[\frac{n_e}{\text{cm}^{-3}} \right] \left[\frac{D}{\text{pc}} \right]^3 \left[\frac{\theta_S}{\text{arcsec}} \right]^3, \quad (\text{B.16})$$

B. Physical parameters of H II regions

where m_H is the Hydrogen mass, and V is the volum of a sphere with diameter θ_S . It is also possible to estimate the flux of ionizing photons, \dot{N}_i , necessary to produce the observed ionized region. By considering the Strömgren's sphere model, the balance equation between the number of recombinations and the number of photoionizations within the H II region is

$$\dot{N}_i = \frac{4}{3}\pi R_S^3 n_e^2 \alpha^{(2)} \quad (\text{B.17})$$

with R_S the Strömgren's radius, \dot{N}_i the number of photons with $\lambda < 912\text{\AA}$ per unit of time emitted by the protostar, and $\alpha^{(2)}$ the recombination coefficient to the level 2 or higher (recombinations to level 1 produce a ionizing photon, thus they must not be considered), which can be estimated as $3 \times 10^{-13} [T_e]^{-3/4} \text{ cm}^3 \text{ s}^{-1}$, with T_e in K. In practical units, the flux of ionizing photons is

$$\left[\frac{\dot{N}_i}{\text{s}^{-1}} \right] = 8.852 \times 10^{40} \left[\frac{S_\nu}{\text{Jy}} \right] \left[\frac{\nu}{\text{GHz}} \right]^{0.1} \left[\frac{T_e}{10^4 \text{ K}} \right]^{0.35} \left[\frac{D}{\text{pc}} \right]^2. \quad (\text{B.18})$$

With the flux of ionizing photons, and assuming the H II region is produced by a single star, we can estimate the spectral type of the ionizing star using the tables of Panagia (1973), Thompson (1984), Vacca et al. (1996), or Diaz-Miller et al. (1998).

B.3 Optically thick H II regions

It is important to note, that not all H II regions are optically thin at centimeter wavelengths. In the last years, observations toward several H II regions have revealed a number of objects being exceptionally small ($< 0.05 \text{ pc}$) and dense ($n_e > 10^6 \text{ cm}^{-3}$; $EM > 10^9 \text{ pc cm}^{-6}$), the so-called hypercompact H II regions (see ?, for a review). In this kind of H II regions, the turnover frequency is located at frequencies $\gtrsim 20 \text{ GHz}$, resulting in a spectral energy distribution with the optically thick regime detectable at radio wavelengths (see Figure B.1).

It is obvious that we can not use equations of Section B.2 to estimate the physical parameters of hypercompact H II regions. The most appropriate way to estimate their physical parameters is by constructing the spectral energy distribution, and fitting it to the expression

$$\begin{aligned} S_\nu &= B_\nu(T_e) (1 - e^{-\tau_{ff}(\nu)}) \Omega_{\text{source}} \\ &= \frac{2h\nu^3}{c^2} \frac{1}{e^{h\nu/kT_e} - 1} (1 - e^{-\tau_{ff}(\nu)}) \Omega_{\text{source}}, \end{aligned} \quad (\text{B.19})$$

where the optical depth and angular size of the source are defined by

$$\tau_{ff}(\nu) = 0.08235 \left[\frac{EM}{\text{cm}^{-6} \text{ pc}} \right] \left[\frac{T_e}{\text{K}} \right]^{-1.35} \left[\frac{\nu}{\text{GHz}} \right]^{-2.1}, \quad (\text{B.20})$$

$$\Omega_{\text{source}} = \frac{\pi}{4 \ln 2} \theta_S^2. \quad (\text{B.21})$$

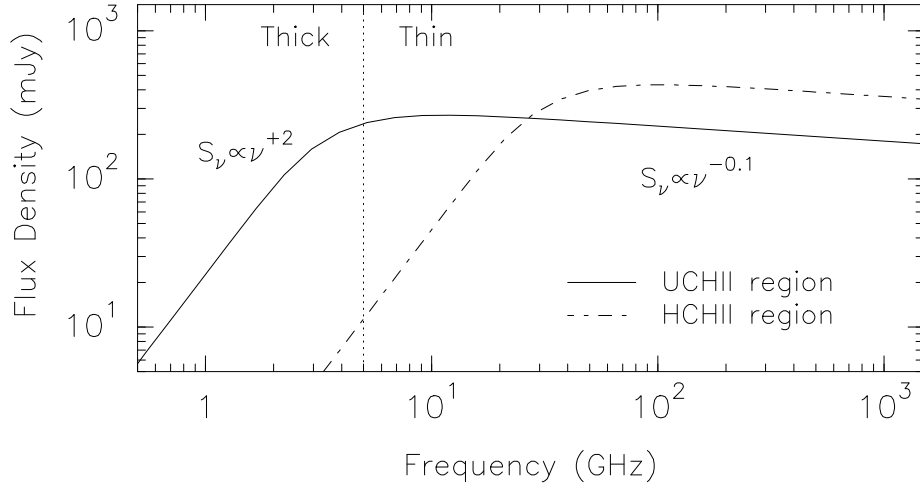


Figure B.1: Radio spectrum of thermal bremsstrahlung emission from a spherical, homogeneous, isothermal H II region. The solid line corresponds to an H II region with the optically thin ($S_\nu \propto \nu^{-0.1}$) regime at radio wavelengths, and with the turnover frequency (vertical dotted line) at 5 GHz. The dot-dashed line corresponds to an HCH II region, optically thick ($S_\nu \propto \nu^{+2}$) in the radio regime, and with a turnover frequency at 50 GHz.

Note that we are still assuming homogeneous H II regions. To obtain the physical parameters we only have to find the values of EM (or n_e) and θ_S that better fit the observational data (assuming some certain value for T_e , e. g., 10^4 K). Since the angular size of the source is usually determined observationally, we only have to find the best emission measure that fits our data.

In Section B.5, we introduce the `HIIREGIONS.f` program that allow the user to fit the spectral energy distribution of any H II region, obtaining its physical parameters.

B.4 H II regions with density gradient

We can now try to estimate and model non-homogeneous H II regions. The easiest way is to assume the electron density depends on the distance from the ionizing protostar in a power-law distribution, $n_e \propto r^{-q}$. Olsson (1975) and Panagia and Felli (1975) deal with this assumption and calculate the spectral energy distributions of non-homogeneous H II regions. In the program `HIIREGION.f` (see Section B.5) you can also fit the observational data of such non-homogeneous H II regions.

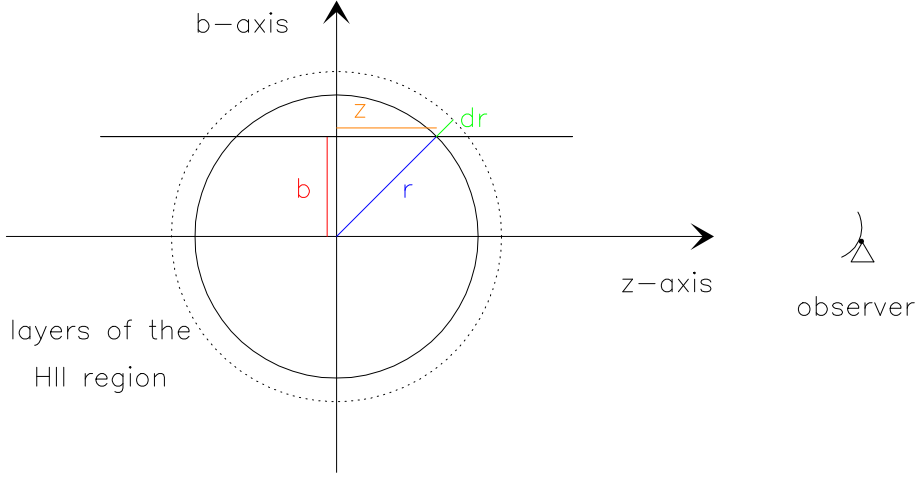


Figure B.2: Scheme of a spherical, non-homogeneous H II region. We assume the H II region is divided into different shells of inner and outer radius r and $r + dr$. The observer's line of sight corresponds to the z -axis.

The two main equations to be solved, assuming $n_e = n_i$, are

$$S_\nu = \int_{\Omega_{\text{source}}} \frac{2h\nu^3}{c^2} \frac{1}{e^{h\nu/kT_e} - 1} (1 - e^{-\tau_{ff}(\nu)}) d\Omega \quad (\text{B.22})$$

$$\tau_{ff}(\nu) = \int_{\text{line of sight}} 0.08235 \left[\frac{n_e^2}{\text{cm}^{-6}} \right] \left[\frac{T_e}{\text{K}} \right]^{-1.35} \left[\frac{\nu}{\text{GHz}} \right]^{-2.1} dl. \quad (\text{B.23})$$

One way to solve these integrations is taking into account the adimensional variables z and b (see Figure B.2). In this scheme, the spherical H II region can be divided into different shells with inner and outer radii r and $r + dr$, respectively. If the observer is located in the z -axis, we can divide the region in cylinders of radius b . Thus, we can first calculate the elemental flux density of each cylinder, and then integrate over all the range of radii b . The emission measure can be expressed as

$$\begin{aligned} EM &= \int_{\text{line of sight}} n_e^2 dz \\ &= \int_b^\infty n_e^2(r) \frac{r dr}{\sqrt{r^2 - b^2}}, \end{aligned} \quad (\text{B.24})$$

where we have used the relation $r^2 = b^2 + z^2$. By introducing a power-law distribution in density, $n_e = n_0(r/r_0)^{-q}$, we obtain

$$EM(b) = 2 \times \int_b^\infty n_0^2 \left(\frac{r}{r_0} \right)^{-2q} \frac{r dr}{\sqrt{r^2 - b^2}}, \quad (\text{B.25})$$

note that we have introduced a factor of 2, that accounts for the two sides of the sphere (i.e., to the left and to the right of the b -axis in Figure B.2). The solution to the integral

Table B.1: Gamma functions and spectral indices^a for different density gradients

power q^b	$\Gamma[q]$	$\Gamma[(q-1)+1/2]$	$EM(b)^c$	α^{thick}	$\alpha^{\text{intermediate}}$	α^{thin}
2	1	$\sqrt{\pi}/2$	$\propto b^{-3}$	+2.0	+0.6	-0.1
3	2	$3\sqrt{\pi}/4$	$\propto b^{-5}$	+2.0	+1.16	-0.1
4	6	$15\sqrt{\pi}/8$	$\propto b^{-7}$	+2.0	+1.4	-0.1
5	24	$105\sqrt{\pi}/16$	$\propto b^{-9}$	+2.0	+1.53	-0.1

^a Spectral indices α ($S_\nu \propto \nu^\alpha$) at centimeter wavelengths for different electron density power-laws.

^b Power q , of the electron density power-law, $n_e \propto r^{-q}$.

^c Proportionality of the emission measure (Eq. B.26) in function of the coordinate b (see Fig. B.2).

of Equation B.25 is

$$\begin{aligned}
 EM(b) &= 2 \times (n_0 r_0^q)^2 \int_b^\infty \frac{r^{1-2q} dr}{\sqrt{r^2 - b^2}} \\
 &= (n_0 r_0^q)^2 \sqrt{\pi} \frac{\Gamma[(2q-1)/2]}{\Gamma[q]} b^{1-2q},
 \end{aligned} \tag{B.26}$$

where $\Gamma[x]$ is the Gamma function. In Table B.1 we list the values of the Gamma function in Equation B.26 for different values of q . Using the result of the emission measure (Equation B.26) we can calculate the optical depth as

$$\tau_{ff}(\nu) = 0.08235 \left[\frac{EM(b)}{\text{cm}^{-6} \text{ pc}} \right] \left[\frac{T_e}{\text{K}} \right]^{-1.35} \left[\frac{\nu}{\text{GHz}} \right]^{-2.1}. \tag{B.27}$$

Finally, we can use Equations B.26 and B.27 to solve Equations B.22 and B.23. We can numerically integrate EM (or τ_{ff}) over b , in a range of values that cover the extension of our radiocontinuum source.

Observationally, we can determine which is the most appropriate power-law density distribution (see Figure B.3). Each density distribution produces three well differentiated regions in the spectral energy distribution: an optically thick regime with a spectral index of +2 (i. e., $S_\nu \propto \nu^2$), an optically thin regime with the typical spectral index of -0.1 (i. e., $S_\nu \propto \nu^{-0.1}$), and an intermediate regime with a spectral index between -0.1 and +2. The intermediate spectral index directly depends on the power-law distribution (value of q ; Table B.1). For a density distribution $n_e \propto r^{-2}$, the intermediate spectral index is +0.6 (equal to the spectral index of a biconical, collimated ionized stellar wind; Reynolds 1986). For a density distribution $n_e \propto r^{-4}$, the intermediate spectral index is +1.4.

B. Physical parameters of H II regions

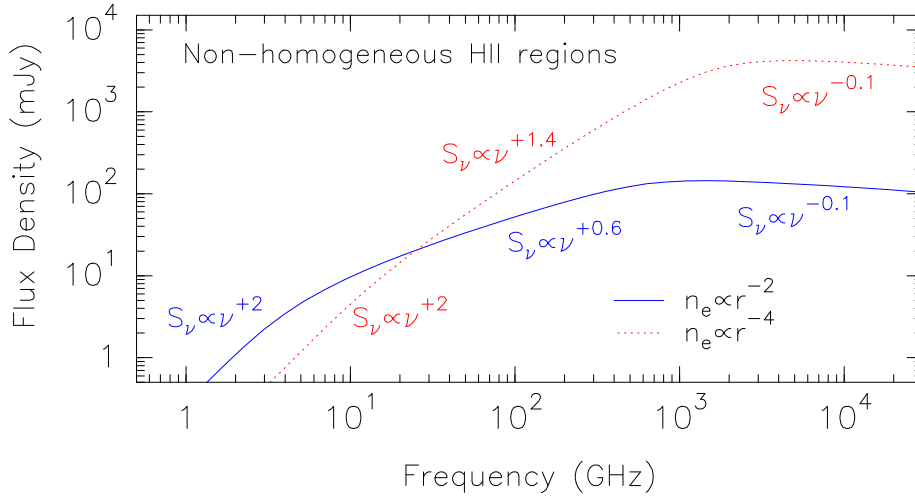


Figure B.3: Thermal bremsstrahlung spectra for spherical, non-homogeneous H II regions. The blue solid line corresponds to a non-homogeneous H II region with a density gradient in the form $n_e \propto r^{-2}$, we can appreciate three different regimes: the optically thick regime with a spectral index of +2, the intermediate regime with +0.6, and the optically thin regime with -0.1 . The red dotted line corresponds to a non-homogeneous H II region with a density gradient in the form $n_e \propto r^{-4}$. The three different regimes are also visible, with the spectral index of the intermediate regime equal to +1.4.

B.5 Program HIIregions.f

Álvaro Sánchez-Monge¹ developed a FORTRAN 77 program to estimate the physical parameters of H II regions and to fit the spectral energy distributions: `HIIregions.f`². The program can be used to fit not only the H II region spectra but also the spectral energy distribution of up to two dust (modified blackbodies) components. You only need an input file `SOURCE.dat` with the observational data of your source, with the format:

```
SOURCE      !source
2000.        !dist
1            !ndat
2            !nfow
3.60d+01  8.4601d+0  1.42d-03  0.29d-03  0.80d+00  0.80d+00
1            !next
2            !nfowext
6.00d+01  4.8601d+0  -1.90d-03  -0.01d-03  1.00d+00  1.00d+00
```

¹You can contact him (me) in asanchez@am.ub.es

²A version of this program can be found at <http://www.am.ub.es/~asanchez/utilities/HIIregions>

The `SOURCE.dat` input file must have a small header including the name of the source (it must be the same as the name of the input file, i.e., `SOURCE`) and the distance to the source in parsec (in the example it corresponds to 2000 pc). The `ndat` integer parameter indicates the number of observational data you want to introduce, and the `nfow` integer parameter indicates if you want to read the wavelength (`nfow=1`) or the frequency (`nfow=2`) from your list of observational inputs. The list of observational data inputs must contain six different numbers: the **wavelength in mm**, the **frequency in GHz**, the **flux density and its error in Jy**, and the **angular size of the source, major and minor axis, in arcsec**. The `next` and `nfowext` integer parameters are similar to the `ndat` and `nfow` inputs, but they refer to the list of observational data inputs listed at the end of the file. This observational data inputs have the same structure as the previous ones, and they refer to those extra observational data not directly related with the ionized gas, i.e., data at millimeter or submillimeter wavelengths associated with the dust envelope, or upper/lower limits at each wavelength.

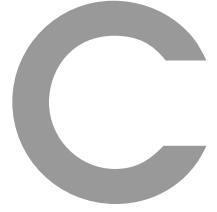
To compile and execute the FORTRAN 77 code you can use the executable file `g77g` also provided in the webpage. You should type:

```
$ g77g HIIregions
$ ./HIIregions
```

When executing the program you will find a menu with different options, each option contains a submenu that allows you to change different parameters, from physical parameters associated with the dust envelope or H II region to parameters related with the aspect of the axis in the plot. The main menu reads as

```
*****
***** Main Menu *****
0.- Exit program
1.- Input data file
2.- Modify dust envelope parameters
3.- Modify disk component parameters
4.- Modify homogeneous HII region parameters
5.- Modify density gradient HII region parameters
6.- Modify plot parameters
```

You should be able to follow the instructions provided in the different menus, in order to properly fit the spectral energy distribution of your target. Any comment, question, doubt, suggestion or whatever can be sent to: asanchez@am.ub.es.



Dust mass estimation

Young stellar objects, formed within galactic molecular clouds, are surrounded by large amounts of gas and dust. The dust grains (only 1% with respect to the mass of the gas) absorb the radiation (with wavelengths shorter than the grain sizes, typically around $0.01 \mu\text{m}$ and $1 \mu\text{m}$) emitted by the protostar, causing high extinction at optical wavelengths in star-forming regions. The absorbed radiation is then reemitted as continuum emission at longer wavelengths, mainly at infrared and (sub)millimeter wavelengths, due to the low temperature of dust.

C.1 Fundamental equations of dust emission

Dust emission can be approximated by a modified blackbody law characterized by the temperature of dust, T_d . Such a spectrum corresponds to a blackbody law, $B_\nu(T_d)$, with an optical depth τ_ν that depends on frequency. The intensity emitted at a given frequency ν is given by

$$I_\nu = B_\nu(T_d) (1 - e^{-\tau_\nu}), \quad (\text{C.1})$$

where the Planck function is

$$B_\nu(T_d) = \frac{2h\nu^3}{c^2} \frac{1}{e^{h\nu/kT_d} - 1}, \quad (\text{C.2})$$

with h the Planck constant, c the speed of light and k the Boltzmann constant. By integrating the specific intensity over the angular size of the source Ω_{source} , we obtain the flux density

$$S_\nu = \int_{\Omega_{\text{source}}} B_\nu(T_d) (1 - e^{-\tau_\nu}) d\Omega, \quad (\text{C.3})$$

C. Dust mass estimation

which, for an homogeneous source, turns into

$$S_\nu = B_\nu(T_d) (1 - e^{-\tau_\nu}) \Omega_{\text{source}}. \quad (\text{C.4})$$

The angular size of the source can be obtained observationally from the angular diameter, θ_S , as $\Omega_{\text{source}} = (\pi/4 \ln 2) \theta_S$, and the optical depth, τ_ν , is proportional to the column mass density along the line of sight, l ,

$$\tau_\nu = \int_{\text{line of sight}} \kappa_\nu \rho \, dl, \quad (\text{C.5})$$

with κ_ν being the absorption coefficient per unit of total mass (gas and dust) density. In the millimeter and submillimeter range, κ_ν is generally well described by

$$\left[\frac{\kappa_\nu}{\text{cm}^2 \text{ g}^{-1}} \right] = \kappa_0 \left[\frac{\nu}{1000 \text{ GHz}} \right]^\beta, \quad (\text{C.6})$$

with β , the dust emissivity index, taking values close to 2 in the interstellar medium, and between 1 and 2 in most star-forming regions, depending on the composition of dust grains, and on variations of the homogeneity and size of the region (Walker et al. 1990; Mezger et al. 1991). The value of κ_0 is not well known. Generally accepted values can be found in Beckwith et al. (1990), $0.1 \text{ cm}^2 \text{ g}^{-1}$ at 1000 GHz, and in Ossenkopf and Henning (1994), who compute and tabulate the opacity dust in dense protostellar cores for different gas densities between 1 μm and 1.3 mm. Note that the values provided by Ossenkopf & Henning are dust opacities, if we want to compute the total (gas and dust) mass (see below) we need to take into account the gas-to-dust ratio. Since the dust is generally a 1% of the mass of gas, we must divide the Ossenkopf & Henning dust opacities by 100 to obtain total (gas and dust) mass opacities.

The mass of gas and dust can be estimated from the observed flux density. From Equation C.4, and assuming optically thin emission, we can write

$$\begin{aligned} S_\nu &\simeq B_\nu(T_d) \Omega_{\text{source}} \tau_\nu = B_\nu(T_d) \frac{A}{D^2} \kappa_\nu \int_{\text{line of sight}} \rho \, dl \\ &= B_\nu(T_d) \kappa_\nu \frac{M_{\text{d+g}}}{D^2}, \end{aligned} \quad (\text{C.7})$$

where A is the area of the source and D is the distance to the source, and we have defined the mass of gas and dust as $M_{\text{d+g}} = A \int \rho \, dl$. From Equation C.7 it is possible to write

$$M_{\text{d+g}} = \frac{S_\nu D^2}{B_\nu(T_d) \kappa_\nu}, \quad (\text{C.8})$$

or in practical units

$$\left[\frac{M_{\text{d+g}}}{M_\odot} \right] = 0.00325 \left[\frac{\nu}{\text{THz}} \right]^{-3} \left[\frac{\kappa_\nu}{\text{cm}^2 \text{ g}^{-1}} \right] \left[\exp \left(0.048 \frac{[\nu/\text{GHz}]}{[T_d/\text{K}]} \right) - 1 \right] \left[\frac{S_\nu}{\text{Jy}} \right] \left[\frac{D}{\text{kpc}} \right]^2, \quad (\text{C.9})$$

which, introducing the absorption coefficient per unit of total mass (Equation C.6) of Beckwith et al. (1990), i. e., $\kappa_0 = 0.1 \text{ cm}^2 \text{ g}^{-1}$, results in

$$\left[\frac{M_{\text{d+g}}}{M_\odot} \right] = 0.0325 \left[\frac{\nu}{1000 \text{ GHz}} \right]^{-(3+\beta)} \left[\exp \left(0.048 \frac{[\nu/\text{GHz}]}{[T_{\text{d}}/\text{K}]} \right) - 1 \right] \left[\frac{S_\nu}{\text{Jy}} \right] \left[\frac{D}{\text{kpc}} \right]^2. \quad (\text{C.10})$$

From the total mass, we can estimate the volumn density, $n_{\text{d+g}}$, and column density, $N_{\text{d+g}}$, of dust and gass. Since the major contribution to gas is due to molecular Hydrogen, H_2 , it is commong to find in the litetature that authors refer to these two variables as n_{H_2} and N_{H_2} , respectively. Assuming a spherical cloud, the volumn density comes from

$$n_{\text{H}_2} = \frac{1}{\mu m_{\text{H}}} \frac{M_{\text{d+g}}}{(4/3)\pi R^3}, \quad (\text{C.11})$$

where μ is the mean molecular mass per Hydrogen atom, m_{H} is the Hydrogen mass, and R is the radius of the cloud. In practical units it reads as

$$\left[\frac{n_{\text{H}_2}}{\text{cm}^{-3}} \right] = 2.95 \times 10^8 \left[\frac{M_{\text{d+g}}}{M_\odot} \right] \left[\frac{\mu}{2.3} \right]^{-1} \left[\frac{\theta_{\text{S}}}{\text{arcsec}} \right]^{-3} \left[\frac{D}{\text{kpc}} \right]^{-3}. \quad (\text{C.12})$$

The column density, N_{H_2} , can be obtained from

$$N_{\text{H}_2} = \int_{\text{line of sight}} n_{\text{H}_2} dl, \quad (\text{C.13})$$

or in practical units

$$\left[\frac{N_{\text{H}_2}}{\text{cm}^{-2}} \right] = 2.21 \times 10^{24} \left[\frac{M_{\text{d+g}}}{M_\odot} \right] \left[\frac{\mu}{2.3} \right]^{-1} \left[\frac{\theta_{\text{S}}}{\text{arcsec}} \right]^{-2} \left[\frac{D}{\text{kpc}} \right]^{-2}. \quad (\text{C.14})$$

It is important to note, that typical uncertainties in the mass estimation can be around a factor of 5, due to the large uncertainties involved in the distance determination.

We have introduced the opacity laws of Beckwith et al. (1990) and Ossenkopf and Henning (1994). However, there are other useful works that deal with the estimation of the gas and dust mass from radio continuum observations at (sub)millimeter wavelengths. Hildebrand (1983) and Beuther et al. (2005) use the opacities given in Hildebrand (1983) obtaing the equations

$$\left[\frac{M_{\text{d+g}}}{M_\odot} \right] = \frac{2.0 \times 10^{-2}}{J_\nu(T_{\text{d}})} \frac{a}{0.1 \text{ } \mu\text{m}} \frac{\rho}{3 \text{ g cm}^{-3}} \frac{R}{100 \text{ Jy}} \left(\frac{D}{\text{kpc}} \right)^2 \left(\frac{\nu}{1.2 \text{ THz}} \right)^{-(3+\beta)}, \quad (\text{C.15})$$

$$\left[\frac{N_{\text{d+g}}}{\text{cm}^{-2}} \right] = \frac{1.25 \times 10^{12}}{J_\nu(T_{\text{d}}) \Omega_{\text{source}}} \frac{a}{0.1 \text{ } \mu\text{m}} \frac{\rho}{3 \text{ g cm}^{-3}} \frac{R}{100 \text{ Jy}} \left(\frac{\nu}{1.2 \text{ THz}} \right)^{-(3+\beta)}, \quad (\text{C.16})$$

where $J_\nu(T_{\text{d}}) = [\exp(h\nu/kT_{\text{d}}) - 1]^{-1}$, and a , ρ , and R are the grain size, grain mass density, and gass-to-dust ratio. Frau et al. (2010) provide in their Appendix A the equations to

C. Dust mass estimation

estimate the mass and column density without the assumption of optically thin emission. They estimate the optical depth as

$$\tau_\nu = -\ln \left(1 - \frac{S_\nu}{\Omega_{\text{source}} B_\nu(T_d)} \right), \quad (\text{C.17})$$

and the mass and column density as

$$N_{\text{d+g}} = \int n_{\text{d+g}} dl = \int \frac{\rho}{\mu m_{\text{H}}} dl = \frac{\tau_\nu}{\mu m_{\text{H}} \kappa_\nu}, \quad (\text{C.18})$$

$$M_{\text{d+g}} = \mu m_{\text{H}} D^2 N_{\text{d+g}} \Omega_{\text{source}}, \quad (\text{C.19})$$

where μ is the mean molecular mass per Hydrogen atom, and m_{H} is the Hydrogen mass.



Molecular Column Density Calculation

D.1 Column Density Calculation

D.1.1 Radiative transfer equation

The specific intensity of the radiation, I_ν , that is propagated through the empty space is constant along the path it follows. If radiation interacts with matter in some region of the space, the matter will absorb a fraction of the radiation and will emit at the same time its own radiation. The intensity variation through the path x can be described with the *absorption coefficient* κ_ν (the attenuation per length unit at the frequency ν), and with the *emission coefficient* j_ν (intensity produced per length unit). The equation that provides the variation of the intensity per unit of length, taking into account these two coefficients, is the *radiative transfer equation*

$$\frac{dI_\nu}{dx} = -\kappa_\nu I_\nu + j_\nu. \quad (\text{D.1})$$

The emission coefficient j_ν has dimensions of $\text{erg s}^{-1} \text{cm}^{-3} \text{sr}^{-1} \text{Hz}^{-1}$, while the absorption coefficient κ_ν has dimensions of cm^{-1} . The inverse of κ_ν has units of length and is known as the *mean free path*, of the radiation or photon: $l_\nu = 1/\kappa_\nu$. Its physical meaning is the mean distance travelled by a photon of frequency ν before it is absorbed. The propagation in empty space corresponds to the particular case where $\kappa_\nu = j_\nu = 0$, i.e., without any radiation-matter interaction.

We can define the absorption and emission coefficients with the absorption and emission

D. Molecular Column Density Calculation

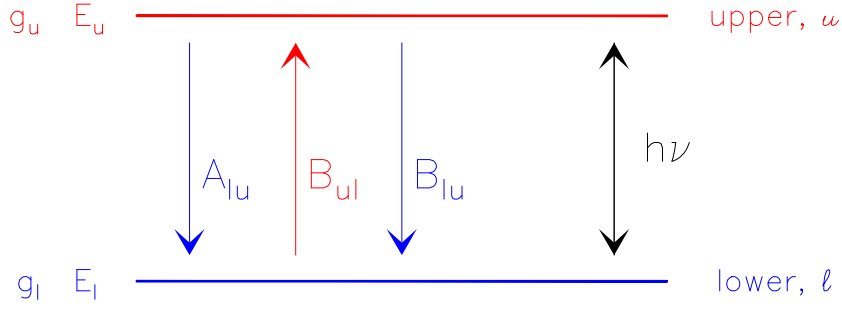


Figure D.1: Scheme of a two-energy level system, u and l are the upper (red) and lower (blue) levels, separated by an energy $h\nu$. Each level is characterized by an energy E and a degeneracy g . The absorption and emission Einstein coefficients characterize the population between both levels.

Einstein coefficients. Thus, the emission coefficient can be defined as

$$j_\nu = \frac{n_u A_{ul}}{4\pi} h\nu_{ul} \phi(\nu), \quad (\text{D.2})$$

where subindices u and l refers to the upper and lower levels (see Fig. D.1), n_u is the density of particles in the upper level, ν_{ul} is the frequency of the transition, h is the Planck constant, $\phi(\nu)$ is the line profile, and A_{ul} is the *Einstein spontaneous emission coefficient*. The absorption coefficient is defined as

$$\kappa_\nu = \frac{n_l B_{lu} - n_u B_{ul}}{4\pi} h\nu_{ul} \phi(\nu), \quad (\text{D.3})$$

where n_l is the density of particles in the lower level, B_{lu} is the *Einstein absorption coefficient*, and B_{ul} is the *Einstein stimulated emission coefficient*.

D.1.2 Optical depth, source function and temperatures

In some cases it is useful to rewrite the radiative transfer equation in terms of two new variables: the *optical depth* τ_ν (adimensional) and the source function \mathcal{S}_ν (with dimensions of intensity), both defined from the absorption and emission coefficients as follows

$$d\tau_\nu = \kappa_\nu dx, \quad (\text{D.4})$$

$$\mathcal{S}_\nu = \frac{j_\nu}{\kappa_\nu}. \quad (\text{D.5})$$

Thus, the radiative transfer equation can be written as

$$\frac{dI_\nu}{d\tau_\nu} = -I_\nu + \mathcal{S}_\nu, \quad (\text{D.6})$$

which solution can be expressed as

$$I_\nu = I_\nu^0 e^{-\tau_\nu} + \mathcal{S}_\nu (1 - e^{-\tau_\nu}), \quad (\text{D.7})$$

where I_ν^0 is the intensity for $\tau_\nu = 0$.

We can define the *excitation temperature* T_{ex} as the temperature associated with the source function, i. e., the excitation temperature is the temperature (usually, function of the frequency) for which the value of the source function is equal to the value of a Planck function for a given frequency ν ,

$$\mathcal{S}_\nu = B_\nu(T_{\text{ex}}) = \frac{2h\nu^3}{c^2} \frac{1}{e^{h\nu/kT_{\text{ex}}} - 1}. \quad (\text{D.8})$$

Similarly, we can define the *brightness temperature* T_{B} as the temperature (usually, function of frequency) for which the intensity I_ν is equal to the value of the Planck function for a given frequency ν ,

$$I_\nu = B_\nu(T_{\text{B}}) = \frac{2h\nu^3}{c^2} \frac{1}{e^{h\nu/kT_{\text{B}}} - 1}. \quad (\text{D.9})$$

At low frequencies or high temperatures, we can use the Rayleigh-Jeans approximation ($h\nu \ll kT$) and obtain

$$I_\nu \simeq \frac{2k\nu^2}{c^2} T_{\text{B}}, \quad (\text{D.10})$$

with the intensity proportional to the brightness temperature. Since this proportionality between intensity and temperature is useful, but it is only applicable in the Rayleigh-Jeans regime, we can define the *radiation temperature* T_{R} , that in the Rayleigh-Jeans approximation is equal to the brightness temperature,

$$I_\nu = \frac{2k\nu^2}{c^2} T_{\text{R}}, \quad (\text{D.11})$$

but in general it is written as

$$T_{\text{R}} = J_\nu(T_{\text{B}}) = \frac{h\nu/k}{e^{h\nu/kT_{\text{B}}} - 1}, \quad (\text{D.12})$$

where J_ν is the energy in units of temperature.

The solution to the radiative transfer equation (Equation D.7) can be written in terms of temperatures (taking into account Equations D.8 and D.9) as follow

$$T_{\text{R}} \equiv J_\nu(T_{\text{B}}) = J_\nu(T_{\text{bg}}) e^{-\tau_\nu} + J_\nu(T_{\text{ex}}) (1 - e^{-\tau_\nu}), \quad (\text{D.13})$$

where J_ν is the energy in units of temperature, T_{B} is the brightness temperature, T_{ex} is the excitation temperature, T_{bg} is the background temperature assumed to be 2.74 K which corresponds to the background intensity I_ν^0 , and T_{R} is the radiation temperature.

D.1.3 Molecular column density

In this Appendix we will briefly present how to calculate the molecular column density, by assuming a simple two-level molecule model (see Fig. D.1), and that all the molecular levels can be described by a single excitation temperature. You can find more detailed discussions on radiative processes in Spitzer (1978) and Estalella and Anglada (1999).

From the general definitions of the source function (Equation D.5) and the excitation temperature (Equation D.8), we can directly obtain

$$j_\nu = B_\nu(T_{\text{ex}}) \kappa_\nu. \quad (\text{D.14})$$

Since we want to evaluate the observed radiation over a measured spectral line profile and along a specific line-of-sight, we need to integrate Equation D.14 over these two parameters:

$$\iint j_\nu \, d\nu \, dx = \iint B_\nu(T_{\text{ex}}) \kappa_\nu \, d\nu \, dx. \quad (\text{D.15})$$

Substituting Equations D.2 and D.8 into this equation results in

$$\iint \frac{n_u A_{ul}}{4\pi} h\nu_{ul} \phi(\nu) \, d\nu \, dx = \iint \frac{2h\nu_{ul}^3}{c^2} \frac{1}{e^{h\nu_{ul}/kT_{\text{ex}}} - 1} \kappa_\nu \, d\nu \, dx. \quad (\text{D.16})$$

If we integrate over x we obtain

$$\frac{N_u A_{ul}}{4\pi} h\nu_{ul} \int \phi(\nu) \, d\nu = \frac{2h\nu_{ul}^3}{c^2} \frac{1}{e^{h\nu_{ul}/kT_{\text{ex}}} - 1} \int \tau_\nu \, d\nu, \quad (\text{D.17})$$

where the monochromatic frequency ν_{ul} can be taken out of the integral, and the column density N_u (the number of molecules in the energy level u integrated over the pathlength dx) and the optical depth τ_ν along the path x , are defined as

$$N_\nu \equiv \int_{\text{line of sight}} n_\nu \, dx \quad (\text{D.18})$$

$$\tau_\nu \equiv \int_{\text{line of sight}} \kappa_\nu \, dx \quad (\text{D.19})$$

Since $\int \phi_\nu \, d\nu = 1$, and writing the optical depth in terms of the velocity (using $\int \tau_\nu \, d\nu = (\nu_{ul}/c) \int \tau_v \, dv$, where c is the speed of light), we obtain from Equation D.17

$$\frac{N_u A_{ul}}{4\pi} h\nu_{ul} = \frac{2h\nu_{ul}^4}{c^3} \frac{1}{e^{h\nu_{ul}/kT_{\text{ex}}} - 1} \int \tau_v \, dv. \quad (\text{D.20})$$

Additionally, the optical depth in terms of the velocity can be rewritten in terms of the maximum optical depth τ_0 (at the center of the line) and the linewidth Δv , using the profile function $\phi_v(v)$,

$$\tau_v = \tau_0 \Delta v \phi_v(v). \quad (\text{D.21})$$

Substituting Equation D.21 into Equation D.20, and using $\int \phi_v dv = 1$, we can finally obtain

$$\tau_0 \Delta v = \frac{c^3}{8\pi \nu_{ul}^3} N_u A_{ul} \left(e^{h\nu_{ul}/kT_{\text{ex}}} - 1 \right). \quad (\text{D.22})$$

Solving for the column density in level u , N_u , in Equation D.22 results in the following

$$N_u = \frac{8\pi \nu_{ul}^3}{c^3} \frac{1}{A_{ul}} \frac{\tau_0 \Delta v}{\left(e^{h\nu_{ul}/kT_{\text{ex}}} - 1 \right)}. \quad (\text{D.23})$$

It is important to note that we have only assumed a two-level molecule model to derive an expression to calculate the column density of a molecular transition, i. e., no assumptions on (local) thermodynamic equilibrium have been used. In order to estimate the total molecular column density, we will assume that all the molecular levels are well described by a single excitation temperature. Thus the population of each level i is given by the *Boltzmann equation*

$$\frac{N_i}{N_u} = \frac{g_i}{g_u} e^{-(E_i - E_u)/kT_{\text{ex}}}, \quad (\text{D.24})$$

where g_u and E_u are the upper state degeneracy and energy, and g_i and E_i are the degeneracy and energy for the level i . The total molecular column density can be obtained from the sum of all the i -level column densities as follow

$$N_{\text{mol}} = \sum_{\text{all levels}} N_i = N_u \sum_{\text{all levels}} \frac{g_i}{g_u} e^{-(E_i - E_u)/kT_{\text{ex}}}. \quad (\text{D.25})$$

We can define the partition function Q (check Equation D.50 in Section D.1.5) as

$$Q \equiv \sum_{\text{all levels}} g_i e^{-E_i/kT_{\text{ex}}}. \quad (\text{D.26})$$

Taking into account the partition function (Equation D.26), and solving for the molecular column density, N_{mol} , in Equation D.25 results in

$$N_{\text{mol}} = N_u \frac{Q}{g_u} e^{E_u/kT_{\text{ex}}}. \quad (\text{D.27})$$

Thus, Equations D.23 and D.27 can be used to calculate the molecular column density from astronomical observations. We *only* need to know the excitation temperature, T_{ex} , the observed linewidth, Δv , and the optical depth at the center of the line, τ_0 , together with constants (specific for each molecule and transition) that will be explained in next sections.

D.1.4 Observational terms

As said in the previous section, we need some observational parameters to estimate the molecular column density: T_{ex} , Δv , and τ_0 . The determination of these three observational parameters is slightly different depending on the kind of transition. Thus, at this point

D. Molecular Column Density Calculation

we must differentiate between single transitions, and transitions with hyperfine structure. We will focus our analysis taking into account that we have obtained the observational parameters via a CLASS¹ fit of the spectra. However, most of these parameters can also be obtained from fits done with other softwares. Additionally, we must take into account the coupling between the radiation and the telescope (e. g., filling factor effects).

Line temperature and filling factor

When observing a spectral line, the observed intensity, I_ν^{ON} , includes both contribution from the line emission and from the background continuum emission

$$I_\nu^{\text{ON}} = I_\nu^0 e^{-\tau_\nu} + \mathcal{S}_\nu (1 - e^{-\tau_\nu}). \quad (\text{D.28})$$

The baseline subtraction consists in subtracting the intensity of the background continuum emission, $I_\nu^{\text{OFF}} = I_\nu^0$ (i. e., the intensity where $\tau_\nu = 0$), to the line emission. At this point, the spectral line intensity can be written as

$$I_\nu = I_\nu^{\text{ON}} - I_\nu^{\text{OFF}} = [\mathcal{S}_\nu - I_\nu^0] (1 - e^{-\tau_\nu}), \quad (\text{D.29})$$

and in units of temperature, we can define the line temperature, T_L , as

$$I_\nu = \frac{2k\nu^2}{c^2} T_L(\nu). \quad (\text{D.30})$$

Similar to Equation D.11, the line temperature is a radiation temperature, $T_L = J_\nu(T_B)$. Using the line temperature and the opacity in terms of the velocity, we can write Equation D.32 as

$$T_L(v) = [J_\nu(T_{\text{ex}}) - J_\nu(T_{\text{bg}})] (1 - e^{-\tau_v}). \quad (\text{D.31})$$

The line intensity at the center of the line is

$$T_0 = [J_\nu(T_{\text{ex}}) - J_\nu(T_{\text{bg}})] (1 - e^{-\tau_0}). \quad (\text{D.32})$$

It is worth to note that the line intensity is positive (*emission line*) when $T_{\text{ex}} > T_{\text{bg}}$. We will see negative line intensity (*absorption line*) when $T_{\text{ex}} < T_{\text{bg}}$. The later can happen when we are observing some molecular line transition (e. g., NH_3) toward a hotter/brighter continuum background source (e. g., an hypercompact H II region).

The line temperature defined in Equation D.31 describes the spectral line temperature of the source, but this value may differ from the temperature measured with the telescope. The relation between the observed radiation (main beam temperature, T_{MB}) and the radiation of the source (line temperature, T_L) depends on the angular size of the source (Ω_{source}) and the beam size of our observations (Ω_{beam}) through a factor known as *filling factor*, f ,

$$T_{\text{MB}} = f T_L, \quad (\text{D.33})$$

¹CLASS can be found in the software package GILDAS, Grenoble Image and Line Data Analysis System, see <http://www.iram.fr/IRAMFR/GILDAS>.

which is < 1 for unresolved sources ($\Omega_{\text{source}} \ll \Omega_{\text{beam}}$) and $f \simeq 1$ for resolved sources ($\Omega_{\text{source}} > \Omega_{\text{beam}}$). The angular size (Ω) can be expressed in terms of the Full Width at Half Maximum (FWHM; θ) as

$$\Omega = \frac{\pi}{4 \ln 2} \theta^2 \simeq 1.133 \theta^2. \quad (\text{D.34})$$

The filling factor, one of the main uncertainties when estimating the column density, can be roughly estimated (Araya et al. 2005) as

$$f = \frac{\theta_{\text{source}}^2}{(\theta_{\text{source}}^2 + \theta_{\text{beam}}^2)}, \quad (\text{D.35})$$

where θ_{source} and θ_{beam} are the source FWHM and the beam FWHM. The latter is also known as the Half-Power Beam Width (HPBW). In practical situations we can assume the filling factor to be ~ 1 for interferometric observations, and < 1 for single-dish observations.

Single transitions

When observing a single transition, a CLASS fit of the spectra provides us with four parameters: the integrated area of the line \mathcal{A} (in K km s⁻¹), the central velocity of the line v_{LSR} (in km s⁻¹), the linewidth Δv (in km s⁻¹), and the main beam temperature of the line T_{MB} (in K). We note that it is interesting (advisable) to have the spectra in units of temperature and velocity. If you have it in intensity (Jy beam⁻¹) and/or frequency (Hz), you should be able to convert it easily into K and km s⁻¹ by using the Doppler equation $dv = -c/\nu_{ul} d\nu$ and

$$\left[\frac{T_{\text{MB}}}{K} \right] = 1.22 \times 10^3 \left[\frac{I_\nu}{\text{mJy beam}^{-1}} \right] \left[\frac{\theta_{\text{beam}}}{\text{arcsec}} \right]^{-2} \left[\frac{\nu_{ul}}{\text{GHz}} \right]^{-2}. \quad (\text{D.36})$$

Out of all the terms that the CLASS fit provides you, the linewidth and the main beam temperature are the ones you need to estimate the molecular column density. Hereafter, we will use ν instead of ν_{ul} , to simplify the notation.

From T_{MB} you can obtain the excitation temperature T_{ex} (necessary in Equations D.23 and D.27). Using Equations D.31, D.33 and D.35 we can relate the measured temperature T_{MB} with the excitation temperature T_{ex} . Thus, solving for T_{ex} results in

$$T_{\text{ex}} = \frac{h\nu/k}{\ln \left[\frac{h\nu/k}{T_{\text{L}}/(1-\exp(-\tau_0)) + J_\nu(T_{\text{bg}})} + 1 \right]}. \quad (\text{D.37})$$

Remember, that for interferometric observations $T_{\text{L}} \simeq T_{\text{MB}}$, and in the case of single-dish observations we can estimate f through Equation D.35 assuming a source size. The opacity at the center of the line, τ_0 , can be obtained by observing different isotopologues of a molecule (e.g., CS and C³⁴S, CO and ¹³CO) as follow (from Equation D.31)

$$\frac{T_{\text{L}}^{\text{iso}}}{T_{\text{L}}^{\text{main}}} = \left[\frac{J_\nu^{\text{iso}}(T_{\text{ex}}) - J_\nu^{\text{iso}}(T_{\text{bg}})}{J_\nu^{\text{main}}(T_{\text{ex}}) - J_\nu^{\text{main}}(T_{\text{bg}})} \right] \left[\frac{1 - e^{-\tau_0^{\text{iso}}}}{1 - e^{-\tau_0^{\text{main}}}} \right], \quad (\text{D.38})$$

D. Molecular Column Density Calculation

where *iso* and *main* refer to two different isotopologues. By assuming that $J_\nu^{\text{iso}}(T) \simeq J_\nu^{\text{main}}(T)$ (i.e., the frequency of both isotopologues are similar), and taking into account that $\tau_0^{\text{main}} = R \tau_0^{\text{iso}}$ (where R is the *main* to *iso* abundance ratio), we obtain

$$\frac{T_L^{\text{iso}}}{T_L^{\text{main}}} = \left[\frac{1 - e^{-\tau_0^{\text{iso}}}}{1 - e^{-R \tau_0^{\text{iso}}}} \right]. \quad (\text{D.39})$$

If we do not have observations of two or more isotopologues we may assume some value for τ_0 (e.g., 0.1–0.3, if we are not sure if the transition is optically thin, $\tau < 1$; or optically thick, $\tau > 1$).

Hyperfine transitions

In the case of hyperfine transitions, the CLASS fit provides us with $A \times \tau_m$, v_{LSR} , Δv , and τ_m , where τ_m is the opacity of the main line (it corresponds to the opacity at the center of the line of one of the hyperfine lines), and A is

$$A = f (J_\nu(T_{\text{ex}}) - J_\nu(T_{\text{bg}})), \quad (\text{D.40})$$

where f is the filling factor. Thus, for hyperfine transitions, and taking into account Equations D.31 and D.33, we can write

$$T_{\text{MB}} = \frac{A \times \tau_m}{\tau_m} (1 - e^{-\tau_m}). \quad (\text{D.41})$$

As in the case of single transitions, we need to calculate the excitation temperature to estimate the column density. Substituting Equation D.41 into Equation D.37 (with $T_{\text{MB}} = f T_L$), and taking into account that, for the main line, $\tau_0 = \tau_m$, we can write

$$T_{\text{ex}} = \frac{h\nu/k}{\ln \left[\frac{h\nu/k}{(A \times \tau_m / (\tau_m f)) + J_\nu(T_{\text{bg}})} + 1 \right]}. \quad (\text{D.42})$$

D.1.5 Molecular (catalogued) terms

In previous sections we have explained how to obtain the observational terms. However there are some terms in Equations D.23 and D.27 which are specific (different) for each molecule. You can find definitions and expressions for all these terms in Townes and Schawlow (1975) and Gordy and Cook (1984). In this document we will present theoretical expressions and how to obtain the values for each molecule using two molecular databases: the Cologne Database for Molecular Spectroscopy (CDMS²) and the Jet Propulsion Laboratory Molecular Spectroscopy (JPL³).

²<http://www.astro.uni-koeln.de/cdms/>

³<http://spec.jpl.nasa.gov/>

Einstein coefficient A_{ul}

The Einstein spontaneous emission coefficient has the form

$$A_{ul} = \frac{64\pi^4 \nu_{ul}^3}{3hc^3} |\mu_{ul}|^2, \quad (\text{D.43})$$

where $|\mu_{ul}|^2$ is the dipole moment of the transition, and is defined as $\mathcal{S}\mu^2/g_u$, where \mathcal{S} is the line strength, μ is the molecular dipole moment, and g_u is the degeneracy of the upper level. In some texts you can find $|\mu_{ul}|^2 = \mathcal{S}\mu^2$. In our case we will use the expression given in the CDMS and JPL databases, and thus, the Einstein coefficient is calculated as

$$A_{ul} = \frac{64\pi^4 \nu_{ul}^3}{3hc^3} \frac{\mathcal{S}\mu^2}{g_u}, \quad (\text{D.44})$$

where the degeneracy of the upper level, g_u , is given in databases (see Section D.1.5), and the line strength times squared dipole moment, $\mathcal{S}\mu^2$, can be calculated as

$$\mathcal{S}\mu^2 = \frac{3hc}{8\pi^3} \frac{I(T)}{\nu_{ul}} \frac{Q(T)}{e^{-E_l/kT} - e^{-E_u/kT}}, \quad (\text{D.45})$$

or in practical units

$$\left[\frac{\mathcal{S}\mu^2}{\text{erg cm statC}^{-2} \text{ Debye}^{-2}} \right] = \quad (\text{D.46})$$

$$2.4025 \times 10^4 \left[\frac{10^{\log(I^{300})}}{\text{nm}^2 \text{ MHz}} \right] Q^{300} \left[\frac{\nu_{ul}}{\text{MHz}} \right]^{-1} \frac{\exp(4.796 \times 10^{-3} [E_l/\text{cm}^{-1}])}{1 - \exp(-1.6 \times 10^{-7} [\nu_{ul}/\text{MHz}])},$$

with ν_{ul} the frequency of the transition in MHz, E_l the lower state energy in cm^{-1} , Q^{300} the partition function at 300 K (see Section D.1.5), and $\log(I^{300})$ the base 10 logarithm of the integrated intensity at 300 K (obtained from databases, see Section D.1.5).

Partition function Q

The total partition function Q , which is needed to estimate the total column density from the column density of a single molecular transition $u \rightarrow l$, can be expressed in terms of their translational and internal components

$$Q(T) = Q_{\text{tr}}(T) Q_{\text{int}}(T). \quad (\text{D.47})$$

As is explained in Appendix A of Araya et al. (2005), the translational partition function, Q_{tr} , is not needed to estimate the total column density. Thus, we only need to calculate the internal partition function Q_{int} (hereafter, Q to simplify notation).

In general, the coupling between vibration, rotation and electronic modes can be neglected, and thus the internal partition function can be factorized as

$$Q_{\text{int}}(T) = Q_{\text{elec}}(T) Q_{\text{vibr}}(T) Q_{\text{rot}}(T), \quad (\text{D.48})$$

D. Molecular Column Density Calculation

where $Q_{\text{elec}} = 1$ for molecules in ground electronic singlet Σ states (most stable organic molecules at ordinary temperatures fulfill this condition under astrophysical conditions). The vibrational partition function Q_{vib} under the harmonic-oscillator approximation (e.g., Herzberg 1991; Araya et al. 2005) can be expressed as

$$Q_{\text{vibr}}(T) = \prod_i \left(1 - e^{-\nu_i hc/kT}\right)^{-d_i}, \quad (\text{D.49})$$

where the product is done for all vibrational modes of frequency ν_i (expressed, as is customary, in cm^{-1}) and degeneracy d_i . Finally, the rotational partition function Q_{rot} can be expressed as

$$Q_{\text{rot}}(T) = \sum_i \left(g_i e^{-E_i/kT}\right), \quad (\text{D.50})$$

where the sum is done for all rotational transitions of energy E_i and degeneracy g_i .

By assuming that the vibrational modes are negligible (i.e., $Q_{\text{vibr}} \simeq 1$) we can write $Q \simeq Q_{\text{rot}}$, and by approximating the sum by an integral we can write simplified expressions for the partitions function for different kind of molecules. For linear molecules (e.g., CO, CS, OCS, N_2H^+) the partition function is approximated by

$$Q \simeq Q_{\text{rot}} = \frac{kT}{hB_0} + \frac{1}{3} + \frac{1}{15} \frac{hB_0}{kT} + \dots \simeq \frac{kT}{hB_0}, \quad (\text{D.51})$$

and for symmetric-top (e.g., CH_3CN , NH_3) and asymmetric-top (e.g., HNCO , H_2CO , NH_2D) molecules the partition function is approximated by

$$Q \simeq Q_{\text{rot}} \simeq \left[\frac{\pi k^3 T^3}{h^3 A_0 B_0 C_0} \right]^{1/2}, \quad (\text{D.52})$$

where A_0 , B_0 and C_0 are the rotational molecular constants, that can be found in the databases or in some books (e.g., Townes and Schawlow 1975; Gordy and Cook 1984). For linear molecules $A_0 = C_0 = 0$, for symmetric-top molecules $A_0 = C_0 \neq 0$, and for asymmetric-top molecules $A_0 \geq B_0 \geq C_0$ (a prolate symmetric top corresponds to $B_0 = C_0$, and an oblate symmetric top to $B_0 = A_0$).

In some cases the vibrational partition function is not negligible (as reported by Araya et al. 2005, in the case of the CH_3CN). In order to avoid tedious calculations of the partition function for each molecule, we can use some estimations of the partition function (including rotational and vibrational terms) available in the CDMS and JPL databases (see Section D.3). In these two databases we can find a document file for each molecule with the value of the partition function at different temperatures (usually from 7 up to 300 K). The method we use in the program `ColDens.f` (see Section D.4) consists in using the partition function values provided by the databases. First of all, we have to calculate the excitation temperature of our transition (Equations D.37 or D.42). From the databases we can obtain the value of the molecular partition function for different temperatures, thus we can obtain a list of pair of values (Q , T). These pair of values can be fitted, in a first

order approximation, by the Equations D.51 or D.52. Thus, if we want to obtain the value of the partition function at our excitation temperature T_{ex} , we should interpolate (fit) the pair of values (Q, T) , and evaluate the partition function at our estimated excitation temperature.

Upper state degeneracy g_u

The upper state degeneracy g_u depends on each molecule and transition. You can find detailed descriptions on this in Townes and Schawlow (1975) and Gordy and Cook (1984). A molecular level is generally described by a set of quantum and pseudo-quantum numbers. For linear molecules we only have to take into account the rotational quantum number J , while for symmetric and asymmetric top molecules we have to take into account J , and other pseudo-quantum numbers such as K , K_a , K_c , and for hyperfine structure we have to include F_1 , F (see Townes and Schawlow 1975; Gordy and Cook 1984). Here we will describe⁴ how to estimate g_u in some cases (useful for most molecules of astrophysical interest). The upper state degeneracy can be factorized as

$$g_u = g_{J_u} g_K g_{\text{nuclear}}, \quad (\text{D.53})$$

where g_{J_u} is the rotational degeneracy of the upper level given by

$$g_{J_u} = 2 J_u + 1, \quad (\text{D.54})$$

g_K is the degeneracy associated with the internal quantum number K in symmetric and asymmetric top molecules, given by

$$g_K = \begin{cases} 1 & \text{for } K = 0, \text{ and for all linear and asymmetric top molecules} \\ 2 & \text{for } K \neq 0 \text{ in symmetric top molecules only} \end{cases} \quad (\text{D.55})$$

and g_{nuclear} is the nuclear spin degeneracy which takes account of the statistical weights associated with identical nuclei in a nonlinear molecule with symmetry (which most nonlinear molecules have). When there is no symmetry and no nuclear hyperfine splitting, each molecular rotational level will have a degeneracy

$$g_{\text{nuclear}} = \prod_i (2I_i + 1), \quad (\text{D.56})$$

where I_i is the spin of the i^{th} nucleus and where the product is taken over all nuclei of the molecule. Symmetry and hyperfine splitting changes g_{nuclear} for all practical cases. You can find a complete description on the calculation of spin degeneracies in Chapter 3 of ?. In Table D.1 of this document we list the values of the nuclear degeneracies for some molecules with symmetry: C_{2v} and C_{3v} molecules⁵.

⁴From the document elaborate by Jeff Mangnum (NRAO) and Yancy Shirley (University of Arizona), that can be found in <https://safe.nrao.edu/wiki/pub/Main/MolInfo/column-density-calculation.pdf>

⁵ C_{2v} and C_{3v} symmetries refer to those molecules with two or three identical nuclei. The number of symmetry states for a molecule are determined by the number of configurations within which the

D. Molecular Column Density Calculation

Table D.1: Nuclear statistical weight factors for C_{2v} and C_{3v} molecules^a

Identical nuclei	Spin	J_u	K	g_{nuclear}
2	$\frac{1}{2}, \frac{3}{2}, \dots$	any	even	$(2I_i + 1)I_i$
2	$\frac{1}{2}, \frac{3}{2}, \dots$	any	odd	$(2I_i + 1)(I_i + 1)$
2	0, 1, 2, ...	any	odd	$(2I_i + 1)(I_i + 1)$
2	0, 1, 2, ...	any	even	$(2I_i + 1)I_i$
3	any	even	$= \dot{3}$	$\frac{1}{3}(2I_i + 1)(4I_i^2 + 4I_i + 3)$
3	any	even or odd	$\neq \dot{3}$	$\frac{1}{3}(2I_i + 1)(4I_i^2 + 4I_i)$

^a From Gordy and Cook (1984), Table 3.2 and 3.3.

As can be seen from Townes and Schawlow (1975) and Gordy and Cook (1984), the calculation of the degeneracies for some kind of molecules can be a tedious work. Thus we can take profit of the already created databases CDMS and JPL. Both databases have different tables for each molecule. These tables contain several lines, and each line is referred to an specific transition, which reads as follows

```
1872169.0570 0.2000 -1.3865 3 887.6325 165 -32503 30327 325 26 324
1872505.7621 0.2374 -2.3388 3 1107.9703 55 32503 30327 622 26 621
```

with the frequency of the line (in MHz), and its uncertainty (in MHz); the base 10 logarithm of the integrated intensity at 300 K (in $\text{nm}^2 \text{ MHz}$); the degree of freedom in the rotational partition function (0 for atoms, 2 for linear molecules, and 3 for non-linear molecules); the lower state energy (in cm^{-1}); the upper state degeneracy g_u ; a molecular tag (where a negative value indicates that both line frequency and uncertainty are experimental values); coding⁶ of the quantum numbers; and finally the quantum numbers.

At this point, it is important to note that in some databases common factors have been factorized in order to keep Q and g_u small. Therefore, it is strongly advisable to compare Q/g_u rather than Q from various databases. Thus, if we are using the partition function of CDMS/JPL database we have to use the degeneracy given in CDMS/JPL. In the program `ColDens.f` (see Section D.4) we use the degeneracies given by the databases. Non-trivial spin-statistical weight ratios are given explicitly in the documentation of a given molecule (also available in the databases, see Section D.3). When estimating column densities of molecules with hyperfine splitting (for example) it is important to read carefully the documentation provided for these given species, since we may have to multiply the column density obtained from the program `ColDens.f` by a certain factor.

wavefunction of the molecule is unchanged with a rotation of π about a symmetry axis and a reflection of π through the symmetry plane.

⁶You can find a description of the coding in <http://www.astro.uni-koeln.de/node/477#qnfmt>

Upper state energy E_u

The upper state energy E_u can be obtained from $E_u = E_l + h\nu_{ul}$, or in a usable form

$$E_u = \frac{hc}{k} E_l + \frac{h}{k} \nu_{ul}, \quad (\text{D.57})$$

$$\left[\frac{E_u}{K} \right] = 1.4338 \left[\frac{E_l}{\text{cm}^{-1}} \right] + 4.799 \times 10^{-5} \left[\frac{\nu_{ul}}{\text{MHz}} \right], \quad (\text{D.58})$$

where the energy of the lower level, E_l , can be found in the database (see section D.1.5). Note that with this expression, E_u is in units of temperature, thus, in all those equations (e. g., Equations D.23 and D.27) where we have to calculate E_u/kT we can use the simplified expression E_u/T where energy and temperature are given in units of temperature (K).

D.1.6 Summary of equations: step-by-step guide

In this section we want to write only those equations you really need to estimate the molecular column density. Details on how to obtain all these equations are explained in previous sections. The idea of this section is to provide the user with a step-by-step guide to explain the main steps you should follow to obtain N_u and N_{mol} from the initial observational parameters.

A. Observational terms (Section D.1.4)

The first step is to obtain observational information. From your observations you will obtain some observational terms, different if you are observing a single transition or a transition with hyperfine structure. **Single transitions** fitted with CLASS provide you main beam temperature T_{MB} and linewidth Δv . You must assume an opacity τ_0 . **Hyperfine transitions** fitted with CLASS provide you $A \times \tau_m$, the linewidth Δv , and the opacity of the main line τ_m . The **filling factor** f can be assumed to be ~ 1 for interferometric observations, and can be estimated for single-dish observations as

$$f = \frac{\theta_{\text{source}}^2}{(\theta_{\text{source}}^2 + \theta_{\text{beam}}^2)},$$

where θ_{source} is the angular diameter of the source size, and θ_{beam} is the angular diameter of the beam.

B. Excitation temperature (Section D.1.2)

The **excitation temperature** T_{ex} is directly obtained from the observational terms following two different expressions. For single transitions we can use

$$T_{\text{ex}} = \frac{h\nu/k}{\ln \left[\frac{h\nu/k}{(T_{\text{MB}}/f)/(1-\exp(-\tau_0)) + J_\nu(T_{\text{bg}})} + 1 \right]},$$

D. Molecular Column Density Calculation

and for transitions with hyperfine structure we can use

$$T_{\text{ex}} = \frac{h\nu/k}{\ln \left[\frac{h\nu/k}{(A \times \tau_{\text{m}}/\tau_{\text{mf}}) + J_{\nu}(T_{\text{bg}})} + 1 \right]},$$

where h is the Planck constant, k is the Boltzmann constant, ν is the frequency of the transition (ν_{ul}), T_{bg} is the background temperature assumed to be 2.74 K, and J_{ν} is the energy in units of temperature and reads

$$J_{\nu}(T) = \frac{h\nu/k}{e^{h\nu/kT} - 1}.$$

C. Catalogued terms (Section D.1.5)

From molecular databases (CDMS and JPL) we can obtain estimations for other terms involved in the calculation of the molecular column density. The **Einstein spontaneous emission coefficient** A_{ul} is obtained by

$$A_{ul} = \frac{64\pi^4 \nu_{ul}^3}{3hc^3} \frac{\mathcal{S}\mu^2}{g_u},$$

where g_u is the **upper state degeneracy** given directly in the databases, and $\mathcal{S}\mu^2$ is the **line strength** estimated as

$$\left[\frac{\mathcal{S}\mu^2}{\text{erg cm statC}^{-2} \text{ Debye}^{-2}} \right] = 2.4025 \times 10^4 \left[\frac{10^{\log(I^{300})}}{\text{nm}^2 \text{ MHz}} \right] Q^{300} \left[\frac{\nu_{ul}}{\text{MHz}} \right]^{-1} \frac{\exp(4.796 \times 10^{-3} [E_l/\text{cm}^{-1}])}{1 - \exp(-1.6 \times 10^{-7} [\nu_{ul}/\text{MHz}])},$$

where the partition function at 300 K, Q^{300} , and the base 10 logarithm of the intensity at 300 K, $\log(I^{300})$, are given in the databases, and the **upper state energy** E_u is calculated as

$$\left[\frac{E_u}{K} \right] = 1.4338 \left[\frac{E_l}{\text{cm}^{-1}} \right] + 4.799 \times 10^{-5} \left[\frac{\nu_{ul}}{\text{MHz}} \right],$$

where the energy of the lower level E_l is given in the databases.

D. Molecular column density (Section D.1.3)

Finally, we can estimate the **column density of the transition**, N_u , as

$$N_u = \frac{8\pi \nu_{ul}^3}{c^3} \frac{\tau_0 \Delta\nu}{A_{ul} (e^{h\nu_{ul}/kT_{\text{ex}}} - 1)},$$

and the **total molecular column density**, N_{mol} , as

$$N_{\text{mol}} = N_u \frac{Q}{g_u} e^{E_u/kT_{\text{ex}}},$$

where Q is the partition function given in the databases.

D.2 Rotational diagrams

To be written, but you can check Goldsmith and Langer (1999) for a detailed description. (Here we can describe the “new” method).

D.3 Resources from databases (CDMS and JPL)

As indicated in previous sections, we can use the resources of some molecular spectroscopy databases to estimate the column density of several molecules without calculating the partition function, degeneracies and so on, independently for each molecule. Two examples of databases are the Cologne Database for Molecular Spectroscopy (CDMS⁷) and the Jet Propulsion Laboratory Molecular Spectroscopy (JPL⁸). In Figure D.2 we show a screenshot of the home webpages for both databases.

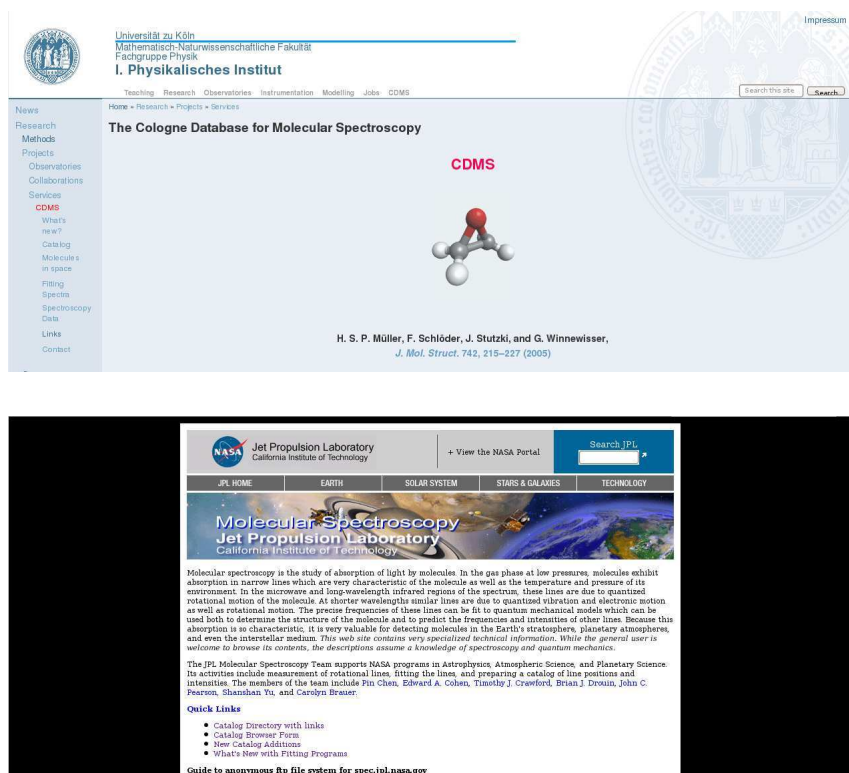


Figure D.2: Database webpages. **Top:** Screenshot of the CDMS database home page. **Bottom:** Screenshot of the JPL database home page.

⁷CDMS can be found in <http://www.astro.uni-koeln.de/cdms/>

⁸JPL can be found in <http://spec.jpl.nasa.gov/>

D. Molecular Column Density Calculation

D.3.1 The Cologne Database for Molecular Spectroscopy, CDMS

CDMS is a molecular spectroscopy database developed by the Universitat zu Koln. You can find a detailed description of the project in the webpage or in Müller et al. (2001, 2005). You can gain access to the catalog by clicking in *Catalog* and then *Entries*, on the left menu bar of the home webpage. You will find a webpage with a list of molecules and different links/documents for each molecule. You must select those files named **HTML** and **eXXXXXX.cat**, where **XXXXXX** is the tag number of the molecule. The **HTML** file is an ascii table (Fig. D.3 bottom) with the information specified at the end of section D.1.5, i.e., frequency, intensity, upper state degeneracy, lower state energy, quantum numbers of the molecular transitions for the chosen molecule. The **eXXXXXX.cat** file (Fig. D.3 top) contains the information of the molecule that you need to estimate column densities, e.g., names of the molecule, dipole moment, the rotational molecular constants, the partition function at different temperatures.

CH₃CN, $v=0$

Methyl cyanide, acetonitrile, cyanomethane, $v=0$

Species tag	041505	Lines Listed	1728
Version	1*	Frequency / GHz	<1864
Date of Entry	Dec. 2009	Max. J	99
Contributor	H. S. P. Müller	log STR0	-7.0
		log STR1	-8.5
		Isotope Corr.	0.0
		Egy / cm ⁻¹	0.0
		μ_a / D	3.9220
		μ_b / D	
		μ_c / D	
		A / MHz	158099.0
		B / MHz	9198.8991
		C / MHz	= B
		Q(500.0)	48625.8971 (21788.9238)
		Q(300.0)	14683.6324 (10118.2635)

This entry is a combined CDMS and JPL entry.
The latest combined fit has been reported by
(1) H. S. P. Müller, B. J. Drouin, and J. G. Pearson, 2009, *Astron. Astrophys.* **506**, 1487.
This work provides new data in the 1.58 – 1.63 THz region. Additional, extensive data between 91 and 1192 GHz were published in
(2) G. Cazzoli and G. Pizzanelli, 2006, *J. Mol. Spectrosc.* **240**, 153.
As in that work, additional data were taken from
(3) S. G. Kukolich, D. J. Ruben, J. H. S. Wang, and J. R. Williams, 1973, *J. Chem. Phys.* **58**, 3155;
from
(4) S. G. Kukolich, 1982, *J. Chem. Phys.* **76**, 97;
and from
(5) D. Boucher, J. Burie, J. Demaison, A. Dubulle, J. Legrand, and B. Segard, 1977, *J. Mol. Spectrosc.* **64**, 390.
The purely K-dependent terms were determined through $\Delta K = 3$ infrared loops from
(6) R. Anttila, V.-M. Hönemann, M. Koivusaari, and R. Paso, 1993, *J. Mol. Spectrosc.* **157**, 198.
The predictions should be reliable throughout with the exception of K = 14 transitions between about J = 36 and 48 which are perturbed by a weak resonant interaction with $v_a = 1$.
*N hyperfine splitting may be resolvable at low values of J and possibly at the highest K. Therefore,

(For units and further details on the catalog entries see the [General](#) section.)

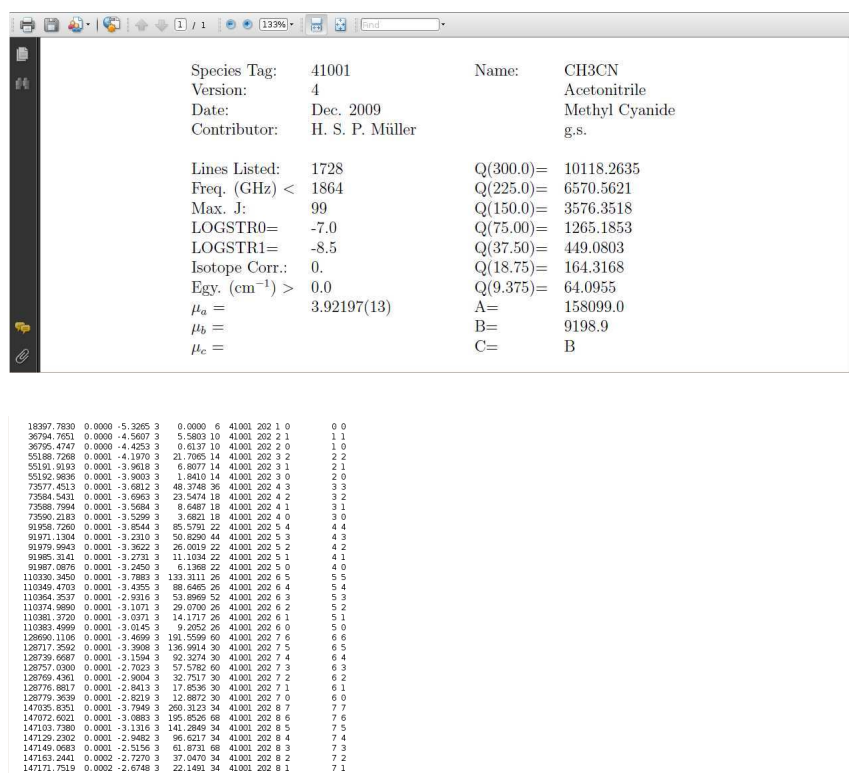
frequency|uncert.|intens.|E.lower||tag||quantum nos: up:low|molecule

18397.7830	0.0000	-5.3265	3	0.0000	6	41505 202 1 0	0 0	CH ₃ CN, $v=0$
36794.7651	0.0000	-4.5607	3	5.5803	10	41505 202 2 1	1 1	CH ₃ CN, $v=0$
36795.4747	0.0000	-4.4253	3	0.6137	10	41505 202 2 0	1 0	CH ₃ CN, $v=0$
55186.7268	0.0001	-4.1970	3	21.7065	14	41505 202 3 2	2 2	CH ₃ CN, $v=0$
55191.9193	0.0001	-3.9618	3	6.8077	14	41505 202 3 1	2 1	CH ₃ CN, $v=0$
55192.9836	0.0001	-3.9003	3	1.8410	14	41505 202 3 0	2 0	CH ₃ CN, $v=0$
72577.4513	0.0001	-3.6612	3	48.3748	26	41505 202 4 3	3 3	CH ₃ CN, $v=0$
72584.5431	0.0001	-3.6963	3	23.5474	18	41505 202 4 2	3 2	CH ₃ CN, $v=0$
72588.7994	0.0001	-3.5684	3	8.6487	18	41505 202 4 1	3 1	CH ₃ CN, $v=0$
72590.2183	0.0001	-3.5269	3	3.6621	18	41505 202 4 0	3 0	CH ₃ CN, $v=0$
91958.7260	0.0001	-3.8544	3	85.5791	22	41505 202 5 4	4 4	CH ₃ CN, $v=0$
91971.1304	0.0001	-3.2310	3	50.8290	44	41505 202 5 3	4 3	CH ₃ CN, $v=0$
91976.8943	0.0001	-3.3622	3	26.0019	22	41505 202 5 2	4 2	CH ₃ CN, $v=0$
91985.3141	0.0001	-3.2731	3	11.1034	22	41505 202 5 1	4 1	CH ₃ CN, $v=0$
91987.0876	0.0001	-3.2450	3	6.1368	22	41505 202 5 0	4 0	CH ₃ CN, $v=0$
110330.3450	0.0001	-3.7883	3	133.3111	26	41505 202 6 5	5 5	CH ₃ CN, $v=0$
110340.4703	0.0001	-3.4355	3	88.6465	26	41505 202 6 4	5 4	CH ₃ CN, $v=0$
110364.3537	0.0001	-2.9316	3	53.8969	52	41505 202 6 3	5 3	CH ₃ CN, $v=0$
110374.9890	0.0001	-3.1071	3	29.0700	26	41505 202 6 2	5 2	CH ₃ CN, $v=0$
110381.3720	0.0001	-3.0371	3	14.1717	26	41505 202 6 1	5 1	CH ₃ CN, $v=0$
110383.4069	0.0001	-3.0143	3	9.2652	26	41505 202 6 0	5 0	CH ₃ CN, $v=0$
128660.1106	0.0001	-3.4699	3	191.5599	60	41505 202 7 6	6 6	CH ₃ CN, $v=0$
128717.3592	0.0001	-3.3908	3	136.9014	30	41505 202 7 5	6 5	CH ₃ CN, $v=0$
128726.6687	0.0001	-3.1594	3	62.3274	30	41505 202 7 4	6 4	CH ₃ CN, $v=0$
128757.0300	0.0001	-2.7023	3	57.5782	60	41505 202 7 3	6 3	CH ₃ CN, $v=0$
128769.4361	0.0001	-2.9004	3	32.7517	30	41505 202 7 2	6 2	CH ₃ CN, $v=0$
128776.8817	0.0001	-2.8413	3	17.8536	30	41505 202 7 1	6 1	CH ₃ CN, $v=0$
128779.3639	0.0001	-2.8219	3	12.8872	30	41505 202 7 0	6 0	CH ₃ CN, $v=0$
147035.6351	0.0001	-3.7949	3	260.3123	84	41505 202 8 7	7 7	CH ₃ CN, $v=0$
147032.6021	0.0001	-3.0881	3	195.8526	68	41505 202 8 6	7 6	CH ₃ CN, $v=0$

Figure D.3: CDMS: **Top**: Screenshot of the eXXXXXX.cat file for CH₃CN. **Bottom**: Screenshot of the HTML file for CH₃CN.

D.3.2 Jet Propulsion Laboratory, Molecular Spectroscopy, JPL

JPL Molecular Spectroscopy is a facility developed by the Jet Propulsion Laboratory of the California Institute of Technology. Documentation explaining more details of the database can be found in the webpage and in Pickett (1991) and Pickett et al. (1998). You can gain access to the catalog by clicking in *Catalog Directory with links*. You will find a webpage with a list of molecules and different links/documents for each molecule. You must select those files named `cXXXXXX.cat` and `pdf`, where `XXXXXX` is the tag number of the molecule. The `cXXXXXX.cat` file is an ascii table (Fig. D.4 bottom) with the information specified at the end of section D.1.5, i. e., frequency, intensity, upper state degeneracy, lower state energy, quantum numbers of the molecular transitions for the chosen molecule. The `pdf` file (Fig. D.4 top) contains the information of the molecule that you need to estimate column densities, e. g., names of the molecule, dipole moment, the rotational molecular constants, the partition function at different temperatures.



The figure consists of two screenshots from the JPL Molecular Spectroscopy database. The top screenshot shows the 'pdf' file for CH₃CN, displaying molecular parameters and transition data. The bottom screenshot shows the 'cXXXXXX.cat' file for CH₃CN, displaying a table of transition data.

Species Tag:	41001	Name:	CH ₃ CN
Version:	4		Acetonitrile
Date:	Dec. 2009		Methyl Cyanide
Contributor:	H. S. P. Müller		g.s.
Lines Listed:	1728	Q(300.0)=	10118.2635
Freq. (GHz) <	1864	Q(225.0)=	6570.5621
Max. J:	99	Q(150.0)=	3576.3518
LOGSTR0=	-7.0	Q(75.00)=	1265.1853
LOGSTR1=	-8.5	Q(37.50)=	449.0803
Isotope Corr.:	0.	Q(18.75)=	164.3168
Egy. (cm ⁻¹) >	0.0	Q(9.375)=	64.0955
μ_a =	3.92197(13)	A=	158099.0
μ_b =		B=	9198.9
μ_c =		C=	B

18397.7830	0.0000	-5.3205	3	0.0000	6	41001	202	1	0	0	0
36794.7651	0.0000	-4.5607	3	5.5803	10	41001	202	2	1	1	1
36795.4747	0.0000	-4.4253	3	0.6137	10	41001	202	2	0	1	0
55188.7288	0.0001	-4.1970	3	21.7065	14	41001	202	3	2	2	2
55191.9193	0.0001	-3.9618	3	6.8077	14	41001	202	3	1	2	1
55192.9836	0.0001	-3.9003	3	1.8410	14	41001	202	3	0	2	0
73577.4513	0.0001	-3.6812	3	48.3748	36	41001	202	4	3	3	3
73584.5431	0.0001	-3.6963	3	23.5474	18	41001	202	4	2	3	2
73588.7994	0.0001	-3.5684	3	8.6487	18	41001	202	4	1	3	1
73590.2183	0.0001	-3.5299	3	3.6521	18	41001	202	4	0	3	0
91958.7280	0.0001	-3.8544	3	65.5793	22	41001	202	5	4	4	4
91971.1304	0.0001	-3.2310	3	50.8290	44	41001	202	5	3	4	3
91979.9943	0.0001	-3.3622	3	26.0019	22	41001	202	5	2	4	2
91985.3041	0.0001	-3.2731	3	11.1034	22	41001	202	5	1	4	1
91987.0876	0.0001	-3.2450	3	6.1388	22	41001	202	5	0	4	0
110330.3450	0.0001	-3.7883	3	133.3111	26	41001	202	6	5	5	5
110349.4703	0.0001	-3.4355	3	88.6465	26	41001	202	6	4	5	4
110394.5537	0.0001	-2.9316	3	53.8969	52	41001	202	6	3	5	3
110374.8880	0.0001	-3.1071	3	29.0700	26	41001	202	6	2	5	2
110381.3720	0.0001	-3.0371	3	14.1717	26	41001	202	6	1	5	1
110383.4999	0.0001	-3.0145	3	9.2552	26	41001	202	6	0	5	0
128690.1106	0.0001	-3.4699	3	191.5599	60	41001	202	7	6	6	6
128717.5562	0.0001	-3.3908	3	136.9614	30	41001	202	7	5	6	5
128739.6687	0.0001	-3.1504	3	62.5274	30	41001	202	7	4	6	4
128757.0300	0.0001	-2.7023	3	57.5782	60	41001	202	7	3	6	3
128769.4361	0.0001	-2.9004	3	22.7517	30	41001	202	7	2	6	2
128776.8817	0.0001	-2.8413	3	17.6536	30	41001	202	7	1	6	1
128779.3639	0.0001	-2.8219	3	12.8872	30	41001	202	7	0	6	0
147035.8351	0.0001	-3.7949	3	260.3123	34	41001	202	8	7	7	7
147072.6021	0.0001	-3.0883	3	195.8526	68	41001	202	8	6	7	6
147103.7380	0.0001	-3.1316	3	141.2849	34	41001	202	8	5	7	5
147129.2302	0.0001	-2.9462	3	96.6217	34	41001	202	8	4	7	4
147149.0683	0.0001	-2.5156	3	61.8731	68	41001	202	8	3	7	3
147163.2441	0.0002	-2.7270	3	37.0470	34	41001	202	8	2	7	2
147171.7519	0.0002	-2.6748	3	22.1491	34	41001	202	8	1	7	1

Figure D.4: JPL: **Top:** Screenshot of the pdf file for CH₃CN. **Bottom:** Screenshot of the cXXXXXX.cat file for CH₃CN.

D.4 Program ColDens.f

Álvaro Sánchez-Monge⁹ developed a FORTRAN 77 program to estimate column densities and make rotational diagrams: `ColDens.f`¹⁰. The program can be used to calculate column densities of almost all kind of molecules., you only need to write the information of the specific molecule (if it does not exist yet) in a `MMMM.mol` file, where `MMMM` is the name of the molecule, saved in a directory `libmol`. In this file you must introduce the information, in a specific format (described in a `README` file that comes together with the code), of the molecule (e. g., rotational molecular constants, partition function at different temperatures, if the molecule is linear, symmetric-top or asymmetric-top) and at the end of the file you have to introduce the molecular transitions you want to study. All the information required to create the `MMMM.mol` file can be found in the CDMS and JPL databases (as explained in Section D.3).

You can also create an input file `SSSS.rd`, to create a rotational diagram from this file. This file, that is saved in the directory `rotdia`, contains observational information indicating the molecule, the frequency of the transition, the main beam temperature of the line, the linewidth, the integrated area, the optical depth, the source size, and the beam size. The format of the `SSSS.rd` file is also explained in the `README` file.

When executing the program you will find a menu with different options

```
*****
**** Main Menu ****
0.- Exit program
1.- Choose molecule lib file (.mol)      molecule
2.- Choose molecular transition
    Frequency (MHz)                      220743.0106
3.- Observational parameters
4.- Print results on terminal
5.- Rotational diagram (CH3CN et al.)
```

You should be able to follow the instructions given in the different menus, in order to properly estimate the column density. Any comment, question, doubt, suggestion or whatever can be sent to: asanchez@am.ub.es.

⁹You can contact him (me) in asanchez@am.ub.es

¹⁰A version of this program can be found in <http://www.am.ub.es/~asanchez/utilities/ColDens>

D.5 Astrophysical constants and conversion factors[†]

Constant	Symbol	Number
<i>Mathematical constants</i>		
Number pi	π	3.141 592 653 6
Euler's constant	e	2.718 281 828 5
<i>Physical constants</i>		
Speed of light	c	$2.997\,924\,58 \times 10^{10}$ cm s ⁻¹
Planck constant	h	$6.626\,075\,5 \times 10^{-27}$ erg s
		$6.626\,075\,5 \times 10^{-34}$ J s
		$4.135\,671\,5 \times 10^{-15}$ eV s
Boltzmann constant	k	$1.380\,658 \times 10^{-16}$ erg K ⁻¹
		$1.380\,658 \times 10^{-23}$ J K ⁻¹
		$8.617\,385 \times 10^{-5}$ eV K ⁻¹
Gravitation constant	G	$6.672\,59 \times 10^{-8}$ dyn cm ² g ⁻²
		$6.672\,59 \times 10^{-11}$ m ³ kg ⁻¹ s ⁻²
<i>Units of distance</i>		
Astronomical unit	AU	$1.495\,978\,706\,6 \times 10^{13}$ cm
Parsec	pc	$3.085\,677\,6 \times 10^{18}$ cm
		3.261 563 8 light (Julian) year
		206 264.806 AU
Light (Julian) year	-	$9.460\,730\,472 \times 10^{17}$ cm
Solar radius	R_{\odot}	$6.955\,08 \times 10^{10}$ cm
<i>Units of mass</i>		
Solar mass	M_{\odot}	$1.989\,1 \times 10^{33}$ g
Mass of electron	m_e	$5.485\,799\,03 \times 10^{-28}$ g
Mass of proton	m_p	$1.672\,623\,1 \times 10^{-24}$ g
Mass of neutron	m_n	$1.674\,928\,6 \times 10^{-24}$ g
Mass of ¹ H atom	m_H	$1.673\,534\,4 \times 10^{-24}$ g
<i>Units of time</i>		
Julian year	-	3.155 76 SI seconds
		525 960 minutes
		8766 hours
		365.25 days
<i>Units of energy, electric charge and flux density</i>		
Solar luminosity	L_{\odot}	3.845×10^{33} erg s ⁻¹
Elementary charge	e	$4.803\,206\,8 \times 10^{-19}$ C
		$1.602\,177\,33 \times 10^{-20}$ esu
Joule	J	10 ⁷ erg
Electron Volt	eV	$1.602\,176\,46 \times 10^{-19}$ J
		$1.602\,176\,46 \times 10^{-12}$ erg
Jansky	Jy	10^{-23} erg s ⁻¹ cm ⁻² Hz ⁻¹
		10^{-26} W m ⁻² Hz ⁻¹
Debye	D	10 ⁻¹⁸ statC cm

[†] From Cox (1999)